Bioresource Processing Research Institute of Australia (BioPRIA)
Food and Dairy GRIP
Department of Chemical and Biological Engineering
Faculty of Engineering
Monash University

ENGINEERING SUSTAINABLE NANOCELLULOSE SUPERABSORBENTS: CHARACTERIZATION AND APPLICATION

by

Laila Hossain
B. Eng. & M. Eng. (Chemical)

A thesis submitted for the degree of Doctor of Philosophy
at Monash University in 2021, Chemical and Biological Engineering

October 2021

THIS PAGE HAS BEEN INTENTIONALLY LEFT BLANK

“There is nothing like a dream to create the future”

Victor Hugo

THIS PAGE HAS BEEN INTENTIONALLY LEFT BLANK

Copyright notice

Laila Hossain

General Declaration

This thesis is an original work of my research and contains no material which has been accepted for the award of any other degree or diploma at any university or equivalent institution and that, to the best of my knowledge and belief, this thesis contains no material previously published or written by another person, except where due reference is made in the text of the thesis.

Signature: ……

Print Name: Laila Hossain

Date: 7th October, 2021

Table of Contents

Monash University

Thesis including published works declaration

I hereby declare that this thesis contains no material which has been accepted for the award of any other degree or diploma at any university or equivalent institution and that, to the best of my knowledge and belief, this thesis contains no material previously published or written by another person, except where due reference is made in the text of the thesis.

This thesis includes three original papers published in peer reviewed journals (Chapter 2, Chapter 3 and Chapter 4), and three manuscripts under preparation (Chapter 1, Chapter 5 and Chapter 6). The core theme of the thesis is Engineering sustainable nanocellulose superabsorbents, characterization and applications. The ideas, development and writing up of all the papers in the thesis were the principal responsibility of myself, the student, working within the Department of Chemical and Biological Engineering, Monash University, under the supervision of Professor Gil Garnier, and Dr. Joanne Tanner.

(The inclusion of co-authors reflects the fact that the work came from active collaboration between researchers and acknowledges input into team-based research.)

In the case of three published chapters my contribution to the work involved the following:

Thesis Chapter	Publication Title	Status *(published, in press, accepted or returned for revision, submitted)*	Nature and % of student contribution	Co-author name(s) Nature and % of Co-author's contribution*	Co-author(s), Monash student Y/N*
2	*Modulating nanocellulose hydrogels and cryogels strength by crosslinking and blending*	*Published*	*88%. Key ideas, experimental work, analysis of results and writing first draft*	*1) Vikram Singh Raghuwanshi (2%) experimental work.* *2) Joanne Tanner (5%) feedback and editing* *3) Gil Garnier (5%) feedback and editing.*	*No* *No* *No*
3	*Structure and swelling of cross-linked nanocellulose foams*	*Published*	*74%. Key ideas, experimental work, analysis of results and writing first draft*	*1) Vikram Singh Raghuwanshi (15%) experimental work and analysis of results* *2) Joanne Tanner (2%) feedback and editing* *3) Chun-Ming Wu (2%) experimental work* *4) Olga Kleinerman (3%) experimental work* *5) Yachin Cohen (2%) experimental work, feedback and editing* *6) Gil Garnier (2%) feedback and editing*	*No* *No* *No* *No* *No* *No*

4	*Absorption kinetics of nanocellulose foams: Effect of ionic strength and surface charge*	*Published*	*78%. Key ideas, experimental work, analysis of results and writing first draft*	*1) Emily Eastman (5%) analysis of results* *2) Monica De Rango (5%) analysis of results* *3) Vikram Singh Raghuwanshi (2%) feedback and editing* *4) Joanne Tanner (5%) feedback and editing* *5) Gil Garnier (5%) feedback and editing*	*Yes* *Yes* *No* *No* *No*

**If no co-authors, leave fields blank*

I have renumbered sections of submitted or published papers in order to generate a consistent presentation within the thesis.

Student name: Laila Hossain

Student signature: **Date:** 7th October, 2021

I hereby certify that the above declaration correctly reflects the nature and extent of the student's and co-authors' contributions to this work. In instances where I am not the responsible author I have consulted with the responsible author to agree on the respective contributions of the authors.

Main Supervisor name: Gil Garnier

Main Supervisor signature: **Date:** 7th October, 2021

Acknowledgements

First of all, I would like to thank Allah (the God Almighty) for giving me the patience, determination and strength during this course of work.

The work presented in this thesis was conducted under the supervision of Prof. Gil Garnier and Dr. Joanne Tanner. I would like to express my gratitude to Gil for his constant support and encouragement throughout the journey. I admire Gil for his leadership, enthusiasm and energy to encourage me in every difficult situation during the study. His suggestions and guidance helped me to publish my research work in the top level of journals. The learning I have got from him will certainly help me to develop my career in future. I extend my gratitude to my co-supervisor, Dr. Joanne Tanner, a creative researcher, always ready to offer creative ideas to answer my questions. She always helped me to improve my writing skill and taught me how to make science more aesthetic.

Thanks to Meat and Livestock Australia (MLA) and Monash University for providing the scholarships and necessary facilities to undertake this degree.

I acknowledge my friends and colleagues in BioPRIA: David Mendoza, Diana Alves, Gloria Arenas, Mahdi Naseri-Nosar, Maisha Maliha, Maoqi Lin, Rodrigo Curvello and Ruth Barajas Ledesma for your continuous support. You all enriched my PhD journey with joy and happiness, without any doubt. Thanks for your support during my milestones by attending and asking questions. I also acknowledge Llyza Mendoza, who helped me at the beginning of my PhD to understand the PhD journey. She helped me during the first few months of PhD by giving her valuable suggestions and guidance. I used to get inspired from her critical thinking and ways to find out easy solutions for difficult problems. I would also like to thank CEPA (Chemical Engineering Postgraduate Association) team, we arranged a successful conference together besides doing social events in the department. During this time, I learnt a lot from the team. I would also like to thank my friends Debarati, Afifa and Nazneen for inspiring me all the time. Their support and motivation have made this journey more enjoyable.

I would like to acknowledge my mentor, Dr. Mohidus Samad Khan, whose inspiration and support motivated me to do something extraordinary in a prestigious institute, like Monash University. I always admire his ways of thinking, efficiency and dedication to work.

I acknowledge all the staff in BioPRIA for their friendly and cooperating attitude. Special thanks to Janette Anthony who has always been very caring and affectionate. Thanks to Scot Sharman to give me training on different equipment, help me with the safety rules and regulations and cheering me up with funny jokes. I express my gratitude to Vikram Singh Raghuwanshi for his always ready to help nature.

I also acknowledge Annie Lewis, Kim Phu and Lilyanne Price. Annie is the Administrative Officer of Food and Dairy GRIP who has been always very caring. Annie organized a number of workshops which really helped me to interact with people from different backgrounds, know industrial perception of research and develop skills for future. Kim Phu is the departmental safety officer who was always there to solve my problems regarding safety and SWI. Kim is a nice lady who always supported the HDR students including me. Lilyanne is the Academic Programs Manager in the department whose time to time assistance made my PhD journey smoother.

And my parents, who don’t need any formal acknowledgement. Because of them, I am going to complete the doctoral degree. They have made me who I am today.

Abstract

Global demand for superabsorbent polymer is increasing and it is estimated that the market will reach 19.64 billion USD by 2030. It is a major challenge to meet this high demand in a sustainable and environmentally benign way as most of the commercial superabsorbent polymers are fossil fuel derived, non-biodegradable, non-sustainable and non-renewable. This lack of sustainability has driven the development of sustainable superabsorbents from natural alternatives, such as cellulose, the most abundant biopolymer in the world. Cellulose is easy to functionalize, readily available, low cost and renewable. Nanocellulose, which is fibrillated cellulose of nanometer scale, has very high aspect ratio, strength and liquid absorption capacity, making it suitable to functionalize into a superabsorbent polymer. However, despite recent advances, the potential of nanocellulose-based superabsorbent remains unrealized, due to the lack of fundamental understanding of the relationship between production methods, structure, and superabsorbent properties. This understanding is critical to enable the nanocellulose superabsorbent properties to be engineered and tuned for specific applications. Therefore, this thesis aims to determine the missing fundamental relationships between physical, mechanical, chemical and biological properties of nanocellulose superabsorbents to develop performant and biodegradable material for use in specific applications including food, personal hygiene, agriculture, and diagnostics.

This research has been conducted in two broad sections. The first part focuses on the manipulating the preparation methods and method parameters to engineer the mechanical, physical and chemical properties of nanocellulose superabsorbents for different applications. The mechanical properties are tuned using different crosslinkers and blending nanocellulose fibers with cellulose crystals, which successfully improved the material strength. Characterization and testing of these modified nanocellulose superabsorbents shows a distinct difference in the water absorption and transport mechanism for neat and crosslinked materials due to the structural changes induced by fiber bundle swelling and network compactness/openness resulted from physical and chemical change in the structure.

The effect of ionic strength of the fluid to be absorbed and degree of oxidation of the nanocellulose are presented. Ionic strength affects the absorption capacity of the superabsorbent. The absorption capacity of nanocellulose superabsorbent is 25% higher in MilliQ water compared to 0.9 wt% NaCl after 5 minutes. Changing the degree of oxidation affects the superabsorbent porosity, which in turn affects the absorption kinetics, which can thus be tuned. Fundamentals of absorption phases

and the understanding of the intrinsic properties of the material are expanded, enabling further customization and application-specific tailoring of nanocellulose superabsorbents.

To highlight the environmental compatibility of these materials, the biodegradability of the neat and crosslinked nanocellulose superabsorbents is quantified under enzymatic conditions. Rapid degradation of crosslinked superabsorbent indicates that crosslinking does not reduce the biodegradation rate in comparison to neat nanocellulose superabsorbent indicating that the engineered material is environmentally benign as planned.

To demonstrate that the aim of the thesis has been achieved, an application-specific nanocellulose superabsorbent material is developed for use as a glucose sensor to detect glucose concentrations in human blood in the second part of the thesis. The colorimetric sensor is developed by immobilizing glucose oxidase in nanocellulose superabsorbent with favorable properties of rheological strength and surface charge. The sensor is stained with phenol red, and shows a distinct and specific color change when blood plasma containing glucose is added. The sensor pH changes due to the oxidation of glucose catalyzed by glucose oxidase, resulting in a visibly detectable color change. This nanocellulose based colorimetric sensor can indicate concentrations of glucose between 7 mM and 13 mM in human blood by a color change from red to orange. The successful transferability of this concept to the potential prototype design not only demonstrates achievement of the thesis aim, but also has the potential for future commercial applications for glucose and other biological analytes detection.

This thesis contributes significantly to the fundamental knowledge of nanocellulose superabsorbent and successfully applies the developed knowledge to engineer tunable materials for specific applications. This research critically analyzes and modulates the nanocellulose superabsorbent properties in order to provide a pathway to the production of renewable, sustainable alternatives to the current fossil-fuel derived synthetic superabsorbent polymers.

List of Publications

Peer-reviewed journal papers

The following published and submitted papers are included in the body of this thesis as individual chapters. The sections of these published papers have been renumbered in order to generate a consistent presentation within the thesis. Papers in the published format are included as Appendix II.

1. Hossain, L., Raghuwanshi, V. S., Tanner, J., & Garnier, G. (2021). Modulating nanocellulose hydrogels and cryogels strength by crosslinking and blending. Colloids and Surfaces A: Physicochemical and Engineering Aspects, 127608.

2. Hossain, L., Raghuwanshi, V. S., Tanner, J., Wu, C. M., Kleinerman, O., Cohen, Y., & Garnier, G. (2020). Structure and swelling of cross-linked nanocellulose foams. Journal of colloid and interface science, 568, 234-244.

3. Hossain, L., Eastman, E., De Rango, M., Raghuwanshi, V. S., Tanner, J., & Garnier, G. (2021). Absorption kinetics of nanocellulose foams: Effect of ionic strength and surface charge. Journal of Colloid and Interface Science, 601, 124-132.

The following published papers are not included in the main body of this thesis and can be found in their published format in Appendix III.

1. Hossain, L., Maliha, M., Barajas-Ledesma, R., Kim, J., Putera, K., Subedi, D., Tanner, J., Barr, J.J., Holl, M.M.B. & Garnier, G. (2021). Engineering laminated paper for SARS-CoV-2 medical gowns. Polymer, 222, 123643.

2. Barajas-Ledesma, R. M., Hossain, L., Wong, V. N., Patti, A. F., & Garnier, G. (2021). Effect of the counter-ion on nanocellulose hydrogels and their superabsorbent structure and properties. Journal of Colloid and Interface Science, 599, 140-148.

3. Mendoza, D. J., Hossain, L., Browne, C., Raghuwanshi, V. S., Simon, G. P., & Garnier, G. (2020). Controlling the transparency and rheology of nanocellulose gels with the extent of carboxylation. Carbohydrate Polymers, 245, 116566.

4. Mendoza, L., Hossain, L., Downey, E., Scales, C., Batchelor, W., & Garnier, G. (2019). Carboxylated nanocellulose foams as superabsorbents. Journal of colloid and interface science, 538, 433-439.

List of Figures

Chapter 1

Chapter 2

Chapter 3

List of Tables

List of Abbreviations

3D	Three-dimensional
BEK	Bleached Eucalyptus Kraft
SAP	Superabsorbent polymer
CNC	Cellulose nanocrystal
MCC	Microcrystalline cellulose
CNF	Cellulose nanofibers
COO^-	Carboxyl groups
CO_2	Carbon dioxide
EDC	N-(3-Dimethylaminopropyl)-N-ethylcarbodiimide hydrochloride
HMDA	Hexamethylenediamine
NaBr	Sodium bromide
NaClO	Sodium hypochlorite
$NaIO_4$	Sodium periodate
NaOH	Sodium hydroxide
NC	Nanocellulose
SAXS	Small angle x-ray scattering
SANS	Small angle neutron scattering

SEM	Scanning electron microscopy
HR-SEM	High resolution scanning electron microscopy
TEMPO	(2,2,6,6-Tetramethylpiperidin-1-yl) oxyl
Sulfo-NHS	N-hydroxysulfosuccinimide
M_w	Molecular weight
HPLC	High performance liquid chromatography
MLA	Meat and Livestock Australia
H_2SO_4	Sulphuric acid
NPK	Nitrogen/phosphorus/potassium
PEI	Polyethyleneimine

List of Nomenclature

%	Percentage
°	Degree
°C	Celsius
Å	Angstrom
G’	Storage modulus
G"	Loss modulus
η	Viscosity
atm	Atmosphere
cm	Centimetre
g	Gram
h	Hour
kg	Kilogram

L	Litre
M	Molar
m^2	Square metre
m^3	Cubic metre
mg	Milligram
min	Minute
mL	Millilitre
mm	Millimetre
mmol	Millimole
MW	Molecular weight
nm	Nanometre
ppm	Parts per million
rpm	Revolutions per minute
s	Seconds
wt.	Weight
µm	Micrometre

THIS PAGE WAS INTENTIONALLY LEFT BLANK

THIS PAGE WAS INTENTIONALLY LEFT BLANK

CHAPTER 1
INTRODUCTION AND LITERATURE REVIEW

THIS PAGE WAS INTENTIONALLY LEFT BLANK

Chapter 1: Introduction and Literature Review

1.1 Introduction

The global superabsorbent polymer (SAP) market was at 9.68 billion USD in 2020 and it is expected to hit 19.64 billion USD by 2030 [1]. The most common widely used SAP is sodium polyacrylate which accounts for 91.4% (volume percentage compared to other SAPs) in 2020 [2]. These non-biodegradable, petrochemical-based polymers are piled up in landfills every year and take many of years to decompose [3]. The hazardous leachate from these areas is also harmful for aquatic life. The motivation of this thesis is therefore to develop a sustainable, renewable, biodegradable SAP and tune the polymer properties for different applications. Polysaccharide-based alternatives to petrochemical SAPs are gaining attention for their renewable and biodegradable characteristics. In particular, cellulose is gaining momentum because of its non-toxicity, abundance, low cost, biocompatibility and favorable surface functionality [4].

Cellulose naturally exists in plants and is also expressed by certain bacterial strains. It is composed of D-glucose monomers connected by β-1,4-glycosidic linkages [5]. Nanocellulose can be produced from different cellulose sources such as wood, cotton, bagasse, bamboo, ramie, corn straw, rice straw and coconut shell [6-15]. The properties of produced nanocellulose depends on the type of source and the fibrillation process followed to produce it [16, 17]. Breaking the native cellulose into nanocellulose fibers increases its aspect ratio, mechanical properties, flexibility and surface area. These properties can be exploited to generate highly porous, foam-like materials with superabsorbent properties similar to and in some cases surpassing those of petrochemical-based SAPs. Nanocellulose SAPs are suitable for a wide range of applications such as for diapers, meat packaging, diagnostic and agricultural water retention aids [18-23]. Figure 1-1 shows the various applications of cellulose-based SAPs where applications shown shaded region are those discussed in this review.

Nanocellulose SAPs have a broad range of potential applications due to their low density, high porosity, high specific surface area and high absorption capacity [24, 25]. These properties can be tuned and modulated for specific applications. Modification of nanocellulose-based SAPs to include different functional groups further enables sensitive applications, such as meat packaging, optical sensors, insulators and agricultural water retention aids [26-28].

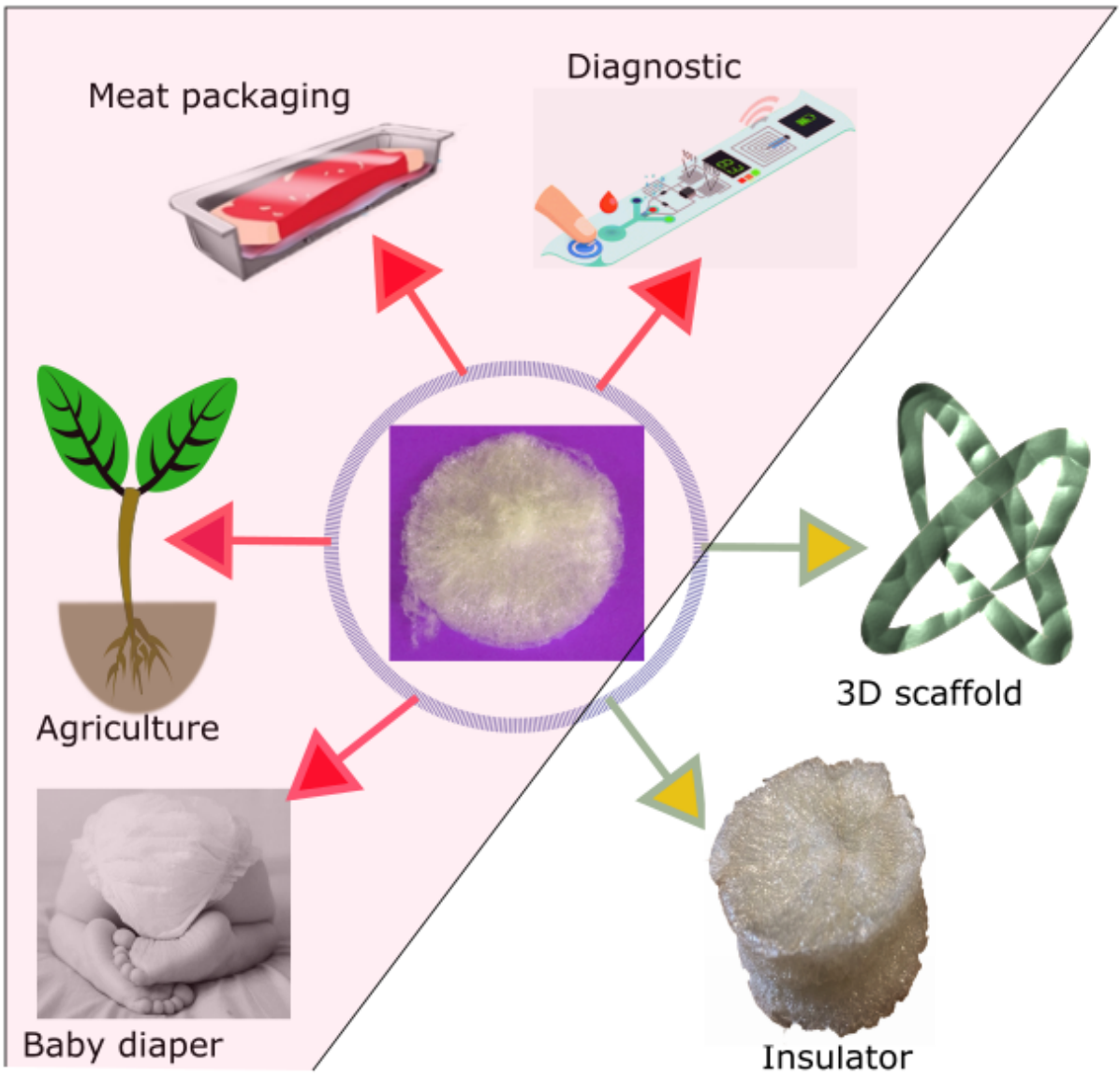

Figure 1-1: Different applications of nanocellulose-based SAP. Diagnostic image is reproduced with permission from [29].

The required properties and performance of SAPs vary significantly depending on the applications, in particular, porosity, absorption rate, capacity, water retention capacity and mechanical strength. For personal hygiene or baby care products, it is assumed that SAPs need to absorb large amounts of fluid in a short time under an applied load. Agricultural applications require both high water absorption capacity and controlled release of water under the load exerted by plants and the soil layer [30]. For meat packaging applications, it seems that it requires the SAPs to have controlled absorption rate and capacity to avoid dehydration of the meat itself. Nanocellulose SAPs for diagnostics are mainly used for their excellent properties

of immobilization of biomolecules inside the structure and increasing their shelf life at room temperature. Understanding the absorption capacity, kinetics and mechanical strength are crucial for tuning SAPs for various applications. To date, these properties, their development during production, and their relationship to the SAP structure have not been adequately quantified or analyzed for packaging, agriculture, personal care product and diagnostic applications. Doing so will enable SAPs with properties tuned specifically for each application to be produced.

This chapter critically reviews the current status of nanocellulose-based SAP production and applications and quantifies the structure-property relationship to link the fundamental properties with applications to better engineer the material. Properties and preparation procedures of cellulose-based SAPs are discussed, followed by an exposition on the effect of drying on the SAP structure. The relevant fluid absorption mechanisms, mechanical strength of SAP and the effect of absorbate solution properties on the SAP absorption phenomena are examined. Several critical applications of cellulose are reviewed in detail, linking SAP structure with the desired properties for those applications. Finally, this review gives a roadmap directing the future research and functionalization required to maximize the benefit of producing and using nanocellulose SAPs for advanced applications.

1.2 Properties of cellulose SAPs

Cellulose-based SAPs have low density (less than 5 mg/cm^3) and high porosity (over 99%) [31]. These structural properties enable these materials to absorb a large amount of water. Table 1-1 presents a summary of reported cellulose SAPs and some of their important properties: pore size, absorption capacity and ion sensitivity. These properties depend on the SAP preparation method, functionalization, and drying technique (discussed in the following sections). SAP properties can be modulated to better match the intended final application by adjusting the preparation method or adding a specific polymer to the cellulose base to enhance or achieve a desired property. For example, chitosan has been combined with cellulose superabsorbent to impart antibacterial properties [32]. Lignin-cellulose composites have been made to produce hydrophobic materials [33]. Similarly, other polymers could be combined with cellulose to have efficient SAP for specific final products.

Table 1-1: Literatures on cellulose-based SAPs.

Article	Cross linker	Drying technique	Pore size	Absorption capacity	Ionic sensitivity	Reference
Preparation of superabsorbent resin with fast water absorption rate based on hydroxymethyl cellulose sodium and its application	N,N'-Methylenebisacrylamide	Blast drying at 60 °C	-	1329 g distilled water /g	-	[34]
Superabsorbent hydrogels based on cellulose for smart swelling and controllable delivery	Epichlorohydrin (ECH)	Freeze drying	-	1050 g distilled water/g	0.76	[35]
Salt-Tolerant Superabsorbent Polymer with High Capacity of Water-Nutrient Retention Derived from Sulfamic Acid-Modified Starch	N,N'-methylene-bis-acrylamide	Blast drying at 50 °C	-	1026 g deionized water/g	0.86	[36]
Biocompatible cellulose-based superabsorbent hydrogels with antimicrobial activity	Epichlorohydrin	-	-	983.9 g ultrapure water/g	-	[37]
Dual crosslinked carboxymethyl cellulose/polyacrylamide interpenetrating hydrogels with highly enhanced mechanical strength and superabsorbent properties	Ethylene glycol diglycidyl ether	Drying at 60 °C and lyophilization	80-100 µm	962 g distilled water/g	-	[38]
Fabrication and characterization of a starch-based superabsorbent hydrogel composite reinforced with cellulose nanocrystals from potato peel waste	N,N'-Methylenebisacrylamide	Freeze drying	-	921 g distilled water/g	-	[39]

Synthesis and swelling behaviors of carboxymethyl cellulose-based superabsorbent resin hybridized with graphene oxide	N,N'-Methylenebisacrylamide	Drying at 70 ºC	-	750 g distilled water/g	-	[40]
Sustainable Production of Cellulose-Based Hydrogels with Superb Absorbing Potential in Physiological Saline	Epichlorohydrin	Oven drying at 50-60 ºC	300-600 µm	725 g distilled water/g	0.84	[41]
Biodegradable superabsorbent hydrogels derived from cellulose by esterification crosslinking with 1,2,3,4-butanetetracarboxylic dianhydride	1,2,3,4-butanetetracarboxylic dianhydride	Drying under reduced pressure	-	720 g water/g	-	[42]
Natural Cellulose-Chitosan Cross-Linked Superabsorbent Hydrogels with Superior Swelling Properties	Carboxymethylated chitosan	Oven drying at 60 ºC	350-600 µm	610 g distilled water/g	-	[43]
Superabsorbent materials derived from hydroxyethyl cellulose and bentonite: Preparation, characterization and swelling capacities	N,N′-methylenebisacrylamide and sodium hydroxide	-	-	538 g distilled water/g	-	[44]
Enhanced Swelling and Responsive Properties of Pineapple Peel Carboxymethyl Cellulose-g-poly(acrylic acid-co-acrylamide) Superabsorbent Hydrogel by the Introduction of Carclazyte	N,N'-Methylenebisacrylamide	Oven drying at 50 ºC	-	515.24 g distilled water/g	0.93	[45]
Development of poly(acrylic acid)/nanofibrillated cellulose superabsorbent composites by ultraviolet light induced polymerization	Photo crosslinked at 365 nm UV light	Oven drying at 105 ºC	-	512 g distilled water/g	-	[46]

Superabsorbent hydrogels via graft polymerization of acrylic acid from chitosan-cellulose hybrid and their potential in controlled release of soil nutrients	Thiourea formaldehyde	Oven drying at 70 °C	-	390 g distilled water /g	0.90	[47]
Synthesis of carboxymethylcellulose/ starch superabsorbent hydrogels by gamma-irradiation	Without any crosslinker, by gamma-irradiation	Drying at 70 °C	-	350 g water/g	0.89	[48]
A facile and efficient strategy for the fabrication of porous linseed gum/cellulose superabsorbent hydrogels for water conservation	Epichlorohydrin	Vacuum drying	18-28 µm	320 g distilled water/g	-	[49]
Preparation and properties of novel corn straw cellulose–based superabsorbent with water-retaining and slow-release functions	N,N'-methylene-bis-acrylamide	Vacuum freeze drying	-	303.2 g deionized water/g	-	[50]
Biodegradable poly (lactic acid)/cellulose-based superabsorbent hydrogel composite material as water and fertilizer reservoir in agricultural applications	1-ethyl-3-(3-dimethylami-nopropyl) carbodiimide hydrochloride	Oven drying at 45 °C	-	300 g water/g	-	[51]
Synthesis of cellulose-based superabsorbent hydrogels by high-energy irradiation in the presence of crosslinking agent	N,N'-methylene-bis-acrylamide	Drying at 60 °C	-	275 g water/g	0.79	[52]
Synthesis of Grafted Nanofibrillated Cellulose-Based Hydrogel and Study of Its Thermodynamic, Kinetic, and Electronic Properties	N,N'-methylene-bis-acrylamide	Vacuum drying at 40 °C	-	250 g distilled water/g	-	[53]

Cellulose hydrogels prepared from micron-sized bamboo cellulose fibers	-	Freeze drying	-	230 g water/g	-	[54]
Environmentally friendly superabsorbent fibers based on electrospun cellulose nanofibers extracted from wheat straw	Sodium acrylate	-	Nanometer range	225 g distilled water	0.08	[55]
Eco-friendly superabsorbent polymers based on carboxymethyl cellulose strengthened by TEMPO-mediated oxidation wheat straw cellulose nanofiber	Citric acid	Drying at 23 ºC	Macro and micro	200 g water/g	0.73-0.98	[56]
A novel wheat straw cellulose-based semi-IPNs superabsorbent with integration of water-retaining and controlled-release fertilizers	N,N'-Methylenebisacrylamide	Drying at 75 ºC	-	178.45 g distilled water/g	-	[57]
Chemically Cross-Linked Cellulose Nanocrystal Aerogels with Shape Recovery and Superabsorbent Properties	Hydrazone	Drying in a critical point dryer	<50 nm and >1µm	160 g water /g	-	[23]
Novel superabsorbent materials from bacterial cellulose	Polyethylene glycol diacrylate	Oven drying at 50 ºC	350-600 µm	125 g distilled water/g	0.77	[58]
Superabsorbent crosslinked carboxymethyl cellulose-PEG hydrogels for potential wound dressing applications	Citric acid	Drying at 80 ºC	-	~100 g deionized water/g	-	[59]

Potential of cellulose-based superabsorbent hydrogels as water reservoir in agriculture	1-ethyl-3-(3-dimethylaminopropyle) carbodiimide hydrochloride	Oven drying at 45 ^{o}C	-	80 g distilled water/g	-	[60]
Synthesis and characterization of hydrogels from cellulose acetate by esterification crosslinking with EDTA dianhydride	Ethylenediaminetetraacetic dianhydride	-	-	72 cm^3 distilled water/g	-	[61]
Proposed cross-linking model for carboxymethyl cellulose /starch superabsorbent polymer blend	Aluminum Sulfate Octadecahydrate	Drying at 100 ^{o}C	-	58 g distilled water/g	-	[62]
Phosphoric acid-mediated green preparation of regenerated cellulose spheres and their use for all-cellulose cross-linked superabsorbent hydrogels	Citric acid	Freeze drying	-	40 g distilled water/g	-	[63]
Preparation and characterization superporous hydroxypropyl methylcelulose gel beads	Divinylsulfone	Drying at room temperature	-	37.4 g distilled water/g	-	[64]
Superabsorbent sodium carboxymethyl cellulose membranes based on a new cross-linker combination for female sanitary napkin applications	Sodium trimetaphosphate (STMP) and aluminium sulphate (AlS)	Drying at 60 ^{o}C	26.6±5 µm	27.5 g distilled water /g	-	[65]
Superabsorbent crosslinked bacterial cellulose biomaterials for chronic wound dressings	Citric acid	Drying at room temperature	-	25 g distilled water/g	-	[66]

High strength of hemicelluloses based hydrogels by freeze/thaw technique	Physical cross linking between hemicelluloses, polyvinyl alcohol (PVA) and chitin nanowhiskers by repeated freeze/thaw cycles	Freeze drying	-	21 g distilled water/g	-	[67]
Superabsorbent and fully biobased protein foams with a natural cross-linker and cellulose nanofibers	Genipin	Freeze drying	-	17.1 g water /g	0.47	[68]
Superabsorbent hydrogel composite based on copolymer cellulose/poly (vinyl alcohol)/CNT	Glutaraldehide	Drying at room temperature	-	8.4 g water/g	-	[69]

1.3 Preparation of nanocellulose SAP

Cellulose is a polymeric chain of glucose units which can be derived from plant matter or bacterial strains. Cellulose derivation from bacterial strain is difficult and expensive. Therefore, majority of cellulose is derived from plant sources. In plant matter, cellulose is arranged in a highly organized hierarchical structure, as shown in Figure 1-2. Plant cell walls (P) can be divided into three secondary walls: S1, S2 and S3 (depending on the orientation of cellulose nanofibril) and middle lamella (mL). Encased within the plant cell wall are cellulose bundles which are entangled together with other components such as lignin and hemicellulose [70]. These cellulose bundles contain several strands of microfibrils (or, nanocellulose) ranging from 5 to 20 nm. Within an individual microfibril, elementary fibrils of 1.5 to 3.5 nm are tightly contained and bonded together through extensive hydrogen bonding [71, 72].

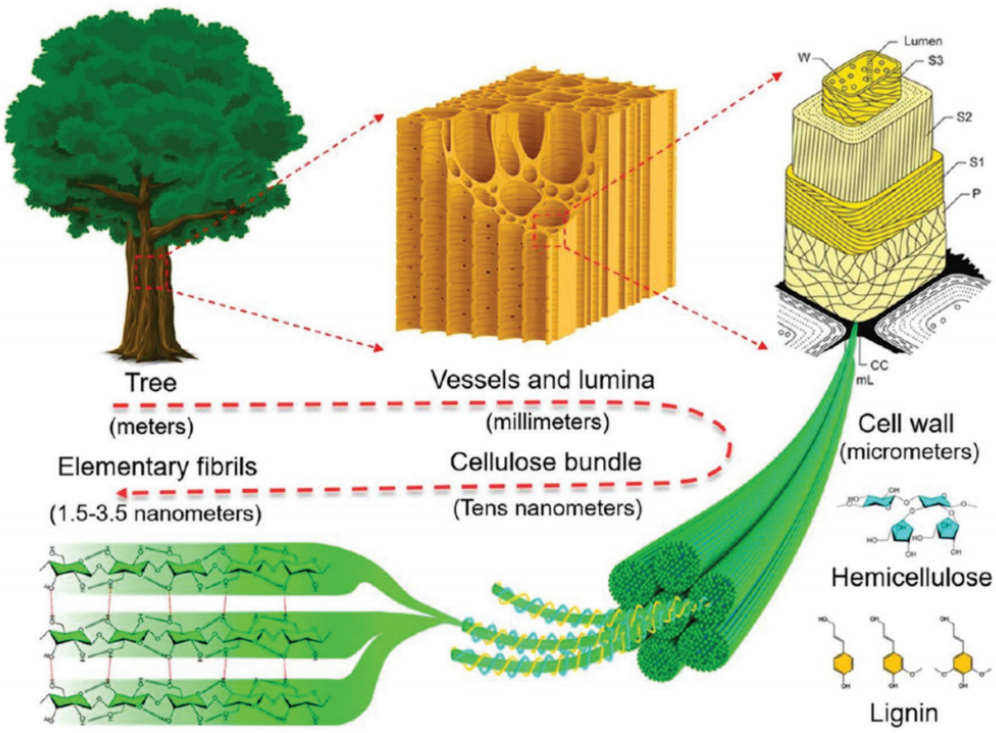

Figure 1-2: Graphical illustration of the hierarchical structure of wood, and the composition of cell wall. The term "CC" in the figure represents cell corner. Reprinted with permission from [72-74] Copyright 2018, American Chemical Society; Copyright 2017, American Chemical Society; Copyright 2006, Springer.

Breaking down cellulose into nanometer units produces nanocellulose. Nanocellulose can be divided into two categories: cellulose nano fiber (CNF) and cellulose nano crystal (CNC) depending on the presence or absence of amorphous and crystalline regions in the material. Nanocrystalline cellulose (NCC or CNC), also known as nanowhiskers, appears as cylindrical rods with typical diameters of 3-5 nm and lengths of 20-1000 nm [75]. Cellulose nanofibers (CNFs) are long fibers which possess far higher aspect ratios (up 500) [76]. Due to their high aspect ratio, CNFs can be combined to form entangled porous structures with high swelling capacity [77]. CNC alone cannot form fiber entanglement and because of their crystalline nature they have low swelling capacity. For these reasons, CNC is mostly used as filler and strength modifier to reinforce superabsorbent composite structures [39].

Preparation of SAPs from CNF involves two main steps: (i) hydrogel preparation and (ii) drying of hydrogel (Figure 1-3). There are different techniques for both of these steps. Any functionalization or chemical modification is done as part of the hydrogel preparation, and mainly impacts the chemical properties of the resulting SAP, sometimes the physical structure as well. For example, crosslinking or extensive oxidation can change the pore size of the resultant SAP. The drying techniques mainly dictates the physical structure (porosity, structural homogeneity, specific surface area etc.) of SAP.

1.3.1 Hydrogel preparation

The first step to develop SAP is hydrogel preparation. Hydrogels are three-dimensional networks consisting of physically or chemically crosslinked hydrophilic polymers. There are various treatment methods, such as, enzymatic [78], mechanical [79] and chemical [80] to produce CNF that is suitable for hydrogel preparation. Among these, chemical treatment is the most popular due to its low energy consumption and benefit of producing high quality functionalized CNF [81]. Popular chemical pre-treatment methods include carboxymethylation, periodate oxidation, and TEMPO mediated oxidation. These pre-treatment methods introduce or modify functional groups on the cellulose polymer chains, increasing the repulsive forces within and between fibers, which improves fiber separation and liberation of CNF from cellulose. Of these methods, TEMPO-mediated oxidation is considered one of the most effective methods to prepare CNF hydrogel [82]. Figure 1-3 shows the preparation of hydrogel and SAP from wood pulp. The TEMPO oxidation process selectively converts the cellulose surface primary alcohol groups to carboxylate groups.

The anionic carboxylate groups along the cellulose chain introduces electrostatic repulsion between the fibers which allows liberation of fibers when under high shear forces such as homogenization [83] (Figure 1-3). TEMPO-oxidized, homogenized nanocellulose directly forms hydrogel after crossing specific nanocellulose concentration threshold (0.1 wt% for TEMPO oxidized fiber) [83]. The colloidal stability of the hydrogel is driven by fiber entanglement and electrostatic repulsion between the negative carboxylic groups.

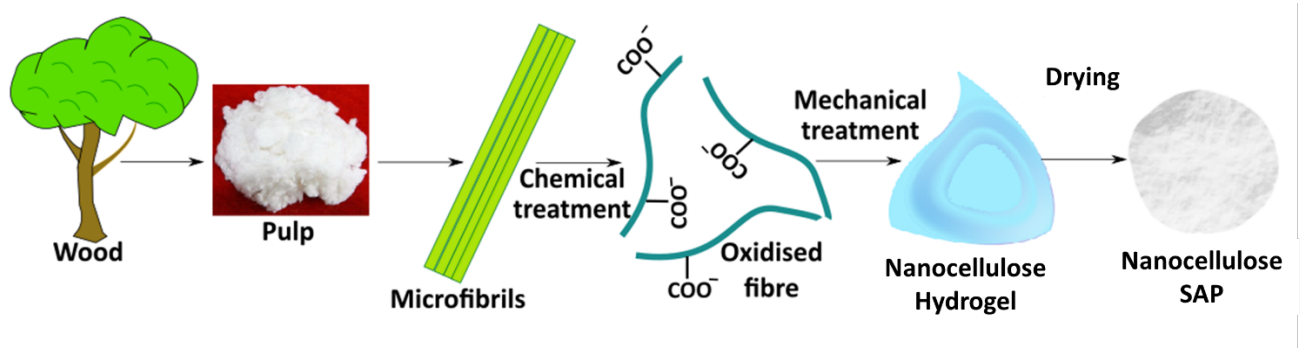

Figure 1-3: Preparation of nanocellulose hydrogel by TEMPO oxidation followed by drying to produce nanocellulose SAP.

The hydrogel structure can be strengthened by various types of physical and chemical crosslinking. Physical crosslinking phenomena include hydrogen bonding, electrostatic interactions, van der Waals forces, and ionic and hydrophobic interactions [84]. In chemical crosslinking, cellulose chains are linked by covalent bonds. Chemical crosslinking can be achieved by various techniques, such as, using crosslinker, initiation with enzymes, using photosensitive agents or reaction between functionals groups of polymers [85, 86]. Chemically crosslinked hydrogels are stronger (higher tensile, shear and bending properties) compared to physical crosslinking [87].

1.3.2 Drying of the hydrogel

The second step of SAP preparation is drying of the developed hydrogel. Hydrogel drying techniques include freeze drying, spray drying, spray freeze drying, oven drying, and supercritical drying. The choice of drying technique depends on the initial hydrogel solid concentrations and the final application, as drying methods directly influences the final SAP properties. The structural differences in SAP depending on drying techniques are discussed on section 1.4.

Freeze drying (lyophilization) is the most common technique for removing water from hydrogel to prepare nanocellulose SAPs. The freeze drying process consists of two main steps: (i) ice crystal growth and (ii) ice sublimation [88]. The free water and a part of the bound water in the hydrogel is transformed into ice in the first step. These ice crystals act as porogens, or pore molds, influencing the dried SAP structure [89]. Sublimation follows at a temperature range of -20 ^{o}C to -50 ^{o}C, under a lower pressure than that of triple point of water to minimize the aggregation of the cellulose particles and preserve the pore structure formed by the ice from step (i) [90]. The dried SAP produced by this method is called cryogel [91]. Freeze drying is particularly suitable for heat sensitive materials. The main drawback of freeze drying is non-uniform ice crystal formation during pre-freezing procedure (first step) and the high energy cost of the sublimation step [92]. The non-uniform ice crystal formation can be overcome by directional freeze drying which can produce honeycomb like pores in the transverse direction and regular directional tunnels in the longitudinal direction [93, 94].

Spray drying is a drying operation where a suspension (in this case a nanocellulose hydrogel) is passed through a nozzle as fine droplets into a drying tower that is continually flushed with hot air [88]. There are three main stages in the spray drying process: (i) dispersion of the hydrogel in the form of droplets, (ii) contact of hydrogel droplets with hot air, and (iii) solvent evaporation and formation of solid particles [95]. Spray freeze drying, another common technique, is a combination of spray drying and freeze drying. Spray freeze drying can be divided into two steps: (i) the hydrogel is sprayed through an atomizer and the atomized droplets are frozen by contact with a cryogenic solvent (usually liquid nitrogen), and (ii) frozen droplets are dried by sublimation [96, 97]. Spray freeze drying is lower cost compared to freeze drying as the reduced particle size increases the surface mass transfer coefficient resulting in higher drying rate and therefore a lower specific energy requirement for drying [98]. However, spray drying process has low thermal efficiencies due to the large volumes of air circulating inside the dryer chamber without contacting the particles [99].

In oven drying, the nanocellulose hydrogel is dried in an oven operating at 105 ^{o}C with flowing air. The oven drying process can be represented into three steps: (i) the constant rate drying period, (ii) the first falling rate drying period, and (iii) the second falling rate drying period [100-102]. In the constant rate drying period, water evaporation occurs from the bulk fluid, the capillary force increases as a function of water evaporation, and cellulose nanofibers move closer together as liquid water is removed from the fiber network [103]. The first falling rate drying period begins

when the water in the hydrogel has evaporated to the point that cellulose nanofiber surfaces begin to be exposed. In this period, water evaporation primarily takes place at the cellulose nanofiber surfaces, while the capillary force reaches its maximum and vapor diffusion starts to dominate the drying rate. During this period, cellulose nanofibers also move closer [103]. Drying enters the second falling rate drying period when the water transfer rate from the interior of cellulose nanofiber suspension to the exposed surface is smaller than the water diffusion rate through an individual fiber to the fiber surface. In this stage, the distance between nanocellulose fibers becomes much smaller due to the combined effect of capillary action and diffusion forces, enabling strong intermolecular hydrogen bonds to develop between the surface functional groups of the nanocellulose fibers, eventually forming a continuous fiber network [103]. The nanocellulose SAP produced in this method is called xerogel [104]. While oven drying is cost effective, fiber agglomeration (hornification) is a common disadvantage (see Section 1.4).

Supercritical drying is a drying technique where the solvent elimination is achieved without creating a two-phase system by reducing the related capillary forces, and decompressing the system to atmospheric pressure while keeping the solvent in the gas phase [88]. Alcohol, acetone or carbon dioxide can be used as the solvent [105]. Carbon dioxide is the most commonly used solvent in supercritical drying due to its easily achievable critical temperature and pressure (31.3 ^{o}C and 72.9 atm) [106]. Supercritical drying involves a two-way mass transfer of CO_2 and hydrogel solvent to and from the wet hydrogel. First, the liquid (water) in hydrogel expands due to dissolution of CO_2. Secondly, the CO_2 content in the hydrogel pores increases until the supercritical conditions are attained. Hydrogel dried in this process is called aerogel after drying [107]. The presence of supercritical CO_2 in the pores displaces the water, without altering its surface tension, which avoids the pore collapse phenomenon typically observed with other drying methods [108]. Supercritical drying is, however, relatively expensive mainly due to fluid compression [109-111]. It is therefore only suitable for high value, precise applications such as drug delivery or other biomedical applications [112].

1.4 Effect of drying method on the SAP structure

The SAP form and structure are greatly influenced by the hydrogel drying method. The SAP can be produced as a film, foam or powder, and the porous structure, specific surface area, and absorption capacity can be tuned by playing with the hydrogel drying methods.

The morphology of a freeze dried SAP depends on the freezing conditions and can vary from a foam-like open porous structure to a small-pored structure, depending on the freeze drying conditions [113]. Material with larger pores (several microns to several hundred microns) can be obtained by ice templating (slower freezing: -20 ^{o}C) [114, 115]. Faster freezing rates or cryo-protectant addition can mitigate this effect and produce smaller pores by producing smaller ice crystals [116]. A homogeneous fiber structure with small pores can also be obtained by rapid cooling [106]. The specific surface area of SAP can be increased by the replacement of water by tert-butanol prior to freeze drying. The specific surface area of SAP prepared by replacement of water by tert-butanol was shown to be around twelve times higher than that of SAP prepared by freeze drying directly from the water-based hydrogel. The capillary action of tert-butanol during the drying process is lower than that of water, resulting in less fiber network shrinkage and hence higher final SAP surface area [117-119].

Spray drying and spray freeze drying are used by many industries for the production of powders [120]. The final morphology of a spray dried or spray freeze dried SAP powder depends on the concentration and the size of the solids in the suspension or hydrogel, the type of the atomizer (nozzle), the temperature and the velocity of the drying air, and the cyclone separation conditions (cyclone separator diameter affects the differential pressure and hence particle size of the final product) [121, 122]. Spray freeze drying is advantageous for the drying of nanocellulose as the rapidity of spray freeze drying in comparison to traditional freeze drying protects the nanocellulose fiber structure from deformation due to ice crystal growth [96].

During oven drying at 105 ^{o}C, hornification of fibers increases, destroying the fiber network structure and resulting in micro-irregularities. Hornification is an irreversible process leading to loss of elasticity and flexibility of the fibers [123-125]. It occurs in fiber cell walls due to the formation of strong hydrogen bonds between the cellulose molecules in the fiber cell walls [126, 127] during the drying process [128, 129]. The removal of water from the cell wall of fibers causes the collapse of the pores and closure of capillary voids during the oven drying process [130, 131]. Closure of pore spaces in the fiber wall makes fiber stiffer as well as reduces swelling ability and therefore lower absorption capacity [128, 132-134]. Drying at lower temperatures of 50 ^{o}C has been shown to reduce this effect, producing a glassy sheet-like structure with very high water absorption capacity of 207.25 g/g [135].

Supercritical CO_2 drying results in highly porous network with high specific surface area and low shrinking rate [136]. Supercritical CO_2 drying of TEMPO oxidized fiber has produced very large

specific surface area, which is 500-600 m^2/g [137]. It has also been shown that the SAP formed by supercritical drying results in a more homogeneous pore structure compared to that of freeze drying.

1.5 Fluid absorption mechanism in nanocellulose SAP

The fluid absorption mechanism in nanocellulose SAP is critical to determine the absorption kinetics and absorption capacity and engineer the material for final applications. There is limited knowledge on the fluid absorption mechanism, absorption phase and absorption kinetics of nanocellulose SAP. Most of the fundamental study on cellulose absorption is done on paper [124, 138, 139]. Fluid absorption in paper can be described as a combination of wicking and fiber swelling [140].

Wicking is the spontaneous transport of liquid into a porous medium by the action of capillary pressure [141]. Capillary pressure (P) is a function of the surface tension of the liquid (γ), contact angle (Θ), and radius of pore (r_i) and its magnitude is given by the Laplace equation (eqn 1) [126].

$$P = \frac{2\times\gamma\times cos\theta}{r_i} \quad \ldots\ldots 1$$

Liquid wicking kinetics through porous media can be described by the Lucas-Washburn equation by considering the pore space as a bundle of capillary tubes of varying diameter embedded in the solid matrix [127, 128]. The location of liquid front (L) can be expressed as by the Washburn equation as given in eqn 2 [123, 124, 128, 129].

$$L = \sqrt{\frac{D_e\,\gamma\,cos\theta}{4\,\eta}}\, t^{0.5} \quad \ldots\ldots ...2$$

Where effective pore diameter, $D_e = \frac{D_h^2}{D_c}$

D_h is hydraulic pore diameter and D_c is capillary pore diameter

If the capillary and hydraulic diameters are equal ($D_c = D_h = D_e$), eqn 2 can be rewritten as

$$L = \sqrt{\frac{D_c\,\gamma\,cos\theta}{4\,\eta}}\, t^{0.5} \quad \ldots\ldots ...3$$

The above equation was modified by Laughlin [125].

$$L = a\, t^K \quad \ldots\ldots ..4$$

Where k may have values lower than 0.5 depending on the types of material.

Where η = liquid viscosity and K = wicking coefficient [126]

Fiber swelling is the swelling of nanocellulose fibers due to absorption of fluid molecules. Fiber swelling in paper due to liquid absorption can be described by the modified Washburn equation [130].

$$L = \sqrt{\frac{R_o \gamma \cos\theta}{4 \eta}} \left[t - \frac{a}{R_o} t^2 + \frac{a^2}{3R_o^2} t^3\right]^{0.5} \ldots\ldots\ldots\ldots\ldots\ldots\ldots\ldots\ldots\ldots\ldots\ldots\ldots\ldots\ldots 5$$

Where R_o is the initial value of hydraulic radius (R_h) and a is a constant representing the swelling effect [124].

The overall absorption kinetics (wicking and fiber swelling together) for cellulose SAP can be represented by the first-order expression based on Fick's second law of diffusion, as shown by eqn 6 [142].

$$\frac{dQ}{dt} = k\,(Q_{\max} - Q) \ldots\ldots\ldots\ldots\ldots\ldots\ldots\ldots\ldots\ldots\ldots\ldots\ldots\ldots\ldots\ldots\ldots\ldots\ldots\ldots 6$$

Here, Q_{max} is the absorption capacity at equilibrium; Q is absorption capacity at any time t, k is first-order rate constant which depends on the fiber particle radius and on the diffusion coefficient [143]

Integrating eqn 1 between 0 and the maximum value Q_{max} yields eqn 7 [142].

$$Q_t = Q_{max}\,(1-e^{-kt}) \ldots\ldots\ldots\ldots\ldots\ldots\ldots\ldots\ldots\ldots\ldots\ldots\ldots\ldots\ldots\ldots\ldots\ldots\ldots\ldots\ldots 7$$

The first order rate constant (k) can be determined experimentally using eqn 6 or 7.

The absorption kinetics of nanocellulose SAPs need to be studied as a function of wicking and fiber swelling. There is limited knowledge on how to tune the nanocellulose SAPs structure to control the absorption kinetics. Further the fundamental knowledge of absorption phenomenon and mechanism can be modelled using the above equations. This also facilities the comparison between experimental data and simulated results. These models help to understand the in-detail fluid absorption mechanism in nanocellulose SAPs.

1.6 Mechanical strength of SAP

Mechanical properties (tensile, compression or shear) of SAPs are important for their final applications. Different types of crosslinking (physical or chemical) are used to achieve the desired mechanical properties [144]. Chemical crosslinking forms strong bonds between the cellulose fibers compared to physical crosslinking. Common examples of physical crosslinkers include methylene-bis-acrylamide, ethylene glycol dimethacrylate (EGDMA), 1,1,1- trimethylolpropane triacrylate (TMPTA), and tetraalyloxy ethane (TAOE) [145, 146]. Epichlorohydrin, hexamethylenediamine (HMDA), aldehydes and aldehyde-based reagents, urea derivatives, and carbodiimides are also used as crosslinkers for cellulose based SAP [147, 148]. However, most of the chemical crosslinkers are not environment friendly which limits their applications. To avoid the harmful effect if chemical crosslinkers, citric acid is being using nowadays to crosslinked cellulose fibers [149]. Blending cellulose fiber with cellulose crystals can also improve the mechanical strength [150] while maintaining the sustainability. However, there is limitation on the nanocellulose SAP mechanical strength, especially for compressive strength, which is critical for various applications of SAP such as meat packaging or baby diaper. There is limited knowledge on increasing the compressive strength of nanocellulose SAP in a sustainable way.

1.7 Effect of fluid properties on absorption

The structure of nanocellulose SAP is important to dictate the absorption kinetics and absorption capacity as already described in the previous sections. Next, the fluid to be absorbed also determines the effectiveness of the SAP. Therefore, the fluid properties need to be considered when choosing production methods and tuning the SAP structural properties. The combination of SAP structure and fluid properties dictate the ultimate SAP performance.

1.7.1 Effect of temperature

Absorption capacity and kinetics depend on fluid viscosity, according to the modified Washburn Equation (Eqn 5), and fluid viscosity in turn depends on temperature. Temperature requirements for superabsorbent applications, including food packaging, agriculture, and infant and personal care products, typically vary from 4 ^{o}C (refrigeration) to 37 ^{o}C (body temperature). These SAP

applications involve the absorption of a range of fluids, including water, saline solutions, and blood. The temperature dependence of the viscosity of these solutions is given in Figure 1-4.

According to eqn 5, increasing fluid viscosity, η, will reduce the distance travelled through the absorbent by the fluid. Water viscosity decreases with temperature between 4 and 37 °C (Figure 1-4), which indicates that the absorption rate and distance travelled will increase over this range, increasing total absorption capacity. However, these is no literature directly relating fluid viscosity with nanocellulose SAP absorption kinetics, and therefore no correlation available with which to directly assess the potential impact of temperature on nanocellulose SAP behavior.

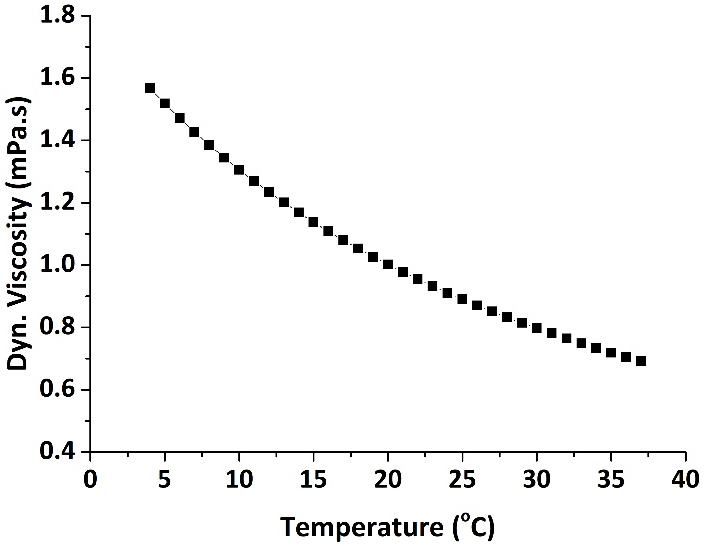

Figure 1-4: Change of water viscosity for a temperature range of 4-37 °C [151].

1.7.2 Effect of ionic strength

Ionic strength of the liquid to be absorbed affects the swelling capacity of the SAPs. A significant decrease in absorption capacity has been observed for salt-containing solutions [37, 152, 153]. This is due to decrease of electrostatic repulsion between the charged groups on the fiber surface, which induces a charge screening effect and has been theoretically proved by Florey [154]. The valency of ions in the liquid absorbate further affects the swelling capacity; the higher the valency of the ions, the lower the swelling of the fibers because of the stronger charge screening effect caused by multi-valent ions [155-157]. Besides that, hydrophilic groups in the nanocellulose (such as carboxylic groups) SAP complexes with the ions present in the solution by surface crosslinking,

which hinders the water molecule penetration through the nanocellulose matrix [158, 159]. This phenomenon is illustrated in Figure 1-5 [160] where the absorption capacity is the highest for monovalent ions (NaCl) and the lowest for trivalent ions ($AlCl_3$).

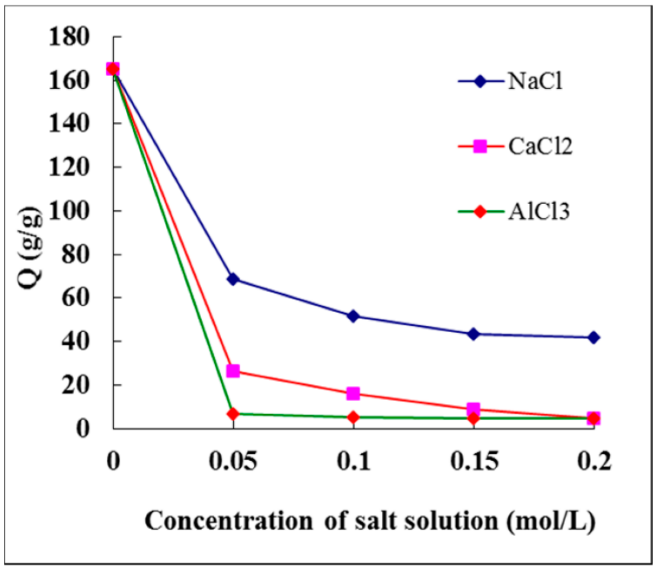

Figure 1-5: Absorption capacity (Q) of superabsorbent in different salt solutions. Reprinted from [160].

Equilibrium swelling capacity also decreases with increasing ionic strength of the liquid absorbate due to the reduced osmotic pressure difference between the nanocellulose matrix and the ionic solution in comparison to pure water. This is supported by the Donan equilibrium theory, which states that a high concentration of mobile counterions in an external solution can reduce the osmotic pressure inside a polymer matrix, resulting in matrix shrinkage [35, 161, 162]. The swelling of the nanocellulose SAP can be determined by Flory's equation (eqn 8) which is dependent on ionic strength of external solution [163].

$$Q^{5/3} \approx \frac{(\frac{i}{\frac{1}{2V_u S^2}})^2 + \left(\frac{1}{2} - x_1\right)V_1}{\frac{V_E}{V_o}} \quad \ldots\ldots 8$$

Here, Q = swelling degree of the polymer

i/V_u = charge density of the SAP

S = ionic strength of the external solution

$\left(\frac{1}{2} - x_1\right) V_1$ = affinity between SAP and solvent

$\frac{V_E}{V_o}$ = SAP crosslinking density

The ionic sensitivity of nanocellulose SAP, or indeed any absorbent, can also be expressed as the salt sensitivity, calculated by eqn 9, which indicates how susceptible the SAP absorption capacity is to changes in the ionic strength of the fluid to be absorbed. Higher salt sensitivity indicates a higher loss of absorbency for that particular SAP in an ionic (salt) solution. So, lower salt sensitivity is preferred for SAP where high performance in ionic solutions is required.

Salt sensitivity, $f = 1 - \frac{Qs}{Qd}$ …9

Here, Qs is the water absorption capacity in saline water or ionic solution and Qd is water absorption capacity in deionized water [164].

Reduced absorption capacity in ionic solution results from the charge screening effect. This charge screening effect can be moderated by introducing sulfate ions into the SAP structure during hydrogel preparation. Sulfate groups ionize more easily compared to carboxylic groups resulting in less association with the mobile ions in the solution to be absorbed and lower salt sensitivity [165]. The introduction of non-anionic amide groups on the cellulose surface can also reduce the salt sensitivity [166].

Nanocellulose SAP can be engineered utilizing the fundamental knowledge of structure-property relationship. Tuning the structure by playing with preparation technique can produce nanocellulose SAP with different porosity, specific area, absorption capacity etc. Therefore, understanding the application and therefore, choosing the most appropriate method is vital for the preparation of nanocellulose SAP.

1.8 Tuning cellulose SAP properties for packaging, personal care, diagnostic and agriculture products

Cellulose SAPs are an excellent choice for existing and emerging applications, especially when the world is moving towards sustainability. These materials can be used for a variety of applications, if proper care is taken during SAP preparation and production to achieve the required material properties. Different applications have different key parameters, such as: absorption

capacity and kinetics, ionic strength of the fluid, temperature and applied load. These different variables are already reviewed in the previous sections which dictates the final properties of SAP required for specific applications. This fundamental knowledge of structure-property relationships helps to optimize the SAP structure for final applications.

1.8.1 Meat packaging products

The soaker pad (absorbent pad) for meat packaging is used to absorb the excess moisture released from meat pieces. They are typically made of sodium polyacrylate, which is not biodegradable. More than 750 million soaker pads are used in Australia every year only for meat packaging. These take many years to degrade and cost us a large amount every year for landfill. Moreover, this type of soaker pad is not efficient enough for red meat packaging. There are often liquid pools around the meat which looks unappetizing, promotes bacterial growth, and accelerates meat spoilage [167]. This creates obstacles for long term storage and exporting packaged fresh meat. These issues with lack of sustainability and unacceptable or inconsistent performance have driven researchers to explore alternative options for renewable, sustainable and performant soaker pads for meat packaging.

Cellulose SAPs are an attractive option to be used in soaker pads for food applications. However, the SAP needs to be especially designed and functionalized for this application, as it must absorb fluids which contain water, protein, iron, and water-soluble vitamins. For example, drip loss from raw beef contains around 11% protein which is mainly sarcoplasmic proteins, including myoglobin, lactic acid and glycolytic enzymes [168-170]. These components (protein and others) increase the drip loss viscosity compared to that of pure water. In retail products, drip loss can be 15 mL to 60 mL depending on the meat type and mass. So, the cellulose SAP needs efficiently and effectively to absorb this amount of drip loss, while not acting as a desiccant or removing moisture from the meat itself. Moreover, SAPs need to be performant at shelf temperature of 4 °C. Nanocellulose SAPs for this application therefore require the following properties: slow absorption rate compatible with the released drip loss rate from meat pieces and not desiccating the meat at 4 °C, capacity to absorb protein molecules related to the drip loss composition and required mechanical strength during absorption to avoid disintegration when in operation under the load of the meat.

By applying and expanding upon the knowledge summarized in Sections 1.3 to 1.7 above, nanocellulose SAPs could be developed with specific porosity and absorption kinetics compatible

with the blood release rate from meat pieces to efficiently absorb the drip loss. Protein molecules are usually 3 to 6 nm in size. Nanocellulose SAPs with porosity larger than 6 nm would therefore be theoretically capable of absorbing the protein molecules from drip loss. Usually nanocellulose SAPs pore sizes are larger than 6 nm irrespective of the drying method as observed in Table 1-1 for different types of cellulose SAP. However, pore size can be tuned by changing the cooling rate in freeze drying [114, 115] or homogeneous pore structure can be achieved by supercritical drying [108]. Tunable absorption kinetics can be achieved by varying the pore sizes during hydrogel preparation or drying. Efficient drip loss absorption can hinder microbial growth, hence can improve the appearance and shelf life of meat [171]. Figure 1-6 shows a conceptual drawing of a comparison between a commercial soaker pad and a sustainable cellulose SAP-based pad.

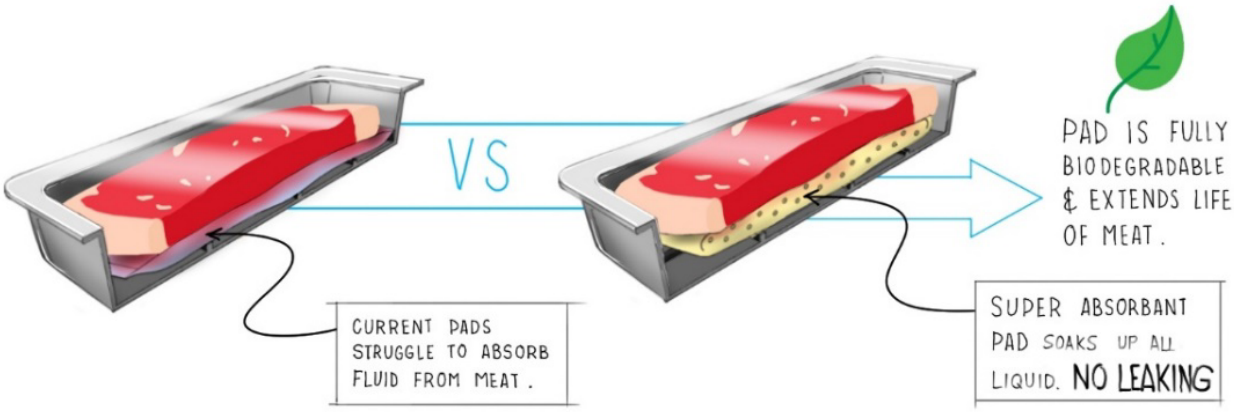

Figure 1-6: Conceptual performance comparison of commercial soaker pad vs sustainable cellulose pad for meat packaging.

1.8.2 Personal care products

Superabsorbent polymers (cross linked polyacrylates) were first used in baby diapers in Germany and France in 1980 [146, 172]. Similar products were introduced in Japan with less SAP followed by the introduction of thinner diapers in other Asian countries, US and Europe [146]. Nowadays, most commercial SAPs are made of sodium-based polymers (mainly sodium polyacrylate), which are fossil-derived, non-renewable and non-sustainable. The annual production of sodium polyacrylate based SAP is estimated to be around 2 million metric tons where disposable diapers accounts for 74% of the market [173]. Disposable diapers are the third largest single consumer

items in landfill [174]. This huge amount of landfill waste takes many years to decompose [3]. The detrimental effects of landfill, such as: greenhouse gas emissions and global warming, has led the scientists to look for sustainable, renewable and biodegradable options. Replacing the fossil derived SAP with a renewable material is still of direct benefit even if the other components in these products remain the same. However, changing the complete diaper design to make it complete biodegradable should be, of course, the ultimate goal.

There are several criteria which need to be fulfilled for a new SAP material to be used for baby diapers. They are: absorption capacity of an ionic solution (urine), a fast absorption rate, water holding or retention capacity under shear (baby weight, movement and comfort). Urine consists mainly of water, urea, salt and pigment compounds. A nanocellulose SAP for this application should therefore be able to absorb an ionic solution. 0.9 wt% NaCl solution is commonly used to mimic the ionic strength of urine [140]. Absorption capacity under load (AUL) is usually measure at a pressure of 21000 dynes/cm^2 (around 0.3 psi) for baby diaper applications [175]. Industrially accepted absorption under load values are between 18 to 30 g/g. However, AUL of 45-50 g/g enables thinner diapers with less superabsorbent, reducing production cost and improving product aesthetics [176]. This absorption under load can be achieved by developing SAP with good mechanical integrity by crosslinking methods as in Section 1.6.

Water retention capacity under shear is measured by centrifuge retention capacity (CRC). The centrifuge retention capacity or saline water retention capacity of tempo oxidized cellulose nanofiber is higher than that of commercial SAP [177]. This is due to the high porosity and high surface area of nanocellulose superabsorbent, which allows improved penetration of saline solution inside the structure [178, 179]. The porosity and surface area of nanocellulose SAP can be modulate by selecting the appropriate drying technique and parameters, as mentioned in section 1.4. However, the centrifuge retention capacity gives an indirect measure of SAP performance, not directly related to SAP absorption capacity under baby weight. So, the SAP needs to be tested under baby weight i.e. absorption capacity when under load at 37 ºC, as fluid viscosity changes with temperature (section 1.7.1). Additionally, the mechanical integrity and how to improve that integrity under load have not been investigated (section 1.6). Finally, the complete biodegradable design of the diaper needs to be developed to complement the nanocellulose SAP.

The main challenge associated with the development of a sustainable, biodegradable baby diapers is the combination of all the required layers. Figure 1-7 shows a proposed design for a biodegradable baby diaper design. There are four different layers: (i) semi-permeable layer, (ii)

distribution layer, (iii) superabsorbent material and (iv) hydrophobic layer. The top, semi-permeable layer will direct the urine flow only in inward direction which will keep the top sheet in contact with baby skin dry (which is required for comfort). The distribution layer, made of cotton fluff, will distribute the urine uniformly into the nanocellulose SAP layer. The final hydrophobic layer, potentially made of PLA, prevents leakage through the back side. The four proposed layers can easily be integrated and joined by heat sealing. It is therefore the development and tuning of cellulose SAP for baby diaper applications, as described above, that is required to further develop and realize this prototype.

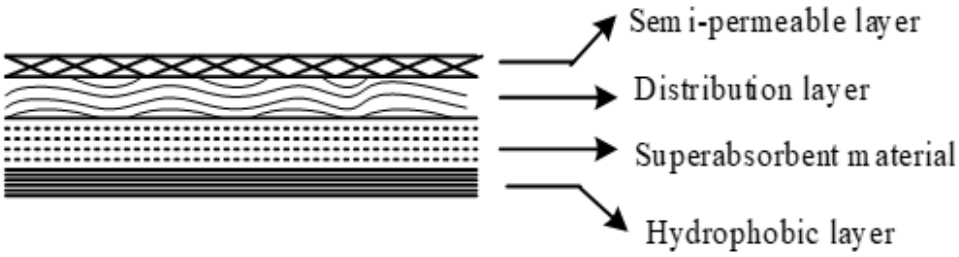

Figure 1-7: Conceptual prototype design for baby diaper.

1.8.3 Diagnostic products

Due to its biocompatibility, low cost, easy functionality and non-toxic nature, cellulose is gaining attention for biosensors and microfluidic paper-based analytical devices (μPADs) [180]. There are numerous reports on paper-based biosensors for diagnostic applications [181-186]. Paper-based devices are also being used for capturing and storing biomolecules such as DNA, protein, enzymes etc. In particular, immobilization of enzymes on an appropriate substrate can increase their stability and preserve their activity [187]. There are several common immobilization techniques available, shown in Figure 1-8, including adsorption, crosslinking, encapsulation, covalent bonding and entrapment. However, immobilization of enzymes can cause some denaturation depending on the immobilization technique, pH, temperature, and buffer solution [188].

Nanocellulose SAPs are therefore a promising medium for enzyme immobilization, as the physical properties of nanocellulose hydrogel from which the superabsorbent is made can be tuned to match the ideal conditions required for immobilization, preservation and use of a particular enzyme, including pH, temperature, and ionic strength [189-194]. Nanocellulose SAP has also has a very high, tunable surface area, which improves interaction with and binding of the enzyme and the

fiber network [137, 195-197]. The dried nanocellulose SAP matrix can also preserve the enzyme stability and improve ease of handling, ease of use, and shelf life of the enzyme. Furthermore, a reduction of enzyme activity often occurs in 2D substrates [198-201]. 3D hydrogel networks can overcome these limitations and preserve enzymes within the structure, ensuring the sensitivity of nanocellulose SAP-based biosensors [202].

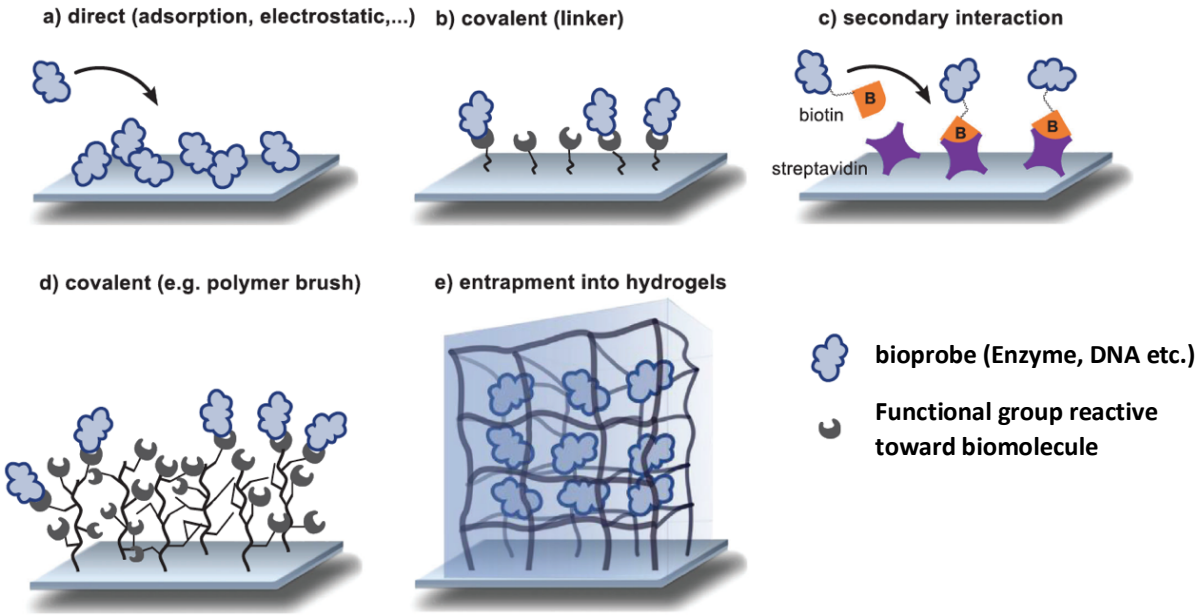

Figure 1.8: Representation of the possible bioprobe immobilization techniques: (a) direct, (b) covalent, (c) secondary interaction, (d) covalent and (e) entrapment into hydrogel. Reproduced with permission from [203] Copyright 2021, Wiley Online Library.

Immobilized enzyme stability has already been demonstrated in nanocellulose SAPs [204]. Glucose oxidase was immobilized in a nanocellulose network, and shown to change color as expected in the presence of different glucose concentrations. This enzyme-containing SAP was incorporated into a microfluidic device to develop a point of care glucose sensor [205]. Glucose oxidase immobilized in TEMPO oxidized nanocellulose has also been shown to detect glucose in urine [206]. However, most of the nanocellulose SAP based biosensor are not direct indicators, and require pre- or post-treatment to determine blood glucose levels, which is not appropriate for home use. So, further research and device design for a simple, user-friendly glucose sensor and visual indicator is required. This will require the nanocellulose SAP with controlled absorption

capacity of the analytes (human blood in case of glucose sensor) and ability to incorporate enzymes inside the porous structure.

1.8.4 Agriculture

The agricultural sector plays a vital role to ensure food security, where it has been estimated that global demand for food will double food production by 2050 [207]. To meet this demand, in an environmentally benign and sustainable way, is a major challenge in agriculture, especially because this industry uses about 70% of the water available for human consumption worldwide [208, 209]. Climate change and droughts have significantly decreased water availability in recent years, threatening the world's agricultural development in the future. The use of SAPs as agricultural aids offers a way to address and mitigate this challenge. However, most commercial SAPs are non-biodegradable, fossil-fuel derived polymers such as polyacrylates (PAs) or polyacrylamides (PAMs), which has greatly limited their commercial applications because of possible environmental risk. This lack of sustainability has led to the development of materials derived from natural polymers such as starch, pectin, and guar gum, chitosan and alginate [210]. However, these materials are still produced as composites with PA/PAM, limiting their sustainability and biodegradability, and thus not solving the problem [211].

Nanocellulose SAPs have the potential to increase soil water retention, significantly reducing irrigation water consumption. They can function as 'water reservoirs', increasing the water availability to plants and allowing them to survive longer under water stress. Cellulose is also 100% biodegradable. Depending on the weather conditions, temperature and moisture, cellulose decomposition mostly occurs within 16 to 30 days [212, 213]. As cellulose biodegrades *in situ* in the soil, is also provides an excellent source of labile carbon to soil-based microbes, providing them the energy needed for growth and to perform important functions to develop healthy soil via nutrient cycling and fertilization.

Functionalizing the nanocellulose SAP to introduce nutrients to the fiber network expands the application range of this material to function not only as a water retention aid, but also as a carrier for agrochemicals, as the SAP capable of administering a controlled-release of nutrients according to plant demand, thereby increasing crop yield. Nitrogen/phosphorus/potassium (NPK) can be encapsulated in carboxymethyl cellulose (CMC) based SAPs to facilitate slow release of NPK fertilizers [214]. The fertilizer in this material was continuously released over a period of 10 days.

Further *in vivo* testing studies on cucumber plants demonstrated a more significant development of cucumber seeds supplemented with this material (Figure 1-9).

Though there are a few studies on the performance of nanocellulose SAP in agriculture [215, 216], a comprehensive and systematic analysis is required to fully understand the effect of nanocellulose SAP on soils and plant growth from the fundamental perspective. Different soils have different properties and ionic strengths, which affect the SAP performance, so it's critical to analyze effect of ionic strength and evaluate the relative Nanocellulose SAP salt sensitivity. The release kinetics needs to be controlled for nutrient delivery which can be achieved by tuning the pore size or functionalization. With proper analysis and quantification, nanocellulose SAP can be engineered for agricultural applications by tuning their structure and properties.

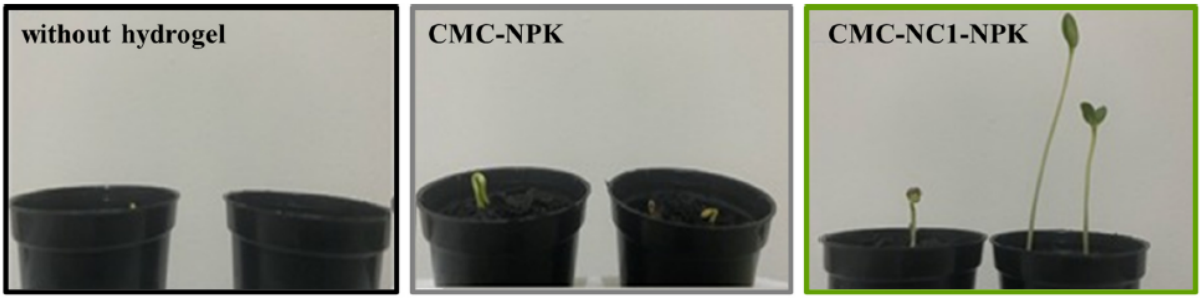

Figure 1-9: In vivo tests of cucumber seeds grown in soil (a) without SAP, (b) with SAP and NPK fertilizer and (c) with SAP filled with nanocellulose and NPK fertilizers. Reprinted with permission from [214], Copyright 2021, Elsevier.

1.9 Perspectives

Nanocellulose SAP represents a new class of bio-based material capable of absorbing a large volume of fluid while maintaining its own structure. This renewable, biodegradable, non-toxic material can be functionalized and engineered by utilizing simple methods, such as TEMPO oxidation, homogenization and drying to prepare novel SAPs with application-specific absorption properties. Though there is literature on the development and properties of nanocellulose SAPs, extensive studies on nanocellulose SAP structure-property relationship does not exist, and is still required to successfully tailor the properties, without resorting to the creation of composites with non-renewable, non-biodegradable and non-sustainable petrochemically-derived additives. There is limited knowledge on nanocellulose SAP mechanical strength, absorption fundamentals, absorption phases, fiber-fiber interaction phenomenon, absorption kinetics and biodegradation rate

for crosslinked/neat SAPs. The relation between the key variables, preparation conditions and structural changes is poorly understood. Furthermore, how this nanocellulose SAP can be utilized for novel applications is poorly understood. Therefore, a fundamental comprehensive study is required to fully understand nanocellulose SAP structure and how this structure can be modulated by careful choice of the hydrogel production, drying and functionalization methods and method parameters.

1.10 Gaps in knowledge

The literature review indicated significant gaps in knowledge which are hindering the development of nanocellulose SAP for with application-specific properties. The following gaps need to be addressed:

1. There is limited knowledge on how crosslinking is related to SAP mechanical strength. The absorption capacity of physically/chemically crosslinked and cellulose fibrils/biopolymer blended SAP remains poorly described.
2. The lack of understanding on the effect of the fibrous network structure on the swelling of nanocellulose-based SAP and the structural changes during drying of swollen SAP.
3. The lack of knowledge on the absorption kinetics, absorption phases and absorption mechanism with differences in nanocellulose SAP structure at the various critical length and time scales of interest, particularly for SAP exhibiting rapid absorption kinetics.
4. The limited understanding of crosslinked nanocellulose SAP biodegradation in soil.
5. The limited application of engineered nanocellulose SAP for novel applications, such as, diagnostics (for example blood glucose detection in human blood), highlighting the unexplored potential of nanocellulose SAP for the efficient and user-friendly device development for diagnostic.

1.11 Research Objectives

Performant, sustainable, renewable SAPs are required to replace the current commercial petrochemical-based SAP. This research aims to increase the knowledge of the relationship between production methods, structure and properties of nanocellulose SAPs to address this

challenge and enable the development of nanocellulose SAPs with tunable, application-specific properties.

The following specific research objectives are achieved in this study:

1. Engineer and characterize TEMPO oxidized nanocellulose SAP by controlling crosslinking density/type and by adding crystalline cellulose to improve the mechanical strength.
2. Understand and quantify the relationship between the structure and swelling behavior of nanocellulose SAPs upon water absorption and drying.
3. Quantify the effect of the nanocellulose fiber surface charge on the structure, absorption kinetics, capacity and absorption mechanism of nanocellulose SAP for water and ionic fluids.
4. Measure the rate of biodegradation of nanocellulose SAP as a function of nanocellulose crosslinking, enzyme concentration and correlate the biodegradation rate with crosslinked SAP structure.
5. Develop a nanocellulose based biosensor to detect glucose concentration in human blood- a novel application of nanocellulose SAP by applying the prior knowledge and outcomes from objectives 1 to 4 to demonstrate that this research has addressed the gaps in knowledge and achieved the overall aim to enable the development of application specific nanocellulose SAPs.

1.12 Thesis Outline

This thesis is presented in the format of "Thesis by Publications" according to Monash University Guidelines. It consists of five experimental chapters of which three are already published and the other two are manuscripts under preparation. All published manuscripts are reformatted for a consistent presentation whilst the text remains unchanged. The original publications are provided in Appendix II.

The following is the thesis structure outlining the aims, conducted research and outcomes.

Chapter 1: Introduction and Literature Review

This chapter critically reviews the current knowledge and understanding of nanocellulose SAPs, and their fundamental physical and chemical properties. It includes an overview of nanocellulose SAP production methods, and presents nanocellulose SAP properties, absorption mechanisms and the requirements to use nanocellulose SAPs in advanced applications, including meat packaging, personal care products, agriculture and diagnostics. The existing limitations are highlighted and further research required to overcome the limitations has been evaluated.

Chapter 2: Modulating Nanocellulose Hydrogels and Cryogels Strength by Crosslinking and Blending

Hossain, L., Raghuwanshi, V. S., Tanner, J., & Garnier, G. (2021). Modulating nanocellulose hydrogels and cryogels strength by crosslinking and blending. Colloids and Surfaces A: Physicochemical and Engineering Aspects, 127608. DOI: 10.1016/j.colsurfa.2021.127608

Impact factor: 4.539

This chapter investigates the production of nanocellulose SAPs with high mechanical strength via crosslinking and blending. The mechanical properties of the SAPs (both hydro- and cryogel) are characterized from rheological and compressive strength perspectives. Nanocellulose SAP is functionalized with crosslinkers and blended with cellulose nanocrystals (CNC) to improve the mechanical sustainability while maintaining absorption capacity with applied load for different applications, such as baby diaper or meat packaging.

Chapter 3: Structure and Swelling of Cross-linked Nanocellulose Foams

Hossain, L., Raghuwanshi, V. S., Tanner, J., Wu, C. M., Kleinerman, O., Cohen, Y., & Garnier, G. (2020). Structure and swelling of cross-linked nanocellulose foams. Journal of colloid and interface science, 568, 234-244. DOI: 10.1016/j.jcis.2020.02.048

Impact factor: 8.128

This chapter quantifies the relation between the structure and swelling behavior of cross-linked nanocellulose foam/SAP. Physically and chemically crosslinked nanocellulose SAPs are saturated with water and measured using a combination of small angle scattering and cryogenic high

resolution (HR) SEM techniques. Comparison of crosslinked and non-crosslinked nanocellulose SAPs is presented to differentiate the structures and reveal the water transport mechanisms inside the structure.

Chapter 4: Absorption Kinetics of Nanocellulose Foams: Effect of Ionic strength and Surface Charge

Hossain, L., Eastman, E., De Rango, M., Raghuwanshi, V. S., Tanner, J., & Garnier, G. (2021). Absorption kinetics of nanocellulose foams: Effect of ionic strength and surface charge. Journal of Colloid and Interface Science, 601, 124-132. DOI: 10.1016/j.jcis.2021.05.092

Impact factor: 8.128

Nanocellulose SAP absorption kinetics and capacity is tuned by using TEMPO oxidation methods to manipulate the nanocellulose surface charge (COO^-), which affects swelling by altering the SAP porosity and pore structure. Tunable absorption kinetics enable the successful engineering of SAP material for applications where controlled rate of absorption is required.

Chapter 5: Effect of Crosslinking on Nanocellulose Superabsorbent Biodegradability

Nanocellulose SAP and the effect of crosslinking on biodegradability are analyzed in this chapter by quantifying biodegradation under enzymatic condition. Nanocellulose SAP biodegradation is quantified in sandy soil by analyzing microbial activity and hydrolysis of remaining product at different enzyme and solid (SAP) concentrations. The findings are compared with SAP in soil without enzyme to evaluate the accelerated biodegradation effect caused by enzyme.

Chapter 6: Point of Care Nanocellulose Sensor for Glucose Detection in Blood

A novel application of nanocellulose SAP is presented to demonstrate the final goal of preparing application specific SAPs. Enzyme immobilized nanocellulose SAP based colorimetric sensor is developed to detect glucose level in human blood. This pH based colorimetric sensor is evaluated to detect glucose concentration of 7 mM to 13 mM and potential device design is proposed to transfer this concept as a commercial product. This concept of colorimetric biosensor opens the opportunity of developing colorimetric sensors to detect infectious diseases in human body.

Chapter 7: Conclusion and Perspectives

The overall understanding from this thesis is summarized in this last chapter. The perspective for the application of nanocellulose SAP by tuning its properties in food, personal care product and diagnostic are presented.

1.13 References

1. Precedence Research. *Super Absorbent Polymers Market Size to Hit US$ 19.94 Bn by 2030*. 2021; Available from: https://www.globenewswire.com/fr/news-release/2021/02/09/2171789/0/en/Super-Absorbent-Polymers-Market-Size-to-Hit-US-19-94-Bn-by-2030.html.
2. Market;, S.A.P.S. *Super Absorbent Polymers (SAP) Market by Type (Sodium Polyacrylate, Polyacrylate/Polyacrylamide, Copolymers), Application (Personal Hygiene, Agriculture, Medical, Industrial, Packaging, Construction, Oil & Gas), Region - Global Forecast to 2026*. 2021; Available from: https://www.marketsandmarkets.com/Market-Reports/super-absorbent-market-177336849.html.
3. Passauer, L., T. Hallas, E. Bäucker, G. Ciesielski, S. Lebioda, and U. Hamer, *Biodegradation of hydrogels from oxyethylated lignins in model soils.* ACS Sustainable Chemistry & Engineering, **3**(9).2015. 1955-1964.
4. Curvello, R., V.S. Raghuwanshi, and G. Garnier, *Engineering nanocellulose hydrogels for biomedical applications.* Advances in colloid and interface science.2019.
5. Kadla, J.F. and R.D. Gilbert, *Cellulose structure: A review.* Cellulose Chemistry and Technology, **34**.2000. 197-216.
6. Rajinipriya, M., M. Nagalakshmaiah, M. Robert, and S. Elkoun, *Importance of agricultural and industrial waste in the field of nanocellulose and recent industrial developments of wood based nanocellulose: a review.* ACS Sustainable Chemistry & Engineering, **6**(3).2018. 2807-2828.
7. Inamochi, T., R. Funahashi, Y. Nakamura, T. Saito, and A. Isogai, *Effect of coexisting salt on TEMPO-mediated oxidation of wood cellulose for preparation of nanocellulose.* Cellulose, **24**(9).2017. 4097-4101.
8. Morais, J.P.S., M. de Freitas Rosa, L.D. Nascimento, D.M. do Nascimento, and A.R. Cassales, *Extraction and characterization of nanocellulose structures from raw cotton linter.* Carbohydrate polymers, **91**(1).2013. 229-235.
9. Hsieh, Y.-L., *Cellulose nanocrystals and self-assembled nanostructures from cotton, rice straw and grape skin: a source perspective.* Journal of materials science, **48**(22).2013. 7837-7846.
10. Syafri, E., A. Kasim, H. Abral, G.T. Sulungbudi, M. Sanjay, and N.H. Sari, *Synthesis and characterization of cellulose nanofibers (CNF) ramie reinforced cassava starch hybrid composites.* International journal of biological macromolecules, **120**.2018. 578-586.
11. Mandal, A. and D. Chakrabarty, *Isolation of nanocellulose from waste sugarcane bagasse (SCB) and its characterization.* Carbohydrate Polymers, **86**(3).2011. 1291-1299.
12. Li, J., X. Wei, Q. Wang, J. Chen, G. Chang, L. Kong, J. Su, and Y. Liu, *Homogeneous isolation of nanocellulose from sugarcane bagasse by high pressure homogenization.* Carbohydrate polymers, **90**(4).2012. 1609-1613.

13. Brito, B.S., F.V. Pereira, J.-L. Putaux, and B. Jean, *Preparation, morphology and structure of cellulose nanocrystals from bamboo fibers.* Cellulose, **19**(5).2012. 1527-1536.
14. Hernandez, C., F. Ferreira, and D. Rosa, *X-ray powder diffraction and other analyses of cellulose nanocrystals obtained from corn straw by chemical treatments.* Carbohydrate polymers, **193**.2018. 39-44.
15. Wan, C., Y. Lu, Y. Jiao, C. Jin, Q. Sun, and J. Li, *Ultralight and hydrophobic nanofibrillated cellulose aerogels from coconut shell with ultrastrong adsorption properties.* Journal of Applied Polymer Science, **132**(24).2015.
16. Sacui, I.A., R.C. Nieuwendaal, D.J. Burnett, S.J. Stranick, M. Jorfi, C. Weder, E.J. Foster, R.T. Olsson, and J.W. Gilman, *Comparison of the properties of cellulose nanocrystals and cellulose nanofibrils isolated from bacteria, tunicate, and wood processed using acid, enzymatic, mechanical, and oxidative methods.* ACS applied materials & interfaces, **6**(9).2014. 6127-6138.
17. Deepa, B., E. Abraham, N. Cordeiro, M. Mozetic, A.P. Mathew, K. Oksman, M. Faria, S. Thomas, and L.A. Pothan, *Utilization of various lignocellulosic biomass for the production of nanocellulose: a comparative study.* Cellulose, **22**(2).2015. 1075-1090.
18. Demilecamps, A., C. Beauger, C. Hildenbrand, A. Rigacci, and T. Budtova, *Cellulose–silica aerogels.* Carbohydrate polymers, **122**.2015. 293-300.
19. Fu, J., S. Wang, C. He, Z. Lu, J. Huang, and Z. Chen, *Facilitated fabrication of high strength silica aerogels using cellulose nanofibrils as scaffold.* Carbohydrate polymers, **147**.2016. 89-96.
20. Jaxel, J., G. Markevicius, A. Rigacci, and T. Budtova, *Thermal superinsulating silica aerogels reinforced with short man-made cellulose fibers.* Composites Part A: Applied Science and Manufacturing, **103**.2017. 113-121.
21. Stoyneva, V., D. Momekova, B. Kostova, and P. Petrov, *Stimuli sensitive super-macroporous cryogels based on photo-crosslinked 2-hydroxyethylcellulose and chitosan.* Carbohydrate Polymers, **99**.2014. 825-830.
22. Pääkkö, M., J. Vapaavuori, R. Silvennoinen, H. Kosonen, M. Ankerfors, T. Lindström, L.A. Berglund, and O. Ikkala, *Long and entangled native cellulose I nanofibers allow flexible aerogels and hierarchically porous templates for functionalities.* Soft Matter, **4**(12).2008. 2492-2499.
23. Yang, X. and E.D. Cranston, *Chemically cross-linked cellulose nanocrystal aerogels with shape recovery and superabsorbent properties.* Chemistry of Materials, **26**(20).2014. 6016-6025.
24. De France, K.J., T. Hoare, and E.D. Cranston, *Review of hydrogels and aerogels containing nanocellulose.* Chemistry of Materials, **29**(11).2017. 4609-4631.
25. Niinivaara, E. and E.D. Cranston, *Bottom-up assembly of nanocellulose structures.* Carbohydrate Polymers, **247**.2020. 116664.
26. Barajas-Ledesma, R.M., L. Hossain, V.N. Wong, A.F. Patti, and G. Garnier, *Effect of the counter-ion on nanocellulose hydrogels and their superabsorbent structure and properties.* Journal of Colloid and Interface Science, **599**.2021. 140-148.
27. Wu, B., G. Zhu, A. Dufresne, and N. Lin, *Fluorescent aerogels based on chemical crosslinking between nanocellulose and carbon dots for optical sensor.* ACS applied materials & interfaces, **11**(17).2019. 16048-16058.
28. Sun, Y., Y. Chu, W. Wu, and H. Xiao, *Nanocellulose-based lightweight porous materials: A review.* Carbohydrate Polymers.2020. 117489.
29. Smith, S., J.G. Korvink, D. Mager, and K. Land, *The potential of paper-based diagnostics to meet the ASSURED criteria.* RSC advances, **8**(59).2018. 34012-34034.

30. Guancha-Chalapud, M., *Natural fibers for hydrogels production and their applications in agriculture.* Acta Agronómica, **66**(4).2017. 495-505.
31. Jiang, F. and Y.-l. Hsieh, *Amphiphilic superabsorbent cellulose nanofibril aerogels.* J. Mater. Chem. A, **2**(18).2014. 6337-6342.
32. Tyagi, P., R. Mathew, C. Opperman, H. Jameel, R. Gonzalez, L. Lucia, M. Hubbe, and L. Pal, *High-strength antibacterial chitosan–cellulose nanocrystal composite tissue paper.* Langmuir, **35**(1).2018. 104-112.
33. Yeap, R.Y., *The potential of lignin to increase the hydrophobicity of micro/nanofibrillated cellulose (MNFC)*. 2020, University of British Columbia.
34. Cheng, S., X. Liu, J. Zhen, and Z. Lei, *Preparation of superabsorbent resin with fast water absorption rate based on hydroxymethyl cellulose sodium and its application.* Carbohydrate polymers, **225**.2019. 115214.
35. Chang, C., B. Duan, J. Cai, and L. Zhang, *Superabsorbent hydrogels based on cellulose for smart swelling and controllable delivery.* European Polymer Journal, **46**(1).2010. 92-100.
36. Zhao, C., M. Zhang, Z. Liu, Y. Guo, and Q. Zhang, *Salt-tolerant superabsorbent polymer with high capacity of water-nutrient retention derived from sulfamic acid-modified starch.* ACS omega, **4**(3).2019. 5923-5930.
37. Peng, N., Y. Wang, Q. Ye, L. Liang, Y. An, Q. Li, and C. Chang, *Biocompatible cellulose-based superabsorbent hydrogels with antimicrobial activity.* Carbohydrate polymers, **137**.2016. 59-64.
38. Jeong, D., C. Kim, Y. Kim, and S. Jung, *Dual crosslinked carboxymethyl cellulose/polyacrylamide interpenetrating hydrogels with highly enhanced mechanical strength and superabsorbent properties.* European Polymer Journal, **127**.2020. 109586.
39. Olad, A., F. Doustdar, and H. Gharekhani, *Fabrication and characterization of a starch-based superabsorbent hydrogel composite reinforced with cellulose nanocrystals from potato peel waste.* Colloids and Surfaces A: Physicochemical and Engineering Aspects, **601**.2020. 124962.
40. Wang, Z., A. Ning, P. Xie, G. Gao, L. Xie, X. Li, and A. Song, *Synthesis and swelling behaviors of carboxymethyl cellulose-based superabsorbent resin hybridized with graphene oxide.* Carbohydrate polymers, **157**.2017. 48-56.
41. Alam, M.N., M.S. Islam, and L.P. Christopher, *Sustainable Production of Cellulose-Based Hydrogels with Superb Absorbing Potential in Physiological Saline.* ACS Omega, **4**(5).2019. 9419-9426.
42. Kono, H. and S. Fujita, *Biodegradable superabsorbent hydrogels derived from cellulose by esterification crosslinking with 1,2,3,4-butanetetracarboxylic dianhydride.* Carbohydrate Polymers, **87**(4).2012. 2582-2588.
43. Alam, M.N. and L.P. Christopher, *Natural cellulose-chitosan cross-linked superabsorbent hydrogels with superior swelling properties.* ACS Sustainable Chemistry & Engineering, **6**(7).2018. 8736-8742.
44. Adair, A., A. Kaesaman, and P. Klinpituksa, *Superabsorbent materials derived from hydroxyethyl cellulose and bentonite: Preparation, characterization and swelling capacities.* Polymer Testing, **64**.2017. 321-329.
45. Dai, H. and H. Huang, *Enhanced swelling and responsive properties of pineapple peel carboxymethyl cellulose-g-poly (acrylic acid-co-acrylamide) superabsorbent hydrogel by the introduction of carclazyte.* Journal of agricultural and food chemistry, **65**(3).2017. 565-574.

46. Wen, Y., X. Zhu, D.E. Gauthier, X. An, D. Cheng, Y. Ni, and L. Yin, *Development of poly (acrylic acid)/nanofibrillated cellulose superabsorbent composites by ultraviolet light induced polymerization.* Cellulose, **22**(4).2015. 2499-2506.
47. Essawy, H.A., M.B. Ghazy, F. Abd El-Hai, and M.F. Mohamed, *Superabsorbent hydrogels via graft polymerization of acrylic acid from chitosan-cellulose hybrid and their potential in controlled release of soil nutrients.* International journal of biological macromolecules, **89**.2016. 144-151.
48. Fekete, T., J. Borsa, E. Takács, and L. Wojnárovits, *Synthesis of carboxymethylcellulose/starch superabsorbent hydrogels by gamma-irradiation.* Chemistry Central Journal, **11**(1).2017. 46.
49. Zhang, H., Q. Luan, Q. Huang, H. Tang, F. Huang, W. Li, C. Wan, C. Liu, J. Xu, and P. Guo, *A facile and efficient strategy for the fabrication of porous linseed gum/cellulose superabsorbent hydrogels for water conservation.* Carbohydrate polymers, **157**.2017. 1830-1836.
50. Wang, W., S. Yang, A. Zhang, and Z. Yang, *Preparation and properties of novel corn straw cellulose–based superabsorbent with water-retaining and slow-release functions.* Journal of Applied Polymer Science, **137**(32).2020. 48951.
51. Calcagnile, P., T. Sibillano, C. Giannini, A. Sannino, and C. Demitri, *Biodegradable poly (lactic acid)/cellulose-based superabsorbent hydrogel composite material as water and fertilizer reservoir in agricultural applications.* Journal of Applied Polymer Science, **136**(21).2019. 47546.
52. Fekete, T., J. Borsa, E. Takács, and L. Wojnárovits, *Synthesis of cellulose-based superabsorbent hydrogels by high-energy irradiation in the presence of crosslinking agent.* Radiation Physics and Chemistry, **118**.2016. 114-119.
53. Khalilzadeh, M.A., S. Hosseini, A.S. Rad, and R.A. Venditti, *Synthesis of Grafted Nanofibrillated Cellulose-Based Hydrogel and Study of Its Thermodynamic, Kinetic, and Electronic Properties.* Journal of Agricultural and Food Chemistry, **68**(32).2020. 8710-8719.
54. Zhang, X., Y. Wang, C. Lu, and W. Zhang, *Cellulose hydrogels prepared from micron-sized bamboo cellulose fibers.* Carbohydrate Polymers, **114**.2014. 166-169.
55. Petroudy, S.R.D., S.A. Kahagh, and E. Vatankhah, *Environmentally friendly superabsorbent fibers based on electrospun cellulose nanofibers extracted from wheat straw.* Carbohydrate Polymers, **251**.2021. 117087.
56. Petroudy, S.R.D., J. Ranjbar, and E.R. Garmaroody, *Eco-friendly superabsorbent polymers based on carboxymethyl cellulose strengthened by TEMPO-mediated oxidation wheat straw cellulose nanofiber.* Carbohydrate Polymers, **197**.2018. 565-575.
57. Li, X., Q. Li, Y. Su, Q. Yue, B. Gao, and Y. Su, *A novel wheat straw cellulose-based semi-IPNs superabsorbent with integration of water-retaining and controlled-release fertilizers.* Journal of the Taiwan Institute of Chemical Engineers, **55**.2015. 170-179.
58. Chaiyasat, A., S. Jearanai, L.P. Christopher, and M.N. Alam, *Novel superabsorbent materials from bacterial cellulose.* Polymer International, **68**(1).2019. 102-109.
59. Capanema, N.S., A.A. Mansur, A.C. de Jesus, S.M. Carvalho, L.C. de Oliveira, and H.S. Mansur, *Superabsorbent crosslinked carboxymethyl cellulose-PEG hydrogels for potential wound dressing applications.* International journal of biological macromolecules, **106**.2018. 1218-1234.
60. Demitri, C., F. Scalera, M. Madaghiele, A. Sannino, and A. Maffezzoli, *Potential of Cellulose-Based Superabsorbent Hydrogels as Water Reservoir in Agriculture.* International Journal of Polymer Science, **2013**.2013.

61. Senna, A.M., K.M. Novack, and V.R. Botaro, *Synthesis and characterization of hydrogels from cellulose acetate by esterification crosslinking with EDTA dianhydride.* Carbohydrate Polymers, **114**.2014. 260-268.
62. Braihi, A.J., S.I. Salih, F.A. Hashem, and J.K. Ahmed, *Proposed cross-linking model for carboxymethyl cellulose/starch superabsorbent polymer blend.* International Journal of Materials Science and Applications, **3**(6).2014. 363-369.
63. Kassem, I., Z. Kassab, M. Khouloud, H. Sehaqui, R. Bouhfid, J. Jacquemin, and M. El Achaby, *Phosphoric acid-mediated green preparation of regenerated cellulose spheres and their use for all-cellulose cross-linked superabsorbent hydrogels.* International journal of biological macromolecules, **162**.2020. 136-149.
64. Liu, C., N. Wei, S. Wang, and Y. Xu, *Preparation and characterization superporous hydroxypropyl methylcellulose gel beads.* Carbohydrate Polymers, **78**(1).2009. 1-4.
65. Reshma, G., C. Reshmi, S.V. Nair, and D. Menon, *Superabsorbent sodium carboxymethyl cellulose membranes based on a new cross-linker combination for female sanitary napkin applications.* Carbohydrate Polymers, **248**.2020. 116763.
66. Ciecholewska-Juśko, D., A. Żywicka, A. Junka, R. Drozd, P. Sobolewski, P. Migdał, U. Kowalska, M. Toporkiewicz, and K. Fijałkowski, *Superabsorbent crosslinked bacterial cellulose biomaterials for chronic wound dressings.* Carbohydrate Polymers, **253**.2021. 117247.
67. Guan, Y., J. Bian, F. Peng, X.-M. Zhang, and R.-C. Sun, *High strength of hemicelluloses based hydrogels by freeze/thaw technique.* Carbohydrate Polymers, **101**.2014. 272-280.
68. Capezza, A.J., Q. Wu, W.R. Newson, R.T. Olsson, E. Espuche, E. Johansson, and M.S. Hedenqvist, *Superabsorbent and fully biobased protein foams with a natural cross-linker and cellulose nanofibers.* Acs Omega, **4**(19).2019. 18257-18267.
69. Khoerunnisa, F., Y. Hendrawan, O.D. Sonjaya, and O.D. Putri, *Superabsorbent hydrogel composite based on copolymer cellulose/poly (vinyl alcohol)/CNT*. 2016.
70. Gibson, L.J., *The hierarchical structure and mechanics of plant materials.* Journal of the royal society interface, **9**(76).2012. 2749-2766.
71. Khan, A., T. Huq, R.A. Khan, B. Riedl, and M. Lacroix, *Nanocellulose-based composites and bioactive agents for food packaging.* Critical reviews in food science and nutrition, **54**(2).2014. 163-174.
72. Chen, C. and L. Hu, *Nanocellulose toward advanced energy storage devices: structure and electrochemistry.* Accounts of chemical research, **51**(12).2018. 3154-3165.
73. Song, J., C. Chen, C. Wang, Y. Kuang, Y. Li, F. Jiang, Y. Li, E. Hitz, Y. Zhang, B. Liu, A. Gong, H. Bian, J.Y. Zhu, J. Zhang, J. Li, and L. Hu, *Superflexible Wood.* ACS Applied Materials & Interfaces, **9**(28).2017. 23520-23527.
74. Agarwal, U.P., *Raman imaging to investigate ultrastructure and composition of plant cell walls: distribution of lignin and cellulose in black spruce wood (Picea mariana).* Planta, **224**(5).2006. 1141.
75. George, J. and S. Sabapathi, *Water soluble polymer-based nanocomposites containing cellulose nanocrystals*, in *Eco-friendly Polymer Nanocomposites*. 2015, Springer. p. 259-293.
76. Sharma, P.R., B. Zheng, S.K. Sharma, C. Zhan, R. Wang, S.R. Bhatia, and B.S. Hsiao, *High aspect ratio carboxycellulose nanofibers prepared by nitro-oxidation method and their nanopaper properties.* ACS Applied Nano Materials, **1**(8).2018. 3969-3980.
77. Chen, Y., L. Zhang, Y. Yang, B. Pang, W. Xu, G. Duan, S. Jiang, and K. Zhang, *Recent progress on nanocellulose aerogels: preparation, modification, composite fabrication, applications.* Advanced Materials, **33**(11).2021. 2005569.

78. Pääkkö, M., M. Ankerfors, H. Kosonen, A. Nykänen, S. Ahola, M. Österberg, J. Ruokolainen, J. Laine, P.T. Larsson, and O. Ikkala, *Enzymatic hydrolysis combined with mechanical shearing and high-pressure homogenization for nanoscale cellulose fibrils and strong gels.* Biomacromolecules, **8**(6).2007. 1934-1941.
79. Sim, G., *Carboxylated Cellulose Pulp Fibers: From Fundamentals to Applications*. 2016, McGill University Libraries.
80. Matsuki, S., H. Kayano, J. Takada, H. Kono, S. Fujisawa, T. Saito, and A. Isogai, *Nanocellulose Production via One-Pot Formation of C2 and C3 Carboxylate Groups Using Highly Concentrated NaClO Aqueous Solution.* ACS Sustainable Chemistry & Engineering, **8**(48).2020. 17800-17806.
81. Rol, F., B. Vergnes, N. El Kissi, and J. Bras, *Nanocellulose production by twin-screw extrusion: simulation of the screw profile to increase the productivity.* ACS Sustainable Chemistry & Engineering, **8**(1).2019. 50-59.
82. Sanchez-Salvador, J.L., C. Campano, C. Negro, M.C. Monte, and A. Blanco, *Increasing the Possibilities of TEMPO-Mediated Oxidation in the Production of Cellulose Nanofibers by Reducing the Reaction Time and Reusing the Reaction Medium.* Advanced Sustainable Systems, **5**(4).2021. 2000277.
83. Mendoza, L., W. Batchelor, R.F. Tabor, and G. Garnier, *Gelation mechanism of cellulose nanofibre gels: A colloids and interfacial perspective.* Journal of Colloid And Interface Science, **509**.2018. 39-46.
84. Kayra, N. and A.Ö. Aytekin, *Synthesis of cellulose-based hydrogels: Preparation, formation, mixture, and modification.* Cellulose-Based Superabsorbent Hydrogels.2019. 407-434.
85. Khan, S., A. Ullah, K. Ullah, and N.-u. Rehman, *Insight into hydrogels.* Designed monomers and polymers, **19**(5).2016. 456-478.
86. Ullah, F., M.B.H. Othman, F. Javed, Z. Ahmad, and H.M. Akil, *Classification, processing and application of hydrogels: A review.* Materials Science and Engineering: C, **57**.2015. 414-433.
87. Ermis, M., S. Calamak, G.C. Kocal, S. Guven, N.G. Durmus, I. Rizvi, T. Hasan, N. Hasirci, V. Hasirci, and U. Demirci, *Hydrogels as a new platform to recapitulate the tumor microenvironment*, in *Handbook of nanomaterials for cancer theranostics*. 2018, Elsevier. p. 463-494.
88. Zimmermann, M.V., C. Borsoi, A. Lavoratti, M. Zanini, A.J. Zattera, and R.M. Santana, *Drying techniques applied to cellulose nanofibers.* Journal of Reinforced Plastics and Composites, **35**(8).2016. 628-643.
89. Grenier, J., H. Duval, F. Barou, P. Lu, D. Letourneur, and B. David. *Pore formation in hydrogel scaffolds textured by freeze-drying*. in *MATERIAUX 2018*. 2018.
90. Voronova, M.I., A.G. Zakharov, O.Y. Kuznetsov, and O.V. Surov, *The effect of drying technique of nanocellulose dispersions on properties of dried materials.* Materials letters, **68**.2012. 164-167.
91. Korhonen, O. and T. Budtova, *All-cellulose composite aerogels and cryogels.* Composites Part A: Applied Science and Manufacturing, **137**.2020. 106027.
92. Jiang, H., M. Zhang, and B. Adhikari, *21 - Fruit and vegetable powders*, in *Handbook of Food Powders*, B. Bhandari, et al., Editors. 2013, Woodhead Publishing. p. 532-552.
93. Chen, Y., L. Zhou, L. Chen, G. Duan, C. Mei, C. Huang, J. Han, and S. Jiang, *Anisotropic nanocellulose aerogels with ordered structures fabricated by directional freeze-drying for fast liquid transport.* Cellulose, **26**(11).2019. 6653-6667.

94. Lou, C.-W., X. Zhou, X. Liao, H. Peng, H. Ren, T.-T. Li, and J.-H. Lin, *Sustainable cellulose-based aerogels fabricated by directional freeze-drying as excellent sound-absorption materials.* Journal of Materials Science, **56**(33).2021. 18762-18774.
95. OW, O. and P. PR, *Spray drying (spray drying) of plant extracts: foundations and applications.* J Pharmacog, **20**.2009. 641-650.
96. Jiménez-Saelices, C., B. Seantier, B. Cathala, and Y. Grohens, *Spray freeze-dried nanofibrillated cellulose aerogels with thermal superinsulating properties.* Carbohydrate polymers, **157**.2017. 105-113.
97. Luy, B. and H. Stamato, *Spray freeze drying.* Drying Technologies for Biotechnology and Pharmaceutical Applications.2020. 217-237.
98. Ishwarya, S.P., C. Anandharamakrishnan, and A.G. Stapley, *Spray-freeze-drying: A novel process for the drying of foods and bioproducts.* Trends in Food Science & Technology, **41**(2).2015. 161-181.
99. Cheng, F., X. Zhou, and Y. Liu. *Methods for improvement of the thermal efficiency during spray drying*. in *E3S Web of Conferences*. 2018. **53**: p. 01031. EDP Sciences.
100. Brinker, C.J. and G.W. Scherer, *Sol-gel science: the physics and chemistry of sol-gel processing*. 2013: Academic press.
101. GW, S., *Theory of drying.* J Am Ceram Sco **73**.1990. 3–14.
102. Mujumdar, A.S. and S. Devahastin, *Fundamental principles of drying*, in *Mujumdar's Practical Guide to Industrial Drying: Principles, Equipment and New Developments*. 2000, Exergex, Brossard, Canada. p. 1-22.
103. Peng, Y., D.J. Gardner, and Y. Han, *Drying cellulose nanofibrils: in search of a suitable method.* Cellulose, **19**(1).2012. 91-102.
104. Yamasaki, S., W. Sakuma, H. Yasui, K. Daicho, T. Saito, S. Fujisawa, A. Isogai, and K. Kanamori, *Nanocellulose Xerogels With High Porosities and Large Specific Surface Areas.* Frontiers in Chemistry, **7**(316).2019.
105. Şahin, İ., Y. Özbakır, Z. Inönü, Z. Ulker, and C. Erkey, *Kinetics of supercritical drying of gels.* Gels, **4**(1).2018. 3.
106. Lavoine, N. and L. Bergström, *Nanocellulose-based foams and aerogels: processing, properties, and applications.* Journal of Materials Chemistry A, **5**(31).2017. 16105-16117.
107. Hüsing, N. and U. Schubert, *Aerogels—airy materials: chemistry, structure, and properties.* Angewandte Chemie International Edition, **37**(1-2).1998. 22-45.
108. Long, L.-Y., Y.-X. Weng, and Y.-Z. Wang, *Cellulose aerogels: Synthesis, applications, and prospects.* Polymers, **10**(6).2018. 623.
109. Walters, R.H., B. Bhatnagar, S. Tchessalov, K.-I. Izutsu, K. Tsumoto, and S. Ohtake, *Next generation drying technologies for pharmaceutical applications.* Journal of pharmaceutical sciences, **103**(9).2014. 2673-2695.
110. Singh, R., M. Singh, S. Bhartiya, A. Singh, D. Kohli, P.C. Ghosh, S. Meenakshi, and P. Gupta, *Facile synthesis of highly conducting and mesoporous carbon aerogel as platinum support for PEM fuel cells.* International Journal of Hydrogen Energy, **42**(16).2017. 11110-11117.
111. He, S. and X. Chen, *Flexible silica aerogel based on methyltrimethoxysilane with improved mechanical property.* Journal of Non-Crystalline Solids, **463**.2017. 6-11.
112. Pakowski, Z., *Modern methods of drying nanomaterials.* Transport in porous media, **66**(1).2007. 19-27.
113. Beaumont, M., H. Rennhofer, M. Opietnik, H.C. Lichtenegger, A. Potthast, and T. Rosenau, *Nanostructured cellulose II gel consisting of spherical particles.* ACS Sustainable Chemistry & Engineering, **4**(8).2016. 4424-4432.

114. Guastaferro, M., E. Reverchon, and L. Baldino, *Polysaccharide-Based Aerogel Production for Biomedical Applications: A Comparative Review.* Materials, **14**(7).2021. 1631.
115. Zaman, A., F. Huang, M. Jiang, W. Wei, and Z. Zhou, *Preparation, properties, and applications of natural cellulosic aerogels: a review.* Energy and Built Environment, **1**(1).2020. 60-76.
116. Rey, L. and J.C. May, *Freeze-drying/lyophilization of pharmaceutical & biological products, revised and expanded*. 2004: CRC Press.
117. Sehaqui, H., Q. Zhou, and L.A. Berglund, *High-porosity aerogels of high specific surface area prepared from nanofibrillated cellulose (NFC).* Composites science and technology, **71**(13).2011. 1593-1599.
118. Ishida, O., D.-Y. Kim, S. Kuga, Y. Nishiyama, and R.M. Brown, *Microfibrillar carbon from native cellulose.* Cellulose, **11**(3-4).2004. 475-480.
119. Nemoto, J., T. Saito, and A. Isogai, *Simple freeze-drying procedure for producing nanocellulose aerogel-containing, high-performance air filters.* ACS applied materials & interfaces, **7**(35).2015. 19809-19815.
120. Mujumdar, A.S., *Handbook of industrial drying*. 2014: CRC press.
121. Peng, Y., Y. Han, and D.J. Gardner, *Spray-drying cellulose nanofibrils: effect of drying process parameters on particle morphology and size distribution.* Wood and Fiber Science, **44**(4).2012. 448-461.
122. Ekdahl, A., D. Mudie, D. Malewski, G. Amidon, and A. Goodwin, *Effect of spray-dried particle morphology on mechanical and flow properties of felodipine in PVP VA amorphous solid dispersions.* Journal of pharmaceutical sciences, **108**(11).2019. 3657-3666.
123. Kissa, E., *Wetting and wicking.* Textile Research Journal, **66**(10).1996. 660-668.
124. Masoodi, R. and K.M. Pillai, *Darcy's law-based model for wicking in paper-like swelling porous media.* AIChE Journal, **56**(9).2010. 2257-2267.
125. Laughlin, R.D. and J.E. Davies, *Some Aspects of Capillary Absorption in Fibrous Textile Wicking.* Textile Research Journal, **31**(10).1961. 904-910.
126. Mhetre, S. and R. Parachuru, *The effect of fabric structure and yarn-to-yarn liquid migration on liquid transport in fabrics.* The Journal of The Textile Institute, **101**(7).2010. 621-626.
127. Washburn, E.W., *The dynamics of capillary flow.* Physical review, **17**(3).1921. 273.
128. Markl, D., S. Yassin, D.I. Wilson, D.J. Goodwin, A. Anderson, and J.A. Zeitler, *Mathematical modelling of liquid transport in swelling pharmaceutical immediate release tablets.* International journal of pharmaceutics, **526**(1-2).2017. 1-10.
129. Kamath, Y., S. Hornby, H.-D. Weigmann, and M. Wilde, *Wicking of spin finishes and related liquids into continuous filament yarns.* Textile Research Journal, **64**(1).1994. 33-40.
130. Schuchard, D.R. and J.C. Berg, *Liquid transport in composite cellulose—superabsorbent fiber networks.* Wood and Fiber Science, **23**(3).2007. 342-357.
131. Mao, N. and S. Russell, *Capillary pressure and liquid wicking in three-dimensional nonwoven materials.* Journal of Applied Physics, **104**(3).2008. 034911.
132. Hearle, J. and P. Stevenson, *Nonwoven fabric studies: Part III: The anisotropy of nonwoven fabrics.* Textile Research Journal, **33**(11).1963. 877-888.
133. Mao, N. and S. Russell, *Anisotropic liquid absorption in homogeneous two-dimensional nonwoven structures.* Journal of applied physics, **94**(6).2003. 4135-4138.
134. Chen, H. and M. Fan, *Chitosan/carboxymethyl cellulose polyelectrolyte complex scaffolds for pulp cells regeneration.* Journal of Bioactive and Compatible Polymers, **22**(5).2007. 475-491.

135. Barajas-Ledesma, R.M., A.F. Patti, V.N. Wong, V.S. Raghuwanshi, and G. Garnier, *Engineering nanocellulose superabsorbent structure by controlling the drying rate.* Colloids and Surfaces A: Physicochemical and Engineering Aspects, **600**.2020. 124943.
136. Wang, Z., W. Zhu, R. Huang, Y. Zhang, C. Jia, H. Zhao, W. Chen, and Y. Xue, *Fabrication and Characterization of Cellulose Nanofiber Aerogels Prepared via Two Different Drying Techniques.* Polymers, **12**(11).2020. 2583.
137. Kobayashi, Y., T. Saito, and A. Isogai, *Aerogels with 3D ordered nanofiber skeletons of liquid-crystalline nanocellulose derivatives as tough and transparent insulators.* Angewandte Chemie International Edition, **53**(39).2014. 10394-10397.
138. Liu, Z., J. Hu, Y. Zhao, Z. Qu, and F. Xu, *Experimental and numerical studies on liquid wicking into filter papers for paper-based diagnostics.* Applied Thermal Engineering, **88**.2015. 280-287.
139. Akinli-Kocak, S., *The influence of fiber swelling on paper wetting.*2001.
140. Hossain, L., E. Eastman, M. De Rango, V.S. Raghuwanshi, J. Tanner, and G. Garnier, *Absorption kinetics of nanocellulose foams: Effect of ionic strength and surface charge.* Journal of Colloid and Interface Science, **601**.2021. 124-132.
141. Raja, D., V. Ramesh Babu, G. Ramakrishnan, and M. Senthilkumar, *Effect of cyclic stress on the transverse wicking behaviour of cotton/lycra knitted fabrics.* Journal of The Textile Institute, **104**(5).2013. 502-510.
142. Esteves, L.P. *On the absorption kinetics of superabsorbent polymers*. in *International RILEM Conference on Use of Superabsorbent Polymers and Other New Additives in Concrete*. 2010: p. 77-84. RILEM Publications SARL.
143. Yiamsawas, D., W. Kangwansupamonkon, O. Chailapakul, and S. Kiatkamjornwong, *Synthesis and swelling properties of poly[acrylamide- co-(crotonic acid)] superabsorbents.* Reactive and Functional Polymers, **67**(10).2007. 865-882.
144. Kim, C.H., H.J. Youn, and H.L. Lee, *Preparation of cross-linked cellulose nanofibril aerogel with water absorbency and shape recovery.* Cellulose, **22**(6).2015. 3715-3724.
145. Chavda, H. and C. Patel, *Effect of crosslinker concentration on characteristics of superporous hydrogel.* International journal of pharmaceutical investigation, **1**(1).2011. 17.
146. Zohuriaan-Mehr, M.J. and K. Kabiri, *Superabsorbent polymer materials: a review.* Iranian polymer journal, **17**(6).2008. 451.
147. Sinha, S., *Biodegradable superabsorbents: Methods of preparation and application—A review*, in *Fundamental Biomaterials: Polymers*. 2018, Woodhead Publishing. p. 307-322.
148. Hossain, L., V.S. Raghuwanshi, J. Tanner, C.-M. Wu, O. Kleinerman, Y. Cohen, and G. Garnier, *Structure and swelling of cross-linked nanocellulose foams.* Journal of Colloid and Interface Science, **568**.2020. 234-244.
149. Kaya, M., *Super absorbent, light, and highly flame retardant cellulose-based aerogel crosslinked with citric acid.* Journal of Applied Polymer Science, **134**(38).2017. 45315.
150. Zhang, T., Y. Zhang, X. Wang, S. Liu, and Y. Yao, *Characterization of the nano-cellulose aerogel from mixing CNF and CNC with different ratio.* Materials Letters, **229**.2018. 103-106.
151. Viscosity of Water. *Viscosity Table- Measurement Data*. Available from: https://wiki.anton-paar.com/au-en/water/.
152. Chen, Y., Y. Zhang, F. Wang, W. Meng, X. Yang, P. Li, J. Jiang, H. Tan, and Y. Zheng, *Preparation of porous carboxymethyl chitosan grafted poly (acrylic acid) superabsorbent by solvent precipitation and its application as a hemostatic wound dressing.* Materials Science and Engineering: C, **63**.2016. 18-29.
153. Yang, Y., Z. Tong, Y. Geng, Y. Li, and M. Zhang, *Biobased polymer composites derived from corn stover and feather meals as double-coating materials for controlled-release and*

water-retention urea fertilizers. Journal of agricultural and food chemistry, **61**(34).2013. 8166-8174.
154. Flory, P.J., *Principles of polymer chemistry*. 1953: Cornell University Press.
155. Nelson, P. and C. Kalkipsakis, *The carboxymethylation of a eucalypt kraft pulp.* Tappi, **47**(2).1964. 107.
156. Nelson, P. and C. Kalkipsakis, *The behavior of salts of a carboxymethylated eucalypt kraft pulp.* Tappi, **47**(3).1964. 170-176.
157. Scallan, A. and J. Grignon, *The effect of cations on pulp and paper properties.* Svensk papperstidning, **2**.1979. 40-47.
158. Shah, L.A., M. Khan, R. Javed, M. Sayed, M.S. Khan, A. Khan, and M. Ullah, *Superabsorbent polymer hydrogels with good thermal and mechanical properties for removal of selected heavy metal ions.* Journal of cleaner production, **201**.2018. 78-87.
159. Sadeghi, M. and Z.G. Kouchak, *Swelling kinetics study of hydrolyzed carboxymethylcellulose-poly (sodium acrylate-co-acrylamide) superabsorbent hydrogel with salt-sensitivity properties.*2007.
160. Cheng, W.-M., X.-M. Hu, D.-M. Wang, and G.-H. Liu, *Preparation and characteristics of corn straw-Co-AMPS-Co-AA superabsorbent hydrogel.* Polymers, **7**(11).2015. 2431-2445.
161. Chang, C., M. He, J. Zhou, and L. Zhang, *Swelling behaviors of pH-and salt-responsive cellulose-based hydrogels.* Macromolecules, **44**(6).2011. 1642-1648.
162. Zhao, Y., J. Kang, and T. Tan, *Salt-, pH-and temperature-responsive semi-interpenetrating polymer network hydrogel based on poly (aspartic acid) and poly (acrylic acid).* Polymer, **47**(22).2006. 7702-7710.
163. Lanthong, P., R. Nuisin, and S. Kiatkamjornwong, *Graft copolymerization, characterization, and degradation of cassava starch-g-acrylamide/itaconic acid superabsorbents.* Carbohydrate Polymers, **66**(2).2006. 229-245.
164. Fan, Y., M. Zhang, and L. Shangguan, *Synthesis of a novel and salt sensitive superabsorbent hydrogel using soybean dregs by UV-irradiation.* Materials, **11**(11).2018. 2198.
165. Llanes, L., P. Dubessay, G. Pierre, C. Delattre, and P. Michaud, *Biosourced Polysaccharide-Based Superabsorbents.* Polysaccharides, **1**(1).2020. 51-79.
166. Pourjavadi, A., H. Ghasemzadeh, and H. Hosseinzadeh, *Preparation and swelling behaviour of a novel anti-salt superabsorbent hydrogel based on kappa-carrageenan and sodium alginate grafted with polyacrylamide.* e-Polymers, **4**(1).2004.
167. Ohlsson, T. and N. Bengtsson, *Minimal processing technologies in the food industries*. 2002: Elsevier.
168. Berlin, K.D., *Mechanism and Theory in Organic Chemistry, Second Edition.* Journal of Chemical Education, **59**(4).1982. A143.
169. Savage, A.W., P.D. Warriss, and P.D. Jolley, *The amount and composition of the proteins in drip from stored pig meat.* Meat science, **27**(4).1990. 289.
170. Huff-Lonergan, E. and A. Sosnicki, *Water-holding capacity of fresh meat.* Fact Sheet, **4669**.2002.
171. Eker, B., *A QUALITY ENHANCING PRACTICE IN THE PACKAGING OF CHICKEN MEAT.* Center for Quality.2015.
172. Buchholz, F.L., *Superabsorbent polymers: an idea whose time has come.* Journal of chemical education, **73**(6).1996. 512.
173. Future Market Insights (FMI). *Super absorbent polymer (SAP) market—Global industry analysis, size and forecast.*; Available from: https://www.futuremarketinsights.com/reports/super-absorbent-polymer-market (2015–2020).

174. Ajmeri, J. and C. Ajmeri, *Developments in the use of nonwovens for disposable hygiene products*, in *Advances in Technical Nonwovens*. 2016, Elsevier. p. 473-496.
175. Ehrnsperger, B. and U.F. Schoenborn, *Absorbent cores for absorbent diapers having reduced thickness and improved liquid handling and retention performance and comprising a super absorbent polymer*. 2007, Google Patents.
176. Buchholz, F.L. and N.A. Peppas, *Superabsorbent polymers: science and technology*. 1994: ACS Publications.
177. Patiño-Masó, J., F. Serra-Parareda, Q. Tarrés, P. Mutjé, F.X. Espinach, and M. Delgado-Aguilar, *TEMPO-oxidized cellulose nanofibers: a potential bio-based superabsorbent for diaper production.* Nanomaterials, **9**(9).2019. 1271.
178. Tarrés, Q., H. Oliver-Ortega, M. Llop, M.À. Pèlach, M. Delgado-Aguilar, and P. Mutjé, *Effective and simple methodology to produce nanocellulose-based aerogels for selective oil removal.* Cellulose, **23**(5).2016. 3077-3088.
179. Mendoza, L., L. Hossain, E. Downey, C. Scales, W. Batchelor, and G. Garnier, *Carboxylated nanocellulose foams as superabsorbents.* Journal of colloid and interface science, **538**.2019. 433-439.
180. Ratajczak, K. and M. Stobiecka, *High-performance modified cellulose paper-based biosensors for medical diagnostics and early cancer screening: A concise review.* Carbohydrate polymers, **229**.2020. 115463.
181. Noiphung, J., T. Songjaroen, W. Dungchai, C.S. Henry, O. Chailapakul, and W. Laiwattanapaisal, *Electrochemical detection of glucose from whole blood using paper-based microfluidic devices.* Analytica chimica acta, **788**.2013. 39-45.
182. Khan, M.S., G. Thouas, W. Shen, G. Whyte, and G. Garnier, *Paper diagnostic for instantaneous blood typing.* Analytical chemistry, **82**(10).2010. 4158-4164.
183. Mahato, K., A. Srivastava, and P. Chandra, *Paper based diagnostics for personalized health care: Emerging technologies and commercial aspects.* Biosensors and Bioelectronics, **96**.2017. 246-259.
184. Kuswandi, B. and A.A. Ensafi, *Perspective—Paper-based biosensors: Trending topic in clinical diagnostics developments and commercialization.* Journal of The Electrochemical Society, **167**(3).2019. 037509.
185. Jiang, Q., Y.J. Chandar, S. Cao, E.D. Kharasch, S. Singamaneni, and J.J. Morrissey, *Rapid, point-of-care, paper-based plasmonic biosensor for Zika virus diagnosis.* Advanced Biosystems, **1**(9).2017. 1700096.
186. Liu, B., D. Du, X. Hua, X.Y. Yu, and Y. Lin, *Paper-based electrochemical biosensors: from test strips to paper-based microfluidics.* Electroanalysis, **26**(6).2014. 1214-1223.
187. Mateo, C., J.M. Palomo, G. Fernandez-Lorente, J.M. Guisan, and R. Fernandez-Lafuente, *Improvement of enzyme activity, stability and selectivity via immobilization techniques.* Enzyme and microbial technology, **40**(6).2007. 1451-1463.
188. Sulaiman, S., M.N. Mokhtar, M.N. Naim, A.S. Baharuddin, and A. Sulaiman, *A review: potential usage of cellulose nanofibers (CNF) for enzyme immobilization via covalent interactions.* Applied biochemistry and biotechnology, **175**(4).2015. 1817-1842.
189. Richter, A., G. Paschew, S. Klatt, J. Lienig, K.-F. Arndt, and H.-J.P. Adler, *Review on hydrogel-based pH sensors and microsensors.* Sensors, **8**(1).2008. 561-581.
190. Klouda, L., *Thermoresponsive hydrogels in biomedical applications: A seven-year update.* European Journal of Pharmaceutics and Biopharmaceutics, **97**.2015. 338-349.
191. Tudor, A., L. Florea, S. Gallagher, J. Burns, and D. Diamond, *Poly (ionic liquid) semi-interpenetrating network multi-responsive hydrogels.* Sensors, **16**(2).2016. 219.
192. Jochum, F.D. and P. Theato, *Temperature-and light-responsive smart polymer materials.* Chemical Society Reviews, **42**(17).2013. 7468-7483.

193. Wang, T., X. Yu, Y. Li, J. Ren, and X. Zhen, *Robust, self-healing, and multistimuli-responsive supergelator for the visual recognition and separation of short-chain cycloalkanes and alkanes.* ACS applied materials & interfaces, **9**(15).2017. 13666-13675.
194. Xiong, X., C. Wu, C. Zhou, G. Zhu, Z. Chen, and W. Tan, *Responsive DNA-based hydrogels and their applications.* Macromolecular rapid communications, **34**(16).2013. 1271-1283.
195. Kim, J., J.W. Grate, and P. Wang, *Nanobiocatalysis and its potential applications.* Trends in biotechnology, **26**(11).2008. 639-646.
196. Wang, P., S. Dai, S. Waezsada, A.Y. Tsao, and B.H. Davison, *Enzyme stabilization by covalent binding in nanoporous sol-gel glass for nonaqueous biocatalysis.* Biotechnology and Bioengineering, **74**(3).2001. 249-255.
197. Lee, J., Y. Lee, J.K. Youn, H.B. Na, T. Yu, H. Kim, S.M. Lee, Y.M. Koo, J.H. Kwak, and H.G. Park, *Simple synthesis of functionalized superparamagnetic magnetite/silica core/shell nanoparticles and their application as magnetically separable high-performance biocatalysts.* Small, **4**(1).2008. 143-152.
198. Bertok, T., A. Sediva, A. Vikartovska, and J. Tkac, *Comparison of the 2D and 3D nanostructured lectin-based biosensors for in situ detection of sialic acid on glycoproteins.* International journal of electrochemical science/Electrochemical Science Group, **9**(2).2014. 890.
199. Horgan, A.M., J.D. Moore, J.E. Noble, and G.J. Worsley, *Polymer-and colloid-mediated bioassays, sensors and diagnostics.* Trends in biotechnology, **28**(9).2010. 485-494.
200. Le Goff, G.C., R.L. Srinivas, W.A. Hill, and P.S. Doyle, *Hydrogel microparticles for biosensing.* European polymer journal, **72**.2015. 386-412.
201. Song, H.S., O.S. Kwon, J.-H. Kim, J. Conde, and N. Artzi, *3D hydrogel scaffold doped with 2D graphene materials for biosensors and bioelectronics.* Biosensors and Bioelectronics, **89**.2017. 187-200.
202. Lian, M., X. Chen, Y. Lu, and W. Yang, *Self-assembled peptide hydrogel as a smart biointerface for enzyme-based electrochemical biosensing and cell monitoring.* ACS applied materials & interfaces, **8**(38).2016. 25036-25042.
203. Herrmann, A., R. Haag, and U. Schedler, *Hydrogels and Their Role in Biosensing Applications.* Advanced Healthcare Materials, **n/a**(n/a).2021. 2100062.
204. Uddin, K.M., H. Orelma, P. Mohammadi, M. Borghei, J. Laine, M. Linder, and O.J. Rojas, *Retention of lysozyme activity by physical immobilization in nanocellulose aerogels and antibacterial effects.* Cellulose, **24**(7).2017. 2837-2848.
205. Uddin, K.M.A., V. Jokinen, F. Jahangiri, S. Franssila, O.J. Rojas, and S. Tuukkanen, *Disposable microfluidic sensor based on nanocellulose for glucose detection.* Global Challenges, **3**(2).2019. 1800079.
206. Neubauerova, K., M.C. Carneiro, L.R. Rodrigues, F.T. Moreira, and M.G.F. Sales, *Nanocellulose-based biosensor for colorimetric detection of glucose.* Sensing and Bio-Sensing Research, **29**.2020. 100368.
207. Tilman, D., C. Balzer, J. Hill, and B.L. Befort, *Global food demand and the sustainable intensification of agriculture.* Proceedings of the National Academy of Sciences, **108**(50).2011. 20260-20264.
208. Organisation for Economic Co-operation and Development. *Managing water sustainably is key to the future of food and agriculture*. [cited 2020 12/06/2020]; Available from: https://www.oecd.org/agriculture/topics/water-and-agriculture/.
209. Department of Agriculture, W.a.t.E., . *Water for food*. 2020 [cited 2020 12/06/2020]; Available from: https://www.agriculture.gov.au/water/water-for-food.

210. Pérez-Álvarez, L., L. Ruiz-Rubio, E. Lizundia, and J. Vilas-Vilela, *Polysaccharide-based superabsorbents: synthesis, properties, and applications.* Springer Nature: Cham, Switzerland.2019. 1393-1431.
211. Zhang, M., S. Zhang, Z. Chen, M. Wang, J. Cao, and R. Wang, *Preparation and characterization of superabsorbent polymers based on sawdust.* Polymers, **11**(11).2019. 1891.
212. Hadas, A., L. Kautsky, M. Goek, and E. Erman Kara, *Rates of decomposition of plant residues and available nitrogen in soil, related to residue composition through simulation of carbon and nitrogen turnover.* Soil Biology and Biochemistry, **36**(2).2004. 255-266.
213. Hadas, A., S. Feigenbaum, M. Sofer, J.A.E. Molina, and C.E. Clapp, *Decomposition of Nitrogen-15-Labeled Wheat and Cellulose in Soil: Modeling Tracer Dynamics.* Soil Science Society of America Journal, **57**(4).1993. 996-1001.
214. Bauli, C.R., G.F. Lima, A.G. de Souza, R.R. Ferreira, and D.S. Rosa, *Eco-friendly carboxymethyl cellulose hydrogels filled with nanocellulose or nanoclays for agriculture applications as soil conditioning and nutrient carrier and their impact on cucumber growing.* Colloids and Surfaces A: Physicochemical and Engineering Aspects, **623**.2021. 126771.
215. Sikder, A., A.K. Pearce, S.J. Parkinson, R. Napier, and R.K. O'Reilly, *Recent trends in advanced polymer materials in agriculture related applications.* ACS Applied Polymer Materials, **3**(3).2021. 1203-1217.
216. Chang, L., L. Xu, Y. Liu, and D. Qiu, *Superabsorbent polymers used for agricultural water retention.* Polymer Testing.2020. 107021.

CHAPTER 2
MODULATING NANOCELLULOSE HYDROGELS AND CRYOGELS STRENGTH BY CROSSLINKING AND BLENDING

THIS PAGE WAS INTENTIONALLY LEFT BLANK

Preface

Superabsorbent polymers (SAP) are widely used for a variety of application that ranges from baby diaper to sophisticated sensor development. Their high surface area, high porosity and fast water absorption capacity make them ideal for novel functional applications. Most of the commercial SAPs are petrochemical based and non-renewable. TEMPO mediated oxidized SAP appears as an ideal alternative to these polyacrylic SAPs. However, full structural and swelling characterization is required for TEMPO mediated SAPs to be engineered for their specific application. In this chapter, we studied the mechanical strength of nanocellulose hydrogel and cryogel. Cryogel is the freeze-dried form of the hydrogel, often referred to as nanocellulose foam or SAP. Cryogels structures and properties vary widely for their different applications. For example, the loads sustained by the SAPs (dried hydrogel/cryogel) is specific to its application: the absorbent for food packaging must supports a cut of meat (100-200 g), that for baby diaper must fully swell under the baby (3-10 kg). Cryogel of high compressive strength will not disintegrate when load is applied. Hence, we studied the mechanical strength of SAP in this chapter and modulate the mechanical strength by crosslinking and blending with fibers of different size. This published chapter addresses the first objective of this thesis which is to modulate SAP mechanical strength by crosslinking/blending to have tuneable mechanical strength of nanocellulose SAPs.

THIS PAGE WAS INTENTIONALLY LEFT BLANK

Chapter 2: Modulating Nanocellulose Hydrogels and Cryogels Strength by Crosslinking and Blending

THIS PAGE WAS INTENTIONALLY LEFT BLANK

Modulating nanocellulose hydrogels and cryogels strength by crosslinking and blending

Laila Hossain, Vikram Singh Raghuwanshi, Joanne Tanner, Gil Garnier*

Bioresource Processing Research Institute of Australia (BioPRIA), Department of Chemical Engineering, Monash University, Clayton, Australia

*Corresponding author: gil.garnier@monash.edu

2.1 Abstract

The mechanical strength of hydrogels and cryogels made from carboxylated nanocellulose (NC) fibers can be modulated by chemically/physically crosslinking and blending with different fibrils (shorter/longer). Nano- cellulose hydrogels are produced by oxidizing Bleached Eucalyptus Kraft (BEK) pulp followed by high pressure mechanical treatment. Polyethyleneimine (PEI) and hexamethylenediamine (HMDA) are selected to crosslink nanocellulose hydrogels physically and chemically, respectively. Shorter cellulose nanocrystals (CNC) and longer microcrystalline cellulose (MCC) fibrils are blended with the TEMPO oxidized nano/micro fibers to produce hydrogels of controlled properties. Nanocellulose cryogels are prepared from these hydrogels by a two steps process of freezing and lyophilization. The mechanical properties of nanocellulose hydrogels and cryogels are modulated by controlling the type and density of crosslinking as well as by blending with nano- or microfibrils. Chemical crosslinking (HMDA) increases the hydrogel elastic compression modulus/storage modulus (G′) but does not significantly affect the compressive strength of the cryogel. SAXS reveals the HMDA crosslinked hydrogel to be structurally homogeneous. Physical crosslinking with high molecular weight PEI increases the storage modulus (G′) of nanocellulose hydrogels. Blending a carboxylated nanocellulose fiber suspension with CNC significantly in- creases the cryogel compressive strength. Nanocellulose gel exhibits tunable mechanical strength and absorption capacity from the crosslinking/blending strategy (type and density); this improved fundamental knowledge of the fiber-crosslinker and fiber-cellulose crystal interactions enables greater control and tunability of the properties of hydro- and cryogels for personal and infant care products, as agricultural water retention aids, and for biosensor applications.

2.2 Keywords

Mechanical strength, Nanocellulose, Hydrogel, Cryogel, Cellulose nanocrystal.

2.3 Graphical Abstract

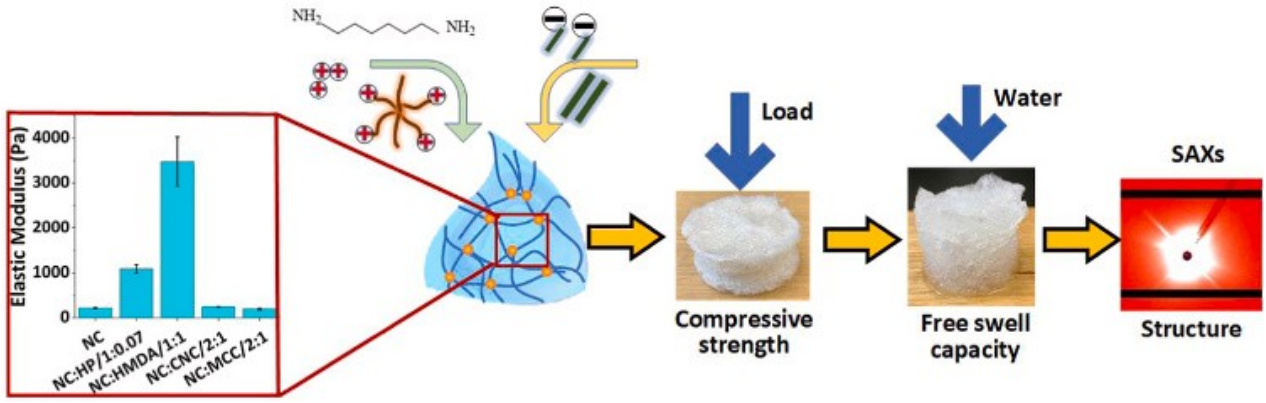

2.4 Introduction

A hydrogel is a three dimensional polymeric network capable of retaining a large volume of water inside its structure [1, 2]. Such polymeric materials have wide-ranging applications as a wet or dried gel, including baby diapers, contact lenses, drug delivery, wound dressing, and tissue engineering, among others [3-7]. The term hydrogel is often used ambiguously to describe both the wet and dried gel forms, although the term “cryogel” describing freeze-dried gels provides clarity [8]. Collectively, hydro- and cryogels can be categorized as synthetic or naturally derived, depending on their raw material [9, 10]. Synthetic hydrogels based on acrylate or acrylamide are the most commonly used for commercial applications, but they are neither renewable nor biodegradable. Common naturally derived hydrogels include alginate, chitosan, collagen, gelatin, starch, hyaluronan, and recently, cellulose [11, 12]. Among those, cellulose-based materials are attractive because of their stiffness, hydrophilicity, ease of functionalization, renewability, biocompatibility, large availability and low cost, making them unique among biodegradable materials [13, 14].

Cellulose is the most abundant biopolymer on Earth. It is found in plants, algae, tunicates and some bacteria [15, 16]. Plant-derived cellulose (and nanocellulose) contains both crystalline and amorphous regions, depending on the local molecular structures [17]. Breaking down the cellulose can produce nanocellulose (NC); it can be produced directly from bacterial strains as well. There

are mainly three types of nanocellulose: (i) cellulose nanofiber (CNF), (ii) cellulose nanocrystal (CNC), and (iii) bacterial cellulose (BC). CNF is prepared either by (i) mechanical treatment, (ii) chemical treatment or (iii) combined chemical and mechanical treatment of plant-derived cellulose. CNF retains both the amorphous and crystalline regions of the original cellulose fibers [18]. CNC is mainly produced by acid hydrolysis of plant-derived cellulose fibers to degrade the amorphous regions and retain the crystalline domains [19]. Bacterial cellulose is produced by microorganisms that excrete pure cellulose directly as nanofibers. In general, nanocellulose is biocompatible and has excellent native gel forming properties [20].

The mechanical properties of a nanocellulose hydrogel govern many of its applications [21] in which crosslinking (type and density) can be a controlling variable. Crosslinking compounds can be broadly categorized as chemical or physical, depending on the type of interaction between the crosslinker and the nanocellulose fiber. Chemical crosslinkers form covalent bonds with nanocellulose fibers. Common examples include methylene-bis-acrylamide, ethylene glycol dimethacrylate (EGDMA), 1,1,1- trimethylolpropane triacrylate (TMPTA), and tetraalyloxy ethane (TAOE) [2, 22]. Epichlorohydrin, hexamethylenediamine (HMDA), aldehydes and aldehyde-based reagents, urea derivatives, and carbodiimides have also been used as crosslinkers for cellulose based hydrogels [23, 24]. Among these, crosslinking of nanocellulose fiber with high carbon amine groups in presence of EDC/sulfo NHS is very efficient with high yield [25].

In physical cross-linking, interacting forces such as hydrogen bonding, electrostatic forces, van der Waals forces, chain entanglements, and ionic and hydrophobic interactions dominate [26]. Physical cross-linking via hydrogen bonding between the carboxyl groups of oxidized cellulose fibers can be achieved by the freeze-thaw technique. The skeletal density of the cellulose fiber matrix is increased upon crystallization of the bulk solvent, which forces the polymer chains to align and form a cohesive network via hydrogen bonding and covalent interaction. Changes in the freeze-thaw cycle affect the resultant hydrogel properties, for example, reduction of porosity [27-29]. High strength polyvinyl alcohol (PVA) hydrogels have been made by this technique, where the strength came from intra and intermolecular hydrogen bonds [30]. The freeze-thaw method has also been used to make high strength hydrogels from hemicellulose, hyaluronic acid and cellulose nano crystal [31-33]. However, the freeze-thawing method has some disadvantages: (i) long cycle times (for example, five cycles or more with 22 hours each) [34] (ii) irregular hydrogel pore spacing and (iii) higher energy consumption due to repeated cycles. Physical crosslinking can also be achieved by the physical interaction of negative cellulose fiber with positive polyelectrolyte molecules, resulting in high mechanical strength. For example, polyethyleneimine

(PEI) has been widely used to crosslink with nanocellulose in the presence of glutaraldehyde [35]. Nanocellulose fibers crosslinked with PEI and allylamine modified PNIPAm particles have been developed and exhibit thermo-responsive behavior [36]. As the definition of physical crosslinking includes hydrogen bonding and ionic/electrostatic interaction [37], the ionic interaction between positive PEI molecules and negative nanocellulose fibers can be designated as physical crosslinking. For a greener physical crosslinking approach, it may be possible to use PEI alone, although there is limited work on this. Therefore, the effect of PEI molecular weights on nanocellulose fibers crosslinking is also poorly understood.

Cryogels are hydrogels that have been dried into porous and highly absorbent structures with high surface area. Cryogels can be produced by supercritical drying, freeze drying, ambient pressure drying, microwave drying, or vacuum drying of hydrogels [38]. Cryogels have been investigated for multifunctional sensor, supercapacitor, insulator, controlled drug release and drug scaffold, and recently, infant care applications [8, 39-43]. The absorption capacity of a cryogel is a critical parameter for all applications, and is related to its cross linking density, internal surface area, and charged functional groups, such as COO^- [44]. Oxidation is the most common treatment to introduce negative hydrophilic COO^- groups on the fiber surface [45, 46]. The hydrophilic functional group (COO^-) of the cryogel network contribute to water absorption while the cross-links between the network chains prevent the cryogel structure from collapsing upon re-wetting [47]. The mechanical/compressive strength of cryogel can also be increased upon cellulose crystal blending [48]. The chain molecules of crystalline cellulose are packed in an orderly manner resulting in higher nanocellulose strength compared to amorphous region [49]. Introducing nano and micro crystal into the nanocellulose cryogel affects the bonding surface area and the total fiber length available for binding.

In spite of their wide commercial use, there is surprisingly limited knowledge describing how physical and chemical crosslinking correlates with hydrogel and cryogel mechanical strength. For example, the change in mechanical strength for hydrogels and cryogels has not been correlated with their physical and chemical crosslinking density. In this study, HMDA is chosen as chemical crosslinker because HMDA is widely known and used due to its six carbon chains, which form chemical crosslinks between nanocellulose fibers more effectively than other low carbon amines. As physical crosslinker, we have used PEI alone to form ionic interaction with nanocellulose fibers while ensuring to avoid any hazardous chemical during gel preparation. Cellulose crystal was blended with nanocellulose fiber to go one step closer towards the sustainability. Blending cellulose crystal is potentially greener option as PEI and HMDA are still chemical additives and

removal of this additives can make the cryogel even greener and sustainable. The effect of cellulose crystals blending has also not been investigated or quantified. In addition, the absorption capacity of physically and chemically crosslinked cryogels, and cryogels produced by blending with cellulose fibrils remains poorly described. There is a need to compare different types of crosslinking and blending agents, and characterize their effect on the mechanical properties of hydrogels and cryogels. Controlling the mechanical strength is important to develop performant superabsorbent when under load; lack of strength can lead to poor performance due to product disintegration.

The objective of this study is therefore to investigate, quantify and control the strength of nanocellulose hydrogels and cryogels. Carboxylated nanocellulose gels were produced that incorporated either: i) a chemical crosslinker (HMDA), ii) a physical crosslinker (PEI) or iii) cellulose crystal. The effect of chemical crosslinking, physical crosslinking, and dissimilar nanocellulose crystals addition on the structural, absorption, and strength properties of nanocellulose hydrogels and cryogels was compared. The structure of the different composites was analyzed by Small Angle X-ray Scattering (SAXS) and related to the properties of these gels for application as renewable, biocompatible and biodegradable superabsorbents. The developed superabsorbent has tunable absorption and mechanical properties which make it suitable to remain integrated under load, such as for meat packaging or baby diaper.

2.5 Methodology

2.5.1 Materials

Bleached Eucalyptus Kraft (BEK) pulp, containing approximately 10 wt.% solids, was obtained from Australian Paper, Maryvale, Australia. 2,2,6,6-Tetramethylpiperidine-1-oxyl (TEMPO), PEI (low molecular weight: M_w ~ 800 Da, M_n ~ 600 Da; high molecular weight: M_w ~ 750,000 Da, M_n ~ 60,000 Da), HMDA, MCC and sodium bromide (NaBr) were purchased from Sigma-Aldrich. CNC suspension (10.3 wt% solid content and 1.1 wt% Sulphur content) was purchased from The University of Maine, USA. Hydrochloric acid (HCl) and Sodium Hydroxide (NaOH) were diluted for solutions as required and were purchased from ACL Laboratories and Merck, respectively. 12 w/v% Sodium Hypochlorite (NaClO) was purchased from Thermo Fisher Scientific and used as received.

2.5.2 Methods

2.5.2.1 Solids concentration

The solids concentration of all samples (i.e. gel or pulp) was determined through oven drying. The sample was weighed before (w_i) and after (w_d) drying. Sample moisture was removed by drying in an oven (Thermoline BTC 9090) at 105°C for at least 6 h. The solids content was calculated as:

$$Solid\ content\ (\%) = \frac{w_d}{w_i} \times 100\%$$

2.5.2.2 TEMPO mediated oxidation

The TEMPO-mediated oxidation of BEK pulp was done by using oxidizing agent NaClO [10]. 25 g BEK pulp (dry weight) was suspended in 2500 mL water containing 0.4g TEMPO and 2.5g NaBr. The 12 w/v% NaClO solution was initially adjusted to pH 10 via addition of 36% HCl. To initiate the oxidation process, 100 mL NaClO was added drop-wise to the suspension whilst stirring. The pH of the reaction was monitored and maintained at 10 through the manual addition of 0.5 M NaOH. The oxidation process was completed in 3 hours. The oxidized fibers were recovered through vacuum filtration and stored refrigerated (2-8°C).

2.5.2.3 Conductometric titration

The carboxylate group content was measured by conductometric titration as reported in previous study [29]. Oxidized pulp samples (approx. 30 mg dry weight) were suspended in 40 mL deionized water. 200 µL of 1% NaCl was added to the suspended sample. The pH of the suspended sample was manually adjusted to between 2.5 and 3 with 0.5 M HCl prior to titration. Titration was accomplished by automated addition of 0.1 M NaOH using a Mettler Toledo T5 titrator. The conductivity of the sample was monitored throughout the titration progress. The carboxyl group content (mmol COO-Na+ /g fiber) was determined by:

$$CC = \frac{c\Delta V}{w} \times 1000$$

where ΔV pertain to the amount of titrant required to neutralize the carboxylic groups (in L), c is the NaOH concentration (mol/L), and w is the sample weight (g).

2.5.2.4 Physical crosslinking

TEMPO-oxidized pulp was dispersed in deionized water at the desired concentration (0.5 g dry fiber in 100 g suspension). Fibrillation was accomplished through a high-pressure homogenizer (GEA Niro Soavi Homogenizer Panda) at 1000 bar for two passes. One-pass homogenized gel was mixed with PEI using an electric hand mixer (ANCO 500). After thorough mixing, the gel was passed through the homogenizer for the second pass, after which physical crosslinking was assumed to have occurred. The samples were stored at 4 °C.

2.5.2.5 Chemical Crosslinking

Oxidized fiber was homogenized at the desired concentration (0.5 g dry fiber in 100 g suspension) at 1000 bar for two passes to produce nanocellulose gel. HMDA was dissolved in deionized water at a concentration of 0.45 g/mL. The nanocellulose gel was crosslinked with this HMDA in ratios of 2:1 and 1:1 (COO^-:NH_2) in presence of EDC/sulfo NHS. The gel was mixed for 5 mins and incubated at room temperature overnight (16 hours).

2.5.2.6 Cellulose crystal blending

TEMPO-oxidized fiber suspension (0.5 g dry fiber in 100 g suspension) was blended with either MCC or CNC at a mass ratio of 2:1. After that fibrillation was achieved in the homogenizer at 1000 bar for two passes to produce the hydrogel.

2.5.2.7 Rheological measurement

Rheological testing of gel samples was performed with an Anton Paar MCR302 rheometer. A cone (0.997°) and plate (49.975 mm) geometry was selected. Testing was performed at ambient temperature (25 °C). A solvent trap was used to ensure stable temperature during measurements. Viscosity was measured at shear rates ranging from 0.5 to 100 s^{-1}. Oscillatory strain sweep was performed from 0.01 to 100% at a constant 1 Hz frequency.

2.5.2.8 Preparation of Nanocellulose Cryogels

The cryogels were prepared by spreading 12 g of gel evenly over the base of a 50 mm petri dish and freezing the sample at -86°C, then freeze-drying (Christ Alpha 2-4 LD Plus) for 2 days.

2.5.2.9 Fourier Transform Infrared (FTIR) spectroscopy

Cryogel samples were analyzed by Fourier Transform Infrared (FTIR) spectroscopy (Agilent Technologies Cary 630 FTIR) which is equipped with a diamond attenuated total reflectance (ATR) accessory. Eight scans were taken at 4 cm^{-1} resolution.

2.5.2.10 Free swell capacity

The cryogel sample was placed in a glass funnel, which is immersed in a container full of testing fluid. To measure the absorption over time, the funnel with the sample was removed from the fluid container and the excess fluid allowed to drain for five minutes. The total mass was then measured at regular intervals of 3 hours. The free swell capacity was then calculated as follows:

$$\text{Free Swell Capacity (FSC)} = \frac{m_t - m_i}{m_i}$$

Where m_t is the mass of the swollen cryogel at a particular time interval and m_i is the initial mass of the dry cryogel.

2.5.2.11 Compression Testing

Cylindrical cryogel samples of 37 mm diameter and 37 mm length were prepared for compressive testing. Force-displacement data for cryogel samples was obtained by Instron model 5965 Universal Testing Machine equipped with 1kN load cell. The testing was done at 23°C and 50% humidity at a compression rare of 5 mm/min. The compressive Young's Modulus was determined from the slope of the initial linear region of the stress-strain curve.

2.5.2.12 SAXS

The SAXS measurements were conducted at the SAXS/WAXS beamline of the Australian Synchrotron. The X-ray energy of 12 keV (wavelength was 1.03 Å) and the sample to detector

distance of 7 m was used for the measurement. All the samples were measured in the transmission mode. A Pilatus 1M detector is used to collect the scattered X-ray photons from the sample. Silver behenate and glassy carbon standards are used to calibrate the scattering vector q and normalized the scattering curve in the absolute scattering cross sections. The scattering vector q is related to the scattering angle 2θ and X-rays wavelength (λ) by the relation $q = \frac{4\pi sin\theta}{\lambda}$. A ScatterBrain software is used to perform the data reduction and radial averaging.

The scattering vector q is used to determine the average inter-particle distance (d) from the correlation peak by the relation $q = \frac{2\pi}{d}$. Moreover, the scattering intensity I (q) at different q range follows different power law as:

$$I(q) = cq^{-\alpha}$$

Where, c is the prefactor and the value α is the characteristic of mass fractals and compact structures. The value of α between 3 and 4 resembles the scattering from the surface and compact structures.

2.6 Results

The structural and strength properties of physically (low molecular weight: LMW and high molecular weight: HMW PEI) and chemically (HMDA) crosslinked gels were quantified. Nanocellulose gel with 1.3 mmol COO^-/g fiber reinforced with cellulose fibrils of different length scales: long (MCC) and short (CNC) were also prepared and their properties compared with those of the crosslinked gels. The composition and identification of all nanocellulose gels are summarized in Table 2-1. The water content of physically crosslinked hydrogel and CNC blended hydrogel is compared with neat hydrogel in Table 2-S1.

Table 2-1: Description and characterization of the nanocellulose gels composition.

Sample code	Sample details
NC	Pure nanocellulose gel
NC:HP/1:0.05	Nanocellulose gel physically crosslinked with 5 w/w% HMW PEI
NC:HP/1:0.07	Nanocellulose gel physically crosslinked with 7 w/w% HMW PEI
NC:LP/1:0.05	Nanocellulose gel physically crosslinked with 5 w/w % LMW PEI
NC:LP/1:0.07	Nanocellulose gel physically crosslinked with 7 w/w% LMW PEI

NC:HMDA/2:1	Nanocellulose gel chemically crosslinked with HMDA at nanocellulose COO^- to amine ratio 2:1
NC:HMDA/1:1	Nanocellulose chemically crosslinked with HMDA with nanocellulose COO^- to amine ratio 1:1
NC:CNC/2:1	Nanocellulose blended with cellulose nano crystal at nanocellulose to CNC blend mass ratio 2:1
NC:MCC/2:1	Nanocellulose blended with MCC at nanocellulose to MCC blend mass ratio 2:1

2.6.1 Physical crosslinked hydrogels

PEI was chosen as the physical crosslinker with nanocellulose hydrogel as it is known to adsorb on cellulose. The molecular weight of PEI plays an important role in determining the hydrogel strength. High molecular weight PEI improved the hydrogel strength significantly. Figure 2-1 shows the rheological properties of hydrogels as a function of concentration for (a) low and (b) high molecular weight PEI. At low shear stress, the elastic modulus (G') is dominant over the viscous modulus (G"), which indicates that the hydrogel behaves more like a solid material under these conditions, as G' represents gel stiffness or strength. After the intersection point of G' and G", the material flows like a liquid as the viscous modulus exceeds the elastic modulus. G" is the viscous or loss modulus; it indicates the portion of the deformation energy that is lost to internal friction during shearing. At first, G" is constant as the gel behaves like a uniform 3D network. G" then increases with increasing shear as micro cracks appear. Initially, the elastic behavior is dominant. As shear increases further, micro cracks grow, merge and develop into continuous macro cracks which result in gel rupture at the highest value of G". Passed this point, the bulk material starts to flow, as indicated by the dominant viscous modulus (G") after the intersection of G' and G", which occurs at the G" maxima.

Adding a low molecular weight PEI as a physical crosslinker weakens the nanocellulose hydrogel. Here, PEI acts a plasticizer and presents no evidence of crosslinking with cellulose. The viscous and elastic moduli of the LP adsorbed hydrogels (NC:LP) are lower than those of the nanocellulose hydrogel (Figure 2-1a). The modulus intersections are also shifted toward higher shear strains, indicating a more cream-like behavior of the hydrogel. The addition of 5 w/w % HP to nanocellulose hydrogels also does not significantly affect their rheological behavior (Figure 2-1b). However, increasing the HP concentration to 7 w/w % significantly increases the mechanical strength (by up to 5 times) compared to pure nanocellulose hydrogel (Figure 2-1a) because of

bridge formation between nanocellulose fibers. The intersection of G' and G" also shifts to lower shear strain with increasing concentration of HP from 5 w/w % to 7 w/w %, indicating non-creamy or brittle hydrogel formation. The types of interaction between nanocellulose and PEI therefore depend on the molecular weight of PEI, which results in different hydrogel rheology.

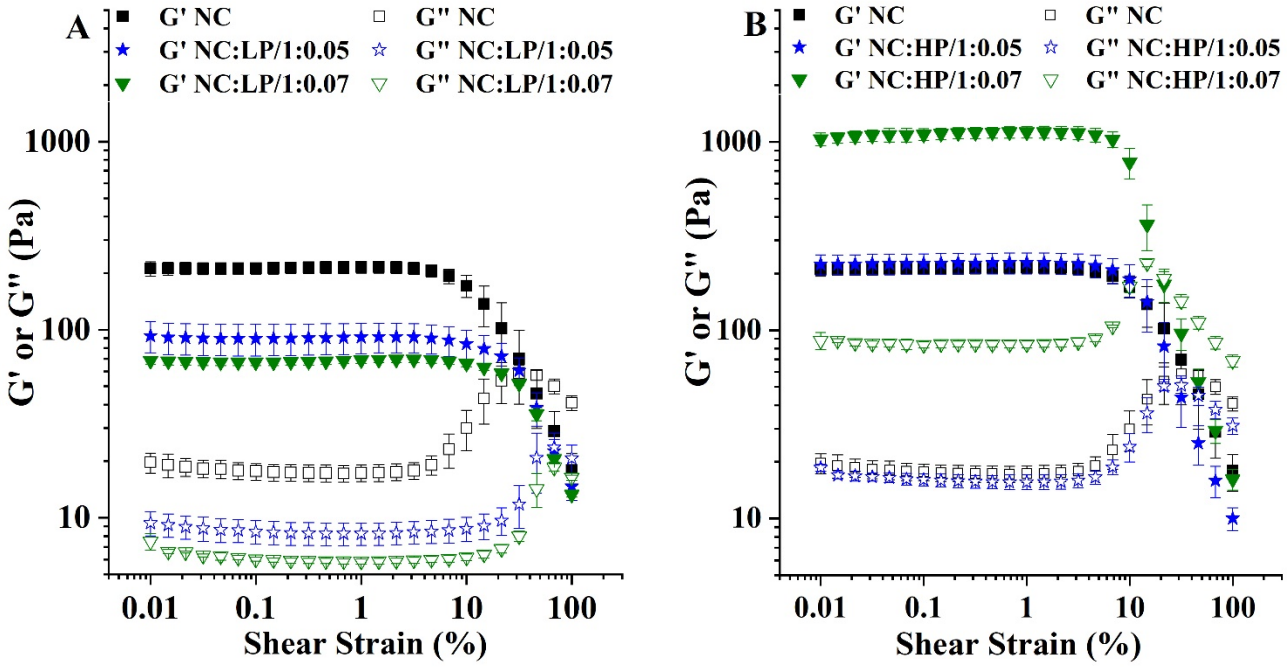

Figure 2-1: Viscoelastic properties of TEMPO-oxidized cellulose hydrogels crosslinked with different concentrations of PEI varying in molecular weight: (A) hydrogels with low molecular weight PEI (LP) and (B) hydrogels with high molecular weight PEI (HP). Two PEI concentrations were tested: 5% and 7%, and the Elastic (G') and viscous (G") moduli were recorded as a function of strain. Oscillation frequency and temperature were kept constant at 1 Hz and 25°C, respectively.

2.6.2 Chemical crosslinked hydrogels

Chemical crosslinking of nanocellulose hydrogel with HMDA significantly increases hydrogel strength (Figure 2-2). Adding HMDA to nanocellulose hydrogel at a carboxyl to amine group ratio of 2:1 results in a four-fold increase in the elastic modulus (G') compared to the neat nanocellulose hydrogel. Increasing the HMDA ratio up to 1:1 augments G' by 15 times. These increases in viscous and elastic moduli result from the formation of amide bonds between nanocellulose hydrogel carboxyl and the HMDA amine groups.

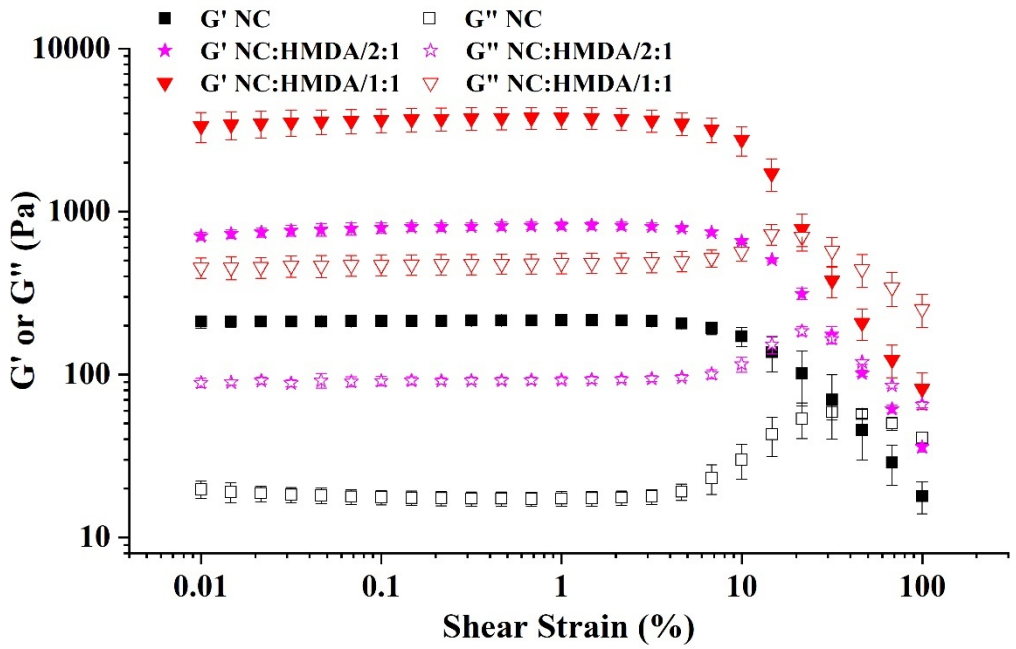

Figure 2-2: Viscoelastic properties of TEMPO-oxidized cellulose hydrogels crosslinked with HMDA at different concentrations. Two NC:HMDA carboxyl to amine group ratio concentrations were tested: 1:1 and 2:1. Elastic (G') and viscous (G") moduli were recorded as a function of strain. Measurements were performed at a frequency of 1 Hz and a temperature of 25°C.

2.6.3 Blending cellulose fibrils to hydrogels

The strength of nanocellulose hydrogels blended with cellulose fibrils of different length scales - microscale with MCC or nanoscale with CNC - was tested (Figure 2-3). These blended hydrogels do not show any significant change in G' or G" compared to the neat nanocellulose hydrogel. However, blending the fibrils shifted the moduli intersections (shown by the vertical dotted lines in Figure 2-3) to a lower shear strain of 10% for NC:CNC/2:1, 21.7% for NC:MCC/2:1 compared to neat NC at 31.7%, indicating the formation of a stronger gel.

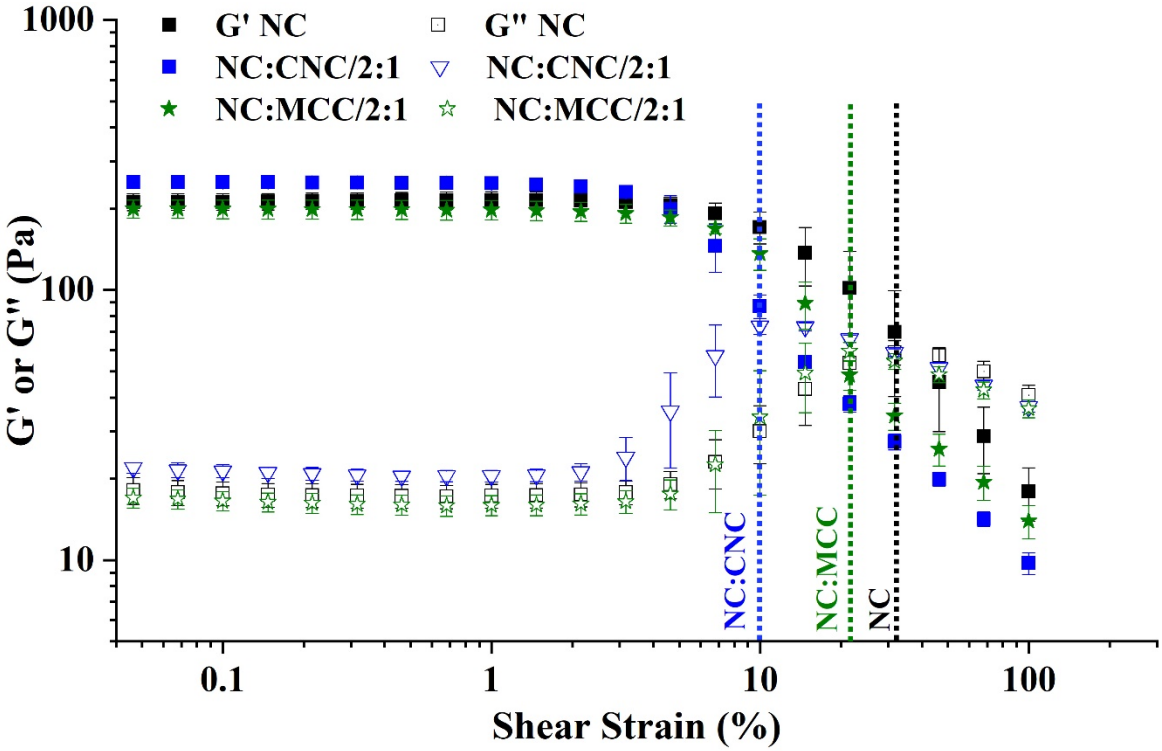

Figure 2-3: Viscoelastic properties of TEMPO-oxidized cellulose hydrogels blended with CNC and MCC. NC:(CNC or MCC) ratio concentrations was set at 2:1. Elastic (G') and viscous (G") moduli were recorded as a function of strain. Measurements were performed at a frequency of 1 Hz and a temperature of 25°C. The moduli intersection points are indicated by the vertical dotted lines.

2.6.4 Nanocellulose cryogels ATR-FTIR

Chemical crosslinking in the HMDA-NC cryogel was confirmed by ATR-FTIR (Figure 2-4). The sharp peak at 1600 cm^{-1} for neat nanocellulose cryogel is due to the C=O stretching of the COO^- group on the oxidized fiber. For the crosslinked sample, C-N bending appears at 1240 cm^{-1} due to the presence of the amine group. C=O stretching from the amide bond is merged with the C=O stretching for COO^- group in the crosslinked sample. Figure 2-S1 shows all other samples FTIR spectra.

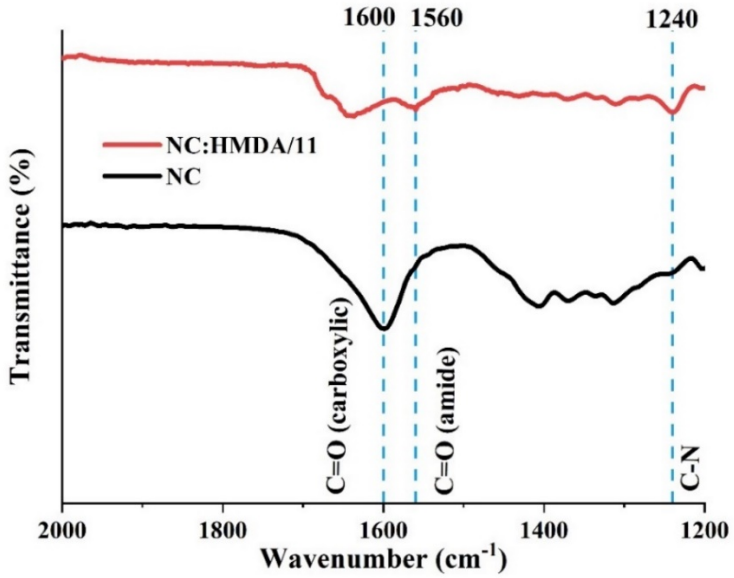

Figure 2-4: ATR-FTIR spectra of pure nanocellulose cryogel and chemically (HDMA) crosslinked cryogel demonstrating effective chemical reaction.

2.6.5 Cellulose cryogels mechanical strength

The compressive strength of the cryogels produced from the neat, crosslinked, and blended nanocellulose hydrogels is shown in Figure 2-5. The cryogel produced from blended hydrogels showed increased mechanical strength. Neither chemical nor physical crosslinking of the hydrogels increased the mechanical strength of their cryogels. The stress-strain curve is shown in Figure 2-S2. Cryogel images at different states (before and after compression, after re absorption) are shown in Figure 2-S3.

2.6.6 Nanocellulose cryogel Free swell capacity

The free swell capacity (FSC) and water retention capacity (WRC) of the neat nanocellulose cryogel are the highest (Figure 2-6). The physically and chemically crosslinked cryogels have the lowest absorption and water retention capacity, while the cryogels blended with CNC and MCC show intermediate performance. Physically and chemically crosslinked cryogels showed a decrease in free swell capacity of 48% and 51% respectively, compared to the neat nanocellulose cryogel.

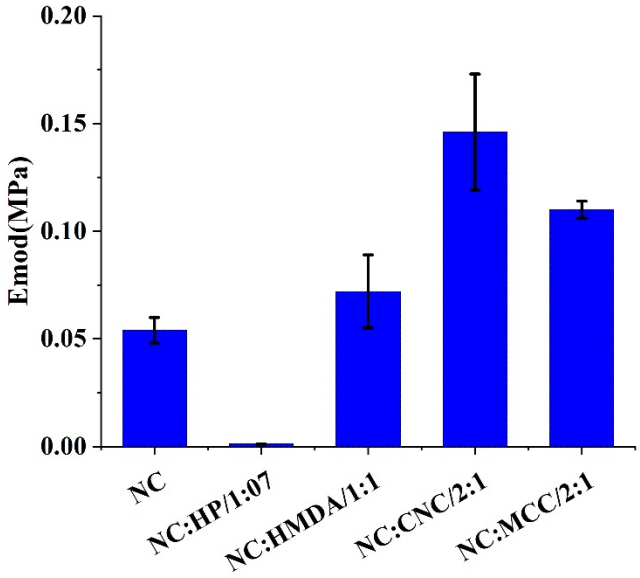

Figure 2-5: Effect of crosslinking and blending on the compressive modulus (E_{mod}) of nanocellulose cryogels.

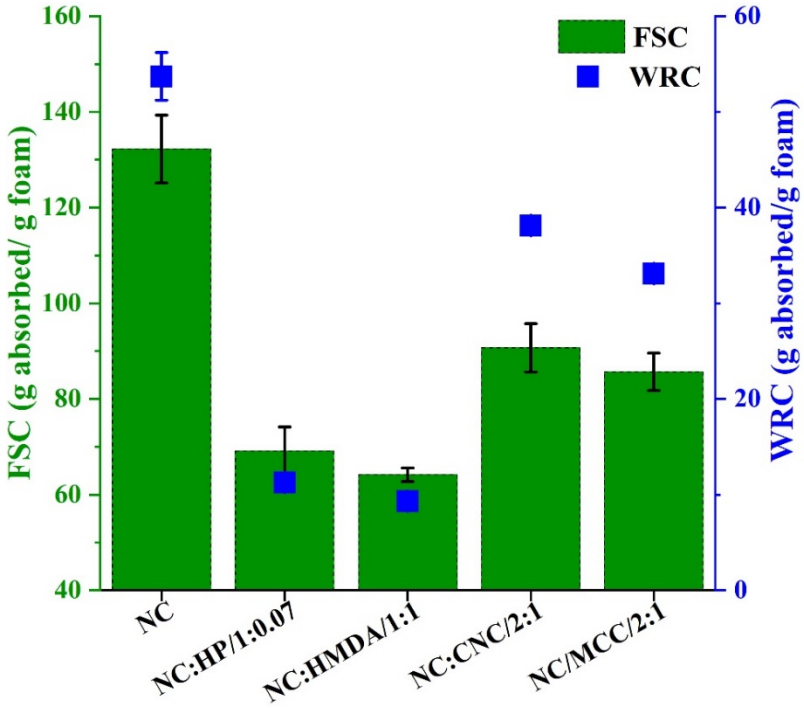

Figure 2-6: Free swell capacity (FSC) and water retention capacity (WRC) of nanocellulose cryogels tested for MilliQ water.

2.6.7 Structural analysis by Small Angle X-ray Scattering (SAXS)

SAXS measurements were performed to reveal the network structure and fiber arrangement, and to visualize the water penetrating the spaces in hydrogel, cryogel and rewetted cryogel samples (Figure 2-7). The different sections of the SAXS curve reveal the fiber structural arrangement at different dimensions before and after water penetration.

For hydrogels, the SAXS curves for neat and crosslinked samples show significant differences, indicating variations in structure (Figure 2-7a). The upturn in the lower q value (0.003 to 0.006 $Å^{-1}$) of all curves indicates that the surface scattering from the large structures of bigger pores/interfibrillar spaces is similar. However, there is noticeable difference in the SAXS curve shape observed between q = 0.003 and 0.2 $Å^{-1}$. The bump in this range is due to the difference in scattering length between the water and the cellulose fibers. The neat nanocellulose hydrogel curve shows a bump between q = 0.015 and 0.22 Å-1, corresponding to a pore size range of 42 – 2.8 nm. The HMDA crosslinked hydrogel shows large bump area between q = 0.01 and 0.23 $Å^{-1}$, indicating a larger pore size range of 63 – 2.7 nm. The HP crosslinked hydrogel shows a bump similar to that of HMDA; however, the bump is more pronounced in the HMDA-crosslinked sample. This indicates that both crosslinked samples have large open structures, but that the HMDA crosslinked sample has a more homogenous distribution of spaces than the HP crosslinked sample. The CNC blended hydrogel shows a shift in the bump towards a q range of between 0.002 and 0.06 $Å^{-1}$, corresponding to a pore size range of 314 – 11 nm. The large size range in the blended sample is due to the repulsion between the cellulose fibers and CNC which forces the network to expand and creates more space between fibers.

For the cryogels, the SAXS curves do not show any significant difference among samples, except for HMDA crosslinked cryogel (Figure 2-7b). The curves follow the power law of q^{-4}, indicating that the cellulose fibers tend to aggregate during drying, and therefore leave large size structures and open-air spaces in the resulting cryogels. However, the HMDA crosslinked sample shows a bump (q = 0.05 to 0.2 $Å^{-1}$), indicating the presence of some smaller size pores of size ranging between 12 - 2 nm in the structure.

Upon rewetting, water is absorbed into both the fibers and the pores of the cryogels. The SAXS curves from rewetted cryogels (Figure 2-7c) show significant differences compared to the dried samples (Figure 2-7b). The bumps in the rewetted sample curves indicate that the scattering from the swollen fibers and the spaces between them are filled with water. In all samples, the bump appears at almost the same q range (0.014 to 0.22 $Å^{-1}$). The corresponding pore size range of the

space is between 45 - 2.8 nm. This indicates the water molecules penetrate and occupy similar sized spaces between fibers in all samples. However, the fiber bundle swelling behavior is significantly different between the samples, as reported previously for PEI and HMDA crosslinked samples [24]. At the low q range (< 0.014 $Å^{-1}$) the power law ranges from $q^{-3.5}$ to q^{-4}, indicating that the larger structure is formed by fiber entanglement and large pores.

The SAXS curves of the rewetted cryogels also differ from their corresponding hydrogels. This qualitatively indicates that the presence and correlation of the water molecules with the network is different in the hydrogels and rewetted cryogels. Therefore, simply rewetting a cryogel does not reform the corresponding hydrogel due to differences in the fiber structure of the hydrogels and cryogels that lead to differences in the interactions of the water molecules with and within the structure upon rewetting.

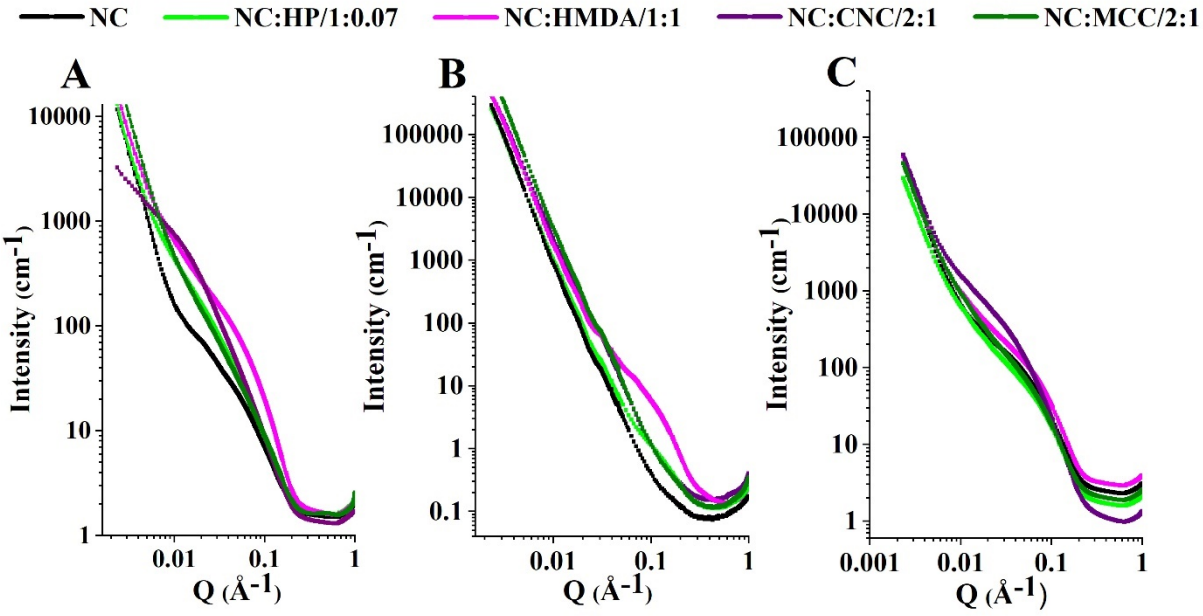

Figure 2-7: Small Angle X-ray (SAXS) measurements of (A) Hydrogel, (B) Cryogel and (C) cryogel rewetted with MilliQ water.

2.7 Discussion

2.7.1 Effect of crosslinking and blending on nanocellulose hydrogels

TEMPO oxidized nanocellulose hydrogels are made of entangled nanocellulose fibrils held together by electrostatic stabilization [50]. Here, chemical or physical crosslinkers and cellulose fibrils are used to modify the properties of the hydrogels. Physical crosslinking of nanocellulose

hydrogel with a dendrimer polyelectrolyte such as PEI affects the rheological properties (to higher or lower elastic moduli) depending on the polymer molecular weight. Chemical crosslinking with HMDA increases the elastic moduli of the gel because of strong amide bond formation between the negative carboxylic group of cellulose and the positive amine of HMDA. Blending nano or micro cellulose fibrils does not have any significant effect on the elastic or viscous moduli of the hydrogel.

PEI molecular weight plays an important role in the hydrogel rheology. For the low molecular weight polyelectrolytes of high charge density, neutralization of the nanocellulose fiber charge occurs by the positively charged PEI amine group [51, 52] (Figure 2-8A), decreasing inter-fiber repulsion between the COO^- groups. The LP molecule is too short to link COO^- groups and form a bridge between nanocellulose fibers and therefore acts as a plasticizer, increasing the liquid-like behavior of the hydrogel. This is indicated by the low G' and G" measured for LP crosslinked hydrogel (Figure 2-1) [53]. Conversely, bridging between the PEI amine groups and nanocellulose fiber COO^- groups does occur for HP [54, 55] (Figure 2-8b), as revealed by the increase of G' and G" by up to 5 times for HP crosslinked hydrogel over the neat nanocellulose hydrogel.

Chemical crosslinking with HMDA produces a strong chemical bond, resulting in higher elastic and viscous moduli for the chemically crosslinked hydrogel than for the physically crosslinked hydrogel. The strong crosslinking density of the HMDA sample was 1.40 mol/m^3, and HP crosslinked hydrogel has a lower crosslinking density of 0.44 mol/m^3.

CNC has a strong negative surface charge which repels the negative charge of oxidized nanocellulose fibers (Figure 2-8C). MCC particles have no specific surface charge, resulting in gels with a heterogeneous structure, as indicated by the SAXs curve (Figure 2-7A and Figure 2-8D). As a result, the blended hydrogel with CNC has a much more homogeneous structure compared to the blended MCC hydrogel, as revealed by a hump in SAXS scattering for CNC blended hydrogel (Figure 2-7A). However, the rheological properties of MCC and CNC blended hydrogels are not significantly different to those of the neat hydrogel. This is because they do not form fiber-fiber bonds, unlike those created in crosslinked hydrogels.

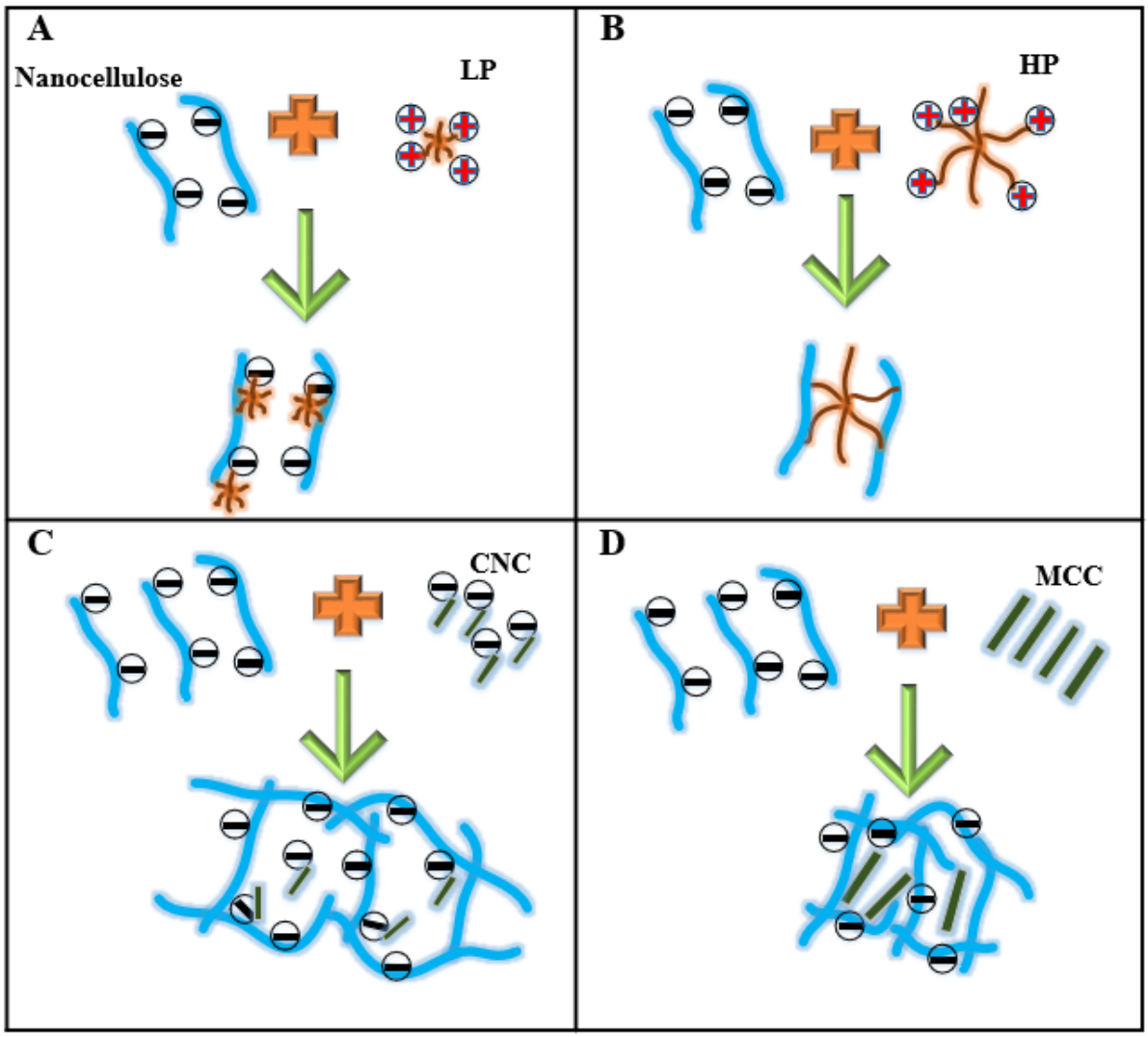

Figure 2-8: Schematic representation of the crosslinking interaction and blending agents with nanocellulose (A) nanocellulose with LP, (B) nanocellulose with HP, (C) nanocellulose with CNC and (D) nanocellulose with MCC.

2.7.2 Effect of crosslinking and blending on nanocellulose cryogels

Nanocellulose hydrogels are freeze dried into cryogels. Crosslinking or blending a nanocellulose hydrogel prior to drying affects the mechanical and absorption properties of the resulting cryogel differently depending on the crosslinking or blending type and density. In this study, the mechanical properties of cryogels were quantified by compressive strength and their absorption capacities measured by free swell capacity measurements followed by centrifugation to determine the water retention capacity.

The HP crosslinked cryogel structure is very open compared to the original nanocellulose one, as revealed by SAXs analysis (Figure 2-7). Structural openness is also visible in these samples via optical microscopy and SEM imaging, as shown in Figure 2-S4 and 2-S5. The HP crosslinked cryogel shows the lowest compressive strength due to its more open and brittle structure [24]. The compressive strength of the chemically crosslinked (HMDA) cryogel does not change significantly, compared to the neat sample, as the small HMDA molecules only crosslink between adjacent fibers, which does not increase the compressive modulus of the corresponding cryogel. Blended CNC hydrogels result in corresponding cryogels with a significantly increased compressive strength of 0.146 MPa compared to 0.054 MPa for the neat nanocellulose cryogel. This increase in mechanical strength is supported by literature where CNC incorporation with cellulose nanfiber (CNF) produces cryogel with 0.165 MPa of compressive strength when CNF to CNC ratio is 1:3 [48]. CNC has a much smaller particle diameter (~5 nm) than MCC (~50 μm). The surface area of reinforcement provided by CNC is four orders of magnitude higher than for MCC, resulting in a higher area of interaction, increased structural reinforcement, and therefore the highest mechanical strength results for CNC-NC blended cryogel.

The neat nanocellulose cryogel shows the highest absorption capacity, while chemically and physically crosslinked cryogels have similar, lower absorption capacity, despite their significant structural differences. The compact structure of the chemically crosslinked hydrogel, which is a result of the amide-COO^- bond formation, hinders water penetration within the pores of the material, resulting in a lower absorption capacity than the neat cryogel. The open structure of the physically crosslinked cryogel cannot contain as much water, therefore also resulting in lower absorption capacity [24] and water retention capacity than that of the neat cryogel. For cryogels made by blending MCC or CNC, the absorption properties decrease in comparison to those of the neat sample because of the lower availability of COO^- groups and the incorporation of cellulose crystals, which hinder water penetration inside the structure (Figure 2-6).

Physical and chemical crosslinking with HP and HMDA, respectively, does increase the mechanical strength of the resulting hydrogel, but not that of the corresponding cryogel. The CNC blended NC cryogel shows increased compressive strength due to the higher area of reinforcement resulting from the incorporation of the small, rod shaped, negatively charged CNC particles. So, although hydrogels and cryogels are simply different forms of a nanocellulose gel having the same original chemical composition, their mechanical strengths vary significantly as a function of crosslinking and blending.

2.8 Conclusion

A family of cellulose hydrogels and cryogels was developed from TEMPO oxidized cellulose nanofibers (CNF) by incorporating physical and chemical crosslinkers or by blending with cellulose fibrils of different relative lengths. The effect of the type of crosslinking or cellulose crystal addition on the mechanical properties of both the hydrogel and corresponding cryogel was quantified. Gel properties were measured by rheology, mechanical strength, and absorption capacity; structure was quantified by SAXS, optical and scanning electron microscopy. Differences in the properties were related to differences in the hydrogel and cryogel composition, structure and mechanical strength.

Chemically crosslinked hydrogel showed the highest strength compared to all other hydrogel because of strong chemical bond between nanocellulose and the crosslinker. Hydrogels physically crosslinked with high molecular weight PEI had higher elastic and viscous moduli than neat nanocellulose hydrogel due to fiber bridging. Crosslinking with a low molecular weight PEI reverses the behavior, showing decreased elastic and viscous moduli due to charge neutralization. This highlights the effect of PEI molecular weight on the strength of oxidized cellulose nanofiber gels. The addition of CNC or MCC to CNF to create a blended hydrogel had no significant effect on the rheological properties.

The highest cryogel compressive strength was achieved by blending CNC with CNF. Chemical crosslinking with HMDA did not affect the cryogel compressive strength significantly. However, physical crosslinking with high molecular weight PEI significantly decreased the compressive strength of the nanocellulose cryogel by opening up its structure. The neat nanocellulose cryogel has the highest free swell capacity and water retention capacity as it has the highest concentration of available COO^- groups.

This study quantifies the effect of chemical and physical crosslinking and cellulose crystal blending on the structure and mechanical properties of NC hydrogels and cryogels. These results improve the understanding of the hydrogel-cryogel structure-property relationships and facilitate the development of tunable hydrogel and cryogel materials for food, agriculture and diagnostic applications.

2.9 Acknowledgements

Financial support was received from Meat and Livestock Australia (grant number P.PSH. 0890). The authors acknowledge Australian Synchrotron for the facilities used. Thanks to Assoc Professor Rico Tabor for the rheological facilities.

2.10 References

1. Kiatkamjornwong, S., *Superabsorbent polymers and superabsorbent polymer composites.* Sci. Asia, **33**(1).2007. 39-43.
2. Zohuriaan-Mehr, M.J. and K. Kabiri, *Superabsorbent polymer materials: a review.* Iranian polymer journal, **17**(6).2008. 451.
3. Masuda, F. *Trends in the development of superabsorbent polymers for diapers*. in *ACS symposium series*. 1994.
4. Caló, E. and V.V. Khutoryanskiy, *Biomedical applications of hydrogels: A review of patents and commercial products.* European Polymer Journal, **65**.2015. 252-267.
5. Li, J. and D.J. Mooney, *Designing hydrogels for controlled drug delivery.* Nature Reviews Materials, **1**(12).2016. 1-17.
6. Li, J., A. Celiz, J. Yang, Q. Yang, I. Wamala, W. Whyte, B. Seo, N. Vasilyev, J. Vlassak, and Z. Suo, *Tough adhesives for diverse wet surfaces.* Science, **357**(6349).2017. 378-381.
7. Tang, J.D., C. Mura, and K.J. Lampe, *Stimuli-responsive, pentapeptide, nanofiber hydrogel for tissue engineering.* Journal of the American Chemical Society, **141**(12).2019. 4886-4899.
8. García-González, C., M. Alnaief, and I. Smirnova, *Polysaccharide-based aerogels—Promising biodegradable carriers for drug delivery systems.* Carbohydrate Polymers, **86**(4).2011. 1425-1438.
9. Zavan, B., R. Cortivo, and G. Abatangelo, *Hydrogels and tissue engineering*, in *Hydrogels*. 2009, Springer. p. 1-8.
10. Barajas-Ledesma, R.M., A.F. Patti, V.N. Wong, V.S. Raghuwanshi, and G. Garnier, *Engineering nanocellulose superabsorbent structure by controlling the drying rate.* Colloids and Surfaces A: Physicochemical and Engineering Aspects, **600**.2020. 124943.
11. Cui, X., J.J. Lee, and W.N. Chen, *Eco-friendly and biodegradable cellulose hydrogels produced from low cost okara: towards non-toxic flexible electronics.* Scientific reports, **9**(1).2019. 1-9.
12. Tang, G., B. Zhou, F. Li, W. Wang, Y. Liu, X. Wang, C. Liu, and X. Ye, *Advances of Naturally-derived and Synthetic Hydrogels for Intervertebral Disc Regeneration.* Frontiers in Bioengineering and Biotechnology, **8**.2020. 745.
13. Sannino, A., C. Demitri, and M. Madaghiele, *Biodegradable cellulose-based hydrogels: design and applications.* Materials, **2**(2).2009. 353-373.
14. Barajas-Ledesma, R.M., L. Hossain, V.N. Wong, A.F. Patti, and G. Garnier, *Effect of the counter-ion on nanocellulose hydrogels and their superabsorbent structure and properties.* Journal of Colloid and Interface Science, **599**.2021. 140-148.
15. Vazquez, A., M.L. Foresti, J.I. Moran, and V.P. Cyras, *Extraction and production of cellulose nanofibers*, in *Handbook of polymer nanocomposites. Processing, performance and application*. 2015, Springer. p. 81-118.
16. Trache, D., M.H. Hussin, C.T.H. Chuin, S. Sabar, M.N. Fazita, O.F. Taiwo, T. Hassan, and M.M. Haafiz, *Microcrystalline cellulose: Isolation, characterization and bio-*

composites application—A review. International Journal of Biological Macromolecules, **93**.2016. 789-804.
17. Chen, Y., X. Jiang, H. Wu, and L. Zheng, *Thermal behavior of complex model with the cellulose II and amorphous chain.* Journal of Theoretical and Computational Chemistry, **19**(03).2020. 2040004.
18. Habibi, Y., H. Chanzy, and M.R. Vignon, *TEMPO-mediated surface oxidation of cellulose whiskers.* Cellulose, **13**(6).2006. 679-687.
19. Abitbol, T., A. Rivkin, Y. Cao, Y. Nevo, E. Abraham, T. Ben-Shalom, S. Lapidot, and O. Shoseyov, *Nanocellulose, a tiny fiber with huge applications.* Current opinion in biotechnology, **39**.2016. 76-88.
20. Ahmed, S. and S. Ikram, *Chitosan based scaffolds and their applications in wound healing. Achiev Life Sci 10: 27–37*. 2016.
21. Dias, O.A.T., S. Konar, A.L. Leão, W. Yang, J. Tjong, and M. Sain, *Current state of applications of nanocellulose in flexible energy and electronic devices.* Frontiers in Chemistry, **8**.2020.
22. Chavda, H. and C. Patel, *Effect of crosslinker concentration on characteristics of superporous hydrogel.* International journal of pharmaceutical investigation, **1**(1).2011. 17.
23. Sinha, S., *Biodegradable superabsorbents: Methods of preparation and application—A review*, in *Fundamental Biomaterials: Polymers*. 2018, Woodhead Publishing. p. 307-322.
24. Hossain, L., V.S. Raghuwanshi, J. Tanner, C.-M. Wu, O. Kleinerman, Y. Cohen, and G. Garnier, *Structure and swelling of cross-linked nanocellulose foams.* Journal of Colloid and Interface Science, **568**.2020. 234-244.
25. Hermanson, G.T., *Bioconjugate techniques*. 2013: Academic press.
26. Kayra, N. and A.Ö. Aytekin, *Synthesis of cellulose-based hydrogels: Preparation, formation, mixture, and modification.* Cellulose-Based Superabsorbent Hydrogels.2019. 407-434.
27. Jiang, F. and Y.-l. Hsieh, *Super water absorbing and shape memory nanocellulose aerogels from TEMPO-oxidized cellulose nanofibrils via cyclic freezingthawing.* J. Mater. Chem. A, **2**(2).2013. 350-359.
28. Liu, L., L. Bai, A. Tripathi, J. Yu, Z. Wang, M. Borghei, Y. Fan, and O.J. Rojas, *High axial ratio nanochitins for ultrastrong and shape-recoverable hydrogels and cryogels via ice templating.* ACS nano, **13**(3).2019. 2927-2935.
29. Zainal, S.H., N.H. h Mohd, N. Suhaili, F.H. Anuar, A.M. Lazim, and R. Othaman, *Preparation of Cellulose-based Hydrogel: A Review.* Journal of Materials Research and Technology.2020.
30. Zhang, X., W. Huo, S. Yan, Y. Chen, K. Gan, J. Liu, and J. Yang, *Innovative application of PVA hydrogel for the forming of porous Si3N4 ceramics via freeze-thaw technique.* Ceramics International, **44**(11).2018. 13409-13413.
31. Guan, Y., J. Bian, F. Peng, X.-M. Zhang, and R.-C. Sun, *High strength of hemicelluloses based hydrogels by freeze/thaw technique.* Carbohydrate Polymers, **101**.2014. 272-280.
32. Zhang, H., F. Zhang, and J. Wu, *Physically crosslinked hydrogels from polysaccharides prepared by freeze–thaw technique.* Reactive and Functional Polymers, **73**(7).2013. 923-928.
33. Butylina, S., S. Geng, and K. Oksman, *Properties of as-prepared and freeze-dried hydrogels made from poly (vinyl alcohol) and cellulose nanocrystals using freeze-thaw technique.* European Polymer Journal, **81**.2016. 386-396.
34. Butylina, S., S. Geng, K. Laatikainen, and K. Oksman, *Cellulose nanocomposite hydrogels: From formulation to material properties.* Frontiers in chemistry, **8**.2020.

35. Kabir, S.F., P.P. Sikdar, B. Haque, M.R. Bhuiyan, A. Ali, and M. Islam, *Cellulose-based hydrogel materials: chemistry, properties and their prospective applications.* Progress in biomaterials, **7**(3).2018. 153-174.
36. Syverud, K., H. Kirsebom, S. Hajizadeh, and G. Chinga-Carrasco, *Cross-linking cellulose nanofibrils for potential elastic cryo-structured gels.* Nanoscale research letters, **6**(1).2011. 1-6.
37. Hu, W., Z. Wang, Y. Xiao, S. Zhang, and J. Wang, *Advances in crosslinking strategies of biomedical hydrogels.* Biomaterials science, **7**(3).2019. 843-855.
38. El-Naggar, M.E., S.I. Othman, A.A. Allam, and O.M. Morsy, *Synthesis, drying process and medical application of polysaccharide-based aerogels.* International journal of biological macromolecules, **145**.2020. 1115-1128.
39. Zhuo, H., Y. Hu, Z. Chen, and L. Zhong, *Cellulose carbon aerogel/PPy composites for high-performance supercapacitor.* Carbohydrate polymers, **215**.2019. 322-329.
40. Budtova, T., *Cellulose II aerogels: A review.* Cellulose, **26**(1).2019. 81-121.
41. Patiño-Masó, J., F. Serra-Parareda, Q. Tarrés, P. Mutjé, F.X. Espinach, and M. Delgado-Aguilar, *TEMPO-oxidized cellulose nanofibers: a potential bio-based superabsorbent for diaper production.* Nanomaterials, **9**(9).2019. 1271.
42. Thapliyal, P.C. and K. Singh, *Aerogels as promising thermal insulating materials: An overview.* J. Mater, **2014**(10).2014.
43. Ulker, Z. and C. Erkey, *An emerging platform for drug delivery: Aerogel based systems.* Journal of Controlled Release, **177**.2014. 51-63.
44. Alam, M.N. and L. Christopher, *Natural Cellulose-Chitosan Crosslinked Superabsorbent Hydrogels with Superior Swelling Properties.* ACS Sustainable Chemistry & Engineering, **6**(7).2018. 8736-8742.
45. Mendoza, D.J., L. Hossain, C. Browne, V.S. Raghuwanshi, G.P. Simon, and G. Garnier, *Controlling the transparency and rheology of nanocellulose gels with the extent of carboxylation.* Carbohydrate Polymers, **245**.2020. 116566.
46. Barajas, R.M., V. Wong, K. Little, A.F. Patti, and G. Garnier, *Carboxylated Nanocellulose Superabsorbent: Biodegradation and Soil Water Retention Properties.*2021.
47. Ahmed, E.M., *Hydrogel: Preparation, characterization, and applications: A review.* Journal of Advanced Research, **6**(2).2015. 105-121.
48. Zhang, T., Y. Zhang, X. Wang, S. Liu, and Y. Yao, *Characterization of the nano-cellulose aerogel from mixing CNF and CNC with different ratio.* Materials Letters, **229**.2018. 103-106.
49. Burhani, D., A.A. Septevani, R. Setiawan, L.M. Djannah, M.A. Putra, S.S. Kusumah, and D. Sondari, *Self-Assembled Behavior of Ultralightweight Aerogel from a Mixture of CNC/CNF from Oil Palm Empty Fruit Bunches.* Polymers, **13**(16).2021. 2649.
50. Curvello, R., V.S. Raghuwanshi, and G. Garnier, *Engineering nanocellulose hydrogels for biomedical applications.* Advances in colloid and interface science.2019.
51. Gregory, J., *Rates of flocculation of latex particles by cationic polymers.* Journal of Colloid and Interface Science, **42**(2).1973. 448-456.
52. Adachi, Y., L. Feng, and M. Kobayashi, *Kinetics of flocculation of polystyrene latex particles in the mixing flow induced with high charge density polycation near the isoelectric point.* Colloids and Surfaces A: Physicochemical and Engineering Aspects, **471**.2015. 38-44.
53. Gregory, J. and S. Barany, *Adsorption and flocculation by polymers and polymer mixtures.* Advances in colloid and interface science, **169**(1).2011. 1-12.

54. Wang, T.K. and R. Audebert, *Flocculation mechanisms of a silica suspension by some weakly cationic polyelectrolytes.* Journal of colloid and interface science, **119**(2).1987. 459-465.
55. Zhou, Y. and G.V. Franks, *Flocculation mechanism induced by cationic polymers investigated by light scattering.* Langmuir, **22**(16).2006. 6775-6786.

THIS PAGE WAS INTENTIONALLY LEFT BLANK

CHAPTER 3
STRUCTURE AND SWELLING OF CROSS-LINKED NANOCELLULOSE FOAMS

THIS PAGE WAS INTENTIONALLY LEFT BLANK

Preface

The TEMPO oxidized nanocellulose SAP/cryogel/foam has tunable mechanical properties which was achieved in the previous chapter (chapter 2). Next, it is crucial to understand the structural differences between a neat and a crosslinked nanocellulose SAP/foam after swelling or drying (deswelling). This is to efficiently engineer the material for its specific applications. This chapter quantifies the fiber bundle swelling for both the neat and crosslinked nanocellulose foam. Nanocellulose foam saturated with H_2O/D_2O is analyzed by small angle X ray and Neutron scattering to determine the structural change upon water absorption. Furthermore, the structural effect during deswelling/drying is mathematically determined.

Neat nanocellulose SAP has the highest absorption capacity; however, physical or chemical crosslinking decreases the absorption capacity by changing structure. The structural change is critical as it determines the absorption or swelling ability of the nanocellulose foam. This structural change measured by small angle scattering technique is complemented by high resolution scanning electron microscopy. This fundamental knowledge of structural change upon crosslinking and the resultant effect on water absorption confirms the good engineerability of nanocellulose SAP for advanced applications.

THIS PAGE WAS INTENTIONALLY LEFT BLANK

Chapter 3: Structure and Swelling of Cross-linked Nanocellulose Foams

THIS PAGE WAS INTENTIONALLY LEFT BLANK

Structure and swelling of cross-linked nanocellulose foams

Laila Hossain[a], Vikram Singh Raghuwanshi[a], Joanne Tanner[a], Chun- Ming Wu[b], Olga Kleinerman[c], Yachin Cohen[c] and Gil Garnier[a]*

[a]Bioresource Processing Research Institute of Australia (BioPRIA), Monash University, Clayton, Victoria-3800, Australia

[b]National Synchrotron Radiation Research Center, Hsinchu 30076, Taiwan

[c]Technion - Israel Institute of Technology, Haifa, Israel

* For Correspondence: Gil.Garnier@Monash.edu

3.1 Abstract

Hypothesis: The water absorption capacity of nanocellulose (NC) foam is tailored by crosslinking with polyethyleneimine (PEI) and hexamethylenediamine (HMDA). The interaction of amine groups in PEI and HMDA with the carboxylic groups (COO^-) of NC affects the foam structure which reduces its swelling capacity.

Experiments: Functionalized NC foams were prepared by TEMPO (2,2,6,6, tetramethylpiperidine-1-oxyl) oxidation of bleached pulp, followed by fibrillation into a hydrogel, adding a crosslinker and freeze drying the hydrogel into a foam. The structure of the NC foam characterized by rheology, SANS (Small Angle Neutron Scattering), SAXS (Small Angle X-ray Scattering) and cryo-SEM (cryo-Scanning Electron Microscopy) was related to absorption and swelling properties.

Findings: The NC foam has the highest water absorption capacity at 132 g water/g foam. PEI-NC foam has a water absorption capacity of 71 g water/g foam, which further decreases to 47 g water/g foam for the HMDA-NC foam. Small angle scattering reveals the elementary fibril of NC is 3–5 nm thick and forms fiber bundles. In water, these bundles swell differently for the different types of foam which affects the water absorption capacity of the network. The structural analysis of the foam was related to the swelling capacity. The structure of NC foam can be engineered for specific applications for biomedical, agriculture or food industries.

3.2 Keywords

Nanocellulose; hydrogel; foam; crosslinking; absorption capacity; swelling; SAXS, SANS, FTIR.

3.3 Graphical Abstract

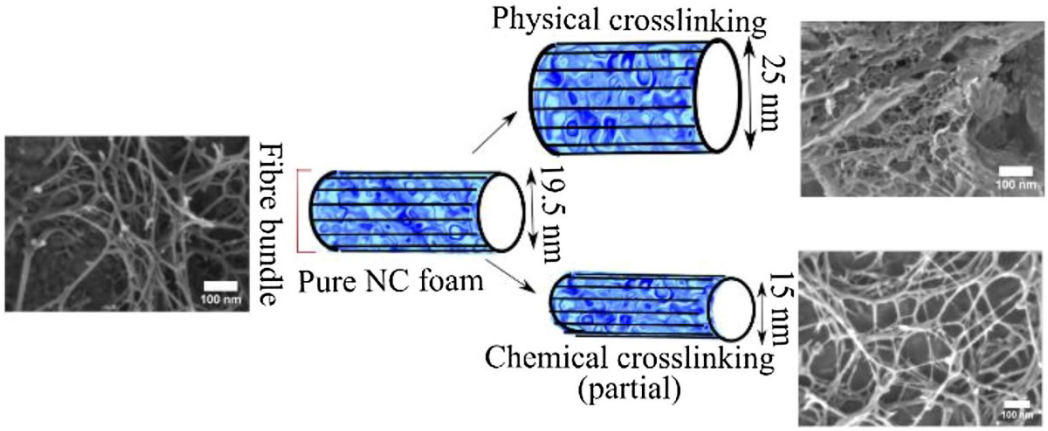

3.4 Introduction

Hydrogels are hydrophilic physically or chemically crosslinked polymeric network materials which contain a large amount of water in their structure [1]. Hydrogels can be divided into two categories: biopolymer-based hydrogels and synthetic hydrogels- depending on their source. Biopolymer based hydrogels have attracted particular attention because of their biocompatibility, biodegradability and high water absorption capacity [2].

Cellulose is the most abundant naturally occurring polymer and can be used to form hydrogels. Cellulose nanofibers, extracted from wood pulp through combinations of chemical and mechanical treatment, consist of semi-flexible fibrils [3]. Among the chemical methods, 2,2,6,6,-tetramethylpiperidine-1-oxyl (TEMPO) mediated oxidation is a widely known technique to introduce carboxylic groups (COO−) to the fiber surface [4]. The electrostatic repulsion between the negative carboxylic groups facilitates the formation of a hydrogel upon mechanical treatment. There are many promising applications of these nanocellulose (NC) hydrogels in the biomedical, food and agriculture fields due to their large surface area, large water absorption capacity, sustainability and biocompatible characteristics [5].

Many crosslinking agents with cellulose based hydrogels have been investigated to achieve better mechanical property, control release of biological fluid and adsorption of specific particles. Epichlorohydrin, urea derivatives, aldehydes and aldehyde based reagents and carbodiimides are the most commonly used crosslinkers for cellulose based hydrogels [6]. Due to the toxicity and potential environmental hazard of these crosslinkers, research has targeted more suitable green crosslinker for NC. Chitosan, citric acid, succinic anhydride, polyethyleneimine (PEI) [7-11] have

all been investigated to minimize potential hazards. PEI is a highly branched dendrimer of high cationic charge density [12, 13] which attracts the negative COO− group of oxidized fibers. As a non-hazardous polymer, PEI is used to physically crosslink the NC gel in this study. Hexamethylenediamine (HMDA) is used as a chemical crosslinker to compare the effect of chemical crosslinking in NC foam. In this study, NC foams are partially chemically crosslinked with HMDA to improve strength without important detrimental effect on absorption capacity of the foam.

NC foam can be produced by drying NC hydrogel. The resulting foam is highly porous (up to 99.7% porosity), of ultra-low density (10 mg/cm^3) [14, 15] and can absorb water at more than 100 times its own dry weight. The absorption capacity depends on the chemical composition of the cellulose itself, as well as its surface area and pore size distribution, and the temperature, pH and ionic strength of the solution being absorbed [6, 16]. The porosity and internal structure of NC foams largely dictate the absorption capacity and rate. This distinct structure of NC foams makes them unique compared to foam prepared from cellulose instead of NC. The absorption capacity can further be controlled by physical or chemical crosslinking the NC fibers. The higher the extent of crosslinking, the lower the absorption capacity due to compact structure [17, 18]. Therefore, determination of the extent of structural change due to crosslinking is critical to the characterization and understanding the mechanism behind the absorption capacity of NC foam.

Analyzing NC foams upon swelling and de-swelling is particularly challenging, given their high-water content and low solid content. A wide range of techniques have been used to characterize NC hydrogels [19] and dried foams; these include SEM and TGA [20], AFM [21], and SANS, SAXS and DLS [22]. Small Angle Scattering techniques, which enable representative analysis through the use of relatively large sample volumes, is emerging as an attractive NC foam characterization method [19]. SAXS of TEMPO oxidized hydrogels was studied at different fiber concentrations to characterize the effect of fiber concentration. This was compared with the gel rheological properties to better understand the gelation mechanism [23]. Mao et al. used SAXS and SANS to characterize TEMPO oxidized homogenized cellulose nanofibers and the data were fitted using ribbon, parallelepiped and Gaussian-approximated parallelepiped models to calculate width and thickness of NC cross section [22]. In another study, microbial NC was studied dry and swollen to quantify the structure by a combination of Ultra SANS and SANS [24]. However, the effect of the fibrous network structure on the swelling capacity of NC-based foam was not explored, nor was the structure related to the swelling hysteresis in these studies.

It is the objective of this study to understand and quantify the relation between the structure and swelling behavior of NC-based foams. It is clear that, although powerful and applicable, SAXS and SANS characterization alone is insufficient to achieve this. In this study, a series of model physically and (partially) chemically crosslinked NC foams were saturated with H2O/D2O and measured using a combination of small angle scattering and cryogenic high resolution (HR) SEM techniques for the first time. Fiber swelling behavior was measured and nano-scale structural changes related with changes in swelling capacities for different types of crosslinking were quantified. Thus, NC gel-foam properties have been directly related to and shown to control the absorption capacity of the foam via crosslinking. Attenuated total reflectance-Fourier transform infrared (ATR-FTIR) spectroscopy is performed to complement the cryogenic HR-SEM imaging technique and verify the effect of crosslinking on chemical composition and morphological structure. Comparison of crosslinked and non-crosslinked foam is presented to differentiate the structures and reveal the water transport mechanisms inside the structure. Insight into the mechanism of fiber bundle swelling on absorption capacity is also provided.

3.5 Methodology

3.5.1 Materials

Bleached Eucalyptus Kraft (BEK) pulp (approximately 10 wt% solids) was obtained from Australian Paper, Maryvale, Australia. 2,2,6,6-Tetramethylpiperidine-1-oxyl (TEMPO), Polyethyleneimine (PEI) of two different molecular weights (high molecular weight: Mn ~ 60,000; Mw ~ 750,000 and low molecular weight: Mn ~ 600; Mw ~ 800) and sodium bromide (NaBr) were purchased from Sigma-Aldrich. Hydrochloric acid (HCl) and Sodium Hydroxide (NaOH) were purchased from ACL Laboratories and Merck, respectively. HMDA was purchased from Chem-Supply. 12 w/v% Sodium Hypochlorite (NaClO) was purchased from Thermo Fisher Scientific and used as received. Milli-Q® water was collected from Merck Milli-Q® water purification system (Direct-Q® 3UV-R).

3.5.2 Methods

3.5.2.1 TEMPO mediated oxidation

The TEMPO-mediated oxidation process used in this investigation is based on a previously developed method [25]. There are two versions: the high charge and low charge methods, which

yield 1.4 mmol and 0.6 mmol of carboxylate groups per gram dry weight of fiber, respectively. 25 g BEK pulp (dry weight) was suspended in 2500 mL water containing 0.4 g TEMPO and 2.5 g NaBr. In each case, a NaClO solution (12 w/v%) was initially adjusted to pH 10 by the addition of 32% HCl. To initiate the oxidation process, 100 mL NaClO (for high charge) or 75 mL NaClO (for low charge) were added drop-wise to the suspension whilst stirring. The pH of the reaction was monitored online and maintained at pH 10 by addition of 0.5 M NaOH. The oxidation process was completed in 3 h for the high charge (1.4 mmol/g) and 2 h for the low charge method (0.6 mmol/g). The oxidized fibers were recovered through filtration and stored refrigerated (2–8 °C). To produce hydrogel, TEMPO-oxidized pulp was dispersed in deionized water at a required concentration (0.5 wt% fiber concentration). Fibrillation is attained through a high-pressure homogenizer (GEA Niro Soavi Homogenizer Panda) at 1000 bar for two passes. The oxidation process is critical to produce hydrogel as unoxidized fiber suspensions do not generate hydrogel. This hydrogel structure together with freeze drying process produces the porous foam structure.

3.5.2.2 Determining solids concentration

The solids concentration of all gels and pulps was determined through oven drying. The sample was weighed before (w_i) and after (w_d) drying. Sample moisture was removed by evaporation at 105°C for at least 6 hours. The solids content was calculated as:

$$Solid\ content\ (\%) = \frac{w_d}{w_i} \times 100\%$$

3.5.2.3 Conductometric titration

The carboxylate group (COO^-) content was measured by conductometric titration as reported in revious studies [26, 27]. Approximately 30 mg (dry weight) of oxidized pulp was dispersed in 40 mL deionized water. 200 µL (1 wt%) NaCl was added to the dispersed sample. The pH of the sample was adjusted between 2.5 and 3 before titration with 0.5 M HCl. Titration was done by controlled addition of 0.1 M NaOH using a Mettler Toledo T5 titrator. The conductivity of the sample was monitored throughout the titration progress. The carboxyl group content (mmol COO^- /g fiber) was determined by using the following equation.

$$CC = \frac{c(V_2 - V_1)}{w} \times 1000$$

where V_1 and V_2 denote the amount of titrant required to neutralize the carboxylic groups (L), c is the NaOH concentration (mol/L), and w is the sample weight (g).

3.5.2.4 PEI incorporation

PEI was dissolved in deionized water at a concentration of 0.005 mg/mL. One-passed homogenized gel was mixed with PEI using a hand blender. Two different molecular weights of PEI (high molecular weight PEI: H_PEI = 750,000 Da and low molecular weight PEI: L_PEI = 800 Da) were used. The NC gel was mixed with PEI at a mass ratios of 1: 0.07 (NC:PEI). The resulting mixture was then passed through the homogenizer again. All the passes through the homogenizer were performed at 1000 bar. PEI at lower concentration (NC:PEI = 1:0.05) was also studied with NC which showed similar swelling behavior but lower gel strength compared to NC:PEI = 1:0.07. Only NC:PEI = 1:0.07 sample was considered for this study as it increased the mechanical property (strength) of the gel compared to pure NC gel.

3.5.2.5 HMDA incorporation

HMDA was dissolved in deionized water at a concentration of 0.45 mg/mL. The NC gel was mixed with the HMDA solution at stoichiometric ratios of 1:4 and 1:8 (COO^-:NH_2). HMDA does not react with NC at room temperature or below room temperature if no reagent (such as EDC/NHS) is used to activate the COO^- group in NC. So, the resulting mixture was cured at 80 °C for 1 h in an oven. The final cross-linked gel was removed and stored at 4 °C. The molecular structure of PEI and HMDA is shown in Figure 3-1. The NC_HMDA hydrogels/foams are named as below:

Table 3-1: Description of NC_HMDA hydrogels/foams composition.

NC_HMDA samples	Name
COO^-:NH_2 = 1:2	NC_HMDA_12
COO^-:NH_2 = 1:4	NC_HMDA_14
COO^-:NH_2 = 1:8	NC_HMDA_18

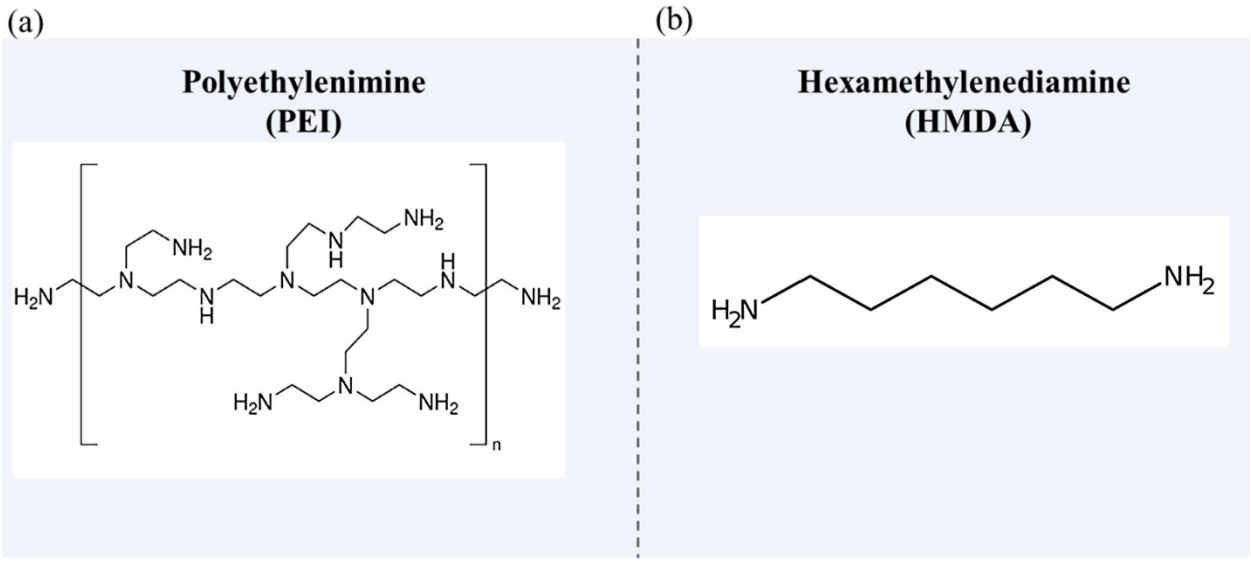

Figure 3-1. Molecular structures of the crosslinking agents: (a) PEI and (b) HMDA.

3.5.2.6 Gel rheology measurement

Rheological testing was performed with an Anton Paar MCR302 rheometer at 25 °C. A cone (0.997°) and plate (49.975 mm) geometry were selected. A solvent trap was used to make sure steady temperature during measurements. Amplitude sweep was done from 0.01 to 100% at a constant frequency of 1 Hz.

3.5.2.7 High-resolution scanning electron microscopy (HR-SEM)

Gel morphologies were imaged by high-resolution scanning electron microscopy (HR-SEM) using cryogenic sample preparation method. Sample preparation was carried out in a controlled-environment vitrification system (CEVS) [28], followed by complete sublimation of vitrified water. Approximately 3 µL of gel was placed between two gold planchettes, and the "sandwiched" gel vitrified by rapid immersion in liquid nitrogen. The vitrified sample was loaded on a specimen holder, which was subsequently transferred under cryogenic conditions into the pumped BAF060 freeze-fracture replication system (Leica, Vienna), the stage of which was pre-cooled to -160 °C. In the BAF060 unit, the sample was fractured and stabilized until the vacuum reached 10^{-6} mBar, maintaining the temperature around -160 °C. To remove the water phase, the temperature of the sample was raised to -100 °C, at which water has a vapor pressure of about 10^{-5} mBar. The sample was maintained at this temperature for two hours to ensure complete water sublimation. This combination of the high vacuum and low temperature provides ideal conditions to achieve water

removal and preserve the mechanical strength of the frozen gel. Subsequently, the liquid nitrogen flow was turned off, and the sample kept inside the BAF060 under vacuum until ambient temperature was reached. This final slow temperature ramp mitigates collapse of the gel structure. The freeze-dried sample was transferred directly to the SEM in the sample holder via the cryogenic port of the microscope (Leica, Vienna). Unlike classical freeze-drying procedures, no shadowing or conductive coating was applied to the sample. Imaging was performed by a Zeiss Ultra Plus high-resolution scanning electron microscope equipped with a Schottky field-emission electron gun and a unique Gemini electron-beam column design (Carl Zeiss SMT GmbH Oberkochen, Germany). To achieve high-resolution images, close to the isoelectric (no-charging) point, the microscope was operated at 1 kV electron beam energy. Images were acquired by mixing signals from a classical Evart-Thornley and a high-resolution In-the-Lens secondary electron (SE) detectors, at working distance of about 3.5 mm.

3.5.2.8 Fourier transform infrared (FTIR) spectroscopy

The crosslinked foams were tested by ATR-FTIR using the Agilent Cary 630 FTIR Spectrometer. The freeze dried foams were tested for the FTIR spectra to determine the type of crosslinking.

3.5.2.9 Preparation of NC foams

To prepare the foams, 15 g of gel was spread evenly onto a 55 mm petri dish. The sample was frozen at -80°C, then freeze-dried (Christ Alpha 2-4 LD Plus) for 2 days. The freeze-dried samples (pure nanocellulose foam: NC foam, nanocellulose crosslinked with high molecular weight PEI: NC_H_PEI foam and nanocellulose crosslinked with HMDA having stoichiometric ratio of 1:8 for COO^-:NH_2 = NC_HMDA_18 foam) are shown in Figure 3-2.

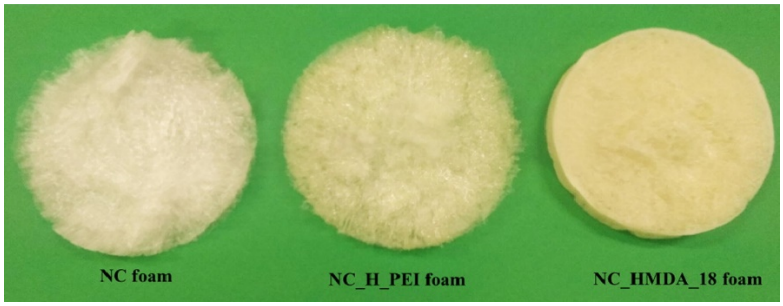

Figure 3-2. Picture of the three types of foams: NC foam, and NC foam crosslinked with high molecular weight PEI and HMDA, respectively.

3.5.2.10 Free swell capacity

15 g of gel sample was freeze-dried in a 55 mm petri dish to produce a NC foam which was tested for free swell capacity. The sample was deposited in a funnel (funnel filter glass, 75 mm diameter) and placed in a beaker full of Milli Q® water. The water absorbed was measured at regular intervals up to 3 hours. Before measuring the weight of water absorbed, the funnel with the sample was removed from the fluid container and kept on an inclined surface for five minutes for the excess liquid drip off.

The free swell capacity was then calculated as follows:

$$\text{Free Swell Capacity (FSC)} = \frac{m_t - m_i}{m_i}$$

Where m_t is the mass of the swollen foam at a particular time interval and m_i is the initial mass of the foam.

3.5.2.11 Small Angle Neutron and Small Angle X-ray Scattering

Small-angle neutron scattering (SANS) measurements were performed at the Time-of-Flight BILBY beamline at the Australian Nuclear Science and Technology Organization (ANSTO), NSW, Australia. The wavelength of 6 Å was conducted by using its neutron-velocity selector (NVS). Two detector carriage lengths were used to cover the Q-range from 0.00254 to 0.31$Å^{-1}$. The foam samples were placed in demountable cells of wall thickness 2 mm. D_2O was used to hydrate the samples.

The data collected were reduced by using the Mantid software with the BILBY package. The background of the empty cell was subtracted from each sample measured without D_2O, and the D_2O scattering was subtracted from the hydrated samples. The raw data was normalized to the absolute scattering values by the pre-calibrated scattering curve of D_2O.

Small angle X-ray Scattering (SAXS) was performed at the SAXS/WAXS beamline of the Australian Synchrotron [29]. The foam was measured in-situ during dehydration. SAXS measurements were made at an energy of 12 keV (λ =1.033 Å) at a sample to detector distance of 7 m (q range:0.001 and 0.1 Å-1). The scattered photons were collected using a PILATUS 1 M detector (pixel size 172 µm × 172 µm). Q scale was calibrated using the standard silver behenate.

Data reduction and radial averaging of scattering curves was performed by the beamline specific Scatter Brain software.

3.6 Results

The free swell capacity of NC foam and crosslinked NC foams is tested by immersion into MilliQ® water. The free swell capacity of the foam is related to the morphological and internal structure, which are determined by HR-SEM and small angle scattering (X-rays and neutrons). The foam internal structure is quantified by network stiffness, swollen bundle diameter and structure compactness to determine the effect of crosslinking on the foam structure. Hydration-dehydration study are also performed to estimate the effect of dehydration/drying time on nanostructure.

3.6.1 Swelling behavior of NC foams

Swelling is tested by immersing the NC foams in MilliQ® water. Figure 3-3 shows the free swell capacity (in g water/g foam) for the pure NC, NC_PEI and the NC_HMDA_18 foams. The free swell capacity for the pure NC foam is 132 g water/g foam. Foams from PEI and HDMA treated NC have a reduced free swell capacity of 71 g water/g foam and 47 g water/g foam, respectively.

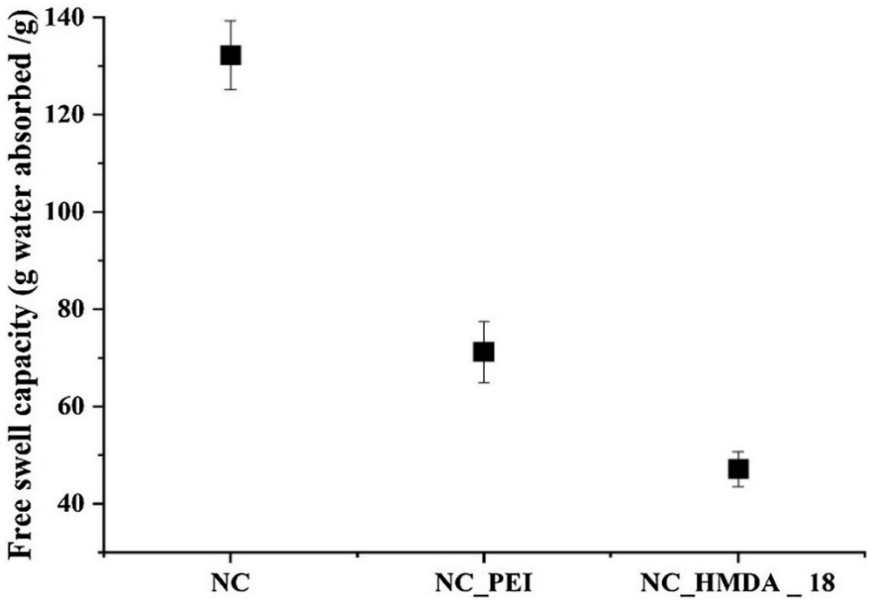

Figure 3-3. Comparison of the free swelling capacity for the different NC foams.

3.6.2 Morphological structure

High-resolution scanning electron microscopy (HR-SEM) is performed on gel samples prepared by the cryogenic method to evaluate the morphology of the pure NC, NC_PEI and NC_HMDA gels. All gels show highly crosslinked and reticulated structures with low fibrous solid content, as expected.

The HR-SEM micrographs of NC (Figure 3-4a) and NC_HMDA gels (Figure 3-4c) show the distribution of cellulose fibers (of diameter 10-30 nm) creating porous structures with large pores of diameter ranging from 50 to 200 nm.

The HR-SEM micrograph of the NC_PEI gel presents a different morphological structure and fiber distribution (Figure 3-4b). The NC_PEI gel has a flake-like and fluffy structure.

3.6.3 FTIR spectra of modified NC foams

Freeze dried NC, NC_PEI and NC_HMDA foams are analyzed by ATR-FTIR. Figure 3-5a compares the ATR-FTIR spectra of NC and NC_PEI foams. Both spectra are similar in shape, indicating that PEI induces no significant chemical change to the NC foam chemical bonding.

Figure 3-5b shows the spectra of NC and NC_HMDA foams. The NC spectra display the representative COO^- group peak at 1599 cm^{-1} corresponding to the C=O stretch. The C=O stretch peak shifts to a broader peak in the amide crosslinked foam (NC_HMDA) at 1589 cm^{-1}. As this was partial crosslinking, the C=O stretch is not very prominent. FTIR spectra for complete crosslinking of NC with HMDA is provided in Figure 3-S1 of the supplementary information section.

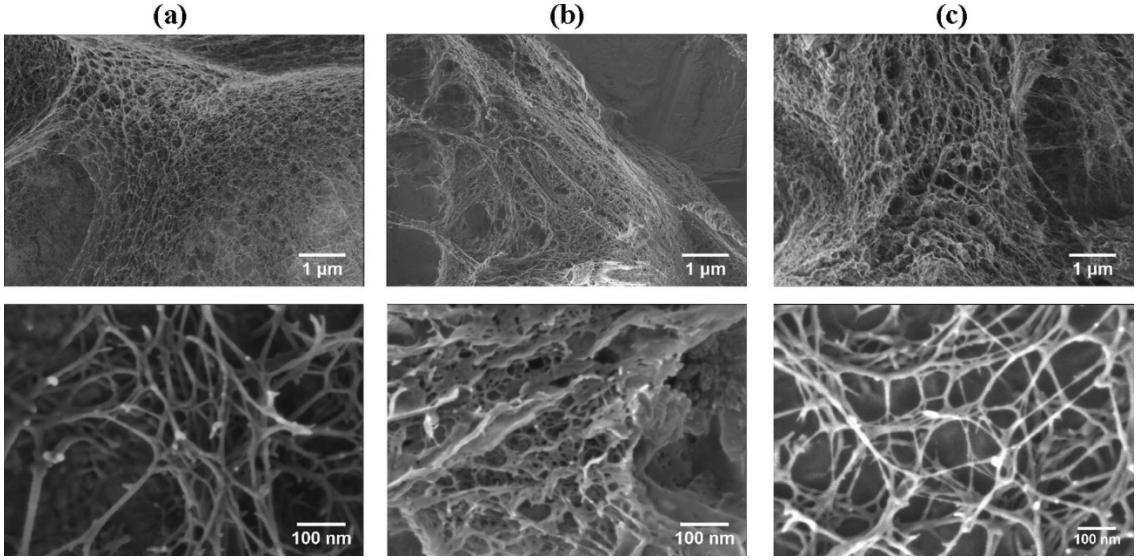

Figure 3-4. HR-SEM images of (a) NC gel, (b) NC_ H_PEI (NC:H_PEI = 1:0.125) gel and (c) NC_HMDA_12 gel at complementary magnifications.

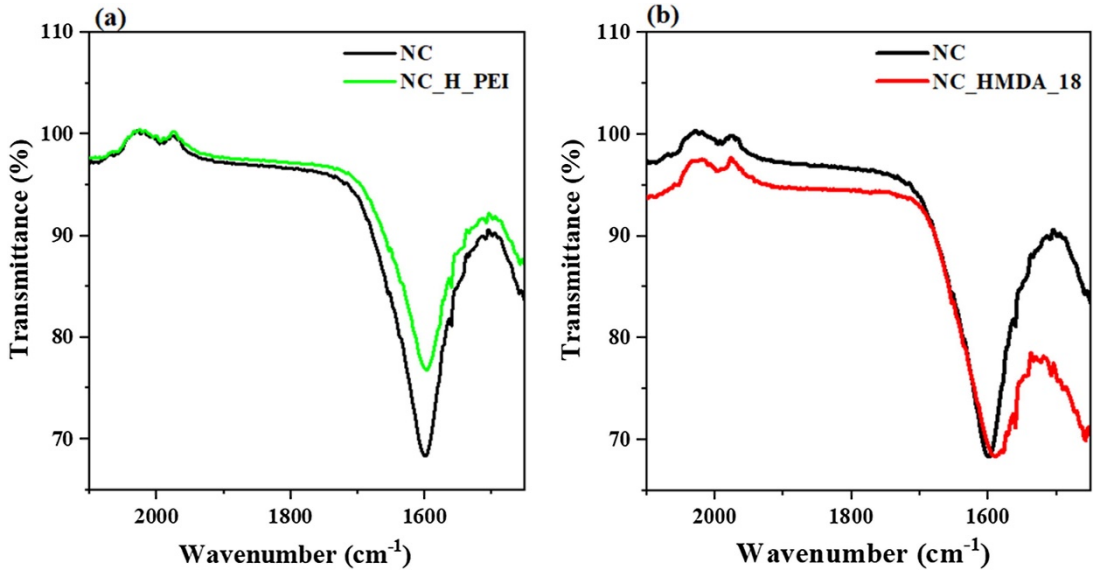

Figure 3-5. ATR-FTIR spectra for (a) pure NC and NC_H_PEI foam, (b) pure NC and NC_HMDA_18 foam.

3.6.4 Rheological properties of crosslinked gel

The viscoelastic behavior of the NC gel and, NC_PEI and NC_HMDA crosslinked gels, is quantified by rheology (Figure 3-6). The Elastic (G′) and Viscous (G″) moduli of the 3 gels were measured in oscillatory flow mode as a function of shear strain. There are four observations of interest. The first is that the rheology of all three gels is dominated by the elastic regime: G′ remains higher than G″ over most of the strain range. The second is that all three gels have a clear and fairly similar linear viscosity region (LVR) that drops at a strain of 10%. The strain at which the LVR regime drops is a little higher for NC_HMDA gels, indicating stronger cohesion between the NC fibers. The third observation is that PEI increases the elastic modulus of NC gels (G') by a factor of 5 compared to the NC gel, while HMDA provides no increase; increase in G' gives an indication of the relative crosslinking densities. Fourth, the slope of the elastic curve (G') after linear viscoelastic region (LVR) for NC_HMDA_18 and NC_H_PEI became steeper compared to NC gel which is also showing some gel crosslinking. The crosslinking densities of these samples calculated from the elastic moduli are provided in Table 3-S1.

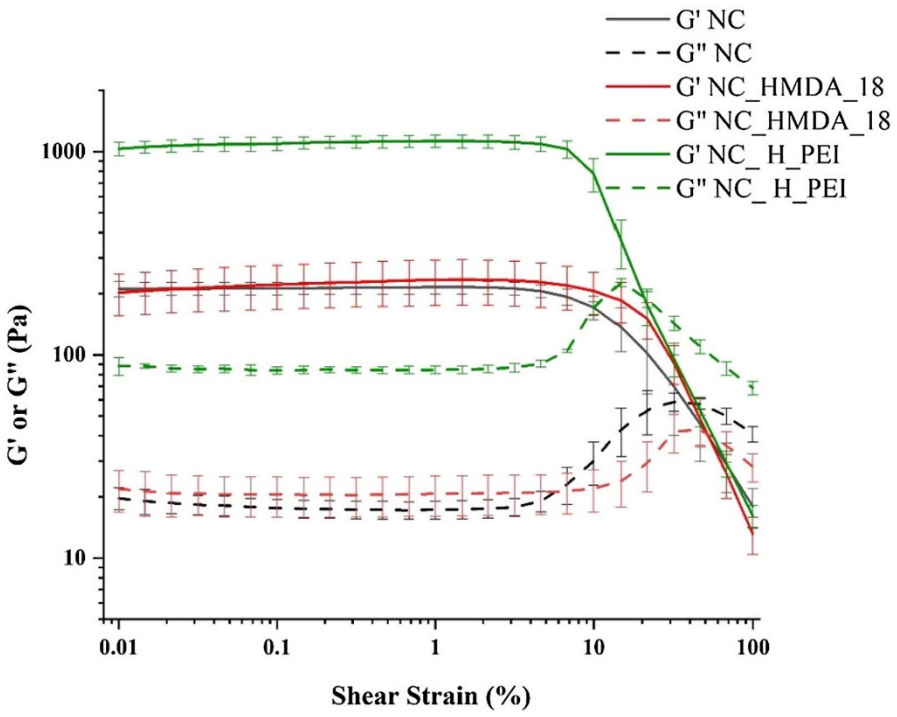

Figure 3-6. Rheological spectra of pure NC, NC_H_PEI and NC_HMDA_18 hydrogel: dynamic strain sweep (25 °C) at a frequency of 1 Hz.

3.6.5 Structural change of foam upon swelling

NC foams are characterized in the dried and hydrated states by Small Angle Neutron (SANS) and X-ray Scattering (SAXS). SANS and SAXS are both non-destructive methods that provide average structural information of nanomaterials using a relatively large sample volume compared to other techniques [30, 31].

Figure 3-7a shows the SANS scattering curves for NC foams made from fibers of two different charges (*HSC*: 1.4 mmol COO^-/g fiber and *LSC*: 0.6 mmol COO^- / g fiber). In the dried state, both materials show the same scattering profile with no evidence of organized structure. The slope of the scattering curve ($q<0.02$ Å^{-1}) displays q^{-4} power law behavior, which indicates scattering from large size aggregated fibers. NC fiber charge density did not affect the gel network structure.

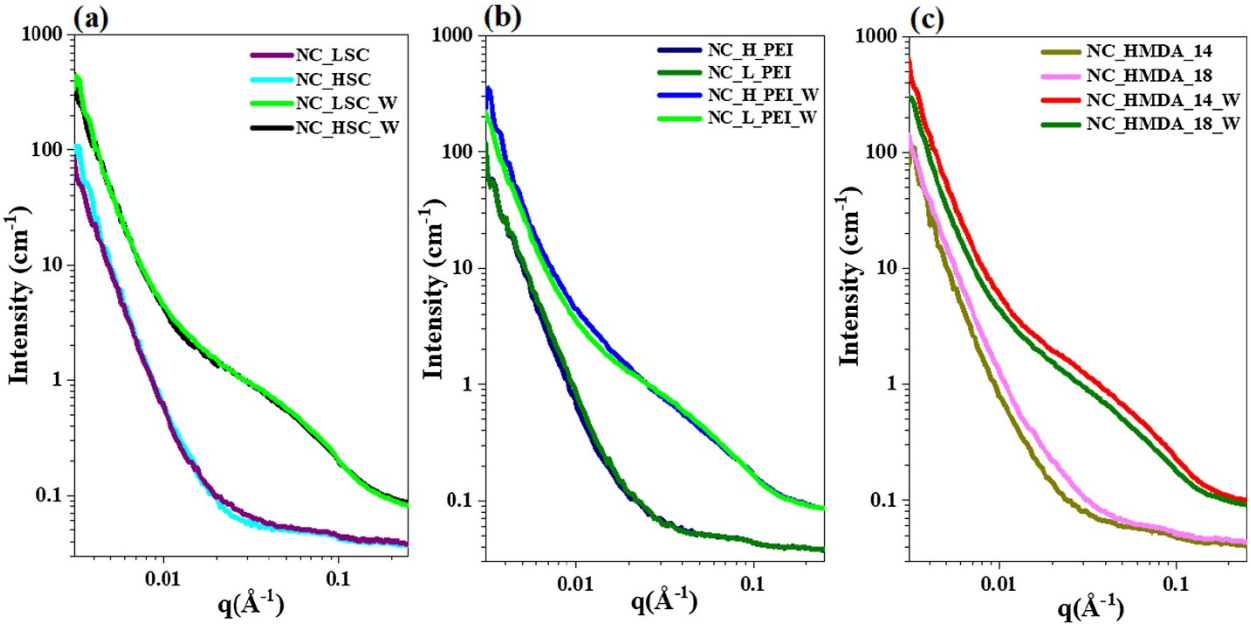

Figure 3-7. SANS intensity-q relationships for dry and saturated (w denotes water saturated foam) foams with hump made from NC gels original, NC_H_PEI and NC_HMDA. (a) Effect of surface charge, (b) physical crosslinking and (c) chemical crosslinking on the foam.

Upon hydrating the sample with D_2O, a significant hump appears in SANS profile (Figure 3-7a) in the q range of 0.02-0.1 Å^{-1}. This hump corresponds to a change in the structure in the size range 1-30 nm. Both HSC and LSC samples show the same structure scattering profile, indicating that the charge of the cellulose fibers has no effect on the structure upon hydration of the freeze-dried

foam. The upturn in the data at low q values ($q< 0.02$ Å^{-1}) in the hydrated SANS curves indicates inhomogeneity of the large-scale structures.

Figure 3-7b shows the SANS curve for the NC foams made with PEI of different molecular weights (750,000 Da and 800 Da). No structure change is observed for the freeze-dried samples. However, upon hydration, a minor change in slope can be seen (Figure 3-7b) which is attributed to the change in PEI molecular weight.

The SANS curves of the NC_HMDA foams show noticeable changes in the scattering curve intensity upon hydration and for freeze dried condition. (Figure 3-7c). However, the structures of the scattering curve profile are identical. The freeze-dried NC_HMDA_18 shows higher scattering than the NC_HMDA_14 foam. Upon hydration with D_2O, the NC_HMDA_14 foam absorbs more water and shows higher scattering intensity compared to NC_HMDA_18.

3.6.6 Probing fibrous structure by different models

The structural information from the scattering curves are extracted by fitting with three different models. These are: (i) the flexible elliptical cylinder model with the power law [32]; (ii) the mass fractals model with power law [33] and (iii) the Debye-Bueche and Lorentzian function [34]. The first model calculates the cross section and the diameter of the fiber with the stiffness of the network structure in terms of persistence length. The second model characterizes the mass fractal distribution in the hydrated foam structures. The third model quantifies the large and small correlation lengths. Detailed model description is provided in supplementary information 3-S1.

The scattering data is fitted by the flexible ellipsoidal cylinder model to quantify the elementary fibril dimension. This model considers ellipsoidal cross-sectional rods defined by the cross-section minor radius r_a, the axis ratio r_b/r_a, the persistence length (l_p) and the contour length (L) [35]. The Kuhn length, which is a measure of stiffness, is twice the persistence length [23]. The contour length represents the length of the chain [36].

Fitting all samples (q range: 0.01- 0.2 Å^{-1}) with the flexible elliptical cylinder model yields average cross-sectional fiber dimensions of 3×5 nm using an assumed contour length of 1000 nm [35]. The current results complement a previous study on TEMPO oxidized homogenized cellulose nanofiber which showed that the width and thickness of the cross section are 2 nm and 8 nm, respectively [22].

The persistence length (network stiffness) evaluated with the flexible cylinder model is shown in Figure 3-8a. For the pure NC foam, the persistence length is 9 nm and increases to 12 nm for NC_H_ PEI foam. The NC_HMDA foam indicating that partial chemical crosslinking results in a higher persistence length.

Fitting the SANS data with the mass fractal model combined with the power law q^{-4} (q range 0.004-0.2 $Å^{-1}$) reveals the cut-off length (Figure 3-8b) to be equivalent to the swollen fiber bundle dimension, which is between 12 and 26 nm. The NC_H_PEI foam swells more than NC_L_PEI indicating that increasing the molecular weight of PEI increases fiber bundle swelling. However, the NC_HMDA foam did not swell much and the bundle size reduced to 14 nm. The NC_HMDA_14 foam has its fiber bundles swelling to 17 nm, which decreased to 14 nm upon increasing the HMDA concentration (1:8) for NC_HMDA_18 foam.

The calculated mass fractal dimensions reveal the compactness/openness of the network structure (Figure 3-8c). The pure NC foam has a fractal dimension of 1.2. Adding the low molecular weight PEI (NC_L_PEI) does not change the dimension significantly, and the high molecular weight PEI (NC_H_PEI) provides foams with a mass fractal dimension of 1.1. The NC_HMDA_14 and NC_HMDA_18 foam show increase in mass fractal dimensions to 1.3 and 1.4, respectively, for foams at the low and high HMDA ratio. The low values of the fractal dimensions indicate the openness of the structure. However, the differences in the fitted values may not be significant and other factors in structure heterogeneities may contribute to differences in fractal dimensions calculated via the mass fractal analytical method.

The correlation length evaluated by the Debye-Bueche and Lorentzian function indicates the large and small scale heterogeneities in the swollen fiber bundles and in the network. The smaller correlation length of 3-5 nm represents the dimensions of the elementary fibril unit. The higher correlation length (Figure 3-8d) was obtained between the size range of 70- 90 nm. These concentration fluctuations occur due to the distributions of the large cellulose fibers bundle size or pore size. The highest correlation length was found for the H-PEI NC foam, which indicates a loose structure. For pure NC foam, the correlation length was 79 nm resulting from the big pores or large size fiber bundles. For the NC-HMDA foam, the correlation lengths decreased as HMDA concentration increased.

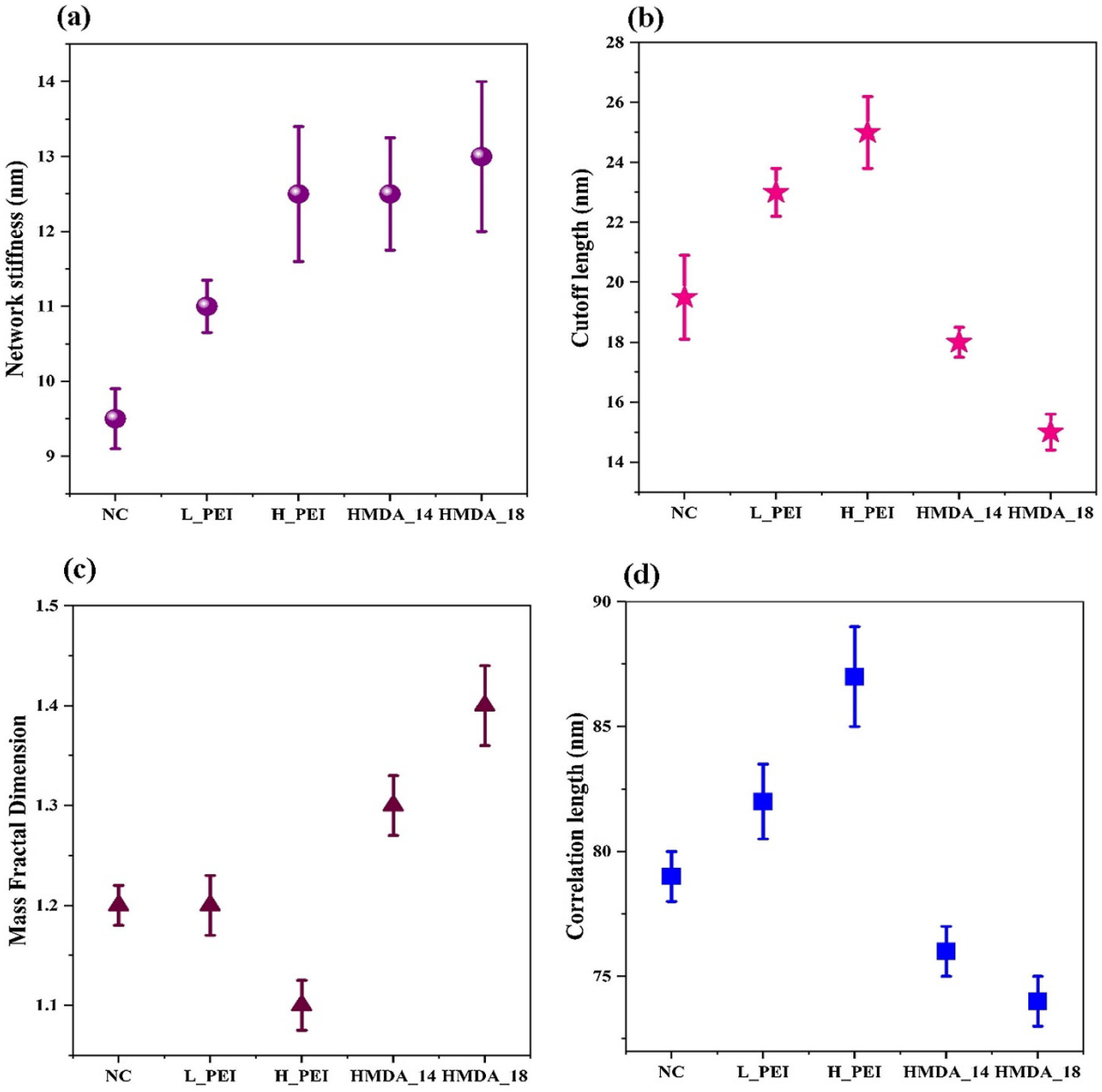

Figure 3-8. Structural characterization of swollen NC foam based on SANS data: (a) network stiffness, (b) cut-off length, (c) mass fractal dimension and (d) correlation length. (L_PEI = NC with 7% LMW PEI; H_PEI = NC with 7% HMW PEI; HMDA_14: NC with HMDA and COO^- : NH_2 = 1:4; HMDA_18: NC with HMDA and COO^- : NH_2 = 1:8).

3.6.7 NC foam hydration and dehydration behavior

SAXS experiments were performed at the SAXS/WAXS beamline of the Australian Synchrotron to evaluate the hydration and drying behavior of NC foam. The freeze-dried foam was hydrated with MilliQ water. Figure 3-9 compares the SAXS curves of the original freeze dried NC foam

structure (designated as blank) to the hydrated NC foams after 10, 13 and 15 minutes during drying under ambient conditions (Figure 3-9).

A sharp hump is observed at saturated condition in the q range between 0.03-2 $Å^{-1}$. The sharp hump started decaying with time and after 15 minutes, the hump completely disappeared. But the profile of freeze-dried foam (blank in Figure 3-9a) and the once saturated dried foam (15 min in Figure 3-9a) is different. This indicates that the foam does not return to its original structure after drying from saturated condition.

All foams show an asymptotic decay of q^{-4} at low q region ($q < 0.03$ A^{-1}), originating from a smooth interface of fiber bundle (Figure 3-9a). The scattering curves were fitted with the mass fractal combined with the power law model, which calculates the cut-off length and the mass fractal dimensions (Figure 3-9b).

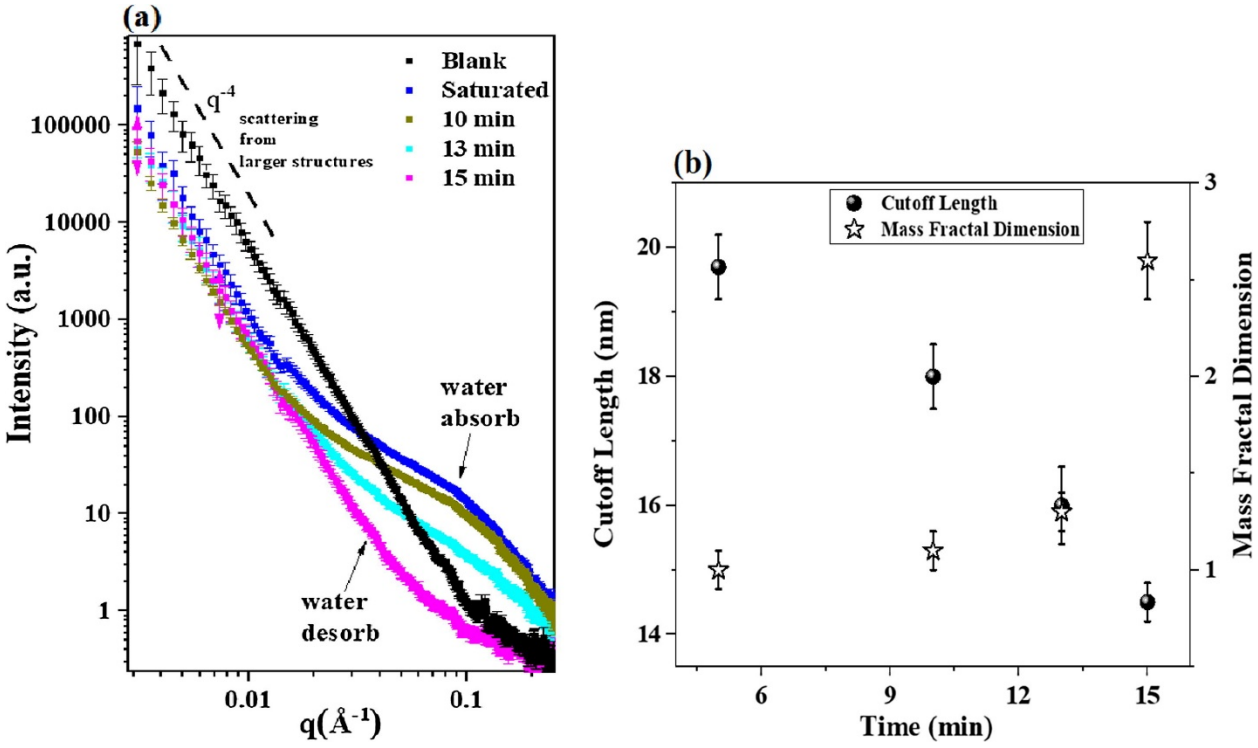

Figure 3-9. Structural change of NC foam upon swelling and deswelling in SAXS: (a) SAXS intensity-q relationships for NC foam (Blank is dry sample and others are after X min of saturation in water where X = saturated, 10, 13 and 15 min) and (b) cutoff length and mass fractal dimension for NC foam.

The saturated NC foam shows a cut-off length (swollen fiber bundle diameter) of 19 nm and a mass fractal dimension of 1 (Figure 3-9b). Upon ambient drying, the cut-off length decreased to 14 nm, indicating the removal of water from the structure, which increases the compactness or shrinkage of the NC fiber bundle. The mass fractal dimension increased to 2.6 which complements the cut-off length results.

3.7 Discussion

The swelling behavior of freeze-dried NC foam crosslinked with PEI (physically) and HMDA (partially chemically) was studied and related to water absorption. The measured free swell capacity of NC foam (132 g water/g foam) indicates that the pure NC foam has a higher absorption capacity than the PEI (65 g water/g foam) and HMDA (48 g water/g foam) crosslinked NC foams (Figure 3-3). This is attributed to a combination of two mechanisms directly related to crosslinking: (i) differences in the physical structure of the foams and (ii) screening of some of the native carboxyl groups on the NC fibers. The zeta potential of selected samples is shown in Table 3-S2 of the supplementary information section. NC foam is composed of entangled, TEMPO oxidized homogenized cellulose nanofiber bundles. The TEMPO reaction oxidizes the secondary OH of the C6 carbon of cellulose into a carboxyl (COO^-) group. The pure NC foam has a carboxylic concentration of 1.4 mmol COO^-/g fiber. The negatively charged carboxyl groups interacts with water molecules which increases water absorption capacity of the NC fiber structure [27].

The fiber bundles of NC foam structure are made of elementary fibrils (elementary fibril shown in Figure 3-10) units of cross section 3 nm × 5 nm as determined by fitting the SANS curves with the flexible elliptical cylinder model. When the NC foam is soaked in water, the liquid diffuses by capillary flow between the elementary fibrils and interferes with the carboxyl groups (H bonding) resulting in swelling of fiber bundles (Figure 3-10). NC foam fiber bundles swell up to 19.5 nm, which is larger than the NC_HMDA foam (15 nm) but smaller than the NC_PEI foam (25 nm).

The NC_PEI foam fiber bundles swell more (25 nm) at the nanoscale but this type of foam absorbs less water (65 g absorbed/g foam) at the macroscale compared to the pure NC foam (132 g water/g foam). During homogenization of PEI with NC fiber, the big molecules of PEI (MW = 750,000 Da) may diffuse into the fiber bundle, expanding the bundle structure (Figure 3-10) and establishing some physically crosslinking with carboxyl groups. This hypothesis of a more open structure is corroborated by the mass fractal dimension of 1.1 (calculated from the SANS curves

fitting) which indicates that the NC_PEI structure is less compact than that of pure NC foam. The cryogenic HR-SEM micrographs complement the SANS analysis showing the open flake like structure of the NC_PEI foam (Figure 3-4). The PEI crosslinked NC fiber shows a high network stiffness with a persistence length of 12.8 nm (Figure 3-8a) which is higher than that for the pure NC foam (9 nm). Higher network stiffness upon crosslinking is also shown by the rheology results (Figure 3-6), as the slope of the PEI crosslinked gel is steeper than for the pure NC gel.

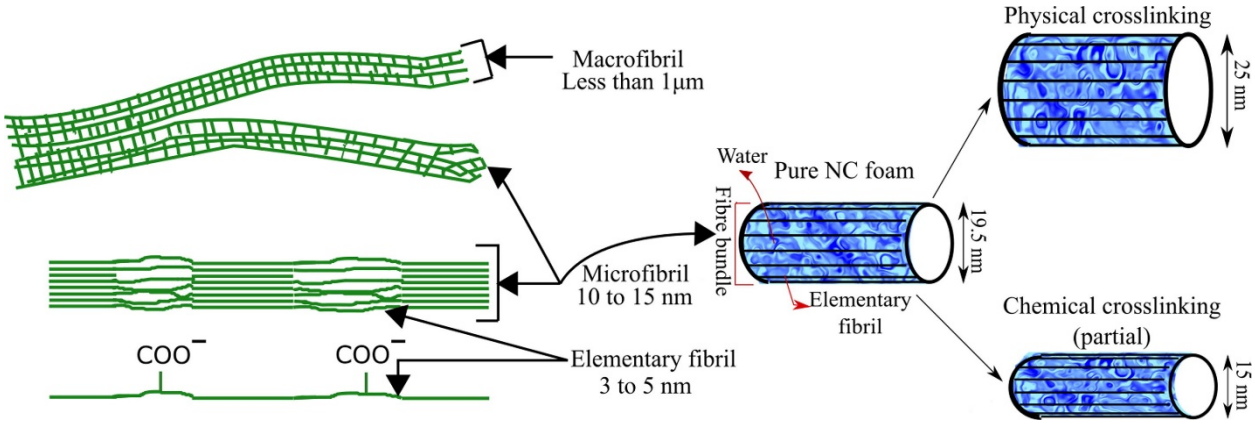

Figure 3-10. Schematic diagram showing the length scale of the NC gel. A flexible ellipsoidal cylinder model was selected to measure the effect of PEI (physical crosslinking) and HMDA (partial chemical crosslinking) on the NC fiber bundle swelling.

Upon contact with water, the water molecules diffuse into the NC_PEI fiber bundles and through the pores formed by the network of crosslinked fiber bundles. The open and fluffy structure of NC_PEI foam accommodates most of the water in the network, resulting in higher fiber bundle swelling.

However, at the macroscale, the lower water absorption capacity of NC_PEI (Figure 3-3) results from the open and stiff fibrous network in this sample, combined with screening of some of the COO− groups by the primary, secondary and tertiary amine groups of the adsorbed PEI molecules (Figure 3-1).

In contrast, in NC_HMDA foam, the HMDA molecules can diffuse into the NC fiber bundle. Due to the smaller size of the HMDA molecule (MW HMDA = 116.2 Da) and their interaction with the COO− groups in the fiber bundle, the resultant NC_HMDA fiber bundle structure is more tightly bound together, and therefore it shrinks [37]. The NC_HMDA foam thus has a more compact fibrous network than the pure NC and NC_PEI foams (Figure 3-8c and Figure 3-10) as

shown by the calculated NC_HMDA_18 mass fractal dimension of 1.4. The compactness of the foam structure increased with the HMDA concentration, as shown by the mass fractal results (Figure 3-8c) which increases the extent of crosslinking.

NC_HMDA foam showed the lowest swelling capacity (48 g water/g foam). This is due to the compactness of fiber bundle which restricts and hinders the water diffusion and penetration in the fiber bundle structure. The tighter structure also reduces the swelling of the fiber bundle to 15 nm. Another reason which contributes to the reduction of water absorption capacity is the screening of some COO− groups by the two primary amine groups from each molecule of HMDA.

The SAXS hydration-drying study quantifies the structure compactness upon swelling and deswelling. For the dry foam, SAXS shows a power law behavior which indicates scattering from the surface of aggregated fibers. During swelling, the fiber bundles and pores accommodate water. The water penetrates into the fiber bundle and the inter-elementary fibril distance increases which opens the fiber bundle. This is seen by the low mass fractal (1.0) value after saturation. Upon drying, the water from the bundles evaporates and the inter-elementary fibril distance decreases, as structure shrinks, and the elementary fibrils aggregate inside the bundle. This leads to an increase in the compactness of the internal structure of the bundles as revealed by the increased mass fractal dimension (2.5).

Interestingly, the freeze-dried foam structure differs from the dehydrated sample (Figure 3-9). The fiber bundle dimension, represented by the cut-off length, decreased from 19 nm to 14 nm upon hydration and subsequent ambient drying. The swollen hydrated fiber bundle has higher cut-off length and upon drying, the water evaporates and the fiber bundle shrinks to their decreased cut-off length 14 nm. This increased compactness is attributed to the formation of aggregates during room temperature drying. Freeze drying sublimation occurs at temperature ranging from −20 °C to −50 °C, at a lower pressure than for the triple point of water, to deliberatively minimize the aggregation of cellulose fibers [38]. However, during ambient drying, the NC fibers have the ability to migrate, resulting in aggregation as water evaporates [39].

The combined effect of physical entrapment and COO^- groups give pure NC foam a higher water absorption capacity than PEI/HMDA modified foams. In contrast, network stiffness increases with PEI and HMDA crosslinking. Therefore, NC foam structure and swelling capacity can be controlled by crosslinking the fiber structure using PEI and HMDA of varying molecular weights and concentrations.

3.8 Conclusion

This study relates the NC gel-foam properties to their structure controlled by physical and partial chemical crosslinking. The structure and swelling behavior of freeze-dried NC foams based on TEMPO oxidized NC gels were investigated. NC gels were crosslinked physically and chemically (partially) by the addition of PEI and HMDA, respectively. The gels were characterized by rheology to assess the level of crosslinking and by HR-SEM for morphology evaluation. The chemical composition of the foams was analyzed by FTIR, and their water absorption capacity determined. SANS and SAXS analysis were performed on the dried foams and saturated foams at different levels of drying.

Functionalized NC foam networks can absorb up to 132 times their own weight in liquid. Water diffusion inside the cellulose nanofibrils swells the constitutive fiber bundle up to 19.5 nm. NC-PEI crosslinking expands the foam structure, which results in higher fiber bundle swelling at the nanoscale (25 nm), but lower absorption capacity at the macroscale (71 g/g) compared to the pure NC foam. In contrast, NC-HMDA crosslinking creates a more compact foam. The NC-HDMA fiber bundle swelling was only 15 nm due to the restriction of migration of water into the more compact fibrous network.

The hydration-dehydration behavior of NC foam shows the change of fiber bundle diameter during drying, confirming fiber bundle shrinkage from 19 nm to 14 nm upon drying. As drying progresses, the fiber bundle structure becomes more and more compact. After drying (air drying), the fiber bundle structure does not return to its original freeze-dried NC foam structure because of the different drying method.

Carboxylated nanocellulose foams have been prepared as superabsorbent in a previous study [27]. Crosslinking NC foams with PEI and HMDA can be used as a method to control and tailor the swelling capacity of NC foams. Cellulose nanofiber structure has been studied in dry and aqueous suspension [15, 40]. However, previous studies did not explore the structural change of crosslinked NC foams nor the mechanism of hydration-dehydration. In this study, structural change was analyzed in the context of swelling upon water absorption for crosslinked foam. Relating the fiber swelling capacity to the internal fibrous structure of a NC foam allows to engineer this material for specific and targeted food, agriculture, personal care and biomedical applications.

3.9 Acknowledgment

This work was supported by Food and Dairy Graduate Research Industry Partnership, Victorian Government, Monash University and Meat and Livestock Australia (MLA). The authors acknowledge the SAXS/WAXS beamline at the Australian Synchroton and BILBY SANS beamline at the Australian Nuclear Science and Technology Organization (ANSTO). Electron microscopy preparations and imaging were done at the Technion Center for Electron Microscopy of Soft Matter, and we acknowledge Prof. Yeshayahu (Ishi) Talmon and Dr. Naama Koifman for their valuable assistance and discussions.

3.10 References

1. Astrini, N., L. Anah, and A. Haryono, *Crosslinking Parameter on the preparation of cellulose based hydrogel with divynilsulfone.* Procedia Chemistry, **4**.2012. 275-281.
2. Shen, X., J.L. Shamshina, P. Berton, G. Gurau, and R.D. Rogers, *Hydrogels based on cellulose and chitin: fabrication, properties, and applications.* Green Chem., **18**(1).2015. 53-75.
3. Quennouz, N., S.M. Hashmi, H.S. Choi, J.W. Kim, and C.O. Osuji, *Rheology of cellulose nanofibrils in the presence of surfactants.* Soft Matter, **12**(1).2016. 157-164.
4. Saito, T. and A. Isogai, *TEMPO-mediated oxidation of native cellulose. The effect of oxidation conditions on chemical and crystal structures of the water-insoluble fractions.* Biomacromolecules, **5**(5).2004. 1983.
5. Abraham, E., B. Deepa, L. Pothan, M. Jacob, S. Thomas, U. Cvelbar, and R. Anandjiwala, *Extraction of nanocellulose fibrils from lignocellulosic fibres: A novel approach.* Carbohydrate Polymers, **86**(4).2011. 1468-1475.
6. Sannino, A., C. Demitri, and M. Madaghiele, *Biodegradable cellulose-based hydrogels: design and applications.* Materials, **2**(2).2009. 353-373.
7. Alam, M.N. and L. Christopher, *Natural Cellulose-Chitosan Crosslinked Superabsorbent Hydrogels with Superior Swelling Properties.* ACS Sustainable Chemistry & Engineering, **6**(7).2018. 8736-8742.
8. Reddy, N. and Y. Yang, *Citric acid cross-linking of starch films.* Food chemistry, **118**(3).2010. 702-711.
9. Capanema, N.S., A.A. Mansur, A.C. de Jesus, S.M. Carvalho, L.C. de Oliveira, and H.S. Mansur, *Superabsorbent crosslinked carboxymethyl cellulose-PEG hydrogels for potential wound dressing applications.* International journal of biological macromolecules, **106**.2018. 1218-1234.
10. Alam, M.N., M.S. Islam, and L.P. Christopher, *Sustainable Production of Cellulose-Based Hydrogels with Superb Absorbing Potential in Physiological Saline.* ACS Omega, **4**(5).2019. 9419-9426.
11. Zhao, F., E. Repo, Y. Song, D. Yin, S.B. Hammouda, L. Chen, S. Kalliola, J. Tang, K.C. Tam, and M. Sillanpää, *Polyethylenimine-cross-linked cellulose nanocrystals for highly efficient recovery of rare earth elements from water and a mechanism study.* Green Chemistry, **19**(20).2017. 4816-4828.

12. Boussif, O., F. Lezoualc'h, M.A. Zanta, M.D. Mergny, D. Scherman, B. Demeneix, and J.-P. Behr, *A versatile vector for gene and oligonucleotide transfer into cells in culture and in vivo: polyethylenimine.* Proceedings of the National Academy of Sciences, **92**(16).1995. 7297-7301.
13. Lungwitz, U., M. Breunig, T. Blunk, and A. Göpferich, *Polyethylenimine-based non-viral gene delivery systems.* European Journal of Pharmaceutics and Biopharmaceutics, **60**(2).2005. 247-266.
14. Lavoine, N. and L. Bergström, *Nanocellulose-based foams and aerogels: processing, properties, and applications.* Journal of Materials Chemistry A, **5**(31).2017. 16105-16117.
15. Antonini, C., T. Wu, T. Zimmermann, A. Kherbeche, M.-J. Thoraval, G. Nyström, and T. Geiger, *Ultra-Porous Nanocellulose Foams: A Facile and Scalable Fabrication Approach.* Nanomaterials, **9**(8).2019. 1142.
16. Trombino, S., R. Cassano, E. Bloise, R. Muzzalupo, L. Tavano, and N. Picci, *Synthesis and antioxidant activity evaluation of a novel cellulose hydrogel containing trans-ferulic acid.* Carbohydrate Polymers, **75**(1).2009. 184-188.
17. Jensen, O.M. *Water absorption of superabsorbent polymers in a cementitious environment*. in *International RILEM Conference on Advances in Construction Materials Through Science and Engineering*. 2011: p. 22-35. RILEM Publications SARL.
18. Kowalski, G., K. Kijowska, M. Witczak, Ł. Kuterasiński, and M. Łukasiewicz, *Synthesis and Effect of Structure on Swelling Properties of Hydrogels Based on High Methylated Pectin and Acrylic Polymers.* Polymers, **11**(1).2019. 114.
19. Raghuwanshi, V.S. and G. Garnier, *Characterisation of hydrogels: Linking the nano to the microscale.* Advances in Colloid and Interface Science.2019. 102044.
20. Liu, J., C. Zhang, D. Miao, S. Sui, F. Deng, C. Dong, L. Zhang, and P. Zhu, *Preparation and characterization of carboxymethylcellulose hydrogel fibers.* Journal of Engineered Fibers and Fabrics, **13**(3).2018. 155892501801300302.
21. Mendoza, L., W. Batchelor, R.F. Tabor, and G. Garnier, *Gelation mechanism of cellulose nanofibre gels: A colloids and interfacial perspective.* Journal of Colloid And Interface Science, **509**.2018. 39-46.
22. Mao, Y., K. Liu, C. Zhan, L. Geng, B. Chu, and B.S. Hsiao, *Characterization of nanocellulose using small-angle neutron, X-ray, and dynamic light scattering techniques.* The Journal of Physical Chemistry B, **121**(6).2017. 1340-1351.
23. Schmitt, J., V. Calabrese, M.A. Da Silva, S. Lindhoud, V. Alfredsson, J.L. Scott, and K.J. Edler, *TEMPO-oxidised cellulose nanofibrils; probing the mechanisms of gelation via small angle X-ray scattering.* Physical Chemistry Chemical Physics, **20**(23).2018. 16012-16020.
24. Koizumi, S., Y. Tomita, T. Kondo, and T. Hashimoto. *What Factors Determine Hierarchical Structure of Microbial Cellulose–Interplay among Physics, Chemistry and Biology–*. in *Macromolecular symposia*. 2009. **279**(1): p. 110-118. Wiley Online Library.
25. Saito, T., S. Kimura, Y. Nishiyama, and A. Isogai, *Cellulose nanofibers prepared by TEMPO-mediated oxidation of native cellulose.* Biomacromolecules, **8**(8).2007. 2485.
26. da Silva Perez, D., S. Montanari, and M.R. Vignon, *TEMPO-mediated oxidation of cellulose III.* Biomacromolecules, **4**(5).2003. 1417-1425.
27. Mendoza, L., L. Hossain, E. Downey, C. Scales, W. Batchelor, and G. Garnier, *Carboxylated nanocellulose foams as superabsorbents.* Journal of colloid and interface science, **538**.2019. 433-439.
28. Issman, L. and Y. Talmon, *Cryo-SEM specimen preparation under controlled temperature and concentration conditions.* Journal of microscopy, **246**(1).2012. 60-69.

29. Kirby, N.M., S.T. Mudie, A.M. Hawley, D.J. Cookson, H.D. Mertens, N. Cowieson, and V. Samardzic-Boban, *A low-background-intensity focusing small-angle X-ray scattering undulator beamline.* Journal of Applied Crystallography, **46**(6).2013. 1670-1680.
30. Glatter, O. and O. Kratky, *Small angle X-ray scattering*. 1982: Academic press.
31. Raghuwanshi, V.S., M. Ochmann, A. Hoell, F. Polzer, and K. Rademann, *Deep eutectic solvents for the self-assembly of gold nanoparticles: a SAXS, UV–Vis, and TEM investigation.* Langmuir, **30**(21).2014. 6038-6046.
32. Castilla, A.M., E.R. Draper, M.C. Nolan, C. Brasnett, A. Seddon, L.L. Mears, N. Cowieson, and D.J. Adams, *Self-sorted Oligophenylvinylene and Perylene Bisimide Hydrogels.* Scientific reports, **7**(1).2017. 8380.
33. Anitas, E. *Fractal fragmentation and small-angle scattering*. in *Journal of Physics: Conference Series*. 2015. **633**(1): p. 012119. IOP Publishing.
34. Shibayama, M., *Small Angle Neutron Scattering on Gels.* Soft Matter Characterization.2008. 783-832.
35. Courtenay, J.C., S.M. Ramalhete, W.J. Skuze, R. Soni, Y.Z. Khimyak, K.J. Edler, and J.L. Scott, *Unravelling cationic cellulose nanofibril hydrogel structure: NMR spectroscopy and small angle neutron scattering analyses.* Soft matter, **14**(2).2018. 255-263.
36. Klotz, A.R., *DNA Polymer Physics in Complex Nanofluidic Environments*. 2015, PhD thesis (McGill University, Montreal, Quebec).
37. Gao, J., J. Liu, H. Peng, Y. Wang, S. Cheng, and Z. Lei, *Preparation of a low-cost and eco-friendly superabsorbent composite based on wheat bran and laterite for potential application in Chinese herbal medicine growth.* Royal Society open science, **5**(5).2018. 180007.
38. Voronova, M.I., A.G. Zakharov, O.Y. Kuznetsov, and O.V. Surov, *The effect of drying technique of nanocellulose dispersions on properties of dried materials.* Materials letters, **68**.2012. 164-167.
39. Salmén, L. and J.S. Stevanic, *Effect of drying conditions on cellulose microfibril aggregation and "hornification".* Cellulose, **25**(11).2018. 6333-6344.
40. Nechyporchuk, O., M.N. Belgacem, and F. Pignon, *Concentration effect of TEMPO-oxidized nanofibrillated cellulose aqueous suspensions on the flow instabilities and small-angle X-ray scattering structural characterization.* Cellulose, **22**(4).2015. 2197-2210.

THIS PAGE WAS INTENTIONALLY LEFT BLANK

CHAPTER 4
ABSORPTION KINETICS OF NANOCELLULOSE FOAMS: EFFECT OF IONIC STRENGTH AND SURFACE CHARGE

THIS PAGE WAS INTENTIONALLY LEFT BLANK

Preface

TEMPO oxidation of cellulose fiber selectively oxidizes the primary alcohol groups on the fiber's surface to carboxyl groups. This oxidized material followed by homogenization and lyophilization can act as a SAP material. The structural change upon swelling for crosslinked and neat nanocellulose SAP has already been determined in Chapter 3. In chapter 3, we developed nanocellulose SAP with 1.4 mmol COO^- / g fiber surface charge by TEMPO oxidation. In this chapter, we have studied nanocellulose SAP with even higher surface charge to engineer a unique material with high absorbency and tuneability. TEMPO-periodate oxidation of nanocellulose fiber produces a nanocellulose SAP/foam with 1.89 mmol COO^-/ g fiber. This TEMPO-periodate oxidized SAP is compared with TEMPO oxidized SAP in terms of structural change, absorption capacity, absorption kinetics and phases of absorption. The structural differences are quantified by X-ray Computed Tomography and are correlated with absorption kinetics. Quantification of the three absorption phases provides a new fundamental understanding of the material from a structural perspective and in terms of designing nanocellulose SAPs for specific applications. The effect of solution ionic strength on absorption behavior is also determined for both types of nanocellulose SAP (TEMPO oxidized and TEMPO-periodate oxidized). This fundamental chapter quantifies the effect of surface charge and solution ionic strength on nanocellulose SAP structure, their resulting absorption phenomenon which provides the basis to understand the absorption mechanism and kinetics for SAPs varying surface charge density.

THIS PAGE WAS INTENTIONALLY LEFT BLANK

Chapter 4: Absorption kinetics of nanocellulose foams: Effect of ionic strength and surface charge

THIS PAGE WAS INTENTIONALLY LEFT BLANK

Absorption kinetics of nanocellulose foams: Effect of ionic strength and surface charge

Laila Hossain, Emily Eastman, Monica De Rango, Vikram Singh Raghuwanshi, Joanne Tanner, Gil Garnier*

Bioresource Processing Research Institute of Australia (BioPRIA), Department of Chemical Engineering, Monash University, Clayton

*Corresponding author: gil.garnier@monash.edu

4.1 Abstract

Hypothesis: The absorption capacity and kinetics of nanocellulose foams are controlled by the surface charge of the fibers, which affects swelling and determine the porosity and structure of the network.

Experiments: Absorption kinetics were quantified at time scales ranging from fractions of a second to minutes. The mass absorption rate as well as the area profile for the liquid stains were simultaneously measured.

Findings: The absorption profile followed a three-stage mechanism: wicking, transition and fiber swelling. Absorption of fluids differing in ionic strength revealed the critical role played by electrostatic forces. Nanocellulose foam absorption capacity is 25% higher for water than for 0.9 wt% NaCl solution. The absorption kinetics of nanocellulose foam are also tunable by modulating the surface charge. High surface charge nanocellulose foams have slower absorption in water than their low surface charged analogues. This behavior is driven by the lower pore sizes developed in high surface charge foams, as determined by X-ray CT. Small Angle X-ray Scattering revealed structural homogeneity of high surface charge foams upon absorption of water due to high fibrillation and fiber swelling.

4.2 Keywords

Nanocellulose; foam; absorption; X-ray computed tomography; structure; wicking; pore size.

4.3 Graphical Abstract

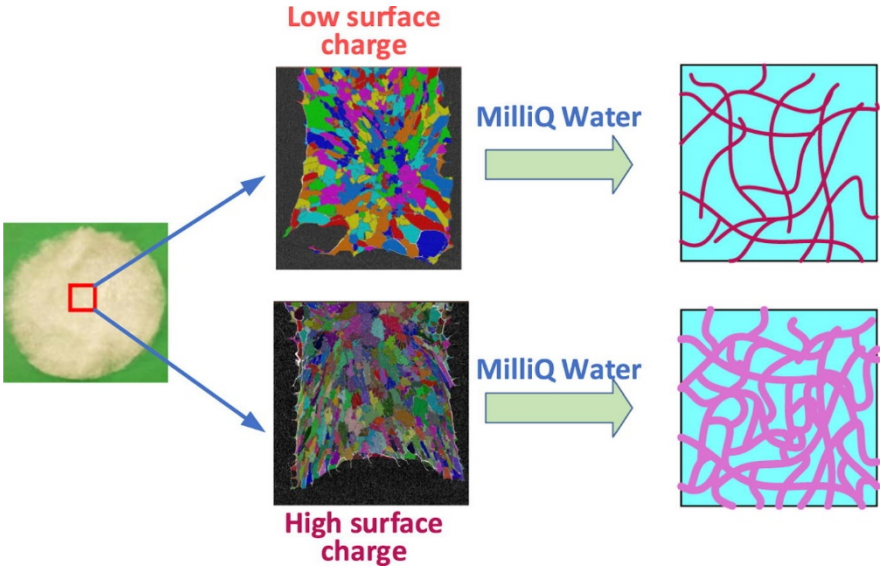

4.4 Introduction

Superabsorbent polymers (SAPs) are three-dimensional, crosslinked, hydrophilic polymer networks capable of absorbing a large volume of water relative to their dry mass [1]. They are used extensively in personal hygiene products, diapers, agriculture, horticulture, biomedical applications, and food packaging [2, 3]. However, most current commercial superabsorbents are based on sodium polyacrylate, a petrochemical-derived polymer which is non-degradable and non-renewable. Several renewable alternatives have been developed using cellulose, starch, gum, chitin and chitosan [4, 5]. Among those, cellulose appears to be the most promising renewable SAPs feedstock due to its worldwide abundance, low cost and inherent biodegradability. Cellulose fiber production is also well known and established on a commercial scale. Further processing of commercial cellulose fibers into carboxylated, nano-sized fibrils, followed by lyophilization, produces nanocellulose foams with superabsorbent properties [6, 7].

Nanocellulose foam material is comprised of entangled nanofibers which create the pores. When in contact with water, these pores and fibers take up water. There are examples in the literatures on fluid absorption in paper like swelling media where absorption occurs by a combination of wicking and fiber swelling [8, 9]. Wicking is the rapid flow of a fluid into the pores that exist between fibers, and is driven by capillary forces. This capillary action occurs when the cohesive force between the fluid molecules and the solid fiber surface is greater than the cohesive force between fluid molecules themselves. Fiber swelling occurs at a smaller length scale and involves

diffusion of the fluid through the fibers themselves. A difference in osmotic pressure between the fibers and the bulk solution in the foam pores provides the driving force for fiber swelling [10]. Swelling of fibers results in partial filling of the interfiber pore spaces and disruption of intrafiber hydrogen bonds between fibers, causing an overall expansion of the material [11].

Via the above mechanisms, nanocellulose foams can and do exhibit superabsorbent properties comparable to commercial SAPs. However, their absorption characteristics depend on a number of variables. For example, foams made with cellulose fibers that have residual associated lignin generally have a lower absorption capacity compared to analogous foams made with pure cellulose fibers due to the hydrophobic nature of lignin [12]. The ionic strength of the liquid to be absorbed can also affect absorption kinetics and capacity due to the influence of ionic strength of the bulk fluid on the osmotic pressure difference that controls fiber swelling. Other factors potentially affecting the superabsorbent properties of nanocellulose foams include the cellulose composition, cellulose surface charge, foam surface area, foam porosity and internal structure, absorbate pH, absorbate temperature and absorbate composition [13].

There are many reports in the literature on the production of nanocellulose foams that claim or demonstrate superabsorbent properties [14-19]. Absorption kinetics have also been determined for various examples of nanocellulose foams at time scales ranging from minutes to days, depending on the saturation duration of the material under investigation [2, 3, 20]. However, no study has yet correlated or quantified the initial absorption rate or phases of the absorption mechanism with differences in either nanocellulose foam structure at the various critical length and time scales of interest, particularly for foams exhibiting rapid (second to minute-scale) absorption kinetics. Moreover, the effect of fiber surface charge and the absorbate solution ionic strength on nanocellulose-based SAPs absorption kinetics, both of which are critical to the tuning of these materials for specific applications, have not been rigorously quantified.

This study investigates the effect of the nanocellulose fiber surface charge on the structure, absorption kinetics, and absorption capacity of nanocellulose foams. Here we demonstrate for the first time that there are three distinct phases of absorption, and present the kinetics of these characteristic phases of fluid absorption in nanocellulose foams. The impact of the combination of different fiber surface charges and solution ionic strengths on this mechanism is also shown, using a 0.9 wt% NaCl solution, to represent the typical ionic strength of body fluids including blood, urine and sweat and demonstrate the suitability of these materials to replace petrochemical SAPs in common commercial applications.

4.5 Experimental

4.5.1 Materials

Bleached Eucalyptus Kraft (BEK) pulp was used as supplied from Australian Paper, Maryvale. 2,2,6,6-Tetramethylpiperidine-1-oxyl (TEMPO), Hydrochloric acid (HCl), Sodium Periodate ($NaIO_4$), Sodium Hydroxide (NaOH) and Sodium Bromide (NaBr) were purchased from Sigma Aldrich. 12 w/v% Sodium Hypochlorite (NaClO) was bought from Thermo Fischer Scientific and used as supplied. Hydrochloric acid (HCl) and Sodium Hydroxide (NaOH) diluted for solutions as required.

4.5.2 Methods

4.5.2.1 TEMPO-mediated oxidation

The TEMPO-mediated oxidation process employed to produce low surface charged fibers was based on a previously developed method [21]. 100 g BEK pulp (dry weight basis) was suspended in 2500 mL water containing 0.4 g TEMPO and 2.5 g NaBr. The 12 w/v% NaClO solution was initially adjusted to pH 10 via addition of 36 w/v% HCl. 100 mL NaClO was added drop-wise to the suspension whilst stirring. The pH of the reaction was maintained at 10 through the addition of 0.5 M NaOH. The oxidation process was deemed to be complete when the pH change was negligible. The oxidized fibers were washed and vacuum filtered until neutral pH was achieved and stored at 4 °C. This preparation method produces oxidized fiber with a surface charge of 1.3 mmol carboxylate (COO–) groups per gram fiber. Fiber produced by this method and foams produced from this fiber are referred to as low surface charge (LSC) in this work. The TEMPO-oxidized pulp was then dispersed in deionized water at a desired concentration. Fibrillation and hydrogel formation were accomplished through a high-pressure homogenizer at 1000 bar with two passes. Nanocellulose foams were prepared by spreading 30 g of gel in a 50 mm petri dish and freezing at −80 °C for 4 h. Once frozen, all samples were freeze-dried for 48 h.

4.5.2.2 One-shot TEMPO-periodate oxidation

The one-shot TEMPO-periodate oxidation process employed to produce high surface charged fibers was based on a previously developed method [22]. 25 g (dry weight basis) of BEK pulp

were suspended in 1200 mL distilled water with 20 g NaBr, 13.5 g NaIO4, and 2 g TEMPO. The outside of the reaction vessel was covered with aluminum foil to prevent photoinduced decomposition of periodate. 120 mL NaClO (12% v/v, pH adjusted to 10.5) was added dropwise under constant stirring. The pH of the reaction was maintained at 10.5 by adding 0.5 M NaOH. After 4 h, the oxidation reaction was stopped by quenching with 10 mL ethanol. The water-insoluble fraction was recovered by vacuum filtration and washed several times with distilled water until a neutral pH in the filtrate stream was achieved. Fibrillation was done in the same way mentioned in section 4.5.2.1. The homogenized gels were then freeze-dried for 48 h. This preparation method produces oxidized fiber with a surface charge of 1.89 mmol carboxylate (COO^-) groups per gram fiber. Fiber produced by this method and foams produced from this fiber are referred to as high surface charge (HSC) in this work.

4.5.2.3 Determination of solids concentration

The solids concentration of sample (i.e. hydrogel or pulp) was determined through oven drying using a previously developed method [13]. The initial weight (w_i) was recorded before the sample was placed in a ventilated oven at 105 °C for at least 4 h and the sample dried to a constant final weight, w_f. The solids content was determined by:

$$Solids\ content\ (\%) = \frac{w_f - w_i}{w_i} \times 100\% \quad (1)$$

4.5.2.4 Determination of carboxylate content

The carboxylate content of the nanocellulose fiber was determined via conductimetric titration using a previously developed method [13]. 0.2 g dry oxidized pulp was suspended in 40 mL deionized water. The sample pH was then lowered to pH 2.5–3 by adding 0.5 M HCl to ensure protonation of all carboxylate groups prior to the beginning of titration. Sample titration was initiated by the addition of 0.1 mL/min 0.1 M NaOH (Mettler Toledo T5 Titrator). The conductivity was monitored throughout the progress of the titration. The amount of carboxylate groups was calculated by:

$$Carboxylate\ content\ \left(\frac{mmol}{g}\right) = \frac{c(V_2 - V_1)}{w} \times 1000 \quad (2)$$

where the difference in V2 and V1 reflects the required amount, in liters, of titrant required to neutralize the carboxylic groups (plateau region of the titration curve), c is the NaOH concentration (mol/L), and w is the dry sample weight (g).

4.5.2.5 Micro-CT analysis

Micro-CT scanning was performed with a Phoenix Nanotom m (GE Sensing & Inspection Technologies GmbH, Wunstorf, Germany) operated using xs control and Phoenix datos|x acquisition software (both GE Sensing & Inspection Technologies).

Foam specimens were mounted on glass rods using a drop of hot glue to at base. The x-ray energy (20 kV and 400 µA) of scans and integration time for x-ray projections (2 s) was optimized to enhance contrast in the foam specimens, which exhibited a very low density relative to the surrounding air. Scans were run at a resolution of 8 µm collecting 1200 projections over a 125-minute period. Volume reconstruction of the micro-CT data was performed using Phoenix datos|x reconstruction software (GE Sensing & Inspection Technologies) applying a median filter and ROI filter during reconstruction. The data was exported as 16-bit volume files for analysis.

Analysis of reconstructed data was conducted using Avizo (Thermo Fisher Scientific). The foam structure was segmented using an interactive threshold and a sample mask created by closing and filling the structure. An inversion of the foam structure within the mask represents the pore space between the foam structure. The segmented volume and volume fraction of foam and pore space was then determined relative to the sample mask. Individual pores were segmented and the pore size distribution produced by labelling and separating the segmented pore space using a Chamfer algorithm, which is based on a watershed analysis of the data.

4.5.2.6 Absorption kinetics

The nanocellulose foam to be tested was cut into 2 cm × 2 cm samples using a laser cutter (EPILOG Laser). The edge of a sample was attached to a metal rod with superglue. The minimum amount of glue required to attach the sample to the rod was used to minimize interference with absorption experiments since the glue is hydrophobic. The rod with sample attached was hung from the hook on the bottom of a balance, so the nanocellulose foam sample was hanging above a reservoir of either deionized water or 0.9% NaCl solution on a height-adjustable stage. The balance was

connected to a laptop via LabX Direct Balance Software to record the weight of the sample at specified time intervals. Three drops of food dye were mixed through the absorbate to provide greater contrast for image analysis. Care was taken to ensure the edge of the sample was parallel to the fluid surface so the entire edge will contact the fluid at the same time. This experimental set-up is shown in Figure 4-1.

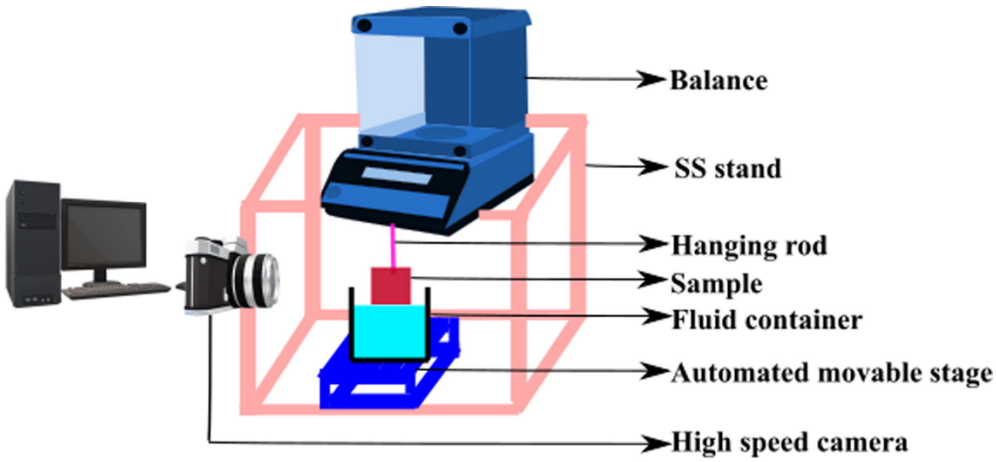

Figure 4-1. Schematic diagram of the testing system to measure simultaneously the absorption kinetics of NC foam as well as the area of the liquid stain.

The pre-weighed sample was slowly lowered by adjusting the reservoir stage height. Care was taken to ensure that both the sample and the absorbate surface remained stationary while moving the stage. Once the edge of the sample was just touching the surface of the absorbate, height adjustment of the stage was stopped. After 5 min, the stage was moved downwards so that the sample was no longer touching the absorbate and the final weight of the saturated sample was recorded. This final weight was divided by the dry weight of the sample to give the weight of absorbate taken up per gram of dry nanocellulose sample.

This experiment was conducted in triplicate with 0.9% NaCl solution and in triplicate with water for vertical orientation of the sample in a controlled environment of 23 °C and 50% relative humidity. A video camera (FLIR Systems, Model: FL3-U3-13E4C-C: 1.3 MP, 60 FPS, e2v EV76C560, Color) was installed to capture images of each absorption trial. The images were converted to binary (black and white) in MATLAB, and the stained area of the sample in the image was used to calculate the area of absorption of the sample.

The results are reported as the average and standard deviation of the calculated absorption areas of the three replicates for each absorbate. The effects of buoyancy and surface tension have not been considered in this study.

4.5.2.7 Small angle X-ray scattering (SAXS)

Small angle X-ray Scattering (SAXS) experiments were conducted at the SAXS/WAXS beamline of the Australian Synchrotron with the assistance of Beamline Scientist Nigel Kirby. An X-ray energy of 12 KeV was used, and the samples were measured in the transmission mode. A 2D Pilatus detector was placed at the long distance of 7 m from the sample to cover a large size range. During measurements samples were first measured in the dried state and later measured as fully wetted with MilliQ water or 0.9% NaCl solution. A glassy carbon and silver behenate standards were used for the calibration. The in-house developed software Scatterbrain was used for data reduction and plotting of the 2D images.

4.6 Results

The absorption kinetics is measured in increments of 0.1 s for five minutes for nanocellulose foams made from fibers of two different surface charges of 1.3 mmol COO^-/g fiber and 1.89 mmol COO^- /g fiber produced from TEMPO and TEMPO-periodate oxidation, respectively. These foams are used separately to absorb MilliQ water and a saline solution (0.9 wt% NaCl). Continuous online image capturing and analysis are performed to quantify the absorption phases at complementary time scales.

4.6.1 Effect of liquid ionic strength

Figure 4-2 illustrates the absorption profile of low surface charge (LSC) nanocellulose foam for MilliQ water and 0.9 wt% NaCl solution to quantify the effect of ionic absorbates on the absorption kinetics. The nanocellulose foam has a larger absorption capacity in water than in saline solution (Figure 4-2). After 5 min, nanocellulose foam absorbed 81 g/g of MilliQ water versus 65 g/g for the NaCl solution. The initial kinetics of nanocellulose foam absorption were measured from the first 10 s (inset of Figure 4-2). After 1 s, the difference in the amount of fluid absorbed is already significant, with 53 g/g of MilliQ water and 38 g/g of NaCl solution. Absorption of NaCl solution

appears to be lower than that of MilliQ water due to Na^+ shielding the COO^- groups of the nanocellulose foam, decreasing its hydrophilicity and reducing the absorption capacity [23].

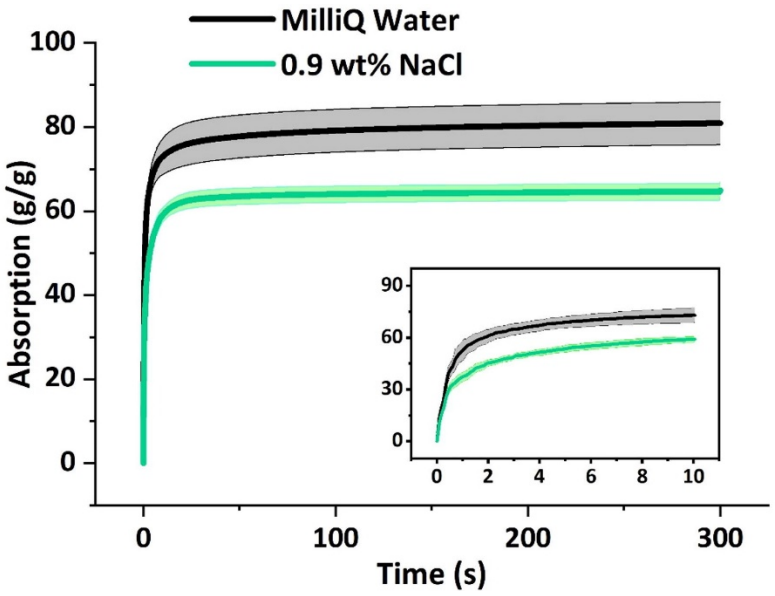

Figure 4-2. Effect of liquid ionic strength on LSC nanocellulose foam absorption kinetics over a period of 5 min for MilliQ water and 0.9 wt% NaCl. The inset shows the effect of ionic strength over 10 s. The solid line represents the average result (n = 3), while the shaded zone indicates the range formed by one standard deviation.

4.6.2 Effect of fiber surface charge

The impact of fiber surface charge on the absorption behavior of nanocellulose foam is measured using foams of two different charge densities: 1.3 mmol COO^-/g (low surface charge, LSC) and 1.89 mmol COO^-/g (high surface charge, HSC). The dimensions of these two different fibers are provided in Table 4-1. The high surface charge fibers are shorter and slightly thinner than the low surface charge fibers.

Table 4-1: Effect of oxidation on fiber dimension and charge [24].

Type of nanocellulose foam	Surface charge (mmol/g)	Fiber length (μm)×dia (nm)
TEMPO oxidized nanocellulose foam (LSC)	1.30	(>1) × (>5)
TEMPO-periodate oxidized nanocellulose foam (HSC)	1.89	(0.5) × (2-4)

The effect of nanocellulose surface charge on absorption kinetics was assessed. Figure 4-3 shows the absorption profiles of LSC and HSC foams for MilliQ water and 0.9 wt% NaCl at different time scales. HSC foam has slower absorption kinetics than LSC at the short time scales (inset of Figure 4-3A), but displays a slightly higher overall absorption capacity after 5 min (Figure 4-3A).

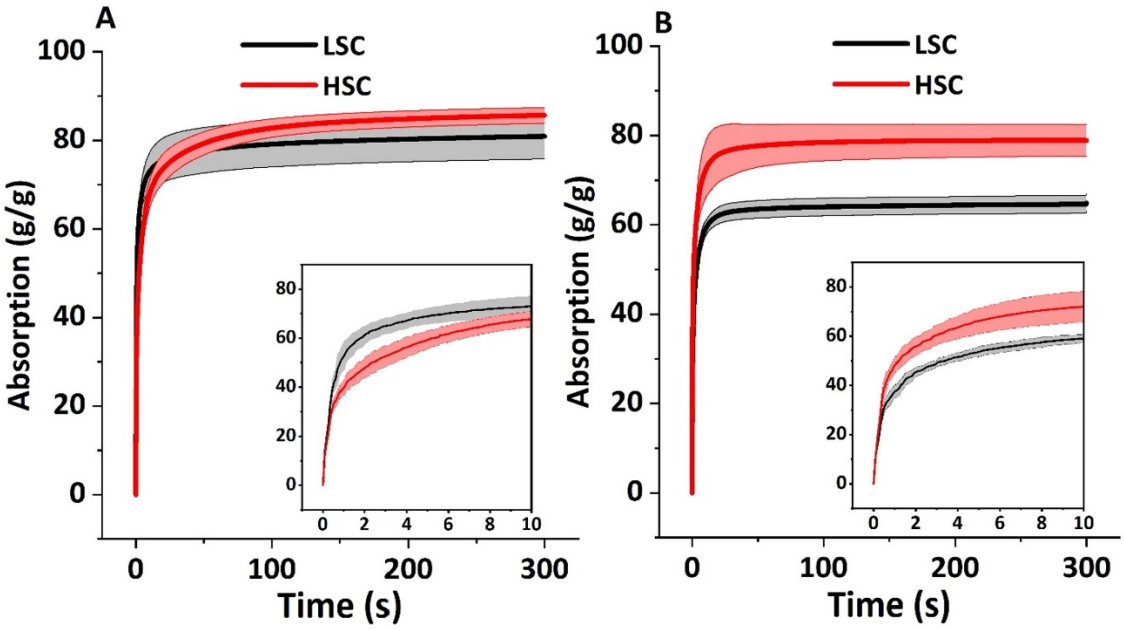

Figure 4-3. Effect of low and high fiber surface charge on the absorption kinetics after 5 min for: (A) MilliQ water and (B) 0.9 wt% NaCl. The insets show the magnified graphs over a 10 s period. The solid line represents the average (n = 3), while the shaded zone indicates the range formed by one standard deviation.

SAXS scattering of the nanocellulose foams in their dry and wet forms was measured (Figure 4-4). For the LSC foam, there are sharp boundaries due to aggregated fibers found under both dry

and wet conditions. This means some structural heterogeneity caused by a lower fibrillation and lower fiber swelling in the dry and wet state, respectively. However, the HSC wet foam in MilliQ water does not show these sharp boundaries. The HSC foam has higher inter-fiber repulsion which results in a higher fibrillation as evidenced from the lower fiber diameter measured (Table 1). This higher fibrillation together with high fiber swelling lead to the structural homogeneity observed for the HSC samples in MilliQ water. However, when HSC foam is wetted with a saline solution, some sharp boundaries from aggregated fibers are formed. This indicates a reduced charge repulsion and fiber swelling due to the high ionic strength of the absorbate.

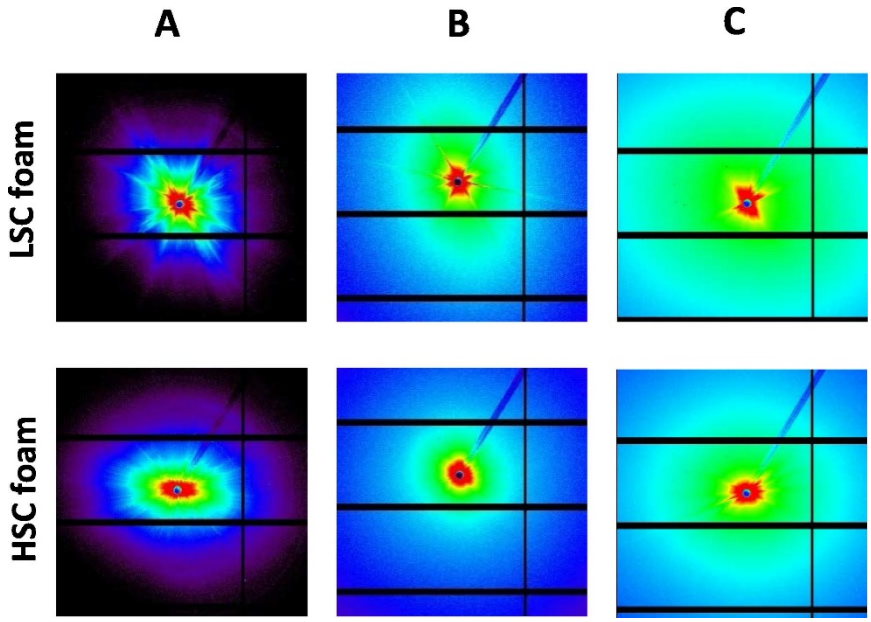

Figure 4-4. SAXS measurements of LSC and HSC nanocellulose foams. (A) Dry foam and wet foam in (B) MilliQ water, and (C) 0.9 wt% NaCl. The first row represents the LSC foam while the second row is for HSC foams.

4.6.3 Structural analysis by micro CT

Structural analysis of the nanocellulose foam samples was performed by X-ray Computed Tomography (CT). Figure 4-5 shows the 3D structures of the nanocellulose foams, the separated pore structure of the foams in the X-Z plane, and their pore size distributions. The HSC foam shows smaller pores than the LSC foam (Figure 4-5E and F). The HSC foam has a higher frequency (~9000) of the smallest pore volumes ($2 \times 10^{-5} - 1 \times 10^{-1}$ mm^3) compared to the LSC foam (~2000). The HSC foam is more homogeneous and denser, as shown by the 3D structure

(Figure 4-5 A-B), due to the smaller pore volumes relative to the LSC foam. The LSC has a wider range of pore size distribution, contributing to structural heterogeneity.

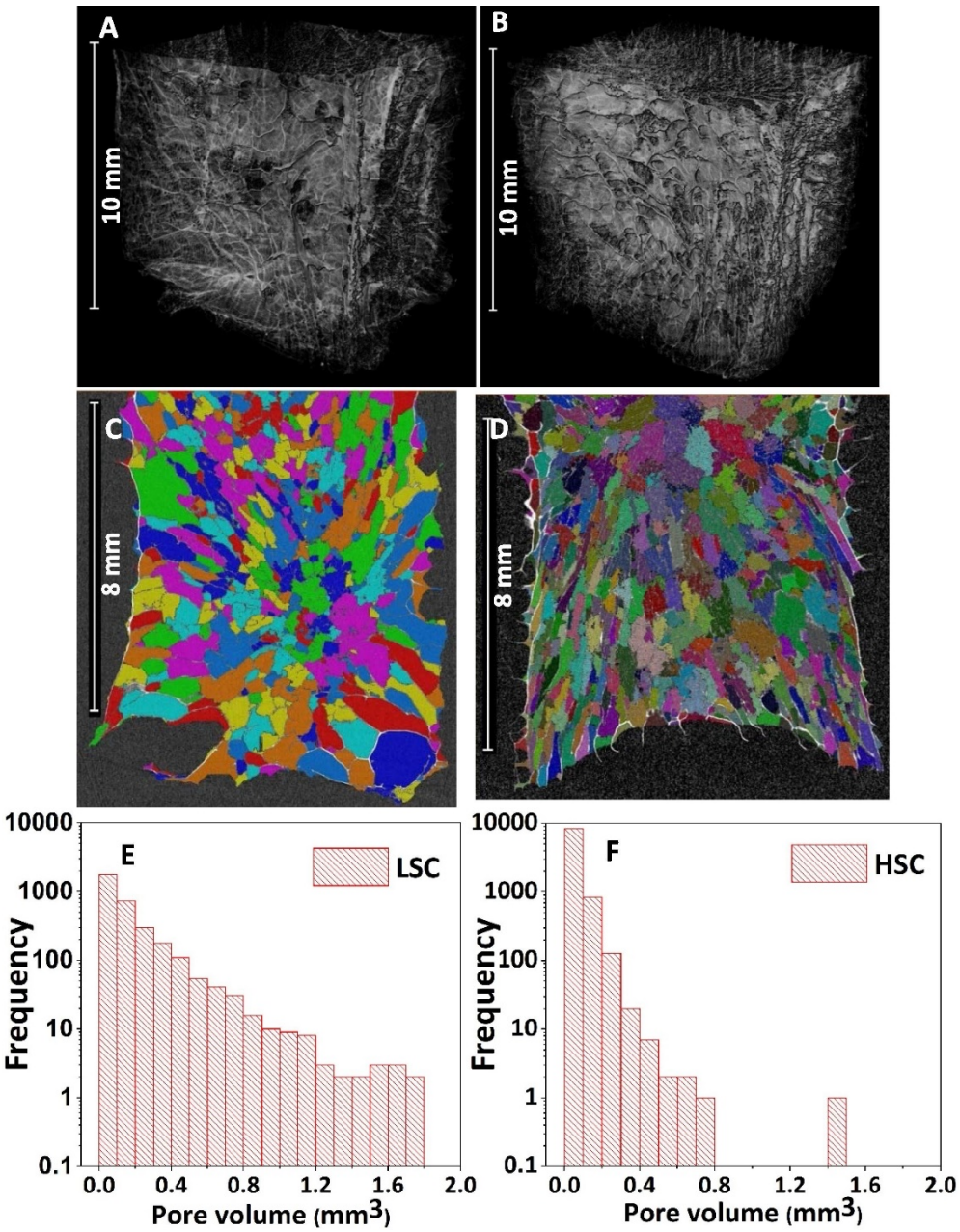

Figure 4-5. Structural analysis of nanocellulose foams by X-ray tomography. 3D structure of: (A) LSC foam, (B) HSC foam; XZ planar slice showing separated pore structure of (C) LSC foam, and (D) HSC foam; pore size distribution of (E) LSC and (F) HSC foam.

4.7 Discussion

4.7.1 Absorption mechanism of nanocellulose foam

The liquid absorption profiles of nanocellulose foams follow an exponential plateau relationship with time and demonstrate the three stages of absorption in nanocellulose foams: wicking, transition phase and fiber swelling. In this work, wicking corresponds well with the period of increasing absorption area as determined by image analysis, and fiber swelling is dominant when absorption continues to increase although the liquid stain area remains constant. Figure 4-6 shows the three different phases of the absorption phenomena by following the size of the liquid stain: wicking (0 to 0.7 s- Phase I); transition (0.7 to 3.8 s- Phase II) and fiber swelling (from 3.8 s- Phase III).

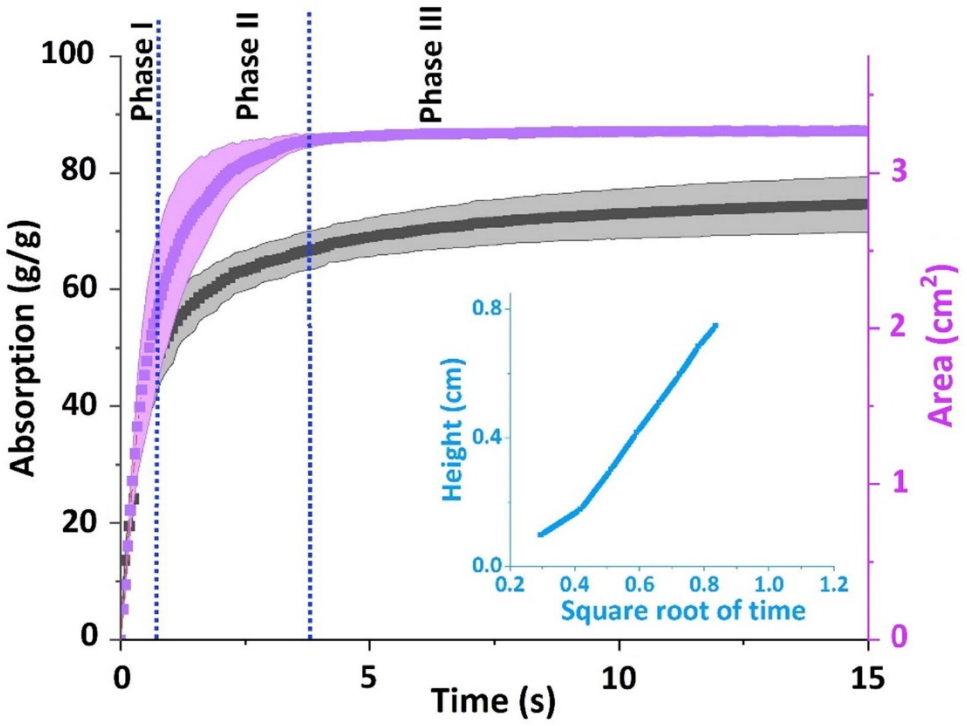

Figure 4-6. Effect of wicking and fiber swelling in LSC nanocellulose foam. The black line indicates absorption and the purple represents the area data. The inset shows the relationship between wicking height and time for phase I. The solid line is the average (n = 3), while the shaded zone indicates the range formed by one standard deviation.

Fluid accommodated by Phase I has been correlated to pore volume in Table 4-2. The fluid absorbed in phase I of Figure 4-3 mainly results from the absorption capacity driven by the pore volume.

Table 4-2: Analysis of pore volume and fluid accommodated by pore volume of the NC foams

Parameter		Volumetric pore density (mm^3/ mm^3)	Fluid accommodated by pore volume (g/g foam)[1]	Fluid absorbed in phase I (g/g foam)[2]	Percentage of fluid accommodated by pore volume after 5 mins absorption
LSC	MilliQ	0.88	42.7	46.8	52.8
	Saline			41.4	65.8
HSC	MilliQ	0.76	35.8	36.2	41.8
	Saline			34.1	45.3

Wicking is driven by capillary forces [25] and is mainly characterized by a high initial absorption rate. The inset of Figure 4-6 shows that the wicking height is proportional to the square root of time for Phase I, following the Lucas- Washburn equation. As absorption progresses and fiber swelling begins to reduce the dimensions of the inter-fiber pore spaces [26], wicking becomes limited and the transport of liquid through the nanocellulose foam structure relies increasingly on diffusion (Phase III) over capillary action following the transition phase (Phase II) [9]. This results in a reduction in the rate of absorption as seen by the decreasing slope which signals the onset of the transition phase (Phase II).

4.7.2 Effect of ionic strength on absorption

The nanocellulose foam absorption capacity for the 0.9 wt% NaCl solution is lower than for MilliQ water (Figure 4-2). This corroborates the findings of Sultana et al. for different SAPs [10]. The

[1] Calculated total amount of fluid that can be accommodated inside the pore structure by calculating pore volume.

[2] Amount of fluid calculated from the straight-line region (phase I as mentioned in Figure 4-6) of Figure 4-3.

nanocellulose foam contains free mobile ions in its structure that exert an osmotic pressure on the fiber network. A difference in osmotic pressure between the fiber network and the absorbate creates a driving force for absorption to occur [27]. Addition of salt to the absorbate reduces the osmotic pressure difference and hence reduces the driving force for absorption. The lower absorption capacity in 0.9 wt% NaCl solution than in MilliQ water is also a consequence of charge shielding as increasing the concentration of free ions in the absorbate reduces the interaction of the nanocellulose carboxylate (COO–) groups with water molecules, therefore decreasing their affinity and absorption propensity [13].

4.7.3 Effect of surface charge on absorption

4.7.3.1 Deionized water

The high surface charge foam exhibits slower absorption kinetics than low surface charge foam for MilliQ water. From the absorption experiments, LSC foam achieved 80% of its total absorption capacity within the first 3 s whereas HSC foam only reached 62% in the same time period (Figure 4-3A). Similarly, after 30 min of free swelling, LSC foam had achieved 75% of its saturation capacity compared to 66% for HSC foam for MilliQ water (Supplementary Info 4-S1). Image analysis of the liquid stain confirms the slower kinetics of the HSC foam compared to the LSC (Figure 4-7A). The slower absorption kinetics and higher saturation capacity indicate that a major part of the absorption capacity of HSC foam results from fiber swelling. The osmotic pressure is increased in HSC foam due to an augmented charge density which facilitates higher fiber swelling in HSC foam compared to LSC foam [28-30].

The slower absorption kinetic of the HSC foam is due to its lower pore size compared to the LSC foam. The HSC foam also has a higher surface charge which improves the efficiency and therefore the extent of fibrillation due to greater electrostatic repulsion combined with less hydrogen bonding [24]. Thus, HSC foam porosity is lower than that of the LSC foam [31]. As flow resistance from small pores decelerates wicking [32], LSC foams exhibit a higher rate of initial absorption compared to HSC foams.

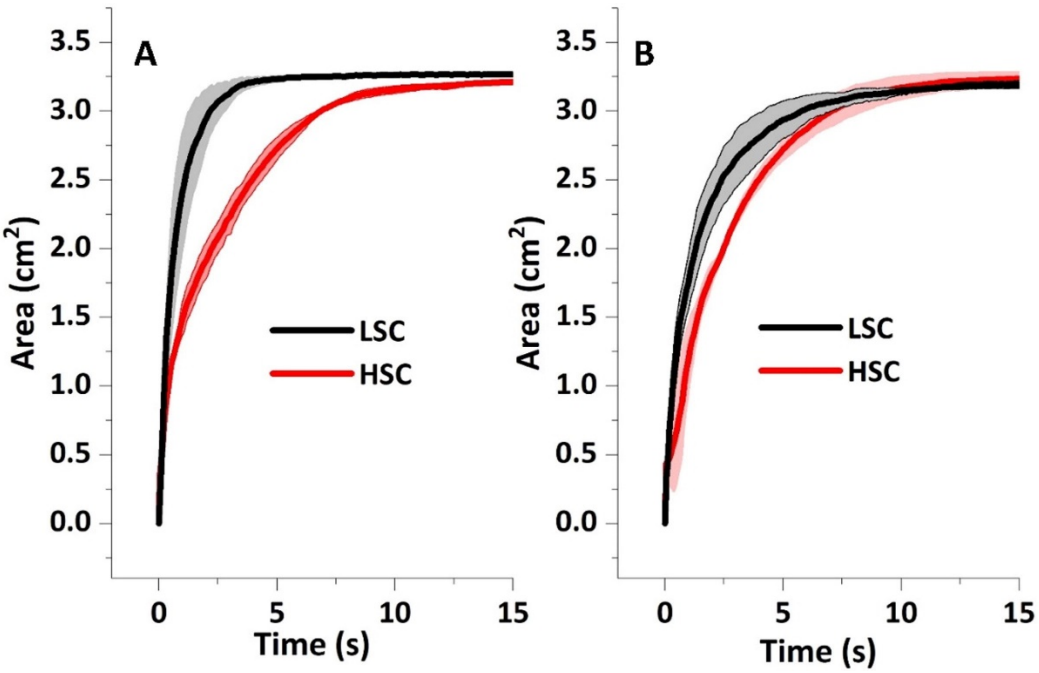

Figure 4-7. Effect of surface charge on the stain area of the absorbed fluid over time for LSC and HSC NC foams, for (A) Milli Q water and (B) 0.9 wt% NaCl. The solid line is the average (n = 3), while the shaded zone indicates the range formed by one standard deviation.

4.7.3.2 0.9 wt% saline solution

HSC foam exhibits similar absorption kinetics but higher absorption capacity than LSC foam when absorbing a NaCl solution (Figure 4-3B). Image analysis confirms that HSC and LSC foams have similar wicking kinetics in a NaCl solution (Figure 4-7B). However, the absorption capacity of HSC is higher (Figure 4-3B) which means fiber swelling is higher for HSC foam compared to that of LSC for NaCl solution.

4.8 Conclusion

Nanocellulose based foams are attractive because of their inherent renewability and biodegradability [33]. Nanocellulose foam with different solid concentrations and surface charges have already been developed [13, 24]. The swelling of natural polymers, cellulose films and superabsorbents has been previously analyzed as a function of pH and ionic strength [28, 34-37]. However, the absorption kinetics, the mechanism and the absorption phases for a fast-swelling foam/superabsorbent have not been reported. In this study, the absorption kinetics of

superabsorbent nanocellulose foams varying in charge density (controlled with the COO– concentration) are measured for MilliQ water and 0.9 wt% NaCl solution and the results interpreted in terms of foam structure and absorption mechanism. The absorption kinetics are measured at time frames ranging from a fraction of a second to a few minutes to elucidate the full absorption mechanism and correlate it with foam structure and porosity.

Kinetics and wicking area data both confirm the occurrence of three distinct stages of absorption. These are: 1) wicking, 2) transition and 3) fiber swelling. Wicking is driven by capillary forces and dominates in the first few seconds of absorption. The wicking rate of nanocellulose foams for MilliQ water depends on pore size, as evidenced from X-ray computed tomography, with higher rates for foams with larger pore sizes. Wicking is followed by the transition phase, after which fiber swelling dominates the absorption mechanism. A high surface charge (density of COO^- groups) increases fiber swelling [38], which is a slower mechanism than wicking. The slower absorption kinetics of high surface charge fiber foam are therefore due to both smaller pore size and higher concentration of COO– groups. When absorbing an ionic solution, fiber swelling is reduced due to charge shielding and, as a result, the maximum absorption capacity of nanocellulose foam is decreased. Small Angle X-ray Scattering analysis corroborates this hypothesis by revealing the occurrence of fiber agglomeration in both high and low surface charge nanocellulose foams for the absorption of NaCl solution.

This fundamental absorption study aims to elucidate the initial absorption mechanism of nanocellulose foam. Using these results, performant biosourced and sustainable nanocellulose foams with the desired structure and absorption kinetics can be engineered. These foams can meet the stringent standards and performance criteria for applications such as baby diapers, personal hygiene products or biosensors, and represent a sustainable alternative to petrochemical-based superabsorbent polymers.

4.9 Acknowledgment

Financial support was received from Meat and Livestock Australia (MLA) [grant number P.PSH.0890]. The authors acknowledge Stephen Mudie, Nigel Kirby from the SAXS/WAXS beamline at the Australian Synchrotron for the SAXS measurement. Moreover, authors acknowledge ANSTO for the beamtime. The authors also thank Micro-Computed Tomography

facilities in University of Melbourne. And thanks to David Mendoza for providing the tempo-periodate oxidized fiber.

4.10 References

1. Zohuriaan-Mehr, M.J. and K. Kabiri, *Superabsorbent polymer materials: a review.* Iranian polymer journal, **17**(6).2008. 451.
2. Barajas-Ledesma, R.M., A.F. Patti, V.N. Wong, V.S. Raghuwanshi, and G. Garnier, *Engineering nanocellulose superabsorbent structure by controlling the drying rate.* Colloids and Surfaces A: Physicochemical and Engineering Aspects, **600**.2020. 124943.
3. Sawut, A., M. Yimit, W. Sun, and I. Nurulla, *Photopolymerisation and characterization of maleylatedcellulose-g-poly (acrylic acid) superabsorbent polymer.* Carbohydrate polymers, **101**.2014. 231-239.
4. Alam, M.N. and L. Christopher, *Natural Cellulose-Chitosan Crosslinked Superabsorbent Hydrogels with Superior Swelling Properties.* ACS Sustainable Chemistry & Engineering, **6**(7).2018. 8736-8742.
5. Mondal, M.I.H., *Cellulose-based superabsorbent hydrogels*. 2019: Springer.
6. Zhang, Y., T. Nypelö, C. Salas, J. Arboleda, I.C. Hoeger, and O.J. Rojas, *Cellulose nanofibrils.* Journal of Renewable Materials, **1**(3).2013. 195-211.
7. De France, K.J., T. Hoare, and E.D. Cranston, *Review of hydrogels and aerogels containing nanocellulose.* Chemistry of Materials, **29**(11).2017. 4609-4631.
8. Soriano, L. and M. Rahman, *Wicking Properties of Brassica Fiber in Three Different Growth Stages.*2016.
9. Akinli-Kocak, S., *The influence of fiber swelling on paper wetting.*2001.
10. Sultana, S., M.S. Rahaman, and S.M.M. Hasnine, *Effect of Salinity on Swelling Behaviors of Superwater Absorbent Hydrogel Prepared from Carboxymethyl cellulose/Acrylamide Blends by Gamma Radiation.* American Journal of Applied and Industrial Chemistry, **2**(2).2018. 20-26.
11. Schuchard, D.R. and J.C. Berg, *Liquid transport in composite cellulose—superabsorbent fiber networks.* Wood and Fiber Science, **23**(3).2007. 342-357.
12. Hubbe, M.A., A. Ayoub, J. Daystar, R. Venditti, and J. Pawlak, *Enhanced Absorbent Products Incorporating Cellulose and Its Derivatives: A Review*, in *BioResources*. 2013. p. 6556-+.
13. Mendoza, L., L. Hossain, E. Downey, C. Scales, W. Batchelor, and G. Garnier, *Carboxylated nanocellulose foams as superabsorbents.* Journal of colloid and interface science, **538**.2019. 433-439.
14. Petroudy, S.R.D., J. Ranjbar, and E.R. Garmaroody, *Eco-friendly superabsorbent polymers based on carboxymethyl cellulose strengthened by TEMPO-mediated oxidation wheat straw cellulose nanofiber.* Carbohydrate Polymers, **197**.2018. 565-575.
15. Nnadi, F. and C. Brave, *Environmentally friendly superabsorbent polymers for water conservation in agricultural lands.* Journal of Soil Science and Environmental Management, **2**(7).2011. 206-211.
16. Patiño-Masó, J., F. Serra-Parareda, Q. Tarrés, P. Mutjé, F.X. Espinach, and M. Delgado-Aguilar, *TEMPO-oxidized cellulose nanofibers: a potential bio-based superabsorbent for diaper production.* Nanomaterials, **9**(9).2019. 1271.

17. Demitri, C., R. Del Sole, F. Scalera, A. Sannino, G. Vasapollo, A. Maffezzoli, L. Ambrosio, and L. Nicolais, *Novel superabsorbent cellulose-based hydrogels crosslinked with citric acid.* Journal of Applied Polymer Science, **110**(4).2008. 2453-2460.
18. Brodin, P.W. and H. Theliander, *Absorbent materials based on kraft pulp: Preparation and material characterization.* BioResources, **7**(2).2012. 1666-1686.
19. Brodin, F.W., Y. Sonavane, and H. Theliander, *Preparation of absorbent foam based on softwood kraft pulp: advancing from gram to kilogram scale.* BioResources, **8**(2).2013. 2099-2117.
20. Olad, A., F. Doustdar, and H. Gharekhani, *Fabrication and characterization of a starch-based superabsorbent hydrogel composite reinforced with cellulose nanocrystals from potato peel waste.* Colloids and Surfaces A: Physicochemical and Engineering Aspects, **601**.2020. 124962.
21. Saito, T., S. Kimura, Y. Nishiyama, and A. Isogai, *Cellulose nanofibers prepared by TEMPO-mediated oxidation of native cellulose.* Biomacromolecules, **8**(8).2007. 2485-2491.
22. Mendoza, D.J., C. Browne, V.S. Raghuwanshi, G.P. Simon, and G. Garnier, *One-shot TEMPO-periodate oxidation of native cellulose.* Carbohydrate polymers, **226**.2019. 115292.
23. Fekete, T., J. Borsa, E. Takács, and L. Wojnárovits, *Synthesis of carboxymethylcellulose/starch superabsorbent hydrogels by gamma-irradiation.* Chemistry Central Journal, **11**(1).2017. 46.
24. Mendoza, D.J., L. Hossain, C. Browne, V.S. Raghuwanshi, G.P. Simon, and G. Garnier, *Controlling the transparency and rheology of nanocellulose gels with the extent of carboxylation.* Carbohydrate Polymers.2020. 116566.
25. Liu, Z., X. He, J. Han, X. Zhang, F. Li, A. Li, Z. Qu, and F. Xu, *Liquid wicking behavior in paper-like materials: mathematical models and their emerging biomedical applications.* Microfluidics and Nanofluidics, **22**(11).2018. 132.
26. Patnaik, A., R.S. Rengasamy, V.K. Kothari, and A. Ghosh, *Wetting and Wicking in Fibrous Materials.* Textile Progress, **38**(1).2006. 1-105.
27. Elliott, M., *Superabsorbent polymers.* Product development scentist for SAP. BASF Aktiengesellschaft ss, **13**.2004.
28. Fält, S., L. Wågberg, and E.-L. Vesterlind, *Swelling of model films of cellulose having different charge densities and comparison to the swelling behavior of corresponding fibers.* Langmuir, **19**(19).2003. 7895-7903.
29. Hanhikoski, S., I. Solala, P. Lahtinen, K. Niemelä, and T. Vuorinen, *Fibrillation and characterization of lignin-containing neutral sulphite (NS) pulps rich in hemicelluloses and anionic charge.* Cellulose.2020.
30. Buchholz, F.L. and A.T. Graham, *Modern superabsorbent polymer technology.* John! Wiley & Sons, Inc, 605 Third Ave, New York, NY 10016, USA, 1998. 279.1998.
31. Wakabayashi, M., S. Fujisawa, T. Saito, and A. Isogai, *Nanocellulose Film Properties Tunable by Controlling Degree of Fibrillation of TEMPO-Oxidized Cellulose.* Frontiers in Chemistry, **8**.2020. 37.
32. Ahmed, S., M.-P.N. Bui, and A. Abbas, *based chemical and biological sensors: Engineering aspects.* Biosensors and Bioelectronics, **77**.2016. 249-263.
33. Klemm, D., E.D. Cranston, D. Fischer, M. Gama, S.A. Kedzior, D. Kralisch, F. Kramer, T. Kondo, T. Lindström, and S. Nietzsche, *Nanocellulose as a natural source for groundbreaking applications in materials science: Today's state.* Materials Today, **21**(7).2018. 720-748.
34. Kabiri, K. and M. Zohuriaan-Mehr, *Superabsorbent hydrogel composites.* Polymers for Advanced Technologies, **14**(6).2003. 438-444.

35. de Lima, G.F., A.G. de Souza, and D.d.S. Rosa. *Nanocellulose as Reinforcement in Carboxymethylcellulose Superabsorbent Nanocomposite Hydrogels*. in *Macromolecular Symposia*. 2020. **394**(1): p. 2000126. Wiley Online Library.
36. Deghiedy, N., *Synthesis and Characterization of Super absorbent Hydrogels Based on Natural Polymers Using Ionizing Radiations*. 2010, Faculty of Science Al-Azhar University (Girls) Cairo In the partial fulfillment for M. Sc. Degree in Chemistry (Organic Chemistry) Submitted by Noha Mohamed Abd El-Salam Deghiedy B. Sc. of Science (Special Chemistry) Faculty of Science, Al-Azhar University.
37. Das, D., P. Prakash, P.K. Rout, and S. Bhaladhare, *Synthesis and Characterization of Superabsorbent Cellulose-Based Hydrogel for Agriculture Application.* Starch-Stärke, **73**(1-2).2021. 1900284.
38. Mayr, M., R. Eckhart, H. Winter, and W. Bauer, *A novel approach to determining the contribution of the fiber and fines fraction to the water retention value (WRV) of chemical and mechanical pulps.* Cellulose, **24**(7).2017. 3029-3036.

CHAPTER 5
EFFECT OF CROSSLINKING ON NANOCELLULOSE SUPERABSORBENT BIODEGRADABILITY

THIS PAGE WAS INTENTIONALLY LEFT BLANK

Preface

Fundamentals aspects of the nanocellulose SAP structure-property relationship were studied in chapter 2 to chapter 4. Sustainable nanocellulose SAP was developed, characterized and the structure was modulated for mechanical strength, absorption capacity and absorption kinetics. The next question surrounds the biodegradation rate and mechanisms for this novel SAP. In this chapter, biodegradation of neat and crosslinked nanocellulose SAP are quantified under enzymatic assisted condition to accelerate the process. Nanocellulose SAP biodegradation is studied in soil with cellulase as enzyme. Neat SAP degradation rate is compared with crosslinked SAP - with and without enzyme. The biodegradation quantification for crosslinked SAP enables the use of crosslinked SAP for specific applications where biodegradation is required.

THIS PAGE WAS INTENTIONALLY LEFT BLANK

Chapter 5: Effect of Crosslinking on Nanocellulose Superabsorbent Biodegradability

THIS PAGE WAS INTENTIONALLY LEFT BLANK

Effect of crosslinking on nanocellulose superabsorbent biodegradability

5.1 Abstract

Superabsorbent polymer (SAP) is an excellent material to absorb and retain a wide range of fluids inside its structure, making it desirable to engineer advanced applications. However, commercial SAPs are petrochemical products and their non-biodegradability and end of life are significant environmental issues. In this study, we have developed a TEMPO oxidized nanocellulose superabsorbent and quantified the effect of crosslinking on biodegradation in soil under enzymatic (cellulase) assisted condition. CO_2 emission shows that both types of SAP emit similar amounts of CO_2. Hydrolysis of residual SAPs in soil after specific time intervals shows that chemically crosslinked SAP degrades more compared to neat nanocellulose SAP. However, without enzyme, their degradation is similar and much lower than under enzymatic condition (after 6 days). These results suggest that nanocellulose SAPs: both neat and crosslinked -can easily and rapidly be degraded at home or in the compost of the garden under proper enzymatic assisted condition.

5.2 Keywords

Crosslinked, SAP, Cellulase, CO_2, biodegradation, inhibition.

5.3 Graphical Abstract

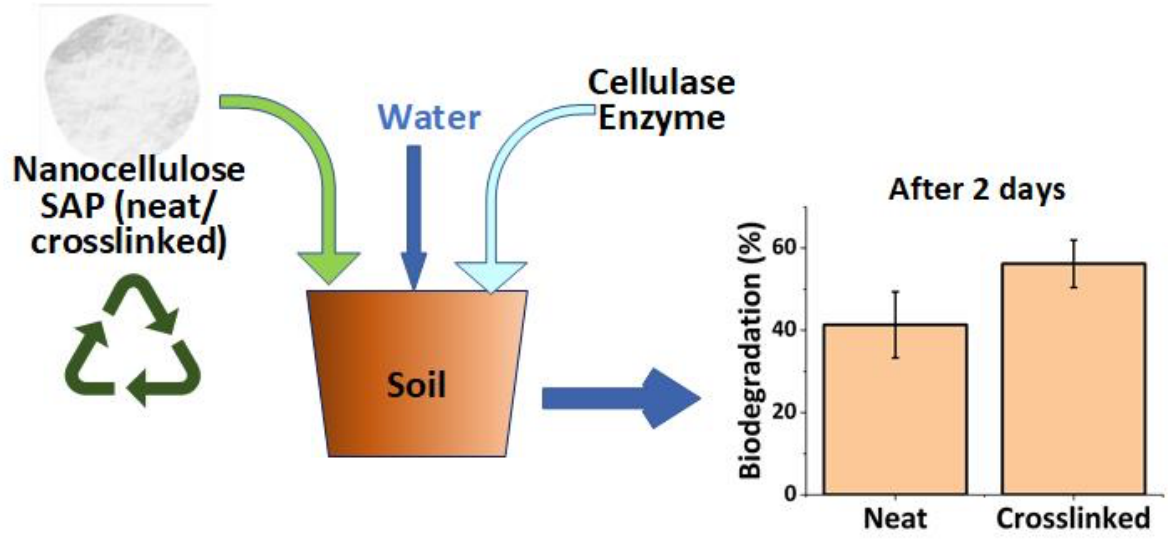

5.4 Introduction

Superabsorbent materials are three dimensional crosslinked polymeric networks able to absorb and retain large amounts of water and aqueous solutions inside their structure [1]. These water absorbing polymers do not dissolve in water as they are crosslinked but swell considerably, even under load [2, 3] because of their hydrophilic functional groups [4]. Superabsorbent polymers (SAPs) can be divided into two groups based on their original source: (i) natural SAP: polysaccharide and polypeptide based; and (ii) synthetic SAPs: petrochemical based such as acrylic based, vinyl acetate or polyethylene glycol [5, 6]. Most of the commercial SAPs are synthetic and can remain in the environment for many years after disposal [7]. Sodium polyacrylate based SAPs are the most commonly used in disposable diaper and feminine hygiene products; they are non-biodegradable and non-renewable. Globally, over 2 million metric tons of acrylate SAPs are being produced annually, of which disposable diapers hold 74% of the market share [8]. Their long-term persistence in the environment is leading climate change, pollution in aquatic life and global warming. These detrimental environmental effects have increased the thirst for sustainable, renewable, biodegradable superabsorbent based on polysaccharide.

Biodegradation is the degradation of a material naturally by microorganisms, such as bacterial, fungi or algae into environmentally acceptable products, such as carbon dioxide, water and biomass [9]. On the other hand, the term “compostable” is used to indicate a material that can be broken down into non-toxic, natural elements (carbon dioxide, water and biomass) with the help of biological organisms to enhance the soil nutritious quality [10]. Biodegradable SAPs are attractive for their abundancy, low cost and non-toxic behavior. Recent research describes several biodegradable polymers, such as cellulose, chitosan, starch, rice husk, raw bran and tulips [11]. Among those, cellulose is of special interest due to its high water holding capacity, abundance, ease of functionalization, full biodegradability, biocompatibility and non-toxicity [12]. TEMPO oxidized nanocellulose SAP has been engineered for different applications such as packaging, baby diapers, agriculture and biomedical [13-16]. High surface charge TEMPO-periodate oxidized nanocellulose produces SAP with high absorption capacity and tunable absorption kinetics [17, 18]. Recent development on cellulose superabsorbent has demonstrated that cellulose based SAP can be engineered specifically to suit their final application.

However, in spite of its widespread used, the biodegradability of acrylate SAPs and even natural SAPs have been very poorly and inconsistently characterized. Further, natural based SAPs require crosslinking to achieve properties similar to acrylate SAPs. A concern is how this crosslinking

might affect their biodegradability. To address this gap, biodegradability of neat and crosslinked nanocellulose SAP is quantified in this study. Soil burial degradation assay is one of the most common tests to quantify the degradation rate [19]. Water hyacinth cellulose-graft-poly(ammonium acrylate-co-acrylic acid) polymer SAP was degraded in garden soil around 25% after 14 days by determining mass loss [19]. Maleylated cellulose-g-poly(acrylic acid) SAP losses around 46.7% weight after 150 days in soil [20]. Another method uses activated sludge where the sample is placed and incubated at 25^{o}C. Biodegradation was measured by quantifying biological oxygen demand (BOD) which detects consumption of oxygen during experiment. Chitin based SAP showed almost complete degradation in this method after 20 days [21]. There is ISO standard (ISO 14855-1:2012) to determine the aerobic biodegradability of plastic materials under controlled conditions by analyzing evolved CO_2 and the sample size and shape [22]. However, these are indirect methods to determine biodegradation by weighing leftover sample mass. Here, we quantify the leftover mass by sample hydrolysis and glucose measurement using high-performance liquid chromatography.

Degradation of cellulose can be accelerated by using enzyme or fertilizer. Cellulase is a class of hydrolytic enzymes which is the specific enzyme for cellulose degradation. The main factors affecting the cellulose degradation process include: substrate composition, crystallinity, hydrophobicity, accessibility (porosity/structure), temperature, pH, nature of enzyme and inhibition effect of reaction products [23]. Enzymatic degradation is slower for crystalline and hydrophobic cellulose [24, 25]. Accessibility of the material to enzymes is another crucial parameter. For cellulosic materials, accessibility of cellulase is around 90% through the internal specific pores [26]. Cellulase adsorption on the outer surface of substrate has a small contribution in the overall adsorption [27]. Substrate structure as well as the reaction environment together with enzyme type thus affect the enzymatic degradation of cellulose.

Enzymatic degradation of cellulose is faster compared to without enzyme and typically achieved in solution. However, in nature, there is cellulase in the soil which can naturally degrade solid cellulose products over time. Much of the household waste which contains SAP are in solid form, for example, disposing baby diapers or absorbent pads in meat packaging. Degrading this product at home in a shorter time span is beneficial to the environment and minimizes the use of fertilizer. The biodegradation of these household products under enzymatic condition is poorly characterized. Moreover, the effect of crosslinking on the superabsorbent enzymatic degradation has not been investigated. The objective of this study is to quantify biodegradation rate of cellulose superabsorbents in sandy soils under enzymatic assisted condition to quantify enzyme and

crosslinking effect. This study can pave the way to consumable SAPs degradation in just a few days in the garden. Moreover, the rapid degradation of crosslinked SAP can guide further product development with strong chemical crosslinking.

5.5 Methodology

5.5.1 Materials

Bleached Eucalyptus Kraft (BEK) pulp was provided by Australian Paper, Maryvale, Australia. 2,2,6,6-tetramethylpiperidine-1-oxyl (TEMPO) and sodium bromide (NaBr) were purchased from Sigma Aldrich. 12 w/v% sodium hypochlorite (NaClO) was purchased from ThermoFisher Scientific. Sodium hydroxide (NaOH) and hydrochloric acid (HCl) were purchased from Merck and ACL Laboratories, respectively and diluted for solution as required. Cellulase (1,4-(1,3:1,4)-β-D-Glucan 4-glucano-hydrolase) from *Trichoderma reesei* was purchased from Merck.

Soil was collected from a vegetable farm located in Cranbourne, Victoria (38°11'6"S; 145°18'50"E). The soil was classified as a Podosol, according to the Australian Soil Classification criteria [28]). Soil was collected at a depth of 0 – 20 cm, air-dried and sieved to >2 mm. A subsample of 200 g was analyzed for range of key physicochemical properties (Table 5-S1). The analysis was conducted by Environmental Analysis Laboratories, at Southern Cross University [29], using Rayment and Lyons [30] standard methods.

5.5.2 Methods

5.5.2.1 TEMPO oxidation

Nanocellulose SAP was produced by three steps: (i) oxidation, (ii) fibrillation and (iii) freeze drying. TEMPO mediated oxidation was followed for the first step which is based on a previously developed method [31]. 25 g (dry weight) BEK pulp was suspended in 2500 mL of deionized water containing 0.4 g TEMPO and 2.5 g NaBr. The pH of 100 mL 12 w/v% NaClO was adjusted to 10 by the addition of 32 w/v% HCl. NaClO was added dropwise to the reaction mixture to initiate the oxidation reaction. The pH of the reaction was maintained by addition of 0.5 M NaOH dropwise throughout the reaction period of 3 hours. The oxidized fiber was washed and vacuum filtered until neutral pH is achieved and then stored at 4^{o}C.

5.5.2.2 Fibrillation of oxidized fibers

TEMPO-oxidized pulp was dispersed in deionized water at the desired concentration (0.5 g dry fiber in 100 g suspension) for further processing. Fibrillation was accomplished through a high-pressure homogenizer (GEA Niro Soavi Homogenizer Panda) at 1000 bar. Fiber suspensions were homogenized for two passes to produce nanocellulose hydrogel.

5.5.2.3 Solids concentration

The solids concentration of all samples (i.e. gel or pulp) was determined through oven drying. The sample was weighed before (w_i) and after (w_d) drying. Sample moisture was removed by drying in an oven (Thermoline BTC 9090) at 105°C for at least 6 h. The solids content was calculated as:

$$Solid\ content\ (\%) = \frac{w_d}{w_i} \times 100\%$$

5.5.2.4 Chemical Crosslinking

Hexamethyldiamine (HMDA) was dissolved in deionized water at a concentration of 0.45 g/mL. The nanocellulose gel was mixed with this HMDA solution in molar ratios of 1:1 (COO^-:NH_2) in presence of EDC and NHS and incubated at room temperature for 16 hours.

5.5.2.5 Preparation of Nanocellulose SAP

The SAPs were prepared by spreading 12 g of gel evenly over the base of a 50 mm petri dish and freezing the sample at -86°C, then freeze-drying (Christ Alpha 2-4 LD Plus) for 2 days.

5.5.2.6 ATR-FTIR

The SAP samples were tested by ATR-FTIR using the Agilent Cary 630 FTIR Spectrometer. The freeze-dried foams were tested for the FTIR spectra to determine the chemical crosslinking.

5.5.2.7 Microbial Activity

Microbial activity test was performed at specific temperature and relative humidity for both samples. For each type, samples were prepared by mixing the SAP at the application rate of 0.25

wt% and 0.5 wt% to prepare 50 g of soil treatment. Deionized water was then added to reach 60% moisture content. Two concentrations of enzyme (cellulase) (HE = 100 µL enzyme/ 7 mL water and LE = 50 µL enzyme / 7 mL water) were mixed with deionized water before adding to the samples. Samples were incubated at 35°C and 80% relative humidity in a temperature/humidity control cabinet (Thermoline L + M – 150-GD).

At appropriate sampling time points (day 1 to day 6) gas samples were collected using the method adapted from van Zwieten [32]. Briefly, soil treatments in containers with known volume and basal area were sealed and gases were allowed to accumulate for 20 minutes. The gases were then collected from the sealed containers using an airtight syringe (SGE Analytical Scientific) and inserted into pre-evacuated 12 mL Exetainers ® vials through a septum. Collected gas samples were analyzed for CO_2 using an Agilent Technologies 7890A Gas Chromatography – Thermal Conductivity Detector (GC-TCD) and GC-Flame Ionization Detector (FID). The detector temperature was 250 °C. Helium was used as the carrier gas at 21 mL/min. The temperature of the column and oven was 60 °C.

The flux rate, F_{CO2} (mg CO_2 / m^2h) was calculated using the following equation:

$$F_{CO2} = \frac{b \times V_{CH} \times MW_{CO2} \times 60 \times 10^6}{A_{CH} \times MV_{corr} \times 10^9}$$

Where, b = CO_2 concentration measured in ppm/min

V_{CH} = measuring chamber volume

MW_{CO2} = molecular weight of CO_2

A_{CH} = basal area of measuring chamber

MV_{corr} = temperature corrected molecular weight = $0.02241 \times \frac{273.15+T}{273.15}$, T = air temperature

5.5.2.8 Biodegradation

SAP biodegradation was evaluated for neat and crosslinked SAPs for 0.25 wt% application rate. Samples were prepared by mixing the SAP with soil to prepare 10 g of soil treatment and water with enzyme (cellulase) was added to reach 60 % moisture content. A control treatment without any SAP was also carried out. Samples were incubated at 35°C and 80% relative humidity in a

temperature/humidity control cabinet (Thermoline L + M – 150-GD). At appropriate sampling time points (day 2, 4, 6) samples were dried in an oven at 60 °C and stored frozen at -20 °C until required.

Acid digestion method adapted from Sluiter [33] was used to quantify biodegradation. This method hydrolyses cellulose samples to glucose and glucuronic acid which can be measured by chromatography. In brief, 3 mL of 72% sulphuric acid was added to 5 g of soil treatment. The treatment was then placed in a hot plate at 30 °C and incubated for 60 min. The mixture was occasionally stirred every 5 to 10 minutes to ensure even acid – treatment contact. Samples were then diluted to 4% sulphuric acid by adding 84 mL of water and autoclaved for 30 minutes at 121 °C. After cooling at room temperature, treatments were neutralized to a pH 5 – 6 using calcium carbonate. Upon neutralization, treatments were then centrifuged at 10,000 rpm for 5 min. The supernatant was collected, filtered through syringe filter (Acrodisk 25 mm 0.2 μm) and analyzed through high performance liquid chromatography (HPLC) using a BioRad Amminex HPX-87H column, 0.005 M sulfuric acid as mobile phase, with a refractive index detector at a temperature of 60 °C and a flow rate of 0.4 mL/min.

5.6 Results

Neat and chemically crosslinked Nanocellulose SAPs samples are analyzed in soil under enzyme assist conditions (cellulase) for microbial activity and biodegradation rate. Microbial activity is determined for day 1 to day 6, whereas biodegradation is quantified by acid hydrolysis for day 2, 4 and 6. Analysis reveals that crosslinked nanocellulose SAP is more biodegradable than the neat SAP.

5.6.1 FTIR

FTIR spectra of SAP (Figure 5-1) shows that chemically crosslinked SAP has C=O stretching at 1560 cm^{-1} due to strong amide bond formation between the COO- group of nanocellulose SAP and the NH_2 group of HMDA. Neat SAP has a peak at 1600 cm^{-1} from COO^- group of TEMPO-oxidized nanocellulose.

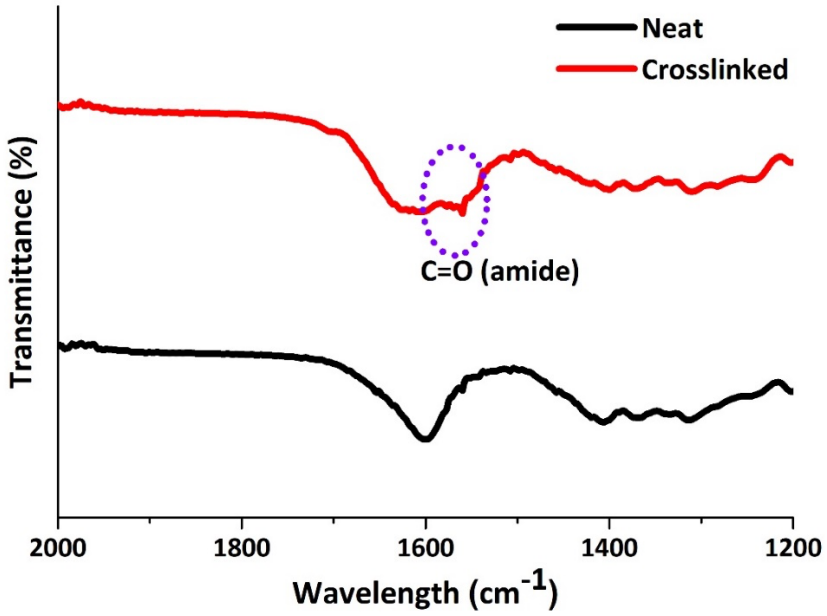

Figure 5-1: FTIR spectra of nanocellulose (neat) and HMDA crosslinked nanocellulose SAPs.

5.6.2 Microbial Activity

In general, for both types of nanocellulose SAPs, CO_2 emission increases with time and enzyme concentration (Figure 5-2). Increase in enzyme concentration increases CO_2 emission which indicates the soil microbial community response is higher when high concentration of enzyme is used. For crosslinked and neat nanocellulose SAPs, the CO_2 emission is similar with overlapping error bars. Figure 5-3 shows the effect of SAPs application rate on the microbial activity for both neat and crosslinked nanocellulose SAPs. There is essentially no difference when using 0.5% SAPs compared to 0.25% which signifies that enzyme addition overcomes the effect of solid concentration in this range.

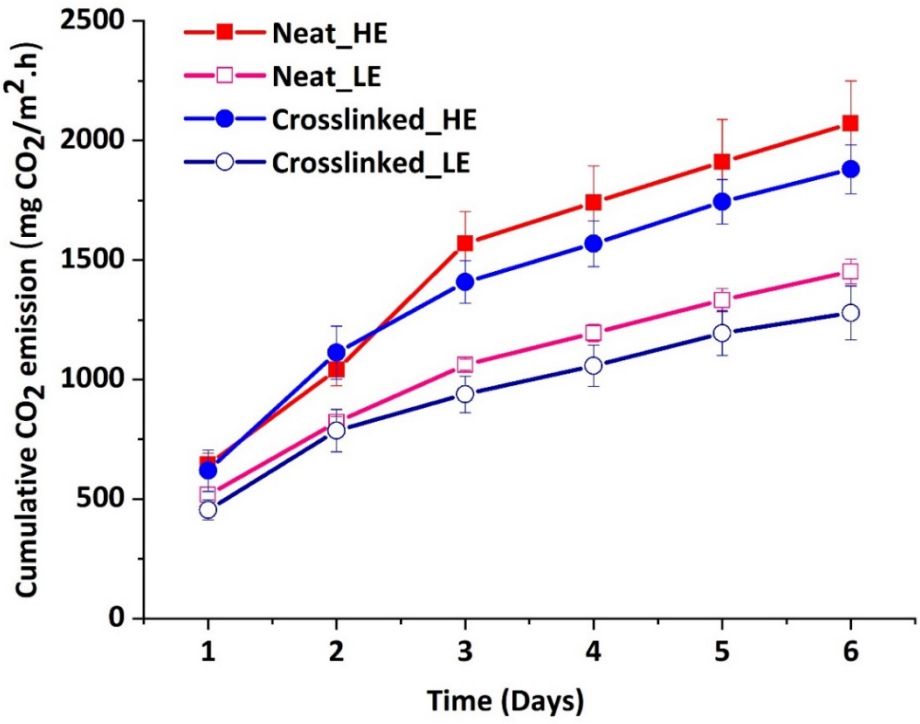

Figure 5-2: Effect of enzyme concentration and crosslinking on microbial activity for neat and crosslinked nanocellulose SAP. HE indicates high enzyme concentration whereas LE refers to low enzyme concentration.

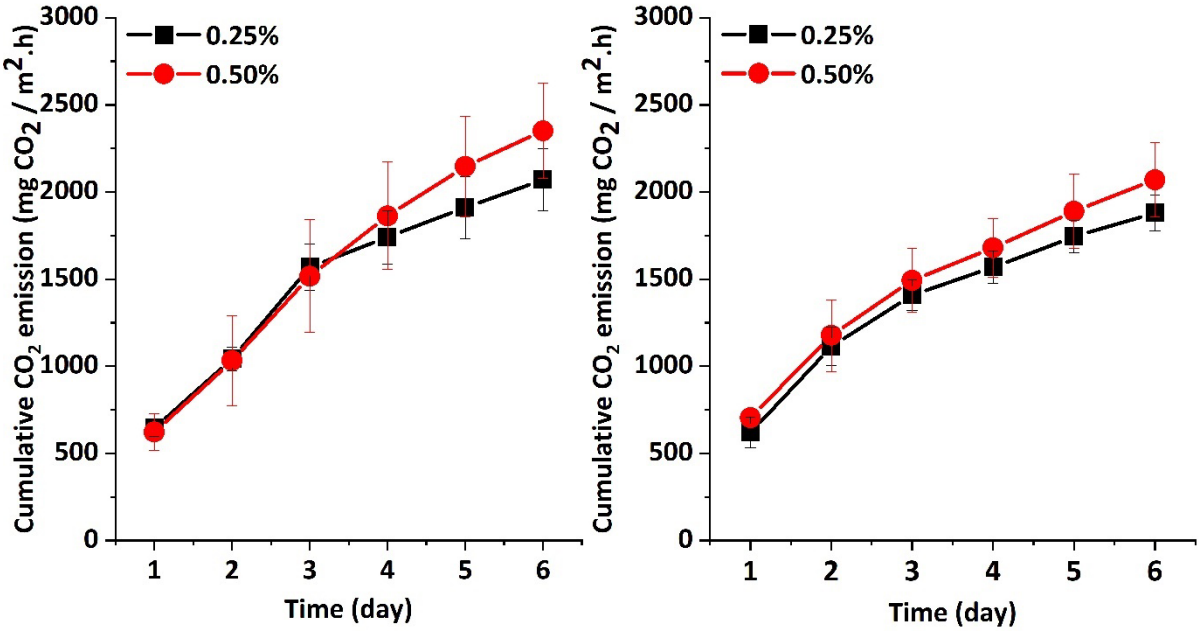

Figure 5-3: Effect of nanocellulose SAP solid concentration on microbial activity with high concentration of enzyme: (a) Neat nanocellulose and (b) crosslinked nanocellulose.

5.6.3 Biodegradation

Figure 5-4 shows the effect of enzyme concentration and crosslinking on biodegradation; this is in terms of mg of SAPs remains in the soil after specific intervals. The degradation rate is almost constant over 6 days. Around 41% SAPs degraded in 2 days for neat SAP and 56% for crosslinked SAP with low enzyme concentration. After day 6, there is 1.51±0.0.08 mg and 0.90±0.21 mg nanocellulose SAP remaining in the soil for neat and crosslinked SAP with low enzyme concentration, respectively. Without enzyme the sample remaining increased to 2.29±0.18 mg for neat and 2.20±0.19 mg for crosslinked SAP while the original sample was 2.5 mg/g soil. Biodegradation rate of crosslinked nanocellulose SAP for high enzyme concentration is also higher compared to neat SAP, as seen from the lower amount of SAP remaining in the soil after day 2 ,4 and 6.

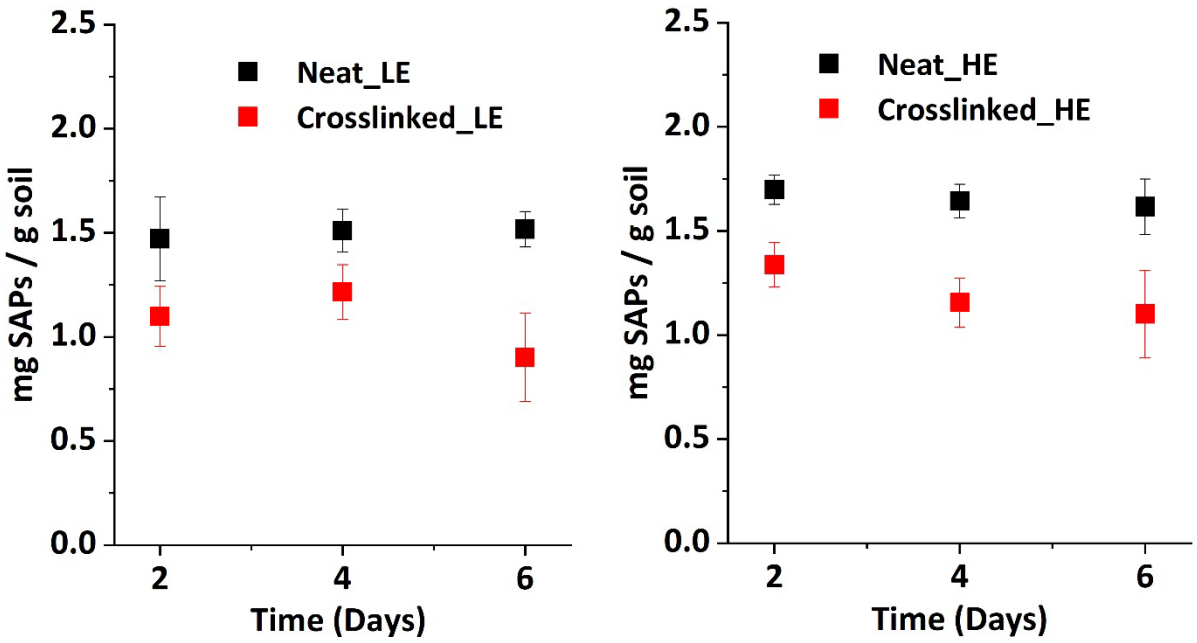

Figure 5-4: Effect of enzyme concentration and crosslinking on the superabsorbent biodegradation in soil. The amount of superabsorbent which remained is reported: (a) low enzyme and (b) high enzyme. LE indicates low enzyme concentration whereas HE indicates high enzyme concentration. Initial sample (SAP) mass was 2.5 mg/g soil.

5.7 Discussion

Enzymatic degradation of nanocellulose SAPs in soil was analyzed at different enzyme and solid concentration. Nanocellulose SAP, both neat or crosslinked, degrades faster under enzymatic assisted condition. The effect of crosslinking and its consequence on the biodegradation rate was evaluated by quantifying microbial activity and residual cellulose in soil at regular time intervals. This analysis confirms the potential and feasibility of fast degradation of cellulose based SAP material using enzyme assisted home compost technology.

Chemically crosslinked nanocellulose SAP does not reduce its biodegradation rate (Figure 5-4). Indeed, similar microbial activity was measured for the degradation of original and Crosslinked nanocellulose SPA (Figure 5-2). Cellulase are big enzymatic protein macromolecules of diameter of 4-6.5 nm and18-21.5 nm length [34]. The nanocellulose SAP has pore size bigger than the enzyme size range as previously quantified [17]. The pores inside the SAPs structure are the main contributors for the accessibility [26] of cellulase. Here, nanocellulose SAP has micron size pores which are at least 1000 times bigger than cellulase enzyme. So, in terms of cellulase accessibility, crosslinked SAP is not creating any hinderance. Moreover, the biodegradation rate is higher for crosslinked SAP. Jarerat et al. showed that addition of gelatin (which has -CONH groups same as HMDA crosslinked SAP) acts as the nitrogen source resulting in increased biodegradation of PLA by *Saccharothrix Waywayandensis* [35]. So, the crosslinked SAP biodegradation is higher in this study because of the presence of nitrogen source in the structure.

Neat nanocellulose SAP biodegrades by around 8% (2.29 mg/g soil left) without enzyme, whereas with enzyme, it reduces by 35-40% after 6 day for both the enzyme concentrations tested. Similarly, for chemically crosslinked SAP, the degradation is around 12% (2.20 mg/g soil left) whereas with enzyme, it degrades to 56-64% after 6 days (for both enzyme concentrations). Addition of cellulases effectively accelerates the breakdown of cellulose SAP – crosslinked or not-to glucose in soils. The microbial activity determined with different solid concentrations (0.25% and 0.5% SAP in soil) does not show difference in microbe response in terms of CO_2 emission, indicating that microbes are responding similarly for higher SAP concentration as well confirming their higher degradability.

The degradation rate for both neat and crosslinked SAP did not change significantly after day 2 (Figure 5-4). Neat and crosslinked SAP degrades around 41% and 56%, respectively, (with low enzyme concentration) after day 2. Enzymatic degradation depends mostly on factors such as temperature, accessibility, structure of substrate and inhibition. Temperature, humidity, moisture

content were kept constant throughout the incubation period. Could product inhibition- from cellulose to cellobiose or glucose formation- affect degradation? To determine product inhibition effect, nanocellulose SAP was mixed with cellobiose in 1:1 ratio and analyzed the biodegradation in soil. From day 2, It is evident that biodegradation (Table 5-S2) is not product inhibited, neither by cellobiose nor by glucose. The sample left in the soil after day 2 was 0.35±0.10 mg sample/g soil from the initial mass of 2.5 mg sample/g soil. This indicates around 79% biodegradation confirming the absence of product inhibition. As cellobiose was added initially, its inhibition would have decreased any biodegradation, which was not the case. Instead adding cellobiose increases the biodegradation as part of the sample was already in the form of cellobiose- so it is rather easier for enzyme to degrades. This findings of higher degradation with initial cellobiose concentration also rules out the possibility of glucose inhibition. The insignificant difference of biodegradation rate after day 2 might therefore be due to enzyme inactivity at 35 ^{o}C after day 2 which slows down the biodegradation.

These new cellulose-based SAP can be used in baby diaper and degraded at home compost. Baby diaper contains around 33.3 wt% SAP [36] while the average weight of a clean diaper without urine is of 41 g [37]. Extrapolating from this study, 2.7 to 5.4 kg soil is required to degrade the SAP of one diaper (containing 13.65 g of nanocellulose SAP) at the 0.5 and 0.25% solid addition in soil, respectively. Around 41% of SAP will be degraded within 2 days when using neat SAP. However, this calculation is based on the weight of commercial SAP used in baby diaper, nanocellulose based SAP can have lower amount in baby diaper composition. Moreover, using food waste in the compost can lower the soil requirements. Additionally, our experiment was done by hydrolyzing the soil with residual sample after specific time interval which limited the use of higher solid concentration in soil in experimental condition. This was just a model study to proof the concept. But in real scenario, higher SAP concentration is expected to apply. The strong sunlight and soil microbes will accelerate the SAP degradation in garden compost.

The rapid biodegradation of nanocellulose based SAP under enzymatic condition, effect of crosslinking and their potential to degradation at garden soil indicates the potential of using cellulose SAP diaper commercially while maintaining the environmental sustainability. The other components of diaper, such as PLA base sheet has already been prepared. The only problematic part is the non-renewable, non-biodegradable SAP. In this study, we have proved that the developed renewable nanocellulose SAP can degrade around 40 to 60% in 2 days under enzymatic assisted conditions. This study not only explores the potential of easy diaper composting but also broadens the opportunity of using the developed SAP for food packaging applications. For food

packaging, there is already different types of sustainable packaging made out of paper except the SAP in absorbent pad. So, replacing the commercial SAP in absorbent pad with our developed SAP can gives the consumers the opportunity to chuck the packaging with absorbent pad in the garden compost.

5.8 Conclusion

TEMPO oxidized nanocellulose-based superabsorbent (SAP) was evaluated for its quick biodegradation in soil- cellulase assisted or not. Using Hexamethylene Diamine (HMDA), the objective was to measure whether chemical crosslinking affects the biodegradation of nanocellulose SAP. The effect of cellulase concentration on neat and crosslinked SAP degradation was analyzed and the microbial activity in soil at different application rates was determined.

The microbial activity of nanocellulose SAP decreases with the decrease of enzyme concentration; however, increasing the SAPs application rate does not affect the microbial activity. Both neat and chemically crosslinked SAPs showed similar microbial activity (in terms of CO_2 emission) indicating similar microbe response. Microbial activity also strongly depends on the nutrient availability and initial microbial biomass availability in the soil [38, 39]. So, high enzyme (cellulase) concentration increases microbial activity for both types of SAPs.

Biodegradation rate quantified by hydrolyzing the remaining cellulose in soil after regular intervals (day 2, 4, and 6) shows difference between neat and crosslinked SAP. HMDA crosslinked nanocellulose degrades faster than the neat. While counter intuitive and differing form CO_2 microbial respiratory experiment, this finding is due to the nitrogen source available in the HMDA structure which increases the degradation rate.

This study quantifies the effect cellulase has for different types of nanocellulose SAPs in terms of SAP structure-enzyme accessibility. Rapid biodegradation of chemically crosslinked SAP facilitates the use of crosslinked SAP without any biodegradability issues. These findings can help develop home based compost or degrade baby diaper in garden soil at short time and grow plants while saving the environment from the harmful effect of petro-chemical based SAPs.

5.9 References

1. Zohuriaan-Mehr, M.J. and K. Kabiri, *Superabsorbent polymer materials: a review.* Iranian polymer journal, **17**(6).2008. 451.
2. Zohuriaan-Mehr, M., H. Omidian, S. Doroudiani, and K. Kabiri, *Advances in non-hygienic applications of superabsorbent hydrogel materials.* Journal of materials science, **45**(21).2010. 5711-5735.
3. Yu, Y., L. Liu, Y. Kong, E. Zhang, and Y. Liu, *Synthesis and properties of N-maleyl chitosan-cross-linked poly (acrylic acid-co-acrylamide) superabsorbents.* Journal of Polymers and the Environment, **19**(4).2011. 926-934.
4. Behera, S. and P.A. Mahanwar, *Superabsorbent polymers in agriculture and other applications: A review.* Polymer-Plastics Technology and Materials, **59**(4).2020. 341-356.
5. Okay, O., *General properties of hydrogels*, in *Hydrogel sensors and actuators*. 2009, Springer. p. 1-14.
6. Sadeghi, M. *Synthesis and swelling behavior of Protein-g-poly Methacrylic acid/kaolin superabsorbent hydrogel composites*. in *AIP Conference Proceedings*. 2008. **1042**(1): p. 318-320. American Institute of Physics.
7. Passauer, L., T. Hallas, E. Bäucker, G. Ciesielski, S. Lebioda, and U. Hamer, *Biodegradation of hydrogels from oxyethylated lignins in model soils.* ACS Sustainable Chemistry & Engineering, **3**(9).2015. 1955-1964.
8. Chazovachii, P.T., M.J. Somers, M.T. Robo, D.I. Collias, M.I. James, E.N.G. Marsh, P.M. Zimmerman, J.F. Alfaro, and A.J. McNeil, *Giving superabsorbent polymers a second life as pressure-sensitive adhesives.* Nature Communications, **12**(1).2021. 1-6.
9. Karak, N., *Biopolymers for paints and surface coatings*, in *Biopolymers and biotech admixtures for eco-efficient construction materials*. 2016, Elsevier. p. 333-368.
10. Philp, J.C., A. Bartsev, R.J. Ritchie, M.-A. Baucher, and K. Guy, *Bioplastics science from a policy vantage point.* New biotechnology, **30**(6).2013. 635-646.
11. Qureshi, M.A., N. Nishat, S. Jadoun, and M.Z. Ansari, *Polysaccharide based superabsorbent hydrogels and their methods of synthesis: A review.* Carbohydrate Polymer Technologies and Applications, **1**.2020. 100014.
12. Mondal, M.I.H., *Cellulose-based superabsorbent hydrogels*. 2019: Springer.
13. Barajas-Ledesma, R.M., L. Hossain, V.N. Wong, A.F. Patti, and G. Garnier, *Effect of the counter-ion on nanocellulose hydrogels and their superabsorbent structure and properties.* Journal of Colloid and Interface Science, **599**.2021. 140-148.
14. Mendoza, L., L. Hossain, E. Downey, C. Scales, W. Batchelor, and G. Garnier, *Carboxylated nanocellulose foams as superabsorbents.* Journal of colloid and interface science, **538**.2019. 433-439.
15. Curvello, R., L. Mendoza, H. McLiesh, J. Manolios, R.F. Tabor, and G. Garnier, *Nanocellulose hydrogel for blood typing tests.* ACS Applied Bio Materials, **2**(6).2019. 2355-2364.
16. Hossain, L., V.S. Raghuwanshi, J. Tanner, C.-M. Wu, O. Kleinerman, Y. Cohen, and G. Garnier, *Structure and swelling of cross-linked nanocellulose foams.* Journal of Colloid and Interface Science, **568**.2020. 234-244.
17. Hossain, L., E. Eastman, M. De Rango, V.S. Raghuwanshi, J. Tanner, and G. Garnier, *Absorption kinetics of nanocellulose foams: Effect of ionic strength and surface charge.* Journal of Colloid and Interface Science, **601**.2021. 124-132.
18. Mendoza, D.J., C. Browne, V.S. Raghuwanshi, G.P. Simon, and G. Garnier, *One-shot TEMPO-periodate oxidation of native cellulose.* Carbohydrate polymers, **226**.2019. 115292.

19. Rop, K., D. Mbui, N. Njomo, G.N. Karuku, I. Michira, and R.F. Ajayi, *Biodegradable water hyacinth cellulose-graft-poly (ammonium acrylate-co-acrylic acid) polymer hydrogel for potential agricultural application.* Heliyon, **5**(3).2019. e01416.
20. Sawut, A., M. Yimit, W. Sun, and I. Nurulla, *Photopolymerisation and characterization of maleylatedcellulose-g-poly (acrylic acid) superabsorbent polymer.* Carbohydrate polymers, **101**.2014. 231-239.
21. Yoshimura, T., I. Uchikoshi, Y. Yoshiura, and R. Fujioka, *Synthesis and characterization of novel biodegradable superabsorbent hydrogels based on chitin and succinic anhydride.* Carbohydrate Polymers, **61**(3).2005. 322-326.
22. Kim, Y.-J., H. Sun, Y.-S. Lee, S.-Y. Lee, S.-J. Ma, M.-N. Kim, and H.-J. Kang, *Determination of the ultimate aerobic biodegradability of plastic materials under controlled composting.* 한국생물공학회: 학술대회논문집.2003. 451-451.
23. Deng, S., *Cellulase activity of soils and the effect of tillage management on enzyme activities in soils*. 1994, IOWA State University: USA. p. 235.
24. Yoshida, M., Y. Liu, S. Uchida, K. Kawarada, Y. Ukagami, H. Ichinose, S. Kaneko, and K. Fukuda, *Effects of cellulose crystallinity, hemicellulose, and lignin on the enzymatic hydrolysis of Miscanthus sinensis to monosaccharides.* Bioscience, biotechnology, and biochemistry, **72**(3).2008. 805-810.
25. Zambrano, M.C., J.J. Pawlak, and R.A. Venditti, *Effects of chemical and morphological structure on biodegradability of fibers, fabrics, and other polymeric materials.* BioResources, **15**(4).2020. 9786.
26. Dutta, S.K. and S. Chakraborty, *Pore-scale dynamics of enzyme adsorption, swelling and reactive dissolution determine sugar yield in hemicellulose hydrolysis for biofuel production.* Scientific reports, **6**(1).2016. 1-13.
27. Baig, K., *Interaction of enzymes with lignocellulosic materials: causes, mechanism and influencing factors.* Bioresources and Bioprocessing, **7**(1).2020. 1-19.
28. Isbell, R.F., *The Australian soil classification*. Second edition. ed, ed. S. National Committee on and Terrain. 2016: Clayton South, VIC, Australia : CSIRO Publishing.
29. Environmental Analysis Laboratory, S.C.U., . *Agricultural soil testing*. 2020 [cited 2020 31/07/2020]; Available from: https://www.scu.edu.au/environmental-analysis-laboratory---eal/analytical-services/agricultural-soil-testing/.
30. Rayment, G.E., *Soil chemical methods Australasia*, ed. D.J. Lyons. 2011, Collingwood, Vic.: Collingwood, Vic. : CSIRO Pub.
31. Saito, T., S. Kimura, Y. Nishiyama, and A. Isogai, *Cellulose nanofibers prepared by TEMPO-mediated oxidation of native cellulose.* Biomacromolecules, **8**(8).2007. 2485.
32. van Zwieten, L., S. Kimber, S. Morris, A. Downie, E. Berger, J. Rust, and C. Scheer, *Influence of biochars on flux of [N.sub.2]O and C[O.sub.2] from Ferrosol.* Australian Journal of Soil Research, **48**.2010. 555+.
33. Sluiter, A., B. Hames, R. Ruiz, C. Scarlata, J. Sluiter, D. Templeton, and D. Crocker, *Determination of structural carbohydrates and lignin in biomass, in: Laboratory Analytical Procedure (LAP).* National Renewable Energy Laboratory.2008.
34. Bubner, P., J. Dohr, H. Plank, C. Mayrhofer, and B. Nidetzky, *Cellulases dig deep: in situ observation of the mesoscopic structural dynamics of enzymatic cellulose degradation.* Journal of Biological Chemistry, **287**(4).2012. 2759-2765.
35. Jarerat, A. and Y. Tokiwa, *Poly (L-lactide) degradation by Saccharothrix waywayandensis.* Biotechnology letters, **25**(5).2003. 401-404.
36. Itsubo, N., M. Wada, S. Imai, A. Myoga, N. Makino, and K. Shobatake, *Life cycle assessment of the closed-loop recycling of used disposable diapers.* Resources, **9**(3).2020. 34.

37. Mirabella, N., V. Castellani, and S. Sala, *Life cycle assessment of bio-based products: A disposable diaper case study.* The International Journal of Life Cycle Assessment, **18**(5).2013. 1036-1047.
38. Cui, J., X. Yuan, Q. Zhang, J. Zhou, K. Lin, J. Xu, Y. Zeng, Y. Wu, L. Cheng, and Q. Zeng, *Nutrient availability is a dominant predictor of soil bacterial and fungal community composition after nitrogen addition in subtropical acidic forests.* PloS one, **16**(2).2021. e0246263.
39. Jiménez, J.J., J.M. Igual, L. Villar, J.L. Benito-Alonso, and J. Abadias-Ullod, *Hierarchical drivers of soil microbial community structure variability in "Monte Perdido" Massif (Central Pyrenees).* Scientific reports, **9**(1).2019. 1-17.

CHAPTER 6
POINT OF CARE NANOCELLULOSE SENSOR FOR GLUCOSE DETECTION IN BLOOD

THIS PAGE WAS INTENTIONALLY LEFT BLANK

Preface

Thus far, each chapter has contributed to defining the potential of nanocellulose SAP for specific applications, such as, baby diapers, agriculture, meat/food packaging and diagnostic. We already studied the fundamentals of tuning the SAP structure and quantified the structure-property relationship. In this chapter, we present a novel application of nanocellulose SAP. The developed SAP is utilized to engineer glucose sensor to detect glucose concentration in human blood. This colorimetric glucose sensor can detect blood glucose level by exploiting the concept of enzyme immobilization and enzyme-catalyzed reaction of glucose. This cheap but accurate and user-friendly colorimetric sensor can determine glucose concentration in the clinical range of 7 mM to 13 mM which can differentiate if a patient is diabetic or not. The concept utilized in this study, is not only helpful to develop glucose sensors, but also can be generalized into a robust platform to prepare nanocellulose SAP-based sensors to determine many medical analytes from body fluids such as urine, blood, saliva or even sweat.

THIS PAGE WAS INTENTIONALLY LEFT BLANK

Chapter 6: Point of Care Nanocellulose Sensor for Glucose Detection in Blood

Point of Care nanocellulose sensor for glucose detection in blood

5.1 Abstract

The increasing incidence of Diabetes Mellitus (DM) represents an alarming global epidemic disproportionately affecting developing nations. Whilst sophisticated, electronic DM diagnostic devices are commonplace in the developed world; cost and electricity reliance makes them unsuitable for many remote or socioeconomically deprived communities. A robust, commercially viable, paper-based diagnostic device would facilitate early diagnosis, greatly ameliorating Diabetes outcomes and reducing the economic burden upon developing countries. A solution may be found in the application of nanocellulose superabsorbent technology from nanocellulose hydrogel. Nanocellulose superabsorbent is an abundant, low cost and biodegradable natural material. It is capable of stabilizing enzymes contained within its structure, thus improving and prolonging enzyme function facilitating the detection of glucose from human blood by an enzyme catalysis reaction of glucose.

Here, we immobilize glucose oxidase within the nanocellulose superabsorbent structure to develop a simple human-readable and visual colorimetric blood glucose sensor. An increase in blood glucose concentration increases the concentration of reaction product which decreases the system pH. A Colorimetric pH-based glucose sensor was developed by immobilizing glucose oxidase and phenol red in a nanocellulose hydrogel followed by lyophilization. The sensor produces a color change from red to orange as pH decreases due to the enzymatic reaction of glucose into glucuronic acid and hydrogen peroxide. This sensor can be used to measure glucose concentrations of 7-13 mM with an accuracy of ±1 mM at temperatures of 4°C to 40°C. Stability tests confirmed that there was no deterioration in enzyme activity after four weeks at room temperature storage of the sensors. A functional prototype device was developed. Successful enzyme immobilization and device transferability demonstrated the future application of nanocellulose biosensor as an economical, and robust, and diagnostic technology for a broad spectrum of diseases.

5.2 Keywords

Immobilization, glucose sensor, shelf life, sensitivity, blood

5.3 Graphical Abstract

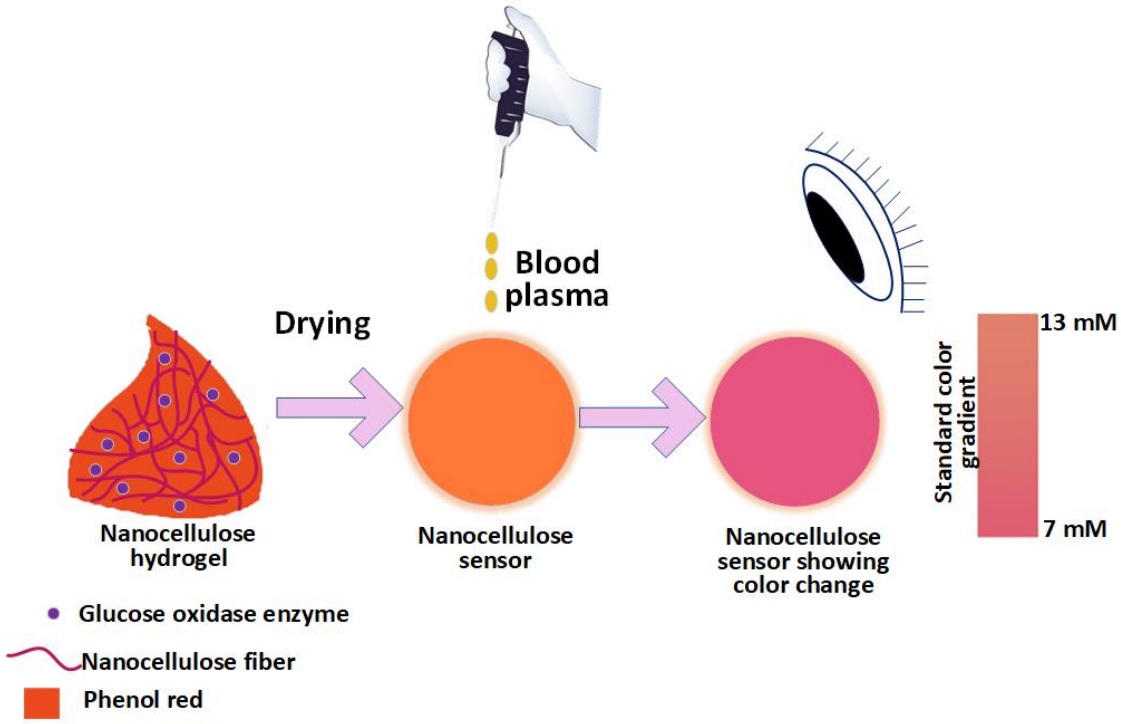

5.4 Introduction

Blood glucose measurement is important as high blood glucose levels are linked to adverse health outcomes in patients with diseases such as diabetics mellitus [1], which can cause serious damage to the kidneys, blood vessels and heart over time. The number of people with diabetes worldwide is expected to double from 171 million in 2000 to 366 million by 2030 [2] with developing countries being the most affected [3]. According to the World Health Organization, around 1.5 million deaths were directly related to diabetes in 2019 [4]. The rate of deaths associated with diabetes increases with remoteness, socioeconomic disadvantage, and ethnicity. In 2018, casualties were as twice as high for remote and very remote communities compared to major cities and four times as high for Aboriginal and Torres Strait Islanders compared to non-Indigenous Australians [5].

There are three main types of diabetes: Type 1, Type 2 and gestational. Type 1 diabetes is an autoimmune disease which results in the inability of the body to produce insulin; it is more common in younger people. Type 2 diabetes develops when the body becomes resistant to the effect of insulin or the body's ability to produce insulin gradually decreases over time, and usually develops in middle age and older people [6, 7]. Gestational diabetes is a form of diabetes that

occurs during pregnancy, which generally resolves following birth. However, women who develop gestational diabetes have an increased risk of developing type 2 diabetes later in life [8]. More than 95% of patients having diabetes are type 2 [9]. Diabetes is diagnosed as having a blood sugar level exceeding 7 mM after fasting or exceeding 11.1 mM two hours after eating [10]. Prediabetes is defined as a blood sugar level exceeding 6.1 mM after fasting or 7.8 mM two hours after eating [11].

Continuous blood glucose monitoring for diabetic people is important to avoid growing health issues. Glucose concentration is the highest in the arterial circulation. However, lab tests are usually performed using venous blood samples. There are a few blood tests done in pathology depending on the patient's conditions which includes glycated haemoglobin (HbA1c), fasting, two hours after having meal, glucose tolerance test and random blood glucose test. Blood glucose level is measured two hours after having a meal to test how the body responds after having a meal. Blood glucose level increases sharply after a meal; however, the pancreas releases insulin to help move the sugar from the blood into the cells of muscles and other tissues. Within 2 hours of a meal, the glucose level should return to normal. Random blood glucose test is done if diabetes is suspected and fasting blood glucose can confirm the diagnosis. HbA1c level is measured for diabetes patients to determine the recent average blood glucose level. It is also helpful to determine prediabetes as it provides the average glucose level for the past two to three months.

There are three basic approaches for measuring blood glucose in the laboratory: the reducing method, the condensation method and the enzymatic method. The reducing method is the oldest where the blood sample is treated with an alkaline copper solution to produce insoluble cuprous oxide. This cuprous oxide is reacted with phospharomolybdate to form a molybdenum blue color complex which is read by spectrophotometer at 420 nm. This method is abandoned in the clinical laboratory as its time consuming and can determine the fructose concentration as well in the blood, which can yield erroneous results. In the condensation approach, O-toluidine reacts with glucose in blood to produce the green colored glucosamine. The intensity of this color complex is also measured by spectrophotometer to detect the glucose level. However, O-toluidine is highly corrosive and toxic, so this approach is also being phased out from the laboratory [12]. The most common method is to centrifuge the whole blood sample to collect plasma and test using a semi-automatic or automatic biochemistry system utilizing enzymes which generates a colorimetric complex of intensity proportional to the glucose concentration [13]. However, most of these lab-based tests are not suitable for home use.

A glucometer is very common to determine glucose level at home from whole blood. Glucose concentration in plasma is usually 10-15% higher than glucose concentration in whole blood. Most laboratories/pathologies measure glucose level in plasma, so there are many glucometers which provide a "plasma equivalent" to compare users results with lab test [14]. In the most common glucometer, the embedded enzyme (glucose oxidase) on the electrode induces an electric current through the strip which is proportional to the glucose amount [15]. These types of conductivity-based biosensors tend to be expensive, and therefore not suitable for a global application of diabetes diagnostics.

A paper-based testing device could provide a solution. Hydrogel and superabsorbent networks provide good 3D media as the sensing or detection locus where enzyme react with glucose and form some detectable complex. Several studies investigated glucose concentration by measuring the swelling or deswelling of hydrogels [16, 17]. Glucose concentration was also determined by fluorescence quenching. Quantum dots (QDs) and carbon dots (CDs) are commonly used for fluorescent labelled sensor to detect glucose. However, reading blood sugar by fluorescent quenching is not feasible for home use. Glucose concentration in sweat, blood and saliva was monitored by the contact angle of analytes on a pH responsive surface or fluorescent nanohybrid [18, 19]. There are also optical sensors which gives different spectra based on glucose concentration and pH [20-23]. Again, spectrum analysis at home is not a feasible option. Dilutions or pre-treatment of human blood is another disadvantage of most methods mentioned. A recent article reports colorimetric detection of glucose from human blood without pre-treatment or dilution. However, a post treatment is required for color intensity determination by eye [24]. Further, aqueous sensors typically limit stability for long term use.

In this study, we explored the potential of nanocellulose hydrogel as a performant diagnostic device. The aqueous and porous structure of hydrogel makes them an exceptional biocompatible medium capable of stabilizing and immobilizing problematic molecules such as enzymes. Enzyme immobilized hydrogels are freeze-dried to produce smart nanocellulose foams/SAP with sensing ability. The colorimetric technique chosen in the detection of diabetes from blood plasma is a pH-based reaction. This technique utilizes glucose oxidase and phenol red to induce a color change from red to orange with the decrease of the foam's pH level. The schematic of the process is given in Figure 6-1.

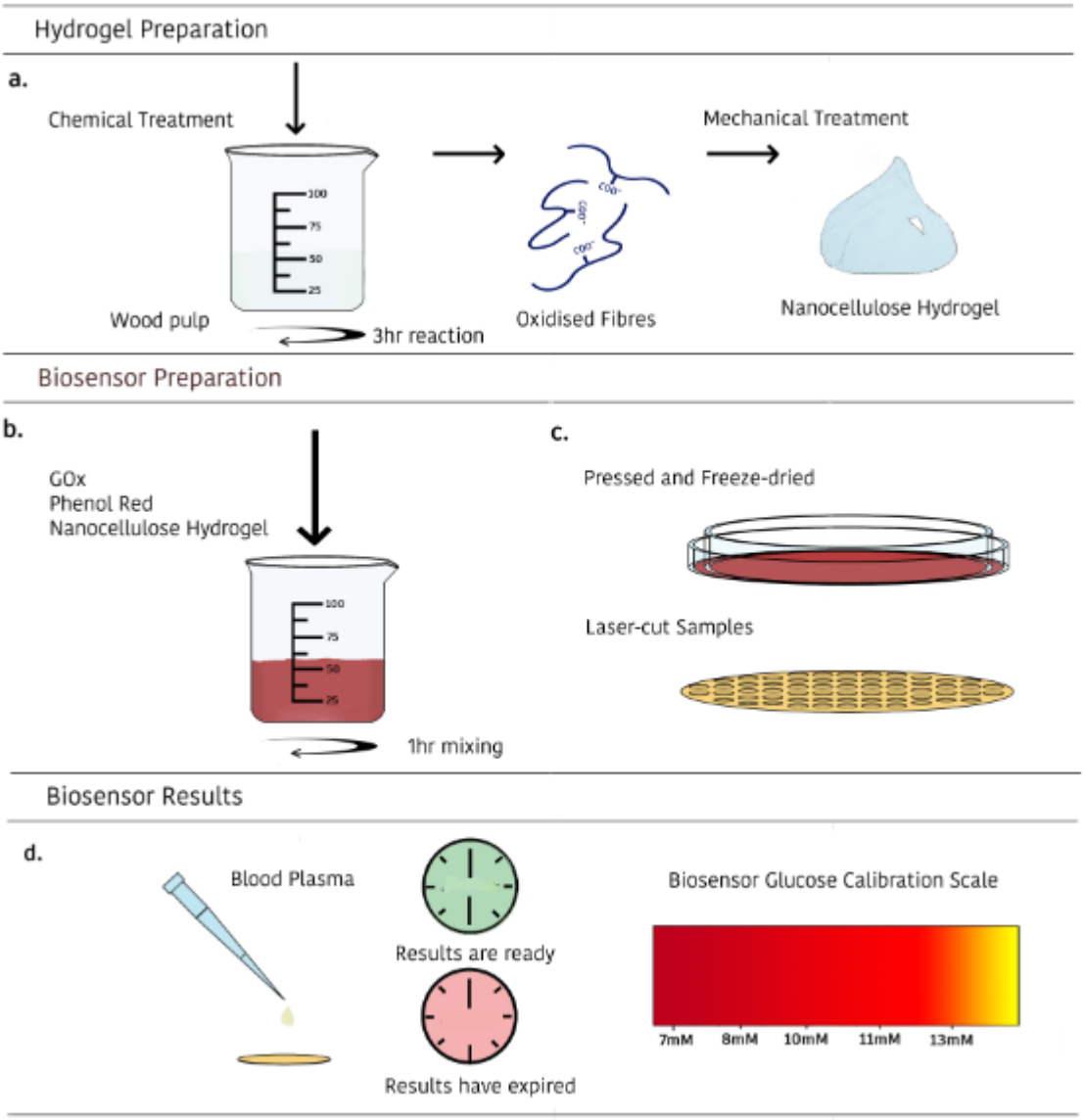

Figure 6-1: Schematic of the preparation and use of the nanocellulose sensing diagnostic for measuring glucose concentration in human blood. First, a nanocellulose hydrogel of controlled COO^- content and rheology is prepared; second, selected enzyme glucose oxidase (GOx) is immobilized onto the nanocellulose hydrogel, freeze dried into a foam with immobilized enzyme (adsorbed and entrapped), and converted into diagnostics; last, blood plasma is introduced – or created by filtration of RBC- and glucose content displayed by color change.

We aim to develop a Point of Care (POC) nanocellulose sensor for the selective detection of glucose in human blood. This can be achieved by separating the red blood cell (RBC) from blood and reacting blood plasma with glucose sensor. For this, we proposed a device design utilizing the concept of microfluidics. The whole blood is passed through a layer where wicking kinetics is

utilized to help the user to determine the optimized reaction time. The selective separation of RBC in a membrane in the next layer allows the blood plasma to travel to the sensor part where the enzyme catalysis reaction decreases system pH and shows a color change. In this study, we only tested the sensor part for reproducibility and accuracy. The developed nanocellulose sensor is tested for a blood plasma glucose range of 7-13 mM which has specific medical interest. The sensitivity and stability at different temperatures indicates the potential of a nanocellulose sensor in a POC device. Finally, quantified shelf life over 4 weeks' time period indicates the biosensors long term usability when storing at room temperature. This enzyme immobilized nanocellulose biosensor can detect human blood glucose concentration within the range of interest (for diabetes patient or to detect prediabetes). This concept also opens the door of developing nanocellulose based sensor to detect other analytes present in body fluid.

5.5 Methodology

5.5.1 Materials

Bleached Eucalyptus Kraft (BEK) pulp was collected from Australian Paper, Maryvale. 2,2,6,6-Tetramethylpiperidine-1-oxyl (TEMPO), sodium Bromide (NaBr), glucose oxidase and phenol red were purchased from Sigma Aldrich. 12 w/v% Sodium Hypochlorite (NaClO) was purchased from ThermoFisher. Sodium hydroxide (NaOH) and Hydrochloric acid (HCl) were purchased from Merck and ACL laboratories, respectively. D(+)-glucose powder was sourced from Merck. Human blood was collected from Australian Red Cross. Glucose colorimetric kit was purchased from Invitrogen.

5.5.2 Methods

5.5.2.1 TEMPO mediated oxidation

The TEMPO-mediated oxidation process employed to produce low surface charged fibers is based on a previously developed method [25]. 100 g BEK pulp is suspended in 2500 mL water containing 0.4 g TEMPO and 2.5 g NaBr. The 12 w/v% NaClO solution is initially adjusted to pH 10 via addition of 32 w/v% HCl. 100 mL NaClO is added drop-wise to the suspension whilst stirring. The pH of the reaction is maintained at 10 through the addition of 0.5 M NaOH. The oxidation process is deemed to be complete when the pH change is negligible. The TEMPO-oxidized pulp

is then dispersed in deionized water at a desired concentration. Fibrillation is accomplished through a high-pressure homogenizer at 1000 bar with two passes. The hydrogel produced by this procedure is stored at 4^{o}C.

5.5.2.2 Preparation of nanocellulose sensor

5 g of nanocellulose hydrogel was mixed with 214.77 µL of 372.5 µM GoX, 100 µL of 0.75% phenol red and mixed with magnetic stirrer for an hour. After one hour, the mixed hydrogel (5 g) was transferred on a petri dish to produce a circle with diameter around 73 mm. The petri dish was previously wrapped with gladwrap to avoid the hydrogel stick to the petri dish surface after drying. Another petri dish wrapped with glad wrap was placed on the top of mixed hydrogel petri dish. Then a fixed weight of glass petri dish was placed on top to press the hydrogel and make a thin layer. This does not produce an exact circle but we tried to keep it as exact as possible with 73 mm diameter. Then this setup with mixed hydrogel was placed into -80^{o}C freezer for at least 4 hours followed by freeze drying in a Christ Alpha 2-4 LD Plus freeze dryer for 24 hours. The dried samples (62.8±5.4 µm thickness) were cut into 8 mm circles by Epilog Laser cutter with a speed of 100% and 3% power. Each circle contains 3±0.2 µL GoX inside its structure.

5.5.2.3 Blood glucose level determination

The glucose concentration in the blood sample received from Australian Red Cross was measured by glucometer (ACCU-CHEK Performa). Some of the blood plasma samples glucose concentrations were measured by Invitrogen Glucose colorimetric detection kit to confirm the accuracy of gluometer. This kit comes with glucose standard solution (320 mg/dL), assay buffer (contains detergent and stabilizers), substrate, horseradish peroxidase (HRP) concentrate, glucose oxidase (GoX) concentrate. 1X GoX and 1X HRP was prepared according to the instructions provided by the supplier. The human blood plasma was diluted at 1:20 into the assay buffer and 20 µL of diluted plasma was added with 25 µL 1X HRP, 25 µL substrate and 25 µL GoX in 96-half area well plate. The colorimetric reaction was analyzed in a Tecan Infinite M Nano plate reader at 560 nm after 30 minutes of incubation. The standard curve for glucose was generated by diluting the glucose standard provided, for a range of glucose concentration of 32 – 0 mg/dL and quantifying the absorbance at 560 nm. The glucose concentrations of unknown samples were read

from the standard curve and multiplied by the dilution factor. A few blood samples glucose concentrations were also measured by Melbourne pathology to confirm the accuracy of glucometer.

5.5.2.4 Spiking glucose concentration in blood plasma

The whole blood samples glucose concentrations were measured by glucometer and then the blood plasma was separated from red blood cells by centrifugation (Eppendorf Centrifuge 5702) at 4500 rpm for 20 minutes. The blood plasma was mixed with glucose solution to have the desired concentration for the blood plasma samples. It was ensured that all of the samples mixed with the same volume of glucose solution to maintain the consistency of the blood plasma dilution (20%).

5.5.2.5 Sensor testing with different temperatures and glucose concentrations

Dried nanocellulose sensor sized 8 mm was placed inside a light box (16×16" dimmable 70 LED light box) and tested for five glucose concentrations: 7, 8, 10, 11 and 13 mM at three different temperatures; cold: 4^{o}C, room: 20^{o}C and hot: 40^{o}C. 10 µL spiked blood plasma was added on the nanocellulose sensor by a 10 µL pipette. Continuous video capturing was done at 4K 60 FPS (frames per second) from the top of a light box by an iPhone from initial to 20 minutes. The light box was used to maintain the consistent light intensity throughout the experiments. 4^{o}C testing was done inside a cool room maintained at 4^{o}C and for 40^{o}C temperature, a hot plate was used. Each test replicated 4 times. The images were extracted from the video file for analyzing at different time intervals.

5.5.2.6 Shelf life testing

Dried nanocellulose sensors were stored at 23^{o}C and 50% RH for four weeks and tested for different glucose concentrations at room temperature as described in section 5.5.2.5.

5.5.2.7 Image analysis

The images at specific times (30s, 1 min, 2 min, 4 min, 7 min and 10 min) were extracted from the captured videos as image file. The backgrounds of these images were removed in Adobe

Photoshop. The image compilation was done in Adobe Photoshop 2021. The color hue of the images was also quantified in Photoshop.

5.6 Results

A new point of care (POC) concept of nanocellulose sensor was developed to directly measure and rapidly report by colorimetry the glucose concentration in human blood. The variables tested include time, glucose concentrations and temperatures; this was to evaluate the glucose diagnostic usability under relevant conditions. Enzyme immobilized glucose sensor is utilized to react with blood glucose which changes the reaction pH and a consequent color change on the sensor. The effect of contact time is studied to optimize the color development reporting glucose concentration and to determine how long the reporting color remains stable. The diagnostic was tested at critical temperatures (4, 20 and 40 ^{o}C) to report the dependency of reaction rate and color intensity with temperature. Diagnostic performance at room temperature (20 ^{o}C), sample stored in the fridge (4 ^{o}C) and during a hot Australian day (40 ^{o}C) was tested.

5.6.1 Glucose assay

Colorimetric glucose assay was conducted by glucose colorimetric kit and analyzed by spectrophotometry. Both tests show similar results (Table 6-1). This confirms the sensitivity and accuracy of glucometer reading. The spectrophotometry test to determine glucose concentrations were performed only for a few samples. This was to calibrate and validate that the glucometer reading is reliable and also that spiked plasma has the correct glucose concentration.

Table 6-1: Comparison of glucose concentration in human blood as determined by spectrophotometry and glucometer.

Sample	Glucometer reading (mM)	Spectrophotometry reading (mM)
Sample 1	4.20	3.48±0.35
Sample 2	7.00	7.84±0.63
Sample 3	9.98	9.61±0.27
Sample 4	10.00	10.09±0.72
Sample 5	13.00	12.77±0.99

5.6.2 Effect of time

Testing time was first optimized to ensure reproducible and sensitive results. Figure 6-2 shows the effect of reaction time ranging from 30s to 10 min for the nanocellulose sensor color at room temperature (20 ºC). Room temperature images show a more stable color development than at cold temperature (Figure 6-S1 in the supp info). For cold temperature, both 7 mM and 10 mM color change over time: 7 mM gets redish while the 10 mM turns orangish with time. A 7 min blood-sensor contact time was determined as optimum for both room and cold temperature reading. This contact time period allows the blood plasma to be properly distributed and generate a stable and measurable color change using nanocellulose foam.

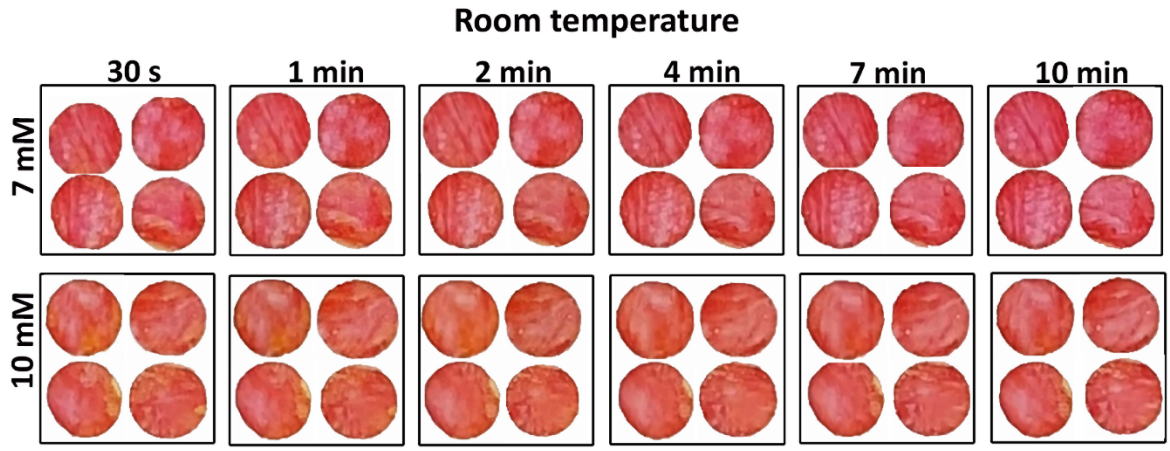

Figure 6-2: Effect of time for nanocellulose sensor colorimetric measurement at room temperature (20±1 ºC) for two different glucose concentrations: 7 mM and 10 mM.

5.6.3 Effect of temperature

Temperature is an important parameter when developing colorimetric sensor based on an enzymatic reaction. Testing was conducted at 4, 20 and 40 ºC. High temperature (40ºC) results in maroon color for 7 mM glucose concentration in blood plasma, while the other temperatures develop a red color (Figure 6-3). There is a slight difference between cold and room; room temperature shows a slightly darker color than cold temperature.

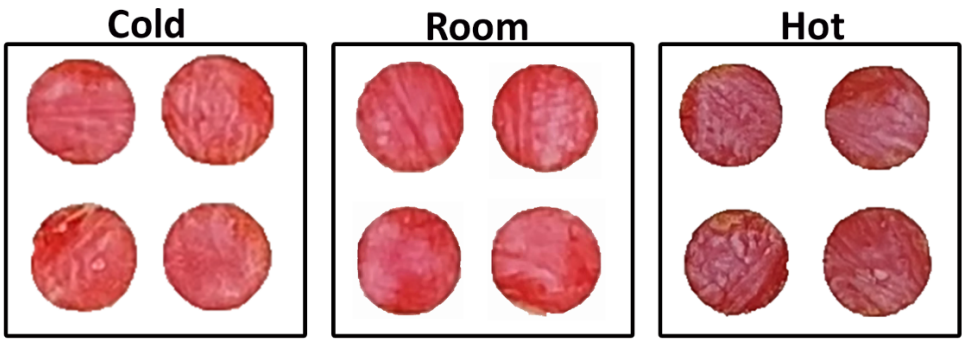

Figure 6-3: Effect of temperature on nanocellulose sensor colorimetric performance for measurement under cold (4±1 ºC), room (20±1 ºC) and hot conditions (40±1 ºC) after 7 min for 7 mM glucose concentration.

5.6.4 Effect of glucose concentration

A colorimetric glucose sensor requires to show visible differences in color in the concentration range of interest. The nanocellulose sensor developed shows a gradual color change as the glucose concentration in blood plasma increases from 7 mM to 13 mM (considering its medical importance) from red to orange (Figure 6-4A). This is because higher glucose concentrations produce higher concentrations of gluconic acid in presence of glucose oxidase which decreases pH, resulting in color change; phenol red changes from red to orange as pH drops.

Quantification of sensor shelf life is important as long-term storage of sensors is a requirement to for economic viability. The nanocellulose sensor was tested after 4 weeks aging at room temperature in airtight container (23 ºC and 50% relative humidity) to quantify its effectivity. Figure 6-4B shows the gradual color change for different glucose concentrations from 7 mM to 13 mM. This color change confirms the activity of glucose oxidase after 4 weeks storage.

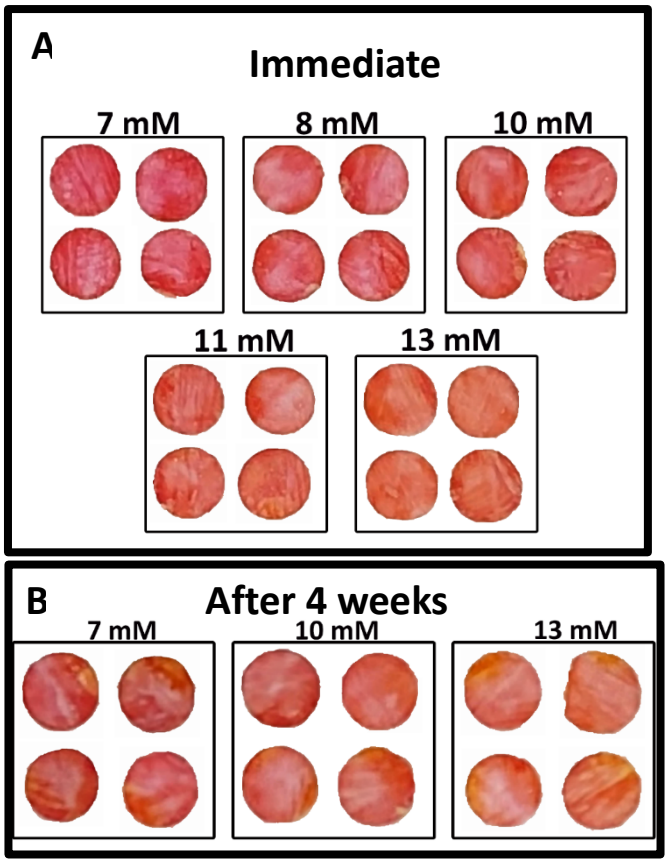

Figure 6-4: Effect of glucose concentration on colorimetric properties for nanocellulose sensor after 7 mins (A) Immediate test and (B) After 4 weeks test.

5.6.5 Diagnostic prototype design

A 3D multilayer laminate based diagnostic device was created. The device had 3 functions to achieve. First, to remove RBC, as only plasma is analyzed for glucose content; second, to measure and display testing reading time; third, to measure and colorimetrically report glucose concentration. The composition and 3D pathway of the device layers is presented in Figure 6-5. This device consists of six layers: (i) hydrophobic layer on the top to avoid any leakage, (ii) adhesive layer to keep the layers together, (iii) wicking layer to monitor reaction time for optimum reading, (iv) membrane layer to separate red blood cells from plasma, (v) detection layer which is the colorimetric sensor part, and, (vi) hydrophobic result window layer. Three microfluidic technologies are implemented within this device: time-controlled wicking channel (layer 3), a paper-based plasma separating membrane (layer 4), and a detection zone (layer 5). However, the

time-controlled wicking channel can be removed if the users can monitor the reaction time by themselves.

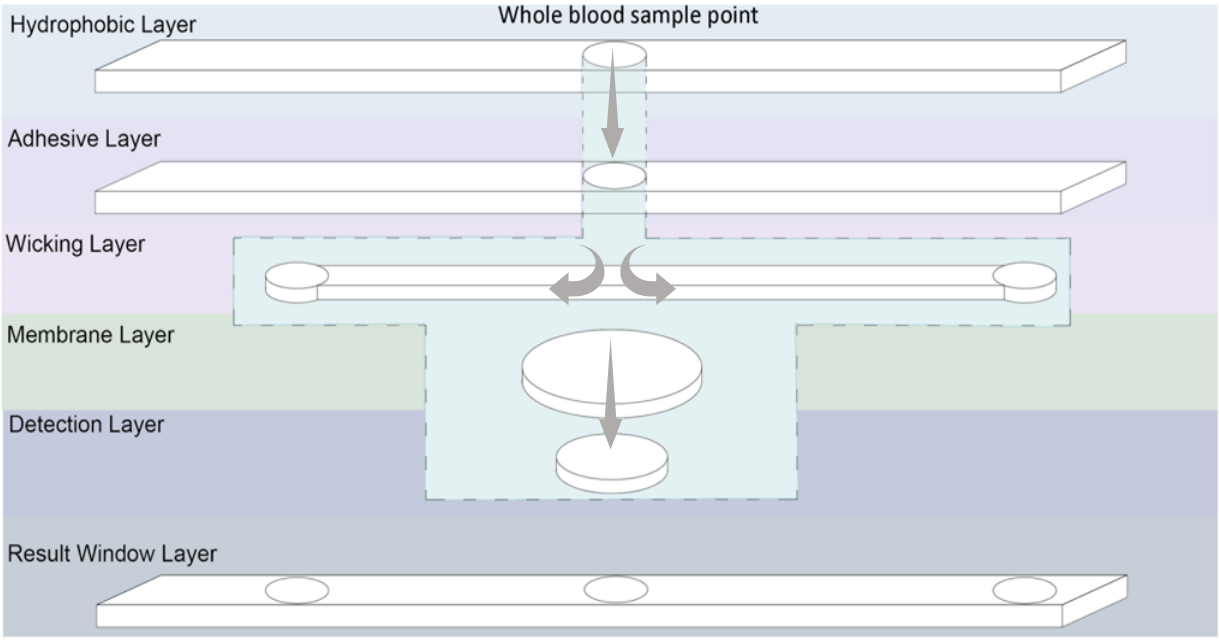

Figure 6-5: Schematic construction of a laminated glucose diagnostic representing the Microfluidic 3D pathway of the handheld device.

The time-controlled wicking channel is selected in such a way that the blood reaches the left corner of the wicking channel at the optimized time, when the glucose concentration needs to be recorded and displayed from the device. The right side of the wicking channel is longer than the left side which requires more time to transport the blood on the right edge indicating the color reading is expired. The wicking speed in the wicking channel can be controlled by the porosity and thickness of the paper used. Tissue paper from Kimberly Clark Experimental Forming Unit (EFU), Neenah (WI), USA was selected; it is available at a range of thickness. Next, paper-based plasma separator reduces the need for whole blood preparation; the end user can apply blood directly to the sample area. The membrane technology utilizes paper pores structure to physically separate larger (7-8µm [26]), pigmented red blood cells; leaving a transparent yellow tinted solution to react within the detection zone [27]. When blood is dropped onto the sample area, it travels through the wicking channel laterally and vertically both. Passing the wicking channel, blood goes to the membrane layer vertically which separates red blood cells and pass the plasma through the membrane to the next layer which is the detection layer. A hydrophobic waxed circle is integrated into the center of the membrane to prevent the reddening membrane from altering the visual reading of the nanocellulose foam. Nanocellulose superabsorbent/foam in the detection layer is adhered to the

membrane to prevent bypassing, the membrane undergoes a waxing process that hydrophobically blocks the fluid from reaching the membrane edges and bypassing the separation process by jumping to adjacent layers. The blood plasma reacts with the enzymes and colorimetry reagents within the nanocellulose superabsorbent resulting in a color change, visible through the middle result window. Once the blood has wicked to the left end of the lateral wicking channels, it can be seen through the result window openings which means the color can be read now.

5.7 Discussion

5.7.1 Governing variables

In this study, we developed a nanocellulose based colorimetric sensor by utilizing its unique properties of high porosity and high surface area. The new sensor is tested for different glucose concentration, reaction time, reaction temperature and stability over 4 weeks' time. The developed sensor shows successful color change at different glucose concentrations confirming its functionality for future use of this sensor in blood glucose determination device.

Glucose oxidase immobilized in nanocellulose oxidizes beta-D-glucose into D-glucono-1,5 lactone, which then hydrolyses into gluconic acid. H_2O_2 is produced as a by-product in this reaction [28]. This acidic medium changes the pH of the system which is indicated by pH sensitive phenol red color change in the sensor. The reaction is noticed to proceed with time in Figure 6-2. Continuous monitoring and video capturing of the reaction indicate that the reaction is quicker at higher temperature. This increase of darkness with temperature in Figure 6-3 reveals that the catalysis reaction of glucose by glucose oxidase is quicker at higher temperature. This is consistent with literature where reaction rate of glucose oxidase was studied at a temperature of 25 to 60^{o} C. The reaction velocity increases with increase in temperature due to increase of second order reaction rate constant [29]. The optimized time to read the sensor color can be different for large temperature difference.

The developed sensor can quantify the difference in glucose concentration in blood plasma by changing color from red to orange (Figure 6-4). Normal blood glucose concentrations for non-diabetics are under 7.8 mM two hours after having meals. Glucose levels in between 7.8 to 11 mM indicates prediabetes and higher than 11 mM is diabetes. Our glucose sensor can consistently determine the difference between 7 and 8 mM-10 mM (Figure 6-4) which determines occurrence of diabetes. The color difference between 10, 11 and 13 mM also differentiates the state between

pre-diabetes and diabetes. The sensor color change is shown as a color gradient in Figure 6-6. This is confirmed with color hue calculation as shown in the image by the horizontal gradient bar. Summary of color theory and the reasons to choose color hue is given in supplementary information (Figure 6-S2 and 6-S3). Color hue of the images changes from 351° to 12° indicating quantitative confirmation of color change. This number can be integrated with any device to show directly glucose concentration number instead of comparing the color with the standard. However, this sensor can work independently without incorporating into an electronic device.

The successful color change of the developed enzyme immobilized pH based nanocellulose sensor motivate us to design a prototype to simulate the real and future product. The conceptual device is designed with the intention of being most applicable to users disadvantaged by poverty, remoteness, electricity, and education. The three step testing procedure follows the ASSURED principles – affordable, specific, sensitive, user-friendly, rapid and robust, equipment free, and deliverable [30].

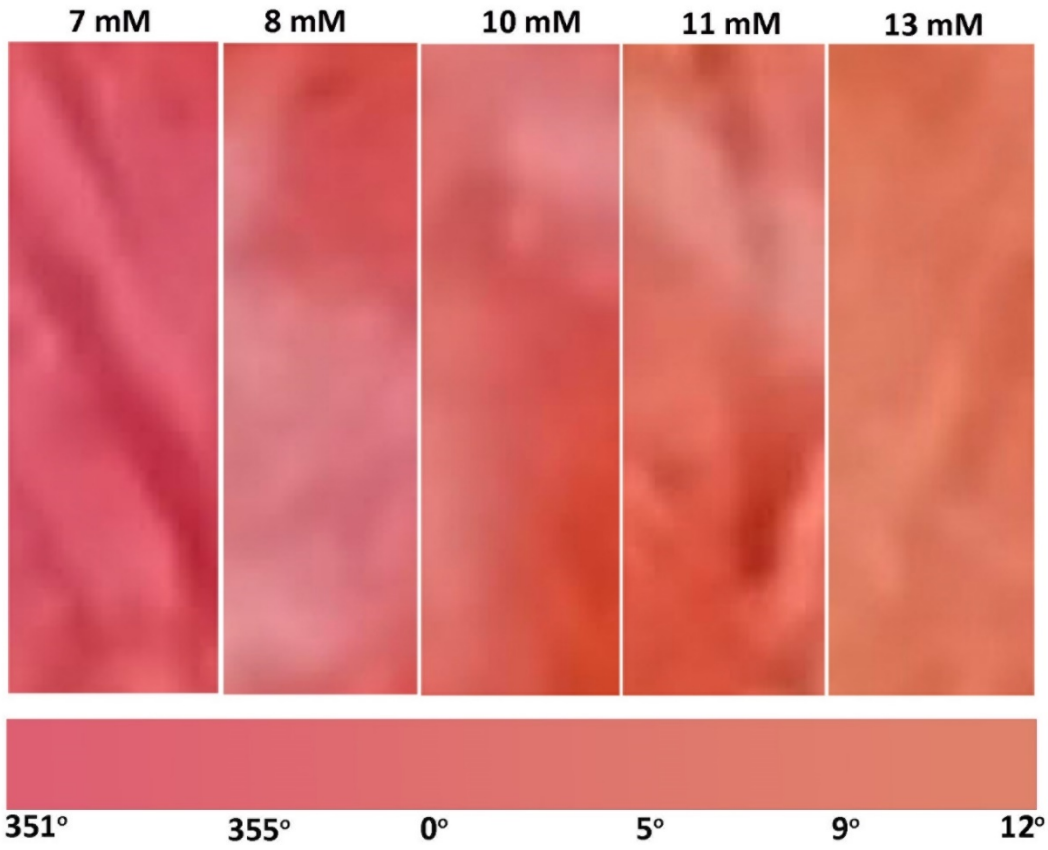

Figure 6-6: Gradient of color change at a glucose range of 7 mM – 13 mM.

5.7.2 Device concept

Figure 6-7 shows the device design for nanocellulose sensor. A single-use diagnostic strip (Figure 6-5) is inserted within the user's reusable plastic casing that details the three-step procedure. A sample of approximately 20 µL of blood– obtained by pricking a finger with a lancet - is dropped onto the whole blood detection zone. Turning the device over, an indicator box at the top will turn red due to blood wicking after a certain time, communicating the nanocellulose diagnostic zone is available to be read for results. The standard color at different glucose concentration is given on the device. Once the bottom indicator box turns red after another specific time, the results have expired. Encouraging a new generation of environmentally conscious single-use diagnostic devices – once testing concludes the biodegradable paper strip may be disposed of with the individual's plastic insertion device kept for reuse.

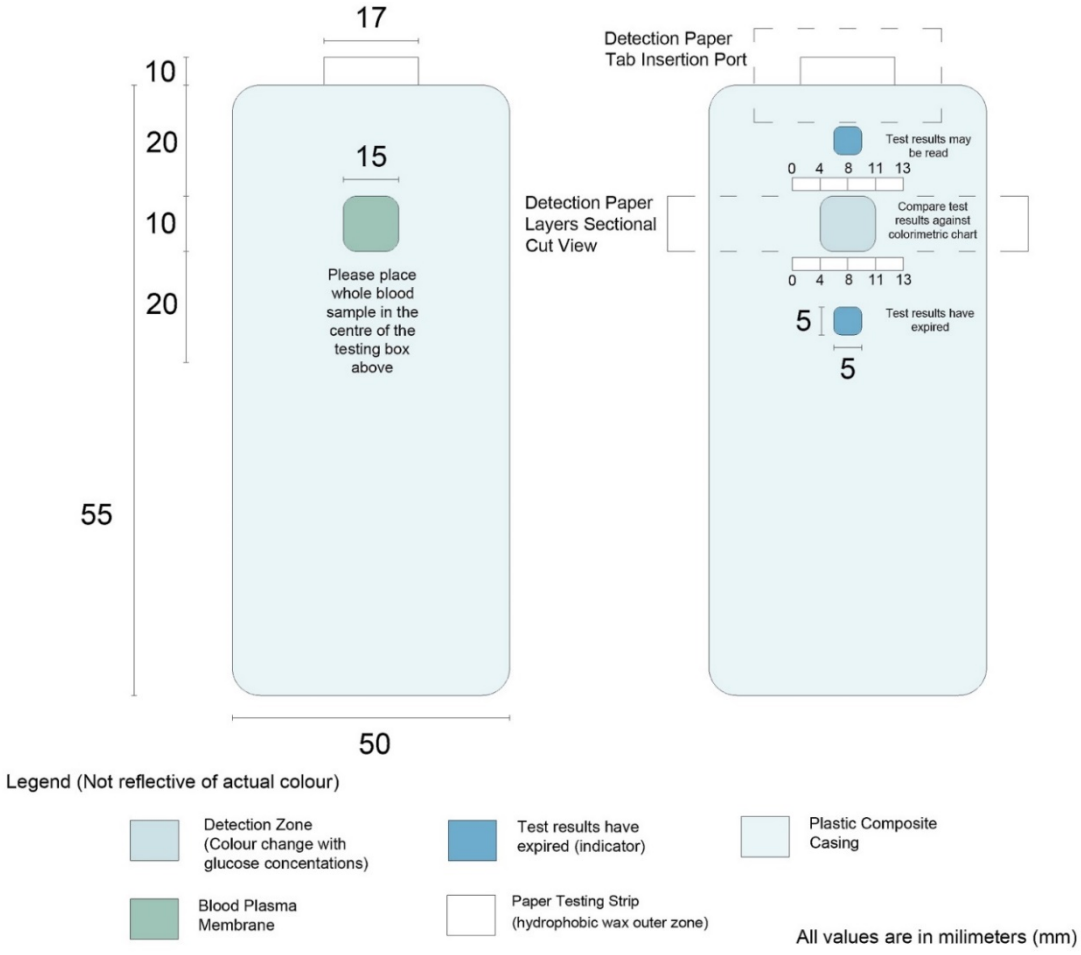

Figure 6-7: Nanocellulose sensor device concept. The numbers on the image shows the distance in mm. The distances are estimated considering user friendly device concept and based on the commercial sensor device available.

5.8 Conclusion

This study investigates the use of nanocellulose superabsorbent as a generic medium for colorimetric methods for the detection of glucose in blood. Applying the concept, a novel handheld paper-based glucose POC diagnostic device was proposed. This colorimetric method was assessed in term of temperature, time and glucose concentrations to develop a robust diagnostic. The color change is determined both qualitatively and quantitively to confirm accuracy and consistency.

Phenol red based glucose oxidase immobilized nanocellulose sensor differentiates glucose concentrations in blood plasma by showing gradual color change from red to orange. It is sensitive in the 7 to 13 mM concentration range of interest for diabetes detection. This immobilized enzyme remains active up to 4 weeks at room temperature, providing the required diagnostic shelf life. This contrasts to the usual 3 weeks shelf life at 4ºC for enzymes in solution. This colorimetric method shows high temperature sensitivity when the temperature is very high at around 40 ºC. Usually the room temperature is maintained within 20-30 ºC where the developed sensor is quite stable. Overall this research succeeded in evaluating the potential of enzyme colorimetry method within a prototype device and highlights there is a future application for economical nanocellulose foam/SAP diagnostic devices.

5.9 References

1. Basiruddin, S. and S.K. Swain, *Phenylboronic acid functionalized reduced graphene oxide based fluorescence nano sensor for glucose sensing.* Materials Science and Engineering: C, **58**.2016. 103-109.
2. Wild, S., G. Roglic, A. Green, R. Sicree, and H. King, *Global prevalence of diabetes: estimates for the year 2000 and projections for 2030.* Diabetes Care, **27**(5).2004. 1047-53.
3. Hossain, P., B. Kawar, and M. El Nahas, *Obesity and Diabetes in the Developing World — A Growing Challenge.* New England Journal of Medicine, **356**(3).2007. 213-215.
4. (WHO);, W.H.O. *Diabetes*. 2021 [cited 2021; Available from: https://www.who.int/news-room/fact-sheets/detail/diabetes.
5. Health, A.I.o. and Welfare, *Diabetes*. 2020, AIHW: Canberra.
6. Isley, W.L. and M.E. Molitch, *Type 1 diabetes.* The Journal of Clinical Endocrinology & Metabolism, **90**(1).2005. E2-E2.
7. Ndisang, J.F., A. Vannacci, and S. Rastogi, *Insulin Resistance, Type 1 and Type 2 Diabetes, and Related Complications 2017.* Journal of diabetes research, **2017**.2017. 1478294-1478294.
8. Australia;, D. *Gestational diabetes*. 2021; Available from: https://www.diabetesaustralia.com.au/about-diabetes/gestational-diabetes/.
9. Kharroubi, A.T. and H.M. Darwish, *Diabetes mellitus: The epidemic of the century.* World journal of diabetes, **6**(6).2015. 850.

10. World Health, O. and F. International Diabetes, *Definition and diagnosis of diabetes mellitus and intermediate hyperglycaemia : report of a WHO/IDF consultation*. 2006, World Health Organization: Geneva.
11. Alberti, K.G. and P.Z. Zimmet, *Definition, diagnosis and classification of diabetes mellitus and its complications. Part 1: diagnosis and classification of diabetes mellitus provisional report of a WHO consultation.* Diabet Med, **15**(7).1998. 539-53.
12. McMilin, J.M., *Clinical Methods: The History, Physical, and Laboratory Examinations*. 3rd ed. Blood Glucose. 1990, Boston: Butterworths.
13. Nguyen, T.B.N., *Blood glucose and enzyme analysis methods of blood glucose: Case in Vietnam.*2018.
14. HN Rajaratnam and S. Pathmanathan, *How reliable are capillary blood glucose measurements?* Sri Lanka Journal of Diabetes Endocrinology and Metabolism, **1**(1).2011. 22-24.
15. Kotwal, N. and A. Pandit, *Variability of capillary blood glucose monitoring measured on home glucose monitoring devices.* Indian journal of endocrinology and metabolism, **16**(Suppl 2).2012. S248-S251.
16. Lin, G., S. Chang, H. Hao, P. Tathireddy, M. Orthner, J. Magda, and F. Solzbacher, *Osmotic swelling pressure response of smart hydrogels suitable for chronically implantable glucose sensors.* Sensors and Actuators B: Chemical, **144**(1).2010. 332-336.
17. Guenther, M., G. Gerlach, T. Wallmersperger, F. Solzbacher, P. Tathireddy, J. Magda, G. Lin, and M. Orthner. *Hydrogel-Based biochemical sensors*. in *Proceedings of 15th international conference on sensors and measurement technology "Sensor+ Test*. 2011: p. 211-215. Citeseer.
18. Gao, Z.F., E.E. Sann, X. Lou, R. Liu, J. Dai, X. Zuo, F. Xia, and L. Jiang, *Naked-eye point-of-care testing platform based on a pH-responsive superwetting surface: Toward the non-invasive detection of glucose.* NPG Asia Materials, **10**(4).2018. 177-189.
19. Cui, Y., W. Duan, Y. Jin, F. Wo, F. Xi, and J. Wu, *Ratiometric Fluorescent Nanohybrid for Noninvasive and Visual Monitoring of Sweat Glucose.* ACS sensors, **5**(7).2020. 2096-2105.
20. Khan, M.R.R., A.V. Watekar, and S.-W. Kang, *Fiber-optic biosensor to detect pH and glucose.* IEEE Sensors Journal, **18**(4).2017. 1528-1538.
21. Song, C., P.E. Pehrsson, and W. Zhao, *Optical enzymatic detection of glucose based on hydrogen peroxide-sensitive HiPco carbon nanotubes.* Journal of materials research, **21**(11).2006. 2817-2823.
22. Lin, X., W. Lin, M. Yang, J. Chen, D. Yu, W. Hong, and X. Chen, *Rapid colorimetric glucose detection via chain reaction amplification of acrylic functionalized Ag@ SiO 2 nanoparticles.* RSC advances, **8**(66).2018. 37729-37734.
23. Wang, Q., T. Dai, P. Sun, X. Wang, and G. Wang, *A colorimetric and ratiometric glucose sensor based on conformational switch of i-motif DNA.* Talanta Open.2020. 100001.
24. Lee, P.-C., N.-S. Li, Y.-P. Hsu, C. Peng, and H.-W. Yang, *Direct glucose detection in whole blood by colorimetric assay based on glucose oxidase-conjugated graphene oxide/MnO 2 nanozymes.* Analyst, **144**(9).2019. 3038-3044.
25. Saito, T., S. Kimura, Y. Nishiyama, and A. Isogai, *Cellulose nanofibers prepared by TEMPO-mediated oxidation of native cellulose.* Biomacromolecules, **8**(8).2007. 2485-2491.
26. Kinnunen, M., A. Kauppila, A. Karmenyan, and R. Myllylä, *Effect of the size and shape of a red blood cell on elastic light scattering properties.* Biomedical optics express, **2**.2011. 1803-14.
27. *Vivid™ Plasma Separation Membrane*. 2021 [cited 2021 04/05/2021]; Available from: https://shop.pall.com/us/en/medical/advanced-materials/diagnostics-2/zidgri78lls.

28. Kornecki, J.F., D. Carballares, P.W. Tardioli, R.C. Rodrigues, Á. Berenguer-Murcia, A.R. Alcántara, and R. Fernandez-Lafuente, *Enzyme production of D-gluconic acid and glucose oxidase: successful tales of cascade reactions.* Catalysis Science & Technology, **10**(17).2020. 5740-5771.
29. Odebunmi, E. and S. Owalude, *Kinetic and thermodynamic studies of glucose oxidase catalysed oxidation reaction of glucose.*2007.
30. Byrnes, S., G. Thiessen, and E. Fu, *Progress in the development of paper-based diagnostics for low-resource point-of-care settings.* Bioanalysis, **5**(22).2013. 2821-2836.

CHAPTER 7
CONCLUSION AND PERSPECTIVES

THIS PAGE WAS INTENTIONALLY LEFT BLANK

Chapter 7: Conclusion and Perspectives

THIS PAGE WAS INTENTIONALLY LEFT BLANK

7.1 Conclusions

Superabsorbent polymers (SAPs) are 3D cross-linked hydrophilic network capable of absorbing a large volume water or fluids inside its structure. They are being widely used for food packaging, agriculture, personal care products and biomedical applications. However, most of the commercial SAPs are petrochemical based, non-biodegradable and non-renewable. Nevertheless, they are widely commercially used to fulfil the global demand. This necessitates the development of sustainable SAPs made from a naturally sourced polymer, such as cellulose, which is abundant and cheap. Breaking down cellulose into nanosized fibers produce nanocellulose which is extremely hydrophilic and eminently suitable for engineering, functionalization, and use as an application specific superabsorbent material.

This thesis details research conducted to enable nanocellulose to be tuned and engineered into a highly performant superabsorbent by manipulating key properties of the material including: mechanical strength, absorption capacity, absorption kinetics, pore structure, and fiber-fiber interaction. The physical, chemical, and mechanical properties of nanocellulose SAPs were investigated to enable a tunable, biodegradable material to be developed for different applications. The success of the developed material and achievement of the overall thesis aim has been demonstrated by applying the new knowledge of the relationships between nanocellulose pre-treatment and production methods, superabsorbent structure, and superabsorbent properties to engineer a nanocellulose superabsorbent-based glucose sensor for the detection of human blood sugar concentrations.

7.1.1 Nanocellulose superabsorbent with high mechanical strength

Mechanical strength of nanocellulose SAP is important to have performant superabsorbent under applied load. This applied load can be different depending on final application, such as for meat packaging or baby diaper. Superabsorbent polymer with high compressive strength will not disintegrate under this applied load. To improve the mechanical strength of neat nanocellulose SAP, the nanocellulose was crosslinked, or blended with crosslinkers or cellulose crystal. Crosslinking successfully increased the rheological and mechanical properties of the precursor hydrogel, but did not improve the mechanical strength (compressive strength) in the final, dried SAP. Blending cellulose nanocrystals into hydrogel increased the compressive strength of dried superabsorbent due to the increase in bonded surface area and total fiber length available for

bonding. Thus, a method of tuning the mechanical strength of nanocellulose SAPs has been demonstrated.

7.1.2 Swelling mechanism of neat and crosslinked superabsorbent

The swelling behavior at nanoscale is dependent on the superabsorbent structure. Physically and chemically crosslinked hydrogels were characterized by rheological methods to quantify the effect of crosslinking and HR-SEM was used for morphological structure evaluation. Small Angle Neutrons and X-ray scattering were used to quantify the structural difference during swelling and drying of saturated SAP.

Functionalized neat nanocellulose SAP can absorb up to 132 times of its initial weight in MilliQ water, and the fiber bundles swell up to 19.5 nm during water absorption. Chemically crosslinked SAP has very compact structure which results in lower fiber bundle swelling of 15 nm where physically (high molecular weight PEI) crosslinked SAP has an open structure, resulting in higher fiber bundle swelling of 25 nm. The hydration-dehydration hysteresis shows the decrease of fiber bundle diameter confirming fiber bundle shrinkage during drying. Thus, it has been shown that absorption properties of nanocellulose SAPs are controlled by physical and chemical crosslinking.

Physical and chemical crosslinking of nanocellulose superabsorbent can be used as a method to control and tailor the swelling capacity of NC foams. Quantification of structural change upon swelling and drying broadens the understanding of swelling phenomenon in nanoscale.

7.1.3 Tunable absorption kinetics of nanocellulose superabsorbent

The absorption kinetics of nanocellulose SAP prepared by TEMPO and TEMPO-periodate oxidation methods were measured from a fraction of a second to few minutes to understand the absorption phases and mechanism. The results indicate the occurrence of three phases: 1) wicking, 2) transition and 3) fiber swelling. Wicking is very rapid and dominant in the first few seconds. Wicking is followed by a transition phase, after which fiber swelling becomes dominant, which is a slower process. Slower absorption kinetics were observed for high surface charge compared to low surface charge nanocellulose SAPs, a phenomenon that is due to the smaller pore size and higher concentration of COO^- groups in high surface charge materials. Fiber swelling was reduced when absorbing in ionic solution due to charge shielding effect form the ions present in the solution.

Nanocellulose SAP absorption kinetics can thus be tuned by manipulating the surface change on nanocellulose fiber. This fundamental relation between the nanocellulose SAP structure and absorption phenomenon helps to develop SAP with controlled absorption kinetics by playing with the structure.

7.1.4 Nanocellulose superabsorbent with fast biodegradation

Biodegradability of nanocellulose SAP is very important along with its performance. The impact of varying the nanocellulose SAP properties, particularly the addition of crosslinker reagents, on biodegradability of the nanocellulose SAP was thus evaluated. Fast biodegradation of crosslinked nanocellulose SAP was demonstrated under enzymatic conditions *in situ* in soil. Cellulase was used to mimic natural soil enzymes, and both neat and crosslinked samples were evaluated and compared. The crosslinked SAP showed around 56% degradation in 2 days compared to neat SAP degradation of around 41%. The higher biodegradation of crosslinked SAP comes from the chemical structure where the presence of -CONH acts as a nitrogen source. So, crosslinking had positive impact on biodegradation, and nanocellulose SAPs were shown to be potentially biodegradable in-home compost or garden soil.

7.1.5 Development of a nanocellulose sensor for glucose detection in human blood

Nanocellulose SAP can be used to immobilize biomolecules, including enzymes inside its structure. Its 3D structure, high surface area, and high porosity are ideal for retention and maintenance of biomolecular activity over time. To address the overall aim of the thesis and apply the newly generated knowledge around the relationships between nanocellulose SAP production methods, resulting structure and properties, functionalized nanocellulose SAP with high porosity and specific surface area was engineered and used to demonstrate a blood glucose sensor. Glucose oxidase was immobilized in the nanocellulose SAP. Incorporation of phenol red inside the SAP structure induces a pH response to the oxidation of blood glucose, which is catalyzed by glucose oxidase. This enzyme immobilized, pH-based colorimetric sensor can differentiate the glucose concentration in human blood for a range of 7-13 mM by showing a visibly detectable color change from red to orange. The color change was stable after 7 min. Increasing the reaction temperature from room temperature to 40 ^{o}C increases the reaction rate in the sensor, but the color change and

correlation to glucose concentration is still visible. The shelf life test after 4 weeks confirmed the sensor stability for long term storage at room temperature. This concept of enzyme immobilized colorimetric sensor clearly demonstrates that nanocellulose SAP materials can be engineered with application specific properties. This concept can be extended to develop other types of biosensors and for wider SAP applications.

7.2 Perspectives

In this thesis, the structure-property relationship of nanocellulose SAPs are established via comprehensive investigation of the rheological properties, mechanical strength, absorption phenomenon and fiber-fiber interactions during absorption by manipulating different variables associated with the pre-treatment and production of the precursor hydrogel and superabsorbent materials.

An interesting avenue to pursue further research can be understanding the similarities and differences in the interactions of nanocellulose with other biopolymers such as starch, hemicellulose, pectin, lignin and chitosan as many applications require mixers of polymers to achieve better characteristics and performance. Additionally, understanding how the biopolymer mixtures affects the cellulose fiber and the interaction between cellulose fiber and other polymers can reveal important information about its fundamental properties- such as charge distribution, hydrophilicity/hydrophobicity and porosity. These insights may better inform the SAP development from a physical and chemical point of view. Investigating the effect and *in situ* efficacy of the addition of biopolymers with antibacterial properties may be beneficial for food packaging application which can increase the product shelf life and consequently reduce the food waste.

Some of the applications of cellulose SAP requires controlled absorption kinetics such as for red meat packaging. The released blood (drip loss) from the meat pieces should be absorbed at a control rate so that there is no forced suction from the meat pieces while maintaining efficient absorption to avoid any visible blood in the surroundings. This thesis has shown that SAPs with high surface charge have slower absorption kinetics. So, mixing high and low surface charged SAPs at different ratios may achieve better controlled absorption capacity required for meat packaging.

For baby diaper application, nanocellulose SAP needs to absorb urine at a quicker rate under baby weight. In this thesis, nanocellulose SAP has engineered with high porosity and larger pores to have quicker absorption kinetics and high mechanical strength to have performant SAP under load. 0.9 wt% NaCl was used to mimic urine ionic strength. Further studies, can be done to quantify the urine absorption rate under baby weight. Next, the nanocellulose SAP needs to be sandwiched between a top and bottom layer. Development of diaper prototype from nanocellulose SAP, testing and comparison with commercial SAP can be done to justify its suitability for diaper application. Finally, techno-economic analysis needs to be done for all commercial applications, not only baby diapers, while keeping in mind landfill cost reduction and possible environmental benefits.

The novel glucose sensor application exemplifies the immense potential for engineered, nanocellulose SAPs with application-specific properties, and opens up new avenues of investigation. For the glucose sensor itself, optimization and uniform homogeneous sample development can improve the current design. Sample collection from diabetes patients and testing on the developed prototype can further inform the commercialization process. The concept can be extended to detect other analytes from body fluid, promoting nanocellulose sensors for diagnostic applications more widely.

Overall, this thesis paves the way for further studies into the adoption of engineered nanocellulose SAPs for food, personal care and diagnostic applications, that will lead to progress in the use and commercialization of this sustainable, biodegradable superabsorbent.

THIS PAGE WAS INTENTIONALLY LEFT BLANK

APPENDIX I
SUPPLEMENTARY INFORMATION

THIS PAGE WAS INTENTIONALLY LEFT BLANK

Modulating nanocellulose hydrogels and cryogels strength by crosslinking and blending

Laila Hossain, Vikram Singh Raghuwanshi, Joanne Tanner, Gil Garnier*

Bioresource Processing Research Institute of Australia (BioPRIA), Department of Chemical Engineering, Monash University, Clayton

*Corresponding author: gil.garnier@monash.edu

Supplementary Information

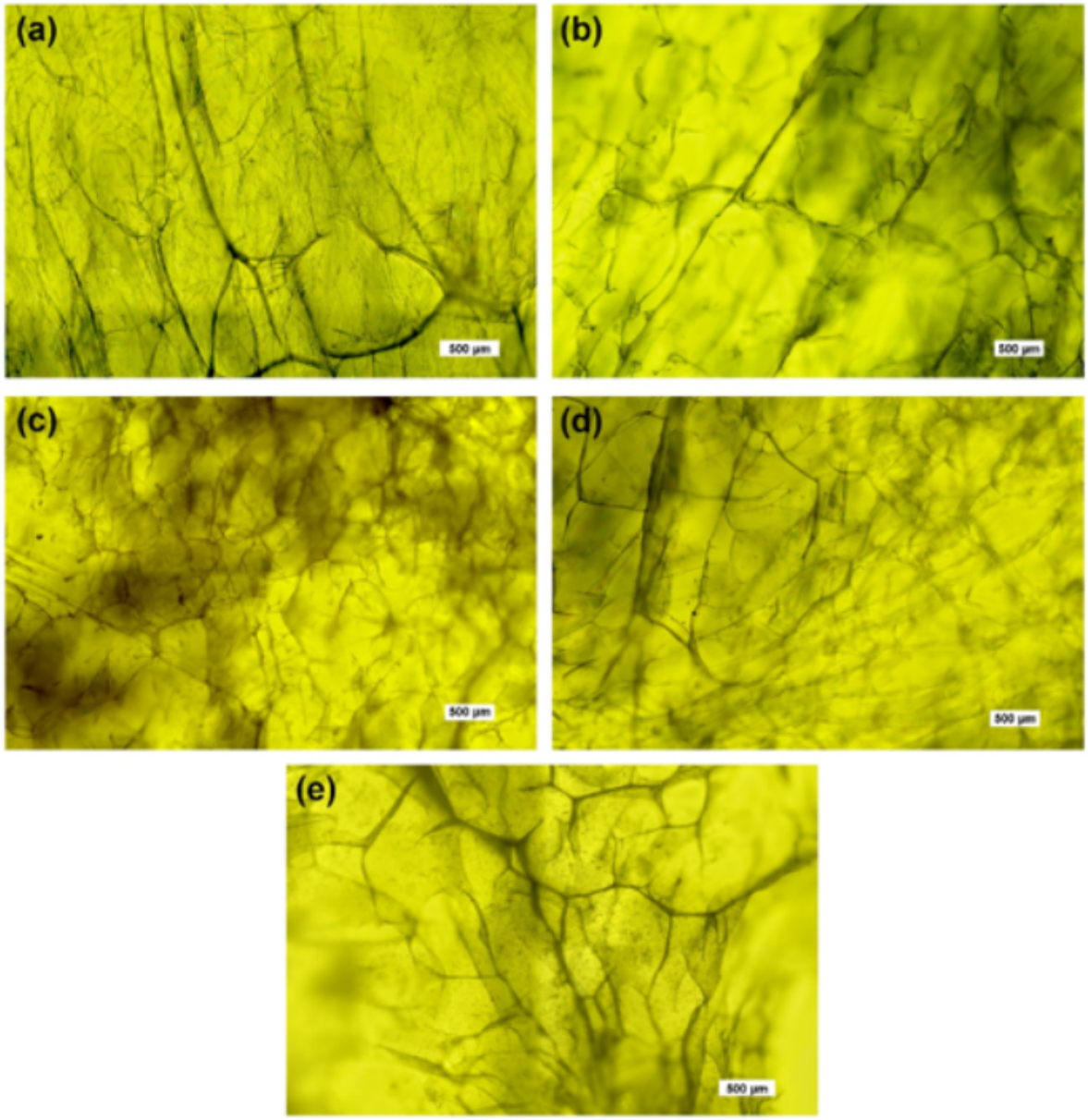

Figure 2-S1: NC cryogel under optical microscope (the scale bars at 500 µm) (a) NC, (b) NC:HP/1:0.07, (c) NC:HMDA/1:1, (d) NC:CNC/2:1 and (e) NC:MCC/2:1.

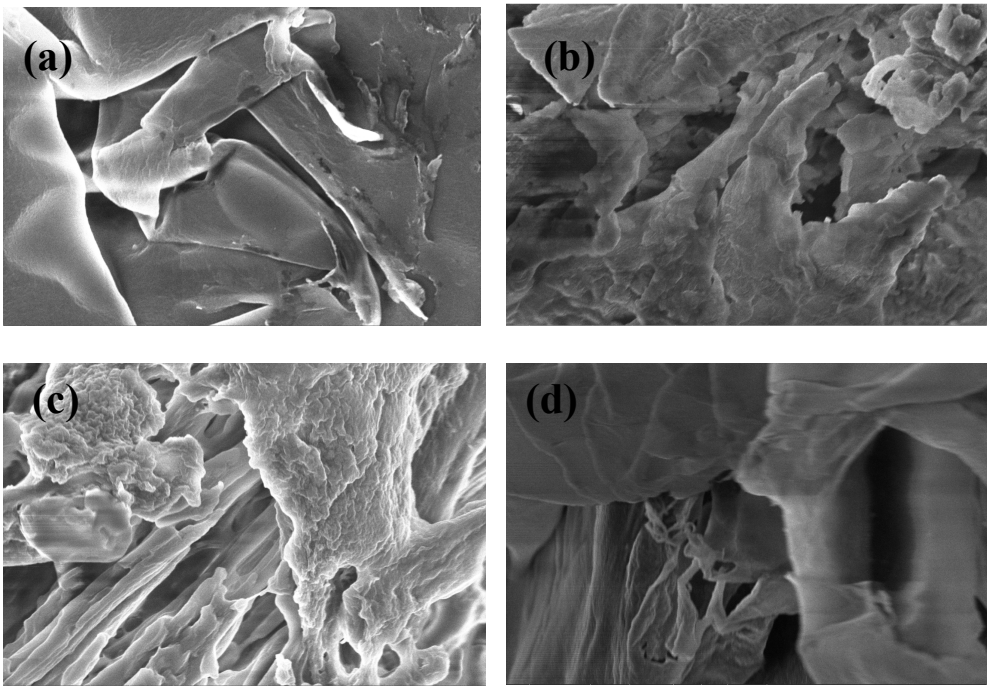

Figure 2-S2: NC cryogel under SEM: scale bar- 2 µm (a) NC, (b) NC:HP/1:0.07, (c) NC:HMDA/1:1, (d) NC:CNC/2:1.

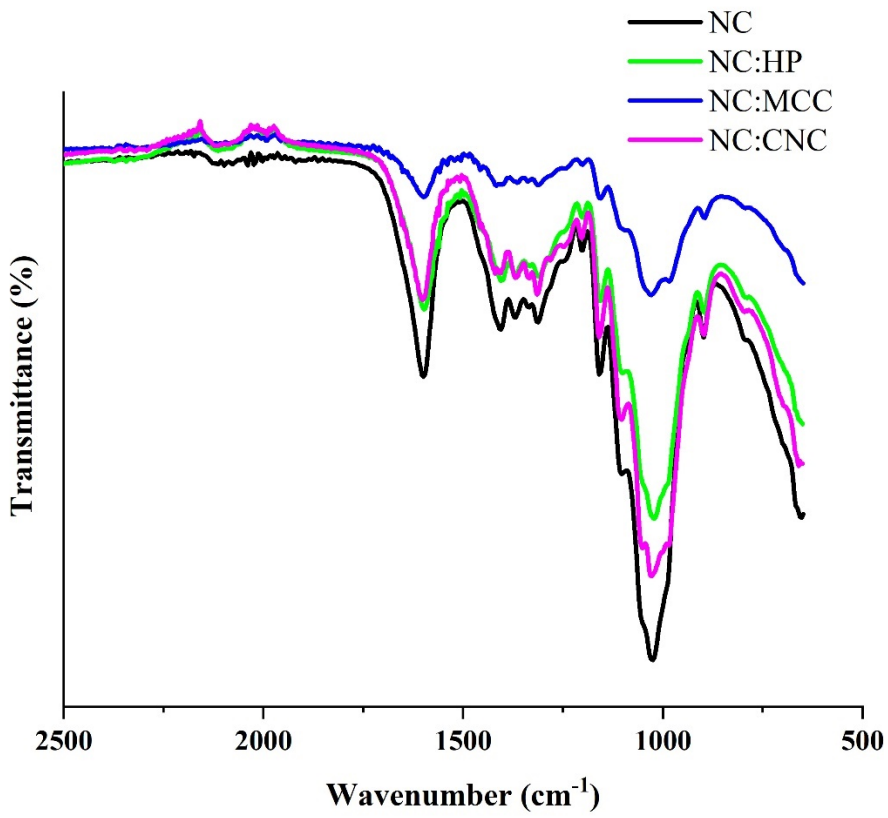

Figure 2-S3: FTIR spectra of physically crosslinked and cellulose fibril blended nanocellulose cryogels.

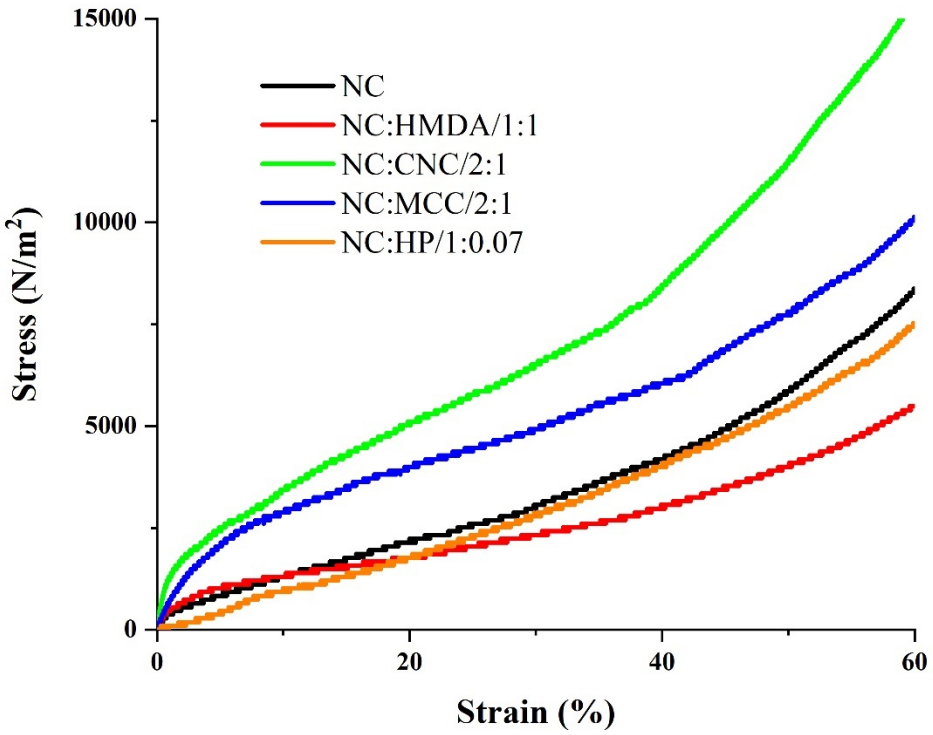

Figure 2-S4: Compression Stress -strain curve for nanocellulose cryogels.

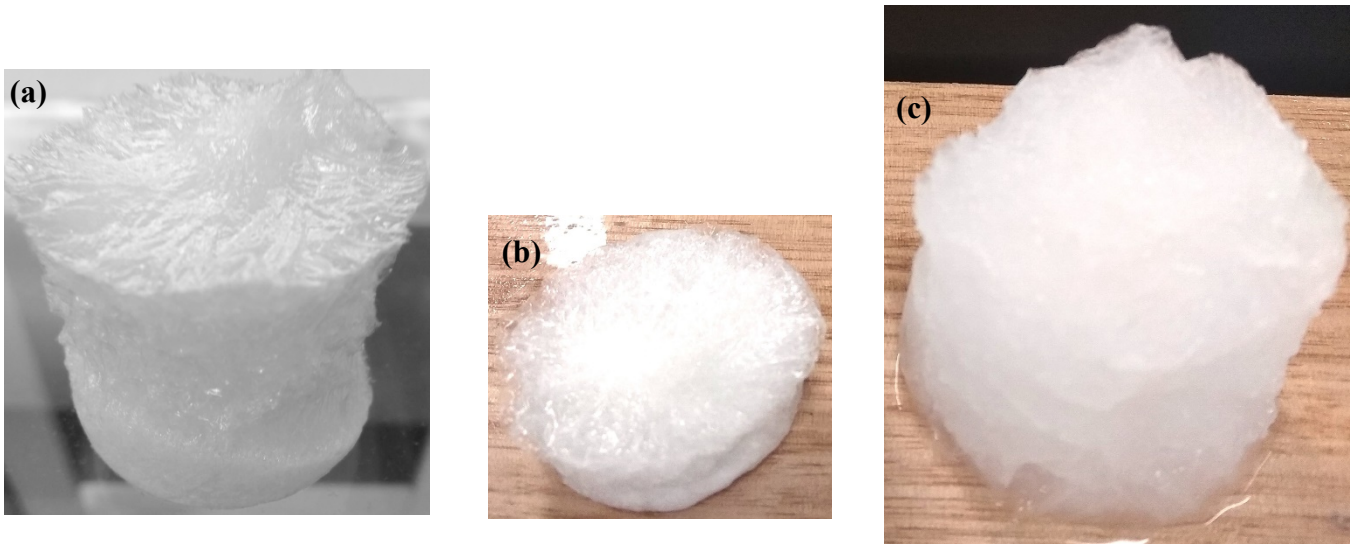

Figure 2-S5: Pictures of the Cryogel at different treatment states: (a) before compression, (b) after compression and (c) after water re-absorption.

Table 2-S1: Hydrogel water content in weight percentage.

Sample	Water percentage
NC	99.52±0.02
NC:HP/1:0.07	99.48±0.02
NC:CNC/2:1	99.28±0.01

Structure and swelling of cross-linked nanocellulose foams

Laila Hossain[a], Vikram Singh Raghuwanshi[a], Joanne Tanner[a], Chun- Ming Wu[b], Olga Kleinerman[c], Yachin Cohen[c] and Gil Garnier[a*]

[a]Bioresource Processing Research Institute of Australia (BioPRIA), Monash University, Clayton, Victoria-3800, Australia

[b]National Synchrotron Radiation Research Center, Hsinchu 30076, Taiwan

[c]Technion - Israel Institute of Technology, Haifa, Israel

Supplementary Information

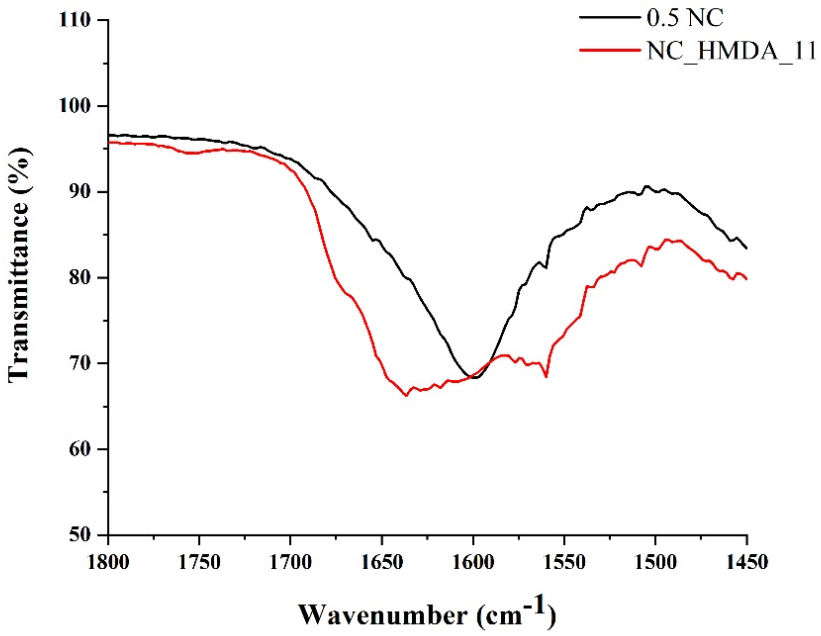

Figure 3-S1: ATR- FTIR spectra for pure NC and NC_HMDA_11 foam for complete crosslinking.

Table 3-S1: Crosslinking density for different types of samples.

Gel sample	Crosslinking density (mmol/m^3)
NC	85±6
NC_HPEI	442±33
NC_HMDA_18	90±22

3-S1: Different models are used to fit the scattering curves. The scatter intensity of different models is defined below:

1. Debye Bueche and Lorentz function

$$I(q) = scale\left[\frac{A}{(1+\xi_1^2 q^2)^2} + \frac{B}{1+\xi_2^2 q^2}\right] + background \quad \text{.....(1)}$$

Where, the first function is the Debye Bueche [1, 2] which includes large correlation length ξ_1, A is a scaling constant. The second function is the Lorentz function [3] which contains information of small correlation length ξ_2, and B is the scaling constant.

2. Mass fractal model

$$I(q) = scale \times P(q)S(q) + \mathrm{a}q^{-\alpha} + background \quad \text{.....(2)}$$

Where, P(q) is the form factor with R as a radius of the building block, and defined as [4]:

$P(q) = F(qR^2))$ with $F(x) = \frac{3[\sin(x) - x\cos(x)]}{x^3}$

The S(q) is related to the mass fractal dimension Dm and cutoff length ζ as:

$$S(q) = \frac{\Gamma(D_m-1)\zeta^{Dm-1}}{[1+(q\zeta)^2]^{\frac{D_m-1}{2}}} \frac{\sin[(D_m-1)\tan^{-1}(q\zeta)]}{q} \quad \text{.....(3)}$$

In eq 2, the term $aq^{-\alpha}$ is the power law with a is the scaling constant and α showed the surface scattering from the distribution of fibers.

3. Flexible cylinder elliptical

$I(q) = scale \times S_{exv}(q) + \mathrm{a}q^{-\alpha} + background$ .....(4)

In the above equation, the excluded volume intensity is defined as $S_{exv}(q)$ is defined as [5, 6]:

$$S_{exv}(q) = w(qR_g)S_{Debye}(q, L, b) + [1 - w(qR_g)][C_1(qR_g)^{-\frac{1}{\upsilon}} + C_2(qR_g)^{-\frac{2}{\upsilon}} + C_3(qR_g)^{-\frac{3}{\upsilon}}] \quad (5)$$

$S_{Debye}(q, L, b) = 2[\exp(-u) + u - 1]/u^2$ .....(6)

$u = \langle R_g^2 \rangle . q^2$ .....(7)

Where, u = ensemble average of the square of the radius of gyration

L = is the contour length

b = statistical segments of the chain (measure of chain flexibility)

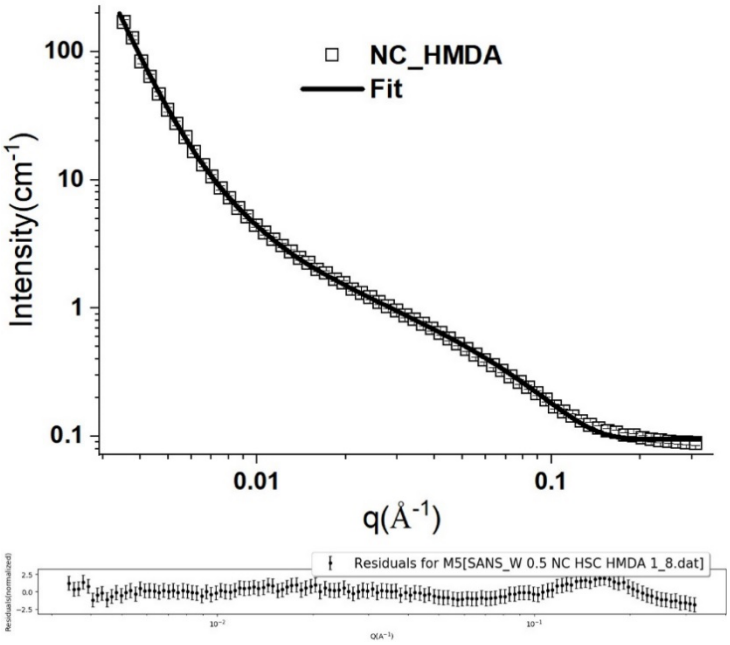

Figure 3-S2: Model validation with experimental data.

In eq 4, the resultant scattering function for the flexible cylinder elliptical is given by

$$S(q, L, b) = S_{exv}(q, L, b) + C\left(\frac{L}{B}\right)\left[\frac{4}{15} + \frac{7}{15u} - \left(\frac{11}{15} + \frac{7}{15u}\right)\exp(-u)\right] b/L \quad .....(8)$$

In eq 4, the term $aq^{-\alpha}$ is the power law with a is the scaling constant and α showed the surface scattering from the distribution of fibers.

Table 3-S2: Zeta potential for different types of samples.

Sample	Ratio of carboxylic group to amine group	Zeta potential (mV)
NC	0	-36±2
NC_HPEI_7	1:1.66	-31±1
NC_LPEI_7	1:1.66	-30±2
NC_HMDA_14	1:4	-27±2
NC_HMDA_18	1:8	-28±4

References

1. Debye, P., H. Anderson Jr, and H. Brumberger, *Scattering by an inhomogeneous solid. II. The correlation function and its application.* Journal of applied Physics, 28(6) (1957) 679-683.
2. Debye, P. and A. Bueche, *Scattering by an inhomogeneous solid.* Journal of Applied Physics, 20(6) (1949) 518-525.
3. Ornstein, L.S. and F. Zernike. *Integral equation in liquid state theory*. in *Proc. Acad. Sci. Amsterdam*. 17 (1914) 793.
4. Mildner, D. and P. Hall, *Small-angle scattering from porous solids with fractal geometry.* Journal of Physics D: Applied Physics, 19(8) (1986) 1535.
5. Pedersen, J.S. and P. Schurtenberger, *Scattering functions of semiflexible polymers with and without excluded volume effects.* Macromolecules, 29(23) (1996) 7602-7612.
6. Chen, W.-R., P.D. Butler, and L.J. Magid, *Incorporating intermicellar interactions in the fitting of SANS data from cationic wormlike micelles.* Langmuir, 22(15) (2006) 6539-6548.

Absorption kinetics of nanocellulose foams: Effect of ionic strength and surface charge

Laila Hossain, Emily Eastman, Monica De Rango, Vikram Singh Raghuwanshi, Joanne Tanner, Gil Garnier*

Bioresource Processing Research Institute of Australia (BioPRIA), Department of Chemical Engineering, Monash University, Clayton

*Corresponding author: gil.garnier@monash.edu

Supplementary Information

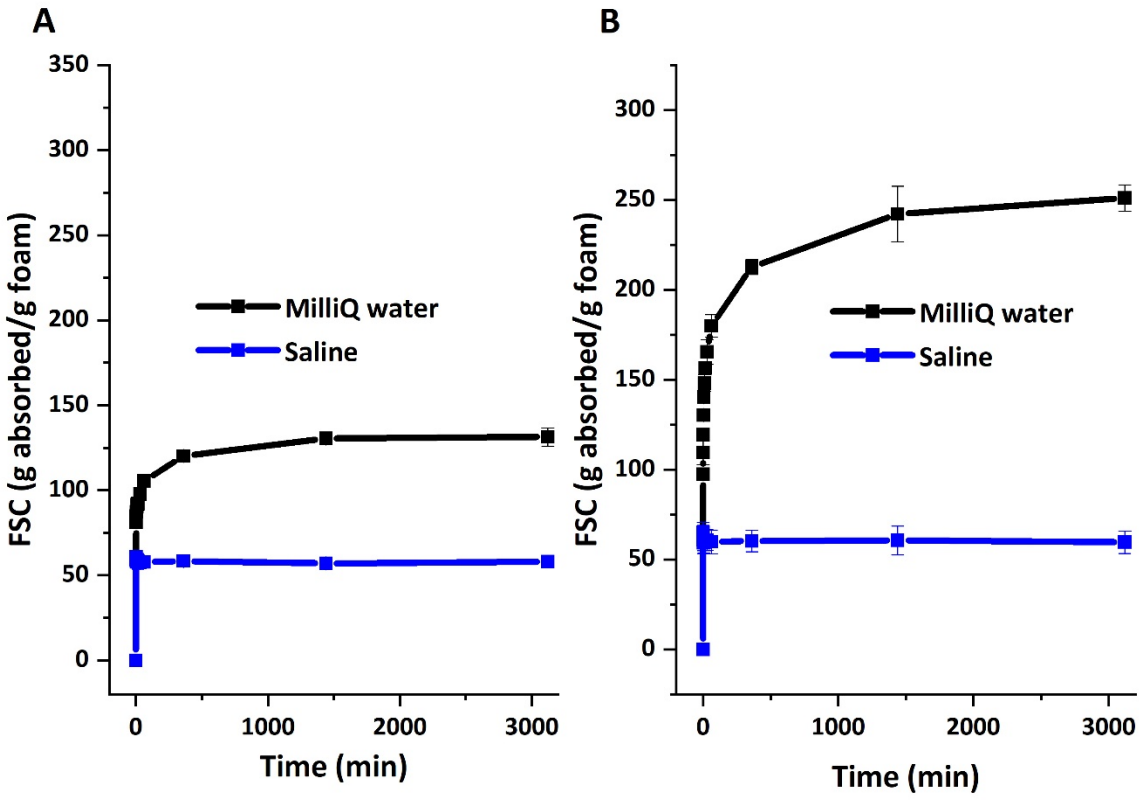

Figure 4-S1: Free swell capacity of NC foams in different absorbates for different surface charges: (A) LSC and (B) HSC.

Effect of Crosslinking on nanocellulose superabsorbent biodegradability

Supplementary Information

Table 5-S1. Characteristics of the Podosol selected for the experiments. Soil was collected from a vegetable farm located in Cranbourne, Victoria, Australia.

Parameter	Podosol
Electrical conductivity (dS/m)*	0.028
pH	6.16
Total Carbon (%)	1.4
Total Nitrogen (%)	0.06
C:N	26
Organic Matter (%)	2.5
Nitrate (mg/Kg)	2.8
Ammonium (mg/Kg)	8.5
Na^+ (mg/Kg)	23
Ca^{2+} (mg/Kg)	316
Mg^{2+} (mg/Kg)	81
K^+ (mg/Kg)	<50
Effective Cation Exchange Capacity ($cmol^+/Kg$)	2.6
Phosphorus (mg/Kg)(Cowell)	14
Zinc (mg/Kg)	3.9
Manganese (mg/Kg)	2.0
Copper (mg/Kg)	0.77
Basic texture	Sandy soil
Water holding capacity (g water/100 g soil)	23

Table 5-S2: Biodegradation of SAP with initial cellobiose addition in the soil to quantify the product inhibition.

Sample	Initial sample mass (mg/g soil)	Sample left after day 2 (mg/g soil)	Biodegradation (%)
NC SAP+cellobiose (1:1)	2.5	0.35±0.10	79±6.77
NC SAP+cellobiose (1:1)	5	2.91±0.07	42±1.4

Point of Care nanocellulose sensor for glucose detection in blood

Supplementary Information

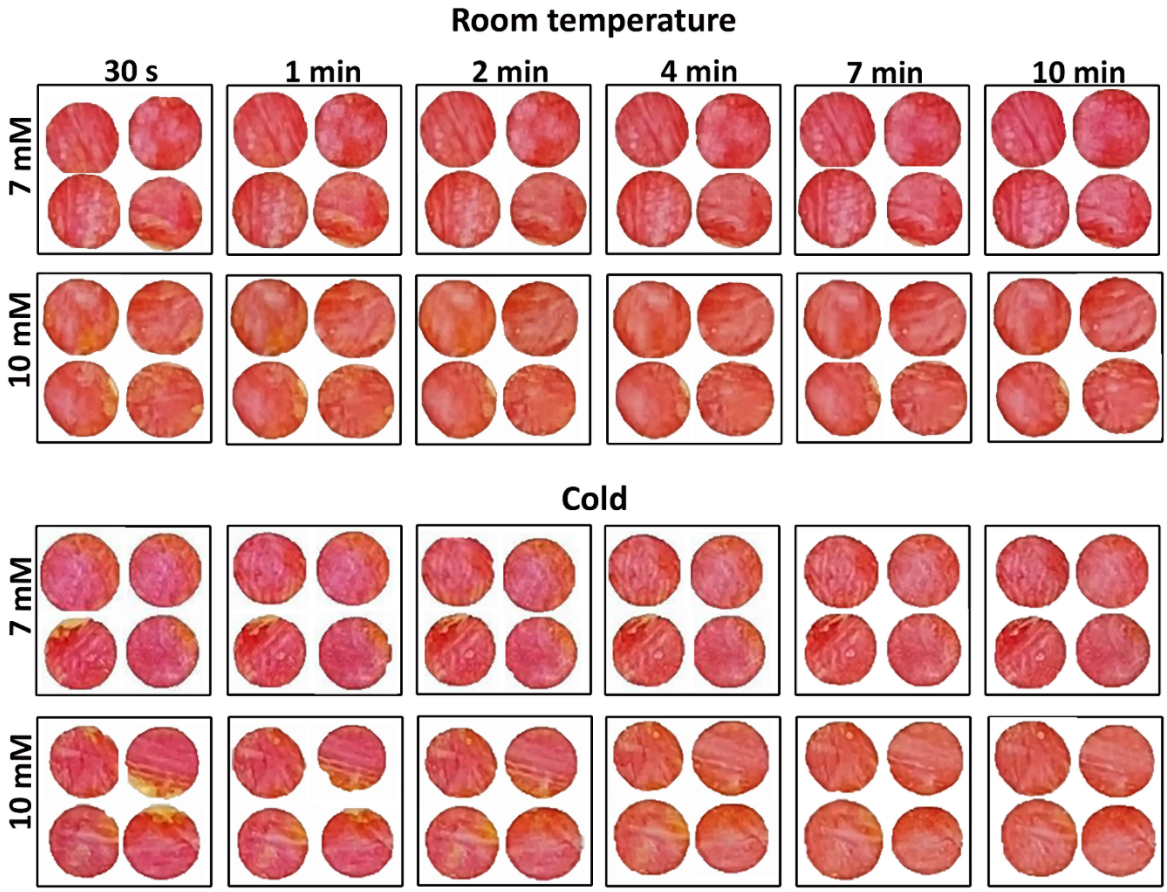

Figure 6-S1: Comparison of color change at a function of reaction time for room and cold temperature.

Color Analysis

There are three primary ways to describe a color: hue, chroma and value. Hue is the dimension of color we instantly experience when we look at the color. Hue distinguishes from one color to another, such as, red, orange, yellow, blue, violet and green. Hue is illustrated by a thermometer in Figure S2 as it describes the color temperature. Value, also called lightness or luminosity, measures the lightness or darkness of a color. Value is described as a circle in the figure S2. Value defines a color on a basis of how close the color is in regards to white or black. Chroma, also called saturation, indicates the degree of intensity or purity. Chroma is indicated by sun in the Figure 6-S2 as it indicates the degree of clarity/ saturation/intensity.

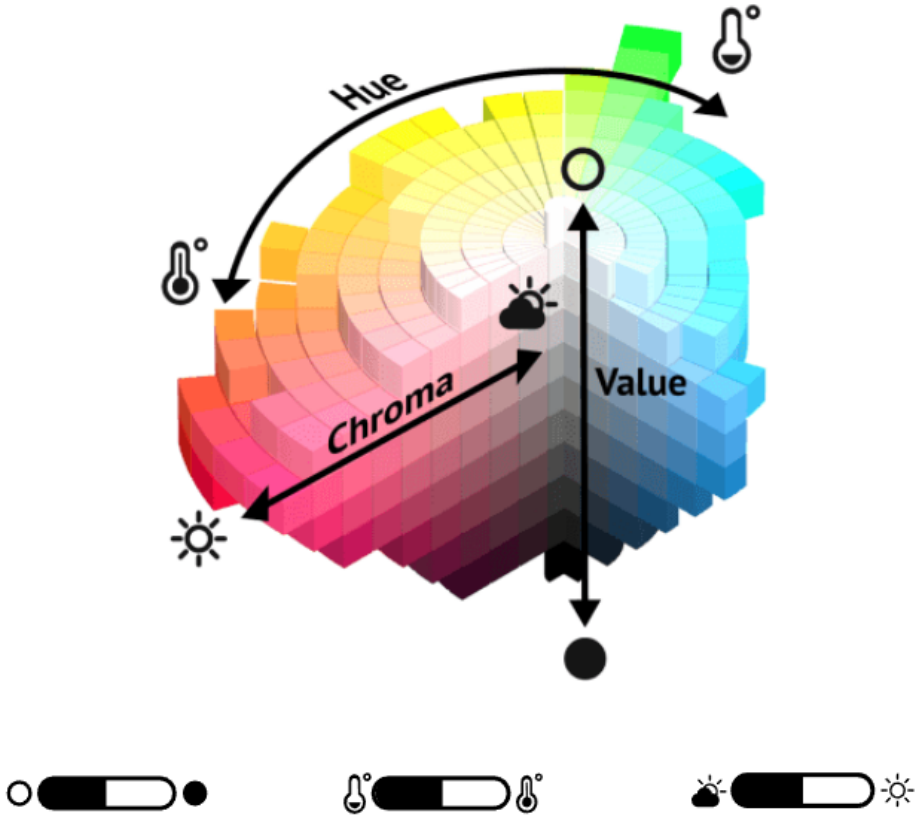

Figure 6-S2: Color scale showing hue, chroma and value [1].

From the above discussion, it is evident that color hue is the best option to describe the color difference as it distinguishes different colors. So, color hue is chosen to distinguish between different samples colors for our glucose sensor described in Figure 6-6. Figure 6-S3 presents the hue wheel indicating different numbers for different colors for a range of 0 to 360^{o}.

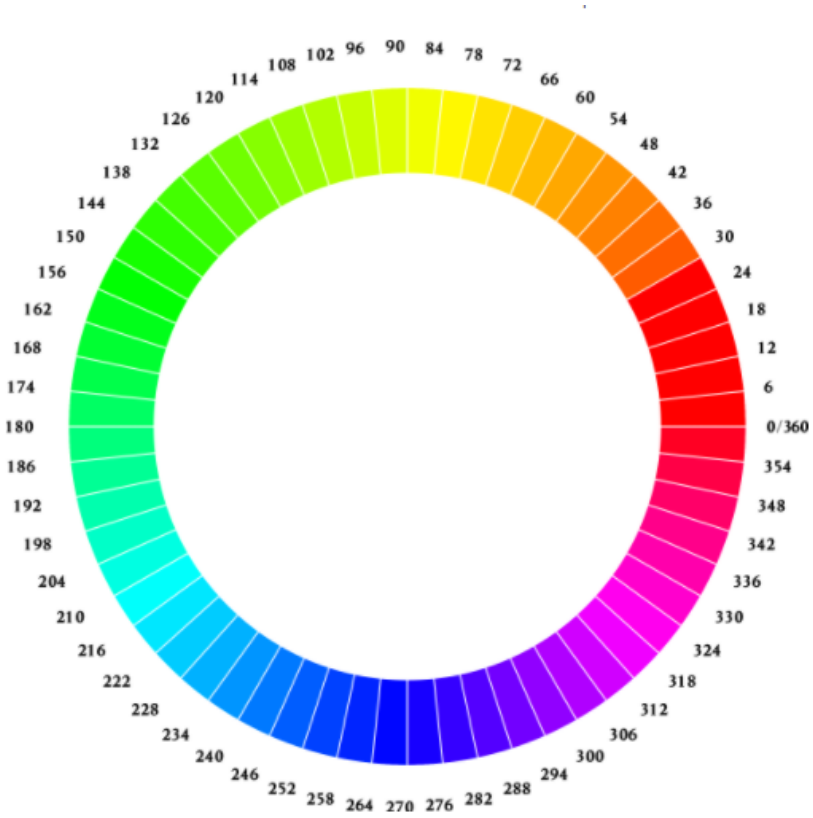

Figure 6-S3: Color wheel indicating different hue colors. The numbers on the wheel are in degrees [2].

References

1. Color & Style. *Compatibility with Color Systems and Names*. Available from: https://en.color-style.com/compatibility/.

2. Pinterest. *Chromatic Wheel 1*. Available from: https://www.pinterest.at/pin/114349278015552260/?amp_client_id=CLIENT_ID(_)&mweb_unauth_id=&simplified=true.

APPENDIX II
PUBLICATIONS INCLUDED IN THESIS IN THEIR PUBLISHED FORMAT

THIS PAGE WAS INTENTIONALLY LEFT BLANK

Colloids and Surfaces A: Physicochemical and Engineering Aspects 630 (2021) 127608

Contents lists available at ScienceDirect

Colloids and Surfaces A: Physicochemical and Engineering Aspects

journal homepage: www.elsevier.com/locate/colsurfa

Modulating nanocellulose hydrogels and cryogels strength by crosslinking and blending

Laila Hossain, Vikram Singh Raghuwanshi, Joanne Tanner, Gil Garnier *

Bioresource Processing Research Institute of Australia (BioPRIA), Department of Chemical Engineering, Monash University, Clayton, Australia

HIGHLIGHTS

- Mechanical properties of crosslinked and blended nanocellulose gels were studied.
- Physical and chemical crosslinking significantly increases hydrogel strength.
- Cryogel strength is increased by CNC blending.
- Chemical crosslinking and CNC blending increase cryogel structure homogeneity.
- Cryogel liquid absorption capacity decreases with crosslinking or blending.

GRAPHICAL ABSTRACT

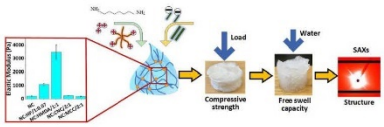

ARTICLE INFO

Keywords:
Mechanical strength
Nanocellulose
Hydrogel
Cryogel
Cellulose nanocrystal

ABSTRACT

The mechanical strength of hydrogels and cryogels made from carboxylated nanocellulose (NC) fibers can be modulated by chemically/physically crosslinking and blending with different fibrils (shorter/longer). Nanocellulose hydrogels are produced by oxidizing Bleached Eucalyptus Kraft (BEK) pulp followed by high pressure mechanical treatment. Polyethyleneimine (PEI) and hexamethylenediamine (HMDA) were selected to crosslink nanocellulose hydrogels physically and chemically, respectively. Shorter cellulose nanocrystals (CNC) and longer microcrystalline cellulose (MCC) fibrils were blended with the TEMPO oxidized nano/micro fibers to produce hydrogels of controlled properties. Nanocellulose cryogels were prepared from these hydrogels by a two steps process of freezing and lyophilization. The mechanical properties of nanocellulose hydrogels and cryogels were modulated by controlling the type and density of crosslinking as well as by blending with nano- or microfibrils. Chemical crosslinking (HMDA) increases the hydrogel elastic compression moduli (G') but does not significantly affect the compressive strength of the cryogel. SAXS reveals the HMDA crosslinked hydrogel to be structurally homogeneous. Physical crosslinking with high molecular weight PEI increases the storage modulus (G') of nanocellulose hydrogels. Blending a carboxylated nanocellulose fiber suspension with CNC significantly increases the cryogel compressive strength. Nanocellulose gel exhibits tuneable mechanical strength and absorption capacity from the crosslinking/blending strategy (type and density); this improved fundamental knowledge of the fiber-crosslinker and fiber-cellulose crystal interactions enables greater control and tunability of the properties of hydro- and cryogels for personal and infant care products, as agricultural water retention aids, and for biosensor applications.

* Corresponding author.
E-mail address: gil.garnier@monash.edu (G. Garnier).

https://doi.org/10.1016/j.colsurfa.2021.127608
Received 29 July 2021; Received in revised form 15 September 2021; Accepted 18 September 2021
Available online 22 September 2021
0927-7757/

1. Introduction

A hydrogel is a three dimensional polymeric network capable of retaining a large volume of water inside its structure [1,2]. Such polymeric materials have wide-ranging applications as a wet or dried gel, including baby diapers, contact lenses, drug delivery, wound dressing, and tissue engineering, among others [3–7]. The term hydrogel is often used ambiguously to describe both the wet and dried gel forms, although the term "cryogel" describing freeze-dried gels provides clarity [8]. Collectively, hydro- and cryogels can be categorised as synthetic or naturally derived, depending on their raw material [9,10]. Synthetic hydrogels based on acrylate or acrylamide are the most commonly used for commercial applications, but they are neither renewable nor biodegradable. Common naturally derived hydrogels include alginate, chitosan, collagen, gelatine, starch, hyaluronan, and recently, cellulose [11,12]. Among those, cellulose-based materials are attractive because of their stiffness, hydrophilicity, ease of functionalization, renewability, biocompatibility, large availability and low cost, making them unique among biodegradable materials [13,14].

Cellulose is the most abundant biopolymer on Earth. It is found in plants, algae, tunicates and some bacteria [15,16]. Plant-derived cellulose (and nanocellulose) contains both crystalline and amorphous regions, depending on the local molecular structures [17]. Breaking down the cellulose can produce nanocellulose (NC) of three different types: (i) cellulose nanofiber (CNF), (ii) cellulose nanocrystal (CNC), and (iii) bacterial cellulose (BC). CNF is prepared either by (i) mechanical treatment, (ii) chemical treatment or (iii) combined chemical and mechanical treatment of plant-derived cellulose. CNF retains both the amorphous and crystalline regions of the original cellulose fibers [18]. CNC is mainly produced by acid hydrolysis of plant-derived cellulose fibers to degrade the amorphous regions and retain the crystalline domains [19]. Bacterial cellulose is produced by microorganisms that excrete pure cellulose directly as nanofibres. In general, nanocellulose is biocompatible and has excellent native gel forming properties [20].

The mechanical properties of a nanocellulose hydrogel govern many of its applications [21] in which crosslinking (type and density) can be a controlling variable. Crosslinking compounds can be broadly categorized as chemical or physical, depending on the type of interaction between the crosslinker and the nanocellulose fiber. Chemical crosslinkers form covalent bonds with nanocellulose fibers. Common examples include methylene-bis-acrylamide, ethylene glycol dimethacrylate (EGDMA), 1,1,1- trimethylolpropane triacrylate (TMPTA), and tetraalyloxy ethane (TAOE) [2,22]. Epichlorohydrin, hexamethylenediamine (HMDA), aldehydes and aldehyde-based reagents, urea derivatives, and carbodiimides have also been used as crosslinkers for cellulose based hydrogels [23,24]. Among these, crosslinking of nanocellulose fiber with high carbon amine groups in presence of EDC/sulfo NHS is very efficient with high yield [25].

In physical cross-linking, interacting forces such as hydrogen bonding, electrostatic forces, van der Waals forces, chain entanglements, and ionic and hydrophobic interactions dominate [26]. Physical cross-linking via hydrogen bonding between the carboxyl groups of oxidized cellulose fibers can be achieved by the freeze-thaw technique. The skeletal density of the cellulose fiber matrix is increased upon crystallization of the bulk solvent, which forces the polymer chains to align and form a cohesive network via hydrogen bonding and covalent interaction. Changes in the freeze-thaw cycle affect the resultant hydrogel properties, for example, reduction of porosity [27–29]. High strength polyvinyl alcohol (PVA) hydrogels have been made by this technique, where the strength came from intra and intermolecular hydrogen bonds [30]. The freeze-thaw method has also been used to make high strength hydrogels from hemicellulose, hyaluronic acid and cellulose nano crystal [31–33]. However, the freeze-thawing method has some disadvantages: (i) long cycle times (for example, five cycles or more with 22 h each) [34] (ii) irregular hydrogel pore spacing and (iii) higher energy consumption due to repeated cycles. Physical crosslinking can also be achieved by the physical interaction of cellulose fiber with positive polyelectrolyte molecules, resulting in high mechanical strength. For example, polyethyleneimine (PEI) has been widely used to crosslink with nanocellulose in the presence of glutaraldehyde [35]. Nanocellulose fibers crosslinked with PEI and allylamine modified PNIPAm particles have been developed and exhibit thermo-responsive behaviour [36]. As the definition of physical crosslinking includes hydrogen bonding and ionic/electrostatic interaction [37], the ionic interaction between positive PEI molecules and negative nanocellulose fibers can be designated as physical crosslinking. For a greener physical crosslinking approach, it may be possible to use PEI alone, although there is limited work on this. Therefore, the effect of PEI molecular weights on nanocellulose fibers crosslinking is also poorly understood.

Cryogels are hydrogels that have been dried into porous and highly absorbent structures with high surface area. Cryogels can be produced by supercritical drying, freeze drying, ambient pressure drying, microwave drying, or vacuum drying of hydrogels [38]. Cryogels have been investigated for multifunctional sensor, supercapacitor, insulator, controlled drug release and drug scaffold, and recently, infant care applications [8,39–43]. The absorption capacity of a cryogel is a critical parameter for all applications, and is related to its cross linking density, internal surface area, and charged functional groups, such as COO^- [44]. Oxidation is the most common treatment to introduce negative hydrophilic COO^- groups on the fiber surface [45,46]. The hydrophilic functional groups (COO^-) of the cryogel network contribute to water absorption while the cross-links between the network chains prevent the cryogel structure from collapsing upon re-wetting [47]. The mechanical/compressive strength of cryogel can also be increased upon cellulose crystal blending [48]. The chain molecules of crystalline cellulose are packed in an orderly manner resulting in higher nanocellulose strength compared to amorphous region [49]. Introducing nano and micro crystal into the nanocellulose cryogel affects the bonding surface area and the total fiber length available for binding.

In spite of their wide commercial use, there is surprisingly limited knowledge describing how physical and chemical crosslinking correlates with hydrogel and cryogel mechanical strength. For example, the change in mechanical strength for hydrogels and cryogels has not been correlated with their physical and chemical crosslinking density. In this study, HMDA is chosen as chemical crosslinker because HMDA is widely known and used due to its six carbon chains, which form chemical crosslinks between nanocellulose fibers more effectively than other low carbon amines. As physical crosslinker, we have used PEI alone to form ionic interaction with nanocellulose fibers while ensuring to avoid any hazardous chemical during gel preparation. Cellulose crystal was blended with nanocellulose fiber to go one step closer towards the sustainability. Blending cellulose crystal is potentially greener option as PEI and HMDA are still chemical additives and removal of this additives can make the cryogel even greener and sustainable. The effect of cellulose crystals blending has also not been investigated or quantified. In addition, the absorption capacity of physically and chemically crosslinked cryogels, and cryogels produced by blending with cellulose crystals remains poorly described. There is a need to compare different types of crosslinking and blending agents, and characterize their effect on the mechanical properties of hydrogels and cryogels. Controlling the mechanical strength is important to develop performant superabsorbent when under load; lack of strength can lead to poor performance due to product disintegration.

The objective of this study is therefore to investigate, quantify and control the strength of nanocellulose hydrogels and cryogels. Carboxylated nanocellulose gels were produced that incorporated either: i) a chemical crosslinker (HMDA), ii) a physical crosslinker (PEI) or iii) cellulose crystal. The effect of chemical crosslinking, physical crosslinking, and dissimilar nanocellulose crystals addition on the structural, absorption, and strength properties of nanocellulose hydrogels and cryogels was compared. The structure of the different composites was analysed by Small Angle X-ray Scattering (SAXS) and related to the

properties of these gels for application as renewable, biocompatible and biodegradable superabsorbents. The developed superabsorbent has tuneable absorption and mechanical properties which make it suitable to remain integrated under load, such as for meat packaging or baby diaper.

2. Methodology

2.1. Materials

Bleached Eucalyptus Kraft (BEK) pulp, containing approximately 10 wt% solids, was obtained from Australian Paper, Maryvale, Australia. 2,2,6,6-Tetramethylpiperidine-1-oxyl (TEMPO), PEI (low molecular weight: M_w ~800 Da, M_n ~600 Da; high molecular weight: M_w ~ 750,000 Da, M_n ~ 60,000 Da), HMDA, MCC and sodium bromide (NaBr) were purchased from Sigma-Aldrich. CNC was purchased from The University of Maine, USA. Hydrochloric acid (HCl) and Sodium Hydroxide (NaOH) were diluted for solutions as required and were purchased from ACL Laboratories and Merck, respectively. 12 w/v% Sodium Hypochlorite (NaClO) was purchased from Thermo Fisher Scientific and used as received.

2.2. Solids concentration

The solids concentration of all samples (i.e. gel or pulp) was determined through oven drying. The sample was weighed before (w_i) and after (w_d) drying. Sample moisture was removed by drying in an oven (Thermoline BTC 9090) at 105 °C for at least 6 h. The solids content was calculated as:

$$Solid\ \ content\ (\%) = \frac{w_d}{w_i} \times 100\%$$

2.3. TEMPO mediated oxidation

The TEMPO-mediated oxidation of BEK pulp was done by using the oxidizing agent NaClO [10]. 25 g BEK pulp (dry weight) was suspended in 2500 mL water containing 0.4 g TEMPO and 2.5 g NaBr. The 12 w/v % NaClO solution was initially adjusted to pH 10 via addition of 36% HCl. To initiate the oxidation process, 100 mL NaClO was added drop-wise to the suspension whilst stirring. The pH of the reaction was monitored and maintained at 10 through the manual addition of 0.5 M NaOH. The oxidation process was completed in 3 h. The oxidized fibers were recovered through vacuum filtration and stored refrigerated (2–8 °C).

2.4. Conductometric titration

The carboxylate group content was measured by conductometric titration as reported in previous study [29]. Oxidized pulp samples (approx. 30 mg dry weight) were suspended in 40 mL deionized water. 200 μL of 1% NaCl was added to the suspended sample. The pH of the suspended sample was manually adjusted to between 2.5 and 3 with 0.5 M HCl prior to titration. Titration was accomplished by automated addition of 0.1 M NaOH using a Mettler Toledo T5 titrator. The conductivity of the sample was monitored throughout the titration progress. The carboxyl group content (mmol COO^-Na^+ /g fiber) was determined by:

$$CC = \frac{c\Delta V}{w} \times 1000$$

where ΔV pertain to the amount of titrant required to neutralize the carboxylic groups (in L), c is the NaOH concentration (mol/L), and w is the sample weight (g).

2.5. Physical crosslinking

TEMPO-oxidized pulp was dispersed in deionized water at the desired concentration (0.5 g dry fiber in 100 g suspension). Fibrillation was accomplished through a high-pressure homogenizer (GEA Niro Soavi Homogenizer Panda) at 1000 bar for two passes. One-pass homogenized gel was mixed with PEI using an electric hand mixer (ANCO 500). After thorough mixing, the gel was passed through the homogenizer for the second pass, after which physical crosslinking was assumed to have occurred. The samples were stored at 4 °C.

2.6. Chemical Crosslinking

Oxidized fiber was homogenised at the desired concentration (0.5 g dry fiber in 100 g suspension) at 1000 bar for two passes to produce nanocellulose gel. HMDA was dissolved in deionized water at a concentration of 0.45 g/mL. The nanocellulose gel was crosslinked with this HMDA in ratios of 2:1 and 1:1 (COO^-:NH_2) in presence of EDC/sulfo NHS. The gel was mixed for 5 mins and incubated at room temperature overnight (16 h).

2.7. Cellulose crystal blending

TEMPO-oxidized fiber suspension (0.5 g dry fiber in 100 g suspension) was blended with either MCC or CNC at a mass ratio of 2:1. After that fibrillation was achieved in the homogeniser at 1000 bar for two passes to produce the hydrogel.

2.8. Rheological measurement

Rheological testing of gel samples was performed with an Anton Paar MCR302 rheometer. A cone (0.997°) and plate (49.975 mm) geometry was selected. Testing was performed at ambient temperature (25 °C). A solvent trap was used to ensure stable temperature during measurements. Viscosity was measured at shear rates ranging from 0.5 to 100 s^{-1}. Oscillatory strain sweep was performed from 0.01% to 100% at a constant 1 Hz frequency.

2.9. Preparation of nanocellulose cryogels

The cryogels were prepared by spreading 12 g of gel evenly over the base of a 50 mm petri dish and freezing the sample at − 86 °C, then freeze-drying (Christ Alpha 2–4 LD Plus) for 2 days.

2.10. Fourier Transform Infrared (FTIR) spectroscopy

Cryogel samples were analysed by Fourier Transform Infrared (FTIR) spectroscopy (Agilent Technologies Cary 630 FTIR) which is equipped with a diamond attenuated total reflectance (ATR) accessory. Eight scans were taken at 4 cm^{-1} resolution.

2.11. Free swell capacity

The cryogel sample was placed in a glass funnel, which is immersed in a container full of testing fluid. To measure the absorption over time, the funnel with the sample was removed from the fluid container and the excess fluid allowed to drain for five minutes. The total mass was then measured at regular intervals of 3 h. The free swell capacity was then calculated as follows:

$$\text{Free Swell } Capacity(\text{FSC}) = \frac{m_t - m_i}{m_i}$$

Where m_t is the mass of the swollen cryogel at a particular time interval and m_i is the initial mass of the dry cryogel.

2.12. Compression testing

Cylindrical cryogel samples of 37 mm diameter and 37 mm length were prepared for compressive testing. Force-displacement data for cryogel samples was obtained by Instron model 5965 Universal Testing Machine equipped with 1 kN load cell. The testing was done at 23 °C and 50% humidity at a compression rare of 5 mm/min. The compressive Young's Modulus was determined from the slope of the initial linear region of the stress-strain curve.

2.13. SAXS

The SAXS measurements were conducted at the SAXS/WAXS beamline of the Australian Synchrotron. The wavelength was 1.03 Å and the measurements were conducted in the transmission mode.

3. Results

The structural and strength properties of physically (low molecular weight: LMW and high molecular weight: HMW PEI) and chemically (HMDA) crosslinked gels were quantified. Nanocellulose gel reinforced with cellulose fibrils of different length scales: long (MCC) and short (CNC) were also prepared and their properties compared with those of the crosslinked gels. The composition and identification of all nanocellulose gels are summarized in Table 1. The water content of physically crosslinked hydrogel and CNC blended hydrogel is compared with neat hydrogel in Table S1.

3.1. Physical crosslinked hydrogels

PEI was chosen as the physical crosslinker with nanocellulose hydrogel as it is known to adsorb on cellulose. The molecular weight of PEI plays an important role in determining the hydrogel strength. High molecular weight PEI improved the hydrogel strength significantly. Fig. 1 shows the rheological properties of hydrogels as a function of concentration for (a) low and (b) high molecular weight PEI. At low shear stress, the elastic modulus (G′) is dominant over the viscous modulus (G"), which indicates that the hydrogel behaves more like a solid material under these conditions, as G′ represents gel stiffness or strength. After the intersection point of G′ and G", the material flows like a liquid as the viscous modulus exceeds the elastic modulus. G" is the viscous or loss modulus; it indicates the portion of the deformation energy that is lost to internal friction during shearing. At first, G" is constant as the gel behaves like a uniform 3D network. G" then increases with increasing shear as micro cracks appear. Initially, the elastic behaviour is dominant. As shear increases further, micro cracks grow, merge and develop into continuous macro cracks which result in gel rupture at the highest value of G". Passed this point, the bulk material starts to flow, as indicated by the dominant viscous modulus (G") after the intersection of G′ and G", which occurs at the G" maxima.

Adding a low molecular weight PEI as a physical crosslinker weakens the nanocellulose hydrogel. Here, PEI acts a plasticizer and presents no evidence of crosslinking with cellulose. The viscous and elastic moduli of the LP adsorbed hydrogels (NC:LP) are lower than those of the nanocellulose hydrogel (Fig. 1a). The modulus intersections are also shifted toward higher shear strains, indicating a more cream-like behaviour of the hydrogel. The addition of 5 w/w % HP to nanocellulose hydrogels also does not significantly affect their rheological behaviour (Fig. 1b). However, increasing the HP concentration to 7 w/w % significantly increases the mechanical strength (by up to 5 times) compared to pure nanocellulose hydrogel (Fig. 1a) because of bridge formation between nanocellulose fibers. The intersection of G′ and G" also shifts to lower shear strain with increasing concentration of HP from 5 w/w % to 7 w/w %, indicating non-creamy or brittle hydrogel formation. The types of interaction between nanocellulose and PEI therefore depend on the molecular weight of PEI, which results in different hydrogel rheology.

Table 1
Description and characterization of the nanocellulose gels composition.

Sample code	Sample details
NC	Pure nanocellulose gel
NC:HP/ 1:0.05	Nanocellulose gel physically crosslinked with 5 w/w% HMW PEI
NC:HP/ 1:0.07	Nanocellulose gel physically crosslinked with 7 w/w% HMW PEI
NC:LP/ 1:0.05	Nanocellulose gel physically crosslinked with 5 w/w % LMW PEI
NC:LP/ 1:0.07	Nanocellulose gel physically crosslinked with 7 w/w% LMW PEI
NC:HMDA/ 2:1	Nanocellulose gel chemically crosslinked with HMDA at nanocellulose COO^- to amine ratio 2:1
NC:HMDA/ 1:1	Nanocellulose chemically crosslinked with HMDA with nanocellulose COO^- to amine ratio 1:1
NC:CNC/2:1	Nanocellulose blended with cellulose nano crystal at nanocellulose to CNC blend mass ratio 2:1
NC:MCC/2:1	Nanocellulose blended with MCC at nanocellulose to MCC blend mass ratio 2:1

3.2. Chemical crosslinked hydrogels

Chemical crosslinking of nanocellulose hydrogel with HMDA significantly increases hydrogel strength (Fig. 2). Adding HMDA to nanocellulose hydrogel at a carboxyl to amine group ratio of 2:1 results in a four-fold increase in the elastic modulus (G′) compared to the neat nanocellulose hydrogel. Increasing the HMDA ratio up to 1:1 augments G′ by 15 times. These increases in viscous and elastic moduli result from the formation of amide bonds between nanocellulose hydrogel carboxyl and the HMDA amine groups.

3.3. Blending cellulose fibrils to hydrogels

The strength of nanocellulose hydrogels blended with cellulose fibrils of different length scales - microscale with MCC or nanoscale with CNC - was tested (Fig. 3). These blended hydrogels do not show any significant change in G′ or G" compared to the neat nanocellulose hydrogel. However, blending the fibrils shifted the moduli intersections (shown by the vertical dotted lines in Fig. 3) to a lower shear strain of 10% for NC:CNC/2:1, 21.7% for NC:MCC/2:1 compared to neat NC at 31.7%, indicating the formation of a stronger gel.

3.4. Nanocellulose cryogels ATR-FTIR

Chemical crosslinking in the HMDA-NC cryogel was confirmed by ATR-FTIR (Fig. 4). The sharp peak at 1600 cm^{-1} for neat nanocellulose cryogel is due to the C=O stretching of the COO^- group on the oxidized fiber. For the crosslinked sample, C-N bending appears at 1240 cm^{-1} due to the presence of the amine group. C=O stretching from the amide bond is merged with the C=O stretching for COO^- group in the crosslinked sample. Fig. S3 shows all other samples FTIR spectra.

3.5. Cellulose cryogels mechanical strength

The compressive strength of the cryogels produced from the neat, crosslinked, and blended nanocellulose hydrogels is shown in Fig. 5. The cryogel produced from blended hydrogels showed increased mechanical strength. Neither chemical nor physical crosslinking of the hydrogels increased the mechanical strength of their cryogels. The stress-strain curve is shown in Fig. S4. Cryogel images at different states (before and after compression, after re absorption) are shown in Fig. S5.

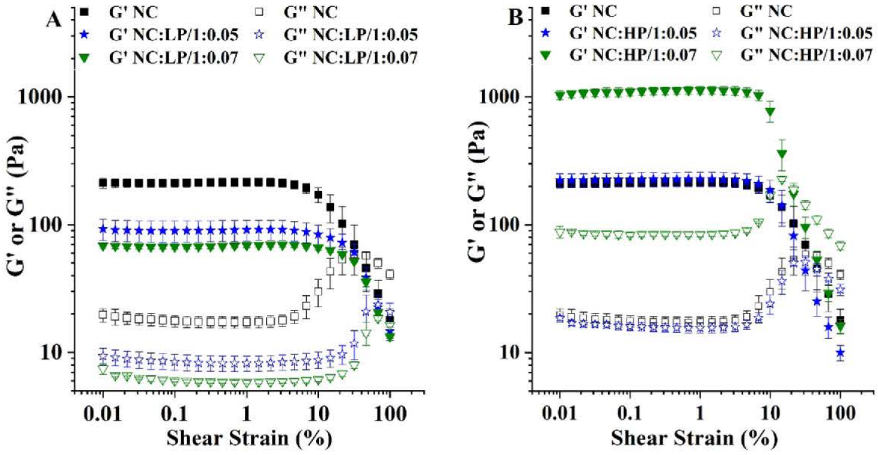

Fig. 1. Viscoelastic properties of TEMPO-oxidized cellulose hydrogels crosslinked with different concentrations of PEI varying in molecular weight: (A) hydrogels with low molecular weight PEI (LP) and (B) hydrogels with high molecular weight PEI (HP). Two PEI concentrations were tested: 5% and 7%, and the Elastic (G′) and viscous (G″) moduli were recorded as a function of strain. Oscillation frequency and temperature were kept constant at 1 Hz and 25 °C, respectively.

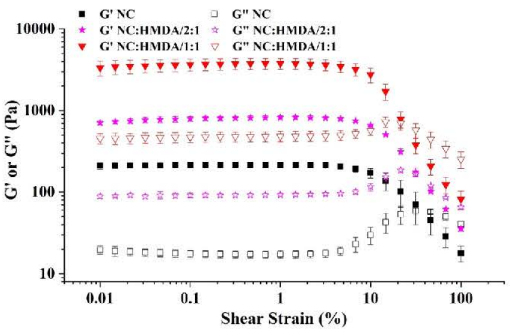

Fig. 2. Viscoelastic properties of TEMPO-oxidized cellulose hydrogels crosslinked with HMDA at different concentrations. Two NC:HMDA carboxyl to amine group ratio concentrations were tested: 1:1 and 2:1. Elastic (G′) and viscous (G″) moduli were recorded as a function of strain. Measurements were performed at a frequency of 1 Hz and a temperature of 25 °C.

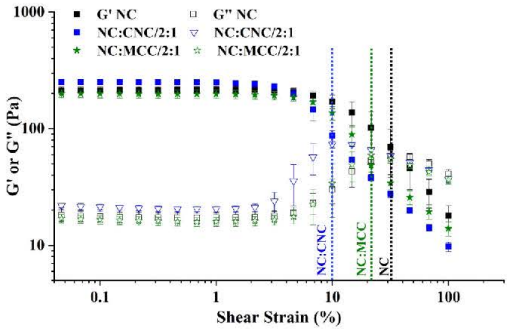

Fig. 3. Viscoelastic properties of TEMPO-oxidized cellulose hydrogels blended with CNC and MCC. NC:(CNC or MCC) ratio concentrations was set at 2:1. Elastic (G′) and viscous (G″) moduli were recorded as a function of strain. Measurements were performed at a frequency of 1 Hz and a temperature of 25 °C. The moduli intersection points are indicated by the vertical dotted lines.

3.6. *Nanocellulose cryogel Free swell capacity*

The free swell capacity (FSC) and water retention capacity (WRC) of the neat nanocellulose cryogel are the highest (Fig. 6). The physically and chemically crosslinked cryogels have the lowest absorption and water retention capacity, while the cryogels blended with CNC and MCC show intermediate performance. Physically and chemically crosslinked cryogels showed a decrease in free swell capacity of 48% and 51% respectively, compared to the neat nanocellulose cryogel.

3.7. *Structural analysis by Small Angle X-ray Scattering (SAXS)*

SAXS measurements were performed to reveal the network structure and fiber arrangement, and to visualize the water penetrating the spaces in hydrogel, cryogel and rewetted cryogel samples (Fig. 7). The different sections of the SAXS curve reveal the fiber structural arrangement at different dimensions before and after water penetration.

For hydrogels, the SAXS curves for neat and crosslinked samples show significant differences, indicating variations in structure (Fig. 7a). The upturn in the lower q value (0.003–0.006 Å $^{-1}$) of all curves indicates that the surface scattering from the large structures of bigger pores/interfibrillar spaces is similar. However, there is noticeable difference in the SAXS curve shape observed between $q = 0.003$ and 0.2 Å $^{-1}$. The bump in this range is due to the difference in scattering length between the water and the cellulose fibers. The neat nanocellulose hydrogel curve shows a bump between $q = 0.015$ and 0.22 Å^{-1}, corresponding to a pore size range of 42–2.8 nm. The HMDA crosslinked hydrogel shows large bump area between $q = 0.01$ and 0.23 Å $^{-1}$, indicating a larger pore size range of 63–2.7 nm. The HP crosslinked hydrogel shows a bump similar to that of HMDA; however, the bump is more pronounced in the HMDA-crosslinked sample. This indicates that both crosslinked samples have large open structures, but that the HMDA crosslinked sample has a more homogenous distribution of spaces than the HP crosslinked sample. The CNC blended hydrogel shows a shift in

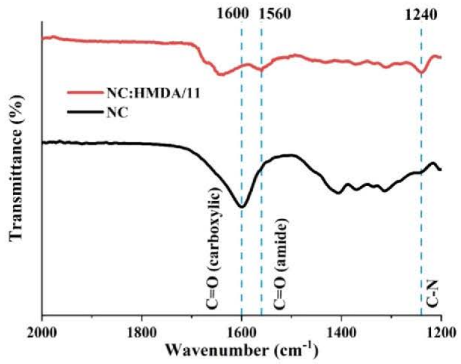

Fig. 4. ATR-FTIR spectra of pure nanocellulose cryogel and chemically (HDMA) crosslinked cryogel demonstrating effective chemical reaction.

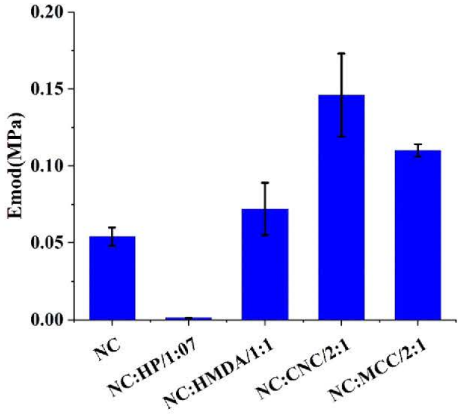

Fig. 5. Effect of crosslinking and blending on the compressive modulus (E_{mod}) of nanocellulose cryogels.

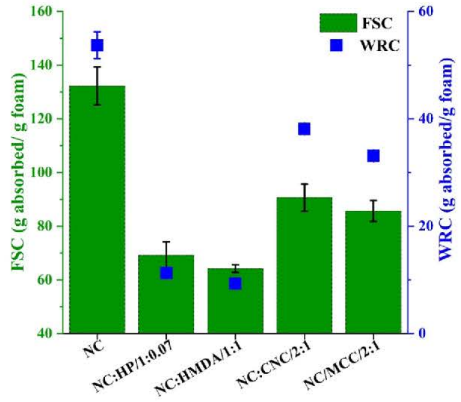

Fig. 6. Free swell capacity (FSC) and water retention capacity (WRC) of nanocellulose cryogels tested for MilliQ water.

the bump towards a q range of between 0.002 and 0.06 Å $^{-1}$, corresponding to a pore size range of 314–11 nm. The large size range in the blended sample is due to the repulsion between the cellulose fibers and CNC which forces the network to expand and creates more space between fibers.

For the cryogels, the SAXS curves do not show any significant difference among samples, except for HMDA crosslinked cryogel (Fig. 7b). The curves follow the power law of q $^{-4}$, indicating that the cellulose fibers tend to aggregate during drying, and therefore leave large size structures and open-air spaces in the resulting cryogels. However, the HMDA crosslinked sample shows a bump ($q = 0.05–0.2$ Å $^{-1}$), indicating the presence of some smaller size pores of size ranging between 12 and 2 nm in the structure.

Upon rewetting, water is absorbed into both the fibers and the pores of the cryogels. The SAXS curves from rewetted cryogels (Fig. 7c) show significant differences compared to the dried samples (Fig. 7b). The bumps in the rewetted sample curves indicate that the scattering from the swollen fibres and the spaces between them are filled with water. In all samples, the bump appears at almost the same q range (0.014–0.22 Å $^{-1}$). The corresponding pore size range of the space is between 45 and 2.8 nm. This indicates the water molecules penetrate and occupy similar sized spaces between fibers in all samples. However, the fiber bundle swelling behavior is significantly different between the samples, as reported previously for PEI and HMDA crosslinked samples [24]. At the low q range (< 0.014 Å $^{-1}$) the power law ranges from q $^{-3.5}$ to q^{-4}, indicating that the larger structure is formed by fiber entanglement and large pores.

The SAXS curves of the rewetted cryogels also differ from their corresponding hydrogels. This qualitatively indicates that the presence and correlation of the water molecules with the network is different in the hydrogels and rewetted cryogels. Therefore, simply rewetting a cryogel does not reform the corresponding hydrogel due to differences in the fiber structure of the hydrogels and cryogels that lead to differences in the interactions of the water molecules with and within the structure upon rewetting.

4. Discussion

4.1. Effect of crosslinking and blending on nanocellulose hydrogels

TEMPO oxidized nanocellulose hydrogels are made of entangled nanocellulose fibrils held together by electrostatic stabilization [50]. Here, chemical or physical crosslinkers and cellulose fibrils are used to modify the properties of the hydrogels. Physical crosslinking of nanocellulose hydrogel with a dendrimer polyelectrolyte such as PEI affects the rheological properties (to higher or lower elastic moduli) depending on the polymer molecular weight. Chemical crosslinking with HMDA increases the elastic moduli of the gel because of strong amide bond formation between the negative carboxylic group of cellulose and the positive amine of HMDA. Blending nano or micro cellulose fibrils does not have any significant effect on the elastic or viscous moduli of the hydrogel.

PEI molecular weight plays an important role in the hydrogel rheology. For the low molecular weight polyelectrolytes of high charge density, neutralization of the nanocellulose fiber charge occurs by the positively charged PEI amine group [51,52] (Fig. 8A), decreasing inter-fiber repulsion between the COO^- groups. The LP molecule is too short to link COO^- groups and form a bridge between nanocellulose fibers and therefore acts as a plasticizer, increasing the liquid-like behavior of the hydrogel. This is indicated by the low G′ and G″ measured for LP crosslinked hydrogel (Fig. 1A) [53]. Conversely, bridging between the PEI amine groups and nanocellulose fiber COO^- groups does occur for HP [54,55] (Fig. 8b), as revealed by the increase of G′ and G″ by up to 5 times for HP crosslinked hydrogel over the neat nanocellulose hydrogel.

Chemical crosslinking with HMDA produces a strong chemical bond,

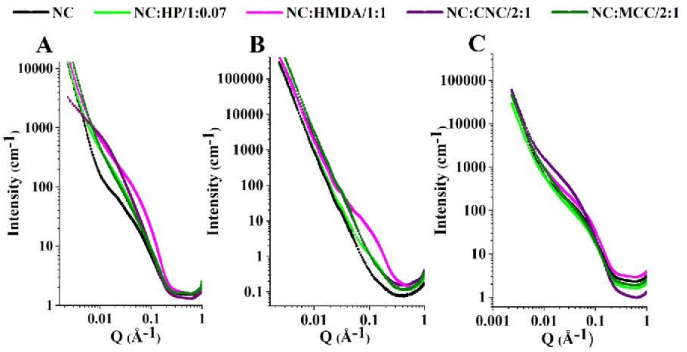

Fig. 7. Small Angle X-ray (SAXS) measurements of (A) Hydrogel, (B) Cryogel and (C) cryogel rewetted with MilliQ water.

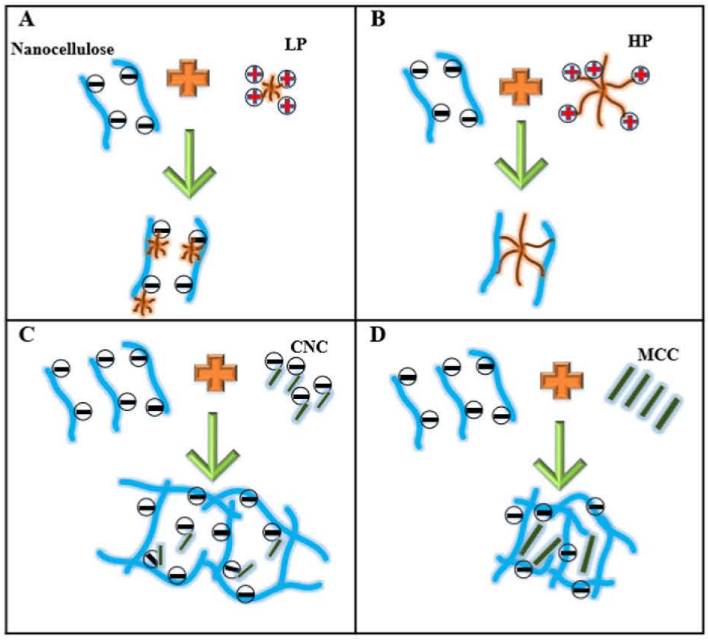

Fig. 8. Schematic representation of the crosslinking interaction and blending agents with nanocellulose (A) nanocellulose with LP, (B) nanocellulose with HP, (C) nanocellulose with CNC and (D) nanocellulose with MCC.

resulting in higher elastic and viscous moduli for the chemically crosslinked hydrogel than for the physically crosslinked hydrogel. The strong crosslinking density of the HMDA sample was 1.40 mol/m^3, and HP crosslinked hydrogel has a lower crosslinking density of 0.44 mol/m^3.

CNC has a strong negative surface charge which repels the negative charge of oxidized nanocellulose fibers (Fig. 8C). MCC particles have no specific surface charge, resulting in gels with a heterogeneous structure, as indicated by the SAXs curve (Figs. 7A and 8D). As a result, the blended hydrogel with CNC has a much more homogeneous structure compared to the blended MCC hydrogel, as revealed by a hump in SAXS scattering for CNC blended hydrogel (Fig. 7A). However, the rheological properties of MCC and CNC blended hydrogels are not significantly different to those of the neat hydrogel. This is because they do not form fiber-fiber bonds, unlike those created in crosslinked hydrogels.

4.2. Effect of crosslinking and blending on nanocellulose cryogels

Nanocellulose hydrogels are freeze dried into cryogels. Crosslinking or blending a nanocellulose hydrogel prior to drying affects the mechanical and absorption properties of the resulting cryogel differently depending on the crosslinking or blending type and density. In this study, the mechanical properties of cryogels were quantified by compressive strength and their absorption capacities measured by free swell capacity measurements followed by centrifugation to determine the water retention capacity.

The HP crosslinked cryogel structure is very open compared to the

original nanocellulose one, as revealed by SAXs analysis (Fig. 7). Structural openness is also visible in these samples via optical microscopy and SEM imaging, as shown in Fig. S1 and S2. The HP crosslinked cryogel shows the lowest compressive strength due to its more open and brittle structure [24]. The compressive strength of the chemically crosslinked (HMDA) cryogel does not change significantly, compared to the neat sample, as the small HMDA molecules only crosslink between adjacent fibers, which does not increase the compressive modulus of the corresponding cryogel. Blended CNC hydrogels result in corresponding cryogels with a significantly increased compressive strength of 0.146 MPa compared to 0.054 MPa for the neat nanocellulose cryogel. CNC has a much smaller particle diameter (~5 nm) than MCC (~50 μm). The surface area of reinforcement provided by CNC is four orders of magnitude higher than for MCC, resulting in a higher area of interaction, increased structural reinforcement, and therefore the highest mechanical strength results for CNC-NC blended cryogel.

The neat nanocellulose cryogel shows the highest absorption capacity, while chemically and physically crosslinked cryogels have similar, lower absorption capacity, despite their significant structural differences. The compact structure of the chemically crosslinked hydrogel, which is a result of the amide-COO^- bond formation, hinders water penetration within the pores of the material, resulting in a lower absorption capacity than the neat cryogel. The open structure of the physically crosslinked cryogel cannot contain as much water, therefore also resulting in lower absorption capacity [24] and water retention capacity than that of the neat cryogel. For cryogels made by blending MCC or CNC, the absorption properties decrease in comparison to those of the neat sample because of the lower availability of COO^- groups and the incorporation of cellulose crystals, which hinder water penetration inside the structure (Fig. 6).

Physical and chemical crosslinking with HP and HMDA, respectively, does increase the mechanical strength of the resulting hydrogel, but not that of the corresponding cryogel. The CNC blended NC cryogel shows increased compressive strength due to the higher area of reinforcement resulting from the incorporation of the small, rod shaped, negatively charged CNC particles. So, although hydrogels and cryogels are simply different forms of a nanocellulose gel having the same original chemical composition, their mechanical strengths vary significantly as a function of crosslinking and blending.

5. Conclusion

A family of cellulose hydrogels and cryogels was developed from TEMPO oxidized cellulose nanofibers (CNF) by incorporating physical and chemical crosslinkers or by blending with cellulose fibrils of different relative lengths. The effect of the type of crosslinking or cellulose crystal addition on the mechanical properties of both the hydrogel and corresponding cryogel was quantified. Gel properties were measured by rheology, mechanical strength, and absorption capacity; structure was quantified by SAXS, optical and scanning electron microscopy. Differences in the properties were related to differences in the hydrogel and cryogel composition, structure and mechanical strength.

Chemically crosslinked hydrogel showed the highest strength compared to all other hydrogel because of strong chemical bond between nanocellulose and the crosslinker. Hydrogels physically crosslinked with high molecular weight PEI had higher elastic and viscous moduli than neat nanocellulose hydrogel due to fiber bridging. Crosslinking with a low molecular weight PEI reverses the behavior, showing decreased elastic and viscous moduli due to charge neutralization. This highlights the effect of PEI molecular weight on the strength of oxidized cellulose nanofiber gels. The addition of CNC or MCC to CNF to create a blended hydrogel had no significant effect on the rheological properties.

The highest cryogel compressive strength was achieved by blending CNC with CNF. Chemical crosslinking with HMDA did not affect the cryogel compressive strength significantly. However, physical crosslinking with high molecular weight PEI significantly decreased the compressive strength of the nanocellulose cryogel by opening up its structure. The neat nanocellulose cryogel has the highest free swell capacity and water retention capacity as it has the highest concentration of available COO^- groups.

This study quantifies the effect of chemical and physical crosslinking and cellulose crystal blending on the structure and mechanical properties of NC hydrogels and cryogels. These results improve the understanding of the hydrogel-cryogel structure-property relationships and facilitate the development of tunable hydrogel and cryogel materials for food, agriculture and diagnostic applications.

CRediT authorship contribution statement

Laila Hossain: Conceptualization, Visualization, Methodology, Investigation, Software, Writing – original draft. **Vikram Singh Raghuwanshi:** Software, Writing – review & editing. **Joanne Tanner:** Supervision, Writing – review & editing. **Gil Garnier:** Visualization, Supervision, Writing – review & editing.

Declaration of Competing Interest

The authors declare that they have no known competing financial interests or personal relationships that could have appeared to influence the work reported in this paper.

Acknowledgements

Financial support was received from Meat and Livestock Australia (grant number P.PSH. 0890). The authors acknowledge Australian Synchrotron for the facilities used. Thanks to Assoc Professor Rico Tabor for the rheological facilities. The authors also acknowledge Mahdi Naseri-Nosar to provide help with the optical microscope.

Appendix A. Supporting information

Supplementary data associated with this article can be found in the online version at doi:10.1016/j.colsurfa.2021.127608.

References

[1] S. Kiatkamjornwong, Superabsorbent polymers and superabsorbent polymer composites, Sci. Asia 33 (1) (2007) 39–43.
[2] M.J. Zohuriaan-Mehr, K. Kabiri, Superabsorbent polymer materials: a review, Iran. Polym. J. 17 (6) (2008) 451.
[3] F. Masuda, Trends in the Development of Superabsorbent Polymers for Diapers, ACS Symp. Ser. (1994) 88–98.
[4] E. Caló, V.V. Khutoryanskiy, Biomedical applications of hydrogels: a review of patents and commercial products, Eur. Polym. J. 65 (2015) 252–267.
[5] J. Li, D.J. Mooney, Designing hydrogels for controlled drug delivery, Nat. Rev. Mater. 1 (12) (2016) 1–17.
[6] J. Li, A. Celiz, J. Yang, Q. Yang, I. Wamala, W. Whyte, B. Seo, N. Vasilyev, J. Vlassak, Z. Suo, Tough adhesives for diverse wet surfaces, Science 357 (6349) (2017) 378–381.
[7] J.D. Tang, C. Mura, K.J. Lampe, Stimuli-responsive, pentapeptide, nanofiber hydrogel for tissue engineering, J. Am. Chem. Soc. 141 (12) (2019) 4886–4899.
[8] C. García-González, M. Alnaief, I. Smirnova, Polysaccharide-based aerogels—promising biodegradable carriers for drug delivery systems, Carbohydr. Polym. 86 (4) (2011) 1425–1438.
[9] B. Zavan, R. Cortivo, G. Abatangelo, Hydrogels and tissue engineering. Hydrogels, Springer,, 2009, pp. 1–8.
[10] R.M. Barajas-Ledesma, A.F. Patti, V.N. Wong, V.S. Raghuwanshi, G. Garnier, Engineering nanocellulose superabsorbent structure by controlling the drying rate, Colloids Surf. A: Physicochem. Eng. Asp. 600 (2020), 124943.
[11] X. Cui, J.J. Lee, W.N. Chen, Eco-friendly and biodegradable cellulose hydrogels produced from low cost okara: towards non-toxic flexible electronics, Sci. Rep. 9 (1) (2019) 1–9.
[12] G. Tang, B. Zhou, F. Li, W. Wang, Y. Liu, X. Wang, C. Liu, X. Ye, Advances of Naturally Derived and Synthetic Hydrogels for Intervertebral Disk Regeneration, Front. Bioeng. Biotechnol. 8 (2020) 745.
[13] A. Sannino, C. Demitri, M. Madaghiele, Biodegradable cellulose-based hydrogels: design and applications, Materials 2 (2) (2009) 353–373.
[14] R.M. Barajas-Ledesma, L. Hossain, V.N. Wong, A.F. Patti, G. Garnier, Effect of the counter-ion on nanocellulose hydrogels and their superabsorbent structure and properties, J. Colloid Interface Sci. 599 (2021) 140–148.

[15] A. Vazquez, M.L. Foresti, J.I. Moran, V.P. Cyras, Extraction and production of cellulose nanofibers. Handbook of Polymer Nanocomposites. Processing, Performance and Application, Springer,, 2015, pp. 81–118.
[16] D. Trache, M.H. Hussin, C.T.H. Chuin, S. Sabar, M.N. Fazita, O.F. Taiwo, T. Hassan, M.M. Haafiz, Microcrystalline cellulose: isolation, characterization and bio-composites application—a review, Int. J. Biol. Macromol. 93 (2016) 789–804.
[17] Y. Chen, X. Jiang, H. Wu, L. Zheng, Bi-directional tuning of thermal transport in SrCoOx with electrochemically induced phase transitions, Nat. Mater. 19 (03) (2020) 655–662.
[18] Y. Habibi, H. Chanzy, M.R. Vignon, TEMPO-mediated surface oxidation of cellulose whiskers, Cellulose 13 (6) (2006) 679–687.
[19] T. Abitbol, A. Rivkin, Y. Cao, Y. Nevo, E. Abraham, T. Ben-Shalom, S. Lapidot, O. Shoseyov, Nanocellulose, a tiny fiber with huge applications, Curr. Opin. Biotechnol. 39 (2016) 76–88.
[20] S. Ahmed, S. Ikram, Chitosan based scaffolds and their applications in wound healing, Achiev. Life Sci. 10 (2016) 27–37.
[21] O.A.T. Dias, S. Konar, A.L. Leão, W. Yang, J. Tjong, M. Sain, Current state of applications of nanocellulose in flexible energy and electronic devices, Front. Chem. 8 (2020) 420.
[22] H. Chavda, C. Patel, Effect of crosslinker concentration on characteristics of superporous hydrogel, Int. J. Pharm. Investig. 1 (1) (2011) 17–21.
[23] S. Sinha, Biodegradable superabsorbents: methods of preparation and application—a review. Fundamental Biomaterials: Polymers, Woodhead Publishing,, 2018, pp. 307–322.
[24] L. Hossain, V.S. Raghuwanshi, J. Tanner, C.-M. Wu, O. Kleinerman, Y. Cohen, G. Garnier, Structure and swelling of cross-linked nanocellulose foams, J. Colloid Interface Sci. 568 (2020) 234–244.
[25] G.T. Hermanson. Bioconjugate Techniques, Academic press,, 2013.
[26] N. Kayra, A.Ö. Aytekin, Synthesis of cellulose-based hydrogels: preparation, formation, mixture, and modification, Cellul. -Based Superabsorbent Hydrogels (2019) 407–434.
[27] F. Jiang, Y.-l Hsieh, Super water absorbing and shape memory nanocellulose aerogels from TEMPO-oxidized cellulose nanofibrils via cyclic freezingthawing, J. Mater. Chem. A 2 (2) (2013) 350–359.
[28] L. Liu, L. Bai, A. Tripathi, J. Yu, Z. Wang, M. Borghei, Y. Fan, O.J. Rojas, High axial ratio nanochitins for ultrastrong and shape-recoverable hydrogels and cryogels via ice templating, ACS Nano 13 (3) (2019) 2927–2935.
[29] S.H. Zainal, N.H. h Mohd, N. Suhaili, F.H. Anuar, A.M. Lazim, R. Othaman, Preparation of cellulose-based hydrogel: a review, J. Mater. Res. Technol. (2020).
[30] X. Zhang, W. Huo, S. Yan, Y. Chen, K. Gan, J. Liu, J. Yang, Innovative application of PVA hydrogel for the forming of porous Si3N4 ceramics via freeze-thaw technique, Ceram. Int. 44 (11) (2018) 13409–13413.
[31] Y. Guan, J. Bian, F. Peng, X.-M. Zhang, R.-C. Sun, High strength of hemicelluloses based hydrogels by freeze/thaw technique, Carbohydr. Polym. 101 (2014) 272–280.
[32] H. Zhang, F. Zhang, J. Wu, Physically crosslinked hydrogels from polysaccharides prepared by freeze-thaw technique, React. Funct. Polym. 73 (7) (2013) 923–928.
[33] S. Butylina, S. Geng, K. Oksman, Properties of as-prepared and freeze-dried hydrogels made from poly (vinyl alcohol) and cellulose nanocrystals using freeze-thaw technique, Eur. Polym. J. 81 (2016) 386–396.
[34] S. Butylina, S. Geng, K. Laatikainen, K. Oksman, Cellulose nanocomposite hydrogels: from formulation to material properties, Front. Chem. 8 (2020) 655.
[35] S.F. Kabir, P.P. Sikdar, B. Haque, M.R. Bhuiyan, A. Ali, M. Islam, Cellulose-based hydrogel materials: chemistry, properties and their prospective applications, Prog. Biomater. 7 (3) (2018) 153–174.
[36] K. Syverud, H. Kirseborn, S. Hajizadeh, G. Chinga-Carrasco, Cross-linking cellulose nanofibrils for potential elastic cryo-structured gels, Nanoscale Res. Lett. 6 (1) (2011) 1–6.
[37] W. Hu, Z. Wang, Y. Xiao, S. Zhang, J. Wang, Advances in crosslinking strategies of biomedical hydrogels, Biomater. Sci. 7 (3) (2019) 843–855.
[38] M.E. El-Naggar, S.I. Othman, A.A. Allam, O.M. Morsy, Synthesis, drying process and medical application of polysaccharide-based aerogels, Int. J. Biol. Macromol. 145 (2020) 1115–1128.
[39] H. Zhuo, Y. Hu, Z. Chen, L. Zhong, Cellulose carbon aerogel/PPy composites for high-performance supercapacitor, Carbohydr. Polym. 215 (2019) 322–329.
[40] T. Budtova, Cellulose II aerogels: a review, Cellulose 26 (1) (2019) 81–121.
[41] J. Patiño-Masó, F. Serra-Parareda, Q. Tarrés, P. Mutjé, F.X. Espinach, M. Delgado-Aguilar, TEMPO-oxidized cellulose nanofibers: a potential bio-based superabsorbent for diaper production, Nanomaterials 9 (9) (2019) 1271.
[42] P.C. Thapliyal, K. Singh, Aerogels as promising thermal insulating materials: an overview, J. Mater. 2014 (10) (2014) 1–10.
[43] Z. Ulker, C. Erkey, An emerging platform for drug delivery: aerogel based systems, J. Control. Release 177 (2014) 51–63.
[44] M.N. Alam, L. Christopher, Natural cellulose-chitosan crosslinked superabsorbent hydrogels with superior swelling properties, ACS Sustain. Chem. Eng. 6 (7) (2018) 8736–8742.
[45] D.J. Mendoza, L. Hossain, C. Browne, V.S. Raghuwanshi, G.P. Simon, G. Garnier, Controlling the transparency and rheology of nanocellulose gels with the extent of carboxylation, Carbohydr. Polym. 245 (2020), 116566.
[46] R.M. Barajas, V. Wong, K. Little, A.F. Patti, G. Garnier, *Carboxylated Nanocellulose Superabsorbent: Biodegradation and Soil Water Retention Properties*, J. Appl. Polym. Sci. (2021) 51495.
[47] E.M. Ahmed, Hydrogel: preparation, characterization, and applications: a review, J. Adv. Res. 6 (2) (2015) 105–121.
[48] T. Zhang, Y. Zhang, X. Wang, S. Liu, Y. Yao, Characterization of the nano-cellulose aerogel from mixing CNF and CNC with different ratio, Mater. Lett. 229 (2018) 103–106.
[49] D. Burhani, A.A. Septevani, R. Setiawan, L.M. Djannah, M.A. Putra, S.S. Kusumah, D. Sondari, Self-assembled behavior of ultralightweight aerogel from a mixture of CNC/CNF from oil palm empty fruit bunches, Polymers 13 (16) (2021) 2649.
[50] R. Curvello, V.S. Raghuwanshi, G. Garnier, Engineering nanocellulose hydrogels for biomedical applications, Adv. Colloid Interface Sci. 267 (2019) 47–61.
[51] J. Gregory, Rates of flocculation of latex particles by cationic polymers, J. Colloid Interface Sci. 42 (2) (1973) 448–456.
[52] Y. Adachi, L. Feng, M. Kobayashi, Kinetics of flocculation of polystyrene latex particles in the mixing flow induced with high charge density polycation near the isoelectric point, Colloids Surf. A: Physicochem. Eng. Asp. 471 (2015) 38–44.
[53] J. Gregory, S. Barany, Adsorption and flocculation by polymers and polymer mixtures, Adv. Colloid Interface Sci. 169 (1) (2011) 1–12.
[54] T.K. Wang, R. Audebert, Flocculation mechanisms of a silica suspension by some weakly cationic polyelectrolytes, J. Colloid Interface Sci. 119 (2) (1987) 459–465.
[55] Y. Zhou, G.V. Franks, Flocculation mechanism induced by cationic polymers investigated by light scattering, Langmuir 22 (16) (2006) 6775–6786.

Journal of Colloid and Interface Science 568 (2020) 234–244

Contents lists available at ScienceDirect

Journal of Colloid and Interface Science

journal homepage: www.elsevier.com/locate/jcis

Structure and swelling of cross-linked nanocellulose foams

Laila Hossain [a], Vikram Singh Raghuwanshi [a], Joanne Tanner [a], Chun-Ming Wu [b], Olga Kleinerman [c], Yachin Cohen [c], Gil Garnier [a,*]

[a] Bioresource Processing Research Institute of Australia (BioPRIA), Monash University, Clayton, Victoria 3800, Australia
[b] National Synchrotron Radiation Research Center, Hsinchu 30076, Taiwan
[c] Technion – Israel Institute of Technology, Haifa, Israel

GRAPHICAL ABSTRACT

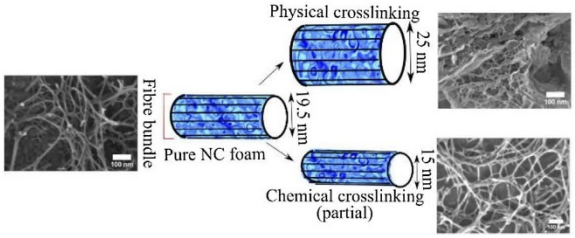

ARTICLE INFO

Article history:
Received 29 December 2019
Revised 12 February 2020
Accepted 13 February 2020
Available online 14 February 2020

Keywords:
Nanocellulose
Hydrogel
Foam
Crosslinking
Absorption capacity
Swelling
SAXS
SANS
FTIR

ABSTRACT

Hypothesis: The water absorption capacity of nanocellulose (NC) foam is tailored by crosslinking with polyethyleneimine (PEI) and hexamethylenediamine (HMDA). The interaction of amine groups in PEI and HMDA with the carboxylic groups (COO^-) of NC affects the foam structure which reduces its swelling capacity.

Experiments: Functionalised NC foams were prepared by TEMPO (2,2,6,6,-tetramethylpiperidine-1-oxyl) oxidation of bleached pulp, followed by fibrillation into a hydrogel, adding a crosslinker and freeze drying the hydrogel into a foam. The structure of the NC foam characterised by rheology, SANS (Small Angle Neutron Scattering), SAXS (Small Angle X-ray Scattering) and cryo-SEM (cryo-Scanning Electron Microscopy) was related to absorption and swelling properties.

Findings: The NC foam has the highest water absorption capacity at 132 g water/g foam. PEI-NC foam has a water absorption capacity of 71 g water/g foam, which further decreases to 47 g water/g foam for the HMDA-NC foam. Small angle scattering reveals the elementary fibril of NC is 3–5 nm thick and forms fiber bundles. In water, these bundles swell differently for the different types of foam which affects the water absorption capacity of the network. The structural analysis of the foam was related to the swelling capacity. The structure of NC foam can be engineered for specific applications for biomedical, agriculture or food industries.

1. Introduction

Hydrogels are hydrophilic physically or chemically crosslinked polymeric network materials which contain a large amount of water in their structure [1]. Hydrogels can be divided into two categories: biopolymer-based hydrogels and synthetic hydrogels-

* Corresponding author.
E-mail address: Gil.Garnier@Monash.edu (G. Garnier).

https://doi.org/10.1016/j.jcis.2020.02.048
0021-9797/

depending on their source. Biopolymer based hydrogels have attracted particular attention because of their biocompatibility, biodegradability and high water absorption capacity [2].

Cellulose is the most abundant naturally occurring polymer and can be used to form hydrogels. Cellulose nanofibers, extracted from wood pulp through combinations of chemical and mechanical treatment, consist of semi-flexible fibrils [3]. Among the chemical methods, 2,2,6,6,-tetramethylpiperidine-1-oxyl (TEMPO) mediated oxidation is a widely known technique to introduce carboxylic groups (COO^-) to the fibre surface [4]. The electrostatic repulsion between the negative carboxylic groups facilitates the formation of a hydrogel upon mechanical treatment. There are many promising applications of these nanocellulose (NC) hydrogels in the biomedical, food and agriculture fields due to their large surface area, large water absorption capacity, sustainability and biocompatible characteristics [5].

Many crosslinking agents with cellulose based hydrogels have been investigated to achieve better mechanical property, control release of biological fluid and adsorption of specific particles. Epichlorohydrin, urea derivatives, aldehydes and aldehyde based reagents and carbodiimides are the most commonly used crosslinkers for cellulose based hydrogels [6]. Due to the toxicity and potential environmental hazard of these crosslinkers, research has targeted more suitable green crosslinker for NC. Chitosan, citric acid, succinic anhydride, polyethyleneimine (PEI) [7–11] have all been investigated to minimise potential hazards. PEI is a highly branched dendrimer of high cationic charge density [12,13] which attracts the negative COO^- group of oxidised fibres. As a non-hazardous polymer, PEI is used to physically crosslink the NC gel in this study. Hexamethylenediamine (HMDA) is used as a chemical crosslinker to compare the effect of chemical crosslinking in NC foam. In this study, NC foams are partially chemically crosslinked with HMDA to improve strength without important detrimental effect on absorption capacity of the foam.

NC foam can be produced by drying NC hydrogel. The resulting foam is highly porous (up to 99.7% porosity), of ultra-low density (10 mg/cm^3) [14,15] and can absorb water at more than 100 times its own dry weight. The absorption capacity depends on the chemical composition of the cellulose itself, as well as its surface area and pore size distribution, and the temperature, pH and ionic strength of the solution being absorbed [6,16]. The porosity and internal structure of NC foams largely dictate the absorption capacity and rate. This distinct structure of NC foams makes them unique compared to foam prepared from cellulose instead of NC. The absorption capacity can further be controlled by physical or chemical crosslinking the NC fibres. The higher the extent of crosslinking, the lower the absorption capacity due to compact structure [17,18]. Therefore, determination of the extent of structural change due to crosslinking is critical to the characterisation and understanding the mechanism behind the absorption capacity of NC foam.

Analysing NC foams upon swelling and de-swelling is particularly challenging, given their high water content and low solid content. A wide range of techniques have been used to characterise NC hydrogels [19] and dried foams; these include SEM and TGA [20], AFM [21], and SANS, SAXS and DLS [22]. Small Angle Scattering techniques, which enable representative analysis through the use of relatively large sample volumes, is emerging as an attractive NC foam characterisation method [19]. SAXS of TEMPO oxidised hydrogels was studied at different fibre concentrations to characterise the effect of fibre concentration. This was compared with the gel rheological properties to better understand the gelation mechanism [23]. Mao et al. used SAXS and SANS to characterise TEMPO oxidised homogenised cellulose nanofibers and the data were fitted using ribbon, parallelepiped and Gaussian-approximated parallelepiped models to calculate width and thickness of NC cross section [22]. In another study, microbial NC was studied dry and swollen to quantify the structure by a combination of Ultra SANS and SANS [24]. However, the effect of the fibrous network structure on the swelling capacity of NC-based foam was not explored, nor was the structure related to the swelling hysteresis in these studies.

It is the objective of this study to understand and quantify the relation between the structure and swelling behaviour of NC-based foams. It is clear that, although powerful and applicable, SAXS and SANS characterisation alone is insufficient to achieve this. In this study, a series of model physically and (partially) chemically crosslinked NC foams were saturated with H_2O/D_2O and measured using a combination of small angle scattering and cryogenic high resolution (HR) SEM techniques for the first time. Fibre swelling behaviour was measured and nano-scale structural changes related with changes in swelling capacities for different types of crosslinking were quantified. Thus, NC gel-foam properties have been directly related to and shown to control the absorption capacity of the foam via crosslinking. Attenuated total reflectance-Fourier transform infrared (ATR-FTIR) spectroscopy is performed to complement the cryogenic HR-SEM imaging technique and verify the effect of crosslinking on chemical composition and morphological structure. Comparison of crosslinked and non-crosslinked foam is presented to differentiate the structures and reveal the water transport mechanisms inside the structure. Insight into the mechanism of fibre bundle swelling on absorption capacity is also provided.

2. Methodology

2.1. Materials

Bleached Eucalyptus Kraft (BEK) pulp (approximately 10 wt% solids) was obtained from Australian Paper, Maryvale, Australia. 2,2,6,6-Tetramethylpiperidine-1-oxyl (TEMPO), Polyethyleneimine (PEI) of two different molecular weights (high molecular weight: $M_n \sim 60{,}000$; $M_w \sim 750{,}000$ and low molecular weight: $M_n \sim 600$; $M_w \sim 800$) and sodium bromide (NaBr) were purchased from Sigma-Aldrich. Hydrochloric acid (HCl) and Sodium Hydroxide (NaOH) were purchased from ACL Laboratories and Merck, respectively. HMDA was purchased from Chem-Supply. 12 w/v% Sodium Hypochlorite (NaClO) was purchased from Thermo Fisher Scientific and used as received. Milli-Q® water was collected from Merck Milli-Q® water purification system (Direct-Q® 3UV-R).

2.2. TEMPO mediated oxidation

The TEMPO-mediated oxidation process used in this investigation is based on a previously developed method [25]. There are two versions: the high charge and low charge methods, which yield 1.4 mmol and 0.6 mmol of carboxylate groups per gram dry weight of fibre, respectively. 25 g BEK pulp (dry weight) was suspended in 2500 mL water containing 0.4 g TEMPO and 2.5 g NaBr. In each case, a NaClO solution (12 w/v%) was initially adjusted to pH 10 by the addition of 32% HCl. To initiate the oxidation process, 100 mL NaClO (for high charge) or 75 mL NaClO (for low charge) were added drop-wise to the suspension whilst stirring. The pH of the reaction was monitored online and maintained at pH 10 by addition of 0.5 M NaOH. The oxidation process was completed in 3 h for the high charge (1.4 mmol/g) and 2 h for the low charge method (0.6 mmol/g). The oxidised fibres were recovered through filtration and stored refrigerated (2–8 °C). To produce hydrogel, TEMPO-oxidised pulp was dispersed in deionised water at a required concentration (0.5 wt% fibre concentration). Fibrillation is attained through a high-pressure homogeniser (GEA Niro Soavi

Homogeniser Panda) at 1000 bar for two passes. The oxidation process is critical to produce hydrogel as unoxidised fibre suspensions do not generate hydrogel. This hydrogel structure together with freeze drying process produces the porous foam structure.

2.3. Determining solids concentration

The solids concentration of all gels and pulps was determined through oven drying. The sample was weighed before (w_i) and after (w_d) drying. Sample moisture was removed by evaporation at 105 °C for at least 6 h. The solids content was calculated as:

$$Solid\ content(\%) = \frac{w_d}{w_i} \times 100\%$$

2.4. Conductometric titration

The carboxylate group (COO^-) content was measured by conductometric titration as reported in previous studies [26,27]. Approximately 30 mg (dry weight) of oxidised pulp was dispersed in 40 mL deionised water. 200 μL (1 wt%) NaCl was added to the dispersed sample. The pH of the sample was adjusted between 2.5 and 3 before titration with 0.5 M HCl. Titration was done by controlled addition of 0.1 M NaOH using a Mettler Toledo T5 titrator. The conductivity of the sample was monitored throughout the titration progress. The carboxyl group content (mmol COO^-/g fibre) was determined by using the following equation.

$$CC = \frac{c(V_2 - V_1)}{w} \times 1000$$

where V_1 and V_2 denote the amount of titrant required to neutralise the carboxylic groups (L), c is the NaOH concentration (mol/L), and w is the sample weight (g).

2.5. PEI incorporation

PEI was dissolved in deionised water at a concentration of 0.005 mg/mL. One-passed homogenised gel was mixed with PEI using a hand blender. Two different molecular weights of PEI (high molecular weight PEI: H_PEI = 750,000 Da and low molecular weight PEI: L_PEI = 800 Da) were used. The NC gel was mixed with PEI at a mass ratios of 1: 0.07 (NC:PEI). The resulting mixture was then passed through the homogeniser again. All the passes through the homogeniser were performed at 1000 bar. PEI at lower concentration (NC:PEI = 1:0.05) was also studied with NC which showed similar swelling behaviour but lower gel strength compared to NC:PEI = 1:0.07. Only NC:PEI = 1:0.07 sample was considered for this study as it increased the mechanical property (strength) of the gel compared to pure NC gel.

2.6. HMDA incorporation

HMDA was dissolved in deionised water at a concentration of 0.45 mg/mL. The NC gel was mixed with the HMDA solution at stoichiometric ratios of 1:4 and 1:8 (COO^-:NH_2). HMDA does not react with NC at room temperature or below room temperature if no reagent (such as EDC/NHS) is used to activate the COO^- group in NC. So, the resulting mixture was cured at 80 °C for 1 h in an oven. The final cross-linked gel was removed and stored at 4 °C. The molecular structure of PEI and HMDA is shown in Fig. 1.

2.7. Gel rheology measurement

Rheological testing was performed with an Anton Paar MCR302 rheometer at 25 °C. A cone (0.997°) and plate (49.975 mm) geometry were selected. A solvent trap was used to make sure steady temperature during measurements. Amplitude sweep was done from 0.01 to 100% at a constant frequency of 1 Hz.

2.8. High-resolution scanning electron microscopy (HR-SEM)

Gel morphologies were imaged by high-resolution scanning electron microscopy (HR-SEM) using cryogenic sample preparation method. Sample preparation was carried out in a controlled-environment vitrification system (CEVS) [28], followed by complete sublimation of vitrified water. Approximately 3 μL of gel was placed between two gold planchettes, and the "sandwiched" gel vitrified by rapid immersion in liquid nitrogen. The vitrified sample was loaded on a specimen holder, which was subsequently transferred under cryogenic conditions into the pumped BAF060 freeze-fracture replication system (Leica, Vienna), the stage of which was pre-cooled to −160 °C. In the BAF060 unit, the sample was fractured and stabilized until the vacuum reached 10^{-6} mBar, maintaining the temperature around −160 °C. To remove the water phase, the temperature of the sample was raised to −100 °C, at which water has a vapor pressure of about 10^{-5} mBar. The sample was maintained at this temperature for two hours to ensure complete water sublimation. This combination of the high vacuum and low temperature provides ideal conditions to achieve water removal and preserve the mechanical strength of the frozen gel. Subsequently, the liquid nitrogen flow was turned off, and the sample kept inside the BAF060 under vacuum until ambient temperature was reached. This final slow temperature ramp mitigates collapse of the gel structure. The freeze-dried sample was transferred directly to the SEM in the sample holder via the cryogenic port of the microscope (Leica, Vienna). Unlike classical freeze-drying procedures, no shadowing or conductive coating was applied to the sample. Imaging was performed by a Zeiss Ultra Plus high-resolution scanning electron microscope equipped with a Schottky field-emission electron gun and a unique Gemini electron-beam column design (Carl Zeiss SMT GmbH Oberkochen, Germany). To achieve high-resolution images close to the isoelectric (no-charging) point, the microscope was operated at 1 kV electron beam energy. Images were acquired by mixing signals from a classical Evart-Thornley and a high-resolution In-the-Lens secondary electron (SE) detectors, at working distance of about 3.5 mm.

2.9. Fourier transform infrared (FTIR) spectroscopy

The crosslinked foams were tested by ATR-FTIR using the Agilent Cary 630 FTIR Spectrometer. The freeze dried foams were tested for the FTIR spectra to determine the type of crosslinking.

2.10. Preparation of NC foams

To prepare the foams, 15 g of gel was spread evenly onto a 55 mm petri dish. The sample was frozen at −80 °C, then freeze-dried (Christ Alpha 2–4 LD Plus) for 2 days. The freeze-dried samples (pure nanocellulose foam: NC foam, nanocellulose crosslinked with high molecular weight PEI: NC_H_PEI foam and nanocellulose crosslinked with HMDA having stoichiometric ratio of 1:8 for COO^-:NH_2 = NC_HMDA_18 foam) are shown in Fig. 2.

2.11. Free swell capacity

15 g of gel sample was freeze-dried in a 55 mm petri dish to produce a NC foam which was tested for free swell capacity. The sample was deposited in a funnel (funnel filter glass, 75 mm diameter) and placed in a beaker full of Milli Q® water. The water absorbed was measured at regular intervals up to 3 h. Before measuring the weight of water absorbed, the funnel with the sample

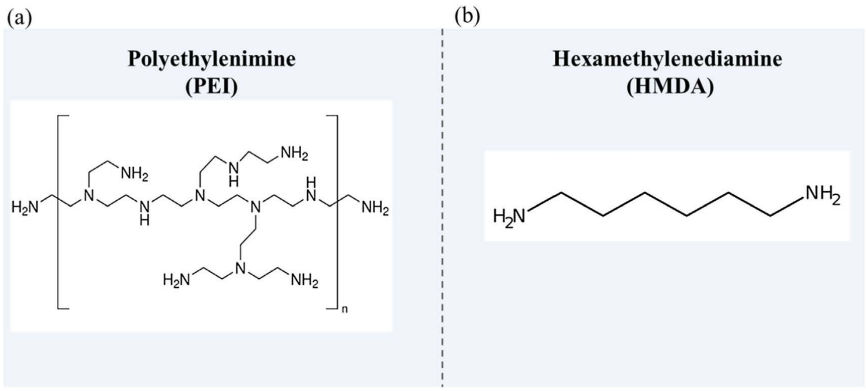

Fig. 1. Molecular structures of the crosslinking agents: (a) PEI and (b) HMDA.

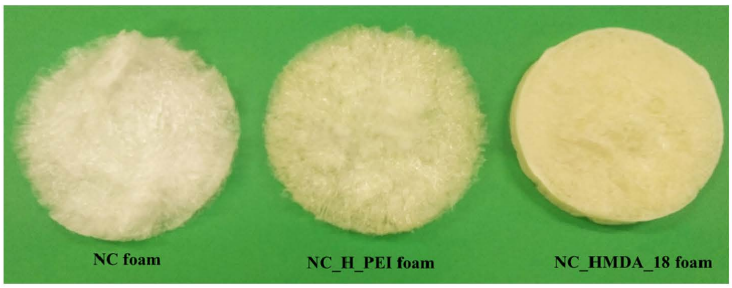

Fig. 2. Picture of the three types of foams: NC foam, and NC foam crosslinked with high molecular weight PEI and HMDA, respectively.

was removed from the fluid container and kept on an inclined surface for five minutes for the excess liquid drip off.

The free swell capacity was then calculated as follows:

$$\text{Free Swell Capacity (FSC)} = \frac{m_t - m_i}{m_i}$$

where m_t is the mass of the swollen foam at a particular time interval and m_i is the initial mass of the foam.

2.12. Small angle neutron and small angle X-ray scattering

Small-angle neutron scattering (SANS) measurements were performed at the Time-of-Flight BILBY beamline at the Australian Nuclear Science and Technology Organisation (ANSTO), NSW, Australia. The wavelength of 6 Å was conducted by using its neutron-velocity selector (NVS). Two detector carriage lengths were used to cover the Q-range from 0.00254 to 0.31 $Å^{-1}$. The foam samples were placed in demountable cells of wall thickness 2 mm. D_2O was used to hydrate the samples.

The data collected were reduced by using the Mantid software with the BILBY package. The background of the empty cell was subtracted from each sample measured without D_2O, and the D_2O scattering was subtracted from the hydrated samples. The raw data was normalised to the absolute scattering values by the pre-calibrated scattering curve of D_2O.

Small angle X-ray Scattering (SAXS) was performed at the SAXS/WAXS beamline of the Australian Synchrotron [29]. The foam was measured in-situ during dehydration. SAXS measurements were made at an energy of 12 keV (λ = 1.033 Å) at a sample to detector distance of 7 m (q range:0.001 and 0.1 $Å^{-1}$). The scattered photons were collected using a PILATUS 1 M detector (pixel size 172 μm × 172 μm). Q scale was calibrated using the standard silver behenate. Data reduction and radial averaging of scattering curves was performed by the beamline specific Scatter Brain software.

3. Results

The free swell capacity of NC foam and crosslinked NC foams is tested by immersion into MilliQ® water. The free swell capacity of the foam is related to the morphological and internal structure, which are determined by HR-SEM and small angle scattering (X-rays and neutrons). The foam internal structure is quantified by network stiffness, swollen bundle diameter and structure compactness to determine the effect of crosslinking on the foam structure. Hydration-dehydration study are also performed to estimate the effect of dehydration/drying time on nanostructure.

3.1. Swelling behaviour of NC foams

Swelling is tested by immersing the NC foams in MilliQ® water. Fig. 3 shows the free swell capacity (in g water/g foam) for the pure NC, NC_PEI and the NC_HMDA_18 foams. The free swell capacity for the pure NC foam is 132 g water/g foam. Foams from PEI and HDMA treated NC have a reduced free swell capacity of 71 g water/g foam and 47 g water/g foam, respectively.

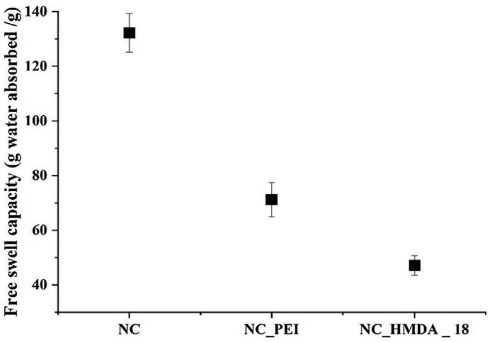

Fig. 3. Comparison of the free swelling capacity for the different NC foams.

3.2. Morphological structure

High-resolution scanning electron microscopy (HR-SEM) is performed on gel samples prepared by the cryogenic method to evaluate the morphology of the pure NC, NC_PEI and NC_HMDA gels. All gels show highly crosslinked and reticulated structures with low fibrous solid content, as expected.

The HR-SEM micrographs of NC (Fig. 4a) and NC_HMDA gels (Fig. 4c) show the distribution of cellulose fibres (of diameter 10–30 nm) creating porous structures with large pores of diameter ranging from 50 to 200 nm.

The HR-SEM micrograph of the NC_PEI gel presents a different morphological structure and fibre distribution (Fig. 4b). The NC_PEI gel has a flake-like and fluffy structure.

3.3. FTIR spectra of modified NC foams

Freeze dried NC, NC_PEI and NC_HMDA foams are analysed by ATR-FTIR. Fig. 5a compares the ATR-FTIR spectra of NC and NC_PEI foams. Both spectra are similar in shape, indicating that PEI induces no significant chemical change to the NC foam chemical bonding.

Fig. 5b shows the spectra of NC and NC_HMDA foams. The NC spectra display the representative COO^- group peak at 1599 cm^{-1} corresponding to the C=O stretch. The C=O stretch peak shifts to a broader peak in the amide crosslinked foam (NC_HMDA) at 1589 cm^{-1}. As this was partial crosslinking, the C=O stretch is not very prominent. FTIR spectra for complete crosslinking of NC with HMDA is provided in Fig. S1 of the supplementary information section.

3.4. Rheological properties of crosslinked gel

The viscoelastic behaviour of the NC gel and, NC_PEI and NC_HMDA crosslinked gels, is quantified by rheology (Fig. 6). The Elastic (G′) and Viscous (G″) moduli of the 3 gels were measured in oscillatory flow mode as a function of shear strain. There are four observations of interest. The first is that the rheology of all three gels is dominated by the elastic regime: G′ remains higher than G″ over most of the strain range. The second is that all three gels have a clear and fairly similar linear viscosity region (LVR) that drops at a strain of 10%. The strain at which the LVR regime drops is a little higher for NC_HMDA gels, indicating stronger cohesion between the NC fibres. The third observation is that PEI increases the elastic modulus of NC gels (G') by a factor of 5 compared to the NC gel, while HMDA provides no increase; increase in G' gives an indication of the relative crosslinking densities. Fourth, the slope of the elastic curve (G') after linear viscoelastic region (LVR) for NC_HMDA_18 and NC_H_PEI became steeper compared to NC gel which is also showing some gel crosslinking. The crosslinking densities of these samples calculated from the elastic moduli are provided in Table S2.

3.5. Structural change of foam upon swelling

NC foams are characterised in the dried and hydrated states by Small Angle Neutron (SANS) and X-ray (SAXS) Scattering. SANS and SAXS are both non-destructive methods that provide average structural information of nanomaterials using a relatively large sample volume compared to other techniques [30,31].

Fig. 7a shows the SANS curves for NC foams made from fibres of two different charges (*HSC*: 1.4 mmol COO^-/g fibre and *LSC*: 0.6 mmol COO^-/g fibre). In the dried state, both materials show

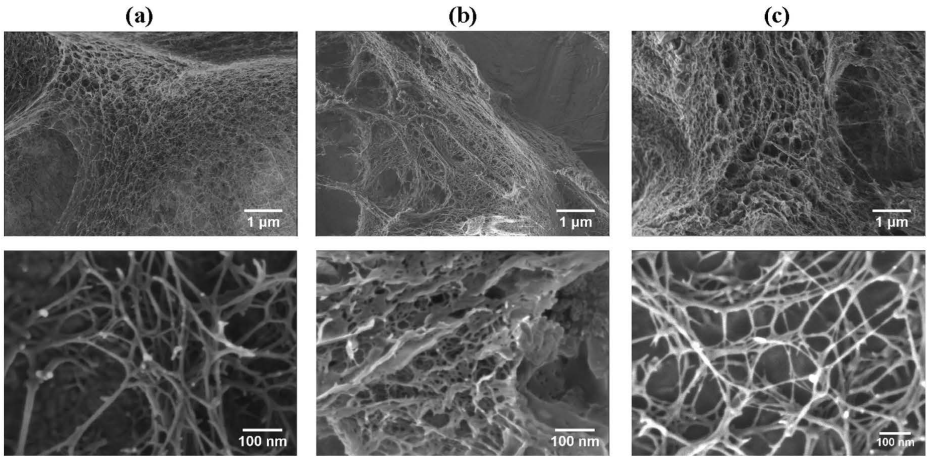

Fig. 4. HR-SEM images of (a) 0.5 NC gel, (b) NC_ H_PEI (NC:H_PEI = 1:0.125) gel and (c) NC_HMDA_12 gel at complementary magnifications.

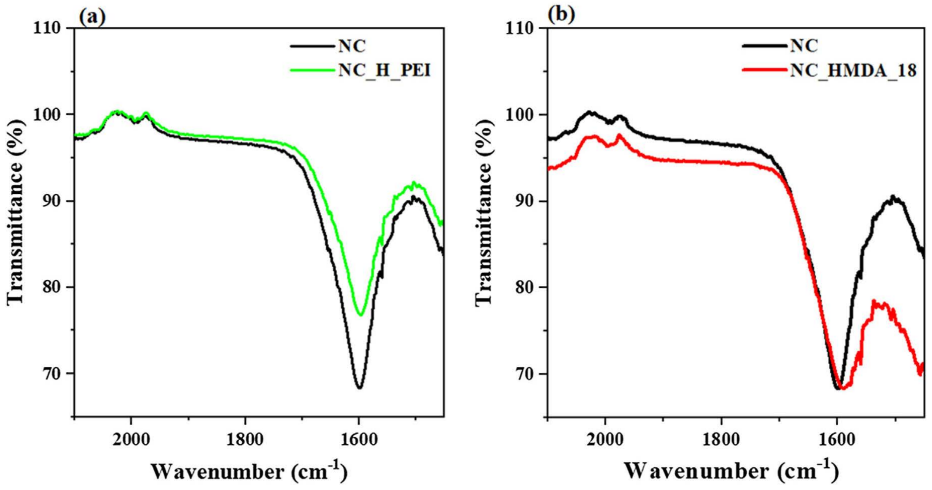

Fig. 5. ATR-FTIR spectra for (a) pure NC and NC_H_PEI foam, (b) pure NC and NC_HMDA_18 foam.

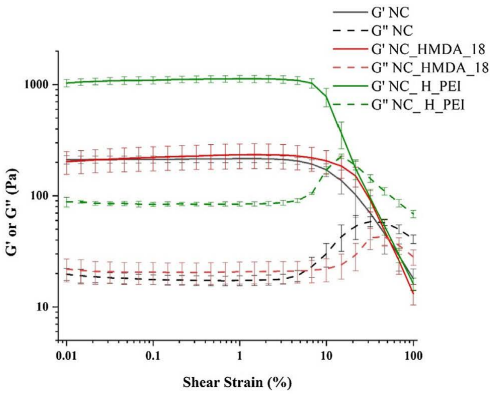

Fig. 6. Rheological spectra of pure NC, NC_H_PEI and NC_HMDA_18 hydrogel: dynamic strain sweep (25 °C) at a frequency of 1 Hz.

the same scattering profile with no evidence of organised structure. The slope of the scattering curve ($q < 0.02$ Å^{-1}) displays q^{-4} power law behaviour, which indicates scattering from large size aggregated fibres. NC fibre charge density did not affect the gel network structure.

Upon hydrating the sample with D_2O, a significant hump appears in SANS profile (Fig. 7a) in the q range of 0.02–0.1 Å^{-1}. This hump corresponds to a change in the structure in the size range 1–30 nm. Both HSC and LSC samples show the same structure scattering profile, indicating that the charge of the cellulose fibres has no effect on the structure upon hydration of the freeze-dried foam. The upturn in the data at low q values ($q < 0.02$ Å^{-1}) in the hydrated SANS curves indicates inhomogeneity of the large-scale structures.

Fig. 7b shows the SANS curve for the NC foams made with PEI of different molecular weights (750,000 Da and 800 Da). No structure change is observed for the freeze-dried samples. However, upon hydration, a minor change in slope can be seen (Fig. 7b) which is attributed to the change in PEI molecular weight.

The SANS curves of the NC_HMDA foams show noticeable changes in the scattering curve intensity upon hydration and for freeze dried condition. (Fig. 7c). However, the structures of the scattering curve profile are identical. The freeze-dried NC_HMDA_18 shows higher scattering than the NC_HMDA_14 foam. Upon hydration with D_2O, the NC_HMDA_14 foam absorbs more water and shows higher scattering intensity compared to NC_HMDA_18.

3.6. Probing fibrous structure by different models

The structural information from the scattering curves are extracted by fitting with three different models. These are: (i) the flexible elliptical cylinder model with the power law [32]; (ii) the mass fractals model with power law [33] and (iii) the Debye-Bueche and Lorentzian function [34]. The first model calculates the cross section and the diameter of the fibre with the stiffness of the network structure in terms of persistence length. The second model characterises the mass fractal distribution in the hydrated foam structures. The third model quantifies the large and small correlation lengths. Detailed model description is provided in supplementary information S3.

The scattering data is fitted by the flexible ellipsoidal cylinder model to quantify the elementary fibril dimension. This model considers ellipsoidal cross-sectional rods defined by the cross-section minor radius r_a, the axis ratio r_b/r_a, the persistence length (l_p) and the contour length (L) [35]. The Kuhn length, which is a measure of stiffness, is twice the persistence length [23]. The contour length represents the length of the chain [36].

Fitting all samples (q range: 0.01–0.2 Å^{-1}) with the flexible elliptical cylinder model yields average cross-sectional fibre dimensions of 3 nm × 5 nm using an assumed contour length of 1000 nm [35]. The current results complement a previous study on TEMPO oxidised homogenised cellulose nanofiber which showed that the width and thickness of the cross section are 2 nm and 8 nm, respectively [22].

The persistence length (network stiffness) evaluated with the flexible cylinder model is shown in Fig. 8a. For the pure NC foam, the persistence length is 9 nm and increases to 12 nm for NC_H_

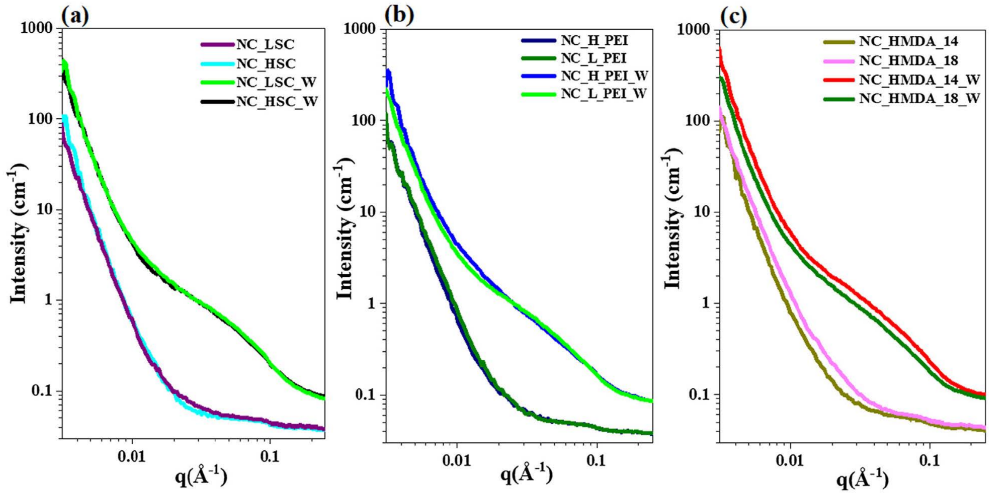

Fig. 7. SANS intensity-q relationships for dry and saturated (w denotes water saturated foam) foams with hump made from NC gels original, NC_H_PEI and NC_HMDA. (a) Effect of surface charge, (b) physical crosslinking and (c) chemical crosslinking on the foam.

PEI foam. The NC_HMDA foam indicating that partial chemical crosslinking results in a higher persistence length.

Fitting the SANS data with the mass fractal model combined with the power law q^{-4} (q range 0.004–0.2 $Å^{-1}$) reveals the cut-off length (Fig. 8b) to be equivalent to the swollen fibre bundle dimension, which is between 12 and 26 nm. The NC_H_PEI foam swells more than NC_L_PEI indicating that increasing the molecular weight of PEI increases fibre bundle swelling. However, the NC_HMDA foam did not swell much and the bundle size reduced to 14 nm. The NC_HMDA_14 foam has its fibre bundles swelling to 17 nm, which decreased to 14 nm upon increasing the HMDA concentration (1:8) for NC_HMDA_18 foam.

The calculated mass fractal dimensions reveal the compactness/openness of the network structure (Fig. 8c). The pure NC foam has a fractal dimension of 1.2. Adding the low molecular weight PEI (NC_L_PEI) does not change the dimension significantly, and the high molecular weight PEI (NC_H_PEI) provides foams with a mass fractal dimension of 1.1. The NC_HMDA_14 and NC_HMDA_18 foam show increase in mass fractal dimensions to 1.3 and 1.4, respectively, for foams at the low and high HMDA ratio. The low values of the fractal dimensions indicate the openness of the structure. However, the differences in the fitted values may not be significant and other factors in structure heterogeneities may contribute to differences in fractal dimensions calculated via the mass fractal analytical method.

The correlation length evaluated by the Debye-Bueche and Lorentzian function indicates the large and small scale heterogeneities in the swollen fibre bundles and in the network. The smaller correlation length of 3–5 nm represents the dimensions of the elementary fibril unit. The higher correlation length (Fig. 8d) was obtained between the size range of 70–90 nm. These concentration fluctuations occur due to the distributions of the large cellulose fibres bundle size or pore size. The highest correlation length was found for the H-PEI NC foam, which indicates a loose structure. For pure NC foam, the correlation length was 79 nm resulting from the big pores or large size fibre bundles. For the NC-HMDA foam, the correlation lengths decreased as HMDA concentration increased.

3.7. NC foam hydration and dehydration behaviour

SAXS experiments were performed at the SAXS/WAXS beamline of the Australian Synchrotron to evaluate the hydration and drying behaviour of NC foam. The freeze-dried foam was hydrated with MilliQ® water. Fig. 9 compares the SAXS curves of the original freeze dried NC foam structure (designated as blank) to the hydrated NC foams after 10, 13 and 15 min during drying under ambient conditions (Fig. 9).

A sharp hump is observed at saturated condition in the q range between 0.03 and 2 $Å^{-1}$. The sharp hump started decaying with time and after 15 min, the hump completely disappeared. But the profile of freeze-dried foam (blank in Fig. 9a) and the once saturated dried foam (15 min in Fig. 9a) is different. This indicates that the foam does not return to its original structure after drying from saturated condition.

All foams show an asymptotic decay of q^{-4} at low q region ($q < 0.03$ $Å^{-1}$), originating from a smooth interface of fibre bundle (Fig. 9a). The scattering curves were fitted with the mass fractal combined with the power law model, which calculates the cut-off length and the mass fractal dimensions (Fig. 9b).

The saturated NC foam shows a cut-off length (swollen fibre bundle diameter) of 19 nm and a mass fractal dimension of 1 (Fig. 9b). Upon ambient drying, the cut-off length decreased to 14 nm, indicating the removal of water from the structure, which increases the compactness or shrinkage of the NC fibre bundle. The mass fractal dimension increased to 2.6 which complements the cut-off length results.

4. Discussion

The swelling behaviour of freeze-dried NC foam crosslinked with PEI (physically) and HMDA (partially chemically) was studied and related to water absorption. The measured free swell capacity of NC foam (132 g water/g foam) indicates that the pure NC foam has a higher absorption capacity than the PEI (65 g water/g foam) and HMDA (48 g water/g foam) crosslinked NC foams (Fig. 3). This

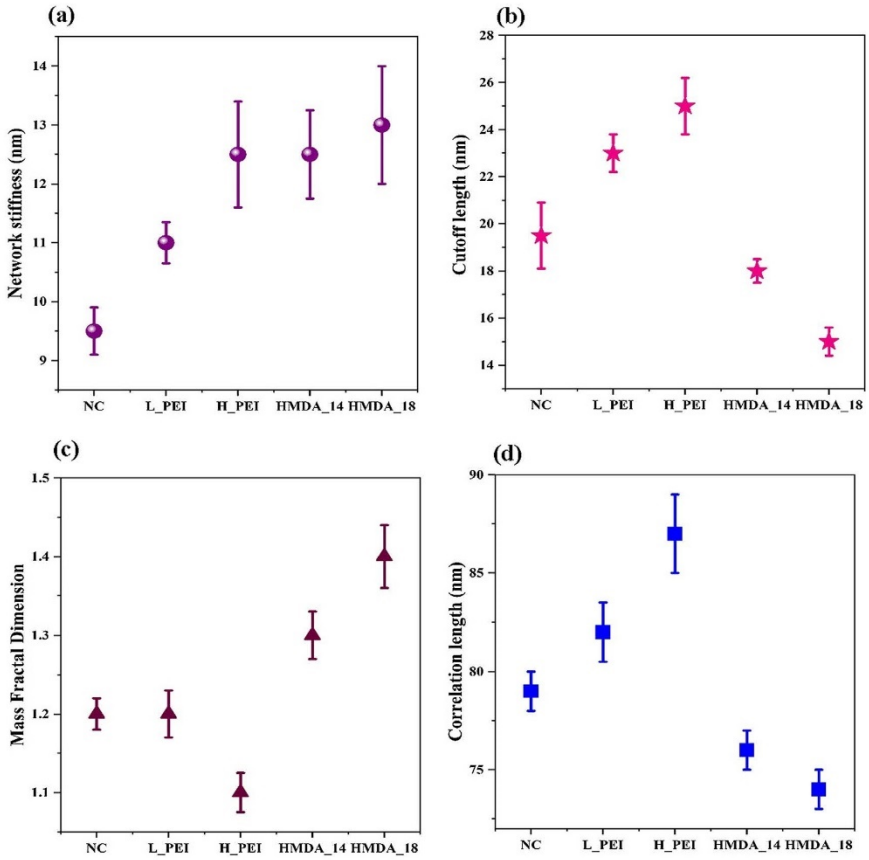

Fig. 8. Structural characterisation of swollen NC foam based on SANS data: (a) network stiffness, (b) cut-off length, (c) mass fractal dimension and (d) correlation length. (L_PEI = NC with 7% LMW PEI; H_PEI = NC with 7% HMW PEI; HMDA_14: NC with HMDA and COO^- : NH_2 = 1:4; HMDA_18: NC with HMDA and COO^- : NH_2 = 1:8).

is attributed to a combination of two mechanisms directly related to crosslinking: (i) differences in the physical structure of the foams and (ii) screening of some of the native carboxyl groups on the NC fibres. The zeta potential of selected samples is shown in Table S4 of the supplementary information section. NC foam is composed of entangled, TEMPO oxidised homogenised cellulose nanofiber bundles. The TEMPO reaction oxidises the secondary OH of the C6 carbon of cellulose into a carboxyl (COO^-) group. The pure NC foam has a carboxylic concentration of 1.4 mmol COO^-/g fibre. The negatively charged carboxyl groups interacts with water molecules which increases water absorption capacity of the NC fibre structure [27].

The fibre bundles of NC foam structure are made of elementary fibrils (elementary fibril shown in Fig. 10) units of cross section 3 nm × 5 nm as determined by fitting the SANS curves with the flexible elliptical cylinder model. When the NC foam is soaked in water, the liquid diffuses by capillary flow between the elementary fibrils and interferes with the carboxyl groups (H bonding) resulting in swelling of fibre bundles (Fig. 10). NC foam fibre bundles swell up to 19.5 nm, which is larger than the NC_HMDA foam (15 nm) but smaller than the NC_PEI foam (25 nm).

The NC_PEI foam fibre bundles swell more (25 nm) at the nanoscale but this type of foam absorbs less water (65 g absorbed/g foam) at the macroscale compared to the pure NC foam (132 g water/g foam). During homogenisation of PEI with NC fibre, the big molecules of PEI (M_W = 750,000 Da) may diffuse into the fibre bundle, expanding the bundle structure (Fig. 10) and establishing some physically crosslinking with carboxyl groups. This hypothesis of a more open structure is corroborated by the mass fractal dimension of 1.1 (calculated from the SANS curves fitting) which indicates that the NC_PEI structure is less compact than that of pure NC foam. The cryogenic HR-SEM micrographs complement the SANS analysis showing the open flake like structure of the NC_PEI foam (Fig. 4). The PEI crosslinked NC fibre shows a high network stiffness with a persistence length of 12.8 nm (Fig. 8a) which is higher than that for the pure NC foam (9 nm). Higher network stiffness upon crosslinking is also shown by the rheology results (Fig. 6), as the slope of the PEI crosslinked gel is steeper than for the pure NC gel.

Upon contact with water, the water molecules diffuse into the NC_PEI fibre bundles and through the pores formed by the network of crosslinked fibre bundles. The open and fluffy structure of

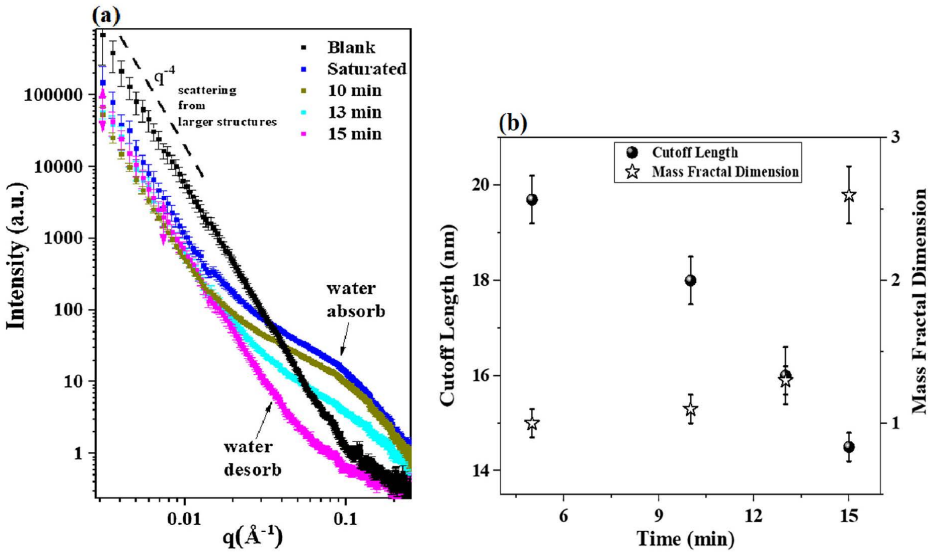

Fig. 9. Structural change of NC foam upon swelling and deswelling in SAXS: (a) SAXS intensity-q relationships for NC foam (Blank is dry sample and others are after X min of saturation in water where X = saturated, 10, 13 and 15 min) and (b) cutoff length and mass fractal dimension for NC foam.

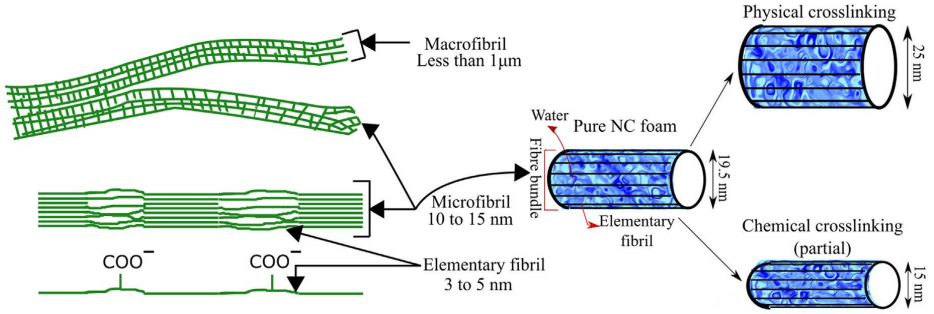

Fig. 10. Schematic diagram showing the length scale of the NC gel. A flexible ellipsoidal cylinder model was selected to measure the effect of PEI (physical crosslinking) and HMDA (partial chemical crosslinking) on the NC fibre bundle swelling.

NC_PEI foam accommodates most of the water in the network, resulting in higher fibre bundle swelling.

However, at the macroscale, the lower water absorption capacity of NC_PEI (Fig. 3) results from the open and stiff fibrous network in this sample, combined with screening of some of the COO^- groups by the primary, secondary and tertiary amine groups of the adsorbed PEI molecules (Fig. 1).

In contrast, in NC_HMDA foam, the HMDA molecules can diffuse into the NC fibre bundle. Due to the smaller size of the HMDA molecule (M_W HMDA = 116.2 Da) and their interaction with the COO^- groups in the fibre bundle, the resultant NC_HMDA fibre bundle structure is more tightly bound together, and therefore it shrinks [37]. The NC_HMDA foam thus has a more compact fibrous network than the pure NC and NC_PEI foams (Fig. 8c and Fig. 10) as shown by the calculated NC_HMDA_18 mass fractal dimension of 1.4. The compactness of the foam structure increased with the HMDA concentration, as shown by the mass fractal results (Fig. 8c) which increases the extent of crosslinking.

NC_HMDA foam showed the lowest swelling capacity (48 g water/g foam). This is due to the compactness of fibre bundle which restricts and hinders the water diffusion and penetration in the fibre bundle structure. The tighter structure also reduces the swelling of the fibre bundle to 15 nm. Another reason which contributes to the reduction of water absorption capacity is the screening of some COO^- groups by the two primary amine groups from each molecule of HMDA.

The SAXS hydration-drying study quantifies the structure compactness upon swelling and deswelling. For the dry foam, SAXS shows a power law behaviour which indicates scattering from the surface of aggregated fibres. During swelling, the fibre bundles and pores accommodate water. The water penetrates into the fibre bundle and the inter-elementary fibril distance increases which opens the fibre bundle. This is seen by the low mass fractal (1.0) value after saturation. Upon drying, the water from the bundles evaporates and the inter-elementary fibril distance decreases, as structure shrinks, and the elementary fibrils aggregate inside the

bundle. This leads to an increase in the compactness of the internal structure of the bundles as revealed by the increased mass fractal dimension (2.5).

Interestingly, the freeze-dried foam structure differs from the dehydrated sample (Fig. 9). The fibre bundle dimension, represented by the cut-off length, decreased from 19 nm to 14 nm upon hydration and subsequent ambient drying. The swollen hydrated fibre bundle has higher cut-off length and upon drying, the water evaporates and the fibre bundle shrinks to their decreased cut-off length 14 nm. This increased compactness is attributed to the formation of aggregates during room temperature drying. Freeze drying sublimation occurs at temperature ranging from −20 °C to −50 °C, at a lower pressure than for the triple point of water, to deliberatively minimise the aggregation of cellulose fibres [38]. However, during ambient drying, the NC fibres have the ability to migrate, resulting in aggregation as water evaporates [39].

The combined effect of physical entrapment and COO^- groups give pure NC foam a higher water absorption capacity than PEI/HMDA modified foams. In contrast, network stiffness increases with PEI and HMDA crosslinking. Therefore, NC foam structure and swelling capacity can be controlled by crosslinking the fibre structure using PEI and HMDA of varying molecular weights and concentrations.

5. Conclusion

This study relates the NC gel-foam properties to their structure controlled by physical and partial chemical crosslinking. The structure and swelling behaviour of freeze-dried NC foams based on TEMPO oxidised NC gels were investigated. NC gels were crosslinked physically and chemically (partially) by the addition of PEI and HMDA, respectively. The gels were characterised by rheology to assess the level of crosslinking and by HR-SEM for morphology evaluation. The chemical composition of the foams was analysed by FTIR, and their water absorption capacity was determined. SANS and SAXS analysis were performed on the dried foams and saturated foams at different levels of drying.

Functionalised NC foam networks can absorb up to 132 times their own weight in liquid. Water diffusion inside the cellulose nanofibrils swells the constitutive fibre bundle up to 19.5 nm. NC-PEI crosslinking expands the foam structure, which results in higher fibre bundle swelling at the nanoscale (25 nm), but lower absorption capacity at the macroscale (71 g/g) compared to the pure NC foam. In contrast, NC-HMDA crosslinking creates a more compact foam. The NC-HDMA fibre bundle swelling was only 15 nm due to the restriction of migration of water into the more compact fibrous network.

The hydration-dehydration behaviour of NC foam shows the change of fibre bundle diameter during drying, confirming fibre bundle shrinkage from 19 nm to 14 nm upon drying. As drying progresses, the fibre bundle structure becomes more and more compact. After drying (air drying), the fibre bundle structure does not return to its original freeze-dried NC foam structure because of the different drying method.

Carboxylated nanocellulose foams have been prepared as superabsorbent in a previous study [27]. Crosslinking NC foams with PEI and HMDA can be used as a method to control and tailor the swelling capacity of NC foams. Cellulose nanofibre structure has been studied in dry and aqueous suspension [15,40]. However, previous studies did not explore the structural change of crosslinked NC foams nor the mechanism of hydration-dehydration. In this study, structural change was analysed in the context of swelling upon water absorption for crosslinked foam. Relating the fibre swelling capacity to the internal fibrous structure of a NC foam allows to engineer this material for specific and targeted food, agriculture, personal care and biomedical applications.

CRediT authorship contribution statement

Laila Hossain: Prepared samples, conducted all experiments and wrote manuscript. **Vikram Singh Raghuwanshi**: Performed SAXS and SANS experiments, data analysis and wrote manuscript. **Joanne Tanner**: Data analysis and wrote manuscript. **Chun-Ming Wu**: Performed SANS experiments. **Olga Kleinerman**: Performed cryo-SEM experiments. **Yachin Cohen**: Performed cryo-SEM experiments, data analysis and wrote manuscript. **Gil Garnier**: Performed data analysis and wrote manuscript.

Declaration of Competing Interest

The authors declare that they have no known competing financial interests or personal relationships that could have appeared to influence the work reported in this paper.

Acknowledgements

This work was supported by Food and Dairy Graduate Research Industry Partnership, Victorian Government, Monash University and Meat and Livestock Australia (MLA). The authors acknowledge the SAXS/WAXS beamline at the Australian Synchroton and BILBY SANS beamline at the Australian Nuclear Science and Technology Organisation (ANSTO). Electron microscopy preparations and imaging were done at the Technion Center for Electron Microscopy of Soft Matter, and we acknowledge Prof. Yeshayahu (Ishi) Talmon and Dr. Naama Koifman for their valuable assistance and discussions.

Appendix A. Supplementary material

Supplementary data to this article can be found online at https://doi.org/10.1016/j.jcis.2020.02.048.

References

[1] N. Astrini, L. Anah, A. Haryono, Crosslinking Parameter on the preparation of cellulose based hydrogel with divynilsulfone, Procedia Chem. 4 (2012) 275–281.
[2] X. Shen, J.L. Shamshina, P. Berton, G. Gurau, R.D. Rogers, Hydrogels based on cellulose and chitin: fabrication, properties, and applications, Green Chem. 18 (1) (2015) 53–75.
[3] N. Quennouz, S.M. Hashmi, H.S. Choi, J.W. Kim, C.O. Osuji, Rheology of cellulose nanofibrils in the presence of surfactants, Soft Matter 12 (1) (2016) 157–164.
[4] T. Saito, A. Isogai, TEMPO-mediated oxidation of native cellulose. The effect of oxidation conditions on chemical and crystal structures of the water-insoluble fractions, Biomacromolecules 5 (5) (2004) 1983.
[5] E. Abraham, B. Deepa, L. Pothan, M. Jacob, S. Thomas, U. Cvelbar, R. Anandjiwala, Extraction of nanocellulose fibrils from lignocellulosic fibres: A novel approach, Carbohydr. Polym. 86 (4) (2011) 1468–1475.
[6] A. Sannino, C. Demitri, M. Madaghiele, Biodegradable cellulose-based hydrogels: design and applications, Materials 2 (2) (2009) 353–373.
[7] M.N. Alam, L. Christopher, Natural cellulose-chitosan crosslinked superabsorbent hydrogels with superior swelling properties, ACS Sustainable Chem. Eng. 6 (7) (2018) 8736–8742.
[8] N. Reddy, Y. Yang, Citric acid cross-linking of starch films, Food Chem. 118 (3) (2010) 702–711.
[9] N.S. Capanema, A.A. Mansur, A.C. de Jesus, S.M. Carvalho, L.C. de Oliveira, H.S. Mansur, Superabsorbent crosslinked carboxymethyl cellulose-PEG hydrogels for potential wound dressing applications, Int. J. Biol. Macromol. 106 (2018) 1218–1234.
[10] M.N. Alam, M.S. Islam, L.P. Christopher, Sustainable production of cellulose-based hydrogels with superb absorbing potential in physiological saline, ACS Omega 4 (5) (2019) 9419–9426.
[11] F. Zhao, E. Repo, Y. Song, D. Yin, S.B. Hammouda, L. Chen, S. Kalliola, J. Tang, K.C. Tam, M. Sillanpää, Polyethylenimine-cross-linked cellulose nanocrystals for highly efficient recovery of rare earth elements from water and a mechanism study, Green Chem. 19 (20) (2017) 4816–4828.
[12] O. Boussif, F. Lezoualc'h, M.A. Zanta, M.D. Mergny, D. Scherman, B. Demeneix, J.-P. Behr, A versatile vector for gene and oligonucleotide transfer into cells in culture and in vivo: polyethylenimine, Proc. Natl. Acad. Sci. 92 (16) (1995) 7297–7301.

[13] U. Lungwitz, M. Breunig, T. Blunk, A. Göpferich, Polyethylenimine-based non-viral gene delivery systems, Eur. J. Pharm. Biopharm. 60 (2) (2005) 247–266.
[14] N. Lavoine, L. Bergström, Nanocellulose-based foams and aerogels: processing, properties, and applications, J. Mater. Chem. A 5 (31) (2017) 16105–16117.
[15] C. Antonini, T. Wu, T. Zimmermann, A. Kherbeche, M.-J. Thoraval, G. Nyström, T. Geiger, Ultra-porous nanocellulose foams: A facile and scalable fabrication approach, Nanomaterials 9 (8) (2019) 1142.
[16] S. Trombino, R. Cassano, E. Bloise, R. Muzzalupo, L. Tavano, N. Picci, Synthesis and antioxidant activity evaluation of a novel cellulose hydrogel containing trans-ferulic acid, Carbohydr. Polym. 75 (1) (2009) 184–188.
[17] O.M. Jensen, Water absorption of superabsorbent polymers in a cementitious environment, in: International RILEM Conference on Advances in Construction Materials Through Science and Engineering, RILEM Publications SARL, 2011, pp. 22–35.
[18] G. Kowalski, K. Kijowska, M. Witczak, Ł. Kuterasiński, M. Łukasiewicz, Synthesis and effect of structure on swelling properties of hydrogels based on high methylated pectin and acrylic polymers, Polymers 11 (1) (2019) 114.
[19] V.S. Raghuwanshi, G. Garnier, Characterisation of hydrogels: Linking the nano to the microscale, Adv. Colloid Interface Sci. 274 (2019) 102044.
[20] J. Liu, C. Zhang, D. Miao, S. Sui, F. Deng, C. Dong, L. Zhang, P. Zhu, Preparation and characterization of carboxymethylcellulose hydrogel fibers, J. Eng. Fibers Fabrics 13 (3) (2018). 155892501801300302.
[21] L. Mendoza, W. Batchelor, R.F. Tabor, G. Garnier, Gelation mechanism of cellulose nanofibre gels: A colloids and interfacial perspective, J. Colloid Interface Sci. 509 (2018) 39–46.
[22] Y. Mao, K. Liu, C. Zhan, L. Geng, B. Chu, B.S. Hsiao, Characterization of nanocellulose using small-angle neutron, X-ray, and dynamic light scattering techniques, J. Phys. Chem. B 121 (6) (2017) 1340–1351.
[23] J. Schmitt, V. Calabrese, M.A. Da Silva, S. Lindhoud, V. Alfredsson, J.L. Scott, K.J. Edler, TEMPO-oxidised cellulose nanofibrils; probing the mechanisms of gelation via small angle X-ray scattering, PCCP 20 (23) (2018) 16012–16020.
[24] S. Koizumi, Y. Tomita, T. Kondo, T. Hashimoto, What factors determine hierarchical structure of microbial cellulose-interplay among physics, chemistry and biology, in: Macromolecular symposia, Wiley Online Library, 2009, pp. 110–118.
[25] T. Saito, S. Kimura, Y. Nishiyama, A. Isogai, Cellulose nanofibers prepared by TEMPO-mediated oxidation of native cellulose, Biomacromolecules 8 (8) (2007) 2485.
[26] D. da Silva Perez, S. Montanari, M.R. Vignon, TEMPO-mediated oxidation of cellulose III, Biomacromolecules 4 (5) (2003) 1417–1425.
[27] L. Mendoza, L. Hossain, E. Downey, C. Scales, W. Batchelor, G. Garnier, Carboxylated nanocellulose foams as superabsorbents, J. Colloid Interface Sci. 538 (2019) 433–439.
[28] L. Issman, Y. Talmon, Cryo-SEM specimen preparation under controlled temperature and concentration conditions, J. Microsc. 246 (1) (2012) 60–69.
[29] N.M. Kirby, S.T. Mudie, A.M. Hawley, D.J. Cookson, H.D. Mertens, N. Cowieson, V. Samardzic-Boban, A low-background-intensity focusing small-angle X-ray scattering undulator beamline, J. Appl. Crystallogr. 46 (6) (2013) 1670–1680.
[30] O. Glatter, O. Kratky, Small Angle X-ray Scattering., Academic press., 1982.
[31] V.S. Raghuwanshi, M. Ochmann, A. Hoell, F. Polzer, K. Rademann, Deep eutectic solvents for the self-assembly of gold nanoparticles: a SAXS, UV–Vis, and TEM investigation, Langmuir 30 (21) (2014) 6038–6046.
[32] A.M. Castilla, E.R. Draper, M.C. Nolan, C. Brasnett, A. Seddon, L.L. Mears, N. Cowieson, D.J. Adams, Self-sorted oligophenylvinylene and perylene bisimide hydrogels, Sci. Rep. 7 (1) (2017) 8380.
[33] E. Anitas, Fractal fragmentation and small-angle scattering, in: Journal of Physics: Conference Series, IOP Publishing. 633(1) (2015) 012119.
[34] M. Shibayama, Small angle neutron scattering on gels, Soft Matter Charact. (2008) 783–832.
[35] J.C. Courtenay, S.M. Ramalhete, W.J. Skuze, R. Soni, Y.Z. Khimyak, K.J. Edler, J.L. Scott, Unravelling cationic cellulose nanofibril hydrogel structure: NMR spectroscopy and small angle neutron scattering analyses, Soft Matter 14 (2) (2018) 255–263.
[36] A.R. Klotz, DNA Polymer Physics in Complex Nanofluidic Environments. PhD thesis (McGill University, Montreal, Quebec), 2015.
[37] J. Gao, J. Liu, H. Peng, Y. Wang, S. Cheng, Z. Lei, Preparation of a low-cost and eco-friendly superabsorbent composite based on wheat bran and laterite for potential application in Chinese herbal medicine growth, R. Soc. Open Sci. 5 (5) (2018) 180007.
[38] M.I. Voronova, A.G. Zakharov, O.Y. Kuznetsov, O.V. Surov, The effect of drying technique of nanocellulose dispersions on properties of dried materials, Mater. Lett. 68 (2012) 164–167.
[39] L. Salmén, J.S. Stevanic, Effect of drying conditions on cellulose microfibril aggregation and "hornification", Cellulose 25 (11) (2018) 6333–6344.
[40] O. Nechyporchuk, M.N. Belgacem, F. Pignon, Concentration effect of TEMPO-oxidized nanofibrillated cellulose aqueous suspensions on the flow instabilities and small-angle X-ray scattering structural characterization, Cellulose 22 (4) (2015) 2197–2210.

Journal of Colloid and Interface Science 601 (2021) 124–132

Contents lists available at ScienceDirect

Journal of Colloid and Interface Science

journal homepage: www.elsevier.com/locate/jcis

Regular Article

Absorption kinetics of nanocellulose foams: Effect of ionic strength and surface charge

Laila Hossain, Emily Eastman, Monica De Rango, Vikram Singh Raghuwanshi, Joanne Tanner, Gil Garnier *

Bioresource Processing Research Institute of Australia (BioPRIA), Department of Chemical Engineering, Monash University, Clayton, VIC-3800, Australia

HIGHLIGHTS

- Nanocellulose foam absorption mechanism follows a three stages process.
- Absorption capacity is reduced as increases the ionic strength of the fluid.
- Foam structure homogeneity increases with fiber's surface charge.
- Absorption kinetics is tailored by controlling fiber's surface charge and foam pore size.

GRAPHICAL ABSTRACT

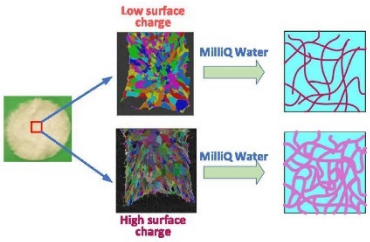

ARTICLE INFO

Article history:
Received 14 April 2021
Revised 13 May 2021
Accepted 15 May 2021
Available online 19 May 2021

Keywords:
Nanocellulose
Foam
Absorption
X-ray computed tomography
Structure
Wicking
Pore size

ABSTRACT

Hypothesis: The absorption capacity and kinetics of nanocellulose foams are controlled by the surface charge of the fibers, which affects swelling and determine the porosity and structure of the network.
Experiments: Absorption kinetics were quantified at time scales ranging from fractions of a second to minutes. The mass absorption rate as well as the area profile for the liquid stains were simultaneously measured.
Findings: The absorption profile followed a three-stage mechanism: wicking, transition and fiber swelling. Absorption of fluids differing in ionic strength revealed the critical role played by electrostatic forces. Nanocellulose foam absorption capacity is 25% higher for water than for 0.9 wt% NaCl solution. The absorption kinetics of nanocellulose foam are also tuneable by modulating the surface charge. High surface charge nanocellulose foams have slower absorption in water than their low surface charged analogues. This behaviour is driven by the lower pore sizes developed in high surface charge foams, as determined by X-ray CT. Small Angle X-ray Scattering revealed structural homogeneity of high surface charge foams upon absorption of water due to high fibrillation and fiber swelling.

1. Introduction

Superabsorbent polymers (SAPs) are three-dimensional, cross-linked, hydrophilic polymer networks capable of absorbing a large volume of water relative to their dry mass [1]. They are used extensively in personal hygiene products, diapers, agriculture, horticulture, biomedical applications, and food packaging [2,3]. However, most current commercial superabsorbents are based on sodium polyacrylate, a petrochemical-derived polymer which is non-degradable and non-renewable. Several renewable alternatives have been developed using cellulose, starch, gum, chitin and chitosan [4,5]. Among those, cellulose appears to be the most promising renewable SAPs feedstock due to its worldwide abundance, low cost and inherent biodegradability. Cellulose fiber production is also well known and established on a

* Corresponding author.
E-mail address: gil.garnier@monash.edu (G. Garnier).

https://doi.org/10.1016/j.jcis.2021.05.092
0021-9797/

commercial scale. Further processing of commercial cellulose fibers into carboxylated, nano-sized fibrils, followed by lyophilization, produces nanocellulose foams with superabsorbent properties [6,7].

Nanocellulose foam material is comprised of entangled fibers which create the pores. When in contact with water, these pores and fibers accommodate water. There are literatures on fluid absorption in paper like swelling media where absorption occurs by a combination of wicking and fiber swelling [8,9]. Wicking is the rapid flow of a fluid into the pores that exist between fibers, and is driven by capillary forces. This capillary action occurs when the cohesive force between the fluid molecules and the solid fiber surface is greater than the cohesive force between fluid molecules themselves. Fiber swelling occurs at a lower length scale and involves diffusion of the fluid through the fibers themselves. A difference in osmotic pressure between the fibers and the bulk solution in the foam pores provides the driving force for fiber swelling [10]. Swelling of fibers results in partial filling of the interfiber pore spaces and disruption of intrafiber hydrogen bonds between fibers, causing an overall expansion of the material [11].

Via the above mechanisms, nanocellulose foams can and do exhibit superabsorbent properties comparable to commercial SAPs. However, their absorption characteristics depend on a number of variables. For example, foams made with cellulose fibers that have residual associated lignin generally have a lower absorption capacity compared to analogous foams made with pure cellulose fibers due to the hydrophobic nature of lignin [12]. The ionic strength of the liquid to be absorbed can also affect absorption kinetics and capacity due to the influence of ionic strength of the bulk fluid on the osmotic pressure difference that controls fiber swelling. Other factors potentially affecting the superabsorbent properties of nanocellulose foams include the cellulose composition, cellulose surface charge, foam surface area, foam porosity, absorbate pH, absorbate temperature and absorbate composition [13].

There are many reports in the literature on the production of nanocellulose foams that claim or demonstrate superabsorbent properties [14–19]. Absorption kinetics have also been determined for various examples of nanocellulose foams at time scales ranging from minutes to days, depending on the saturation duration of the material under investigation [2,3,20]. However, no study has yet correlated or quantified the initial absorption rate or phases of the absorption mechanism with differences in either nanocellulose foam structure at the various critical length and time scales of interest, particularly for foams exhibiting rapid (second to minute-scale) absorption kinetics. Moreover, the effect of fiber surface charge and the absorbate solution ionic strength on nanocellulose-based SAPs absorption kinetics, both of which are critical to the tuning of these materials for specific applications, have not been rigorously quantified.

This study investigates the effect of the nanocellulose fiber surface charge on the structure, absorption kinetics, and absorption capacity of nanocellulose foams. Here we demonstrate for the first time that there are three distinct phases of absorption, and present the kinetics of these characteristic phases of fluid absorption in nanocellulose foams. The impact of the combination of different fiber surface charges and solution ionic strengths on this mechanism is also shown, using a 0.9 wt% NaCl solution, to represent the typical ionic strength of body fluids including blood, urine and sweat and demonstrate the suitability of these materials to replace petrochemical SAPs in common commercial applications

2. Experimental

2.1. Materials

Bleached Eucalyptus Kraft (BEK) pulp was used as supplied from Australian Paper, Maryvale. 2,2,6,6-Tetramethylpiperidine-1-oxyl (TEMPO), Hydrochloric acid (HCl), Sodium Periodate ($NaIO_4$), Sodium Hydroxide (NaOH) and Sodium Bromide (NaBr) were purchased from Sigma Aldrich. 12 w/v% Sodium Hypochlorite (NaClO) was bought from Thermo Fischer Scientific and used as supplied. Hydrochloric acid (HCl) and Sodium Hydroxide (NaOH) diluted for solutions as required.

2.2. Methods

2.2.1. TEMPO-mediated oxidation

The TEMPO-mediated oxidation process employed to produce low surface charged fibers was based on a previously developed method [21]. 100 g BEK pulp (dry weight basis) was suspended in 2500 mL water containing 0.4 g TEMPO and 2.5 g NaBr. The 12 w/v% NaClO solution was initially adjusted to pH 10 via addition of 36 w/v% HCl. 100 mL NaClO was added drop-wise to the suspension whilst stirring. The pH of the reaction was maintained at 10 through the addition of 0.5 M NaOH. The oxidation process was deemed to be complete when the pH change was negligible. The oxidized fibers were washed and vacuum filtered until neutral pH was achieved and stored at 4 °C. This preparation method produces oxidized fiber with a surface charge of 1.3 mmol carboxylate (COO^-) groups per gram fiber. Fiber produced by this method and foams produced from this fiber are referred to as low surface charge (LSC) in this work. The TEMPO-oxidized pulp was then dispersed in deionized water at a desired concentration. Fibrillation and hydrogel formation were accomplished through a high-pressure homogeniser at 1000 bar with two passes. Nanocellulose foams were prepared by spreading 30 g of gel in a 50 mm petri dish and freezing at −80 °C for 4 h. Once frozen, all samples were freeze-dried for 48 h.

2.2.2. One-shot TEMPO-periodate oxidation

The one-shot TEMPO-periodate oxidation process employed to produce high surface charged fibers was based on a previously developed method [22]. 25 g (dry weight basis) of BEK pulp were suspended in 1200 mL distilled water with 20 g NaBr, 13.5 g $NaIO_4$, and 2 g TEMPO. The outside of the reaction vessel was covered with aluminum foil to prevent photoinduced decomposition of periodate. 120 mL NaClO (12% v/v, pH adjusted to 10.5) was added dropwise under constant stirring. The pH of the reaction was maintained at 10.5 by adding 0.5 M NaOH. After 4 h, the oxidation reaction was stopped by quenching with 10 mL ethanol. The water-insoluble fraction was recovered by vacuum filtration and washed several times with distilled water until a neutral pH in the filtrate stream was achieved. The fibers were then freeze-dried for 48 h. This preparation method produces oxidized fiber with a surface charge of 1.89 mmol carboxylate (COO^-) groups per gram fiber. Fiber produced by this method and foams produced from this fiber are referred to as high surface charge (HSC) in this work.

2.2.3. Determination of solids concentration

The solids concentration of sample (i.e. hydrogel or pulp) was determined through oven drying using a previously developed method [13]. The initial weight (w_i) was recorded before the sample was placed in a ventilated oven at 105 °C for at least 4 h and the sample dried to a constant final weight, w_f. The solids content was determined by:

$$Solids\ content(\%) = \frac{w_f - w_i}{w_i} \times 100\% \quad (1)$$

2.2.4. Determination of carboxylate content

The carboxylate content of the nanocellulose fiber was determined via conductimetric titration using a previously developed method [13]. 0.2 g dry oxidized pulp was suspended in 40 mL deionized water. The sample pH was then lowered to pH 2.5–3 by adding 0.5 M HCl to ensure protonation of all carboxylate groups prior to the beginning of titration. Sample titration was initiated by the addition of 0.1 mL/min 0.1 M NaOH (Mettler Toledo T5 Titrator). The conductivity was monitored throughout the progress of the titration. The amount of carboxylate groups was calculated by:

$$Carboxylatecontent\left(\frac{mmol}{g}\right) = \frac{c(V_2 - V_1)}{w} \times 1000 \quad (2)$$

where the difference in V_2 and V_1 reflects the required amount, in litres, of titrant required to neutralize the carboxylic groups (plateau region of the titration curve), c is the NaOH concentration (mol/L), and w is the dry sample weight (g).

2.2.5. Micro-CT analysis

Micro-CT scanning was performed with a Phoenix Nanotom m (GE Sensing & Inspection Technologies GmbH, Wunstorf, Germany) operated using xs control and Phoenix datos|x acquisition software (both GE Sensing & Inspection Technologies).

Foam specimens were mounted on glass rods using a drop of hot glue to at base. The x-ray energy (20 kV and 400 μA) of scans and integration time for x-ray projections (2 s) was optimized to enhance contrast in the foam specimens, which exhibited a very low density relative to the surrounding air. Scans were run at a resolution of 8 μm collecting 1200 projections over a 125-minute period. Volume reconstruction of the micro-CT data was performed using Phoenix datos|x reconstruction software (GE Sensing & Inspection Technologies) applying a median filter and ROI filter during reconstruction. The data was exported as 16-bit volume files for analysis.

Analysis of reconstructed data was conducted using Avizo (Thermo Fisher Scientific). The foam structure was segmented using an interactive threshold and a sample mask created by closing and filling the structure. An inversion of the foam structure within the mask represents the pore space between the foam structure. The segmented volume and volume fraction of foam and pore space was then determined relative to the sample mask. Individual pores were segmented and the pore size distribution produced by labelling and separating the segmented pore space using a Chamfer algorithm, which is based on a watershed analysis of the data.

2.2.6. Absorption kinetics

The nanocellulose foam to be tested was cut into 2 cm × 2 cm samples using a laser cutter (EPILOG Laser). The edge of a sample was attached to a metal rod with superglue. The minimum amount of glue required to attach the sample to the rod was used to minimize interference with absorption experiments since the glue is hydrophobic. The rod with sample attached was hung from the hook on the bottom of a balance, so the nanocellulose foam sample was hanging above a reservoir of either deionized water or 0.9% NaCl solution on a height-adjustable stage. The balance was connected to a laptop via LabX Direct Balance Software to record the weight of the sample at specified time intervals. Three drops of food dye were mixed through the absorbate to provide greater contrast for image analysis. Care was taken to ensure the edge of the sample was parallel to the fluid surface so the entire edge will contact the fluid at the same time. This experimental set-up is shown in Fig. 1.

The pre-weighed sample was slowly lowered by adjusting the reservoir stage height. Care was taken to ensure that both the sample and the absorbate surface remained stationary while moving the stage. Once the edge of the sample was just touching the surface of the absorbate, height adjustment of the stage was stopped. After 5 min, the stage was moved downwards so that the sample was no longer touching the absorbate and the final weight of the saturated sample was recorded. This final weight was divided by the dry weight of the sample to give the weight of absorbate taken up per gram of dry nanocellulose sample.

This experiment was conducted in triplicate with 0.9% NaCl solution and in triplicate with water for vertical orientation of the sample in a controlled environment of 23 °C and 50% relative humidity. A video camera (FLIR Systems, Model: FL3-U3-13E4C-C: 1.3 MP, 60 FPS, e2v EV76C560, Color) was installed to capture images of each absorption trial. The images were converted to binary (black and white) in MATLAB, and the stained area of the sample in the image was used to calculate the area of absorption of the sample.

The results are reported as the average and standard deviation of the calculated absorption areas of the three replicates for each absorbate. The effects of buoyancy and surface tension have not been considered in this study.

2.2.7. Small angle X-ray scattering (SAXS)

Small angle X-ray Scattering (SAXS) experiments were conducted at the SAXS/WAXS beamline of the Australian Synchrotron with the assistance of Beamline Scientist Nigel Kirby. An X-ray energy of 12 KeV was used, and the samples were measured in the transmission mode. A 2D Pilatus detector was placed at the long distance of 7 m from the sample to cover a large size range. During measurements samples were first measured in the dried state and later measured as fully wetted with MilliQ water or 0.9% NaCl solution. A glassy carbon and silver behenate standards were used for the calibration. The in-house developed software Scatterbrain was used for data reduction and plotting of the 2D images.

3. Results

The absorption kinetics is measured in increments of 0.1 s for five minutes for nanocellulose foams made from fibers of two different surface charges of 1.3 mmol COO^-/g fiber and 1.89 mmol COO^-/g fiber produced from TEMPO and TEMPO-periodate oxidation, respectively. These foams are used separately to absorb MilliQ water and a saline solution (0.9 wt% NaCl). Continuous online image capturing and analysis are performed to quantify the absorption phases at complementary time scales.

3.1. Effect of liquid ionic strength

Fig. 2 illustrates the absorption profile of low surface charge (LSC) nanocellulose foam for MilliQ water and 0.9 wt% NaCl solution to quantify the effect of ionic absorbates on the absorption kinetics. The nanocellulose foam has a larger absorption capacity in water than in saline solution (Fig. 2). After 5 min, nanocellulose foam absorbed 81 g/g of MilliQ water versus 65 g/g for the NaCl solution. The initial kinetics of nanocellulose foam absorption were measured from the first 10 s (inset of Fig. 2). After 1 s, the difference in the amount of fluid absorbed is already significant, with 53 g/g of MilliQ water and 38 g/g of NaCl solution. Absorption of NaCl solution appears to be lower than that of MilliQ water due to Na^+ shielding the COO^- groups of the nanocellulose foam,

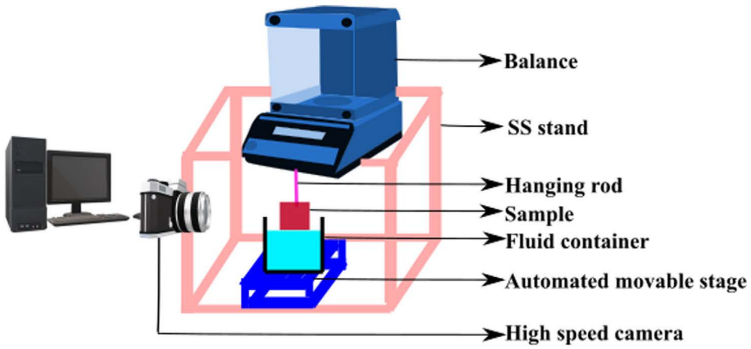

Fig. 1. Schematic diagram of the testing system to measure simultaneously the absorption kinetics of NC foam as well as the area of the liquid stain.

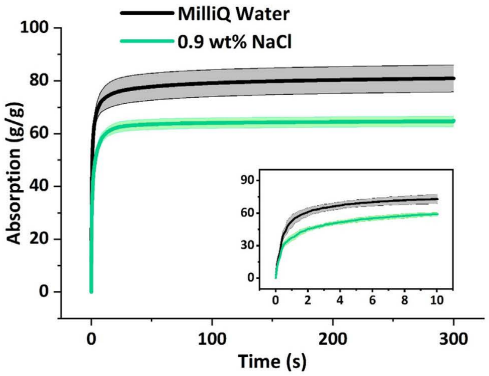

Fig. 2. Effect of liquid ionic strength on LSC nanocellulose foam absorption kinetics over a period of 5 min for MilliQ water and 0.9 wt% NaCl. The inset shows the effect of ionic strength over 10 s. The solid line represents the average result (n = 3), while the shaded zone indicates the range formed by one standard deviation.

decreasing its hydrophilicity and reducing the absorption capacity [23].

3.2. Effect of fiber surface charge

The impact of fiber surface charge on the absorption behavior of nanocellulose foam is measured using foams of two different charge densities: 1.3 mmol COO^-/g (low surface charge, LSC) and 1.89 mmol COO^-/g (high surface charge, HSC). The dimensions of these two different fibers are provided in Table 1. The high surface charge fibers are shorter and slightly thinner than the low surface charge fibers.

The effect of nanocellulose surface charge on absorption kinetics was assessed. Fig. 3 shows the absorption profiles of LSC and HSC foams for MilliQ water and 0.9 wt% NaCl at different time scales. HSC foam has a slower absorption kinetics than LSC at the short time scales (inset of Fig. 3A), but displays a slightly higher overall absorption capacity after 5 min (Fig. 3A).

Table 1
Effect of oxidation on fiber dimension and charge [24].

Type of nanocellulose foam	Surface charge (mmol/g)	Fiber length (μm) × dia (nm)
TEMPO oxidized nanocellulose foam (LSC)	1.30	(>1) × (>5)
TEMPO-periodate oxidized nanocellulose foam (HSC)	1.89	(0.5) × (2–4)

SAXS scattering of the nanocellulose foams in their dry and wet forms was measured (Fig. 4). For the LSC foam, there are sharp boundaries due to aggregated fibers found under both dry and wet conditions. This means some structural heterogeneity caused by a lower fibrillation and lower fiber swelling in the dry and wet state, respectively. However, the HSC wet foam in MilliQ water does not show these sharp boundaries. The HSC foam has higher inter-fiber repulsion which results in a higher fibrillation as evidenced from the lower fiber diameter measured (Table 1). This higher fibrillation together with high fiber swelling lead to the structural homogeneity observed for the HSC samples in MilliQ water. However, when HSC foam is wetted with a saline solution, some sharp boundaries from aggregated fibers are formed. This indicates a reduced charge repulsion and fiber swelling due to the high ionic strength of the absorbate.

3.3. Structural analysis by micro CT

Structural analysis of the nanocellulose foam samples was performed by X-ray Computed Tomography (CT). The three-dimensional separated pores for both LSC and HSC are shown in the videos provided in the supplementary section (V1_LSC and V2_HSC). Fig. 5 shows the 3D structures of the nanocellulose foams, the separated pore structure of the foams in the X-Z plane, and their pore size distributions. The HSC foam shows smaller pores than the LSC foam (Fig. 5E and F). The HSC foam has a higher frequency (~9000) of the smallest pore volumes ($2 \times 10^{-5} - 1 \times 10^{-1}$ mm^3) compared to the LSC foam (~2000). The HSC foam is more homogeneous and denser, as shown by the 3D structure (Fig. 5 A-B), due to the smaller pore volumes relative to the LSC foam. The LSC has a wider range of pore size distribution, contributing to structural heterogeneity.

4. Discussion

4.1. Absorption mechanism of nanocellulose foam

The liquid absorption profiles of nanocellulose foams follow an exponential plateau relationship with time and demonstrate the three stages of absorption in nanocellulose foams: wicking, transition phase and fiber swelling. In this work, wicking corresponds well with the period of increasing absorption area as determined

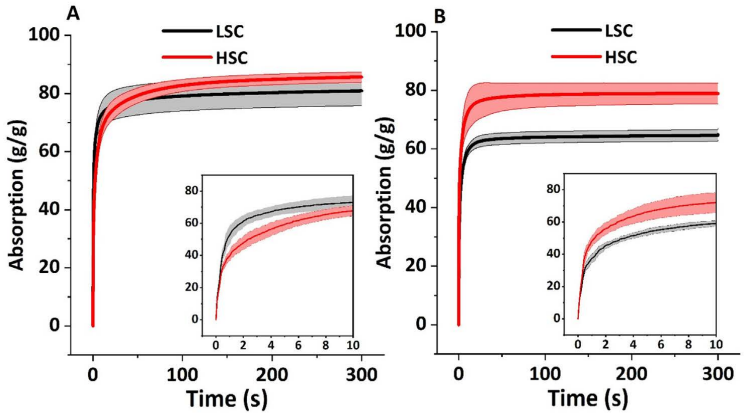

Fig. 3. Effect of low and high fiber surface charge on the absorption kinetics after 5 min for: (A) MilliQ water and (B) 0.9 wt% NaCl. The insets show the magnified graphs over a 10 s period. The solid line represents the average (n = 3), while the shaded zone indicates the range formed by one standard deviation.

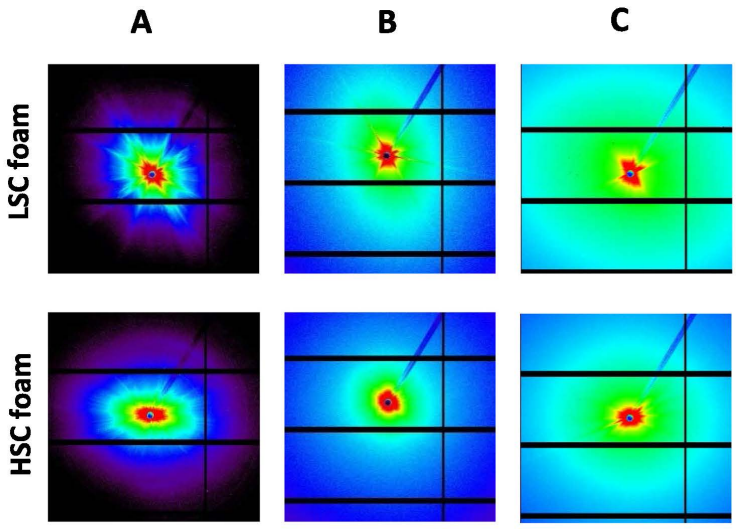

Fig. 4. SAXS measurements of LSC and HSC nanocellulose foams. (A) Dry foam and wet foam in (B) MilliQ water, and (C) 0.9 wt% NaCl. The first row represents the LSC foam while the second row is for HSC foams.

by image analysis, and fiber swelling is dominant when absorption continues to increase although the liquid stain area remains constant. Fig. 6 shows the three different phases of the absorption phenomena by following the size of the liquid stain: wicking (0 to 0.7 s- Phase I); transition (0.7 to 3.8 s- Phase II) and fiber swelling (from 3.8 s- Phase III).

Fluid accommodated by Phase I has been correlated to pore volume in Table 2. The fluid absorbed in phase I of Fig. 3 mainly results from the absorption capacity driven by the pore volume.

Wicking is driven by capillary forces [25] and is mainly characterized by a high initial absorption rate. The inset of Fig. 6 shows that the wicking height is proportional to the square root of time for Phase I, following the Lucas- Washburn equation. As absorption progresses and fiber swelling begins to reduce the dimensions of the inter-fiber pore spaces [26], wicking becomes limited and the transport of liquid through the nanocellulose foam structure relies increasingly on diffusion (Phase III) over capillary action following the transition phase (Phase II) [9]. This results in a reduction in the rate of absorption as seen by the decreasing slope which signals the onset of the transition phase (Phase II).

4.2. Effect of ionic strength on absorption

The nanocellulose foam absorption capacity for the 0.9 wt% NaCl solution is lower than for MilliQ water (Fig. 2). This corroborates the findings of Sultana et al. for different SAPs [10]. The nanocellulose foam contains free mobile ions in its structure that exert an osmotic pressure on the fiber network. A difference in

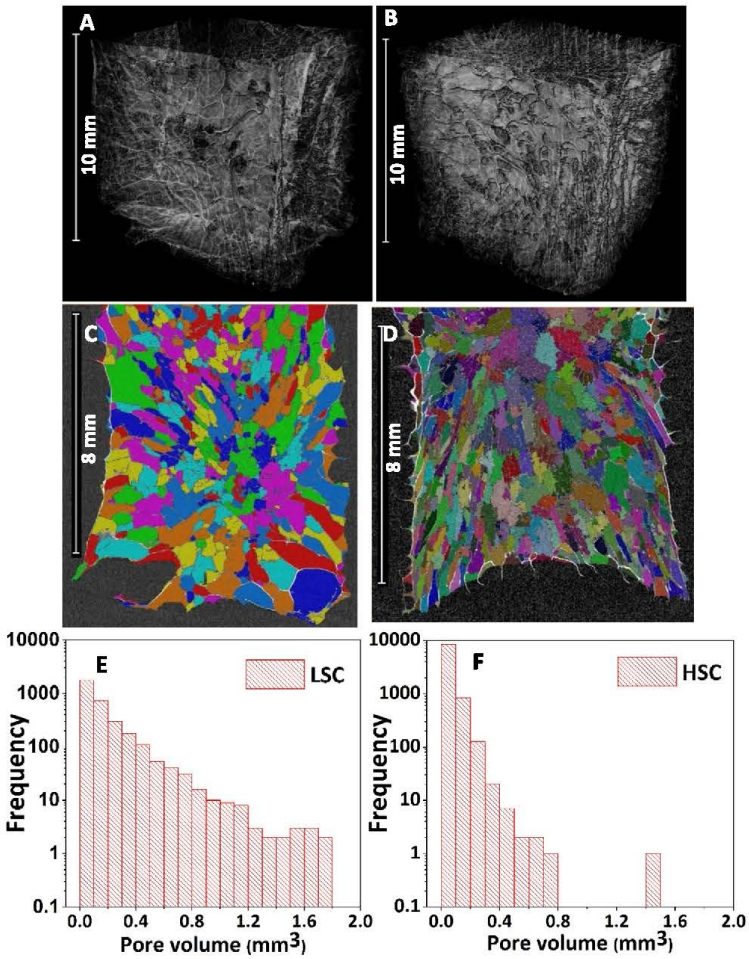

Fig. 5. Structural analysis of nanocellulose foams by X-ray tomography. 3D structure of: (A) LSC foam, (B) HSC foam; XZ planar slice showing separated pore structure of (C) LSC foam, and (D) HSC foam; pore size distribution of (E) LSC and (F) HSC foam.

osmotic pressure between the fiber network and the absorbate creates a driving force for absorption to occur [27]. Addition of salt to the absorbate reduces the osmotic pressure difference and hence reduces the driving force for absorption. The lower absorption capacity in 0.9 wt% NaCl solution than in MilliQ water is also a consequence of charge shielding as increasing the concentration of free ions in the absorbate reduces the interaction of the nanocellulose carboxylate (COO^-) groups with water molecules, therefore decreasing their affinity and absorption propensity [13].

4.3. Effect of surface charge on absorption

4.3.1. Deionised water

The high surface charge foam exhibits slower absorption kinetics than low surface charge foam for MilliQ water. From the absorption experiments, LSC foam achieved 80% of its total absorption capacity within the first 3 s whereas HSC foam only reached 62% in the same time period (Fig. 3A). Similarly, after 30 min of free swelling, LSC foam had achieved 75% of its saturation capacity compared to 66% for HSC foam for MilliQ water (Supplementary Info S1). Image analysis of the liquid stain confirms the slower kinetics of the HSC foam compared to the LSC (Fig. 7A). The slower absorption kinetics and higher saturation capacity indicate that a major part of the absorption capacity of HSC foam results from fiber swelling. The osmotic pressure is increased in HSC foam due to an augmented charge density which facilitates higher fiber swelling in HSC foam compared to LSC foam [28–30].

The slower absorption kinetic of the HSC foam is due to its lower pore size compared to the LSC foam. The HSC foam also has a higher surface charge which improves the efficiency and therefore the extent of fibrillation due to greater electrical repulsion combined with lower hydrogen bonding [24].Thus, HSC foam porosity is lower than that of the LSC foam [31]. As flow resistance from small pores decelerates wicking [32], LSC foams exhibit a higher rate of initial absorption compared to HSC foams.

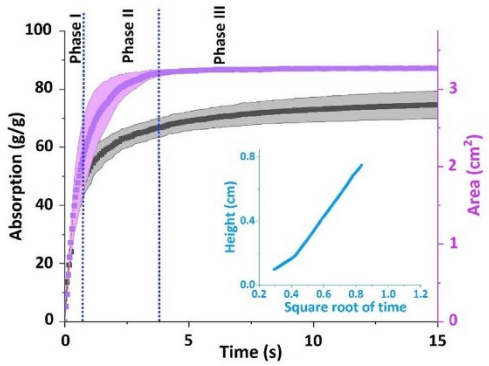

Fig. 6. Effect of wicking and fiber swelling in nanocellulose foam. The black line indicates absorption and the purple represents the area data. The inset shows the relationship between wicking height and time for phase I. The solid line is the average (n = 3), while the shaded zone indicates the range formed by one standard deviation. (For interpretation of the references to color in this figure legend, the reader is referred to the web version of this article.)

4.3.2. 0.9 wt% saline solution

HSC foam exhibits similar absorption kinetics but higher absorption capacity than LSC foam when absorbing a NaCl solution (Fig. 3B). Image analysis confirms that HSC and LSC foams have similar wicking kinetics in a NaCl solution (Fig. 7B). However, the absorption capacity of HSC is higher (Fig. 3B) which means fibre swelling is higher for HSC foam compared to that of LSC for NaCl solution.

5. Conclusion

Nanocellulose based foams are attractive because of their inherent renewability and biodegradability [33]. Nanocellulose foam with different solid concentrations and surface charges have already been developed [13,24]. The swelling of natural polymers, cellulose films and superabsorbents has been previously analysed as a function of pH and ionic strength [28,34–37]. However, the absorption kinetics, the mechanism and the absorption phases for a fast-swelling foam/superabsorbent have not been reported. In this study, the absorption kinetics of superabsorbent nanocellulose foams varying in charge density (controlled with the COO^- concentration) are measured for MilliQ water and 0.9 wt% NaCl solution and the results interpreted in terms of foam structure and absorption mechanism. The absorption kinetics is measured at time frames ranging from a fraction of a second to a few minutes to elucidate the full absorption mechanism and correlate it with foam structure and porosity.

Kinetics and wicking area data both confirm the occurrence of three distinct stages of absorption. These are: 1) wicking, 2) transition and 3) fiber swelling. Wicking is driven by capillary forces and dominates in the first few seconds of absorption. The wicking rate of nanocellulose foams for MilliQ water depends on pore size, as

Table 2
Analysis of pore volume and fluid accommodated by pore volume of the NC foams.

Parameter		Volumetric pore density (mm^3/mm^3)	Fluid accommodated by pore volume (g/g foam)	Fluid absorbed in phase I (g/g foam)	Percentage of fluid accommodated by pore volume after 5 mins absorption
LSC	MilliQ	0.88	42.7	46.8	52.8
	Saline			41.4	65.8
HSC	MilliQ	0.76	35.8	36.2	41.8
	Saline			34.1	45.3

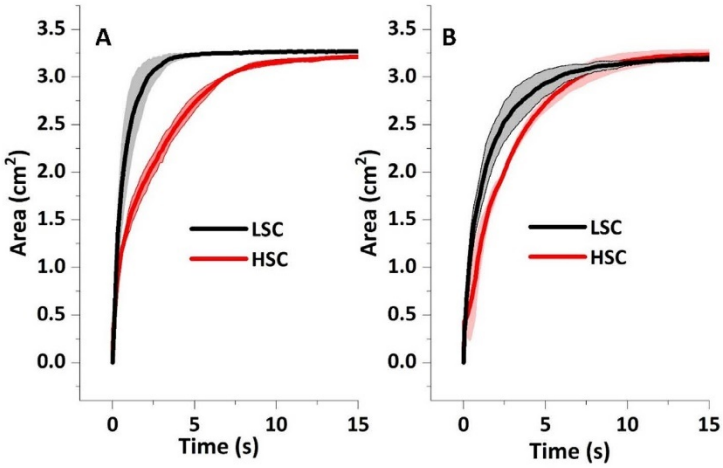

Fig. 7. Effect of surface charge on the stain area of the absorbed fluid over time for LSC and HSC NC foams, for (A) Milli Q water and (B) 0.9 wt% NaCl. The solid line is the average (n = 3), while the shaded zone indicates the range formed by one standard deviation.

evidenced from X-ray computed tomography, with higher rates for foams with larger pore sizes. Wicking is followed by the transition phase, after which fiber swelling dominates the absorption mechanism. A high surface charge (density of COO^- groups) increases fiber swelling [38], which is a slower mechanism than wicking. The slower absorption kinetics of high surface charge fiber foam are therefore due to both smaller pore size and higher concentration of COO^- groups. When absorbing an ionic solution, fiber swelling is reduced due to charge shielding and, as a result, the maximum absorption capacity of nanocellulose foam is decreased. Small Angle X-ray Scattering analysis corroborates this hypothesis by revealing the occurrence of fiber agglomeration in both high and low surface charge nanocellulose foams for the absorption of NaCl solution.

This fundamental absorption study aims to elucidate the initial absorption mechanism of nanocellulose foam. Using these results, performant biosourced and sustainable nanocellulose foams with the desired structure and absorption kinetics can be engineered. These foams can meet the stringent standards and performance criteria for applications such as baby diapers, personal hygiene products or biosensors, and represent a sustainable alternative to petrochemical-based superabsorbent polymers.

CRediT authorship contribution statement

Laila Hossain: Conceptualization, Visualization, Methodology, Investigation, Software, Writing-Original Draft. **Emily Eastman:** Investigation, Softwar. **Monica De Rango:** Investigation, Software. **Vikram Singh Raghuwanshi:** Investigation, Software, Writing-Review & Editing. **Joanne Tanner:** Supervision, Writing- Review & Editing. **Gil Garnier:** Visualization, Supervision, Writing- Review & Editing.

Declaration of Competing Interest

The authors declare that they have no known competing financial interests or personal relationships that could have appeared to influence the work reported in this paper.

Acknowledgment

Financial support was received from Meat and Livestock Australia (MLA) [grant number P.PSH.0890]. The authors acknowledge Stephen Mudie, Nigel Kirby from the SAXS/WAXS beamline at the Australian Synchrotron for the SAXS measurement. Moreover, authors acknowledge ANSTO for the beamtime. The authors also thank Micro-Computed Tomography facilities in University of Melbourne. And thanks to David Mendoza for providing the tempo-periodate oxidized fiber.

Appendix A. Supplementary material

Supplementary data to this article can be found online at https://doi.org/10.1016/j.jcis.2021.05.092.

References

[1] M.J. Zohuriaan-Mehr, K. Kabiri, Superabsorbent polymer materials: a review, Iranian Polymer Journal 17 (6) (2008) 451.
[2] R.M. Barajas-Ledesma, A.F. Patti, V.N. Wong, V.S. Raghuwanshi, G. Garnier, Engineering nanocellulose superabsorbent structure by controlling the drying rate, Colloids Surf. A: Physicochem. Eng. Aspects 600 (2020) 124943.
[3] A. Sawut, M. Yimit, W. Sun, I. Nurulla, Photopolymerisation and characterization of maleylatedcellulose-g-poly (acrylic acid) superabsorbent polymer, Carbohydr. Polym. 101 (2014) 231–239.
[4] M.N. Alam, L. Christopher, Natural Cellulose-Chitosan Crosslinked Superabsorbent Hydrogels with Superior Swelling Properties, ACS Sustain. Chem. Eng. 6 (7) (2018) 8736–8742.
[5] M.I.H. Mondal, Cellulose-based superabsorbent hydrogels, Basel:Springer (2019).
[6] Y. Zhang, T. Nypelö, C. Salas, J. Arboleda, I.C. Hoeger, O.J. Rojas, Cellulose nanofibrils, J. Renewable Mater. 1 (3) (2013) 195–211.
[7] K.J. De France, T. Hoare, E.D. Cranston, Review of hydrogels and aerogels containing nanocellulose, Chem. Mater. 29 (11) (2017) 4609–4631.
[8] L. Soriano, M. Rahman, Wicking Properties of Brassica Fiber in Three Different Growth Stages.(2016).
[9] S. Akinli-Kocak, The influence of fiber swelling on paper wetting.Electronic Theses and Dissertations, 253. (2001).
[10] S. Sultana, M.S. Rahaman, S.M.M. Hasnine, Effect of Salinity on swelling behaviors of superwater absorbent hydrogel prepared from carboxymethyl cellulose/acrylamide blends by gamma radiation, Am. J. Appl. Ind. Chem. 2 (2) (2018) 20–26.
[11] D.R. Schuchard, J.C. Berg, Liquid transport in composite cellulose—superabsorbent fiber networks, Wood Fiber Sci. 23 (3) (2007) 342–357.
[12] M.A. Hubbe, A. Ayoub, J. Daystar, R. Venditti, J. Pawlak, Enhanced absorbent products incorporating cellulose and its derivatives: a review, BioResources. (2013) 6556.
[13] L. Mendoza, L. Hossain, E. Downey, C. Scales, W. Batchelor, G. Garnier, Carboxylated nanocellulose foams as superabsorbents, J. Colloid Interface Sci. 538 (2019) 433–439.
[14] S.R.D. Petroudy, J. Ranjbar, E.R. Garmaroody, Eco-friendly superabsorbent polymers based on carboxymethyl cellulose strengthened by TEMPO-mediated oxidation wheat straw cellulose nanofiber, Carbohydr. Polym. 197 (2018) 565–575.
[15] F. Nnadi, C. Brave, Environmentally friendly superabsorbent polymers for water conservation in agricultural lands, J. Soil Sci. Environ. Manage. 2 (7) (2011) 206–211.
[16] J. Patiño-Masó, F. Serra-Parareda, Q. Tarrés, P. Mutjé, F.X. Espinach, M. Delgado-Aguilar, TEMPO-oxidized cellulose nanofibers: a potential bio-based superabsorbent for diaper production, Nanomaterials 9 (9) (2019) 1271.
[17] C. Demitri, R. Del Sole, F. Scalera, A. Sannino, G. Vasapollo, A. Maffezzoli, L. Ambrosio, L. Nicolais, Novel superabsorbent cellulose-based hydrogels crosslinked with citric acid, J. Appl. Polym. Sci. 110 (4) (2008) 2453–2460.
[18] P.W. Brodin, H. Theliander, Absorbent materials based on kraft pulp: Preparation and material characterization, BioResources 7 (2) (2012) 1666–1686.
[19] F.W. Brodin, Y. Sonavane, H. Theliander, Preparation of absorbent foam based on softwood kraft pulp: advancing from gram to kilogram scale, BioResources 8 (2) (2013) 2099–2117.
[20] A. Olad, F. Doustdar, H. Gharekhani, Fabrication and characterization of a starch-based superabsorbent hydrogel composite reinforced with cellulose nanocrystals from potato peel waste, Colloids Surf., A 601 (2020) 124962.
[21] T. Saito, S. Kimura, Y. Nishiyama, A. Isogai, Cellulose nanofibers prepared by TEMPO-mediated oxidation of native cellulose, Biomacromolecules 8 (8) (2007) 2485–2491.
[22] D.J. Mendoza, C. Browne, V.S. Raghuwanshi, G.P. Simon, G. Garnier, One-shot TEMPO-periodate oxidation of native cellulose, Carbohydr. Polym. 226 (2019) 115292.
[23] T. Fekete, J. Borsa, E. Takács, L. Wojnárovits, Synthesis of carboxymethylcellulose/starch superabsorbent hydrogels by gamma-irradiation, Chem. Cent. J. 11 (1) (2017) 46.
[24] D.J. Mendoza, L. Hossain, C. Browne, V.S. Raghuwanshi, G.P. Simon, G. Garnier, Controlling the transparency and rheology of nanocellulose gels with the extent of carboxylation, Carbohydr. Polym. 245 (2020) 116566.
[25] Z. Liu, X. He, J. Han, X. Zhang, F. Li, A. Li, Z. Qu, F. Xu, Liquid wicking behavior in paper-like materials: mathematical models and their emerging biomedical applications, Microfluid Nanofluid 22 (11) (2018) 132.
[26] A. Patnaik, R.S. Rengasamy, V.K. Kothari, A. Ghosh, Wetting and Wicking in Fibrous Materials, Text. Prog. 38 (1) (2006) 1–105.
[27] M. Elliott, Superabsorbent polymers. Product development scentist for SAP. BASF Aktiengesellschaft ss, 13 2004.
[28] S. Fält, L. Wågberg, E.-L. Vesterlind, Swelling of model films of cellulose having different charge densities and comparison to the swelling behavior of corresponding fibers, Langmuir 19 (19) (2003) 7895–7903.
[29] S. Hanhikoski, I. Solala, P. Lahtinen, K. Niemelä, T. Vuorinen, Fibrillation and characterization of lignin-containing neutral sulphite (NS) pulps rich in hemicelluloses and anionic charge, Cellulose (2020).
[30] F.L. Buchholz, A.T. Graham, Modern superabsorbent polymer technology. Wiley & Sons, Inc, 605 Third Ave, New York, NY 10016, USA, 1998. 279.1998.
[31] M. Wakabayashi, S. Fujisawa, T. Saito, A. Isogai, Nanocellulose film properties tunable by controlling degree of fibrillation of TEMPO-oxidized cellulose, Front. Chem. 37 (8) (2020).
[32] S. Ahmed, M.-P.N. Bui, A. Abbas, Paper-based chemical and biological sensors: engineering aspects, Biosens Bioelectron. 77 (2016) 249–263.
[33] D. Klemm, E.D. Cranston, D. Fischer, M. Gama, S.A. Kedzior, D. Kralisch, F. Kramer, T. Kondo, T. Lindström, S. Nietzsche, Nanocellulose as a natural source for groundbreaking applications in materials science: Today's state, Mater. Today 21 (7) (2018) 720–748.
[34] K. Kabiri, M. Zohuriaan-Mehr, Superabsorbent hydrogel composites, Polym. Adv. Technol. 14 (6) (2003) 438–444.
[35] G.F. de Lima, A.G. de Souza, D.d.S. Rosa, Nanocellulose as reinforcement in carboxymethylcellulose superabsorbent nanocomposite hydrogels, Macromol. Symp. 394 (1) (2020) 2000126. Wiley Online Library.

APPENDIX III
CO-AUTHORED PUBLICATIONS NOT INCLUDED IN THE THESIS

THIS PAGE WAS INTENTIONALLY LEFT BLANK

Polymer 222 (2021) 123643

Contents lists available at ScienceDirect

Polymer

journal homepage: http://www.elsevier.com/locate/polymer

Engineering laminated paper for SARS-CoV-2 medical gowns

Laila Hossain [a,b,1], Maisha Maliha [a,b,1], Ruth Barajas-Ledesma [a,b,1], Jinhee Kim [b], Kevin Putera [b], Dinesh Subedi [c], Joanne Tanner [a,b], Jeremy J. Barr [c], Mark M. Banaszak Holl [b], Gil Garnier [a,b,*]

[a] Bioresource Processing Research Institute of Australia (BioPRIA), Australia
[b] Department of Chemical Engineering, Monash University, VIC, 3800, Australia
[c] School of Biological Sciences, Monash University, VIC, 3800, Australia

ARTICLE INFO

Keywords:
Medical gown
Virus protection
Barrier material
PE laminated Paper
COVID-19
Coating morphology

ABSTRACT

The COVID-19 pandemic has highlighted the need for diversity in the market and alternative materials for personal protective equipment (PPE). Paper has high coatability for tunable barrier performance, and an agile production process, making it a potential substitute for polyolefin-derived PPE materials. Bleached and newsprint papers were laminated with polyethylene (PE) coatings of different thicknesses, and characterised for their potential use as medical gowns for healthcare workers and COVID-19 patients. Thicker PE lamination improved coating homogeneity and water vapour resistance. 49 GSM bleached paper with 16 GSM PE coating showed high tensile and seam strength, and low water vapour transmission rate (WVTR). Phi-X174 bacteriophage testing revealed that paper laminated with 15 GSM coating hinders virus penetration. This research demonstrates that PE laminated paper is a promising material for low cost viral protective gowns.

1. Introduction

In March 2020, the World Health Organisation declared the outbreak of COVID-19 to be a global pandemic. The highly infectious nature of the virus SARS-CoV-2, which causes COVID-19, has made the prevention of person-to-person transmission a critical mechanism to halt the spread of the disease. The use of personal protective equipment (PPE) is therefore vitally important [1]. Without appropriate protection from exposure to the SARS-CoV-2 virus, front-line health care workers are at great personal risk, and represent a critical transmission link to other patients and their families [2]. The rapid spread of COVID-19 and the consequential increase in demand for PPE has resulted in significant worldwide PPE shortages, including medical gowns.

Medical gowns are designed to prevent the transmission of pathogens to the wearer from an infected patient's body fluids [3,4]. These have been shown to be superior to apron-style coverings in the reduction of contamination from splashes [5,6]. According to the American Food, Drug and Cosmetic act [7], PPE used in healthcare facilities is considered to be a medical device. PPE is categorised as either a Class I (low to moderate risk) or Class II (moderate to high risk) device by the USFDA [8]. Medical gowns are classified as Class II medical devices, for which regulatory standards must be met for commercialisation [9]. According to the AAMI PB70 standard, the four tests required for the barrier performance of medical gowns are water, hydrostatic pressure, blood penetration and virus penetration resistance [10]. Based on their performance in these tests, medical gowns are categorised from level 1 (low protection) to level 4 (high protection) [11].

In the absence of genuine and appropriate PPE, many workers have been forced to adopt makeshift solutions, such as wearing plastic garbage bags as gowns, which do not meet any of the above standards [12]. Public Health England sought to mitigate the shortage of appropriate PPE by allowing the use of reusable laboratory coats and patient gowns made of washable, woven fabrics as alternatives to disposable, non-woven gowns [13]. Many PPE manufacturers have increased or introduced the production of reusable gowns to meet the increasing demand [14–16]. However, some products only meet level 2 [17] or level 3 [18] regulatory requirements. Granzow [19] demonstrated that reusable woven fabric gowns have a lower resistance to microorganism and liquid penetration than disposable non-woven polypropylene gowns, which achieve the best liquid penetration resistance.

The global pandemic, spike in demand, and shortage of traditional PPE materials suitable for viral transmission protection has driven biopolymer researchers, virologists, and biomedical experts to collaborate and explore low cost alternative materials for medical gowns and

* Corresponding author. Bioresource Processing Research Institute of Australia (BioPRIA), Australia.
E-mail address: gil.garnier@monash.edu (G. Garnier).
[1] Authors contribute equally.

https://doi.org/10.1016/j.polymer.2021.123643
Received 9 November 2020; Received in revised form 3 March 2021; Accepted 12 March 2021
Available online 19 March 2021
0032-3861/

other PPE [20]. Laminated paper is a non-woven material with significant potential for use as medical gowns. The inherent properties, ubiquitous availability, low cost, and agile paper production and lamination processes make this material widely available, suitable to address the health-care criteria, and able to adapt to rapid changes in demand during a pandemic event or other emergency that results in critical PPE shortage situations. Laminated paper materials are attracting attention for their physical properties, as well as their renewability and biodegradability in many industries including packaging [21–23], superabsorbents [24–27], membranes [28,29] and biomedical [30–32]. However, the use of paper-based protective apparel has not yet been reported.

This study presents engineered and optimised laminated paper composite materials for medical gowns. Paper as the base material provides the mechanical strength, and a thin laminated coating of polyethylene acts as a barrier to increase the level of viral protection of the gowns. The effects of basis weight, laminate thickness, and combinations thereof on the composite performance were determined. The mechanical and barrier properties, viral protection, and liquid resistance of the composites were quantified. The ease of gown manufacture and performance with respect to the regulatory requirements for Level 4 medical gowns were critically evaluated. Finally, bespoke prototypes were designed and manufactured from the optimised laminated paper material, and feedback from health-care workers was sought to demonstrate the application.

2. Methodology

2.1. Materials

Polyethylene was provided by Qenos Pty Ltd. Machine glazed bleached eucalyptus paper and newsprint paper were provided by Opal, Maryvale, VIC, Australia (formerly known as Australian Paper) and Norske Skog Boyer, Australia, respectively. Anhydrous calcium chloride was purchased from Sigma Aldrich. The surfactant polysorbate 80 was purchased from Sigma-Aldrich, Australia. Whatman filter paper 602H was obtained from Bio-Strategy Pty limited Australia.

2.2. Preparation of laminated paper

The base sheets were coated on one or two sides with a blend of low density polyethylene (LDPE) and linear low-density polyethylene (LLDPE), referred to simply as polyethylene (PE) in this paper. Paper samples were coated at Opal Specialty Paper, VIC, Australia (formerly known as Orora) by extrusion coating. In this process, polyethylene is melted at high temperature (300 °C to 320 °C) and pressure, extruded through a slit die and laminated onto a paper substrate at high temperature through a nip roll assembly. The nip roll assembly consists of a rubber-covered pressure roll and water-cooled chill roll. The paper is fed from the rubber-covered pressure roll into the nip where lamination is achieved by pressing the polyethylene and paper layer together. The formed laminate is rapidly cooled down by water-cooled chill roll (15 °C to 30 °C) and collected by a wind-up mechanism. The sample description and composition is given in Table 1.

2.3. Sample thickness

The thickness of the material was measured using the L&W Micrometer (model no. 222). The sample thickness was calculated as the average of 5 random points for 5 replicates.

2.4. Coating defect analysis

2.4.1. Fluorescence and optical imaging

Fluorescence staining was employed to detect defects in the PE coating, followed by optical microscopy in transmission and reflectance mode to visualise the overall coating morphology. In theory, the fluorescence dye should stain defects on PE coating if the nature of the defect is a hole in the coating that exposes the underlying paper. Diluted propidium iodide (PI) solution was prepared by mixing 20 μL of stock solution (10 mM) with 80 μL of deionised water, then passing through a 0.2 μm syringe filter before spraying the solution onto the coated side(s) of the sample. PI droplets on the coated surface were dried by wicking with a delicate task wipe (Kimwipe), and the surface was rinsed with deionised water to remove any residue on the coated surface before a final drying with Kimwipe. Fluorescence images of the pinhole structures were taken with the PE coated side up using a Nikon upright microscope (model DS-Ri2) employing a TRITC filter (Ex 540/24, DM 565, BA 605/55) with 10x objective lens. The entire surface was scanned before capturing images of the location(s) with the largest observed pinholes. Pinhole defects appeared as red spots on the sample during fluorescence imaging. Pinholes were not always visible in the optical images. Transmission (brightfield) and reflectance images were captured sequentially at the same location using the same microscope. Reflectance images were captured with a coloured filter to enhance contrast. A fine tipped marker was used to circle the pinhole location on the PE coating to direct the subsequent acquisition of topography and chemical composition information with AFM-IR.

2.4.2. Atomic force microscopy – infrared spectroscopy (AFM-IR)

The AFM-IR data were collected with a Bruker NanoIR3 system. AFM images of pinholes identified during fluorescence and optical imaging were captured areas of 3 × 3 μm to 30 × 30 μm at 0.7Hz line scan rate with 100–200 pixel density on each edge using contact mode probes (Model: PR-EX-nIR2-10). Two to four height images were stitched together depending on the defect size in order to visualise the defect topography. Four IR spectra within the range 790–1850 cm^{-1} were taken at locations of interest with 18.74% laser power, 2.9% duty cycle, and 2429 pt IR focus spot. The resonant frequency of the tip was tuned to around 265 kHz. IR imaging was performed with IR peaks unique to PE and cellulose – 1464 cm^{-1} and 1062 cm^{-1}, attributed to CH_2 wag and C–O stretch, respectively – to acquire IR maps of the PE-to-cellulose ratio on the coated surface.

Table 1
Description and composition of laminated paper materials examined in this study.

Sample code	Sample Details	
	Base sheet	Laminate
N42/10	Newsprint 42 GSM	Polyethylene 10 GSM
N51/10	Newsprint 51 GSM	Polyethylene 10 GSM
B44/0	Bleached 44 GSM	–
B44/6	Bleached 44 GSM	Polyethylene 6 GSM
B44/10	Bleached 44 GSM	Polyethylene 10 GSM
B44/15	Bleached 44 GSM	Polyethylene 15 GSM
B49/0	Bleached 49 GSM	–
B49/16	Bleached 49 GSM	Polyethylene 16 GSM
15/B49/16	Bleached 49 GSM	Double side coated with Polyethylene 15 GSM and 16 GSM

2.5. Mechanical properties

2.5.1. Tensile strength

Bare and laminated paper samples were tested for tensile strength in accordance with the TAPPI T402 standard using an Instron tensile tester

(model 5965). The samples were cut into 50 mm wide strips by laser cutter and tested at a constant strain rate of 10 mm/min. Five replicates were measured in each direction (machine direction: MD and cross direction: CD). Geometric mean tensile (GMT) was calculated by the square root of the product of the MD tensile load and CD tensile load at break.

$$\mathrm{GMT} = \sqrt{(\text{Tensile load at MD} \times \text{Tensile load at CD})}$$

2.5.2. Tear strength

Tear strength was measured following ASTM D5587-15. Rectangular samples of dimension 150 mm by 75 mm were cut by laser cutter (Epilog Laser). Following the standard, an isosceles trapezoid template of 25 mm by 102 mm was drawn for each sample. A preliminary cut 15 mm long was made at the centre of the 25 mm edge. Samples were tested using an Instron tensile tester (model 5965) at a constant strain rate of 300 mm/min. Five replicates were measured for each direction (machine direction: MD and cross direction: CD) and the arithmetic mean value is reported.

2.5.3. Seam strength

Seam strength was measured following ASTM D751-19. Rectangular samples with a dimension of 50 mm by 203 mm were cut by laser cutter (Epilog Laser). The sample was folded in half with the fold parallel to the short direction of the sample. The fold was sewn in a seam (stitch type: 301) approximately 100 mm from one end using a Janome N190 sewing machine with polyester thread (Gutermann 274 yds/vgs) and a denim needle (denim needle 16; 15 × 1DE). The fold was cut after seaming, and the samples unfolded at the seam or strength testing using an Instron tensile tester (model 5965) at a constant strain rate of 300 mm/min. Five replicates were measured for each direction (machine direction: MD and cross direction: CD) and the arithmetic mean value is reported. For thermofused samples, the samples were folded similarly as described for sewn samples. Then the samples were cut through the fold and thermofused by a heat sealer (Sunbeam VAC 780).

2.5.4. Statistical analysis

The tensile and the seam strengths were analysed to determine the variance in the results from each type of sample, and to determine whether there were statistically significant differences between them. This was done using GraphPad Prism 8.0.2 by one-way analysis of variance (ANOVA) for the whole set of data, followed by Tukey's post hoc test to compare individual samples.

2.6. Barrier properties

2.6.1. Water penetration

Impact penetration tests were evaluated in triplicate following the standard AATCC TM42-2017e [33]. Samples and blotting papers were conditioned at 21 °C and 50% relative humidity for at least 4 h before testing. Once conditioned, each sample was clamped under a spring clamp located at the top of a stand with an inclination of 45°. Another spring clamp with a weigh of 0.5 kg was clamped at the free end of the sample. A previously weighed blotting paper was placed beneath the sample.

A funnel with a spray nozzle at the bottom was placed 0.6 m above the top of the inclined stand (measured from the middle). The nozzle had 25 holes of 1 mm diameter. 500 mL of deionised water was poured into the funnel and allowed to spray under gravity onto the sample. The weight of the blotter paper was measured immediately after the water spraying finished.

2.6.2. Hydrostatic pressure

Hydrostatic pressure tests were performed in triplicate using a set up adapted from the standard AATCC TM127-2018 [34]. Samples were conditioned at 21 °C and 50% relative humidity for at least 4 h before testing. A pre-fabricated polypropylene tube of 15 cm diameter and 100 cm height with two clear plaques at the bottom was used to conduct the tests. Each sample was inserted in between these plaques and tighten with screws. Deionised water was poured inside the tube with the sample at the bottom until leaks were observed. The height of the water in the tube was recorded.

2.6.3. Water vapour transmission rate

The water vapour transmission rate (WVTR) of the samples was measured using the desiccant method according to the standard ASTM E96. The samples were dried in an oven at 105 °C for at least 4 h prior to the test. Permeability cups containing pre-dried calcium chloride were sealed with the laminated side (outside surface) of the samples facing the desiccant, and the paper side (inside surface) facing the environment. The WVTR testing was conducted at 23 °C and 50% relative humidity. The change in mass of the cups with time was recorded and plotted. The slope of the rate of change of mass was used to calculate the water vapour transmission rate.

2.7. Virus protection

2.7.1. Preparation of phage suspension

Bacteriophage Phi-X174 was used in this assay as a model virus as it is non-pathogenic to humans. Phi-X174 was propagated using host *Escherichia coli* C ATCC 13706. The lysate was purified following the Phage-on-Tap protocol [35]. Chloroform extraction was not performed during phage purification of the lysate due to incompatibility with the test materials. The phage titre was determined by the soft agar overlay method, in which phage lysate was diluted 10 fold in bacteriophage nutrient broth [Bacto-tryptone (8.0 ± 0.1) g + Potassium chloride (5.0 ± 0.06) g + Calcium chloride (0.2 ± 0.003) g + Purified water (pH 5.3) (1 000 ± 12.5) ml] with surfactant [poly-sorbate 80 (0.1 ± 0.001 25) ml] to simulate the surface tension range for blood and body fluids.

2.7.2. Penetration test

The resistance of the material to Bacteriophage Phi-X174 was studied using the standard method ISO 16604:2004 (E). Herein, Phi-X174 in liquid was used in contact with the outside surface (laminated side) of the material. 90 mm diameter sample were tested in a penetration cell of diameter 70 mm. The penetration test cell and the samples were steam sterilised at 121 °C and 214 kPa for 15 min before each test. The sample was placed within the penetration cell, and the cell was closed by torqueing the bolts to 2.8 Nm each. The cell was covered with the transparent cover and mounted vertically in the apparatus for the penetration test. The cell was filled with 75 ± 2 mL of approximately 10^7 plaque forming units (pfu)/mL of Phi-X174 (challenge suspension) using a syringe and needle. The liquid was subjected to 0 kPa for 5 min followed by 20 kPa for 5 min. The cell was visually inspected for any sign of visible liquid penetration to the inside surface from the outside surface. At the end of the test, the challenge suspension was collected by opening the drain valve. The inside surface of the material (paper side) was washed with 5 mL of sterile nutrient broth, referred to as assay fluid. The entire surface area was brought into contact with the assay fluid by swirling the cell manually. If penetration was observed visually at any point earlier than the completion of the test, the cell was drained immediately and the assay fluid was collected and examined by viral titration using the soft agar overlay method with the media specified in the ISO 16604:2004 (E) protocol. The total number of plaques was counted. The sample passed the test if the count was less than 1 pfu/mL and vice versa. Positive and negative controls were performed using Whatman filter paper 602H and a heavy gauge polypropylene autoclavable bag material, respectively. All experiments were performed in triplicate.

Settle plates were performed to ensure there was no airborne contamination during any stage of the experiment. The agar plates containing *E. coli C* were exposed for 15–20 min at the locations of phage

titration and the penetration testing area. Material compatibility testing was performed to ensure there was no phage inactivation by the sample or the material of the penetration cell. This was done by pouring 10 mL of the phage suspension of 2200 pfu/ml onto the surface of the test material while it was in the cell. The lysate was then collected after 10 min of exposure to the sample and the cell. Phage titration was performed on this lysate as described above.

2.8. Ash content

The ash in the paper laminate composites were tested using the standard method TAPPI T211. Samples of known mass were combusted in an electrical muffle furnace (Model no. BT7670 Tetlow kilns & furnaces) at 525 °C for 3 h and the mass of the resulting ash was recorded. The moisture content was measured by keeping the samples of known mass in 105 °C for 4 h and recording the dried mass. The ash content was calculated as follows:

$$\text{Ash content } (\%) = \frac{\text{Weight of ash (g)}}{\text{Weight of paper sample (moisture free)(g)}} \times 100$$

3. Results

This study aimed to characterise laminated paper composite materials for their potential use as medical gown. The paper laminate composites were analysed by combining optical microscope and AFM-IR to detect surface composition and topographical heterogeneity of the base sheet-laminate interface, thus relating permeability to composite structure. The mechanical properties of the laminate materials, including tensile strength, seam strength and tear strength, were also analysed to quantify the effect of each layer. The materials were further tested against AAMI PB 70 for level 4 medical gowns, for which the required properties are >30 N for tensile and seam strength and >10 N for tear strength. The barrier properties of the composites were tested against both water and a bacteriophage virus to determine the role and importance of each layer.

3.1. Coating morphology

Laminate integrity is key in achieving the required level of viral protection. However, the PE coating must also be as thin as possible for economic purposes, and to optimise wearer comfort. Further, analysis of the level of adhesion and the morphology of the interface can reveal a new understanding of the diffusion and barrier properties of laminated papers. Here, we combine advanced optical microscopy with AFM-IR analysis to probe and quantify the surface and interface between the layers of laminated paper.

3.1.1. PE coating morphology visualised with optical microscopy and AFM-IR

The surface and interface between the layers of the laminated papers were measured through advanced optical microscopy combined with AFM-IR analysis (Fig. 1). The optical microscopy transmission (brightfield) image shows the underlying cellulose fibres while the reflectance image reveals coating morphology. Pinholes were not readily detectable in the brightfield images, but a faint hue of the dye was occasionally observed. The reflectance images show heterogeneous coating morphology across the samples. The images of the two thinnest laminate layers and base sheet thicknesses (B44/6 and B44/10) show light and dark domains, revealing higher amorphous arrangement of PE chains (dark) than the semi-crystalline domains (light), which is consistent with the AFM-IR observations (Fig. 2) [36]. Samples B44/15, B49/16 and 15/B49/16 show no distinct light and dark domains; however, an overall dense bubble morphology indicates air trapped in the melt.

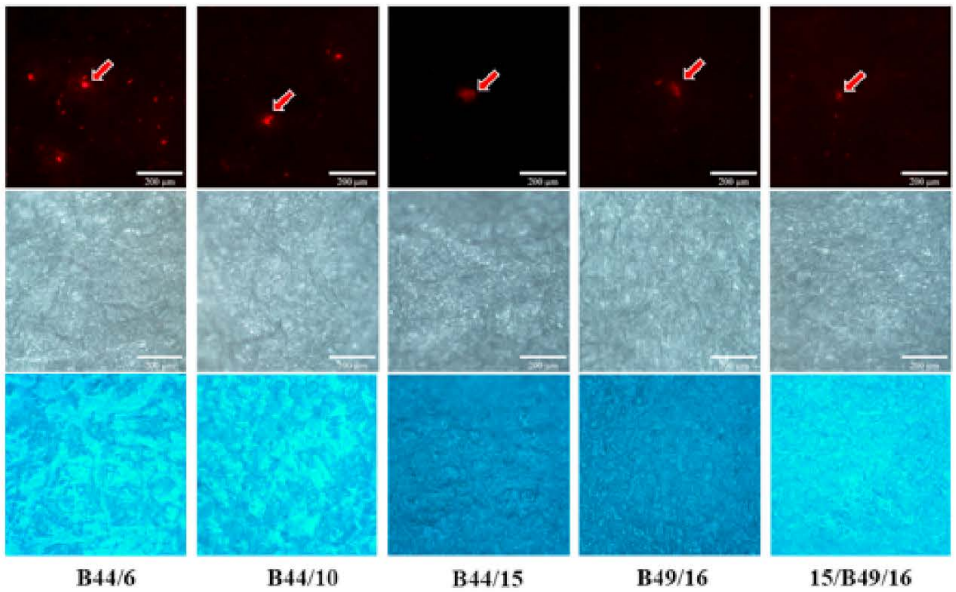

Fig. 1. Optical microscopy of laminate paper composites (scalebar: 200 μm) with PI staining. Fluorescence (top row), transmission (brightfield) (middle row) and reflectance with coloured filter (bottom row) images of propidium-iodide (PI) stained samples with various base sheet and laminate layer thicknesses. Fluorescence images reveal pinholes (in red), brightfield shows cellulose fibres and reflectance images highlight coating morphology. (For interpretation of the references to colour in this figure legend, the reader is referred to the Web version of this article.)

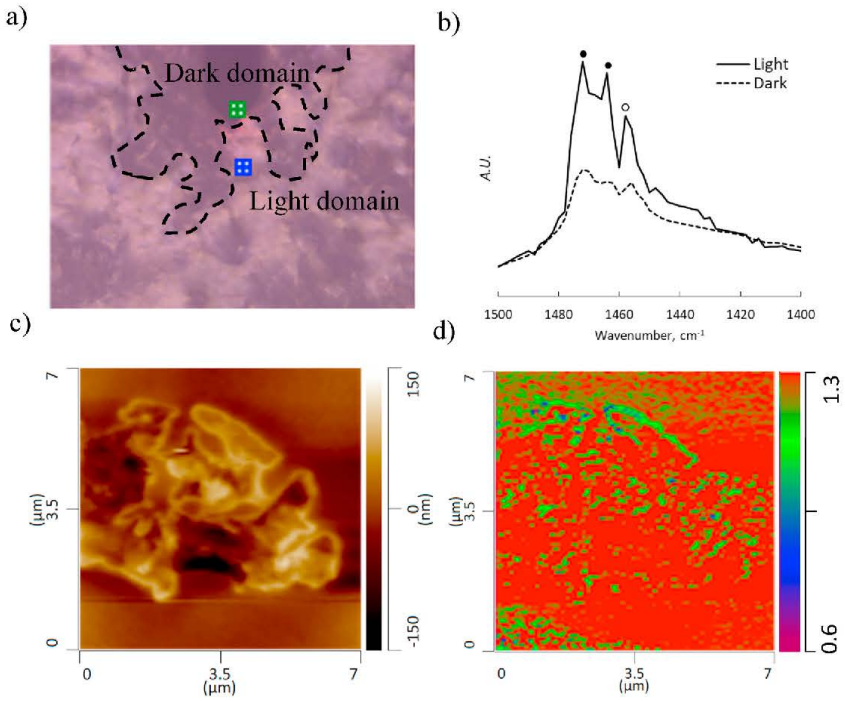

Fig. 2. Characterisation of the heterogeneous coating morphology of sample B44/10: a) NanoIR3 Optical microscopy view (375 × 282 µm) of the coating surface showing light and dark domains. b) AFM-IR spectrum showing the prominent CH_2 bending peaks of semicrystalline PE (solid circles, 1472 cm^{-1}, 1464 cm^{-1}) and amorphous PE (open circle, 1458 cm^{-1}). Dark domains have higher intensity due to semi-crystalline bands compared to the light regions, which show diminished semi-crystalline band signal intensity and similar intensity from the amorphous band. c) AFM topography map of a dark domain showing uneven surface morphology. D) PE (1464 cm^{-1}) -to-Cellulose (1062 cm^{-1}) IR ratio map of region (c) showing distinct PE rich (red) and PE poor (green) areas at the edges of the uneven surface topography. (For interpretation of the references to colour in this figure legend, the reader is referred to the Web version of this article.)

3.1.2. Pinholes visualised with fluorescence microscopy and AFM-IR

The fluorescence and optical images of selected samples after propidium iodide staining are displayed in Fig. 1. Fluorescence images show that the thinner laminate layer has the most pinholes while the thickest base sheet shows the least. The AFM topography images reveal two types of defect morphologies for pinholes. The first morphology is a protrusion of cellulose fibres through the coating from the base sheet due to insufficient amount of coating material (Fig. 3A); the other is a crater-like defect due to uneven coating (Fig. 3b). The AFM-IR shows an increase in the cellulose signal (1064 cm ^{1}) peak closer to the bottom of the crater-like defect than at shallower regions, indicating a thinner layer of the polyethylene coating at the base of the crater. The protruding fibre features give an even stronger cellulose signal at 1064 cm ^{1} in addition to a deformation of the polyethylene peak (1464 cm ^{1}) with lowered intensity and widened base. For protrusion defects, the IR composition map of polyethylene-to-cellulose ratio revealed poor polyethylene coating (Fig. 3c). A simultaneous measurement of the relative stiffness of the material was collected by tracking the resonant frequency of the AFM tip. The protruded defect generated higher frequencies than the surrounding area, indicating that a PE poor region can introduce mechanical heterogeneity, such as domains with high relative stiffness contrast compared to that of surrounding areas due to exposed cellulose material from base sheet (Fig. 3d).

3.2. Mechanical properties

Achieving the required mechanical properties with paper laminate materials, particularly high tensile strength, is expected to be challenging. Here, the effect of the type and thickness of paper base-sheet and the thickness of the PE coating are analysed. The material strength must also be preserved upon gown assembly, therefore two seam options, sewn and fused, are presented and analysed here.

3.2.1. Tensile strength

The mechanical properties of the laminated paper samples were expressed as the geometric mean tensile (GMT) at break point. Results are presented in Fig. 4. The dotted line represents the strength required (30N) for level 4 medical gown materials according to AAMI PB 70. All samples except the two newsprint composites meet the requirement. The newsprint composites (N42/10 and N51/10) have a lower GMT compared to those of bleached paper. These results indicate that pulp type plays an important role in governing the composite strength.

Increasing the thickness of the laminate for the same bleached base-sheet (B44/6, B44/10, B44/16) does not change the GMT significantly, nor does increasing the base sheet grammage from 44 to 49 GSM (B49/0 and B49/16). The effect of laminate thickness is also negligible when paper is coated on a single side. However, coating on both sides (15/B49/16) improves GMT significantly compared to single side coating.

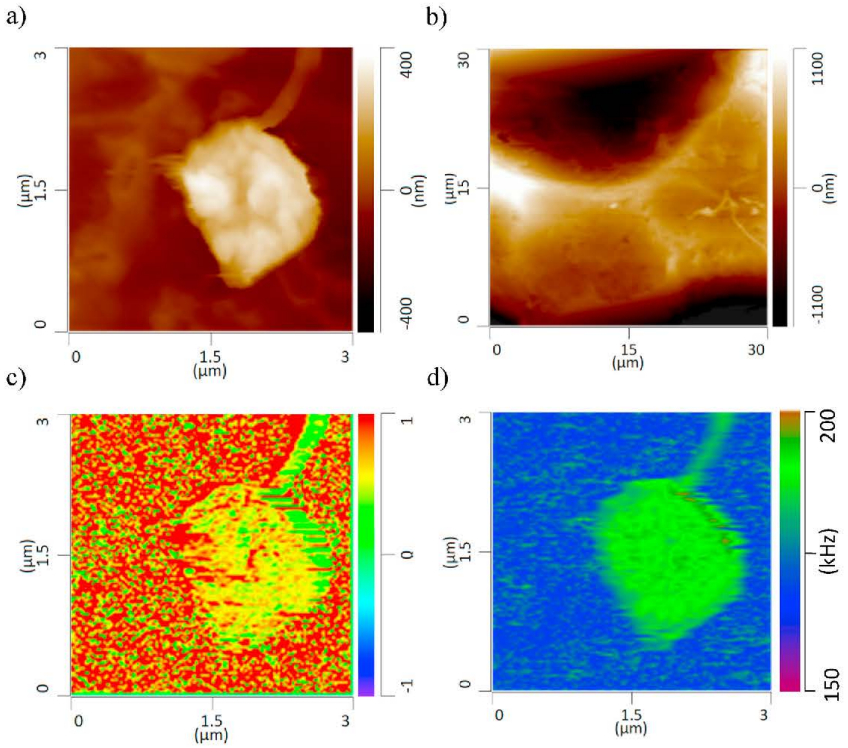

Fig. 3. Evidence of pinhole defect morphologies detected by AFM-IR characterization. a) An AFM topography map of a protruding defect (type 1) and b) An AFM topography map of a concave crater-like defect (type 2). c) PE (1464 cm^{-1}) -to-Cellulose(1062 cm^{-1}) IR ratio map of a protruding defect in A showing reduced IR absorption of 1464 cm^{-1} indicating poor PE coating on cellulose base sheet. d) PLL frequency map showing that protruding defects introduce domains with high relative stiffness contrast.

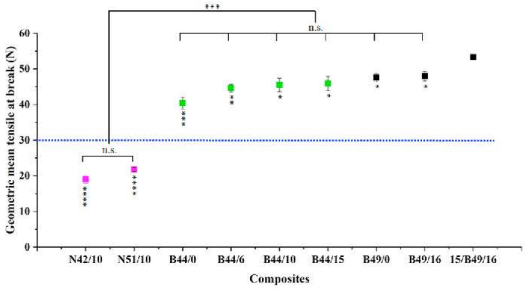

Fig. 4. Geometric mean tensile strength at break point for the different laminate composites. The dotted line shows the AAMI PB 70 requirement. The asterisks brackets show statistically significant differences between the indicated data points and groups. The asterisks below each data point show the level of significance when compared with 15/B49/16. Here, n.s. represents "not statistically significant", * represents $p \leq 0.05$, ** is for $p \leq 0.01$, *** for $p \leq 0.001$ and **** corresponds to $p \leq 0.0001$.

3.2.2. *Seam strength*

Seam strength was measured for both sewn and thermofused sample assemblies (Fig. 5). Slippage occurred for sewn seams at a low force for the unlaminated bleached paper with a 44 GSM base sheet (B44/0). Increasing the laminate thickness on this base sheet (B44/6, B44/10, B44/16) or increasing the base sheet grammage (B49/0) does not affect seam strength significantly. However, when higher GSM base sheets were laminated on one side (B49/16), the seam strength improved considerably. Coating the sample on both sides (15/B49/16) improves the seam strength compared to its single-sided laminated counterpart (B49/16). This material (15/B49/16) has significantly higher seam strength than the unlaminated base sheets (B44/0 and B49/0) and the laminated base sheet with a lower GSM (B44/6,10,15). Therefore, it appears that both base sheet and laminate layers contribute to seam strength.

Thermofused composites did not show any difference in seam strength, irrespective of base sheet grammage, laminate thickness, or double-sided coating. Moreover, none of the thermofused composites samples meet the seam strength required (30 N) for by AAMI PB 70 for level 4 medical gowns (Fig. 5b). However, the thermofuser used here was a kitchen heat seal and thus might not have provided sufficient heat.

3.3. *Barrier properties*

Paper laminate barrier properties are important to ensure protection from the surrounding environment. Here, the effect of the thickness of paper base sheet and the thickness of the coating are evaluated.

3.3.1. *Water resistant*

The water resistance of the composites was measured through

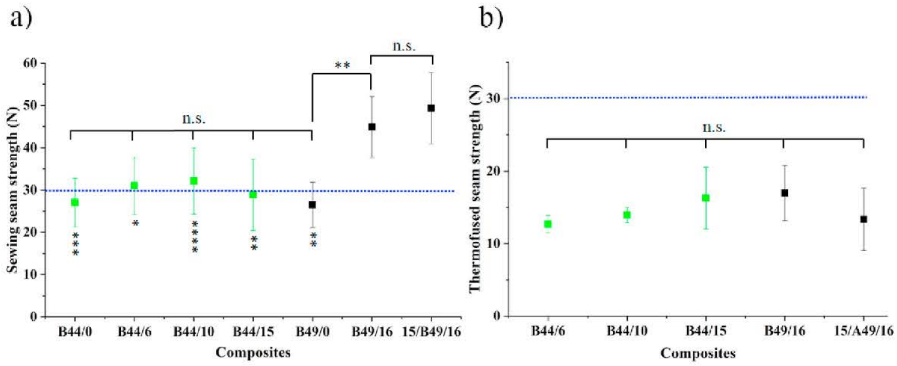

Fig. 5. Seam strength after (a) sewing and (b) thermofusing for the different laminate composites. The dotted line shows the AAMI PB 70 requirement. The asterisks brackets show statistically significant differences between data points and groups. The asterisks below each data point show the level of significance compared to 15/B49/16. Here, n.s. represents not statistically significant, * is $p \leq 0.05$, ** shows $p \leq 0.01$, *** for $p \leq 0.001$ and **** corresponds to $p \leq 0.0001$.

hydrostatic pressure and impact penetration tests with results displayed in Table SI and Fig. 6. The hydrostatic pressure increased with increasing base sheet thickness. However, a more substantial increase was observed when the effect of the laminate was considered simultaneously. For A44/0 and A49/0, hydrostatic pressure was 24 and 37 cm, respectively. These values increased above 98 cm when a coating layer was added.

Water penetration values decreased with increasing base sheet thickness. Similar to the hydrostatic pressure tests, the greatest impact was noted when a laminate layer was included. For A44/0 and A49/0, water penetration was 0.11 and 0.06 g, respectively, decreasing to below 0.3 g when a coating layer was added.

3.3.2. *Water vapour transmission rate*

Materials without a PE layer showed the highest water vapour transmission rate (WVTR) (Fig. 7). WVTR values were similar for different base sheet thickness (A44/0 and A49/0). However, introducing a PE layer to the base sheet decreased the WVTR by 94% for A44/6 (31.3 g/m^2.day) compared to the base sheet A44/0 (530.4 g/m^2.day). Increasing the laminate layer thickness further reduced the WVTR. The lowest WTVR (2.4 g/m^2.day) occurred when a laminate layer was applied to both sides of a base sheet (15/B49/16).

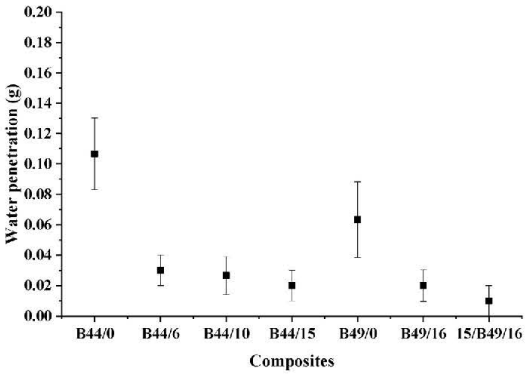

Fig. 6. Water penetration of the different samples.

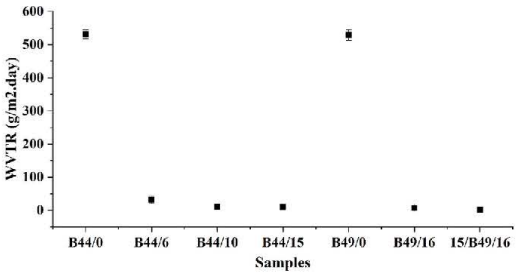

Fig. 7. Water vapour transmission rate for the different laminate composites.

3.4. *Virus protection*

The ability of the laminate materials to resist the penetration of viruses was tested using a surrogate virion Phi-X174 bacteriophage. The penetration of a virus suspension containing 10^7 pfu/mL from one side of the material to the other side was tested. Table S2 shows the resistance of the bleached paper samples coated with laminates of different thickness to virus penetration. The samples with a higher PE lamination passed the penetration tests irrespective of the paper type and base sheet grammage. The samples with low PE lamination (A44/6 and A44/10) failed the penetration test, whereas those with higher lamination (A44/15 and A49/16) could withstand a pressure of 20 kPa without allowing the virus particles to penetrate, thereby passing the test. The double coated sample (15/A49/16) also passed the test. The experimental method was validated with positive and negative controls. The positive control, which was a filter paper having a pore size of 2 μm, provided no barrier to the virus particles. The impermeable polyethylene material, with very low wettability and a small pore size, showed in no penetration of the virus suspension even under pressure.

Virus sizes usually range between 24 and 200 nm. The Phi-X174 bacteriophage tested here was reported to have an icosahedral shape with external spikes on each vertex, with a diameter of 25 nm excluding the spikes [37]. This virus particle is reported to be 34 ± 2 nm in size, including the spikes [38]. The viral species causing the COVID-19 outbreak is SARS-CoV-2. SARS-CoV-2 virions are spherical in shape, also containing glycoprotein spikes, and their diameter ranges from 60

nm to 140 nm [39,40]. SARS-CoV-2 viruses are larger than the microbe tested. It is therefore concluded that materials that provides barrier to the Phi-X174 bacteriophage would also resist penetration by the SARS-CoV-2 virus.

3.5. Ash content

The ash content signifies the presence of inorganic residues from wood pulp, the paper making process, and paper fillers. The ash content of the newsprint (N42/10) and bleached paper (B44/10) having the same laminate coating were 1.35 ± 0.36% and 0.50 ± 0.07%. The ash content of the newsprint sample was significantly higher than the bleached sample. The ash content of the uncoated bleached paper (B44/0) is 0.21 ± 0.12%, which shows that the 10 GSM coating also has some contribution to the ash.

4. Discussion

Paper based materials have never been reported for use as medical gowns. Thus, their prospect in this area remains poorly understood. At first, this material may seem to be an injudicious choice because of its perceived weakness, high porosity and high wicking ability. However, two events have challenged this perception. The first is the COVID crisis that has drastically limited access to typical polyolefin non-woven gown materials, which are predominantly manufactured in Asia [41,42]. In contrast, paper is manufactured on all the inhabited continents, and indeed, in most countries. The second is the advance of paper as an engineered material. Substantial progress in strength and barrier performance has been achieved in the last decade. However, commodity paper has yet to be reported as an accessible medical gown material, without the use of advanced technologies such as nanocellulose and assembling systems. This section has two objectives. The first is to investigate the property-structure relationship of laminated papers in the context of COVID-19 medical gown materials; the second is to determine if and how the current gown standard (AAMI PB 70) can be met with paper technology.

The AAMI PB 70 standard states the mechanical and barrier property requirements for medical gowns. Hence, these were studied to understand the suitability of the base sheet-laminate combination for Level 4 medical gowns, the highest level of protection. Special attention was dedicated to coating homogeneity, which was identified as a critical factor to ensure both reliability and safety of the material in COVID-19 medical gowns.

4.1. Material morphology

Defects in the laminate layer may compromise the barrier and mechanical function of laminated paper during use as COVID-19 surgical and isolation gowns. Due to the sub-micron size of the SARS-CoV-2 virus, a high resolution technique, namely AFM-IR, was utilised to acquire nanoscale structural and composition information regarding material defects by revealing these features with fluorescence staining. The concept is to stain the paper underneath the laminated surface with a fluorescent dye, which gives highly sensitive detection of any defects present.

Fluorescence stained regions, or pinholes, are defects which are more prevalent in composites with lower grammage base sheets, which introduces more pores in the sheet, or thinner laminate layers providing inadequate coverage over the rough paper surface. AFM-IR characterization reveals protruding (type 1) or crater like (type 2) defect morphologies with circular to ellipsoidal shapes that are 1–30 μm on the longest axis. Samples of the lowest base sheet grammage and thinner laminate layers (B44/6) have the largest type 1 and type 2 defects. The number of defects reduces with increasing laminate layer thickness (B44/15); in addition, an increase in base sheet grammage also aids in reducing the number and size of defects. The IR absorption of type 1 defects displays stronger absorptions around 1060 cm^{-1} and a reduced absorption around 1466 cm^{-1}. Type 2 defects exhibit an increase in absorption around 1060 cm^{-1} nearer the bottom of the crater. In addition, the relative stiffness of a type 1 defect is significantly higher than that of the surrounding material. This suggests protruding defects result from the base sheet having little to no coating while crater defects consists of regions with a thinner laminate layer with nano-holes at the bottom of the crater. Both types of defects must be mitigated as defects initiate tears and reduces barrier function, especially type 1 defects. However, mechanical and barrier test results must also be considered when determining the base sheet and laminate layer thicknesses (which determine the minimum number of defects) required for a functional yet economical medical gown.

AFM-IR analysis of light and dark domains visualised with optical microscopy reveals a heterogeneous coating morphology with distinct domains of semi-crystalline (light) and amorphous (dark) arrangement of polyethylene in materials with the lowest base sheet grammage (B44/6 and B44/10). While the nature of these domains does not indicate defects of the laminate layer, it does indicate reduced uniformity and molecular orientation, which may imply poor material function and impact laminate adhesion. Sollogoub et al. used optical microscopy to demonstrate that a substrate surface of higher roughness and lower polymer thickness had poor adhesion because the polymer had not reached the bottom of all the substrate surface irregularities due to the polymer flow being halted by crystallization or solidification [43]. Optical microscopy is thus a simple way to gauge the potential quality of laminate adhesion and to identify macroscopic coating defects.

4.2. Material performance

4.1.1. Effect of base sheet type

Two different types of base sheets were evaluated: Newsprint paper and Bleached Kraft paper. Newsprint paper is made from softwood pulp (yellow pine) by thermomechanical pulping, which involves refining (grinding) under saturated vapour to separate the fibres from wood [44] at temperatures above the glass temperature (T_g) of lignin. Newsprint paper retains most of its lignin and some of the hemicelluloses. In contrast, bleached Kraft paper is produced from hardwood (Eucalyptus) by chemical (Kraft) pulping, followed by bleaching. In Kraft pulping, wood chips are pre-steamed and mixed with a hot mixture of sodium hydroxide, sodium sulphide and water, which reacts with lignin to separate the cellulose fibres [45]. Around 90% of the lignin and most of the hemicelluloses are removed in this process. The chemical composition and wood polymer distribution of the two types of paper are thus significantly different. The most critically different properties are the length and therefore bonding abilities of the fibres with Pine fibres (L = 2 mm and D = 20 μm) being significantly coarser than Eucalyptus fibres (L = 0.8 mm, D = 8 μm).

The base sheet type directly affects strength, measured here as the maximum tensile force at rupture [46]. Composites made from Kraft-based paper are twice as strong (GMT) as bleached newsprint (N42/10 and N51/10). This is attributed to the high lignin content in the newsprint paper, which decreases fibre-fibre bonding by the limiting hydrogen bonding ability and reducing fibre conformability, resulting in a lower GMT. Wet end chemistry is not expected to play any significant role as only retention aids and sizing agents (internal and surface for Bleached Kraft paper) are used; there are no wet/dry strengths agents. Further, the Kraft paper contains no filler while the Newsprint likely contains some $CaCO_3$ from the recycling process. This supposition is supported by the ash content analysis, which shows that the newsprint composites (N42/10) has a higher ash content compared to the bleached Kraft paper (B44/10).

4.1.2. Effect of base sheet and laminate thickness

Virus penetration of these composites is entirely dependent on the laminate thickness; base sheet type and thickness has no effect. Samples

with thin laminate show penetration of the virus suspension from the outside (laminated) surface to the inside. A lower grammage base sheet (44 GSM) can provide full protection to virus particles only when the PE layer is above 15 GSM. Granzow et al. showed that gowns made of polypropylene resist fluid strikethrough and microorganism penetration better than those made of polyester or cotton [19]. Thus, it is the polymer coating on the laminated gowns that dictate the level of virus protection. Image analysis confirms that thinner laminates have a heterogeneous coating morphology, and defects may allow virus penetration. Coating thicknesses above 15 GSM show lower coating heterogeneity and less pinhole defects. Therefore, a thicker laminate coating should provide improved virus protection.

Increasing the laminate layer or base sheet thickness does not result in a statistically significant difference in the tensile strength. This is confirmed by the similar GMT results observed for the 44 GSM base sheet composite tested at three laminate layer thickness. The laminate layer mainly contributes to the flexibility or 'drapability' of the composite, and provides a hydrophobic barrier and viral barrier.

For seam strength, sewing outperforms thermofusing. Sewn seam slippage (displacement of thread) occurs at a low force for the unlaminated bleached paper and for laminated bleached papers with lower base sheet grammage. For the 44 GSM base sheets, increasing the laminate thickness does not affect the seam strength significantly. However, the seam strength improves significantly with laminated (one side) 49 GSM base sheets. Coating the sample on both sides further increases seam strength compared to unlaminated base sheets with the same grammage (B49/0). This indicates that both the base sheet and laminate layer contribute to seam strength. For the thermofused composites, increasing the base sheet thickness or the laminate thickness does not affect the seam strength, which is universally poor.

The presence of the laminate has a conspicuous effect on the barrier properties of the composites. The hydrostatic pressure of the paper composites significantly increases when a laminate layer is added, independent of the laminate thickness. Similar results are observed for water resistance and the water vapour transmission rate of laminated samples, which confirms that the polymer coating is responsible for the permeability and hydrophobicity of these composites [47].

4.1.3. *Meeting standard requirements*

16 GSM polyethylene lamination on a 49 GSM Kraft pulp base sheet is a suitable material for the production of Level 4 isolation gowns, as per the requirements of AAMI PB 70, providing the highest level of protection [10]. According to ASTM F3352-19, the laminated composite developed in this study meets the standard requirements for tensile and seam strength (matching or exceeding 30 N) [48]. The analysis indicates that the best combination is a 49 GSM base sheet with 16 GSM PE layer. Although the tear strength of all the laminated composites is lower than the standard requirement, this can potentially be improved by including a thin polypropylene (PP) layer between the composite base sheet and laminate layer, or with a tape or mesh at the ends, preventing crack propagation.

5. Conclusion

This study investigates polyethylene (PE) laminated paper as a novel material for the manufacture of disposable medical gowns meeting the stringent requirements for SARS-CoV-2 protection. Medical gowns have standards to meet in tensile strength, tear strength, seam strength, water penetration, hydrostatic pressure and viral protection.

Bleached and newsprint papers of varying basis weights were laminated with a polyethylene coating (on one or both sides). The laminated composites were characterised for coating morphology (optical microscopy and IR-AFM), mechanical properties, water resistance, water-vapour permeability and viral penetration. The performance achieved were compared to the medical gown material standards.

The water resistance of the laminated papers meets the standard requirements regardless of the laminate thickness or the base sheet grammage. The mechanical strength of the composite results from the type of paper base sheet, with bleached paper being the strongest. The virus protection is dependent on the laminate thickness; a minimum PE coating of 15 GSM is required for viral resistance, regardless of the paper base sheet. Image analysis of the laminated paper surface reveals coating heterogeneity in thinly coated laminates. A thicker coating is required for achieving a coating morphology free of defects, which is imperative for providing good viral protection. The laminated materials met all tensile and seam strength requirements; however, they failed the tear strength standard. A simple solution might be the addition of a tape or mesh at the ends, thus preventing crack propagation in paper. This research presented and validated PE laminated paper as a new material for medical gown and COVID-19 PPE equipment production.

Declaration of competing interest

The authors declare that they have no known competing financial interests or personal relationships that could have appeared to influence the work reported in this paper.

Acknowledgement

This project was supported by ARC Research Hub for Processing Advanced Lignocellulosics (PALS) and the Australian Pulp and Paper Technical Association (APPITA). The authors would also like to thank Norske Skog and Opal (formerly known as Australian Paper and Orora) for preparation of the composites in their mills. Many thanks to Adele Elice-Invaso (Executive Director, Appita), Frank Farchione (Market Development Manager, Amcor Functional Coatings), Russell Allan (Managing Director, Aurelia Group Consulting) and Howard Burvill (Technical Manager, Independent Consultant) for expertise and providing materials. Thanks to Mr. Long Hoh (Laboratory Manager, Department of Civil Engineer), Mr. John Rebolledo (Technical Officer, Department of Civil Engineer) and Mr. Ross Ellingham (Workshop Assistant, Department of Chemical Engineering) for helping out to prepare the experimental setup. Thanks to Monash Institute of Medical Engineering (MIME) for use of facilities.

Appendix A. Supplementary data

Supplementary data to this article can be found online at https://doi.org/10.1016/j.polymer.2021.123643.

References

[1] N.J. Rowan, J.G. Laffey, Challenges and solutions for addressing critical shortage of supply chain for personal and protective equipment (PPE) arising from Coronavirus disease (COVID19) pandemic - case study from the Republic of Ireland, Sci. Total Environ. 725 (2020) 138532.
[2] L. Vogel, Canada's PPE crisis isn't over yet, say doctors, Can. Med. Assoc. J. 192 (20) (2020) E563. E563.
[3] N. Shimasaki, M. Hara, R. Kikuno, K. Shinohara, A highly sensitive assay using synthetic blood containing test microbes for evaluation of the penetration resistance of protective clothing material under applied pressure, Biocontrol Sci. 21 (3) (2016) 141–152.
[4] F.S. Kilinc, A review of isolation gowns in healthcare: fabric and gown properties, J.Eng. fibres.Fabr 10 (3) (2015), 155892501501000313.
[5] Y. Guo, Y. Li, P.L. Wong, Environment and body contamination: a comparison of two different removal methods in three types of personal protective clothing, Am. J. Infect. Contr. 42 (4) (2014) e39–e45.
[6] Verbeek, J.H., B. Rajamaki, S. Ijaz, R. Sauni, E. Toomey, B. Blackwood, C. Tikka, J. H. Ruotsalainen, and F.S.K. Balci, Personal protective equipment for preventing highly infectious diseases due to exposure to contaminated body fluids in healthcare staff. Cochrane Database Syst. Rev., (4).2020.
[7] U.S. Food and Drug Administration, Enforcement policy for gowns, other aparel, and gloves during the coronavirus disease (COVID-19) public health emergency, in: U.S.D.o.H.a.H. Services, United States of America, 2020.
[8] Administration, U.S.F.D. Medical gowns [cited 2020 27 May]; Available from: https://www.fda.gov/medical-devices/personal-protective-equipment-infection-control/medical-gowns, 2020.

Appendix III

[9] F.S.K. Balci, Isolation gowns in health care settings: laboratory studies, regulations and standards, and potential barriers of gown selection and use, Am. J. Infect. Contr. 44 (1) (2016) 104–111.

[10] A.A.M.I. PB70, Liquid barrier performance and classification of protective apparel and drapes intended for use in health care facilities, Association for the Advancement of Medical Instrumentation, Arlington (VA), 2012.

[11] Association for the Advancement of Medical Instrumentation, Selection and use of protective apparel and surgical drapes in health care facilities, Technical Information Report: TIR11: 2005 (2005).

[12] E. Bowden, C. Campanile, B. Golding, Worker at NYC Hospital where Nurses Wear Trash Bags as Protection Dies from Coronavirus. New York Post, 2020.

[13] Coronavirus BBC, UK Failed to Stockpile Crucial PPE, in BBC, 2020 (United Kingdom).

[14] Ford Ramps up PPE Production amidst Collaboration with Thermo Fisher on COVID-19 Test Kits, in Legal Monitor Worldwide, 2020. NA.

[15] HanesBrands, HanesBrands begins production of medical gowns in addition to cloth face coverings to supplement personal protection supply during COVID-19 pandemic, in: Medical Letter on the CDC & FDA, 2020, p. 1342. Atlanta.

[16] From Sanitizer to Gloves to Gowns, Wisconsin Company Vonco Steps up to Combat COVID-19 in America, in Plus Company Updates, 2020. NA.

[17] Dow, Partners to develop and donate level 2 medical isolation gowns, in: M2 Pharma, NA, 2020.

[18] PPE company starts production of reusable gowns, coveralls in response to COVID-19, in: Legal Monitor Worldwide, NA, 2020.

[19] J.W. Granzow, J.W. Smith, R.L. Nichols, R.S. Waterman, A.C. Muzik, Evaluation of the protective value of hospital gowns against blood strike-through and methicillin-resistant Staphylococcus aureus penetration, Am. J. Infect. Contr. 26 (2) (1998) 85–93.

[20] T. Dargaville, K. Spann, M. Celina, Opinion to address a potential personal protective equipment shortage in the global community during the COVID-19 outbreak, Polym. Degrad. Stabil. (2020) 109162.

[21] M.A. El-Samahy, S.A.A. Mohamed, M.H. Abdel Rehim, M.E. Mohram, Synthesis of hybrid paper sheets with enhanced air barrier and antimicrobial properties for food packaging, Carbohydr. Polym. 168 (Supplement C) (2017) 212–219.

[22] M. Maliha, M. Herdman, R. Brammananth, M. McDonald, R. Coppel, M. Werrett, P. Andrews, W. Batchelor, Bismuth phosphinate incorporated nanocellulose sheets with antimicrobial and barrier properties for packaging applications, J. Clean. Prod. 246 (2019).

[23] G. Rodionova, M. Lenes, Ø. Eriksen, Ø. Gregersen, Surface chemical modification of microfibrillated cellulose: improvement of barrier properties for packaging applications, Cellulose 18 (1) (2011) 127–134.

[24] L. Mendoza, L. Hossain, E. Downey, C. Scales, W. Batchelor, G. Garnier, Carboxylated nanocellulose foams as superabsorbents, J. Colloid Interface Sci. 538 (2019) 433–439.

[25] M.N. Alam, L.P. Christopher, Natural cellulose-chitosan cross-linked superabsorbent hydrogels with superior swelling properties, ACS Sustain. Chem. Eng. 6 (7) (2018) 8736–8742.

[26] A.M.A. Hasan, M.E.-S. Abdel-Raouf, Cellulose-based superabsorbent hydrogels, in: M.I.H. Mondal (Ed.), Cellulose-Based Superabsorbent Hydrogels, Springer International Publishing, Cham, 2019, pp. 245–267.

[27] R.M. Barajas-Ledesma, A.F. Patti, V.N.L. Wong, V.S. Raghuwanshi, G. Garnier, Engineering nanocellulose superabsorbent structure by controlling the drying rate, Colloid. Surface. Physicochem. Eng. Aspect. 600 (2020) 124943.

[28] G. Metreveli, L. Wågberg, E. Emmoth, S. Belák, M. Strømme, A. Mihranyan, A size-exclusion nanocellulose filter paper for virus removal, Advanced Healthcare Materials 3 (10) (2014) 1546–1550.

[29] A. Onur, A. Ng, G. Garnier, W. Batchelor, Engineering cellulose fibre inorganic composites for depth filtration and adsorption, Separ. Purif. Technol. 203 (2018) 209–216.

[30] A. Basu, G. Celma, M. Strømme, N. Ferraz, In vitro and in vivo evaluation of the wound healing properties of nanofibrillated cellulose hydrogels, ACS Applied Bio Materials 1 (6) (2018) 1853–1863.

[31] E. Caló, V.V. Khutoryanskiy, Biomedical applications of hydrogels: a review of patents and commercial products, Eur. Polym. J. 65 (2015) 252–267.

[32] M. Jorfi, E.J. Foster, Recent Advances in Nanocellulose for Biomedical Applications, 2015 n/a-n/a.

[33] AATCC TM42-2017e, *Test Method for Water Resistance: Impact Penetration test*, AATCC, North Carolina, USA, 2017.

[34] AATCC TM127-2018, *Test Method For Water Resistance: Hydrostatic Pressure*, North Carolina, 2018.

[35] N. Bonilla, M.I. Rojas, G. Netto Flores Cruz, S.H. Hung, F. Rohwer, J.J. Barr, Phage on tap-a quick and efficient protocol for the preparation of bacteriophage laboratory stocks, PeerJ 4 (2016), e2261.

[36] H. Hagemann, R. Snyder, A. Peacock, L. Mandelkern, Quantitative infrared methods for the measurement of crystallinity and its temperature dependence: polyethylene, Macromolecules 22 (9) (1989) 3600–3606.

[37] K. Yazaki, Electron microscopic studies of bacteriophage phi X174 intact and "eclipsing" particles, and the genome by the staining, and shadowing method, J. Virol Methods 2 (3) (1981) 159–167.

[38] M.E. Bayer, R.W. DeBlois, Diffusion constant and dimension of bacteriophage phi X174 as determined by self-beat laser light spectroscopy and electron microscopy, J. Virol. 14 (4) (1974) 975–980.

[39] N. Zhu, D. Zhang, W. Wang, X. Li, B. Yang, J. Song, X. Zhao, B. Huang, W. Shi, R. Lu, P. Niu, F. Zhan, X. Ma, D. Wang, W. Xu, G. Wu, G.F. Gao, W. Tan, A novel coronavirus from patients with pneumonia in China, 2019, N. Engl. J. Med. 382 (8) (2020) 727–733.

[40] Y.M. Bar-On, A. Flamholz, R. Phillips, R. Milo, SARS-CoV-2 (COVID-19) by the numbers, eLife 9 (2020), e57309.

[41] J.M.R. Andrew, B. Mike, At war with no Ammo: doctors say shortage of protective gear is drive, in: The New York Times, The New York Times, New York, 2020.

[42] The Food and Drug Administration, FAQs on shortages o surgical masks and gowns during the COVID-19 Pandemic [cited 2020 5/11/2020]; Available from: https://www.fda.gov/medical-devices/personal-protective-equipment-infection-control/faqs-shortages-surgical-masks-and-gowns-during-covid-19-pandemic, 2020.

[43] C. Sollogoub, P. Montmitonnet, Y. Demay, J.-F. Agassant, P. Deparis, Origin of the bubble defect in the extrusion coating process, Polym. Eng. Sci. 51 (2) (2011) 347–357.

[44] Skog Norske, Newsprint [cited 2020 1/10/2020]; Available from: https://www.norskeskog.com/Products/Newsprint, 2020.

[45] J. Fernández-Rodríguez, X. Erdocia, F. Hernández-Ramos, M.G. Alriols, J. Labidi, Lignin separation and fractionation by ultrafiltration, in: Separation of Functional Molecules in Food by Membrane Technology, Elsevier, 2019, pp. 229–265.

[46] A. TUTU, U. YILMAZ, M. ÇGÇEKLER, *Effects of physical Properties of some Papers on offset printing quality*, in *IV*, in: International Multidisciplinary Eurasian Congress, 2017. Rome-Italy.

[47] P.W. Klein, in: Morgan, P. Claypool (Eds.), Fundamentals of Plastics Thermoforming, San Rafael, Calif.: San Rafael, Calif, Morgan & Claypool Publishers, 2009.

[48] F3352-19, A., Standard Specification for Isolation Gowns Intended for Use in Healthcare Facilities, ASTM International, West Conshohocken, PA, 2019.

Journal of Colloid and Interface Science 599 (2021) 140–148

Contents lists available at ScienceDirect

Journal of Colloid and Interface Science

journal homepage: www.elsevier.com/locate/jcis

Regular Article

Effect of the counter-ion on nanocellulose hydrogels and their superabsorbent structure and properties

Ruth M. Barajas-Ledesma [a], Laila Hossain [a], Vanessa N.L. Wong [c], Antonio F. Patti [b], Gil Garnier [a,*]

[a] Bioresource Processing Research Institute of Australia (BioPRIA) and Department of Chemical Engineering, Monash University, Clayton, VIC 3800, Australia
[b] School of Chemistry, Monash University, Clayton, VIC 3800, Australia
[c] School of Earth, Atmosphere & Environment, Monash University, Clayton, VIC 3800, Australia

GRAPHICAL ABSTRACT

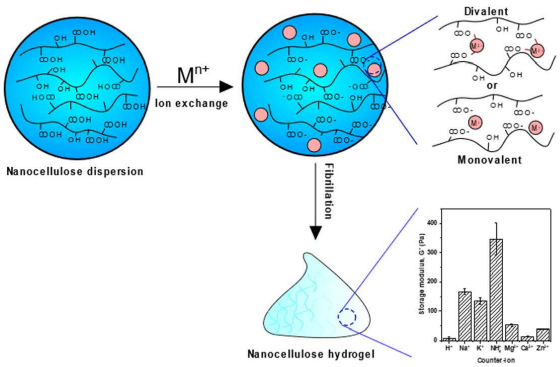

ARTICLE INFO

Article history:
Received 19 February 2021
Revised 12 April 2021
Accepted 13 April 2021
Available online 17 April 2021

Keywords:
Carboxylated nanocellulose
TEMPO
Cation
Valency
Superabsorbent
Gelation
Hydrogel
Foam
Aerogel

ABSTRACT

Hypothesis: Carboxylated nanocellulose gels and superabsorbents (SAPs) can be engineered by ion exchange of TEMPO treated cellulose fibers with different cations prior to shearing, thus creating a nanofibrous network ionically cross-linked. The structure and properties of these materials are highly influenced by the type counter-ion used as it controls both the degree of fibrillation and crosslinking.

Experiments: Functionalised nanocellulose SAPs were made using TEMPO-mediated oxidation followed by ion-exchange before fibrillation into a hydrogel and freeze-drying. Seven different cations were tested: 4 of valency 1 (H, Na, K, NH_4), and 3 of valency 2 (Ca, Mg, and Zn). The effect of the counter-ion on the gelation mechanism and the superabsorbent performance was evaluated. The SAP absorption capacity in deionised water was related to the superabsorbent structure and morphology.

Findings: The gel stability of nanocellulose superabsorbents is governed by the counter-ion type and valency. The viscoelastic properties of all nanocellulose hydrogels are controlled by its elastic regime, that is storage modulus (G′) > loss modulus (G″). The type of cation dictates the rheology of these gels by altering the fibrillation efficiency due to the extent of ionic cross-links occurring before and after fibrillation. The driving force for gelation in monovalent gels is due to the coupling of nanofibrils by physical interactions, creating an electrostatic stabilisation of the ionised COO^- groups at high shear forces. Cation – carboxylate interactions dominate the gelation in divalent gels by supressing the repulsive charges

* Corresponding author.
E-mail address: Gil.Garnier@Monash.edu (G. Garnier).

https://doi.org/10.1016/j.jcis.2021.04.065

generated by the COO^- and also creating interfibril connections via ionic-crosslinks, as confirmed by the zeta potentials. The superabsorption performance is dominated by the counter-ion and is in the order of: $NH_4^+ > K^+ > Na^+ > Mg^{2+} > Zn^{2+} > Ca^{2+}$. NH_4^+-SAPs present the slowest kinetics and the highest absorption capacity. Its high pore area, which extends the number of accessible carboxyl groups that participates in hydrogen bonding with water, is responsible for this behaviour. Nanocellulose SAPs are attractive renewable materials, suited for many applications, including as nutrient cation carriers in agriculture.

1. Introduction

Hydrogels are characterised by cross-linked networks of hydrophilic polymers that hold large amounts of water and remain stable [1–4]. The gelation mechanism is controlled by the density and type of cross-linking, physical or chemical. For physically cross-linked hydrogels, gelation is due to physical interacting forces such as van der Waals, hydrogen bonding, electrostatic and chain entanglements, among others [5]. Chemically cross-linked hydrogels undergo chemical reactions that covalently cross-linked the polymer network. These hydrogels are typically strong and permanent [5]. The formation of ionically-crosslinked hydrogels has been reported when metal salts are added to the polymer network, inducing gelation by screening repulsive charges [6,7].

Hydrogels can be used as superabsorbent polymers (SAPs) by removing the water of the network which, for nanocellulose, is often achieved by freeze-drying [8,9]. The resulting material from freeze-drying appears as a foamy-like structure, also referred to as nanocellulose foam or aerogel [8,10]. Their swelling is dictated by the movement of the counter-ions from outside to inside the superabsorbent, causing an osmotic pressure difference across the network [11]. These materials are found in numerous applications such as hygiene and personal care products [12]. agriculture [13] and biomedicine [14]. In agriculture, SAPs can act as soil conditioners, increasing plant water availability and soil water retention [15,16], and as slow release fertilisers or nutrient carriers [16].

The majority of the available superabsorbents are fossil fuel derived polymers which degrade slowly and raise health and environmental concerns due to the formation of microplastic particles that can be harmful to soil biota [17–19]. These environmental issues have driven the development of superabsorbents from natural polymers, especially those made of starch [20], pectin [21], alginate [22], or cellulose [23,24]. From these, cellulose, the most abundant carbohydrate and biopolymer on earth, is often preferred as source material due its biodegradability, availability and hydrophilicity [16,25]. Cellulose-based SAPs can be produced through the 2,2,6,6-tetramethylpiperidine-1-oxyl (TEMPO)-mediated oxidation of cellulose followed by (freeze)drying. This process converts the primary alcohol groups of cellulose into sodium carboxylate groups [26]. and adds the required electrostatic repulsion which forms nanocellulose hydrogels upon mechanical fibrillation. Nanocellulose-based SAPs are regarded as highly-porous materials with high swelling and water retention properties [8,27].

The sodium ions present in the polymer matrix is not desirable for agricultural related applications of nanocellulose superabsorbents. Adding sodium to soils will have an adverse effect on soil structure, oxygen and water availability and can impose a stress on growing crops, resulting in a decrease of yields or crop failure [28]. The exchange of the counter-ion with others can tailor this material not only as a superabsorbent, but also as a nutrient carrier for plants. Literature suggests that the cation can significantly influence the properties of cellulose-based materials. Homma, Fukuzumi, Saito and Isogai [29] found that the biodegradation rate of TEMPO-oxidised nanofibril films is greatly influenced by the counter-ion; Na^+ are reported to have the fastest rate and Cu^{2+} the lowest. Dong, Snyder, Williams and Andzelm [6] revealed that the storage modulus (G') of cellulose nanofibril hydrogels increase with increasing valency of the metal cation and are strongly associated to the binding energy of the COO^- groups with the nanofibers. Yang, Xu and Han [7] showed that cellulose nanofibers (CNF) covalently cross-linked with polyacrylamide (PAAm) can be reinforced with multivalent cations to create hydrogels of high stiffness and toughness. The addition of these ionic-links between the metal cation and CNF improves hardness and elasticity by 600% compared to pristine gels.

Ionically cross-linked nanocellulose hydrogels can be prepared by subjecting the TEMPO-oxidised nanocellulose to an aqueous salt solution before or after fibrillation, with most of the studies using the latter. This technique consists on adding the salt solution dropwise to a dispersion of TEMPO-oxidised cellulose nanofibers, without stirring, which are left standing overnight [6,7,30,31]. This process selectively substitutes the sodium ions present in the dispersion with another ion of stronger affinity. However, this technique is not only slow – which can sometimes take up to 5 days [30]- but also challenging to scale up, thus limiting the application range.

While several studies investigated the effect that different metal cations have on the gelation of nanocellulose-based hydrogels, none have studied the effect of the different cations on the viscoelastic properties of nanocellulose hydrogels nor associated those to the superabsorption performance. Similarly, while some studies suggested that the addition of salt solution after fibrillation results in the formation of heterogenous clumps and the loss of the gel structure [32]. the effect of the cation on the fibrillation efficiency upon homogenisation is unknown.

Here, TEMPO mediated oxidation was used to prepare carboxylated nanocellulose hydrogels. The oxidised fibres were subjected to an acid wash with HCl to remove all Na^+ cations present, followed by fibre re-suspension in different salt solutions, homogenisation and freeze-drying. The fibrillation efficiency, hydrogel rheology and SAP structure and swelling properties were measured. This study innovates by the technique used to prepare ionically cross-linked SAPs. The addition of these cations can not only assist in the transition of the superabsorbent as a hydro-retentor material to a nutrient carrier material for applications in sustainable agriculture, but also help in understanding the behaviour of superabsorbent in soils where there is a natural mixture of exchangeable cations, including Ca^{2+}, Mg^{2+} and K^+.

2. Materials and methods

2.1. Materials

Bleached Eucalyptus Kraft (BEK) pulp was provided by Australian Paper, Maryvale, Australia with a chemical composition of cellulose (78.8% ± 0.8), hemicellulose (17.7% ± 0.4), lignin (3.2% ± 0.1), extractives (0.3% ± 0.1) and ash (0.2% ± 0.1) [33]. Sodium hypochlorite (NaClO) at 12% w/v was purchased from Thermo Fisher Scientific and used as received. 2,2,6,6-Tetramethylpiperi

dine-1-oxyl (TEMPO) and Sodium bromide (NaBr) were purchased from Sigma-Aldrich. Sodium hydroxide (NaOH) and hydrochloric acid (HCl) were purchased from ACL Laboratories and Merck, respectively, and diluted for solutions as needed. Zinc sulfate monohydrate ($ZnSO_4{\cdot}H_2O$), sodium sulfate anhydrous (Na_2SO_4), ammonium sulfate ($(NH_4)_2SO_4$) and potassium sulfate (K_2SO_4) were purchased from Sigma-Aldrich. Calcium sulfate hemihydrate ($CaSO_4{\cdot}½H_2O$) and Copper (II) sulfate pentahydrate ($CuSO_4{\cdot}5H_2O$) were purchased from Westlab. Magnesium sulfate anhydrous ($MgSO_4$) was purchased from Merck. 70% Nitric acid (HNO_3) was purchased from Ajax Finechem.

2.2. Synthesis of carboxylated cellulose

The oxidation process was based on a previously developed method [26]. In brief, 25 g of BEK pulp (dry basis) was dispersed in 2500 mL of water with 2.5 g and 0.4 g of dissolved sodium bromide and TEMPO, respectively. Prior to the oxidation process, the sodium hypochlorite at 12% w/v was adjusted to pH 10 through the addition of hydrochloric acid at 36% w/v. To achieve a carboxylate content of 1.4 mmol/g of dry fibre, 100 mL of sodium hypochlorite was added drop-wise to the suspension whilst stirring. The pH of the reaction was maintained at 10 by adding 0.5 M NaOH. The reaction was complete when the change in pH was negligible. The oxidised cellulose was washed with deionised water, filtrated and stored refrigerated at 4 °C until required. The sodium carboxylate content of the TEMPO oxidised cellulose was 1.4 mmol/g dry fibre and was measured by conductivity titration [34].

2.3. Ion exchange treatment of carboxylated cellulose

The ion exchange treatment employed was based on a previously reported method [29]. 1 g of the TEMPO-oxidised fibres, containing sodium carboxylate groups, was suspended in 1 L of 0.01 M HCl and stirred for 1 h. The oxidised cellulose pulp was later washed with Milli-Q water and filtrated. The oxidised pulp with protonated carboxyl groups was then re-suspended in 1 L of salt solution and stirred for 3 h at room temperature. The number of moles of salt dissolved in the suspension was fixed to be 10 times as much as the calculated carboxylate groups present in the oxidised cellulose. After 3 h, the salt treated cellulose fibres were washed with Milli-Q water, filtrated and stored refrigerated at 4 °C until required. The following solutions were used for the ion-exchange treatment: hydrochloric acid (HCl), sodium sulfate (Na_2SO_4), zinc sulfate ($ZnSO_4$), potassium sulfate (K_2SO_4), ammonium sulfate ($(NH_4)_2SO_4$), copper (II) sulfate pentahydrate ($CuSO_4$), calcium sulfate ($CaSO_4$), magnesium sulfate ($MgSO_4$). Sulfate anion salts were selected to negate the effect of the anion and for its suitability for agriculture.

2.4. Preparation of nanocellulose hydrogel and superabsorbent

To prepare the nanocellulose hydrogel, the TEMPO-oxidised fibres treated with the various counter-ions were suspended in Milli-Q water to achieve a concentration of solids of 0.5% w/v and fibrillated through high pressure homogenisation (GEA Niro Soavi Homogeniser Panda) at 800 bar and two passes. To produce the nanocellulose superabsorbent, the resulting hydrogel from homogenisation was stored for at least 12 h at −80 °C and freeze-dried for 48 h using a Christ Alpha 2–4 LD Plus.

2.5. Characterisation

Freeze-dried nanocellulose SAP was characterised using a Fourier Transform Infrared (FTIR) spectrometer (Agilent Technologies Cary 630 FTIR).

The counter-ion content in nanocellulose hydrogels was analysed by either elemental analysis (HCNS) using a Perkin Elmer 2400 Series II analyser, for NH_4^+ and H^+ gels, or by inductively coupled plasma – optical emission spectrometry (ICP-OES), for all other ions. For ICP-OES analysis, 3 g of nanocellulose hydrogel was placed in crucibles and ashed using a muffle furnace, based on a previously reported method [35]. Temperature ramped to 600 °C over 3 h and kept for a further 3 h. The metal residues left in the crucible were dissolved using 1 mL of 70% HNO_3 and diluted with Milli-Q water to achieve a total volume of 15 mL. The dissolved metals were then analysed by ICP-OES using a Perkin-Elmer Avio 200. Each sample was analysed in triplicate.

The zeta potential of the nanocellulose hydrogels was measured following the method described by Mendoza, Hossain, Browne, Raghuwanshi, Simon and Garnier [36]. Briefly, 1 mL of each salt treated gel was diluted to a concentration 0.01% and sonicated using an ultrasonic homogeniser at 70% amplitude (ON/OFF, 5 s) and 19.5 kHz for 2 min. Large cellulose fibres were removed by centrifugation for 5 min at 4400 rpm. The zeta potential was measured using a Brookhaven Nanobrook Omni. Each sample was analysed 5 times.

The viscoelastic properties of nanocellulose hydrogels were evaluated using a rheometer (Anton Paar MCR302) at 25 °C. A cone (0.997°) and plate (49.975 mm) geometry was selected for Na^+, K^+ and NH_4^+ and a cup and bob for H^+, Mg^{2+}, Ca^{2+} and Zn^{2+} ions. During the measurements, a solvent trap was employed to maintain a constant temperature. The amplitude sweep was varied from 0.01 to 100% at a constant frequency of 1 Hz.

The morphology of the SAPs was observed using scanning electron microscopy (SEM) (FEI Magellan 400). Nanocellulose foams were placed on a metal stub and coated with an Iridium layer of less than 2 nm thick.

The porosity, pore size distribution and pore properties of all SAPs were measured by mercury porosimetry (Micromeritics Autopore IV). Samples were degassed at 50 °C for at least 24 h prior testing and analysed in triplicates. The testing pressure ranged from 0.1 to 60,000 psia was applied.

The swelling or absorption capacity of nanocellulose SAPs was quantified in Milli-Q water. The swelling rate and absorption were measured by weighing the samples before and after immersion in water over different periods of time (1, 5, 15, 30, 60, 90, and 150 min) at room temperature. The following equation was used to determine the swelling capacity:

$$\textit{Swelling capacity}, Q = \frac{m_t - m_d}{m_d} \quad (1)$$

where m_t refers to the weight of the swollen gel at time t and m_d is the weight of the dried sample.

3. Results

TEMPO oxidised BEK pulp, which had a carboxylate content of 1.4 mmol/g dry fibre and was washed with acid, was first dispersed into different salt solutions of varying valency and cation type and then homogenised under high shear forces, thus forming hydrogels. These hydrogels were characterised in chemical structure and ion content. Rheology was used to evaluate the cross-linking density and fibrillation efficiency. Hydrogels were then lyophilised and the aerogels produced were analysed for morphology, pore size distribution and swelling in water.

3.1. Ion exchange of carboxyl-group counter-ions

The FT-IR spectra and the zeta potential of the hydrogels prepared with the various counter-ions is displayed in Fig. 1a and b, respectively. The presence of a band at 1720 cm^{-1} for the H^+-hydrogel indicates the conversion of the Na^+ carboxylate groups from the TEMPO-mediated oxidation to carboxylic acid groups using the acid treatment (Fig. 1a). All samples with monovalent ions (Na^+, K^+ and NH_4^+) and divalent ions (Mg^{2+}, Ca^{2+} and Zn^{2+}) show a sharp peak at 1600 cm^{-1}, distinctive of the C=O stretching groups, which confirms the presence of the carboxylate functional group which will be associated with the respective counter-ions. Interestingly, the zeta potential of the nanocellulose hydrogels decreased with increasing ion valency. Monovalent hydrogels have a zeta potential ranging from −80 mV to −74 mV; for divalent, it ranges from −50 to −35 mV. Ca^{2+}-hydrogels have the lowest surface charge of all samples (Fig. 1b). The difference between and among the valencies is significant, as previously reported [37].

The degree of counter-ion exchange from the protonated carboxyl group to other cations was evaluated through ICP-OES analysis (Fig. 2). NH_4^+ ions were determined by HCNS analysis, also shown in Fig. 2. Except for Zn^{2+}-gels, the measured counter-ion content of all ions is similar to that calculated by stoichiometry – 1.4 and 0.7 mmol/g dry fibre for mono and divalent cation gels, respectively. This confirms the complete conversion of the protonated carboxyl groups to their respective carboxylate salt. Samples with divalent ions formed cationic carboxylate groups with 1:2 (cation-COO) molar ratio, corresponding to $(COO)_2$-cation structures ionically cross-linked. The increase in the measured counter-ion content of Zn^{2+}-gels higher than the calculated value can be attributed to an excess of salt solution that was not completely removed upon washing.

3.2. Viscoelastic properties

The effect of the counter-ions on the gelation properties of the nanocellulose hydrogels was measured by rheology. The viscosity curves of all gels are presented in Fig. 3a. In general, increasing shear rate decreases viscosity. This is known as a shear-thinning behaviour and is common in nanocellulose gels [38,39]. Gels with divalent ions have lower shear viscosity than those with monovalent ions.

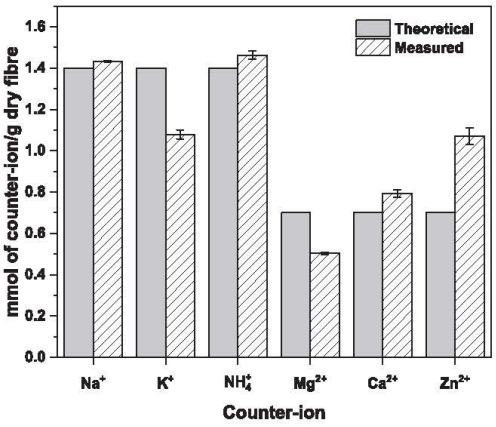

Fig. 2. Counter-ion content of the TEMPO-oxidised nanocellulose sheared after the ion exchange treatment. Measurements are determined from ICP-OES and HCNS analysis. Results are reported as mean ± standard deviation (n = 3).

The storage modulus or solid-like behaviour (G') and the loss modulus or liquid-like behaviour (G") were evaluated as a function of shear strain in oscillatory flow mode (Fig. 3d-e). The viscoelastic properties of the nanocellulose gels is governed by the elastic regime in all cases, noted by a higher G' than G" over the strain range. The storage modulus of the gels decreases with increasing ion valency. Monovalent gels, except those with H^+ ion, exhibit an elastic modulus an order of magnitude higher than all divalent ions providing an indication of fibre crosslinking in between the gel matrix [7]. Gel stiffness, described by the G' values (Fig. 3b), is in the order of $NH_4^+ \gg Na^+ > K^+ > Mg^{2+} > Zn^{2+} > Ca^{2+} > H^+$. Similarly, gel relaxation, described by G" values (Fig. 3c), is in the decreasing order of $NH_4^+ \gg Na^+ > K^+ > Mg^{2+} > Ca^{2+} \sim Zn^{2+} > H^+$. The linear viscoelastic region (LVR) changes for both curves, G' and G", depending on the valency and type of counter-ion. Both hydrogels display a similar LVR regime that drops at a shear strain of 10%. Finally, the difference between the G′ and the G″ values for monovalent gels is an order of magnitude higher than for divalent

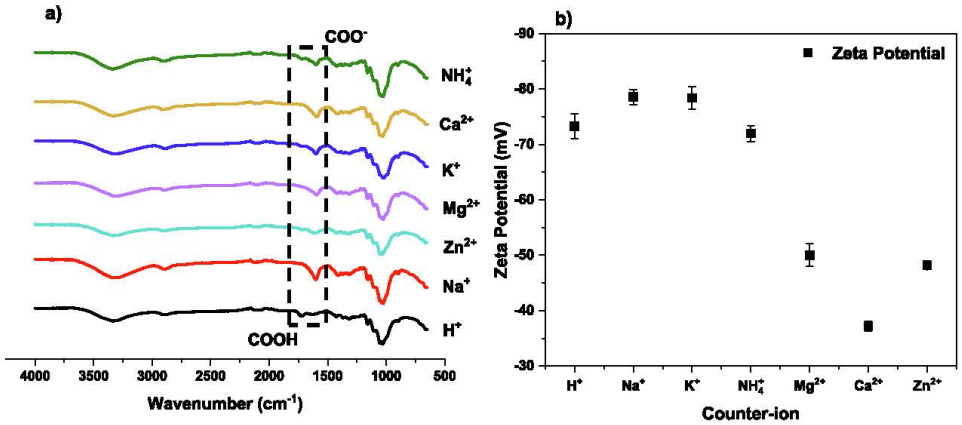

Fig. 1. (a) FT-IR spectra and (b) zeta potential of TEMPO-oxidised nanocellulose pretreated with different counter-ions. The dashed line highlights the absorption bands for COO– and COOH groups. Results are reported as mean ± standard deviation (n = 3).

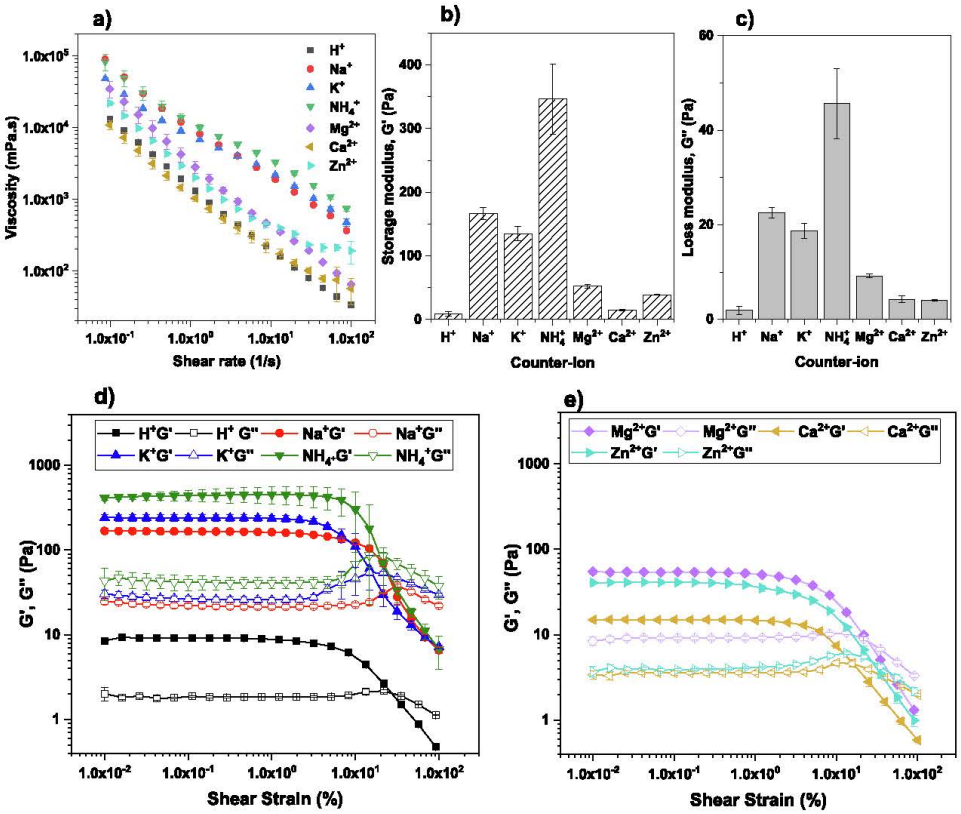

Fig. 3. Rheological properties of TEMPO-oxidised nanocellulose sheared with different counter-ions: (a) viscosity curves, (b) nanocellulose gel stiffness and (c) relaxation represented by the storage modulus (G') and the loss modulus (G"), storage (G') and loss (G") modulus of (d) monovalent and (e) divalent ions. Results are reported as mean ± standard deviation (n = 3).

gels. This suggests that monovalent gels are mostly dominated by the elastic character, whereas divalent and H^+ gels are dictated by both the elastic and the viscous behaviour in the same proportion.

3.3. Morphology

Nanocellulose-based aerogels were prepared by freeze-drying. SEM imaging was employed to analyse the morphology (Fig. 4). The internal structure strongly depends on the counter-ion present in the superabsorbent. Though all treatments produced SAPs with very porous structures, the pore shape, size and fibre arrangement differ. Monovalent ions form SAPs characterised by an entanglement of fibres which results in open and porous three-dimensional assemblies (Fig. 4a-d). Fibres are clearly visible, forming foam structures with pore diameters ranging from 10 to 300 nm. In contrast, superabsorbents with divalent ions are characterised by a more homogeneous and organised structure. Pores are detected, but the cellulose fibres are still connected to each other, not entangled (Fig. 4e-g). Pore diameters range between 30 and 200 nm.

3.4. Pore size

The pore size distribution of the nanocellulose superabsorbents was evaluated using mercury porosimetry (Fig. 5a). Pore size distribution is controlled by the counter-ion present in the SAP. Apart from NH_4^+, all monovalent and divalent ions form SAP with a microporous structure. No visible pores are noted at a scale lower than 2 μm. Superabsorbents made with NH_4^+ counter-ion display a combination of micro, *meso* and macropores of size ranging from 5 nm to up to 100 μm, classified by IUPAC [40].

The pore properties of the superabsorbents is expressed as a function of the counter-ion (Fig. 5a-c). NH_4^+-based superabsorbents exhibit the highest pore area, more than 15 times higher than any of the other SAPs. It also has the smallest pore diameter, in the range of 2–5 nm, which is about 6 times smaller than for the other materials. Apart from this, there are no other major difference observed in the SAPs prepared with the other monovalent and divalent ions. The pore volume is slightly smaller for superabsorbents with monovalent ions than for divalent ions, ranging from 25–30 mL/g and 32–37 mL/g, respectively. The porosity of all the SAPs is in between 90 and 94%, which is typical of freeze-dried superabsorbents [8].

3.5. Swelling

The degree of swelling of the nanocellulose SAPs was quantified in Milli-Q water and evaluated as over time (Fig. 6). All superabsorbents perform similarly, with swelling uptake reaching a plateau after an initial absorption rate. Apart from NH_4^+,

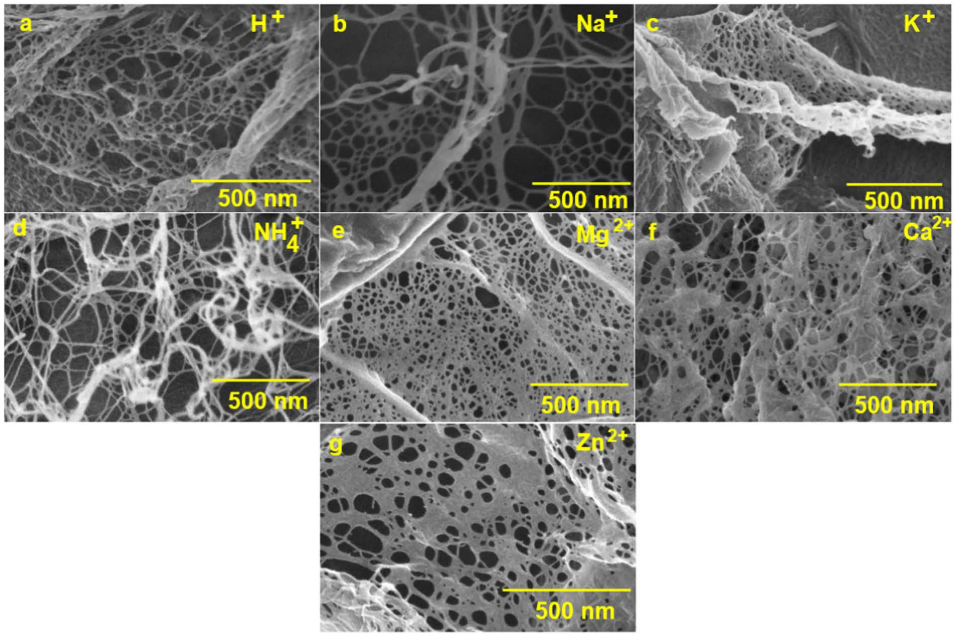

Fig. 4. SEM images of the nanocellulose superabsorbent made from freeze-drying nanocellulose hydrogels of TEMPO-treated cellulose sheared with different counter-ions: (a) H^+, (b) Na^+, (c) K^+, (d) NH_4^+, (e) Mg^{2+}, (f) Ca^{2+} and (g) Zn^{2+}.

superabsorbents show an initial rapid swelling, achieving equilibrium as soon as they are immersed in water. SAP with NH_4^+ counter-ion is characterised a slow swelling rate.

The type of counter-ion dictates the SAP swelling at equilibrium (Fig. 7). Ammonium-based SAP achieves the highest swelling capacity of approximately 130 g water/g dry fibre. This is followed by the other monovalent ions, K^+ and Na^+, in order, respectively. SAPs with valency two ions report a lower swelling capacity, with Ca^{2+} being the lowest of all.

4. Discussion

TEMPO-mediated oxidation is the most commonly used method to produce nanocellulose hydrogels. This introduces sodium carboxylates at the C6 glycosidic position which contributes to the liberation of cellulose fibres upon homogenisation. However, the presence of sodium counter-ions may limit the application range of this material. This study evaluated the effects that different counter-ions have on the properties of both nanocellulose hydrogels and superabsorbents via ion exchange treatment prior fibrillation.

The FT-IR spectra analysis confirms the evidence of the carboxylate groups balanced by different cations or protonated carboxyl groups. This is noted by the presence of their characteristic peak of metal carboxylate group at ~1600 cm^{-1}. However, the intensity of this peak is lower for hydrogels with Zn^{2+} and NH_4^+ ions. In these cases, the FT-IR spectra also show a small peak at ~1720 cm^{-1} which corresponds to protonated carboxyl groups. This suggests that not all the carboxyl groups were converted to the corresponding metal carboxylate group [29,41]. This is because of the pH of $ZnSO_4$ and NH_4SO_4 solutions being 4.8 and 5.5 respectively, which promotes the partial formation of free carboxylic acid.

Except for Zn^{2+}-gels, the addition of multivalent ions forms cation carboxylate groups with molar ratios of 1:1 and 1:2 for monovalent cations (NH_4^+, H^+, Na^+, K^+) and divalent cations (Zn^{2+}, Ca^{2+}, Mg^{2+}), respectively. Divalent cations have a higher solvation volume and binding energy than monovalent cations which allows interfibril interactions, leading to ionic cross-linking between multiple fibres [6]. These ionic links generate strong interactions with numerous carboxylate groups, bridging cellulose nanofibers by attractive forces that screen the electrostatic repulsion between neighbouring nanofibres [7]. This screening effect governs the gel stability and increases with increasing concentration and counter-ion valency [42]. This is confirmed with the surface charge of the hydrogels, being almost half that of monovalent gels, indicating the formation of significant cohesive interactions between nanofibrils due to the strength of these interfibril connections [6]. The surface charge, measured by zeta potential, is related to the physical stability of these gels by electrostatic repulsion of individual fibres. Values higher than +/−30 mV can develop enough repulsive force to reach good colloidal stability. On the other hand, smaller values can lead to flocculation and particle aggregation [43]. In this case, the low zeta potential values of divalent gels, with Ca^{2+}-gels being close to the threshold of agglomeration, led to a decrease in the degree of nanofibrillation, exhibited by the substantial fibril aggregation observed in the nanocellulose dispersion after fibrillation and in the morphology of the aerogels upon drying (Fig. 4) [36]. Fibril aggregation was also observed in gels with H^+ ions. In this case, gel stability is governed by the protonated carboxyl groups which decrease the electrostatic repulsion and surface charge, allowing the fibres to come closer as the van

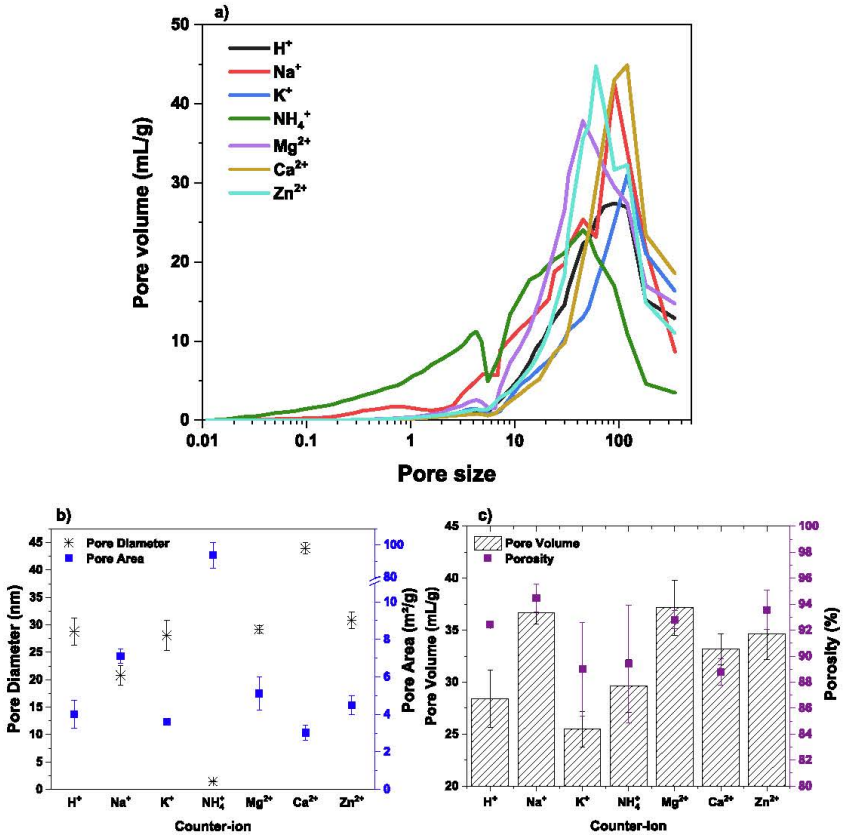

Fig. 5. Pore properties of the nanocellulose superabsorbents with different counter-ions: (a) pore size distribution (b) pore diameter and pore area, and (c) porosity and pore volume. Results are reported as mean +/− standard deviation (n = 3).

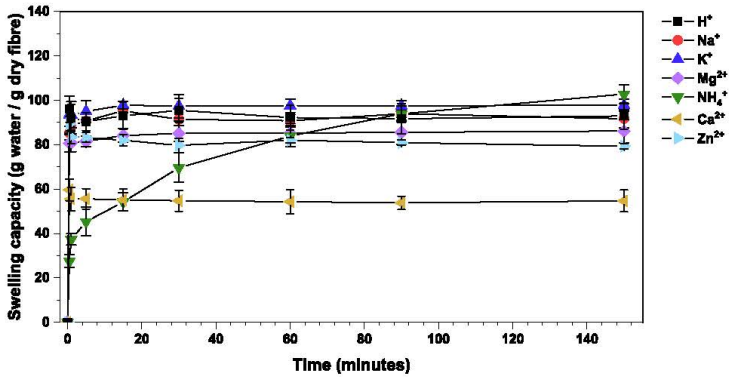

Fig. 6. Effect of the counter-ion on the degree of swelling of nanocellulose superabsorbents over time. Results are reported as mean ± standard deviation (n = 3).

der Waals forces become dominant, resulting in a decrease in the degree of fibrillation [32,44]. In contrast, monovalent ionic gels lack the interfibril cross-linking interactions as observed with the viscoelastic properties. Thus, the driving force for gelation is due to the coupling of nanofibrils by physical interactions that creates an electrostatic stabilisation of the ionised COO^- groups when high

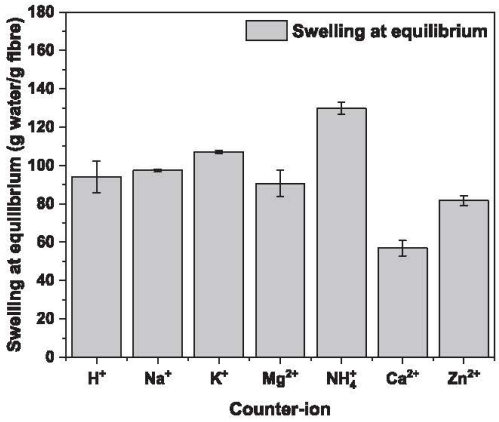

Fig. 7. Effect of the counter-ion on the swelling capacity of nanocellulose superabsorbents at equilibrium. Results are reported as mean +/- standard deviation (n = 3).

shear forces are applied to the oxidised fibres [6,32], forming stronger and more stable materials.

The type of counter-ion governs the superabsorption performance. The interaction of the counter-ion with the cellulose nanofibers can be explained by two main variables. For monovalent ions, the swelling at equilibrium follows the Hofmeister effect. This effect relates the behaviour of hydrophilic colloids in the presence of salts and is attributed to the size and hydration of ions [45]. According to the Hofmeister effect, stability of hydrophilic particles follows the indirect series as: $NH_4^+ > K^+ > Na^+$. Where ions on the left will adsorb more strongly to a hydrophilic substrate [45]. This cation specificity coincides with the measured values of swelling capacity and is attributed to negative volume exclusion entropy generated by the cation hydration. This results in an increase of the strength of the electrostatic repulsive forces which increases the entanglement of nanocellulose fibres [46,47]. Thus, increasing the absorption capacity due to the increase in hydrogen bonding between the COO^- available to interact with water [48] and also contributing to the swelling of the fibre network [10].

These repulsive forces are screened in the presence of divalent cations, as van der Waals forces become dominant and strong cation-carboxylate bonds are created [6]. Cellulose nanofibers come closer, decreasing the fibre ability to entangle upon fibrillation and thus, decreasing the swelling capacity. In this case, swelling is mainly attributed to the available pore volume, where swelling increases with increasing pore volume and decreases in the order of $Mg^{2+} > Zn^{2+} > Ca^{2+}$. This difference in pore volume depending on the counter-ion can be associated to the cation radii, where the increment in ionic radii of valency two cations results in a decrease in swelling (Mg^{2+} (72 pm) < Ca^{2+} (100 pm)) [49].

Lastly, of all the cations studied, NH_4^+ produced gels and superabsorbents with remarkable properties: high gel stiffness and stability, high SAP pore area and swelling, and slow swelling kinetics. Such performance is attributed to the unique ability of the ammonium cation to rotate [50]. This ability creates additional hydrogen bonds between the water molecules and the nanofiber network, resulting in a higher fibrillation efficiency upon homogenisation. This increase in fibre entanglement is observed in the small pore size and wide pore distribution of this SAP (Fig. 4d, 5a and 5b), increasing the pore area by an order of magnitude. This expands the number of available carboxyl groups able to participate with hydrogen bonding, resulting in a high gel stiffness. This also increases the swelling of the nanofibre network and the amount of water adsorbed to the polymer chains, responsible for the high swelling of this superabsorbent [51].

5. Conclusion

A number of nanocellulose hydrogels varying in the extent of cellulose fiberization and ion cross-linking was prepared and freeze-dried into superabsorbents (SAP). Gel and SAP were characterized in terms of rheology, aerogel structure, gelation mechanism and swelling behaviour. Carboxylated nanocellulose was prepared from TEMPO oxidized cellulose followed by ion exchange in a series of salt solutions prior to high shear homogenization into a gel [10]. Seven cations were ion exchanged to the COO^- groups. These are: H^+, Na^+, K^+, NH_4^+, Ca^{2+}, Mg^{2+} and Zn^{2+}; the anion was sulfate. The effect of the cation on the gelation properties and mechanism, superabsorbent structure, swelling capacity and absorption rate was analysed.

FT-IR and ICP-OES analyses confirm the formation of metal carboxylate groups with 1:1 (metal-COO) molar ratio for monovalent cations and 1:2 M ratio for divalent cations, which corresponds to $(COO)_2$-metal structures ionically cross-linked. The gel stability of the nanocellulose is governed by the valency and the type of cation. Gelation in monovalent gels is due to the coupling of nanofibrils by physical interactions which creates an electrostatic stabilisation of the ionised carboxyl groups during the high shear forces of homogenizing [6,32]. In contrast, for divalent gels, the driving force for gelation is due to strong interfibril connections via ionic-crosslinks which screen the repulsive forces between carboxylate groups, enabling fibres to associate together. The type of ion and their interaction with the COO^- groups determine the efficiency of fibrillation during homogenization, which affects the structure of the hydrogels and aerogels made of those. This aerogel structure directly impacts swelling capacity and kinetics. Swelling at equilibrium is in order of: $NH_4^+ > K^+ > Na^+ > Mg^{2+} > Zn^{2+} > Ca^{2+}$. The swelling capacity of monovalent SAPs follows the Hofmeister effect and is related to the size and hydration of ions. For divalent SAPs, absorption is caused by their difference in pore volume given by the ionic radii. The remarkable properties of NH_4^+ gel and SAP, compared to the other cations, are attributed to the ability of the ammonium cation to rotate, which increases the number of available carboxyl groups that engage in hydrogen bonding, resulting in an increase in pore area, gel stiffness and SAP swelling [51].

This study not only demonstrates the potential of nanocellulose-based SAPs with different cations to suit a range of applications but also innovates on the preparation method, that is by performing ion exchange before fibrillation -and not after- resulting in a cheaper and faster process than the conventional treatment. The addition of these cations can assist in the transition of the superabsorbent as a hydro-retentor to a nutrient carrier material, increasing the benefits of this material for agricultural and food use.

CRediT authorship contribution statement

Ruth M. Barajas-Ledesma: Conceptualization, Visualization, Methodology, Investigation, Software, Writing - original draft. **Laila Hossain:** Methodology, Software, Formal analysis, Writing - review & editing. **Vanessa N.L. Wong:** Supervision, Writing - review & editing. **Antonio F. Patti:** Supervision, Writing - review & editing. **Gil Garnier:** Visualization, Supervision, Writing - review & editing.

Appendix III

Declaration of Competing Interest

The authors declare that they have no known competing financial interests or personal relationships that could have appeared to influence the work reported in this paper.

Acknowledgement

Financial support was from the Australian Research Council (ARC), Norske Skog, Visy, the Government of Tasmania and Opal through the Industry Transformation Research Hub Processing Advance Lignocellulosics (PALS) grant IH130100016.

References

[1] E.M. Ahmed, Hydrogel: preparation, characterization, and applications: a review, J. Adv. Res. 6 (2) (2015) 105–121.
[2] S. Ghorbani, H. Eyni, S.R. Bazaz, H. Nazari, L.S. Asl, H. Zaferani, V. Kiani, A.A. Mehrizi, M. Soleimani, Hydrogels based on cellulose and its derivatives: applications, synthesis, and characteristics, Polym. Sci., Ser. A 60 (6) (2019) 707–722.
[3] X. Shen, J.L. Shamshina, P. Berton, G. Gurau, R.D. Rogers, Hydrogels based on cellulose and chitin: fabrication, properties, and applications, Green Chem. 18 (1) (2016) 53–75.
[4] J.R. Gross, The Evolution of Absorbent Materials, in: L. Brannon-Peppas, R.S. Harland (Eds.), Studies in Polymer Science, Elsevier, 1990, pp. 3–22.
[5] R. Curvello, V.S. Raghuwanshi, G. Garnier, Engineering nanocellulose hydrogels for biomedical applications, Adv. Colloid Interface Sci. 267 (2019) 47–61.
[6] H. Dong, J.F. Snyder, K.S. Williams, J.W. Andzelm, Cation-induced hydrogels of cellulose nanofibrils with tunable moduli, Biomacromolecules 14 (9) (2013) 3338–3345.
[7] J. Yang, F. Xu, C.-R. Han, Metal ion mediated cellulose nanofibrils transient network in covalently cross-linked hydrogels: mechanistic insight into morphology and dynamics, Biomacromolecules 18 (3) (2017) 1019–1028.
[8] N. Lavoine, L. Bergström, Nanocellulose-based foams and aerogels: processing, properties, and applications, J. Mater. Chem. A 5 (31) (2017) 16105–16117.
[9] K.J. De France, T. Hoare, E.D. Cranston, Review of hydrogels and aerogels containing nanocellulose, Chem. Mater. 29 (11) (2017) 4609–4631.
[10] L. Mendoza, L. Hossain, E. Downey, C. Scales, W. Batchelor, G. Garnier, Carboxylated nanocellulose foams as superabsorbents, J. Colloid Interface Sci. 538 (2019) 433–439.
[11] J. Grignon, A.M. Scallan, Effect of pH and neutral salts upon the swelling of cellulose gels, J. Appl. Polym. Sci. 25 (12) (1980) 2829–2843.
[12] A. Bashari, A. Rouhani Shirvan, M. Shakeri, Cellulose-based hydrogels for personal care products, Polym. Adv. Technol. 29 (12) (2018) 2853–2867.
[13] T.M. Neethu, P.K. Dubey, A.R. Kaswala, Prospects and applications of hydrogel technology in agriculture, Int. J. Curr. Microbiol. Appl. Sci. 7 (05) (2018) 3155–3162.
[14] R. Curvello, G. Garnier, Cationic cross-linked nanocellulose-based matrices for the growth and recovery of intestinal organoids, Biomacromolecules 22 (2) (2021) 701–709.
[15] M.J. Zohuriaan-Mehr, K. Kabiri, Superabsorbent polymer materials: a review, Iran. Polym. J. 17 (6) (2008) 451–477.
[16] M.R. Guilherme, F.A. Aouada, A.R. Fajardo, A.F. Martins, A.T. Paulino, M.F.T. Davi, A.F. Rubira, E.C. Muniz, Superabsorbent hydrogels based on polysaccharides for application in agriculture as soil conditioner and nutrient carrier: a review, Eur. Polym. J. 72 (2015) 365–385.
[17] Z. Steinmetz, C. Wollmann, M. Schaefer, C. Buchmann, J. David, J. Tröger, K. Muñoz, O. Frör, G.E. Schaumann, Plastic mulching in agriculture. Trading short-term agronomic benefits for long-term soil degradation?, Sci Total Environ. 550 (2016) 690–705.
[18] A.A. Horton, A. Walton, D.J. Spurgeon, E. Lahive, C. Svendsen, Microplastics in freshwater and terrestrial environments: evaluating the current understanding to identify the knowledge gaps and future research priorities, Sci. Total Environ. 586 (2017) 127–141.
[19] L. Ramos, G. Berenstein, E.A. Hughes, A. Zalts, J.M. Montserrat, Polyethylene film incorporation into the horticultural soil of small periurban production units in Argentina, Sci. Total Environ. 523 (2015) 74–81.
[20] P. Chen, W.A. Zhang, W. Luo, Y.e. Fang, Synthesis of superabsorbent polymers by irradiation and their applications in agriculture, J. Appl. Polym. Sci. 93(4) (2004) 1748-1755.
[21] M.R. Guilherme, A.V. Reis, A.T. Paulino, T.A. Moia, L.H.C. Mattoso, E.B. Tambourgi, Pectin-based polymer hydrogel as a carrier for release of agricultural nutrients and removal of heavy metals from wastewater, J. Appl. Polym. Sci. (2010) n/a-n/a.
[22] X. Shi, W. Wang, A. Wang, pH-responsive sodium alginate-based superporous hydrogel generated by an anionic surfactant micelle templating, Carbohydr. Polym. 94 (1) (2013) 449–455.
[23] A. Sannino, C. Demitri, M. Madaghiele, Biodegradable cellulose-based hydrogels: design and applications, Materials 2 (2) (2009) 353–373.
[24] J. De Guzman, K. Dela Peña, J. Ytac Dorothy, T. Tumolva, Synthesis and characterization of ionically-crosslinked κ- carrageenan/sodium alginate/carboxymethyl cellulose hydrogel blends for soil water retention and fertilizer release, Solid State Phenom. 304 (2020) 59–65.
[25] S. Varanasi, R. He, W. Batchelor, Estimation of cellulose nanofibre aspect ratio from measurements of fibre suspension gel point, Cellulose 20 (4) (2013) 1885–1896.
[26] A. Isogai, T. Saito, H. Fukuzumi, TEMPO-oxidized cellulose nanofibers, Nanoscale 3 (1) (2011) 71–85.
[27] Z. Pakowski, Modern methods of drying nanomaterials, Transp. Porous Media 66 (1–2) (2006) 19–27.
[28] E. Bresler, Saline and Sodic Soils Principles-Dynamics-Modeling, 1st ed, Berlin, Heidelberg : Springer Berlin Heidelberg : Imprint: Springer, 1982.
[29] I. Homma, H. Fukuzumi, T. Saito, A. Isogai, Effects of carboxyl-group counter-ions on biodegradation behaviors of TEMPO-oxidized cellulose fibers and nanofibril films, Cellulose 20 (5) (2013) 2505–2515.
[30] H. Dong, J.F. Snyder, D.T. Tran, J.L. Leadore, Hydrogel, aerogel and film of cellulose nanofibrils functionalized with silver nanoparticles, Carbohydr. Polym. 95 (2) (2013) 760–767.
[31] M. Chau, S.E. Sriskandha, D. Pichugin, H. Thérien-Aubin, D. Nykypanchuk, G. Chauve, M. Méthot, J. Bouchard, O. Gang, E. Kumacheva, Ion-mediated gelation of aqueous suspensions of cellulose nanocrystals, Biomacromolecules 16 (8) (2015) 2455–2462.
[32] L. Mendoza, W. Batchelor, R.F. Tabor, G. Garnier, Gelation mechanism of cellulose nanofibre gels: a colloids and interfacial perspective, J. Colloid Interface Sci. 509 (2018) 39–46.
[33] S. Ang, V. Haritos, W. Batchelor, Cellulose nanofibers from recycled and virgin wood pulp: a comparative study of fiber development, Carbohydr. Polym. 234 (2020) 115900.
[34] T. Saito, A. Isogai, TEMPO-mediated oxidation of native cellulose. The effect of oxidation conditions on chemical and crystal structures of the water-insoluble fractions, Biomacromolecules 5 (5) (2004) 1983–1989.
[35] M. Maliha, M. Herdman, R. Brammananth, M. McDonald, R. Coppel, M. Werrett, P. Andrews, W. Batchelor, Bismuth phosphinate incorporated nanocellulose sheets with antimicrobial and barrier properties for packaging applications, J. Cleaner Prod. 246 (2020) 119016.
[36] D.J. Mendoza, L. Hossain, C. Browne, V.S. Raghuwanshi, G.P. Simon, G. Garnier, Controlling the transparency and rheology of nanocellulose gels with the extent of carboxylation, Carbohydr. Polym. 245 (2020) 116566.
[37] R. Prathapan, R. Thapa, G. Garnier, R.F. Tabor, Modulating the zeta potential of cellulose nanocrystals using salts and surfactants, Colloids Surf., A 509 (2016) 11–18.
[38] I. Besbes, S. Alila, S. Boufi, Nanofibrillated cellulose from TEMPO-oxidized eucalyptus fibres: effect of the carboxyl content, Carbohydr. Polym. 84 (3) (2011) 975–983.
[39] O. Nechyporchuk, M.N. Belgacem, F. Pignon, Current progress in rheology of cellulose nanofibril suspensions, Biomacromolecules 17 (7) (2016) 2311–2320.
[40] IUPAC, Compendium of Chemical Terminology, second ed. (the "Gold Book"), Blackwell Scientific Publications, Oxford, 1997.
[41] T. Saito, T. Uematsu, S. Kimura, T. Enomae, A. Isogai, Self-aligned integration of native cellulose nanofibrils towards producing diverse bulk materials, Soft Matter 7 (19) (2011) 8804–8809.
[42] J.N. Israelachvili, Intermolecular and surface forces, third ed., Academic Press, Burlington, Massachusetts, 2011.
[43] E. Joseph, G. Singhvi, Chapter 4 - multifunctional nanocrystals for cancer therapy: a potential nanocarrier, in: A.M. Grumezescu (Ed.), Nanomaterials for Drug Delivery and Therapy, William Andrew Publishing, 2019, pp. 91–116.
[44] A.B. Fall, S.B. Lindström, O. Sundman, L. Ödberg, L. Wågberg, Colloidal stability of aqueous nanofibrillated cellulose dispersions, Langmuir 27 (18) (2011) 11332–11338.
[45] T. Oncsik, G. Trefalt, M. Borkovec, I. Szilagyi, Specific ion effects on particle aggregation induced by monovalent salts within the hofmeister series, Langmuir 31 (13) (2015) 3799–3807.
[46] H. Huang, E. Ruckenstein, Effect of hydration of ions on double-layer repulsion and the hofmeister series, J. Phys. Chem. Lett. 4 (21) (2013) 3725–3727.
[47] E. Ruckenstein, H. Huang, Specific ion effects on double layer forces through ion hydration, Colloids Surf., A 459 (2014) 151–156.
[48] R.M. Barajas-Ledesma, A.F. Patti, V.N.L. Wong, V.S. Raghuwanshi, G. Garnier, Engineering nanocellulose superabsorbent structure by controlling the drying rate, Colloids Surf., A 600 (2020) 124943.
[49] R.D. Shannon, Revised effective ionic radii and systematic studies of interatomic distances in halides and chalcogenides, Acta Crystallogr. Sect. A 32 (5) (1976) 751–767.
[50] J. Guo, L. Zhou, A. Zen, A. Michaelides, X. Wu, E. Wang, L. Xu, J. Chen, Hydration of NH4+ in water: bifurcated hydrogen bonding structures and fast rotational dynamics, Phys. Rev. Lett. 125 (10) (2020) 106001.
[51] Z. Xia, M. Patchan, J. Maranchi, J. Elisseeff, M. Trexler, Determination of crosslinking density of hydrogels prepared from microcrystalline cellulose, J. Appl. Polym. Sci. 127 (6) (2013) 4537–4541.

Carbohydrate Polymers 245 (2020) 116566

Contents lists available at ScienceDirect

Carbohydrate Polymers

journal homepage: www.elsevier.com/locate/carbpol

Controlling the transparency and rheology of nanocellulose gels with the extent of carboxylation

David Joram Mendoza[a], Laila Hossain[a], Christine Browne[a], Vikram Singh Raghuwanshi[a], George P. Simon[b], Gil Garnier[a,*]

[a] Bioresource Processing Research Institute of Australia (BioPRIA), Department of Chemical Engineering, Monash University, Clayton, VIC 3800, Australia
[b] Department of Materials Science and Engineering, Monash University, Clayton, VIC 3800, Australia

ARTICLE INFO

Keywords:
TEMPO-periodate
Nanocellulose fibres
Nanocellulose gels
Transparency
Rheology
Superabsorbent

ABSTRACT

TEMPO and periodate are combined in a one-shot reaction to oxidise cellulose and produce nanocellulose gels with a wide range of degree of substitution (DS). Highly-oxidised cellulose nanofibres with a high charge of −80 mV were produced. The strong electrical repulsion between TEMPO-periodate oxidised nanofibres (TPOF) results in the formation of well-separated nanofibres with a diameter of 2 − 4 nm, albeit depolymerised due to high oxidation. TPOF produces highly-transparent gels due to smaller aspect ratio and high surface charge. These properties induce a reduced viscosity and moduli of the gels by decreasing fibre entanglement. TPOF gels are more stable at basic pH and high ionic strength than TEMPO-oxidised gels due to their higher surface charge. Freeze-dried TPOF gels also exhibit remarkable water holding capacity due to enhanced immobilisation of water molecules. The excellent optical properties of the highly transparent gel for red blood cells analysis open new possibilities in diagnostics application.

1. Introduction

Nanocellulose (cellulose nanocrystals, cellulose nanofibres, bacterial nanocellulose) is a biodegradable and renewable material with excellent mechanical properties, unique optical properties and tunable surface chemistry (Curvello et al., 2019; Dufresne, 2013; Habibi, 2014; Klemm et al., 2009; Nascimento et al., 2018). In particular, cellulose nanofibres (CNFs) are widely used for their inherent flexible elongated structure and their ability to form physically entangled networks at extremely low solids concentration (< 0.3 wt.%). CNFs are commonly prepared by mechanical treatments such as microfluidisation (Hietala, Ämmälä, Silvennoinen, & Liimatainen, 2016; Zimmermann, Pohler, & Geiger, 2004), ultrasound (Chen et al., 2011), high-speed blending (Uetani & Yano, 2011), twin-screw extrusion (Ho, Abe, Zimmermann, & Yano, 2015), and high-pressure homogenisation (Ämmälä, Liimatainen, Burmeister, & Niinimäki, 2013; Mendoza, Batchelor, Tabor, & Garnier, 2018). The major disadvantage of these mechanical treatments is high energy consumption. To address this issue, chemical (Isogai, Saito, & Fukuzumi, 2011; Jiang et al., 2017; Okita, Saito, & Isogai, 2010) and enzymatic (Hu, Tian, Renneckar, & Saddler, 2018; Tarres, Boufi, Mutje, & Delgado-Aguilar, 2017) pre-treatments have been explored to reduce energy consumption and minimise fibre damage.

Carboxylation or oxidation is the most common chemical pre-treatment to prepare CNFs. The introduction of negatively-charged carboxylate groups on the surface of cellulose aids in the mechanical delamination of the fibres into CNFs. Consequently, most oxidised CNFs are used as highly viscous aqueous suspensions which can form hydrogels. Indeed, carboxylated nanocellulose gels have been engineered for biomedical applications (Cheng, Park, & Hyun, 2014; Curvello et al., 2019; Curvello, Raghuwanshi, & Garnier, 2019; Zander, Dong, Steele, & Grant, 2014), drug delivery (Curvello et al., 2019; Fiorati et al., 2020), and superabsorbents (Isobe et al., 2013; Mendoza, Browne, Raghuwanshi, Simon, & Garnier, 2019).

2,2,6,6-Tetramethylpiperidine-1-oxyl (TEMPO)-mediated oxidation, coupled with mechanical fibrillation, remains as the most common method to prepare carboxylated nanocellulose gels. TEMPO is a water-soluble radical catalyst which selectively oxidises alcohol groups to aldehydes and carboxyl groups (Adam, Saha-Moller, & Ganeshpure, 2001; deNooy, Besemer, & vanBekkum, 1996). Isogai et al. have extensively studied and characterised this oxidation protocol for cellulose to prepare carboxylated nanocellulose (Isogai et al., 2011; Okita et al., 2010; Ruizhi et al., 2017; Saito & Isogai, 2004; Shinoda, Saito, Okita, & Isogai, 2012). The properties of TEMPO-oxidised nanocellulose fibres are now very well described in the literature (Isogai et al., 2011;

* Corresponding author.
E-mail address: Gil.Garnier@monash.edu (G. Garnier).

https://doi.org/10.1016/j.carbpol.2020.116566
Received 8 May 2020; Received in revised form 2 June 2020; Accepted 2 June 2020
Available online 10 June 2020

Fig. 1. One-shot TEMPO-periodate oxidation of cellulose; the priary and secondary alcohols are oxidised to carboxylate groups.

Mendoza, Batchelor et al., 2018; Mendoza, Gunawardhana, Batchelor, & Garnier, 2018). However, there is a limited range of degree of substitutions (DS) achievable with TEMPO oxidation, as only the C6 hydroxyl groups can be oxidised.

Previously, we reported a one-shot TEMPO-periodate oxidation protocol to produce carboxylated cellulose with a wide range of degree of substitution (DS) (Mendoza, Browne et al., 2019). By combining periodate with classical TEMPO-mediated oxidation, we showed that cellulose molecules with carboxylate groups in the C6, C2 and C3 positions can be prepared (Fig. 1). In this work, we hypothesise that nanocellulose gels of tunable carboxylate content and thus properties can be produced via TEMPO-periodate oxidation.

A few studies have reported changing the properties of TEMPO-oxidised fibres by manipulating the NaClO concentration (Saito, Kimura, Nishiyama, & Isogai, 2007) or the oxidation time (Benhamou, Dufresne, Magnin, Mortha, & Kaddami, 2014). However, these studies have been limited to aqueous suspensions of nanofibres, often prepared by mild disintegration such as prolonged magnetic stirring. In this study, carboxylated nanocellulose gels are prepared by high-pressure homogenisation of TEMPO-periodate oxidised cellulose fibres. We investigate how TEMPO-periodate oxidation modulates the properties of carboxylated nanocellulose gels over a wide range of carboxylate content measured as COO^-DS. It is our objective to engineer the optical, viscoelastic properties and water-absorbing capacity of nanocellulose gels by controlling the level of carboxylation. We correlate these properties with the structure of the nanocellulose fibres with varying DS. We also highlight how the surface charge affects the stability of these gels at varying pH and ionic strength. Last, the potential of TEMPO-periodate oxidised gels as matrix for red blood cell analysis and diagnostics is demonstrated. We show that TEMPO-periodate oxidation provides high transparency of the gels enabling improved imaging of red blood cells. The excellent transparency of the nanocellulose gel opens new possibilities in gel card-based blood diagnostics. This study aims to engineer nanocellulose gel properties by controlling the level of carboxylation using a combination of TEMPO and periodate oxidation.

2. Materials and methods

2.1. Materials

Never-dried Bleached Eucalyptus Kraft (BEK) pulp of approximately 10 wt.% solids content, was supplied by Australian Paper, Maryvale, Australia. Sodium periodate ($NaIO_4$), 2,2,6,6-tetramethylpiperidine-1-oxyl (TEMPO), and sodium bromide (NaBr) were purchased from Sigma-Aldrich (NSW, Australia). 12 w/v% sodium hypochlorite (NaClO) was purchased from Thermo Fisher Scientific. All chemicals are analytical grade and used without further purification. All materials expressed in mmol/g refer to the dry mass of cellulose.

2.2. Synthesis of carboxylated nanocellulose gels

TEMPO-periodate oxidation of cellulose was based on studies reported previously (Baron et al., 2019; Coseri et al., 2015; Mendoza, Hossain et al., 2019). Approximately 10 g (dry mass basis) of disintegrated BEK pulp was suspended in 1200 mL distilled water containing TEMPO (0.5 mmol/g), NaBr (8.0 mmol/g), and $NaIO_4$(0.1–5 mmol/g). The reaction vessel was covered with aluminium foil to prevent any photoinduced decomposition of periodate. NaClO (12% v/v, pH 10.5, 8 mmol/g) was then added dropwise and the pH was maintained at 10.5 using 0.5 M NaOH. After 4 h, the oxidation reaction was stopped by quenching with 10 mL ethanol. The oxidised fibres were vacuum filtered and washed several times with distilled water until neutral pH was achieved, with the fibres then freeze-dried for 48 h. For comparison, cellulose oxidised with TEMPO/NaBr/NaClO (0 mmol/g $NaIO_4$) was also prepared.

Different solid concentrations of the oxidised fibres (0.1 wt.% to 1.0 wt.%) were prepared by suspending known amounts of the oxidised fibres in water. The suspensions were passed through a high-pressure homogeniser (GEA Niro Soavi Homogeniser Panda) at 1000 bar to produce TEMPO-periodate oxidised (TPOF) and TEMPO oxidised (TOF) nanocellulose gels. Suspensions with less than 1 wt.% were homogenised by two passes, while samples with concentrations greater than 1 wt.% were homogenised using one pass only.

2.3. Characterisation of carboxylated nanocellulose gels

2.3.1. Fourier-transform infrared (FTIR) spectroscopy

Freeze-dried nanofibres were analysed with a Fourier Transform Infrared (FTIR) spectrometer (Agilent Technologies Cary 630 FTIR) equipped with a diamond attenuated total reflectance (ATR) accessory. Eight scans at 4 cm^{-1} resolution were recorded in the range of $4000-500\ cm^{-1}$.

2.3.2. Carboxylate content and degree of substitution (DS)

The carboxylate content and degree of substitution were quantified by conductimetric titration as reported previously (Curvello et al., 2019; Mendoza, Batchelor et al., 2018; Perez, Montanari, & Vignon, 2003). Freeze-dried oxidised nanofibres (ca. 0.1 g) were dispersed in 40 mLl of Milli-Q water. 200 µL of 0.1% NaCl was then added and the pH was adjusted to 2.5 using 0.5 M HCl. Conductimetric titration was performed using a 0.1 N NaOH as titrant operating at a rate of 0.1 mL/min (Mettler Toledo T5 titrator). The carboxylate content (mmol COO^-/g fibre) was calculated by Eq. 1:

$$\text{Carboxylate content}\left(\text{mmol } COO^-/g\right) = \frac{C\,(V_2 - V_1)}{w} \times 1000 \quad (1)$$

where V_2 and V_1 are the volume of titrant required to neutralise the carboxylic groups, C is the NaOH concentration (M), and w is the dry sample weight.

DS is expressed as the ratio of the amount of the sodium carboxylate groups and the total hydroxyl groups in the anhydroglucose unit (AGU). The degree of substitution was calculated by the following equation:

$$\text{Degree of Substitution} = \frac{162 \times C \times (V_2 - V_1)}{w - 111 \times C \times (V_2 - V_1)} \times 100 \quad (2)$$

where V_2 and V_1 are the volume of titrant required to neutralise the carboxylic groups, C is the NaOH concentration (M), w is the dry sample weight and 111 is the molar mass difference of 2,3,6-tricarboxycellulose and AGU.

2.3.3. Degree of polymerisation

The average viscometric degree of polymerisation(DP_v) of the cellulose nanofibres was quantified, as previously reported (Haun, Yoon, Lee, & Weissleder, 2010; Shinoda et al., 2012). About 0.25 g of the oxidised nanofibres were dissolved in 50 mL of 0.5 M copper ethylenediamine for 30 min. The intrinsic viscosities were then measured using a Cannon – Fenske capillary viscometer. These values were converted to DP_v with the Mark–Houwink – Sakurada equation (Saito

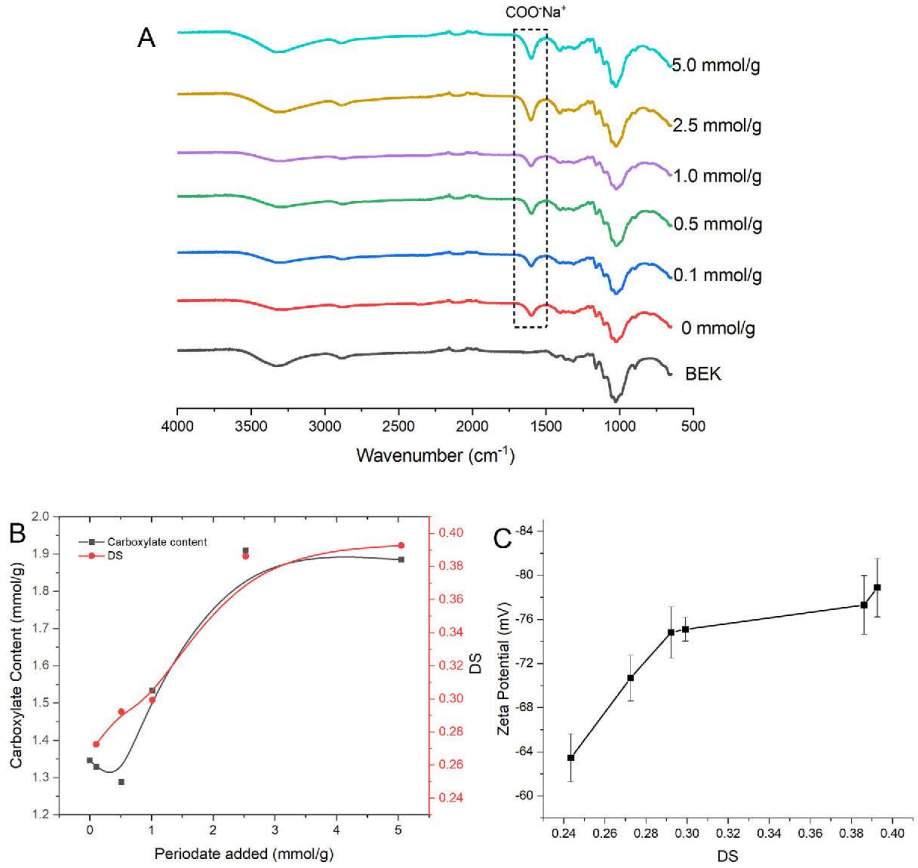

Fig. 2. (a) FTIR spectra of BEK and TEMPO-periodate oxidised nanocellulose at varying periodate concentrations. **(b)** Effect of periodate concentration on the carboxylate content and DS of oxidised nanocellulose gels. **(c)** Effect of DS on the zeta potential of nanocellulose fibres.

et al., 2009), where [η] is the average intrinsic viscosity measured from three replicates:

$$[\eta] = 0.57 \times DP_v \quad (3)$$

2.3.4. Zeta potential

The zeta potential of nanocellulose fibres was measured as previously reported (Okita et al., 2010). Dilute suspensions of the gels (~0.01%) were sonicated for 2 min using an ultrasonic homogeniser at 19.5 kHz and 70% amplitude (ON/OFF, 5 s). Larger fibres were then separated by centrifugation at 12,000 *g* for 5 min. The zeta potential of the supernatants was the average of five measurements using a zeta potential analyser (Brookhaven Nanobrook Omni).

2.3.5. UV–vis spectroscopy

Transmittance spectra of 1 wt.% gels were generated at 300−800 nm using a UV–vis spectrometer (Cary 60 UV–vis Agilent Technologies). Prior to analysis, the gels were centrifuged at 4000 rpm to remove any trapped bubbles.

2.3.6. Rheology studies

Rheological testing of the nanocellulose gels was based on methods reported previously (Mendoza, Batchelor et al., 2018; Mendoza, Batchelor et al., 2018). An Anton Paar MCR302 rheometer, equipped with a cone (0.997°) and plate (49.975 mm) geometry, was used. Viscosity measurements were performed at a shear rate ranging from 0.5–100 s^{-1}. Oscillatory strain sweep was measured from 0.01–100% at a constant frequency (1 Hz). All measurements were performed in triplicates at ambient temperature (25 °C).

2.3.7. Transmission electron microscopy (TEM)

Transmission Electron Microscopy (TEM) was performed using a FEI Tecnai F20. Dilute suspensions of the gels (~ 0.001%) were sonicated with an ultrasonic probe at 70% amplitude for 2 min and were allowed to dry on plasma-cleaned copper grids. The samples were then stained with 2% uranyl acetate, air dried, and examined at 200 kV.

2.3.8. Free swell capacity (FSC)

Freeze-dried nanocellulose gels were placed in a funnel and submerged in deionised water for reabsorption. The water absorbed was measured by weighing the gels at regular intervals up to 92 h. Prior to weighing, the gels were allowed to stand on an inclined surface for five minutes for the excess liquid to run off. The free swell capacity (FSC) is calculated using the following equation:

$$FSC = \frac{m_f - m_i}{m_i} \quad (4)$$

where m_f is the mass of the swollen gel at a particular time and m_i is the initial mass of the gel. All measurements were performed in triplicate.

2.4. Loading of red blood cells on nanocellulose gels

Glycine (300 mM) was dissolved into the gel to balance the osmolality to physiological levels. Reagent red blood cells (3%, AHG Control Cells, Immulab) were diluted in PBS, making up an 0.8% concentration. A volume of 50 μL of the gel was placed on a glass slide and 20 μL of RBCs were loaded in TPOF gels. The RBCs were imaged under an optical microscope (Nikon Eclipse Ni-E Upright Microscope) at 100X magnification.

2.5. Effect of pH and salt concentration on nanocellulose gels

The effect of pH and salt concentration on the stability of 1 wt.% TOF and TPOF gels were determined qualitatively. The pH of the gels was varied from 2–12.5 by the addition of 0.5 M NaOH or 1 M HCl. The salt content of the gels was varied from 0–68.5 mM by adding 3 M NaCl. The gels were then centrifuged at 4,000 rpm for 20 min to separate any released water. The ratio between the initial and final gel height was calculated and expressed as the fibre ratio.

3. Results

3.1. Surface charge

The concentration of carboxylate groups on nanocellulose was determined by FTIR analysis and conductimetric titration. Fig. 2a shows the FTIR spectra of native cellulose and TEMPO-periodate oxidised nanocellulose fibres at varying periodate concentrations. The typical cellulose peaks are observed in all samples: a broad O−H stretching at 3300 cm^{-1} and an sp^3-hybridized C–H stretching at 2900 cm^{-1}(Dufresne, 2012). However, the intensity of these peaks is relatively weak in all TEMPO-periodate oxidised nanocellulose. All oxidised samples show low peak intensities at 1000−1060 cm^{-1}(C−O−C-stretching vibrations), 1201 cm^{-1} (−OH in-plane bending), 1112 cm^{-1} (C−H deformation stretching vibration), and 1165 cm^{-1} (asymmetry stretch vibration), which suggests that some degradation has occurred. The formation of sodium carboxylate groups in all oxidised nanocellulose is shown by the presence of a sharp peak at 1615 cm^{-1}. In general, this sharp peak increases with increasing periodate concentration.

High levels of carboxylate groups (1.27–1.94 mmol COO^-/g fibre) were introduced on nanocellulose by oxidative reactions (Fig. 2b). The carboxylate content and degree of substitution of the nanocellulose fibres increase with periodate concentration. An abrupt increase in carboxylate content and DS is observed at 2.5 mmol/g periodate. This increase in COOH substitution, expressed as DS, increases the nanocellulose charge as measured by zeta potential (Fig. 2c). Interestingly, the TEMPO-periodate oxidised cellulose nanofibres have a significant surface charge, as high as −80 mV.

3.1.1. Optical transmittance

TEMPO and TEMPO-periodate oxidised nanocellulose gels (1 wt.%) of varying carboxylate content were produced (Fig. 3). These gels range from translucent to highly transparent. The gel optical transmittance at 715 nm increases with the level of periodate concentration in the oxidation reaction. The difference in optical transmittance between TOF gel (7%) and TPOF gel (as high as 65%) is significant. DS directly affects the optical transmittance of the gel (Fig. 3); nanocellulose gels transparency increases non-linearly with DS or the level of oxidation.

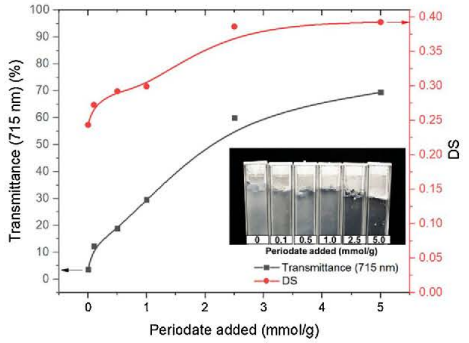

Fig. 3. Effect of periodate concentration on DS and optical transmittance of 1 wt.% nanocellulose gels at 715 nm. Inset: photographs of the oxidised nanocellulose gels.

3.1.2. Morphology and degree of polymerisation

Fig. 4 shows the transmission electron micrographs (TEM) of TEMPO-oxidised (0 mmol IO_4^-/g) and TEMPO-periodate oxidised (2.5 mmol IO_4^-/g) nanocellulose fibres. The oxidised celluloses were fully disintegrated into nanofibres with measured widths less than 4 nm, agreeing with previous reports (Shinoda et al., 2012). Interestingly, TEMPO-oxidation produced long and aggregated nanofibres (> 1 μm long, > 5 nm wide), whereas TEMPO-periodate oxidation led to shorter and better separated individualised nanofibres (< 0.5 μm long, 2−4 nm wide).

The effect of oxidation on the cellulose degree of polymerization (DP) was measured by viscosity. The nanocellulose degree of polymerisation degrades faster than linearly with DS (Fig. 5). A gradual and linear decrease in the DP_v of nanofibres is initially observed for DS ranging from 0.24 to 0.30, followed by a step decrease for DS > 0.30. These results support the TEM analysis; that is, increasing the level of oxidation increases charge density but shortens nanofibres. This corroborates a previous study where the fibril length of TEMPO-oxidised fibres decreased with increasing NaClO concentration (Shinoda et al., 2012). However, because the DS range investigated in this study is much wider than previously reported, cellulose nanofibres of lower fibril length and DP_v are achieved.

3.1.3. Viscoelastic properties

Rheology measured the effects TEMPO-periodate oxidation has on the viscoelastic properties of nanocellulose gels. The viscosity curves of TEMPO (TOF; 0 mmol IO_4^-/g) and TEMPO-periodate (TPOF; 2.5 mmol IO_4^-/g) oxidized nanocellulose gels are presented at different concentration in Fig. 6a. All gels exhibited shear-thinning behaviour: viscosity decreases with an increase in shear rate. This corroborates previous work on TEMPO-oxidised gels (Curvello et al., 2019; Mendoza, Batchelor et al., 2018; Mendoza, Batchelor et al., 2018), but innovates in increasing the carboxylate content or DS tested. TOF gels have a higher zero shear viscosity than TPOF gels at 0.5 and 1 wt.% concentration. The dynamic moduli (G' and G") of the nanocellulose gels are quantified by oscillatory measurements (Fig. 6b). G' describes the dynamic elasticity or solid-like behaviour of the material, while G" is the viscous modulus or the liquid-like behaviour. The strength of TOF and TPOF gels increases with increasing solids concentration. At 0.1 to 0.5 wt.%, TOF gels possess higher dynamic modulus compared to their TPOF counterparts; however, the opposite trend is observed at 1 wt.%.

To understand the opposite trend at 1 wt.%, the effect of periodate concentration and DS on the viscoelastic properties at this concentration was investigated. Fig. 7 reveals that TPOF gels (0.1–5.0 mmol/g IO_4^-) exhibit higher zero-shear viscosity (Fig. 7a) and dynamic moduli (Fig. 7b) than TOF gel (0 mmol/g IO_4^-), confirming the results of

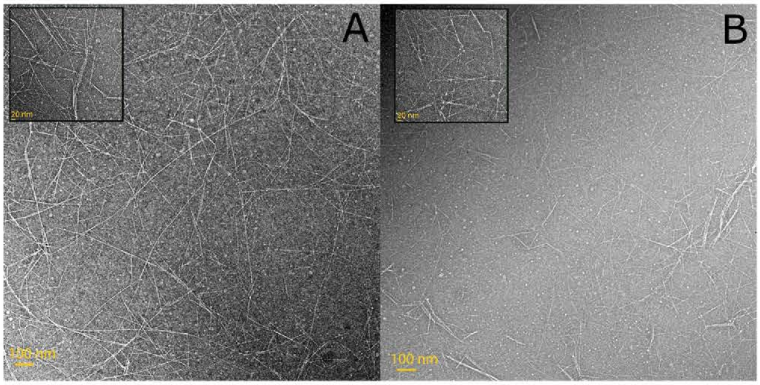

Fig. 4. TEM images of **(a)** TEMPO oxidised cellulose nanofibres (TOF) and **(b)** TEMPO-periodate oxidised nanofibres (TPOF).

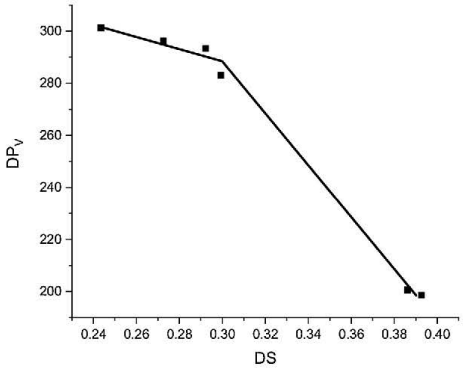

Fig. 5. Effect of the DS on the average viscometric degree of polymerisation (DP_v) of TEMPO-periodate oxidised nanocellulose fibres.

Fig. 6. However, such increases do show a maximum; the gel viscosity and strength started to marginally decrease at DS = 0.30. However, 1 wt.% TPOF gels of DS = 0.38−0.4 exhibit higher viscosity and dynamic moduli than 1 wt.% TOF gel (DS = 0.24). This suggests that DS does not correlate linearly with the viscoelastic properties of carboxylated nanocellulose gels; viscosity and dynamic moduli of the gels are influenced by factors such as solids concentration, aspect ratio, and DS.

3.1.4. Effect of pH and salt concentration on stability

Fig. 8 shows the effect of salt and pH on the stability of 1 wt.% TOF and TPOF gels. The gel stability was quantified with the fibre ratio defined as the gel height after over that before pH and salt treatment. Fig. 8a reveals that TPOF gels remain stable up to 40 mM NaCl, whereas TOF gels release water at only 20 mM NaCl. Both TOF and TPOF gels are unstable under acidic pH but stable over pH ranging from 7 to 11 (Fig. 8b). Interestingly, at pH = 12.5, TPOF gels remain relatively stable, whereas TOF gels released a significant amount of water (fibre ratio = 0.5).

3.1.5. Free swell capacity (FSC)

Carboxylated nanocellulose gels were freeze-dried and their water reabsorption capacity measured. The swelling profile and free swell capacity of the gels at equilibrium are shown in Fig. 9. The swelling of all freeze-dried gels is characterised by an initial abrupt absorption of water during the first 10 h, followed by sustained retention of water until equilibrium (92 h). This study supports previous results (Curvello et al., 2019), but broadens the findings over a much wider range of charge. Consistently, nanocellulose gels treated with higher periodate

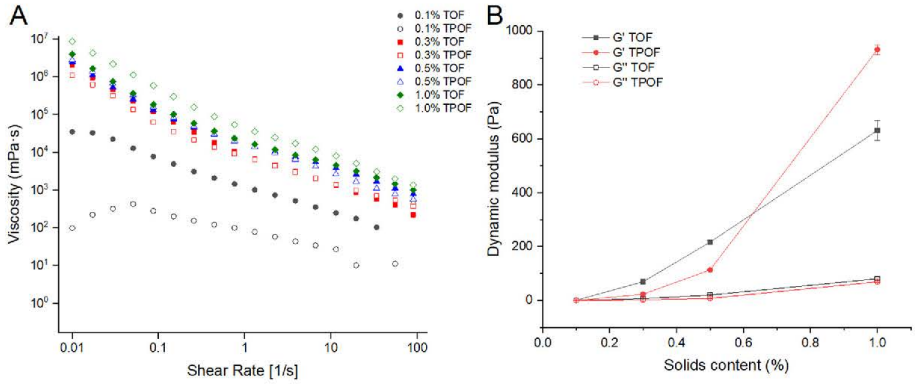

Fig. 6. (a) Viscosity curves of TOF (0 mmol IO_4^- /g) and TPOF (2.5 mmol IO_4^- /g) nanocellulose gels as a function of solids concentration (wt.%). **(b)** Dynamic moduli (Pa) of TOF (0 mmol/g IO_4^-) and TPOF (2.5 mmol/g IO_4^-) gels at different concentrations (wt. %). Measurements were performed at 25 °C and constant frequency (1 Hz). Filled and unfilled symbols represent G' and G'', respectively.

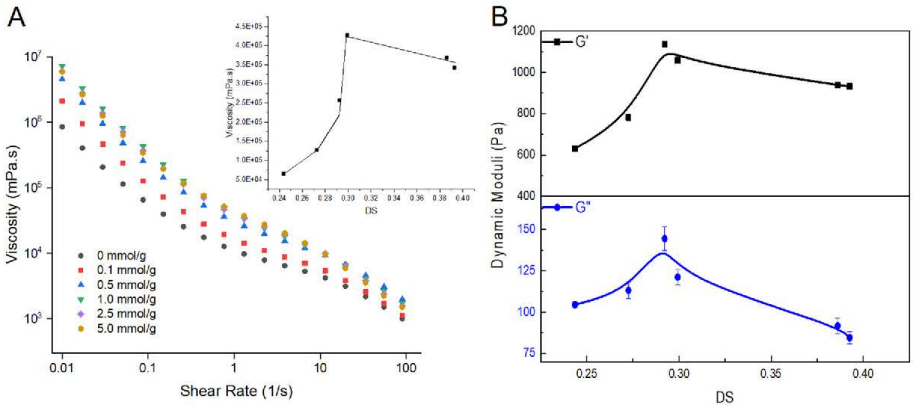

Fig. 7. **(a)** Viscosity curves of carboxylated nanocellulose gels as a function of periodate concentration (mmol/g). Inset shows the effect of DS on the viscosity of the gels at 0.1 s^{-1}. **(b)** Dynamic moduli (Pa) of carboxylated nanocellulose gels as a function of DS. Measurements were performed at 25 °C and constant frequency (1 Hz). Filled and unfilled symbols represent G' and G", respectively.

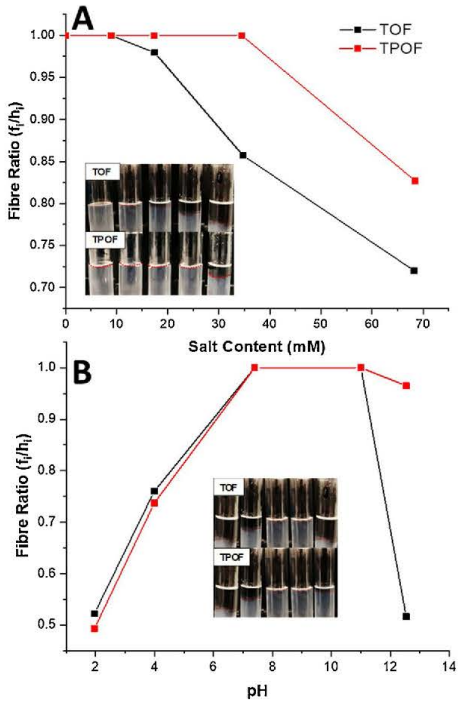

Fig. 8. The effect of **(a)** salt content (mM) and **(b)** pH on the stability of 1 wt.% TOF and TPOF gels. Insets show the release of water from the gels at pH (2-12.5) and salt levels (0-70 mM NaCl).

concentration exhibit a higher FSC. At equilibrium, nanocellulose gels free swell capacity (FSC) increases linearly with DS.

3.1.6. Red blood cells in nanocellulose gels

Reagent red blood cells were loaded in 0.3 wt.% TEMPO-periodate oxidised gels and imaged by optical microscopy. Healthy red blood cells can clearly be imaged in the transparent TPOF gel (Fig. 10). This demonstrates the potential of the gel as a biocompatible media as a matrix for cell imaging and diagnostic application. The high transparency of the gel is attributed to the high oxidation level in TEMPO-periodate oxidation which may not be achievable with TEMPO oxidation alone or mechanical and enzymatic treatments.

4. Discussion

TEMPO-mediated oxidation is the most common chemical pretreatment to carboxylate cellulose and liberate cellulose nanofibres upon homogenisation. However, the COOH substitution can exclusively occur in the C6 glycosidic position, which limits the degree of substitution achievable in carboxylated nanocellulose. In this study, TEMPO-mediated oxidation is combined with periodate in a one-shot reaction to carboxylate cellulose. FTIR and conductimetric titration analyses (Fig. 2) reveal that the addition of periodate controls the level of nanocellulose carboxylation. COOH substitution is higher in TEMPO-periodate oxidation than TEMPO oxidation as evidenced by the significant increase in surface charge (−80 mV) for TPOF nanofibres. This is the most stable and highly-charged nanocellulose fibre that we have prepared to date. This is expected in TEMPO-periodate oxidation, as the C2, C3, and C6 hydroxyl groups can be oxidised to carboxylate groups (Fig. 1). The greater surface charge in TPOF enables a significant increase in the degree of nanofibrillation, as revealed by TEM. The stronger electrical repulsion and decreased hydrogen bonding in TPOF enhanced nanofibrillation relative to TOF. However, at high DS, TPOF fibres start to degrade as indicated by the decrease in DP_v and length (Figs. 4 and 5).

The remarkable increase in surface charge and enhanced nanofibrillation enable the good dispersion of the nanofibres in water to form a gel. The characteristics of the gel are directly associated with the extent of carboxylation of the nanofibrils. Here, we correlate the properties of the nanofibres with the gel transparency, salt and pH stability, rheology, and water absorbency.

Because of the higher charge and better fibrillation in TEMPO-periodate oxidation, the resulting gels are highly transparent (Fig. 3). The strong electrical repulsion between the TPOF fibres hinder their aggregation and thus reduce the light scattering of the gels (Saito et al., 2007). The high transparency of the nanofibres is also attributed to their lower aspect ratio (Carr, Shen, & Hermans, 1977; Carr & Hermans, 1978); that is, the width of the nanofibres are smaller than the wavelength of light which causes the gels to be transparent.

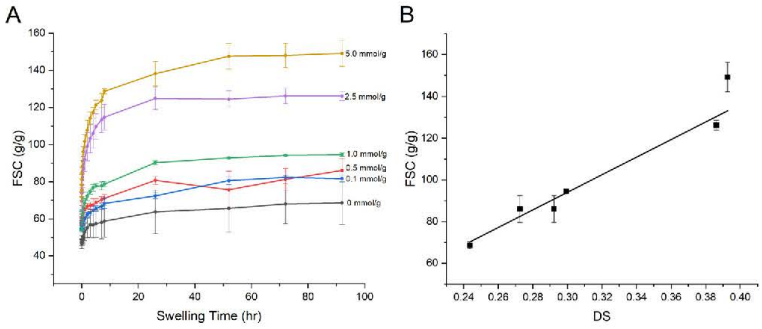

Fig. 9. **(a)** Swelling profile of 1 wt.% freeze-dried carboxylated nanocellulose gels at different periodate concentrations (mmol/g) in water. **(b)**Free swell capacity of freeze-dried carboxylated nanocellulose gels with different DS at equilibrium (92 h).

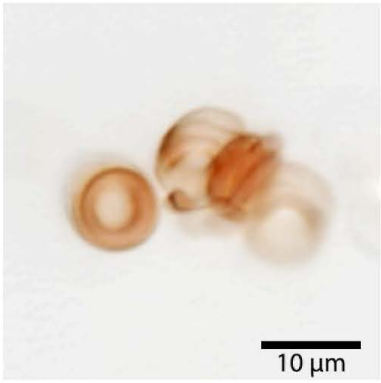

Fig. 10. Optical image of red blood cells in 0.3 wt.% TEMPO-periodate nanocellulose gels at 100x magnification.

The lower aspect ratio and higher surface charge of TPOF nanofibres also explain the reduced viscosity and moduli TPOF gels at 0.1 − 0.5 wt. % (Figs. 6 and 7). At high DS, the nanofibrils are significantly shorter and the probability of fibre entanglement in a dilute suspension is also decreased; resulting in the formation of weakly-networked gels (Benhamou et al., 2014), such as in the case of TPOF gels at 0.1 − 0.5 wt.%. We hypothesise that these fibrils behave like cellulose nanocrystals assembled as liquid crystals where fibre entanglement is limited and repulsive forces are dominant (Urena-Benavides, Ao, Davis, & Kitchens, 2011). These rigid rods tend to percolate and form a gel. Conversely, at 1 wt.%, TPOF gels become stiffer than TOF gels. This is due to the higher fibrillation level resulting from enhanced electrical repulsion leading to a stronger network. However, as seen in Fig. 7, this is only true at DS ≤ 0.3. The gradual decrease in moduli and viscosity with DS is attributed to the lower agglomeration ability of the nanofibres due to higher electrical repulsion (Benhamou et al., 2014; Geng et al., 2018).

The higher charge of TPOF nanofibres also explains the enhanced stability of TPOF gels relative to TOF gels at elevated pH and salt levels (Fig. 8). Increasing the ionic strength effectively screens the negatively-charged carboxylate groups which also decreases the electrical double layer in gels. This results in the destabilisation of the colloidal system and ultimately leads to the collapse of the existing fibre network (Mendoza, Batchelor et al., 2018). TPOF gels, having a higher surface charge than TOF gels, require a greater concentration of salt ions to screen the nanocellulose surface charges. On the other hand, pH severely affects the stability of carboxylated nanocellulose gels. At low pH, the carboxylate groups are protonated resulting in decreased surface potential and electrical repulsion, leading to fibre agglomeration and gel destabilisation (Mendoza, Batchelor et al., 2018). Both TOF and TPOF gels exhibit the same behaviour at acidic and slightly basic conditions. Carboxylated gels are relatively stable at basic pH; however, the effect of ionic strength also needs to be considered. Only the TPOF gel remains stable at pH = 12.5. This is because the ionic strength at pH 12.5 is sufficient to cause TOF gel to collapse.

Increasing the DS of the gels also improves their water holding capacity (Fig. 9). Gels bearing a higher DS or more carboxylate groups can immobilise more water molecules by hydrogen bonding (Hossain et al., 2020; Mendoza, Browne et al., 2019). At 5 mmol IO_4^-/g, the FSC of 1 wt.% TPOF gel is reported to be as much as 150 g/g, which is comparable with commercial superabsorbent polymers such as potassium polyacrylate (Zhang, Feng, & Jin, 2020). TPOF foams can be developed as a green alternative to the current petrochemical-based, irritant and even toxic superabsorbent.

In summary, combining periodate with TEMPO oxidation enables the control of the degree of substitution and surface charge of nanocellulose fibres. Increasing the level of oxidation increases the surface charge and degree of nanofibrillation. However, the nanofibres depolymerise as a consequence of high degree of oxidation (Isogai et al., 2011; Shinoda et al., 2012). The enhanced nanofibrillation, in addition to higher charge, results in very stable and homogeneous nanofibrils forming the gel. These gels are more transparent and exhibit better water-holding capacity and pH and salt stability. High degree of oxidation also induces reduced viscosity and dynamic moduli. The rheology of these gels resembles that of cellulose nanocrystals exhibiting liquid crystal behaviour where electrical repulsion is dominant and fibre entanglement is limited. By controlling the extent of carboxylation of cellulose, we can manipulate the properties of carboxylated nanocellulose gels.

To demonstrate the potential application of the highly transparent gel, we loaded reagent red blood cells and use it as a matrix for storage and analysis. Fig. 10 reveals that red blood cells remain healthy and can be directly imaged whilst loaded inside the gel. The high transparency of the gel allowed clear imaging of the red blood cells. The transparency or cloudiness of the gel is particularly important for imaging and ophthalmic applications (Wang & Han, 2017). The excellent transparency of the nanocellulose gel open new possibilities in diagnostics application.

5. Conclusion

2,2,6,6-Tetramethylpiperidine-1-oxyl (TEMPO)-mediated oxidation coupled with mechanical fibrillation remains as the most common

method to prepare carboxylated cellulose nanofibres. However, the degree of substitution (DS) achievable is limited as only the C6 hydroxyl groups can be oxidised. In this work, TEMPO and periodate are combined in a one-shot reaction to oxidise the C2, C3, and C6 OH groups and produce nanocellulose gels over a wide range of DS. TEMPO-periodate oxidation yields highly-carboxylated cellulose nanofibres (DS = 0.4) with a very high charge of −80 mV. The strong electrical repulsion between the fibres results in the formation of well-separated nanofibres with a diameter of 2−4 nm, although depolymerisation is observed as a consequence of the high oxidation level.

The properties of the gels can be engineered through TEMPO-periodate oxidation/fibrillation. TEMPO-periodate oxidised fibres (TPOF) results in a highly-transparent gel. Their smaller aspect ratio and very high surface charge prevents aggregation and reduces the light scattering of the gels. TEMPO-periodate oxidation also results in gels of reduced viscosity and dynamic moduli. Gel rheology is dependent on the DS and nanofibre concentration. In a dilute regime (0.1−0.5 wt.%), TPOF nanofibres have a low tendency to entangle to form a strong network due to strong electrical repulsion and reduced length. At 1 wt. %, these fibres form a stronger network thanks to an enhanced degree of fibrillation. The TPOF gels have a superior stability at basic pH and high ionic strength due to their high surface charge. Freeze-dried nanocellulose foams prepared from TPOF gels also exhibit remarkable water holding capacity and can immobilise more water molecules by hydrogen bonding. The potential of the highly transparent gel for red blood cells analysis and diagnostic applications is also demonstrated.

CRediT authorship contribution statement

David Joram Mendoza: Conceptualization, Validation, Methodology, Investigation, Software, Writing - original draft. **Laila Hossain:** Methodology, Investigation, Writing - original draft. **Christine Browne:** Validation, Writing - review & editing. **Vikram Singh Raghuwanshi:** Validation, Writing - review & editing. **George P. Simon:** Supervision, Writing - review & editing. **Gil Garnier:** Visualization, Supervision, Writing - review & editing.

Acknowledgements

Funding from the Australian Research Council-Industry Transformation Research Hub; Processing Advanced Lignocellulosics (PALS) [grant number IH170100020] is gratefully acknowledged. Many thanks to Dr. T. Williams, Monash Centre for Electron Microscopy (MCEM), for assistance in TEM analysis and Mr. R Curvello and Ms. D. Alves for help with red blood cells experiment.

References

Adam, W., Saha-Moller, C. R., & Ganeshpure, P. A. (2001). Synthetic applications of nonmetal catalysts for homogeneous oxidations. *Chemical Reviews, 101*(11), 3499–3548.

Ämmälä, A., Liimatainen, H., Burmeister, C., & Niinimäki, J. (2013). Effect of tempo and periodate-chlorite oxidized nanofibrils on ground calcium carbonate flocculation and retention in sheet forming and on the physical properties of sheets. *Cellulose, 20*(5), 2451–2460.

Baron, R. I., Bercea, M., Avadanei, M., Lisa, G., Biliuta, G., & Coseri, S. (2019). Green route for the fabrication of self-healable hydrogels based on tricarboxy cellulose and poly(vinyl alcohol). *International Journal of Biological Macromolecules, 123*, 744–751.

Benhamou, K., Dufresne, A., Magnin, A., Mortha, G., & Kaddami, H. (2014). Control of size and viscoelastic properties of nanofibrillated cellulose from palm tree by varying the TEMPO-mediated oxidation time. *Carbohydrate Polymers, 99*, 74–83.

Carr, M. E., & Hermans, J. (1978). Size and density of fibrin fibers from turbidity. *Macromolecules, 11*(1), 46–50.

Carr, M. E., Jr, Shen, L. L., & Hermans, J. (1977). Mass-length ratio of fibrin fibers from gel permeation and light scattering. *Biopolymers, 16*(1), 1–15.

Chen, W. S., Yu, H. P., Liu, Y. X., Chen, P., Zhang, M. X., & Hai, Y. F. (2011). Individualization of cellulose nanofibers from wood using high-intensity ultrasonication combined with chemical pretreatments. *Carbohydrate Polymers, 83*(4), 1804–1811.

Cheng, J., Park, M., & Hyun, J. (2014). Thermoresponsive hybrid hydrogel of oxidized nanocellulose using a polypeptide crosslinker. *Cellulose, 21*(3), 1699–1708.

Coseri, S., Biliuta, G., Zemljic, L. F., Srndovic, J. S., Larsson, P. T., Strnad, S., & Lindstrom, T. (2015). One-shot carboxylation of microcrystalline cellulose in the presence of nitroxyl radicals and sodium periodate. *RSC Advances, 5*(104), 85889–85897.

Curvello, R., Mendoza, L., McLiesh, H., Manolios, J., Tabor, R. F., & Garnier, G. (2019). Nanocellulose hydrogel for blood typing tests. *ACS Applied Bio Materials, 2*(6), 2355–2364. https://doi.org/10.1021/acsabm.9b00080.

Curvello, R., Raghuwanshi, V. S., & Garnier, G. (2019). Engineering nanocellulose hydrogels for biomedical applications. *Advances in Colloid and Interface Science, 267*, 47–61.

deNooy, A. E. J., Besemer, A. C., & vanBekkum, H. (1996). On the use of stable organic nitroxyl radicals for the oxidation of primary and secondary alcohols. *Synthesis-Stuttgart,* (10), 1153–1174.

Dufresne, A. (2012). *Nanocellulose: From nature to high performance tailored materials.* De Gruyter.

Dufresne, A. (2013). Nanocellulose: A new ageless bionanomaterial. *Materials Today, 16*(6), 220–227.

Fiorati, A., Contessi Negrini, N., Baschenis, E., Altomare, L., Faré, S., Giacometti Schieroni, A., & Melone, L. (2020). TEMPO-nanocellulose/Ca(2+) hydrogels: Ibuprofen drug diffusion and in vitro cytocompatibility. *Materials (Basel, Switzerland), 13*(1), 183.

Geng, L., Mittal, N., Zhan, C., Ansari, F., Sharma, P. R., Peng, X., & Söderberg, L. D. (2018). Understanding the mechanistic behavior of highly charged cellulose nanofibers in aqueous systems. *Macromolecules, 51*(4), 1498–1506.

Habibi, Y. (2014). Key advances in the chemical modification of nanocelluloses. *Chemical Society Reviews, 43*(5), 1519–1542.

Haun, J. B., Yoon, T.-J., Lee, H., & Weissleder, R. (2010). Magnetic nanoparticle biosensors. *WIREs Nanomedicine and Nanobiotechnology, 2*(3), 291–304.

Hietala, M., Ämmälä, A., Siivennoinen, J., & Liimatainen, H. (2016). Fluting medium strengthened by periodate–chlorite oxidized nanofibrillated celluloses. *Cellulose, 23*(1), 427–437.

Ho, T. T. T., Abe, K., Zimmermann, T., & Yano, H. (2015). Nanofibrillation of pulp fibers by twin-screw extrusion. *Cellulose, 22*(1), 421–433.

Hossain, L., Raghuwanshi, V. S., Tanner, J., Wu, C.-M., Kleinerman, O., Cohen, Y., & Garnier, G. (2020). Structure and swelling of cross-linked nanocellulose foams. *Journal of Colloid and Interface Science, 568*, 234–244.

Hu, J., Tian, D., Renneckar, S., & Saddler, J. N. (2018). Enzyme mediated nanofibrillation of cellulose by the synergistic actions of an endoglucanase, lytic polysaccharide monooxygenase (LPMO) and xylanase. *Scientific Reports, 8*(1), 3195.

Isobe, N., Chen, X. X., Kim, U. J., Kimura, S., Wada, M., Saito, T., … Isogai, A. (2013). TEMPO-oxidized cellulose hydrogel as a high-capacity and reusable heavy metal ion adsorbent. *Journal of Hazardous Materials, 260*, 195–201.

Isogai, A., Saito, T., & Fukuzumi, H. (2011). TEMPO-oxidized cellulose nanofibers. *Nanoscale, 3*(1), 71–85.

Jiang, J., Ye, W. B., Liu, L., Wang, Z. G., Fan, Y. M., Saito, T., … Isogai, A. (2017). Cellulose nanofibers prepared using the TEMPO/laccase/O-2 system. *Biomacromolecules, 18*(1), 288–294.

Klemm, D., Schumann, D., Kramer, F., Heßler, N., Koth, D., & Sultanova, B. (2009). Nanocellulose materials - different cellulose, different functionality. *Macromolecular Symposia, 280*(1), 60–71.

Mendoza, L., Batchelor, W., Tabor, R. F., & Garnier, G. (2018). Gelation mechanism of cellulose nanofibre gels: A colloids and interfacial perspective. *Journal of Colloid and Interface Science, 509*, 39–46.

Mendoza, D. J., Browne, C., Raghuwanshi, V. S., Simon, G. P., & Garnier, G. (2019). One-shot TEMPO-periodate oxidation of native cellulose. *Carbohydrate Polymers, 226*, 115292.

Mendoza, L., Gunawardhana, T., Batchelor, W., & Gamier, G. (2018). Effects of fibre dimension and charge density on nanocellulose gels. *Journal of Colloid and Interface Science, 525*, 119–125.

Mendoza, L., Hossain, L., Downey, E., Scales, C., Batchelor, W., & Garnier, G. (2019). Carboxylated nanocellulose foams as superabsorbents. *Journal of Colloid and Interface Science, 538*, 433–439.

Nascimento, D. M., Nunes, Y. L., Figueiredo, M. C. B., de Azeredo, H. M. C., Aouada, F. A., Feitosa, J. P. A., & Dufresne, A. (2018). Nanocellulose nanocomposite hydrogels: technological and environmental issues. *Green Chemistry, 20*(11), 2428–2448.

Okita, Y., Saito, T., & Isogai, A. (2010). Entire surface oxidation of various cellulose microfibrils by TEMPO-mediated oxidation. *Biomacromolecules, 11*(6), 1696–1700.

Perez, D. D., Montanari, S., & Vignon, M. R. (2003). TEMPO-mediated oxidation of cellulose III. *Biomacromolecules, 4*(5), 1417–1425.

Ruizhi, N., Yi, L. L., Yamasaki, S., Lin, J. M., Saito, T., & Isogai, A. (2017). TEMPO-Oxidized Cellulose Nanofiber (TOCN) materials show good biomedical applications. *Abstracts of Papers of the American Chemical Society*, 253.

Saito, T., & Isogai, A. (2004). TEMPO-mediated oxidation of native cellulose. The effect of oxidation conditions on chemical and crystal structures of the water-insoluble fractions. *Biomacromolecules, 5*(5), 1983–1989.

Saito, T., Hirota, M., Tamura, N., Kimura, S., Fukuzumi, H., Heux, L., … Isogai, A. (2009). Individualization of nano-sized plant cellulose fibrils by direct surface carboxylation using TEMPO catalyst under neutral conditions. *Biomacromolecules, 10*(7), 1992–1996.

Saito, T., Kimura, S., Nishiyama, Y., & Isogai, A. (2007). Cellulose nanofibers prepared by TEMPO-mediated oxidation of native cellulose. *Biomacromolecules, 8*(8), 2485–2491.

Shinoda, R., Saito, T., Okita, Y., & Isogai, A. (2012). Relationship between length and degree of polymerization of TEMPO-oxidized cellulose nanofibrils. *Biomacromolecules, 13*(3), 842–849.

Tarres, Q., Boufi, S., Mutje, P., & Delgado-Aguilar, M. (2017). Enzymatically hydrolyzed and TEMPO-oxidized cellulose nanofibers for the production of nanopapers: Morphological, optical, thermal and mechanical properties. *Cellulose, 24*(9),

3943–3954.
Uetani, K., & Yano, H. (2011). Nanofibrillation of wood pulp using a high-speed blender. *Biomacromolecules, 12*(2), 348–353.
Urena-Benavides, E. E., Ao, G. Y., Davis, V. A., & Kitchens, C. L. (2011). Rheology and phase behavior of lyotropic cellulose nanocrystal suspensions. *Macromolecules, 44*(22), 8990–8998.
Wang, K., & Han, Z. (2017). Injectable hydrogels for ophthalmic applications. *Journal of Controlled Release, 268*, 212–224.
Zander, N. E., Dong, H., Steele, J., & Grant, J. T. (2014). Metal cation cross-linked nanocellulose hydrogels as tissue engineering substrates. *ACS Applied Materials & Interfaces, 6*(21), 18502–18510.
Zhang, K., Feng, W., & Jin, C. (2020). Protocol efficiently measuring the swelling rate of hydrogels. *MethodsX, 7*, 100779.
Zimmermann, T., Pohler, E., & Geiger, T. (2004). Cellulose fibrils for polymer reinforcement. *Advanced Engineering Materials, 6*(9), 754–761.

Journal of Colloid and Interface Science 538 (2019) 433–439

Contents lists available at ScienceDirect

Journal of Colloid and Interface Science

journal homepage: www.elsevier.com/locate/jcis

Regular Article

Carboxylated nanocellulose foams as superabsorbents

Llyza Mendoza, Laila Hossain, Emma Downey, Camilla Scales, Warren Batchelor, Gil Garnier *

Bioresource Processing Research Institute of Australia (BioPRIA), Department of Chemical Engineering, Monash University, VIC 3800, Australia

GRAPHICAL ABSTRACT

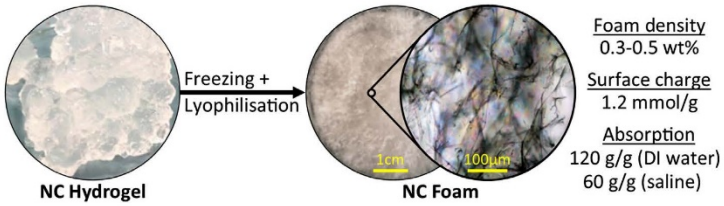

ARTICLE INFO

Article history:
Received 25 October 2018
Revised 29 November 2018
Accepted 30 November 2018
Available online 1 December 2018

Keywords:
Superabsorbent
TEMPO-mediated oxidation
Nanocellulose
Foam
Structure

ABSTRACT

Hypothesis: Carboxylated nanocellulose fibres formed into foam structures can demonstrate superabsorption capacity. Their performance can be engineered by changing process variables.

Experiments: TEMPO-oxidised cellulose nanofibres of varying concentration and surface charge are produced from hardwood kraft pulp. Foams were prepared through a 2-step freezing and lyophilisation process. The absorption capacity of water and saline solution (0.9 wt%) were measured as a function of time and related to the foam structure.

Findings: The absorption capacity of nanocellulose foams can be manipulated from initial gel properties and processing conditions. Pore structure and distribution of nanocellulose foams are dictated by fibre content and charge density and freezing rate. The best performing foams are at 0.3–0.5 wt%, with a carboxylate concentration of 1.2 mmol/g and frozen at −86 °C before freeze-drying, which can absorb 120 g H_2O/g fibre. Fibre surface charge influences the absorption capacity of the foams by dictating the amount of participating carboxylate groups. Absorption capacity in saline (60 g/g) is lower than in deionised water (120 g/g); but is only slightly lower than that of a commercial polyacrylic acid (PAA) SAPs (80 g/g). Nanocellulose foams are attractive renewable alternatives for superabsorbent applications, contributing to a reduction of plastic microspheres.

1. Introduction

Superabsorbent polymer (SAP) hydrogels contain cross-linked network of hydrophilic polymers capable of absorbing large volumes of water [1]. Upon contact with water, the glassy polymers hydrate to form a three-dimensional network which does not dissolve due to the presence of cross-linking [2]. The swelling of these polymer networks is driven by the difference in osmotic pressure inside and outside the gel caused by the movement of the counterions in the system. The high absorption of water molecules is due to a high concentration of COO^- groups able to form hydrogen bonding with water molecules [3]. Although commercial SAPs are usually known for applications in personal care and hygiene products, these materials are also increasingly utilised in agriculture and horticulture [4], biomedical products [5–7], and even wastewater treatment [8,9]. Currently, the majority of superabsorbent products in the market is synthesised from acrylic and acrylamide

* Corresponding author.
E-mail address: gil.garnier@monash.edu (G. Garnier).

https://doi.org/10.1016/j.jcis.2018.11.112
0021-9797/

polymers from petrochemicals which exhibit poor environmental degradability. This lack of sustainability has driven research towards developing alternatives which are renewably sourced and biodegradable.

There are many reports of superabsorbents made from natural polymers in literature. Natural-based SAPs, such as chitosan, gelatine, carrageenan and starch, have been modified to increase water absorption [10,11]. Cellulose, the most abundant biopolymer, has also been studied for its desirable characteristics: biodegradability, renewability, and innate hydrophilicity [12]. Cellulose can be processed into porous materials such as foams [13,14] and different synthesis methods have been explored to functionalise cellulose as a superabsorbent hydrogel [12]. Among those are foam and hydrogel composites made with carboxymethyl cellulose [15–19] and hydroxyethyl cellulose [20,21] used in combination with other polymers and nanoparticles. Another strategy is to graft side groups such as butanetetracarboxyl, acrylic, and acrylamide groups onto the cellulose backbone which results in large absorption of water (~720 g/g) [22,23]. Functionalising the cellulose hydroxyl groups can significantly increase water interactions.

Another method of producing foams is through the production of nanocellulose and manufacture of foams via ice-templating followed by sublimation or via supercritical drying [24]. TEMPO-mediated oxidation is alternative method of functionalising cellulose fibres [25]. This oxidation process selectively converts the primary alcohol (C6) groups into carboxylate groups. The added electrostatic repulsion produces nano-scale fibres upon mechanical fibrillation. Brodin and Theliander initially tested the superabsorbent characteristics of TEMPO-oxidised nanocellulose by varying different process conditions such as pulp types, composition, and oxidation severity [26–29]. Jiang and Hsieh investigated the production of nanocellulose aerogels via cyclic freeze-thawing process and also introduced functionalisation to create oleophilic foams [30–32]. However, the effects of varying foam properties by changing the fibre density were not explored nor related to composite structure. There are limited studies on the effect of processing conditions (i.e. freezing rate) on the performance of nanocellulose foams. Moreover, the kinetics of nanocellulose foam swelling remain unknown.

In this study, we produced nanocellulose superabsorbent foams via a two-step process: (1) TEMPO-mediated oxidation/high-pressure homogenisation to produce a nanocellulose hydrogel [33,34] and (2) freeze-drying the hydrogel to produce nanocellulose foams. The aim of this study is to understand the relationship between process variables (freezing rate) and nanocellulose properties (surface charge and fibre concentration) to the resulting foam structure and absorption characteristics. The swelling kinetics of the foams is also determined. Insight into the mechanism of superabsorbency of these carboxylated nanocellulose foams is demonstrated.

2. Methodology

2.1. Materials

Bleached Eucalyptus Kraft (BEK) pulp, containing approximately 10 wt% solids, was obtained from Australian Paper, Maryvale, Australia. 2,2,6,6-Tetramethylpiperidine-1-oxyl (TEMPO) and sodium bromide (NaBr) were purchased from Sigma-Aldrich. Hydrochloric acid (HCl) and Sodium Hydroxide (NaOH) were diluted for solutions as required and were purchased from ACL Laboratories and Merck, respectively. 12 w/v% Sodium Hypochlorite (NaClO) was purchased from Thermo Fisher Scientific and used as received. Commercial sodium polyacrylate superabsorbent (HySORB R 8130) was provided by BASF.

2.2. TEMPO-mediated oxidation

The TEMPO-mediated oxidation process employed is based on a previously developed method [25]. 100 g BEK pulp was suspended in 2500 mL water containing 0.4 g TEMPO and 2.5 g NaBr. The 12 w/v% NaClO solution was initially adjusted to pH 10 via addition of 36 w/v% HCl. To produce high surface charged fibres, 75 mL NaClO (5 mmol NaClO/g cellulose) was added drop-wise to the suspension whilst stirred. Lower surface charged fibres were produced by adding a lower amount of the primary oxidant (50 mL NaClO, 3.33 mmol/g). The pH of the reaction was maintained at 10 through the addition of 0.5 M NaOH. The oxidation process is deemed to be complete when the pH change is negligible. The oxidised fibres were recovered through filtration and stored refrigerated (2–8 °C).

The TEMPO-oxidised pulp is then dispersed in deionised water at a desired concentration. Fibrillation is accomplished through a high-pressure homogeniser (GEA Niro Soavi Homogeniser Panda) at 1000 bar. Suspensions which contain less than 1 wt% TEMPO-oxidised pulp is homogenised with two passes. More concentrated suspensions are homogenised with only one pass.

2.3. Preparation of nanocellulose foams

Nanocellulose foams were prepared by spreading 15 g gel in a 50 mm petri dish and freezing at either in a freezer for at least 12 h (−20 °C, −80 °C) or in liquid nitrogen (−196 °C). For freezing at −196 °C, the samples were placed in a cold-proof container and liquid nitrogen was poured in ensuring full immersion for 4–5 min. Once frozen, all samples were freeze-dried (Christ Alpha 2–4 LD Plus) for 2 days.

2.4. Determining solids concentration

The solids concentration of any sample (i.e. hydrogel or pulp) is determined through oven drying. The sample is weighed before (w_i) and after (w_d) drying, where the sample moisture is evaporated in a ventilated oven at 105 °C for at least 4 h. The solids content is determined through the following equation:

$$Solids\ content\ (\%) = \frac{w_d}{w_i} \times 100\% \quad (1)$$

2.5. Determining the carboxylate content of nanocellulose

The carboxylate content of the nanocellulose fibre is determined via conductometric titration [35]. 0.1 dry g oxidised pulp is suspended in 40 mL deionised water. 100 µL 1 wt% NaCl is added to the suspension to increase base sample conductivity. The sample pH is then lowered to pH 2.5–3 to protonate all of the carboxylate groups prior to the beginning of titration. Sample titration is initiated by the addition of 0.1 mL/min NaOH (Mettler Toledo T5 titrator). The conductivity is monitored throughout the progress of the titration. The amount of carboxylate groups is then calculated through the following equation:

$$Carboxylate\ Content\ \left(\frac{mmol}{g}\right) = \frac{c(V_2 - V_1)}{w} x100 \quad (2)$$

where V_2 and V_1 pertain to the required amount of titrant to neutralise the carboxylic groups (plateau region in the titration curve), c is the NaOH concentration (mol/L), and w is the dray sample weight.

2.6. Measurement of absorption capacity

The freeze-dried fibres are then allowed to be in contact with deionised water or 0.9 wt% NaCl solution for reabsorption. The foams were repeatedly taken out of immersion and weighed.

Intake of water by the foam is measured in regular intervals up to 2 h. The free swell capacity W is then calculated through the following equation:

$$\textit{Free Swell Capacity},\ W = \frac{m_t - m_i}{m_i} \quad (3)$$

where m_t is the mass of the swollen foam at a particular time interval and m_i is the initial mass of the foam. The results are reported as the average and standard deviation of 3 replicates.

2.7. Imaging of nanocellulose structure

Nanocellulose foams were imaged by optical microscopy (Nikon Eclipse Ni-E Upright Microscope) in bright-field mode at 5x magnification.

2.8. Mercury porosimetry

The pore size distribution, porosity (total and at P = 1 atm), and pore surface area were determined for selected nanocellulose foams via mercury porosimetry (Micromeritics Autopore IV). Nanocellulose foams were cut in small cubes (0.5 × 0.5 × 0.5 cm) by a laser cutter (Epilog Laser Helix). The samples were prepared by initially de-gassing (24 h, 100 °C) followed by testing. Two replicates per sample were tested. In all measurements, the contact angle at the Hg-Foam interface is assumed to be 130° and a testing pressure range from 0.1 to 60,000 psia is applied. The desired values are calculated via the Washburn Equation:

$$D = \frac{-4\gamma\cos\theta}{P} \quad (4)$$

where D is the pore diameter, γ is the surface tension of mercury, θ is the contact angle between the pore wall and mercury, and P is the applied pressure. Important values are reported at either as a result of considering 1 atm (14.7 psia) intrusion pressure or at total maximum porosimetry pressure (60,000 psia/4082 atm).

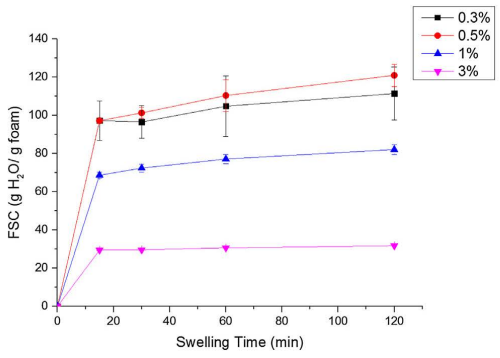

Fig. 1. Free Swell Capacity (FSC) in deionised water of nanocellulose foams (−80 °C) at different solids concentrations as a function of swelling time.

3. Results

The effect of initial gel properties such as the solids concentration and surface charge on the structure and morphology as well as the absorption behaviour of the foams is initially studied (frozen at -80 °C). The effect of freezing rate is then analysed. Lastly, the best performing foam in distilled water is tested with saline and compared against a commercial SAP.

3.1. Effect of gel solids concentration

Fig. 1 shows the free swell capacity (FSC) of nanocellulose foams in deionised water as a function of the initial gel solids concentration in deionised water. In all cases, the initial rapid swelling is followed by a slower absorption process in the 2 h testing period. There is no significant difference between the performance of foams produced from 0.3 wt% and 0.5 wt% (overlapping error bars). Measurement error also increases at lower initial gel concentrations. However, increasing the fibre concentration in gel from 0.5 wt% to 1 and 3 wt% resulted in a decrease in the FSC values.

The pore size distribution of nanocellulose foams was measured by mercury porosimetry as a function of the initial gel solids concentration is shown in Fig. 2A. Calculated foam properties for each of the nanocellulose foams is also summarised in Fig. 2B and C. At increasing initial gel solids concentration, the foam bulk density consistently increases. Foam porosity is calculated at two pressure levels (1 atm and at 4082 atm) to signify pores accessible at atmospheric pressure and the total maximum pore volume, respectively. Total foam porosity is similar (>94%) across all original gel concentrations; however, porosity at 1 atm is halved when the solids content is increased by an order of magnitude. The total pore surface area also decreased with increasing gel solids concentration.

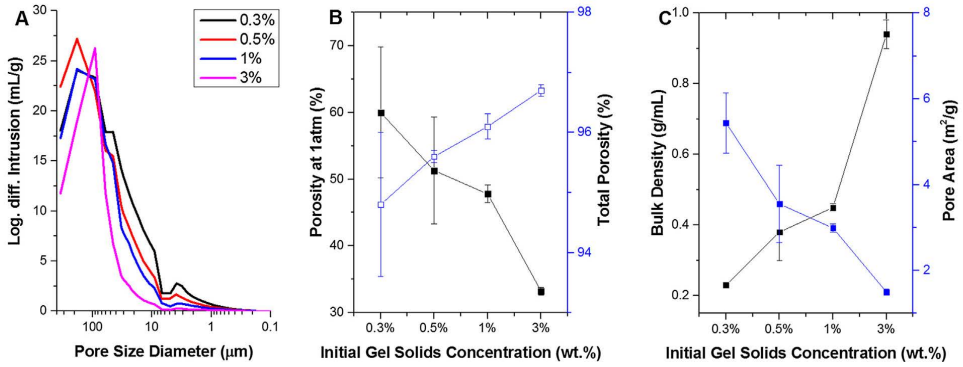

Fig. 2. (A) Pore size distribution of nanocellulose foams (−80 °C) at different solids concentrations. Foam properties such as (B) porosity (1 atm[a] and total[b]), (C) bulk density and pore area derived from mercury porosimetry. Further details on porosimetry data and related calculations are provided in the Supplementary Information. Notes: [a]Porosity at 1 atm is calculated by: $\textit{Porosity}\ (1atm) = \left(1 - \frac{\textit{Bulk Density}\ (1atm)}{\textit{Skeletal Density}}\right) \times 100\%$. [b]Total porosity is calculated by: $\textit{Total Porosity} = \left(\frac{\textit{Pore Volume}}{\textit{Skeletal Volume+Pore Volume}}\right) \times 100\%$.

3.2. Effect of surface charge

Fig. 3 shows the effect of the nanocellulose carboxylate group content on the foam absorption capacity. Lowering the carboxylate group from 1.2 mmol/g to 0.65 mmol/g resulted in lower absorption values for all concentrations tested.

3.3. Effect of freezing rate

The formation of nanocellulose foams is a two-step process which includes freezing of the nanocellulose gels and sublimation of the frozen water. In this study, the effect of freezing rate is studied by freezing at different temperatures (−20 °C, −80 °C, −196 °C). The freezing rate will be the slowest at −20 °C whereas freezing at −196 °C will be the fastest. The lyophilisation step is kept constant in this study. The effect of freezing rate on the performance of nanocellulose foams in absorbing deionised water is shown in Fig. 4A. Aside from 0.3 wt%, foams processed at −80 °C has performed slightly better than −20 °C. Freezing rate was modified to control foam morphology. Freezing at the lowest rate (−20 °C) results in sheet-like structures with interspersed pores (Fig. 4B) whereas at the fastest freezing rate (−196 °C), the pores formed are more uniform (Fig. 4D). At −80 °C, the structure formed is a combination of those from the two freezing rates (Fig. 4C).

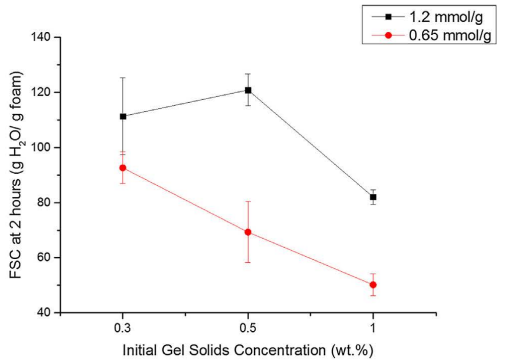

Fig. 3. Effect of cellulose fibre surface charge of nanocellulose foams (−80 °C) at different solids concentration on FSC in deionised water.

3.4. Absorption of saline

Fig. 5 shows the FSC of nanocellulose foam in 0.9 wt% saline. For all foams, lower FSC values are recorded in saline than in deionised water. Absorption after 2 h is very similar for all concentrations tested with capacity ranging between 50 g/g and 70 g/g. The saline absorption capacity of nanocellulose foams were slightly lower to those of commercial SAP (80 g/g).

4. Discussion

4.1. Effect of foam and fibre properties on superabsorbent capacity

In this study, fibre properties, including the initial solids concentration and surface charge, are varied to determine the effect on the superabsorption performance of nanocellulose gels. When the initial gel solids concentration was varied from 0.3 wt% to

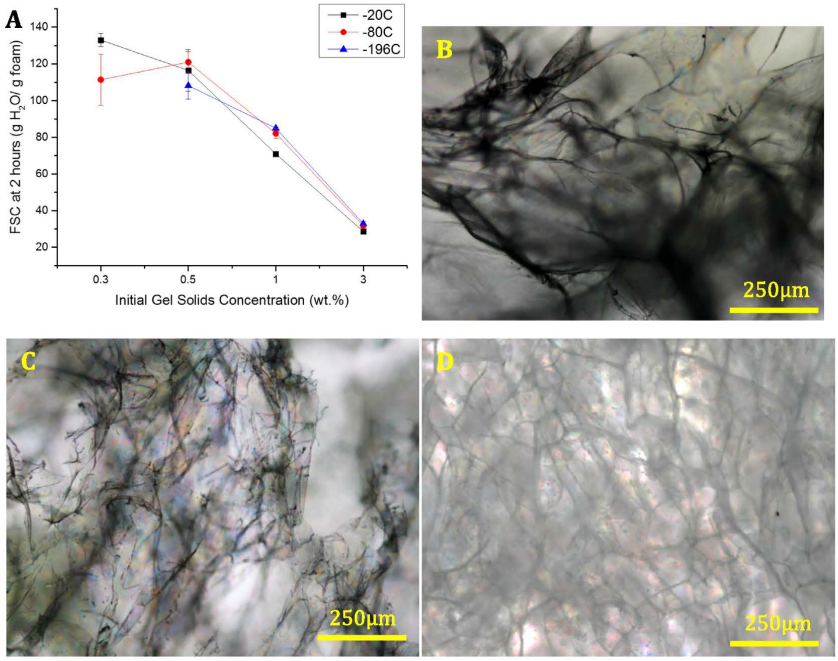

Fig. 4. (A) The effect of freezing rate (initial freezing at −20 °C, −80 °C, and 196 °C) on the FSC in deionised water. Optical microscopy illustrating the effect of freezing at (B) −20 °C (C) −80 °C, and (D) −196 °C on the morphology of nanocellulose foams.

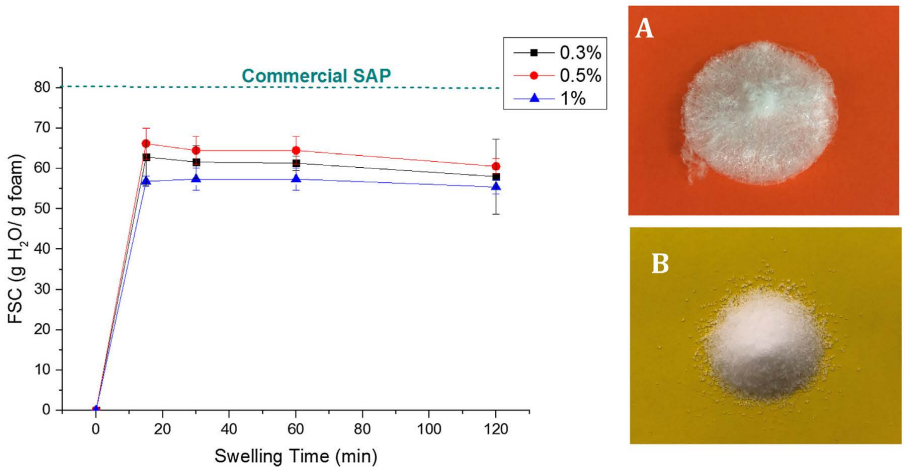

Fig. 5. FSC of nanocellulose (−80 °C) in 0.9 wt% saline as a function of swelling time compared against the equilibrium absorption capacity of a commercial SAP polymer. Images showing a (A) NC foam and (B) commercial SAP polymer.

0.5 wt% (−80 °C), FSC values were similar. However, further increase in the fibre concentration (0.5 wt% to 3 wt%) resulted in lower FSC values due to the limited availability of the foam internal structure because of a narrower pore distribution (Fig. 2). The percentage of accessible pores, quantified by the porosity at 1 atm, decreases with increasing initial solids concentration. For instance, increasing the fibre density by an order of magnitude (0.3 wt% to 3 wt%) resulted in halving (~50% decrease) the available pores at 1 atm. However, the high absorption capacity of nanocellulose cannot be explained merely by the available pore volume shown in Fig. 6. For instance, the foam from 0.5 wt% gel, which is capable of absorbing 120 g/g, has a calculated volume of easily accessible pores of 1.4 mL/g foam (at 1 atm) and a total pore volume of 29 mL/g foam. The available pore volume cannot solely take into account such a large absorption. This means that the 0.5 wt% foam structure needs to significantly expand by a factor four its initial volume. The absorption capacity of nanocellulose can be attributed largely to the swelling of the fibre network leading to physical entrapment of liquid water loosely held between nanofibres by capillary forces. This is in contrast to the absorption mechanism of conventional polyacrylic SAPs which are composed of longer polymer chains (DP = ~20,000 [36], compared to nanocellulose DP = ~600 [37]) with a higher density of COO— groups participating in hydrogen bonding with water.

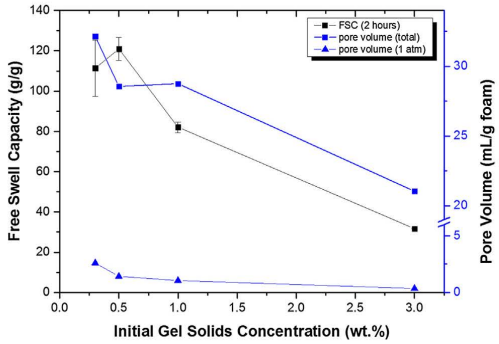

Fig. 6. Effect of the initial gel solids content on the superabsorbent nanocellulose foam FSC (−80 °C) in deionised water (2 h) and available pore volume at 1 atm and total pore volume from mercury porosimetry.

Fibre surface charge is indicative of the amount of COO^- groups which participate to water absorption. Fibrous structures with a higher concentration of COO^- groups can be expected to have higher absorption and FSC values. Nanocellulose fibres have a theoretical and demonstrated upper carboxylate limit of 1.6 mmol/g fibre [38]. Our fibres contain 1.2 mmol COO^-/g fibre, indicating near-complete oxidation of the C6 hydroxyl group. Doubling the carboxylate content on the cellulose polymer resulted in an increase in the absorption capacity (19 g/g to 51 g/g), as shown in Fig. 3.

4.2. Swelling kinetics of nanocellulose foams

The swelling of nanocellulose foams over time can be characterised by two distinct regimes: (a) the initial rapid uptake of absorbate and (b) the asymptotic increase of absorption towards the equilibrium absorption capacity W_∞ (Fig. 1) [39]. Swelling kinetic parameters such as the equilibrium absorption capacity W_∞ (g/g) and swelling rate constant k_s (g/g min) describing the swelling kinetics of the foams can be estimated by assuming a second order rate of swelling of absorption W (g/g) at swelling time t (min) as derived by Schott [40]:

$$\frac{dW}{dt} = k_s(W_\infty - W)^2 \tag{5}$$

Eq. (5) can be linearised by setting the following conditions: $W = 0$ at $t = 0$ and $W = W$ at $t = t$, resulting in Eq. (4):

$$\frac{t}{W} = A + Bt \tag{6}$$

where:

$$B = \frac{1}{W_\infty} \tag{7}$$

$$A = \frac{1}{\left(\frac{dW}{dt}\right)_0} \tag{8}$$

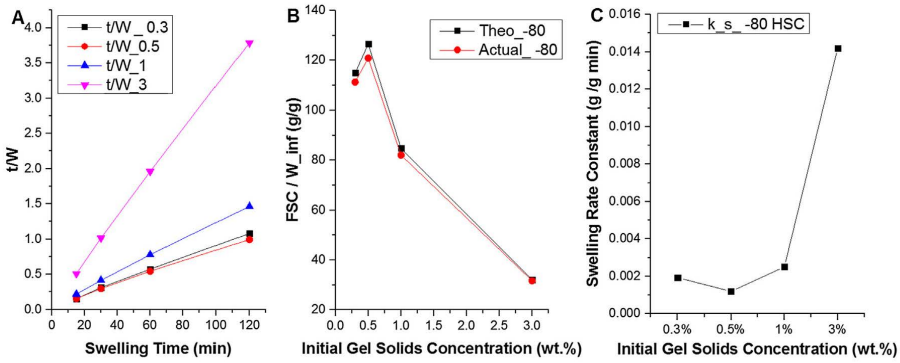

Fig. 7. Calculated swelling kinetic parameters of nanocellulose foams (−80 °C): (A) Linearisation of FSC by Schott's equation (B) equilibrium absorption capacity W_∞ and (C) swelling rate constant.

$$k_s = \frac{1}{AW_\infty^2} \tag{9}$$

Linearising Eq. (6) by plotting *t/W versus t* provides good fit with the experiments ($R^2 > 0.99$) (Fig. 7A). This suggests that the second-order kinetic assumption with respect to capacity is indicative either of a bimolecular mechanism (water-cellulose) or of a system with diffusion constraints. The actual absorption capacity at 2 h is close to the theoretical capacity W_∞, which indicates that the foams reach saturation within the testing period (Fig. 7B). In all concentrations tested, at least 90% of the theoretical capacity was reached within the first 30 min of testing – independent of the initial gel concentration. The foam swelling rate constant is constant between 0.3 wt% and 1 wt% and increased dramatically at 3 wt% (Fig. 7C). The increase in the swelling rate constant at increasing solids content can be due to saturation reached much faster because of smaller pores and numerous inaccessible carboxylate groups leading to an overall lower free swell capacity.

4.3. Effect of freezing rate and absorbate on superabsorbent capacity

The freezing rate of nanocellulose before lyophilisation dictates either nucleation or crystal growth of ice in the gel influencing the nanocellulose porous structure [41]. Freezing at −20 °C promotes the crystallisation of larger ice crystals as the degree of supercooling is low [41]. Hence, large pores are produced in certain regions where the ice crystals are formed, and individual fibres are aggregated forming sheet-like structures together, as seen from Fig. 4B. Freezing at a faster rate (−80 °C) led to an intermediate state wherein there are still sheets formed with the hornified fibres producing a more uniform structure. Vitrification of the network structure is promoted by freezing at a much faster rate (−196 °C) producing a more homogeneous pore structure. This is due to the fibre spacing present within the gel structure (electrostatic repulsion) being maintained upon foam formation. In this instance, the higher rate of freezing promoted the rapid nucleation of smaller ice crystals leading to a more homogenous pore structure [42]. The foams produced at −196 °C however were brittle and difficult to handle in contrast to those treated at −20 °C and −80 °C. Other studies have corroborated with our findings and also reported brittle foams produced from freezing in liquid nitrogen [30,43]. Hence, it was rather difficult to test low solids content foams such as 0.3 wt%; these results were omitted from Fig. 4A. Although, the morphologies of nanocellulose structures are visibly affected by the freezing rate, the absorption capacity remains similar. This could be due to the hornified fibres in foams prepared at −20 °C and −80 °C that separate partially while swelling.

The lower values of absorption in saline compared to deionised water is due to the charge shielding from the ions. This reduces the interaction with the COO^- groups and the water molecules. The saline capacity of the nanocellulose foams is similar to those reported by Theliander et al. with FSCs ranging between 30 and 60 g/g [26–29]. The performance of the nanocellulose foams is slightly lower in contrast to a granulated commercial polyacrylic acid SAP. Further optimising the method to produce the foams may yield similar performance to commercial SAPs.

5. Conclusion

Cellulose-based superabsorbents were investigated as sustainable substitutes for the current acrylic acid and acrylamide-based SAPs. While numerous studies have examined cellulose-based superabsorbents using various methodologies, few have analysed the SAP structure-performance relationship of TEMPO-oxidised nanocellulose foams [26–29,44]. In particular, the effect of fibre content and processing conditions (ie. freezing conditions) were not investigated. Moreover, the kinetics and mechanism of absorption for nanocellulose have not been studied. TEMPO-mediated oxidation produces charged nanocellulose fibres capable of forming cellulosic colloidal gels. The carboxylate groups of TEMPO-oxidised nanocellulose can be exploited for superabsorption. In this study, the potential of TEMPO-oxidised fibres as a superabsorbent polymer is demonstrated. The effect of fibre properties and processing conditions on the resulting nanocellulose foam morphology and its superabsorption performance is determined. Nanocellulose foam density is dictated by the initial gel solids concentration. The best performing foams are at 0.3–0.5 wt% frozen at −80 °C which are capable of absorbing 110–120 g/g H_2O. In general, a higher solids concentration produces foams with a narrower pore size distribution and a lower porosity leading to a decreased absorption performance. Nanocellulose foams follow a pseudo-second order absorption kinetics which is affected by foam density. Freezing temperature affects the foam network structure by dictating whether ice nucleation or crystallisation dominates, expanding or not the fibrous structure. A homogeneous porous structure is formed at the fastest freezing rate (−196 °C) whereas uneven sheet-like formations were observed at lower freezing rates (−20 °C, −80 °C). The free swell capacity remained unaffected even with differences in morphology. Changing the absorbate from deionised water to 0.9 wt% NaCl, mimicking bodily fluids, resulted in

the decrease of free swell capacity (FSC) values due to charge shielding. However, the nanocellulose foam performance in saline is already comparable with granulated polyacrylamide SAPs which have been optimised over the last 3 decades. With the results already achieved, the clear link between process-structure-properties and a robust optimization methodology, matching the properties of the current commercial polyacrylic superabsorbent polymers has become a realistic target for cellulose composites. Absorption behaviour in saline can be further improved by blending nanocellulose with biopolymers and optimising the shape and microstructure of foams. Nanocellulose foams has emerged as a high performance, renewable and biodegradable superabsorbent material for biomedical, personal care and environmental applications.

Acknowledgments

This work was funded by the ARC Bioprocessing Advance Manufacturing Industry Research Transformation (BAMI) Hub IH13100016, Visy, Norske Skog, Orora, Oji Fibre Solutions, Australian Paper and Circa. Special thanks to Anthony De Girolamo (Monash University) for running the porosimetry experiments.

Appendix A. Supplementary material

Supplementary data to this article can be found online at https://doi.org/10.1016/j.jcis.2018.11.112.

References

[1] J.R. Gross, in: Studies in Polymer Science, Elsevier, 1990, p. 3.
[2] H. Omidian, S.A. Hashemi, P.G. Sammes, I. Meldrum, Polymer 39 (1998) 6697.
[3] H. Warson, Modern Superabsorbent Polymer Technology, Wiley-VCH, New York, 2000.
[4] P. Chen, W.A. Zhang, W. Luo, Y.e. Fang, J. Appl. Polym. Sci. 93 (2004) 1748.
[5] J.V. Rogers, W.R. Richter, Y.W. Choi, A.K. Judd, Lett. Appl. Microbiol. 48 (2009) 180.
[6] C. Wiegand, M. Abel, P. Ruth, U.C. Hipler, J. Mater. Sci.: Mater. Med. 22 (2011) 2583.
[7] N. Lavoine, L. Bergström, J. Mater. Chem. A 5 (2017) 16105.
[8] H. Ferfera-Harrar, N. Aouaz, N. Dairi, Polym. Bull. 73 (2016) 815.
[9] M. Dalaran, S. Emik, G. Güçlü, T.B. Iyim, S. Özgümüş, Desalination 279 (2011) 170.
[10] L. Serna-Cock, M.A. Guancha-Chalapud, Acta Agronómica 66 (2017) 495.
[11] X. Xu, B. Bai, C. Ding, H. Wang, Y. Suo, Ind. Eng. Chem. Res. 54 (2015) 3268.
[12] M.A. Hubbe, A. Ayoub, J. Daystar, R. Venditti, J. Pawlak, in: (Ed.)'(Eds.) BioResources, 2013, p 6556.
[13] R. Gavillon, T. Budtova, Biomacromolecules 9 (2008) 269.
[14] R. Sescousse, R. Gavillon, T. Budtova, Carbohydr. Polym. 83 (2011) 1766.
[15] S.R. Djafari Petroudy, J. Ranjbar, E. Rasooly Garmaroody, Carbohydr. Polym. 197 (2018) 565.
[16] A. Olad, H. Zebhi, D. Salari, A. Mirmohseni, A. Reyhani Tabar, Mater. Sci. Eng.: C 90 (2018) 333.
[17] A. Olad, H. Zebhi, D. Salari, A. Mirmohseni, A. Reyhanitabar, J. Porous Mater. 25 (2018) 1325.
[18] A.I. Raafat, M. Eid, M.B. El-Arnaouty, Nucl. Instrum. Methods Phys. Res., Sect. B 283 (2012) 71.
[19] Z. Wang, A. Ning, P. Xie, G. Gao, L. Xie, X. Li, A. Song, Carbohydr. Polym. 157 (2017) 48.
[20] A. Adair, A. Kaesaman, P. Klinpituksa, Polym. Test. 64 (2017) 321.
[21] T. Fekete, J. Borsa, E. Takács, L. Wojnárovits, Carbohydr. Polym. 166 (2017) 300.
[22] H. Kono, S. Fujita, Carbohydr. Polym. 87 (2012) 2582.
[23] H. Dai, H. Huang, J. Agric. Food. Chem. 65 (2017) 565.
[24] L.-Y. Long, Y.-X. Weng, Y.-Z. Wang, Polymers 10 (2018) 623.
[25] T. Saito, S. Kimura, Y. Nishiyama, A. Isogai, Biomacromolecules 8 (2007) 2485.
[26] P.W. Brodin, H. Theliander, BioResources 7 (2012) 1666.
[27] F.W. Brodin, H. Theliander, Cellulose 20 (2013) 1.
[28] F.W. Brodin, Y. Sonavane, H. Theliander, BioResources 8 (2013) 2099.
[29] F.W. Brodin, K. Lund, H. Brelid, H. Theliander, Cellulose 19 (2012) 1413.
[30] F. Jiang, Y.-L. Hsieh, J. Mater. Chem. A 2 (2014) 350.
[31] F. Jiang, Y.-L. Hsieh, J. Mater. Chem. A 2 (2014) 6337.
[32] F. Jiang, Y.-L. Hsieh, ACS Sustain. Chem. Eng. 4 (2016) 1041.
[33] L. Mendoza, T. Gunawardhana, W. Batchelor, G. Garnier, J. Colloid Interface Sci. 525 (2018) 119.
[34] L. Mendoza, W. Batchelor, R.F. Tabor, G. Garnier, J. Colloid Interface Sci. 509 (2018) 39.
[35] D. da Silva Perez, S. Montanari, M.R. Vignon, Biomacromolecules 4 (2003) 1417.
[36] H. Fujita, K. Mitsuhashi, T. Homma, J. Colloid Sci. 9 (1954) 466.
[37] A. Isogai, T. Saito, H. Fukuzumi, Nanoscale 3 (2011) 71.
[38] Y. Okita, T. Saito, A. Isogai, Biomacromolecules 11 (2010) 1696.
[39] X. Shi, W. Wang, A. Wang, Carbohydr. Polym. 94 (2013) 449.
[40] H. Schott, J. Macromol. Sci., Part B 31 (1992) 1.
[41] W.L. Li, K. Lu, J.Y. Walz, Int. Mater. Rev. 57 (2012) 37.
[42] F. Martoïa, T. Cochereau, P.J.J. Dumont, L. Orgéas, M. Terrien, M.N. Belgacem, Mater. Des. 104 (2016) 376.
[43] J. Erlandsson, T. Pettersson, T. Ingverud, H. Granberg, P.A. Larsson, M. Malkoch, L. Wågberg, J. Mater. Chem. A 6 (2018) 19371.
[44] J. Ma, X. Li, Y. Bao, RSC Adv. 5 (2015) 59745.